Bis-perylene diimide macrocycles for chiroptical materials

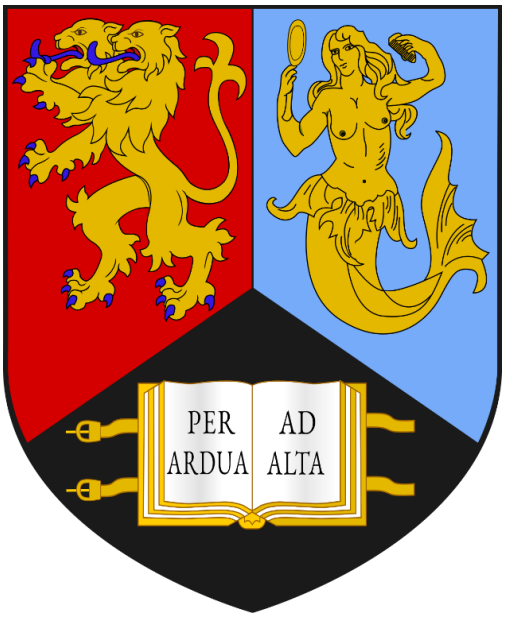

A thesis submitted for the degree of

Doctor of Philosophy

July 2024

Samuel E. Penty

School of Chemistry

University of Birmingham

Abstract

This thesis aims to explore the intramolecular and intermolecular interactions between chiral core-twisted PDIs using a novel bis-PDI macrocyclic scaffold (nicknamed the "Pink Box" due to its colour in solution), with a view towards applications as organic chiroptical materials.

Chapter 1 provides an overview of chiroptical activity and of perylene diimides (PDIs), with an emphasis on their supramolecular self-assembly and on chiral bis-PDI macrocycles.

Chapter 2 outlines the development of the Pink Box macrocyclic scaffold, as well as the characterisation of its intramolecular homochiral PDI-PDI dimer using a range of experimental techniques.

Chapter 3 established a strategy for making the Pink Box macrocycle chirally locked by varying the imide group on the PDIs to prevent an "intramolecular somersault". With stable enantiomers in hand, the aggregation behaviour of enantiopure vs racemic macrocycle samples is studied by UV-vis spectroscopy and X-ray crystallography. It is found that the *intra*molecular PDI-PDI dimer within the macrocycle is always homochiral and H-type, while *inter*molecular PDI-PDI contacts are heterochiral and slip-stacked.

Chapter 4 provides a fundamental understanding of the chiral conformations of "Pink Box" type macrocycles to unlock further potential as efficacious chiroptical materials. A 3rd generation Pink Box macrocycle is developed in which the homochiral stereoisomers can populate two different chiral conformations upon changing the solvent, leading to inversion of the CD spectrum (chiroptical switching). Additionally, a stable heterochiral diastereomer is isolated and shown to exhibit a "slipped-stack" J-type dimer.

Chapter 5 describes the synthesis and characterisation of a series of Pink Box-type macrocycles with alternative linkers, to understand the impact of linker length and rigidity on the interaction between the PDI units in a bis-PDI macrocycle. Guest binding studies are also performed.

Chapter 6 provides a summary of the major conclusions from the research described in this thesis.

Experimental details and methodologies are provided at the end of each research chapter. ***Appendix A*** provides details of the computational studies carried out by Prof Martijn Zwijnenburg to complement the research presented in this thesis.

Acknowledgements

First of all, I must of course thank Dr Tim Barendt for all the great support, guidance, patience and mostly good ideas. It has been a real honour to be your first PhD student along with Angus. I'm sure you will treasure the memory of us forever, just as we will treasure our memories of our time in the TAB Lab. In the same vein I must thank Angus for being there putting up with me from the start. Of course, I must thank all members (past and present) of the now quite large Barendt group. In a broadly chronological order, thank you to Lucy Walker, Alastair Littlewood, Tom Lawson, Jamie Hillis, Emily Cramp, Rob Campbell, Mya Kotecha, Atul Sharma, Denis Hartmann, Becky Kerridge and Claudia Lee for putting up with my music (and Angus'!) and for creating an extremely fun working environment. In fact, I must extend these thanks to everyone in the office and Lab 404 in the Haworth Building (R.I.P).

I must also thank the many people who helped me along the way. Thank you to Prof Martijn Zwijnenburg for performing all computational studies discussed in this thesis and to Robert Pal and his group in Durham for performing CPL measurements (and also for offering me a job!). Massive shout out to Dr Georgia Orton for taking me on a very fun trip to the Diamond Light Source where we obtained my most important crystal structures, and for attempting to teach me crystallography. Also, a big thank you to the people "working behind the scenes" including Trevor Hardy (the single most useful man in the universe) and Dr Cécile le Duff for help with NMR.

I began my PhD in the midst of the COVID pandemic, and being new to Birmingham in the middle of a lockdown would have been pretty depressing were it not for my fabulous housemates Adam and Sam who kept me sane during various quarantines in a leaky mouldy house in Selly Oak. So big thank you. I must also thank all the wonderful friends I have made in Birmingham since then, especially Issy, Dan, Matt, Jack, Kate, and Joe. I must also thank the Wellington Pub, the Spotted Dog, Shabab's, the Bull Ring outdoor market, and Birmingham as a whole.

A huge and really heartfelt thank you to Alice for her love and care and for putting up with me while writing this thesis, which really did take too long.

Last but not least, thank you to my parents Charles and Clarisa and to my sister Sabrina for their unconditional love and support throughout my life.

Samuel E. Penty

Chester-le-Street, County Durham, 18th July 2024

Previously published work

1. The Pink Box: Exclusive Homochiral Aromatic Stacking in a Bis-perylene Diimide Macrocycle.

   S. E. Penty, M. A. Zwijnenburg, G. R. F. Orton, P. Stachelek, R. Pal, Y. Xie, S. L. Griffin, and T. A. Barendt, *J. Am. Chem. Soc.* 2022, **144**, 27, 12290–12298

2. A Chirally Locked Bis-perylene Diimide Macrocycle: Consequences for Chiral Self-Assembly and Circularly Polarized Luminescence

   S. E. Penty, G. R. F. Orton, D. J. Black, R. Pal, M. A. Zwijnenburg, and T. A. Barendt, *J. Am. Chem. Soc.* 2024, **146**, 8, 5470–5479

3. Ultrafast and Coherent Dynamics in a Solvent Switchable "Pink Box" Perylene Diimide Dimer

   G. Bressan, S. E. Penty, D. Green, I. A. Heisler, G. A. Jones, T. A. Barendt and S. R. Meech. Accepted in *Angew. Chem. Int. Ed.* on 3rd July 2024

Glossary of Abbreviations

δ	chemical shift
λ	wavelength
μ	micro
ν	frequency
Δ	change in (a measurement),
°	degree
°C	degrees Celsius
Å	Ångstrom
CD	Circular dichroism
Cgs	Centimetres, grammes, seconds
CP	Circularly polarised
CPL	Circularly polarised
conc.	concentrated
COSY	Correlation spectroscopy
CP-LED	Circularly-polarised light-emitting diode
CT	Charge transfer
CuAAC	copper(I)-catalysed azide–alkyne cycloaddition
d	doublet

dd	doublet of doublets
DCM	Dichloromethane
DFT	Density-functional theory
DIPEA	N,N-di-iso-propylethylamine
DMF	N,N-dimethylformamide
DMSO	dimethyl sulfoxide
DNA	deoxyribonucleic acid
TD-DFT	Time-dependent density-functional theory
DMSO	Dimethyl sulfoxide
EDCC	Enantioselective differential chiral contrast
e.g.	*exempli gratia*
em	emission
eq.,	equiv. equivalent
EPR	Electron paramagnetic resonance
ESI	electrospray ionisation
Et	ethyl
EXSY	Exchange spectroscopy
fsTA	Femtosecond transient absorption
g	gramme
g_{abs}	absorption dissymmetry factor
g_{lum}	luminescence dissymmetry facto

G	Gibbs free energy
HOMO	highest occupied molecular orbital
HPLC	High-performance liquid chromatography
hr.	hour
HSQC	heteronuclear single quantum coherence
ISC	intersystem crossing
J	Joule
J	coupling constant
k	kilo
K	Kelvin
Hz	hertz
LED	Light-emitting diode
L	litre
LUMO	lowest occupied molecular orbital
LSCM	Laser scanning confocal microscopy
MALDI	Matrix-assisted laser desorption/ionization
M	molar
M	mega, molecular ion
m	milli, multiplet,
m	meta
m/z	mass-to-charge ratio

macro	macrocycle
max.	maximum
Me	methyl
min	minute
mol	mole
MS	mass spectrometry
n	nano
NIR	Near infrared
NMR	Nuclear magnetic resonance
NOESY	nuclear Overhauser effect spectroscopy
p	para
PAH	Polyaromatic hydrocarbon
PDI	Perylene diimide
ppm	parts per million
PTCDA	Perylene-3,4,9,10-tetracarboxylic dianhydride
ROESY	Rotating Frame Overhauser Enhancement Spectroscopy
rt	room temperature
s	second, singlet
S_0	Ground state singlet state
S_1	First excited singlet state
SB-CS	Symmetry-breaking charge separation

SET	Single electron transfer
t	triplet
T_1	First excited triplet state
TBA	tetrabutyl ammonium
TBTA	tris[(1-benzyl-1H-1,2,3-triazol-4-yl)methyl]amine
TCE	1,1,2,2-Tetrachloroethane
tert	tertiary
TIPS	Triisopropylsilyl
TLC	Thin layer chromatography
TMS	Trimethylsilyl
TOF	Time of flight
UV	ultra-violet
UV-vis	Ultraviolet-visible
V	volt
vis.	visible
vs.	versus
VT	variable temperature
v/v	volume/volume

Table of contents

Chapter 1: Introduction

1. Introduction

1.1 Introduction to chirality

Chirality is the geometric property of an object that cannot be superimposed onto its mirror image through translations or rotations. Objects that display chirality are termed *chiral* objects. One of the most immediately recognisable chiral objects are our right and left hands (**Figure 1.1**). Indeed, the word *chirality* is derived from the Greek χειρ (kheir), meaning "hand". The term was first coined by Lord Kelvin in 1893,[1] although it is clear from ancient art and architecture that humans have been intuitively aware of the concept for thousands of years.[2] Objects that do not display chirality, such as a sphere or a cube, are termed *achiral*.

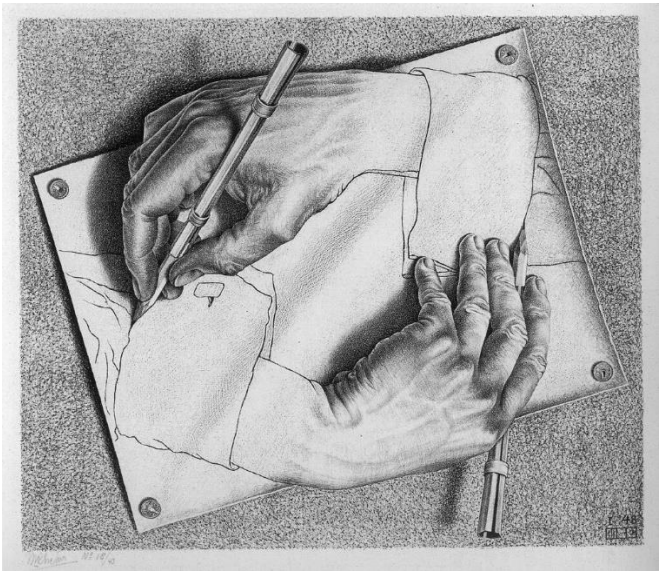

Figure 1.1: Hands are chiral objects. *"Drawing Hands" by M.C. Escher. Reprinted with permission from: M.C. Escher works © 2024 The M.C. Escher Company - the Netherlands.*

Chirality manifests itself throughout the universe at all size scales,[3] from spiral galaxies[4] down to chiral subatomic particles.[5, 6] Of course, for chemists the most relevant chiral objects are chiral molecules. The left- and right-handed counterparts of a chiral molecule are known as *enantiomers*. An equal mixture of left- and right-handed enantiomers is called a *racemic* mixture or a *racemate*. The product of a chemical reaction with racemic starting materials will generally be racemic unless there is an external source of chirality such as a chiral catalyst. Chirality is of immense importance in biology because for most chiral biological building blocks, such as amino acids and sugars, only one enantiomer exists in nature.[7] This leads to

supramolecular chirality in biology, where chiral building blocks assemble into a larger structure that is also chiral, as exemplified by the alpha helix[8, 9] and beta sheet[10] regions of proteins, the DNA double helix,[11] and other chiral biopolymers (**Figure 1.2**).

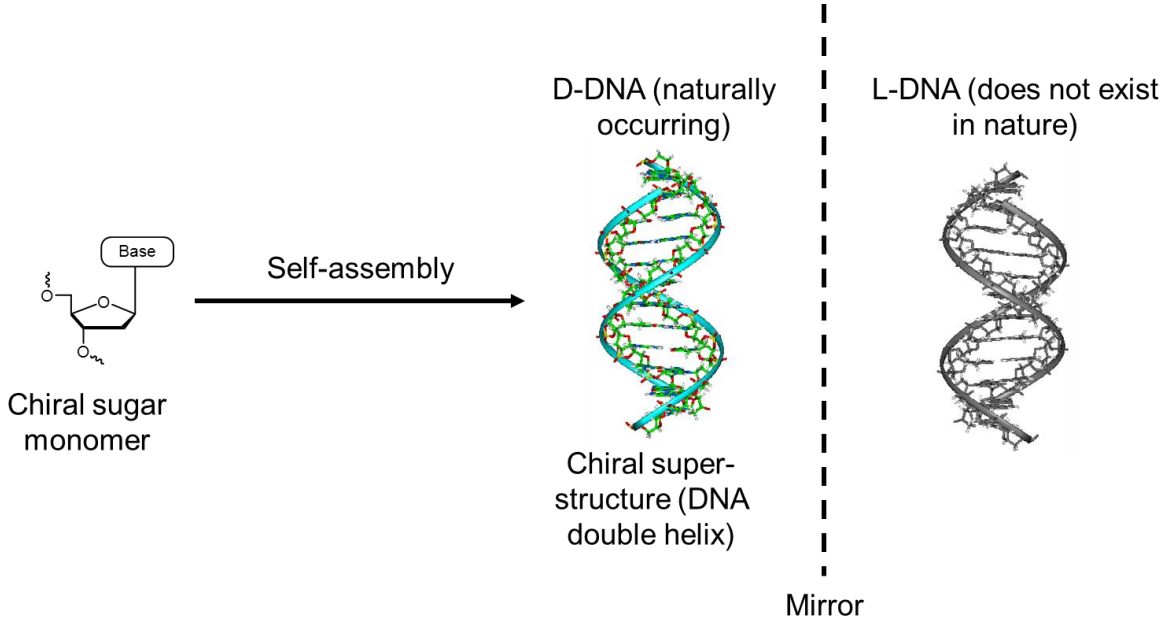

Figure 1.2: Self-assembly of a chiral sugar monomer into a supramolecular chiral structure (the DNA double helix). As all naturally occurring sugar monomers of DNA only exist as one enantiomer, naturally-occurring DNA always has the same helicity. Figure adapted from Wikimedia Commons under a Creative Commons licence.

The source of this biological '*homochirality'* is a major mystery for those studying the origins of life and has been hotly debated for decades.[12-18] Interestingly, in recent years scientists have generated enantiomeric excesses in previously racemic mixtures by irradiation with spin-polarised electrons[19] or circularly polarised (CP) light,[20, 21] and these have been put forward as possible (but by no means proven) causes for the original symmetry-breaking event that led to the evolution of homochirality in biology. Indeed, electromagnetic (EM) radiation, including visible light, can be chiral, as it can exist in left- and right-handed circularly polarised forms (see section 1.2). CP light is a major tool for studying chiral molecules as explained in the next sections.

1.2 Linearly and circularly polarised light

Light is an electromagnetic wave. The electric field of this wave oscillates perpendicularly to the direction of propagation of the wave. Light is referred to as *unpolarised* if the direction of oscillation of the electric field fluctuates randomly over time. If the direction of oscillation if the electric field is well defined, the light is referred to as *polarised*. The two most important types of polarised light are *linearly* and *circularly* polarised light. In linearly polarised (LP) light, the overall electric field oscillates along a single plane. CP light consists of two perpendicular plane polarised waves of equal amplitude but with a phase difference of π/2 (i.e. 90°, one quarter of a wavelength). The resulting electric field vector rotates in a circle around the axis of propagation of the wave, tracing a helix as it travels through space. As a helix is a chiral object, CP light is also chiral, with left- and right-handed mirror-image forms (**Figure 1.3**).[22]

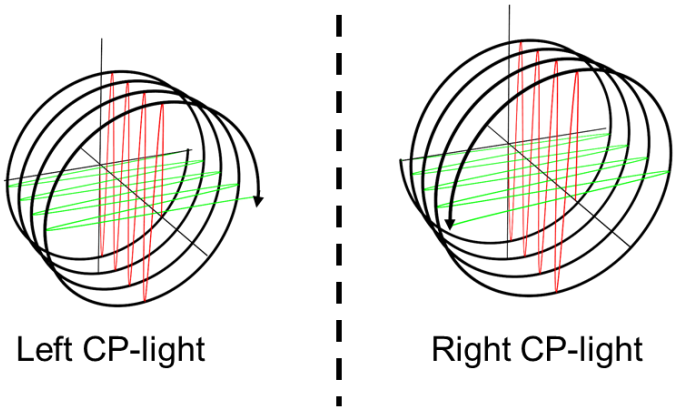

Figure 1.3: Schematic representation of two perpendicular plane polarised electromagnetic waves of equal amplitude but with a phase difference of π/2 (i.e. 90°, one quarter of a wavelength), yielding CP light which can exist as two enantiomeric forms.

1.3 Chiroptical activity

The term 'chiroptical activity' refers to the ability of chiral materials to selectively interact with CP light in terms of absorption, emission, or refraction.[23] This term is often used interchangeably with the historic term 'optical activity' which can refer to the interaction of materials with either linearly or circularly polarised light. Chiroptical activity takes the form of two main properties: *circular birefringence* (CB), referring to refraction of CP light, and *circular dichroism* (CD), referring to absorption and emission of CP light. [24] CB, which is the cause of the optical rotation of linearly polarised light as it passes through a chiral material, was

the first type of optical activity to be discovered[25] and is often simply referred to as 'optical rotation'.[26]

In most chemical literature the term CD is exclusively employed to refer exclusively to the difference between left- and right-handed CP light being absorbed, while the selective emission of CP light is usually referred to as 'circularly polarised luminescence' (CPL). The two enantiomers of a chiral molecule will absorb and emit light of opposite handedness at a given wavelength. The differential absorption or emission of CP light by a material can quantified by the dissymmetry factors g_{abs} for absorption and g_{lum} for emission:

$$g_{\mathrm{abs}} = \frac{\Delta\varepsilon}{\varepsilon} = \frac{\varepsilon_{\mathrm{L}} - \varepsilon_{\mathrm{R}}}{\frac{1}{2}(\varepsilon_{\mathrm{L}} + \varepsilon_{\mathrm{R}})} \quad (1.1)$$

$$g_{\mathrm{lum}} = \frac{\Delta I}{I} = \frac{I_{\mathrm{L}} - I_{\mathrm{R}}}{\frac{1}{2}(I_{\mathrm{L}} + I_{\mathrm{R}})} \quad (1.2)$$

where ε is the molar extinction coefficient of the sample and $\Delta\varepsilon$ is its circular dichroism which is the difference between the molar extinction coefficients for left-handed and right-handed CP light ε_{L} and ε_{R}. By analogy, I is the total emission intensity of the sample and ΔI is the difference in intensity of left-handed I_{L} and right-handed I_{R} CP light emission. The dissymmetry factors g_{abs} and g_{lum} have a maximum value of 2, which represents exclusive absorption or emission of left-handed CP light, while the minimum value of -2 represents exclusive absorption or emission of right-handed CP light. It should be noted that g_{abs} quantifies the dissymmetry of the ground state under thermal equilibrium, while g_{lum} quantifies the dissymmetry of the emissive excited state.

For the emission of CP light, a 2021 review[27] also recommends the use of a parameter termed 'CPL brightness' B_{CPL}:

$$B_{\mathrm{CPL}} = \varepsilon \cdot \Phi \cdot \frac{|g_{\mathrm{lum}}|}{2} \quad (1.3)$$

where ε is the molar extinction coefficient and Φ is the luminescence quantum yield. Comparing materials by B_{CPL} can be more useful in some contexts as many materials with a high g_{lum} may have low values of ε and Φ. [28, 29]

1.4 Physical basis of chiroptical activity

The relationship between quantum mechanics and chiroptical activity was first explored by Rosenfeld in the 1920s.[30] Absorption/emission and CD/CPL bands are characterised by parameters known as dipole (D) and rotational (R) strengths. For convenience, the following discussion will be based on emission/CPL and the corresponding dissymmetry factor g_{lum}, with the corresponding equations for absorption/CD and g_{abs} being completely analogous.

For a chiral molecule in isotropic solution, the CPL ($I_{\mathrm{L}} - I_{\mathrm{R}}$) and total ($I_{\mathrm{L}} + I_{\mathrm{R}}$) emission intensities can be expressed as a function of emission frequency ν as follows [29] (in cgs* units):

$$I_{\mathrm{L}}(\nu) - I_{\mathrm{R}}(\nu) = \frac{16\nu^3\rho(\nu)}{3c^3\hbar^4} R \tag{1.4}$$

$$I_{\mathrm{L}}(\nu) + I_{\mathrm{R}}(\nu) = \frac{8\nu^3\rho(\nu)}{3c^3\hbar^4} D \tag{1.5}$$

where $\hbar$ is the reduced Planck constant, c is the speed of light, and $\rho(\nu)$ is a Gaussian band shape. For an electronic transition from an excited state j to a ground state i, D is defined as:

$$D = \langle \Psi_j | \boldsymbol{\mu} | \Psi_i \rangle^2 \tag{1.6}$$

i.e. it is the square of the transition electric dipole moment $\boldsymbol{\mu}$, where Ψ_j and Ψ_i are the wavefunctions of the excited and ground states.

Rosenfeld showed that R can be expressed as imaginary part of the scalar product between the real vector $\boldsymbol{\mu}$ and the magnetic dipole moment $\boldsymbol{m}$ which is an imaginary vector:

$$R = \mathrm{Im}\left[\langle \Psi_j | \boldsymbol{\mu} | \Psi_i \rangle^2 \cdot \langle \Psi_i | \boldsymbol{m} | \Psi_j \rangle^2 \right] \tag{1.7}$$

where Im refers to the imaginary component of the scalar product. Equation 1.7 is known as the Rosenfeld equation. It can also be more simply expressed in most situations as:

$$R = |\boldsymbol{\mu}||\boldsymbol{m}| \cos\theta \tag{1.8}$$

* Centimetres, grams, seconds

where θ is the angle between the vectors $\boldsymbol{\mu}$ and $\boldsymbol{m}$. From this it can be deduced that chiral materials must have non-orthogonal $\boldsymbol{\mu}$ and $\boldsymbol{m}$ vectors.

By substituting equations 1.4 and 1.5 into equation 1.2 we arrive at:

$$g_{\text{lum}} = \frac{4R}{D} \tag{1.9}$$

If $|\boldsymbol{\mu}| >> |\boldsymbol{m}|$, which is usually the case at the scale of molecules (electric dipole approximation),[31] g_{lum} can be approximated as:

$$g_{\text{lum}} \approx \frac{4|\boldsymbol{m}|}{|\boldsymbol{\mu}|}\cos\theta \tag{1.10}$$

By analogy it can also be shown that:

$$g_{\text{abs}} \approx \frac{4|\boldsymbol{m}|}{|\boldsymbol{\mu}|}\cos\theta \tag{1.11}$$

The chemical consequences of these relationships are explored in the next section.

1.5 Optimising dissymmetry factors in small molecules

From equations 1.10 and 1.11 it is apparent that maximising $|\boldsymbol{m}|$, minimising $|\boldsymbol{\mu}|$, and optimising θ (such that $\boldsymbol{m}$ and $\boldsymbol{\mu}$ are close to parallel or antiparallel) should all be valid strategies for maximising g-factors for molecules. However, as discussed in several excellent reviews, g-factors for small molecules tend to be very small, with the vast majority being $< 10^{-2}$.[32-36] The reasons for this were summarised in a recent review by Fuchter *et al*.[22] The first main reason is that small molecules are obviously very small (often $\sim$ 1 nm or less in length) compared to the wavelength and helical pitch of light (several hundred nm), so the chiral molecules tend not to 'feel' the twist of CP light significantly.[37] Secondly, for *dipole allowed* electronic transitions, which are usually by far the strongest bands in absorption and emission spectra, a small magnetic dipole moment $\boldsymbol{m}$ is dwarfed by a very large electric dipole moment $\boldsymbol{\mu}$. From this it also follows that many molecules with high dissymmetry factors also have low molar extinction coefficients and quantum yield values. Finally, because of molecular geometry the alignment of these dipoles is usually not optimised.

There have been several studies that have shown that increasing the size of a chromophore can significantly enhance the dissymmetry factors.[38, 39] One of the most elegant studies was carried out by Mori, Inoue *et al.* on helicenes, [40] which are interesting systems as the chromophore itself is embedded in a helical framework (**Figure 1.4a)**.[32] Small helicenes in solution display $|g_{\mathrm{abs}}| < 10^{-2}$.[32, 36] The study compared experimental data with computational predictions of CD and CPL spectra for [3]helicene up to [10]helicene.[†] It was found that for the transition that is perpendicular to the C_2 axis of the helicene the $|g_{\mathrm{abs}}|$ increases linearly with $1/n$, where n is the number of benzene rings in the helicene, up to $\mathrm{n} = 6$, followed by a discontinuity between $\mathrm{n} = 6$ and $\mathrm{n} = 7$, and then increases linearly again for $\mathrm{n} > 6$, but with a larger slope. This is interesting because $\mathrm{n} = 6$ corresponds to one full turn of the helix, so for $\mathrm{n} > 6$ the benzene rings on either end of the helix start to overlap. The authors also extrapolated this trend up to a potentially infinite helix, while also considering a computationally-predicted maximal effective conjugation length of $\mathrm{n} \approx 50$ to predict a maximum $|g_{\mathrm{abs}}| \sim 0.09$ for [50]helicene. In practice, studying longer helicenes is hindered by the synthetic difficulty of making these molecules, although synthetic strategies for making some very long helicenes are starting to emerge.[39] More recently, in 2024 a computational study by Miguel and co-workers investigated the calculated $|\boldsymbol{m}|$ in helicenes and other helical molecules such as *ortho*-oligophenylethynylenes (*o*-OPEs).[41] It was found that $|\boldsymbol{m}|$ and hence $|g_{\mathrm{abs}}|$ increase linearly with the inner area of these compounds (**Figure 1.4b**). As such, helicenes and *o*-OPEs behave much like classical solenoids, where the magnetic field generated by a coil bearing an electrical current is proportional to the inner area of the coil. From this "molecular size increases $|g_{\mathrm{abs}}|$ trend" we might expect that chiral polymers and supramolecular aggregates with coupled chromophores should have high dissymmetry factors, and indeed this is often the case, with some polymers displaying $|g_{\mathrm{abs}}| > 1$.[42, 43] Chiroptical activity in supramolecular aggregates with excitonically coupled chromophores will be explored in later sections (1.6, 1.11 and 1.12).

[†] The number in this nomenclature corresponds to the number of benzene rings in the helicene.

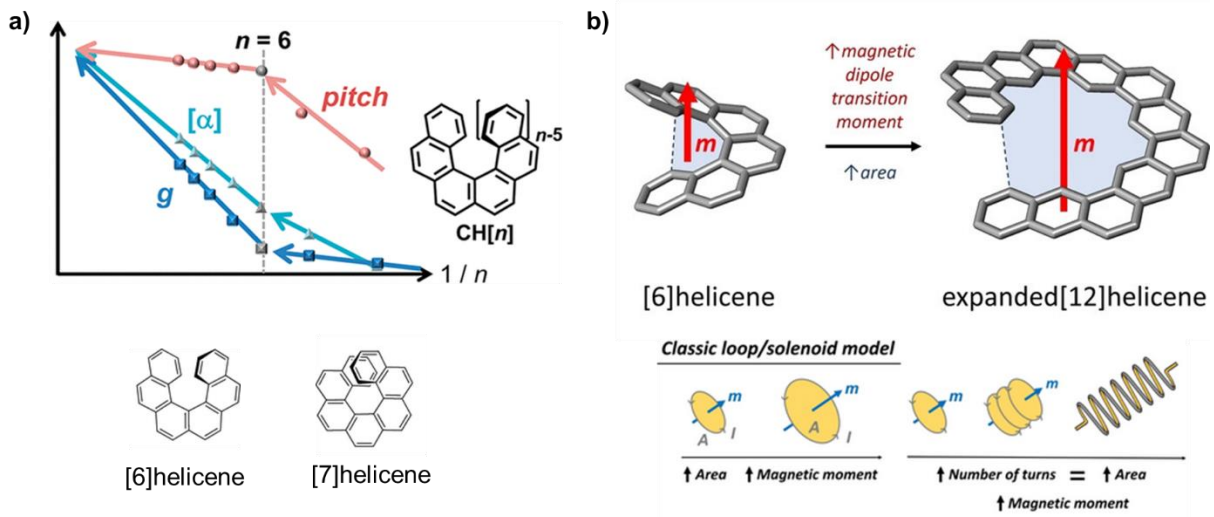

Figure 1.4: a) Schematic depiction of the results from the study by Mori, Inoue *et al.* on helicenes,[40] which shows a linear trend for the absorption dissymmetry factor $\boldsymbol{g}$ as well as the optical rotation $\boldsymbol{\alpha}$ with 1/n where n is the number of benzene rings in the helicene. A discontinuity in this trend is observed between n = 6 and n = 7 as n = 6 corresponds to one full turn of the helix, so after n = 6 benzene rings start to overlap, which perturbs the trend. Adapted with permission from ref. 39. Copyright 2012 American Chemical Society. **b)** Cartoon depiction of the results of the study by Miguel *et al.*[41] which found that $|\boldsymbol{m}|$ and hence $|\boldsymbol{g}_{\mathbf{abs}}|$ increase linearly with the inner area of helicenes and some other helical molecules. Helicenes thus behave much like classical solenoids, where the magnetic field generated by a coil bearing an electrical current is proportional to the inner area of the coil. Adapted with permission from ref. 40. Copyright 2023 The Authors. Angewandte Chemie International Edition published by Wiley-VCH GmbH.

Famously, the highest reported $|g_{\mathrm{lum}}|$ values in the literature have been obtained with chiral lanthanide (III) complexes.[44, 45] This has been achieved by exploiting 'forbidden transitions' to maximise $|\boldsymbol{m}|$ and minimise $|\boldsymbol{\mu}|$ in order to maximise $|g_{\mathrm{lum}}|$ as per equation 1.10.[22] As seen in equations 1.5 and 1.6, the strength of electronic transitions (which determines absorption and emission intensities) depends on the magnitude of $\boldsymbol{\mu}$, which in turn mostly depends on whether the transition obeys a set of quantum mechanical 'selection rules'.[46] For an electronic transition to be 'allowed' (i.e. $\boldsymbol{\mu} \neq 0$) the total spin of the initial and final states must be the same (spin selection rule), but in atoms and centrosymmetric molecules the parity of the wavefunctions of the initial and final states must change (Laporte selection rule). In contrast magnetic dipole transitions are allowed (i.e. $\boldsymbol{m} \neq 0$) if the total spin and parity of the initial and final states is conserved in the transition. For example, $f \rightarrow f$ transitions are electric-dipole forbidden but magnetic-dipole allowed. In Ln(III) complexes, the $4f$ orbitals in the Ln^{3+} ion are highly contracted and largely embedded within the inert core of electrons within the atom.[47,

[48] As a result, Ln^{3+} ions are 'hard' Lewis acids and the $4f$ orbitals are largely unperturbed by the ligands coordinating to the ion. This means that the $f \rightarrow f$ transitions of a chiral Ln(III) complex still obey the selection rules for an atom/centrosymmetric molecule despite the Ln(III) complex possessing a centre of inversion, so they are electric-dipole forbidden but magnetic-dipole allowed. From this one would expect that Ln(III) complexes should display $f \rightarrow f$ transitions with very low absorption/quantum yields (due to low $\boldsymbol{\mu}$**)** but high dissymmetry factors (due to relatively high $\boldsymbol{m}$ and low $\boldsymbol{\mu}$**)**, and this is indeed usually the case. However, Ln(III) complexes with high quantum yields can be rationally designed by harnessing the so-called 'antenna effect' whereby an organic ligand that absorbs strongly at a lower wavelength transfers energy to the Ln^{3+} via non-radiative energy transfer mechanisms, which then radiatively relaxes via an $f \rightarrow f$ transition.[49] Designed using this strategy, the compound in **Figure 1.5a** boasts the highest reported $|g_{\mathrm{lum}}|$ in solution ($|g_{\mathrm{lum}}|$ = 1.4 for the $^5D_0 \rightarrow {}^7F_1$ transition) but still has a comparatively low quantum yield $\Phi = 0.03$.[50, 51] However other Ln(III) complexes that possess both high $|g_{\mathrm{lum}}|$ and high quantum yield have been reported,[44] such as the compounds in **Figure 1.5b** with $|g_{\mathrm{lum}}|$ values of 0.15−0.46 and Φ values of 0.34-0.41.[52]

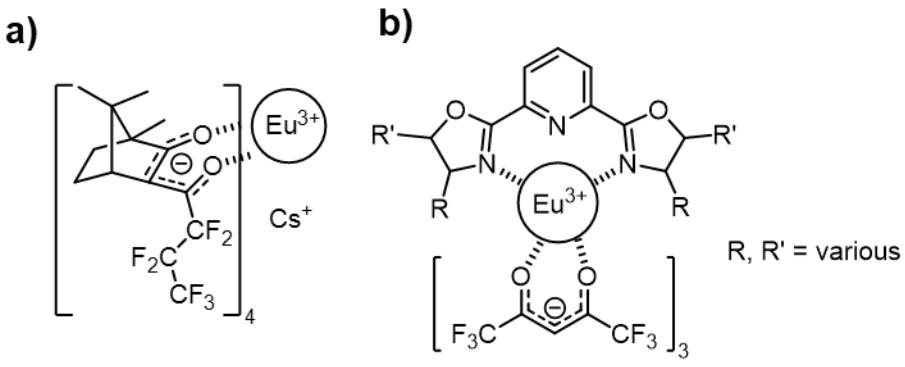

Figure 1.5: a) Structure of the Europium (III) complex reported by Lunkley *et al*. which exhibits the highest reported $|\boldsymbol{g_{lum}}|$ for any molecule in solution. [50, 51] **b)** Structure of the Europium (III) complexes reported by Yuasa *et al*. which exhibit a combination of high $|\boldsymbol{g_{lum}}|$ high quantum yields. [52]

As mentioned earlier, a further possible way of enhancing chiroptical dissymmetry factors is to optimise the alignment of $\boldsymbol{\mu}$ and $\boldsymbol{m}$. This strategy has been utilised most notably in cylinder-shaped chiral π-conjugated macrocycles,[33] with the most impressive of these being reported by Sato, Isobe, *et al* (**Figure 1.6**).[53] In these macrocycles, the π and π* molecular

orbitals extend all the way around the cylindrical molecule, which leads to the sum of local $\boldsymbol{\mu}$ values derived from the chrysene subunits cancelling each other in the xy-plane (the plane of the macrocycle), such that the overall $\boldsymbol{\mu}$ is oriented in the z-axis (i.e. perpendicular to the plane of the macrocycle). Additionally, $\boldsymbol{m}$ originates from the change in angular momentum of an electron during an electronic transition and is proportional to the vector product of the displacement vector $\boldsymbol{r}$ and the electric dipole moment $\boldsymbol{\mu}$ i.e $\boldsymbol{m} \propto \boldsymbol{r} \cdot \boldsymbol{\mu}$ As $\boldsymbol{r}$ radiates towards the outside of the molecular cylinder and $\boldsymbol{\mu}$ lies along the z-axis, the vector $\boldsymbol{r} \cdot \boldsymbol{\mu}$ results in $\boldsymbol{m}$ being oriented antiparallel to $\boldsymbol{\mu}$. As seen in equations 1.10 and 1.11, having parallel or antiparallel $\boldsymbol{\mu}$ and $\boldsymbol{m}$ leads to optimised $|g_{\mathrm{abs}}|$ and $|g_{\mathrm{lum}}|$. Indeed, this macrocycle exhibits the highest reported $|g_{\mathrm{lum}}|$ for a small organic molecule (0.15 at 443 nm) as well as high quantum yield (0.80) and very high $|g_{\mathrm{abs}}|$ (0.17). It must be stressed that these dissymmetry factors are exceptional, and the vast majority of $|g_{\mathrm{abs}}|$ and $|g_{\mathrm{lum}}|$ values reported for small organic molecules in the literature remain $< 10^{-2}$.

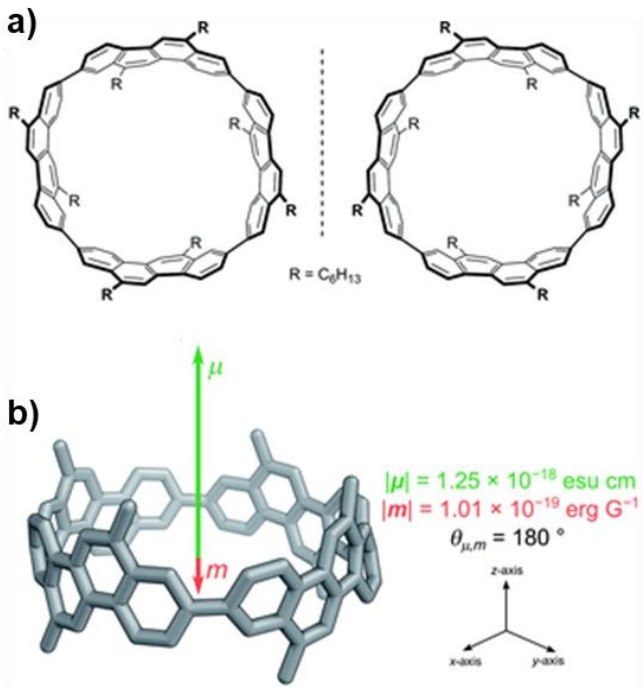

Figure 1.6: a) The two enantiomers of the macrocycle reported by Sato, Isobe, *et al.* [53] **b)** The anti-parallel orientation of the $\boldsymbol{\mu}$ and $\boldsymbol{m}$ transition dipole moments in the *P* enantiomer. Adapted from ref. 22 with permission from the Royal Society of Chemistry.

1.6 Excitonic coupling and chirality

In section 1.4 we explored how chiroptical activity arises from the interplay between CP light and the electric and magnetic dipole moments $\boldsymbol{\mu}$ and $\boldsymbol{m}$ in a chiral molecule. However, in practice it is relatively rare to encounter systems where there is only one electric and one magnetic transition dipole to consider. While there are chromophores that are inherently chiral, such as helicenes, in many other chiral molecules the chromophore (i.e. the part of the molecule that absorbs and emits light) isn't actually chiral if considered in isolation, and its chiroptical activity arises from its orientation relative to other sub-units in the molecule.[54] Furthermore, there are many supramolecular systems where the interactions between chromophores lead to fascinating photophysical and chiroptical effects, and indeed this is the main focus of this thesis. In order to explore the chiroptical effects arising from the interaction between two achiral chromophores in a chiral orientation, it is first necessary to understand the models that best explain the photophysics of these interactions.

1.6.1 Kasha's exciton model

The exciton model accounts for many, but by no means all, photophysical and chiroptical effects observed in supramolecular assemblies.[22] The term 'exciton' refers to a bound pair of an electron and an electron hole that can move in a particle-like manner in an assembly of molecules or atoms,[55] and was first proposed by Frenkel in 1931.[56] The development of the modern exciton model started in the 1930s, when Kirkwood and Kuhn were the first to consider the coupling of transition dipole moments with each other.[57 58] In the 1960s Davydov and Sheka extended these models to treat excitonic effects in molecular crystals[59, 60] and Schellman derived symmetry rules to explain the shape of CD spectra.[61] Around the same time, Kasha and McRae described effects observed upon the aggregation of chromophores in terms of the arrangement of transition dipole moments in various geometries.[62-65] Two limiting cases in this model that are most relevant to this thesis are a face-to-face ("cofacial") arrangement of chromophores, known as an H-aggregate, and a slipped-stack ("head-to-tail") arrangement, known as a J-aggregate.[66] Upon aggregation, H-aggregates show a new band in their UV-vis absorption spectrum that is blue-shifted relative to the absorption of the monomer (hypsochromic shift, hence the term H-aggregate), while J-aggregates show a red-shifted band relative to the monomer (bathochromic shift; for historical reasons the term J-aggregate comes from Jelley who discovered the phenomenon in 1936).[67, 68]

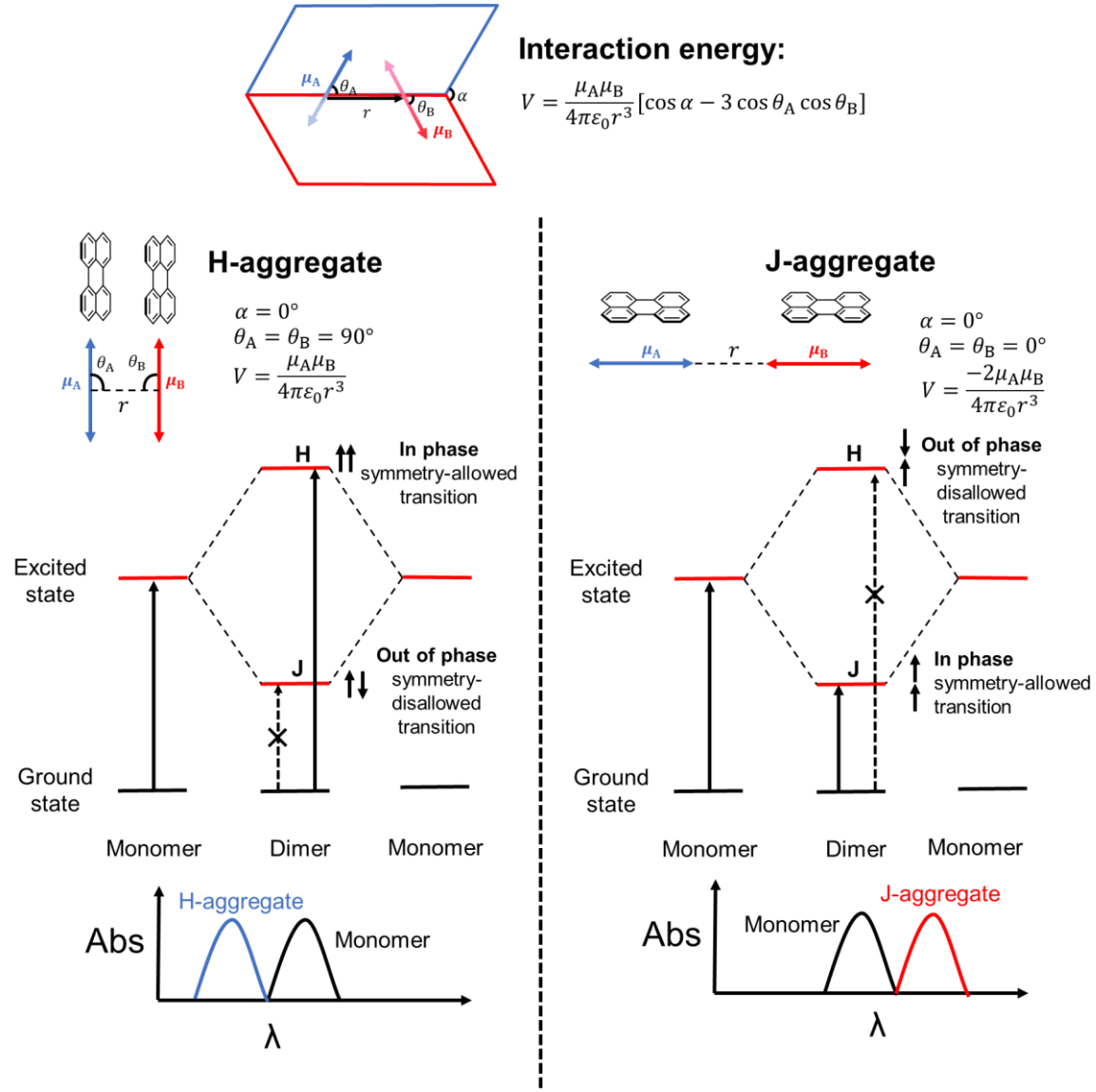

Figure 1.7: Schematic showing the interaction between the transition dipole moments of two nearby molecules in ideal H-type (left) and J-type (right) geometries.

In the exciton model, the interaction between transition dipole moments on nearby molecules is the driving force for excited state delocalisation between the molecules.[69] The simplest form of the exciton model considers the interaction between two equivalent molecules, each with only one excited state. The two degenerate excited states of these molecules combine to form two new states corresponding to the in and out of phase combination of the original excited states (**Figure 1.7**). The new states are separated by an energy gap that is equal to twice the interaction energy V between the transition dipoles. This energy difference is known as "Davydov splitting".[70] The lower energy state is labelled 'J' in **Figure 1.7** while the higher

energy state is labelled 'H'. Absorption and emission from either state can be symmetry-allowed or disallowed depending on the relative orientation of the dipoles. In an ideal H-aggregate ($\theta_A = \theta_B = 90°$, $\alpha = 0°$, **Figure 1.7**), only transitions involving the H-state are symmetry-allowed, hence the blue-shift in the absorption spectrum. In contrast, for an ideal J aggregate ($\theta_A = \theta_B = 0°$, $\alpha = 0°$, **Figure 1.7**) only transitions involving the J state are symmetry-allowed, leading to a red-shifted absorption spectrum.[69] In H-aggregates, a suppression of fluorescence intensity is also observed. This is because fluorescence usually occurs from the lowest excited state (Kasha's rule).[71] H-aggregates can therefore sometimes promote intersystem crossing and phosphorescence, or non-radiative relaxation pathways.[66] In contrast, J-aggregates show no suppression of fluorescence or enhancement of phosphorescence. The results for H- and J-aggregated dimers can also be qualitatively applied to larger aggregates.[66, 72-74]

Perfectly ideal H- and J-aggregates are very rare, and most real-life excitonically coupled systems lie somewhere in between. Indeed, it is possible to transition from an H- to J-aggregate by varying the slip-angle θ ($\theta = \theta_A = \theta_B$) while holding α at 0°. In doing so the system passes through a region known as a "null aggregate" where the interaction between the dipoles disappears and the absorption spectrum of the dimer looks like that of the monomer (at $\theta \approx 54.7356°$, the so-called "magic angle", **Figure 1.8**).[75, 76] Additionally, when the molecules are held face-to-face ($\theta = 90$), they can be rotated by varying the rotation angle α. If the molecules are perpendicularly oriented in a "Greek cross" or "X-aggregate" conformation, such that $\alpha = 90°$, a null aggregate is also observed.[77]

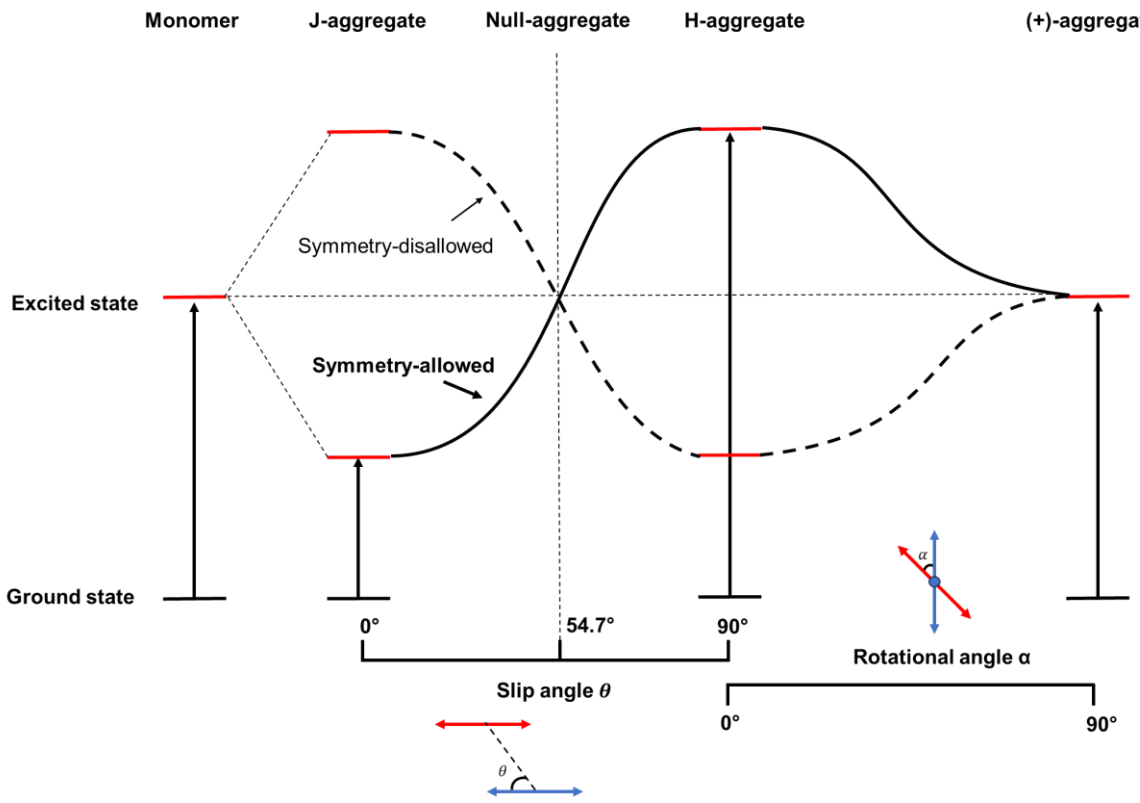

Figure 1.8: Schematic depiction of the relative energy of symmetry-allowed and disallowed electronic transitions in an excitonically coupled dimer as the slip angle $\boldsymbol{\theta}$ and rotational angle $\boldsymbol{\alpha}$ between the two dipole moments are varied.

Kasha's model is generally very successful at describing the basic photophysical properties of many molecular aggregates. However, it has two main drawbacks. Firstly, it does not explain the vibronic fine structure in the absorption and emission spectra of a great deal of aggregating chromophores. For example, in many π-conjugated chromophores the absorption spectrum is dominated by the $S_0 \rightarrow S_1$ electronic transition which is strongly coupled to stretching modes in the chromophore, and as a result the ratio of intensities of the vibronic peaks in this absorption band is sensitive to aggregation. This is discussed in section 1.9 in the context of perylene diimides where the ratio of the 0-0 and 0-1 vibronic peaks A_{0-0}/A_{0-1} decreases upon H-aggregation and increases upon J-aggregation, relative to the spectrum of the monomer. H-aggregation is also typically accompanied by broadening of the absorption bands, while J aggregation is accompanied by a sharpening of the bands. Secondly, Kasha's model only takes into account coupling between transition dipole moments ("Coulomb" or "long-range" coupling) and does not consider the effects of "short-range coupling" mediated by orbital overlap and charge-transfer between chromophores. Detailed theoretical treatments of

vibronic fine structure and short-range coupling in molecular aggregates are beyond the scope of this introduction but both have been explored in great depth by Spano and co-workers.[66, 76, 78]

1.6.2 Excitonic chirality

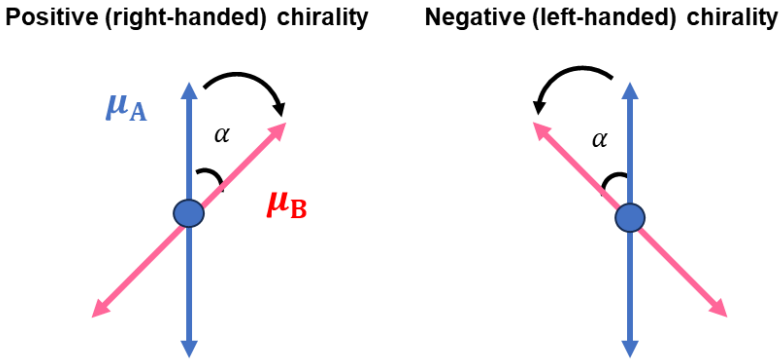

Figure 1.9: Schematic depiction of excitonic chirality between the transition dipole moments of two cofacially-stacked molecules rotated at an angle $\boldsymbol{\alpha}$.

We will now consider the impact of excitonic coupling on chiroptical activity. When the transition dipole moments in excitonically coupled dimers are in a twisted geometry (i.e. $\alpha \neq 0$), they form a chiral object that can interact with CP light (**Figure 1.9**). Studying these chiral exitonic systems allows for the absolute configuration of multi-chromophoric chiral systems to be assigned from their CD spectra. This was first studied by Harada, Nakanishi,[79, 80] and Bayley[81] in the 1970s and recently expanded and formalised by Pescitelli,[82] and Painelli, Sissa, Thomas and co-workers.[69, 83, 84] A characteristic signature of an excitonically-coupled dimer is a "Cotton effect" (also known as "bisignate coupling") in the CD spectrum, where the CD signal varies rapidly with wavelength, crosses zero at the absorption maxima of the band, and then varies again rapidly but with the opposite sign. The circular dichroism for an electronic transition can be predicted by the following relationship:

$$\Delta\varepsilon \propto \boldsymbol{r} \cdot (\boldsymbol{\mu}_A \times \boldsymbol{\mu}_B)V \qquad (1.12)$$

where $\boldsymbol{r}$ is the interchromophoric distance vector, $\boldsymbol{\mu}_A$ and $\boldsymbol{\mu}_B$ are the electric transition dipole moments of the chromophores, and V is the interaction energy between the dipoles. The origin of the Cotton effect can be understood intuitively if for example we consider the in phase and out of phase combinations of dipoles in a face-to-face (H-like) right-handed dimer (**Figure 1.10**).[55] For the higher energy in-phase exciton combination, the dipole moments also form a

right-handed helix, so they interact more strongly with right-handed CP light. In contrast for the lower energy out-of-phase combination, the dipole moments form a left-handed helix, so they interact more strongly with left-handed CP light. Therefore, the electronic transitions involving the in and out of phase excitonic states will have opposite signs in the CD spectrum.

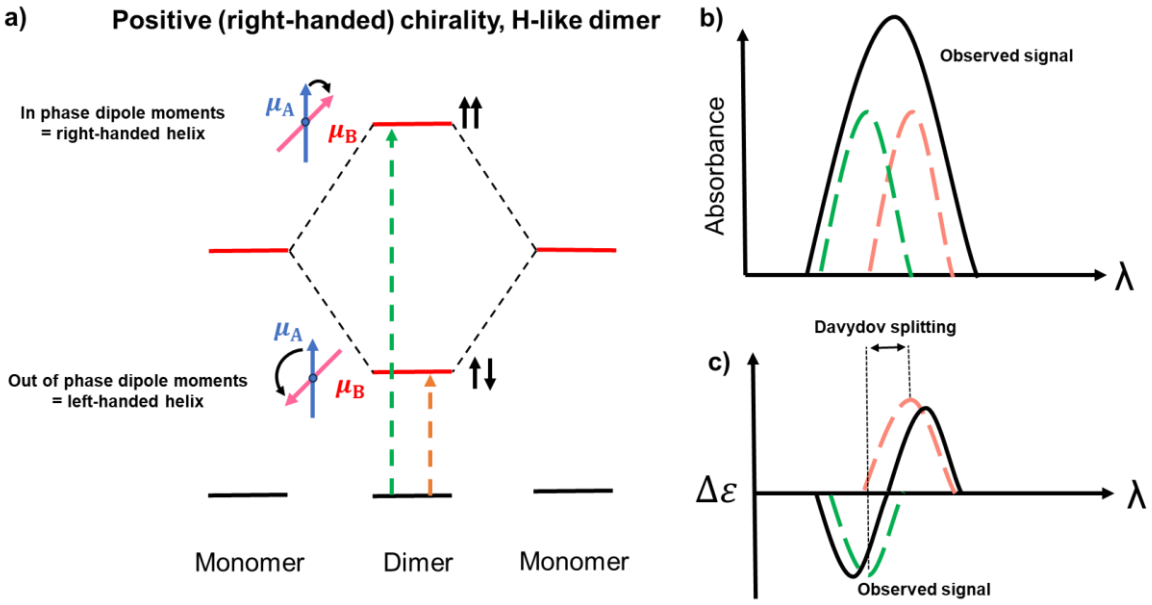

Figure 1.10: a) Energy diagram explaining the origin of Davydov splitting in an excitonically-coupled chiral dimer. **b)** Overall absorption spectrum consisting of the sum of the absorption spectra of both transitions depicted in part **(a)**. **c)** CD spectrum, where the two transitions depicted in part **(a)** appear as two bands with opposite signs. The Davydov splitting energy can be determined from the CD spectrum.

These results for both enantiomers in H- and J-type twisted geometries are summarised in **Figure 1.11a**. Additionally, the results for H- and J-type chiral dimers can be extended to larger aggregates, with H-type aggregates forming helical columnar stacks, while J-aggregates can form "creeper-helical" aggregates (**Figure 1.11b**).[69, 83] Chiral H- and J-type assemblies of perylene diimides (PDIs) and other aromatic molecules are explored in Sections 1.9 and 1.11.

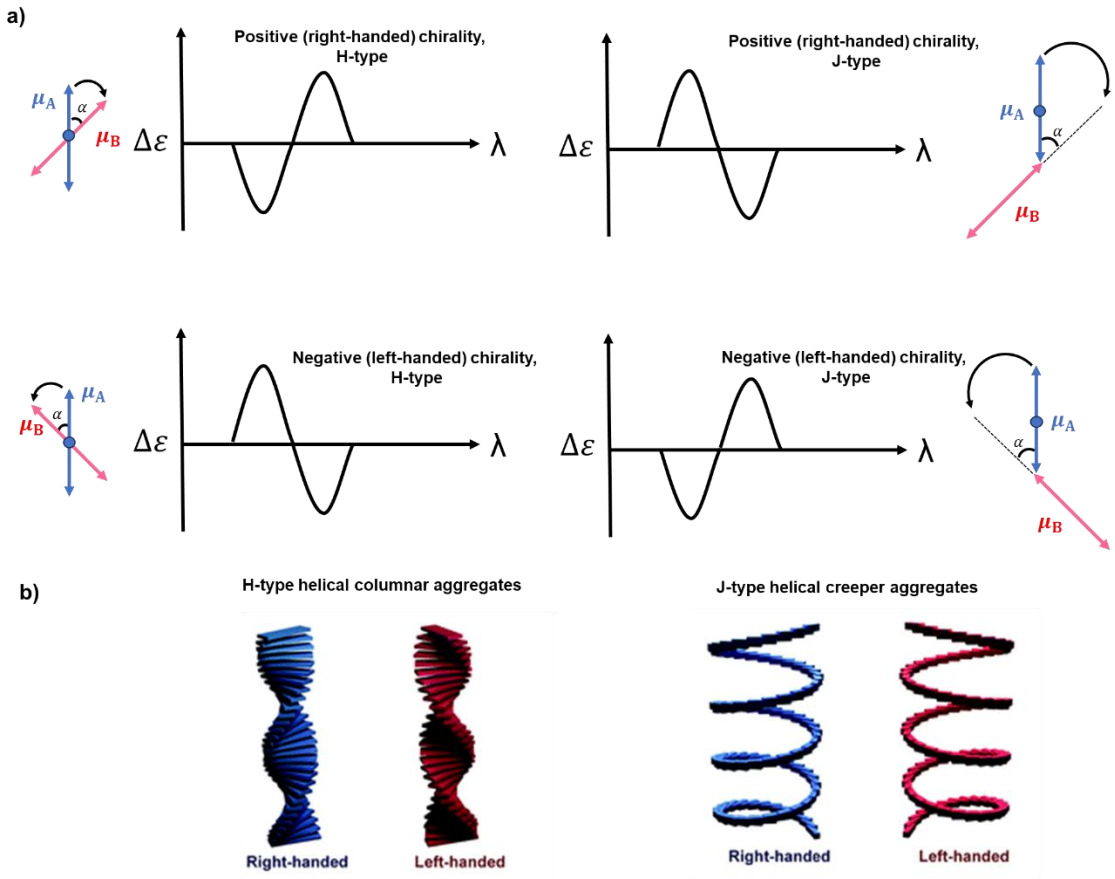

Figure 1.11: a) Schematic depiction of the relative chromophore arrangement in chiral H-type and J-type aggregates, along with the corresponding CD spectral signals predicted by chiral excitonic theory. **b)** Cartoon depiction of multi-chromophore H-type columnar helical aggregates and J-type "creeper" helical aggregates. Adapted from Ref. 69 with permission from the Royal Society of Chemistry.

The model described above only considers coupling between electric transition dipole moments and assumes that any coupling to the magnetic transition dipoles of the two molecules is negligible. If this is not the case,[85] the circular dichroism can be predicted by:

$$\Delta\varepsilon \propto \boldsymbol{r} \cdot (\boldsymbol{\mu}_{\mathrm{A}} \times \boldsymbol{\mu}_{\mathrm{B}}) + \mathrm{Im}[(\boldsymbol{\mu}_{\mathrm{A}} \pm \boldsymbol{\mu}_{\mathrm{B}}) \cdot (\boldsymbol{m}_{\mathrm{A}} \mp \boldsymbol{m}_{\mathrm{B}})] \qquad (1.13)$$

where $\boldsymbol{m}_{\mathrm{A}}$ and $\boldsymbol{m}_{\mathrm{B}}$ are the magnetic transition dipole moments for the two chromophores.

1.7 Chiroptical materials in practice

1.7.1 Techniques

CD spectroscopy is very well established as a powerful analytical tool in chemistry and biochemistry. The spectral shape, sign and magnitude of CD spectra can provide valuable information about molecular and supramolecular structures, such as the helicity and secondary and ternary structures of DNA and proteins.[86] Furthermore, chiral chromophores can be engineered to precisely bind to specific biological molecules to allow for their study by CD spectroscopy.[87] CPL spectroscopy is newer as an analytical tool, but recent developments in CPL spectrometer technology have made it more available.[88] CPL can be very useful as it provides information about the excited states of molecules, rather than the ground state. In addition, CPL-emitting chromophores can be used very much like fluorescent probes commonly used for biological imaging, with the added advantage of being able to add information about chirality to an image. In addition, sensing based on CPL rather than unpolarised light can eliminate the interference of background non-polarised light, allowing for better resolution and sensitivity. The group of Robert Pal in Durham has pioneered the concept of enabling CPL-detection in instruments such as laser scanning confocal microscopes (CPL-LSCM).[89] CPL-LSCM imaging has been used to show that the Λ- and Δ-enantiomers of a known europium complex localise in different organelles within a cell.[89]

1.7.2 Applications

Chiroptical materials also have potential applications in security and information processing as their chirality and interaction with CP light allows them to achieve higher information storage density compared to achiral emitters. For example, the Pal group has also developed a CPL-sensitive camera that has been used to image multilayered security tags consisting of various dyes emitting at different wavelengths and CPL signs which could form the basis for high-security QR codes and bar codes on documents that would be extremely difficult to forge.[90] Systems that provide CPL emission that is responsive to external achiral stimuli such as pH, heat, or specific non-polarised light wavelengths are of interest for similar applications. [91]

Organic light-emitting diodes (OLEDs) are of huge commercial importance and have achieved widespread use in screen displays for devices such as televisions, computer monitors

and mobile phones.[92] However to obtain high image contrast in these devices it is necessary to use an antiglare filter which consists of a circular polariser.[93] This removes most of the ambient light reflecting off the screen, but also has the effect of removing 50% of the non-polarised light emitted by the screen, putting a severe limit of the energy efficiency of such devices (**Figure 1.12)**[94-96] This problem can in principle be overcome by using OLEDs that emit circularly polarised light of the correct handedness to pass through the antiglare polariser without being absorbed. These materials are known as CP-OLEDs and were first reported in 1997 by Meijer and co-workers.[97]

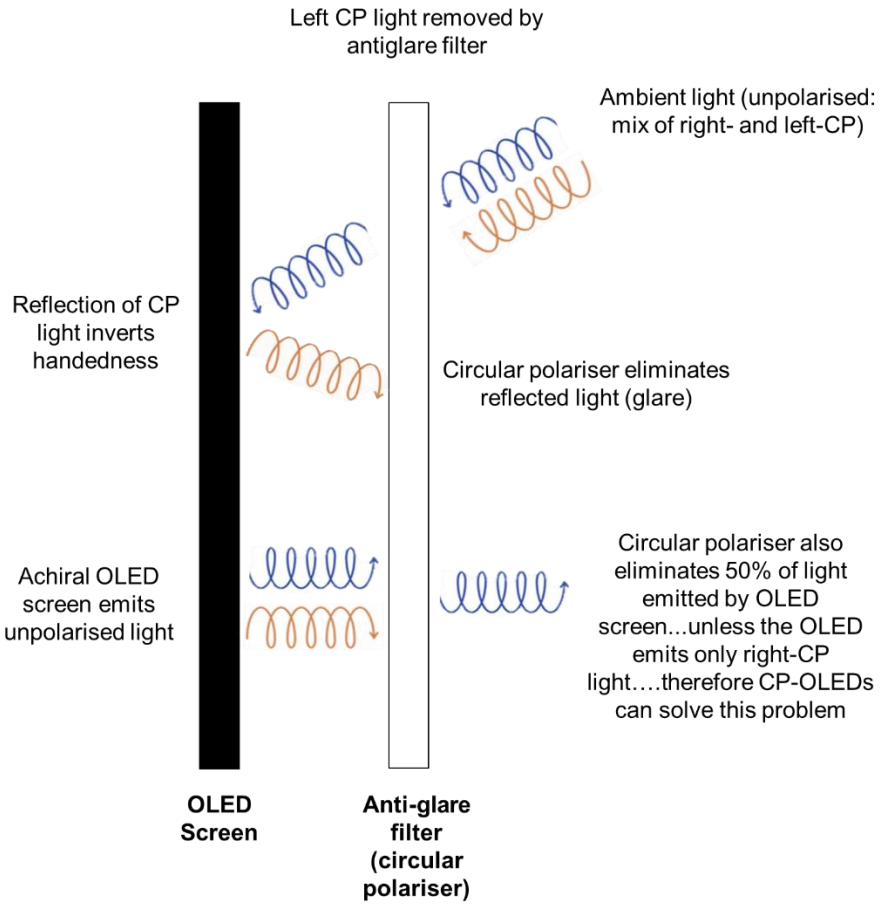

Figure 1.12: Cartoon depiction of an antiglare filter consisting of a circular polariser, and the associated efficiency problem that can be solved by using CP-OLEDs.

Naturally, for a material to be useful for a CP-OLED it must possess both high a high electroluminescence efficiency/brightness and a high electroluminescence dissymmetry factor ($|g_{\mathrm{El}}|$, analogous to $|g_{\mathrm{lum}}|$). This is in general hard to achieve because dissymmetry factors are challenging to optimise as discussed in the previous sections and also because these systems

usually produce excited states in a 1:3 singlet:triplet ratio, but for organic materials often only the singlet excited states are emissive.[94] The field has been largely dominated by polymer systems, with the highest $|g_{\mathrm{El}}|$ value being reported in 2017 in a system consisting of an achiral conjugated polymer and non-emissive chiral dopant.[98] Several groups have developed CP-phosphorescent OLEDs (CP-PHOLEDs) in order to increase the electroluminescence quantum efficiency by allowing the 75% triplet excited state population to be emissive. This can be achieved by exploiting the strong spin-orbit coupling of heavy metals. The first CP-PHOLED, based on a chiral europium (III) complex as a dopant, was reported by Di Bari and co-workers in 2015[51] with a $|g_{\mathrm{El}}|$ of up to 1.0 at 595 nm but still quite low quantum yield. Fuchter, Campbell and co-workers have since developed highly efficient CP-PHOLEDs consisting of chiral platinum complexes with helical chirality with $|g_{\mathrm{El}}|$ values of up to 0.38 at 615 nm and emission brightness large enough to be used in displays. [99]

Another class of organic electronic devices that are of great importance for future technology are organic field effect transistors (OFETs), which use an electric field to control the flow of current through an organic semiconductor material.[100] Several groups have developed CP-sensitive OFETs where the organic semiconductor layer consists of a chiroptical material. For example, Fuchter, Campbell and co-workers have made OFETs using enantiopure helicenes which showed a tenfold increase in drain current upon irradiation with CP light of the correct handedness, compared to no light or light of the opposite handedness (**Figure 1.13**).[101] Other research groups have since developed a range of similar devices, including some using chiral perylene diimide derivatives as the chiroptical material.[102-104] CP-responsive OFETs open up the possibility of CP-light dependent electronic circuits.[94]

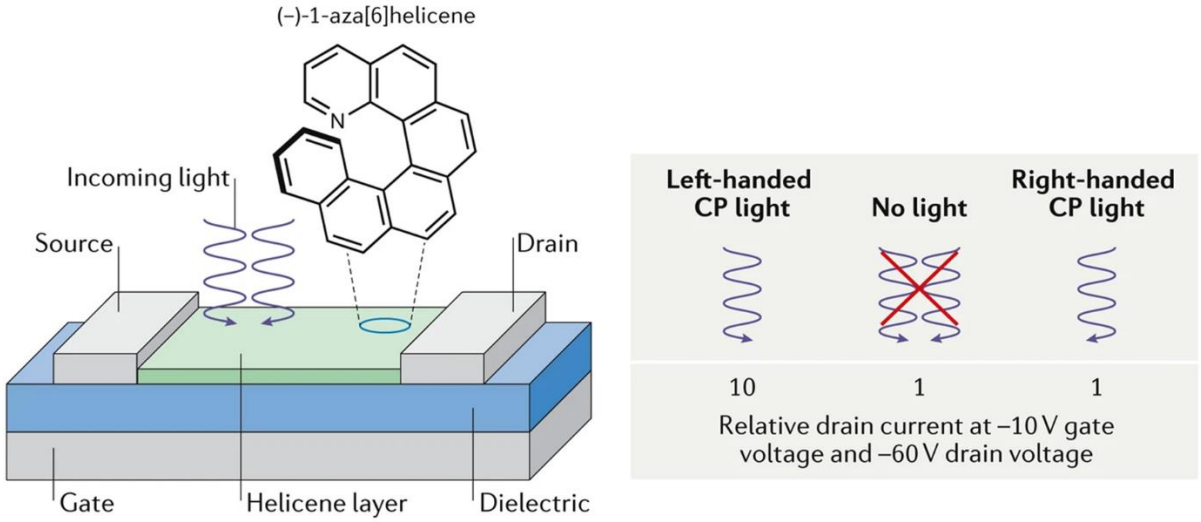

Figure 1.13: Diagram of a CP light-sensitive OFET fabricated using a chiral helicene film.[101] Adapted from ref 101 with permission from Springer Nature.

Finally, as mentioned in section 1.1, the interaction between CP light and chiral materials can be used to induce enantiomeric excesses in chemical reactions. Due to the limited number of substrates that show strong interaction with CP light, these techniques are unlikely to be adopted as a mainstream method of asymmetric synthesis.[22] However, this research is still of fundamental importance as it may provide new understanding on the origins of the homochirality of life, and indeed on the origins of life itself.[105]

1.8 Current challenges in chiroptical materials research

As discussed in the above sections, optimising the absorption and emission dissymmetry factors g_{abs} and g_{lum} up to the theoretical maximum value of 2 remains a challenge. While dissymmetry factors > 1 have been achieved using lanthanides,[50, 51] the highest dissymmetry factors for small organic molecules lag behind significantly (< 0.2 for the best performing small organic molecule, but typically $< 10^{-2}$).[53]

Organic materials are of interest as they have a number of advantages over those containing heavy metals, including a lower cost of raw materials, higher mechanical flexibility, lower processing temperatures and a greater potential for being made biocompatible.[106, 107] Beyond simply optimising dissymmetry factors in organic molecules, a further research aspiration is to produce organic materials that combine high dissymmetry factors with excellent electronic and photophysical properties for use in real-world useful devices. Additionally, as

explored later in this thesis, chiral interactions between organic molecules can be used to control their supramolecular packing,[108] which influences their electronic and photophysical properties in addition to their chiroptical parameters.[109] As discussed in the following sections, one of the most versatile molecular building blocks for exploring all the above is the organic dye perylene diimide (PDI).

1.9 Introduction to perylene diimide chemistry

The chemistry of dyes and pigments is one of the oldest and most well-established fields in synthetic organic chemistry. Driven by industrial demand, numerous dye types were developed in the 19th and early 20th centuries.[110] One such class of dye are the derivatives of perylene-3,4:9,10-tetracarboxylic acid diimide, commonly known as perylene bisimide or perylene diimide and abbreviated as PDI in this thesis. PDIs were first discovered in 1913 by Kardos.[111] Due to their strongly coloured nature and high chemical and thermal stability, PDIs became commonly used as red vat dyes and as coloured finishes for industrial goods.[112] However, because of their insolubility, much of their chemistry and photochemical properties remained undiscovered until chemical modifications that improved their solubility became available later in the 20th century.[113] Since then, PDIs have emerged as excellent fluorescent dyes with long fluorescence lifetimes, high extinction coefficients and an exceptional thermal, chemical and photophysical stability that is very rarely found in other classes of dye.[114, 115] PDIs have consequently been used in a myriad of applications, such as in fluorescence labelling[116] and laser dyes,[117] and in more fundamental studies on light-induced electron transfer processes. The PDI core has been found to possess a very high electron affinity and can therefore form the basis for excellent n-type semiconducting materials.[118-121] For the same reason, PDIs can form stable non-emissive organic radical anions and dianions with strong infrared absorption, with potential applications in photothermal therapy for cancer and photoacoustic imaging.[122-126] Reviews have been published on the synthesis of PDI derivatives,[115] on their structure-property relationships,[127] and on their applications in organic electronic devices[128-130] and in fluorescence spectroscopy,[131] including single molecule fluorescence spectroscopy.[132-134]

PDI-based molecular scaffolds have also been shown to exhibit a rich and varied supramolecular chemistry. Recent reviews have been published exploring the general self-assembly of PDI-containing molecules,[74] PDI hydrogen-bonded architectures,[135] PDI self-assemblies in water,[136] and the applications of water-soluble PDIs in biology.[137] This section

will first discuss the physical and chemical properties of PDIs and will then cover chiral PDI supramolecular assemblies, with an emphasis on chiral π- π interactions, before moving onto bis-PDI macrocycles and other PDI dimers.

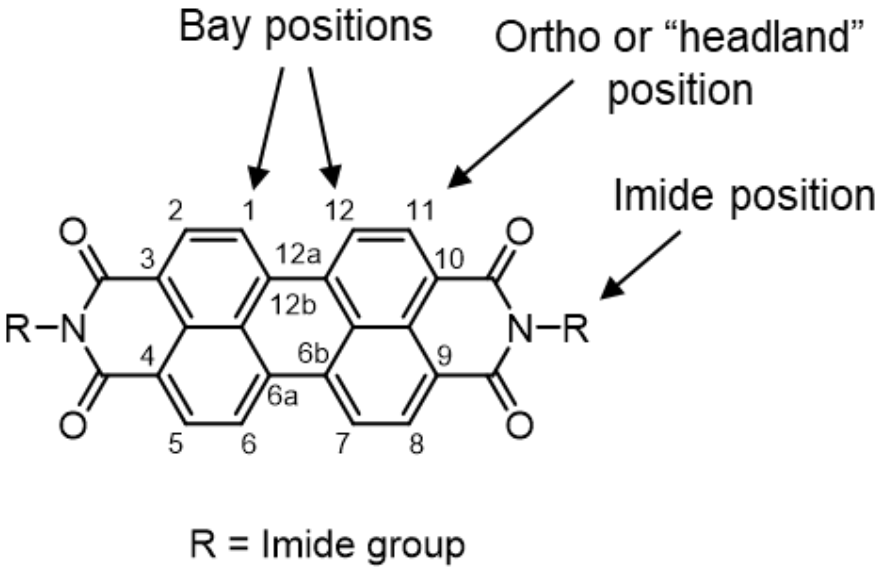

Figure 1.14: Chemical structure of PDI showing the conventional numbering scheme for the perylene core carbon atoms, along with its main functional handles at the *imide, bay* (1,6,7,12) and *headland/ortho* (2,5,8,11) positions.

Figure 1.14 shows the structure of the PDI core. It possesses two main functional handles, known as the imide and bay positions.[74] Substitution is also possible at the ortho/headland positions,[115] although this is less common. A wide variety of substituents may be easily inserted at the imide position via an imide condensation reaction between a relevant amine and PDI's parent anhydride, PTCDA (Perylene-3,4,9,10-tetracarboxylic dianhydride). Imide substituents are mainly used to tune the solubility and aggregation characteristics of the PDI though steric effects,[74] and cannot influence the electronics of the PDI mesomerically. Imide substituents can however influence the optical and redox properties of the PDI core via the inductive effect[138] or via through-space effects such as photo-induced electron transfer (PET).[139, 140]

For many decades, functionalisation at the bay position proved more difficult, requiring harsh conditions to introduce heteroatoms (with generally poor regioselectivity) which could subsequently only be substituted by a handful of nucleophiles.[115] However in recent years, the advent of C-H bond activation and transition metal-catalysed C-C coupling reactions has greatly expanded the synthetic possibilities available at the bay position.[115, 128] Bay substituents

strongly influence the electronic properties of the PDI core both mesomerically and inductively, allowing for tuning of the chromophore for a given application.[127, 141]

Another important property of the PDI core is its high fluorescence quantum yield (typically close to unity in common solvents).[74] This arises from the PDI core being highly rigid, disfavouring vibrational relaxation pathways. Furthermore, the triplet T_1 state is very low in energy relative to the excited singlet S_1 state,[142] making $S_1 \rightarrow T_1$ intersystem crossing an unlikely and therefore slow process relative to radiative decay, according to the energy gap law for radiationless transitions. [143] The two imide groups in PDI also contribute to the high fluorescence quantum yield by making the S_1 state lower in energy than in unfunctionalized perylene, which in turn makes $S_0 \rightarrow S_1$ more energetically accessible. Indeed, the UV-vis absorption band maximum is red-shifted from ~ 440 nm in perylene to ~ 525 nm in a typical PDI.[74] The two imide groups also make PDIs relatively electron poor,[144] which is thought to contribute to the high stability of the PDI core by making it stable to oxidative decomposition pathways that commonly affect other classes of dye with similarly high fluorescence quantum yields.[114] This electron deficiency also results in both the PDI radical anion and dianion being relatively stable species in non-oxidising environments.[145-148]

Through π-π interactions, PDI cores can stack with each other to form dimers or larger assemblies.[74] This leads to a change in the fluorescence quantum yield and a shift in the UV-vis absorption band due to exitonic coupling.[63-66] PDIs most commonly form H-type aggregates, although they can be driven to form J-type aggregates by using hydrogen-bonding substituents,[149] or as explored later in this thesis, by exploiting sterics and chirality.[150]

The compound in **Figure 1.15a** displays typical PDI H-aggregating behaviour.[151] When monomeric, this compound has sharp absorption bands between 400 and 550 nm corresponding to the $S_0 \rightarrow S_1$ electronic transition, with a $\lambda_{max} = 517$ nm and well resolved vibronic bands with an $\varepsilon_{0\text{-}0} / \varepsilon_{0\text{-}1}$ ratio of ~ 1.5. The monomeric emission spectrum is also sharp and is a mirror image of the absorption spectrum, forming a band at 500–650 nm. Upon concentration of the solution, this PDI undergoes H-type aggregation, with the absorption spectrum becoming broader and less structured, with a hypsochromic shift of ~ 27 nm for λ_{max} and a decreased $\varepsilon_{0\text{-}0} / \varepsilon_{0\text{-}1}$ ratio of ~ 0.5. The emission in the aggregated state is characteristic of excimer emission, with a broad, red-shifted band appearing at 600-850 nm.

Meanwhile, the compound in **Figure 1.15b** displays J-aggregating behaviour, with a considerable redshift and sharpening of both the absorption (from λ_{max} = 570 nm to λ_{max} = 642 nm) and emission (from λ_{max} = 602 nm to λ_{max} = 654 nm) bands upon aggregation.[149]

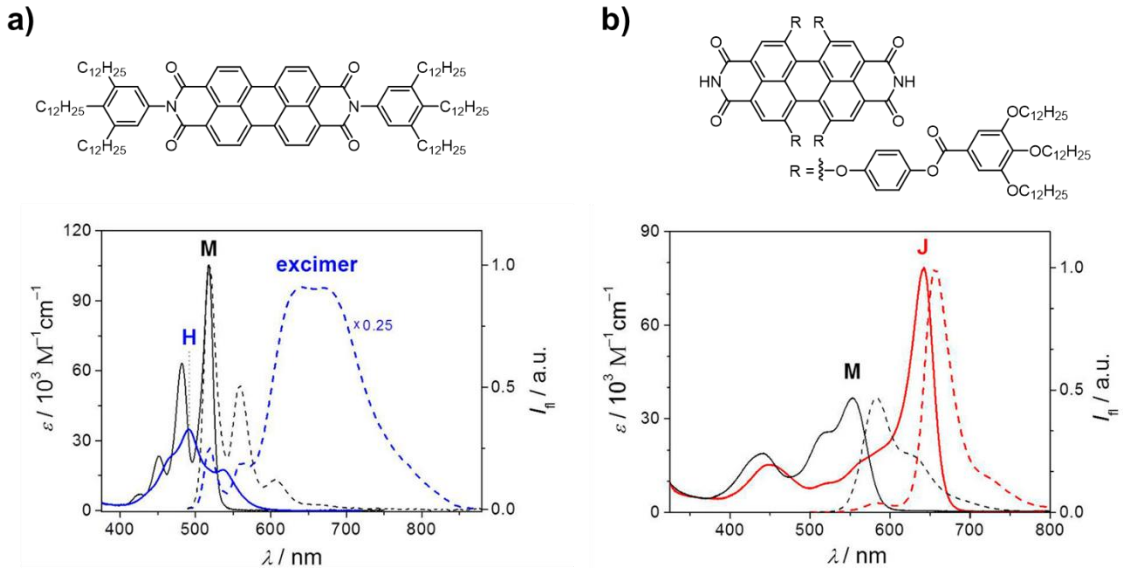

Figure 1.15: a) Structure of a PDI that displays typical H-type aggregation behaviour, alongside the UV-vis-NIR absorption spectra of this PDI in its monomeric state (black solid trace) and in the H-aggregate (blue trace), as well as the emission spectra of this PDI in its monomeric state (black dashed trace) and in the H-aggregate (blue dashed trace).**b)** Structure of a PDI that displays typical J-type aggregation behaviour, alongside the UV-vis-NIR absorption of this PDI in its monomeric state (black solid trace) and in the J-aggregate (red solid trace), as well as the emission spectra of this PDI in the monomeric state (black dashed trace) and in the J-aggregate (red dashed trace). Adapted with permission from ref. 151. Copyright 2006 The Authors. Chemistry A European Journal published by Wiley-VCH GmbH.

1.10 Chirality in PDIs

1.10.1 Inherently chiral twisted PDI cores

Steric repulsion between opposing substituents in the congested bay region will lead to a twisting of the chromophore. This leads to a red-shift and broadening of the $S_0 \rightarrow S_1$ band in the PDI absorption spectrum. For example, a typical core-unsubstituted PDI has an absorption maximum of ~ 535 nm, while in bay-tetraphenyl PDI this band is broader, with less well defined vibronic structure and an absorption maximum at ~ 608 nm.[152] Most interestingly, twisting of the PDI core results in a chiral π-system that can absorb and emit CP light (**Figure 1.16**).[153]

For most bis-functionalised (1,6 or 1,7) PDI cores the energy barrier for interconversion between the two atropisomers is low and interconversion proceeds at room temperature via a planar transition state. However, more stable atropisomers can be obtained through tetra-functionalisation with large substituents such as bromine atoms,[153] allowing for the separation of the atropo-enantiomers though chiral column chromatography. Chiral PDI cores are of great interest for applications in chiroptical materials,[154] including circularly polarised light emitting diodes (CP-LEDs),[115, 155] and in supramolecular chiral recognition.[153, 156]

The system for classifying the inherent chirality of PDIs has not yet been standardised in the literature, leading to different conventions being used.[157] PDI chirality can be considered according to the rules of the axial chirality of the two naphthalene units of the PDI, with substituents at the 1,6,7,12 positions (labelled X and Y in **Figure 1.16**) being assigned priorities according to the Cahn-Ingold-Prelog rules. Amongst others, the Nuckolls[158] and Barendt groups[108, 159] have used this system..[160] Enantiomers of axially chiral compounds are usually given the labels *R* and *S*, although for PDIs the labels ***P*** and ***M*** are often used instead.

Alternatively, the chirality of PDIs can be considered in terms of the helical orientation of the "front" and "back" naphthalene units with the enantiomers being labelled ***P*** and ***M***. Helical chirality labels have the advantage of being independent of substituent priority. Furthermore, for twisted bay-tetrasubstituted PDIs where all four bay substituents are identical, only helical chirality labels can be used.

In this literature review chapter, PDI cores will be labelled according to the rules of helical chirality. However, in the research chapters of this thesis, axial chirality labels are used to keep consistency with the recent publications based on the work in this thesis.[159, 161]

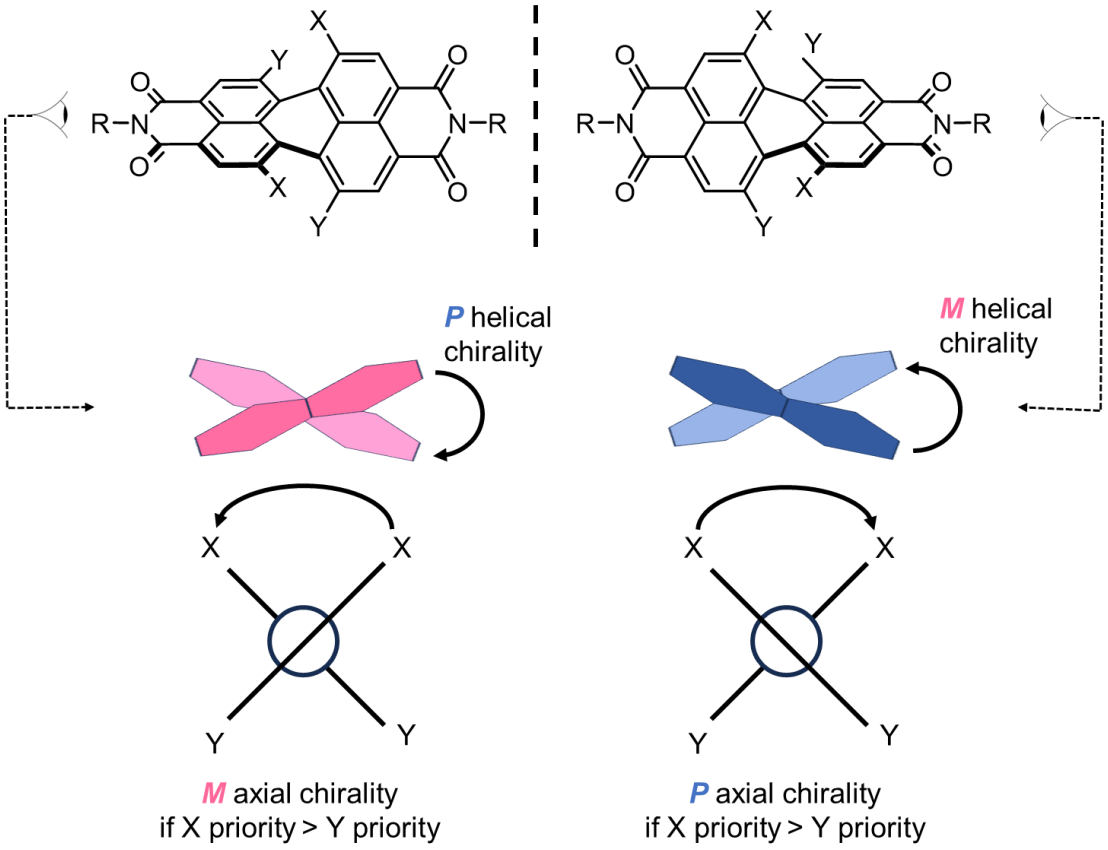

Figure 1.16: Summary of axial and helical chirality systems used to label chiral twisted PDI cores.

In 2007 some of the first reports of stable, separable PDI enantiomers were published by Osswald, Würthner and co-workers, via two very different approaches. [153, 156]

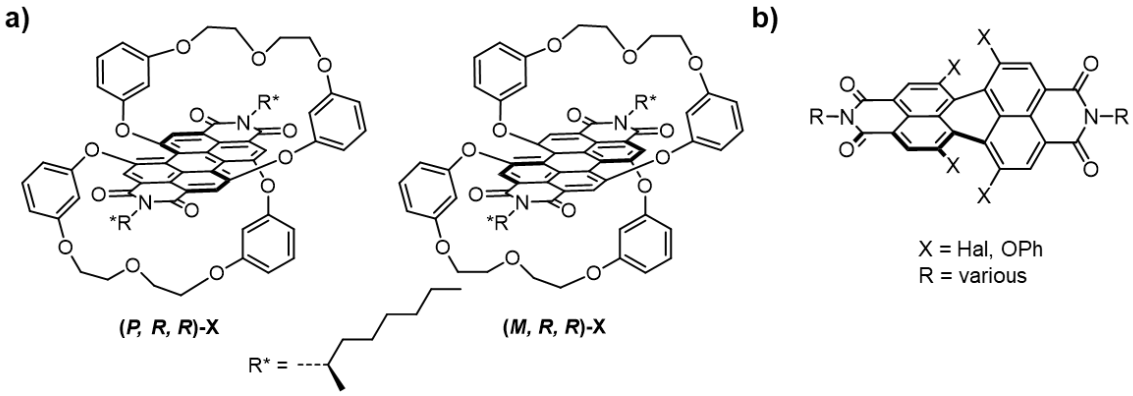

Figure 1.17: The first examples of stable PDI atropo-enantiomers reported by Osswald, Würthner and co-workers, achieved by either macrocyclic strapping **(a)** [156] or bulky bay groups such as Br atoms **(b)**. [153]

The first strategy reported involved the use of macrocyclic "straps" connecting the 1,7 and 6,12 positions to induce a twist of the PDI core (**Figure 1.17a**).[156] This built on the results

of earlier work with similar systems that showed that shortening the length of the macrocyclic straps increased the degree of strain and twisting of the PDI core.[162] The authors realised that if the macrocyclic straps were short enough, the energy barrier for enantiomer interconversion would be too high for racemisation to occur. Thus, the chiral PDI core is configurationally stable. The use of a chiral imide group R* at the imide positions means that the system as a whole exists as two epimers ((*P*,*R*,*R*) and (*M*,*R*,*R*)) that can be separated by HPLC and differentiated by ^{1}H NMR spectroscopy. The absolute stereochemistry of these isomers was assigned using CD spectroscopy and quantum chemical CD calculations.

The second strategy reported involved the use of bulky Br substituents to prevent interconversion between the two twisted PDI atropisomers (**Figure 1.17b**).[153] In this study the authors also explored the effects of bay substituent size on the dihedral twist angle θ of the PDIs and on their racemisation free energy barriers $\Delta G^{\neq}$. They found that both θ and $\Delta G^{\neq}$ increase as the sum of the van der Waals radii of the bay substituents increases. For example, bay-tetrafluoro PDI has $\theta \sim 20°$ and $\Delta G^{\neq} = 40$ kJ mol^{-1} while bay-tetrabromo PDI has $\theta \sim 40°$ and $\Delta G^{\neq} = 118$ kJ mol^{-1}. Here it is worth noting a study by LaPlante and co-workers on atropisomer stability where it is estimated that compounds with racemisation barriers $\Delta G^{\neq} > 125$ kJ mol^{-1} can be considered configurationally stable.[163] Indeed, while the bay-tetra-bromo PDI enantiomers are stable enough to be studied in depth by CD spectroscopy and other techniques, they do racemise slowly. At an elevated temperature of 363 K, complete racemisation was observed after 1.5 days in solution. Interestingly, the widely used bay-tetraphenoxy-PDI is not chirally stable due to the flexibility of this group ($\Delta G^{\neq} = 90$ kJ mol^{-1}).

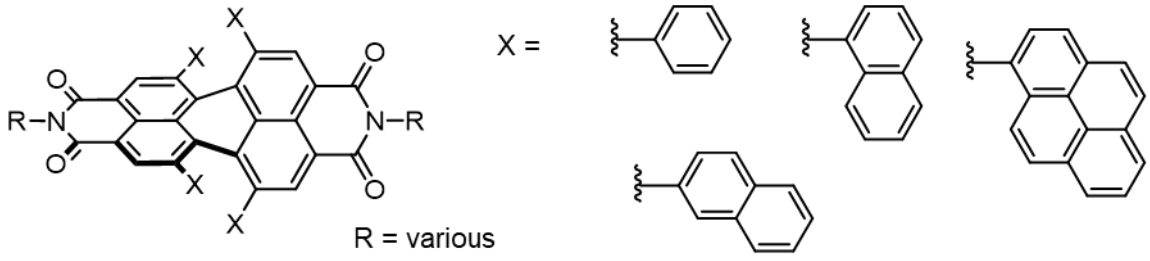

Figure 1.18: Bay-arylated PDIs reported by the groups of Zhu, [164] Hoffmann, [152] and Würthner. [165]

Since the studies by Osswald *et al.* , a number of stable bay-tetrasubstituted PDIs have been reported. Amongst these, bay-arylated PDIs have shown particularly promising properties

for use in organic electronic devices and chiroptical materials (**Figure 1.18**). The groups of Zhu and Hoffman were the first to capitalise on transition metal-catalysed C-C coupling reactions to synthesise tetraarylated PDIs, with the Zhu group reporting the first synthesis of a bay-tetraphenyl PDI in 2006,[164] although its enantiomers were not isolated and studied by CD spectroscopy until the Hoffmann group did so in 2014.[152] In 2021, Renner *et al*. published a study of various tetraarylated PDIs, focusing on their conformation, atropoisomeric stability, solid state packing, and chiroptical properties.[165] The authors found the enantiomers of the tetraarylated-PDIs to be configurationally stable, with bay-tetraphenyl PDI having a PDI twist angle $\theta = 34°$ and a $\Delta G^{\neq} = 119$ kJ mol^{-1}, which is virtually the same as that of bay-tetrabromo-PDI. Furthermore, they had relatively good chiroptical properties for small organic molecule standards, with very red-shifted CPL spectra, with bay-tetra-2-naphthyl PDI emitting at 655 nm with a $|g_{\mathrm{lum}}|$ of ~ 1×10^{-3}.

1.10.2 PDI cores fused with helical motifs

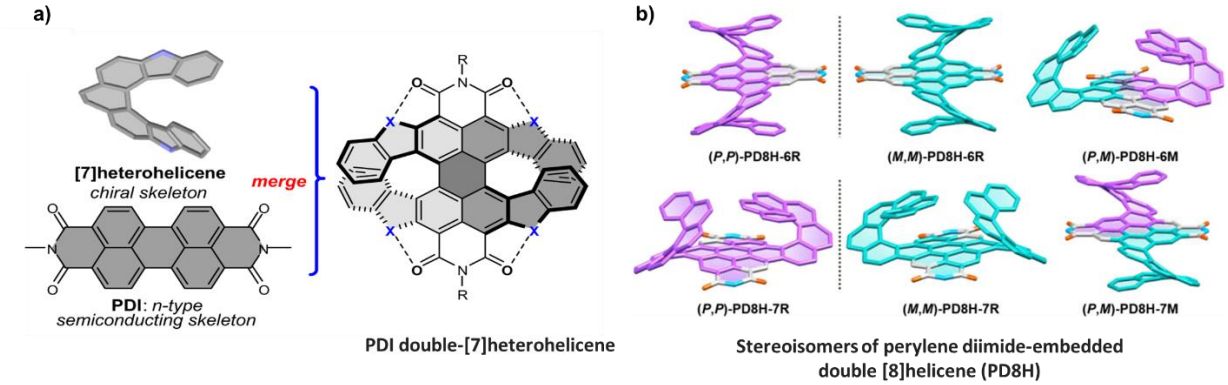

Figure 1.19: PDI cores fused with helical motifs reported by **a)** Zhang, Hak Oh, Lin and co-workers[104] and **b)** Liu, Jiang, Wang and co-workers.[166] Adapted with from ref 104 with permission from Springer Nature and 166 with permission from the American Chemical Society.

Another exciting strategy for generating chirality in PDIs is to fuse the PDI core with further aromatic rings in order to integrate it within a larger helical architecture. The aim of these systems is generally to combine the excellent photophysical and electronic properties of PDIs with the very attractive chiroptical properties of systems like helicenes. Perhaps the simplest of these designs was reported by Zhang, Hak Oh, Lin and co-workers in 2021, which involved fusing 4 heterocyclic rings to both the bay and ortho positions of the PDI core in order to generate a so-called "*ortho*-π-extended PDI double-[7]heterohelicene"(**Figure 1.19a**).[104] The resulting system maintains many of PDI's desirable electronic properties and the π-extension of the PDI skeleton brings about near-infrared (NIR) light absorption up to 780 nm as well as improved charge-transport ability. Excitingly, the PDI core inherits the high chiroptical activity of the embedded helicene motifs, with a $|g_{\mathrm{abs}}|$ value of 1.4×10^{-2} at 628 nm. For context, this is over an order of magnitude higher than the $|g_{\mathrm{abs}}|$ of regular twisted PDIs such as the previously-discussed bay-tetraphenyl PDI which has a $|g_{\mathrm{abs}}|$ value of ~ 1.3×10^{-3}.

In a similar vein, Liu, Jiang, Wang and co-workers reported a "perylene diimide-embedded double [8]helicene" architecture in 2020 which was synthesised by fusing a [6]helicene motif with PDI (**Figure 1.19b**).[166] Because of the structural features of PDI and [6]helicene, this system exists as six different isomers (two pairs of enantiomers and two meso isomers). These were separated and isolated by HPLC and their chiroptical properties were studied alongside their packing in racemic and enantiopure crystals. These systems also had

excellent $|g_{abs}|$ values of up to 1.4 × 10^{-2}, as well as fluorescence quantum yields of up to 30 %, which is high for the standards of extended helicenes.

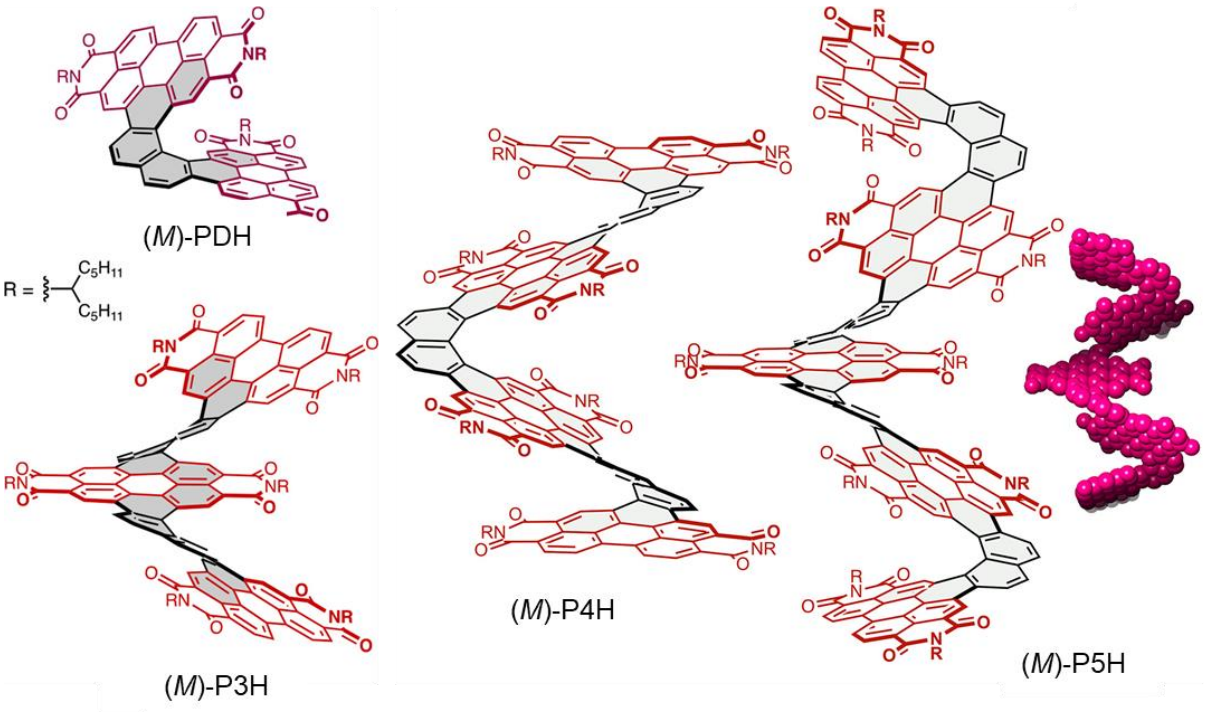

Figure 1.20: PDI-helicene nanoribbons reported by Nuckolls and co-workers. [39, 167, 168] Adapted from ref. 168 with permission. Copyright 2020 American Chemical Society.

Starting in 2016, the Nuckolls group has produced some of the largest PDI-helicene systems, by fusing multiple PDI cores with each other via naphthalene units, resulting in "nanoribbons" containing up to 5 PDI cores.[39, 167, 168] In general, increasing the length and number of PDI cores in the nanoribbons increases the $|g_{abs}|$ values almost linearly in the 400–420 nm region, increasing from ~ 2 × 10^{-3} for the two-PDI core analogue PDH to 1.7 × 10^{-2} for the five-PDI core P5H analogue. The differences in chiroptical properties for the two-PDI and three-PDI analogues are explored in detail in a follow-up computational study.[169] It suggests that the amplification of chiroptical properties in the 400 nm region in the three-PDI nanoribbon P3H results from excitonic coupling between the two [6]helicene units in the P3H nanoribbon, which is not possible in the two-PDI PDH nanoribbon that only contains one [6]helicene. These compounds exhibit some of the largest $\Delta\varepsilon$ values ever recorded, with the five-PDI analogue P5H exhibiting $\Delta\varepsilon$ = 1920 M^{-1} cm^{-1} at 420 nm, although it does not translate into a truly massive

$|g_{abs}|$ because of the high extinction coefficient ε at these wavelengths. The CPL of these compounds has not yet been studied.

1.11 Intermolecular chiral PDI assemblies

1.11.1 Chirality in aggregates of planar PDIs

In the absence of factors such as hydrogen-bonding motifs or sterically bulky substituents, PDIs most commonly assemble to form face-to-face H-type stacks in order to maximise π–π interactions.[74] For PDIs bearing no substituents at the imide or bay positions, computational studies suggest that a rotational displacement of 30° and a distance of 3.4 Å is the energy minimum for π–stacked PDIs in the ground state.[170]

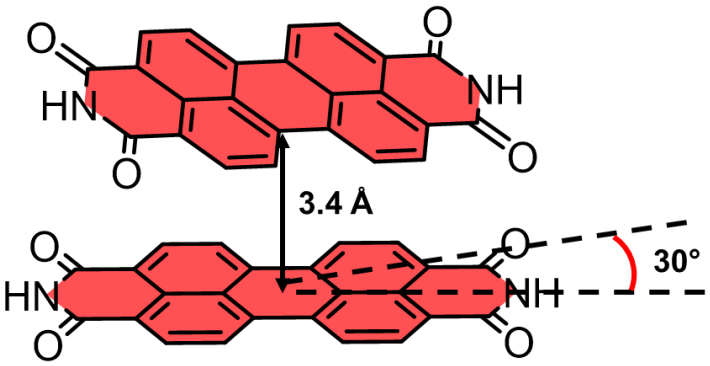

Figure 1.21: Ideal PDI dimer geometry in the absence of other substituents (PDI-PDI distance = 3.4 Å, rotational displacement = 30°) according to computational studies.[170]

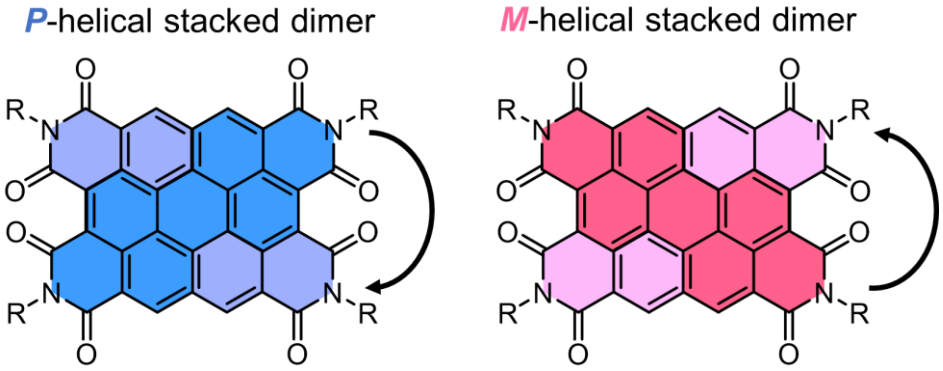

Figure 1.22: ***P***- and ***M***- helically chiral PDI dimers.

When considering the PDI assemblies, a further source of chirality is the relative orientation between PDI cores. This type of chirality can be present even when the PDI cores

are planar and unfunctionalised at the bay positions and is described in terms of helical chirality (**Figure 1.22**).

Naturally, in the absence of chiral substituents, both the *M*- and *P*- helical conformations are energetically identical, so PDI stacks will be rotationally disordered or at best will exist as racemic mixtures of *M*- and *P*- helical stacks. [171] The introduction of chiral substituents at the imide position is now a very well established strategy for influencing the helicity of planar PDI stacks, and has been covered extensively in reviews.[74, 172] The helicity of these stacks can be detected and assigned using CD spectroscopy. Some of the most interesting of these stacks include those made from planar PDIs bearing natural chiral groups at the imide positions, including amino acids,[173] peptides,[174] and sugars.[175-177] Some of these helical stacks are water-soluble, and have been used for specific molecular recognition of chiral proteins.[178] However, in this section we will focus on PDI chiral assemblies governed by the inherent chirality of chiral π–π interactions between twisted PDI cores.

1.11.2 Aggregation of twisted PDI cores governed by chiral π–π stacking

Aggregation constants quantify the strength of the binding of PDIs into an aggregate, and can often be determined by UV-vis titration experiments where the change in the spectrum corresponding to the formation of the aggregate is monitored as the concentration of PDI is increased. These experiments are discussed in detail in **Chapter 3**.

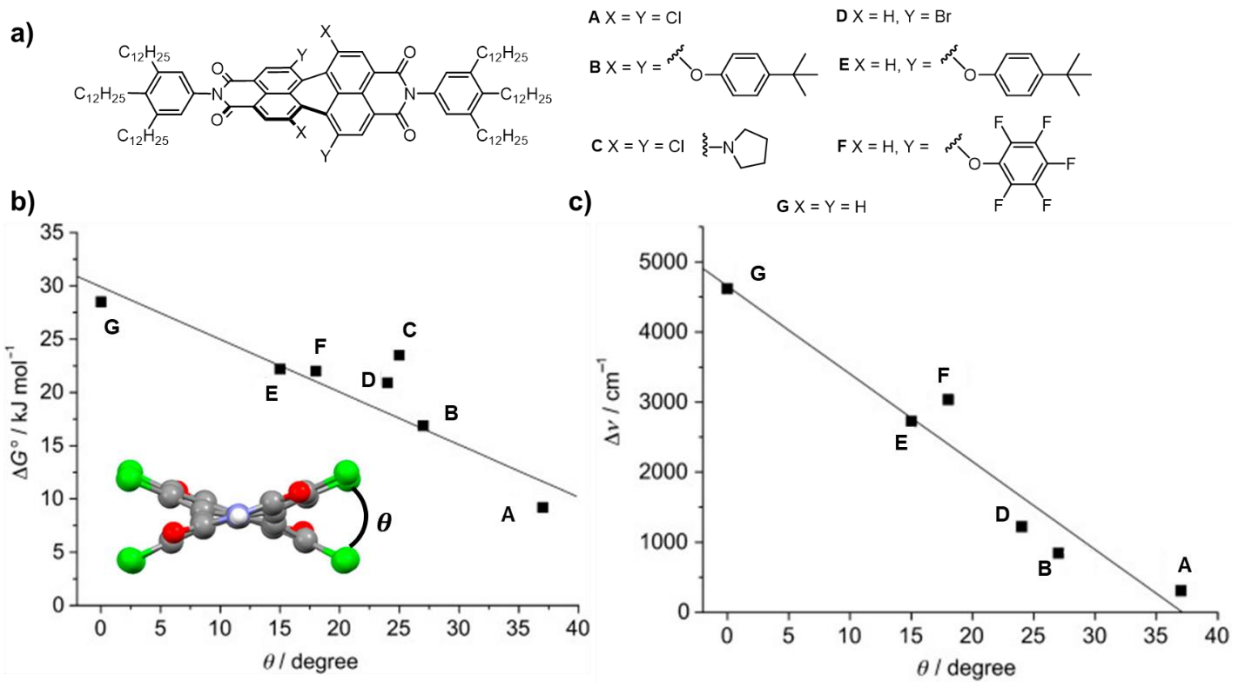

Figure 1.23: a) PDI derivatives used in a study by the Würthner group on the effects of core twisting on self-assembly of PDIs in solution and in liquid crystals. [150] **b)** correlation between the Gibbs free energy of π–π stacking and the PDI core twist angle $\boldsymbol{\theta}$. **c)** Correlation of the spectroscopic energy difference $\boldsymbol{\Delta\nu}$ (in wavenumbers) between the monomeric emission maximum and the maximum of the aggregate emission band with the core twist angle $\boldsymbol{\theta}$. Adapted with permission from ref. 150. Copyright 2006 The Authors. Chemistry A European Journal published by Wiley-VCH GmbH.

Due to the steric effects of bay substituents and their inherent twisted geometry, twisted PDI cores typically have aggregation constants at least two orders of magnitude lower than those of bay-unsubstituted planar PDIs.[74] An early study on the effects of core twisting on self-assembly of PDIs in solution and in liquid crystals was carried out by the Würthner group in 2006 (**Figure 1.23**).[150] It was found that there is a good correlation between the Gibbs free energy of π–π stacking and the PDI core twist angle θ, with the interaction strength decreasing as θ increases (**Figure 1.23b**). For the aggregate excited state, the strength of the π–π interaction can also be quantified by the spectroscopic energy difference $\Delta\nu$ (in wavenumbers)

between the monomeric emission maximum and the maximum of the aggregate emission band. For all these systems, the aggregate emission was red-shifted relative to the monomer band. However, this red-shift $\Delta\nu$ decreases as θ increases, and for bay-tetrachloro-PDI A (**Figure 1.23**) it is almost negligible, implying that it does not aggregate. Additionally, the authors were able to use UV-vis data (in solution) and crystallographic data (in the liquid crystalline phase) to make conclusions about the geometry of these aggregates. They found that the more sterically encumbered and more twisted bay-tetrasubstituted PDIs aggregate to form J-type slipped stacks (**Figure 1.24a**), while the less twisted and less sterically encumbered bay-disubstituted PDIs display cofacial, rotationally-displaced H-type aggregation (**Figure 1.24b**).

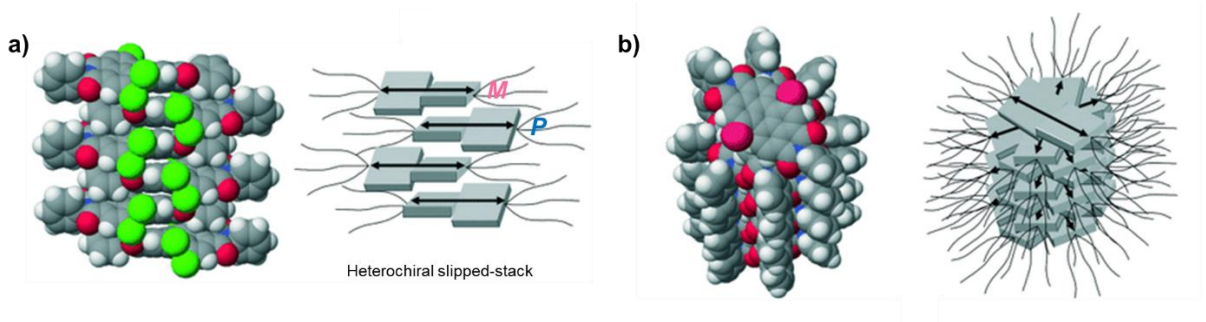

Figure 1.24: a) Slip-stacked J-type aggregate geometry adopted by the more sterically encumbered and more twisted bay-tetrasubstituted PDIs. **b)** Cofacial, H-type aggregate geometry adopted by the less sterically encumbered and less twisted bay-disubstituted PDIs. Whilst the initial paper by Würthner and co-workers[150] makes no mention of chirality, it is clear from the cartoon depictions of these stacks provided by the authors that J-type aggregation should preferentially occur between PDIs of opposite chirality (heterochiral aggregation), while cofacial H-type aggregation should occur between PDIs of the same chirality (homochiral aggregation). Adapted with permission from ref. 150. Copyright 2006 The Authors. Chemistry A European Journal published by Wiley-VCH GmbH.

Whilst at this point the authors make no mention of chirality, it is clear from the cartoon depictions of these stacks provided by the authors that J-type aggregation should preferentially occur between PDIs of opposite chirality (heterochiral aggregation), while cofacial H-type aggregation should occur between PDIs of the same chirality (homochiral aggregation). Later work, including the work described in this thesis,[108, 159] has shown that this is indeed the case. The authors also showed that in some solvents, bay-substituted PDIs preferentially form dimers before forming larger aggregates. For the case of 1,7-disubstituted PDIs they suggested that this is because, upon twisting, both bay substituents on the 1,7-PDI core point out on the same face

of the PDI, resulting in the PDI having one face that is less sterically hindered than the other face and therefore more available for stacking with another PDI (**Figure 1.25**).

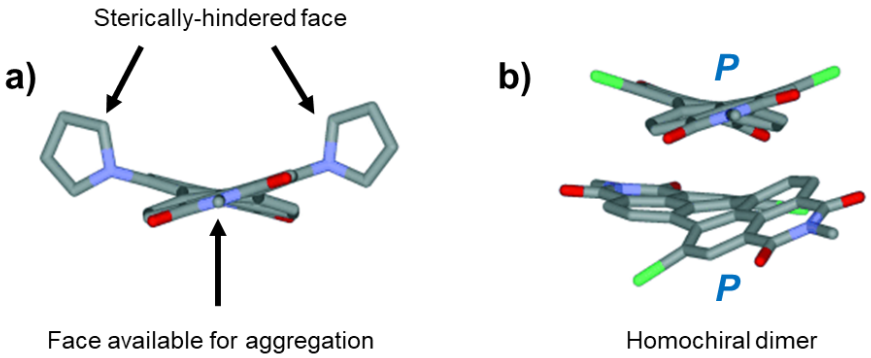

Figure 1.25: a) Depiction of the two faces of a 1,7-disubstituted twisted PDI. One face is less sterically encumbered than the other, making it more available for aggregation with other PDIs. This means that these PDIs tend to initially form dimers before forming larger aggregates, as shown in **(b)**. Adapted with permission from ref. 150. Copyright 2006 The Authors. Chemistry A European Journal published by Wiley-VCH GmbH.

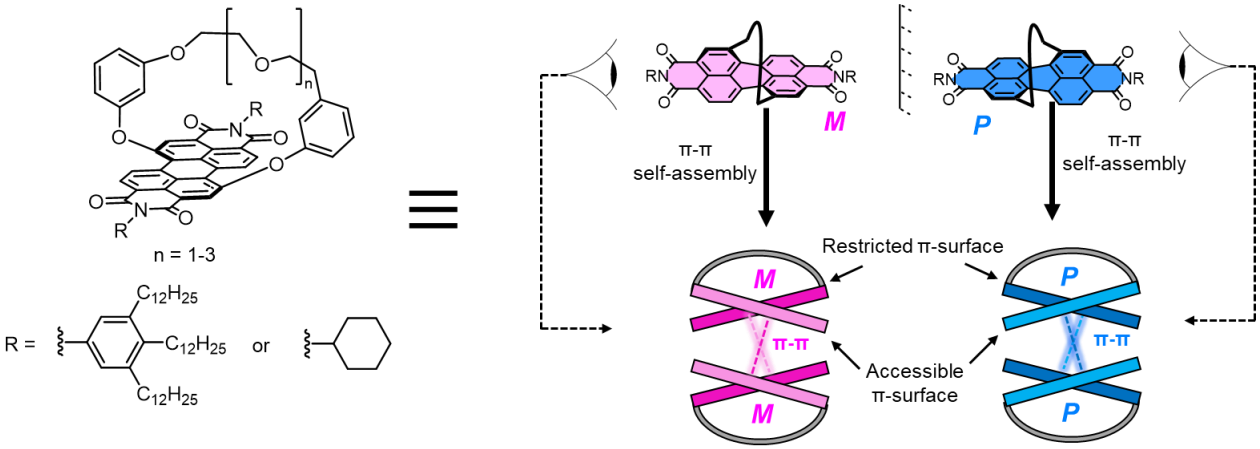

Figure 1.26: Chirally-locked 1,7-strapped PDIs reported by Safont-Sempere *et al.* [179-181] In these systems, one of the PDI faces is completely blocked by the macrocyclic strap, such that π–π stacking can only occur on one PDI face, leading to the exclusive formation of dimers.

This concept of 1,7-PDIs having two distinct faces with different stacking properties is most dramatically exemplified in a series of studies by the Würthner group led by Safont-Sempere where the self-assembly of chirally-locked 1,7-strapped PDIs was studied (**Figure 1.26**).[179-181] In these systems, one of the PDI faces is completely blocked by the macrocyclic

strap, such that π–π stacking can only occur on one PDI face, leading to the exclusive formation of dimers. Through single crystal X-ray crystallography and UV-vis aggregation titrations on enantiopure and racemic samples, the authors were able to show that these PDI assemble preferentially into cofacial H-type homochiral dimers. This can be rationalised by the better overlap of π-surfaces due to a complementary geometry in a homochiral dimer compared to a heterochiral dimer. Analysis of the concentration-dependent CD spectra showed that upon aggregation a Cotton effect appears in the spectrum corresponding to the formation of an *M*-helical dimer for a dimer of *P*-helical PDI cores, and vice-versa. Furthermore, it was shown that the length of the macrocyclic straps (n=1-3, **Figure 1.26**), which affects the rigidity of the twisted chiral conformation of the PDIs, also affects the fidelity of the homo-chiral self-sorting.[180] Studies of some of these systems in the liquid crystal phase showed that they still preferentially assemble into homochiral dimers within columnar stacks, but contacts between dimers are preferentially heterochiral, although the interactions between dimers are not driven by π–π stacking. [181]

1.11.3 J-type aggregation of chiral twisted PDIs driven by hydrogen bonding

In addition to PDI core-twist angle and sterics, a further powerful way to control the stacking of PDI cores is through the introduction of hydrogen-bonding (H-bonding) motifs. Introduction of H-bonding groups at the imide positions has turned out to be a very reliable way of making J-type aggregates.[149, 182] An interesting conclusion can be drawn from considering homochiral and heterochiral slipped-stack packing geometries: homochiral slipped-stacks will necessarily adopt a supramolecular arrangement with a helical pitch, while heterochiral ones will not and can instead form a more dense brickwork type arrangement (**Figure 1.27**).

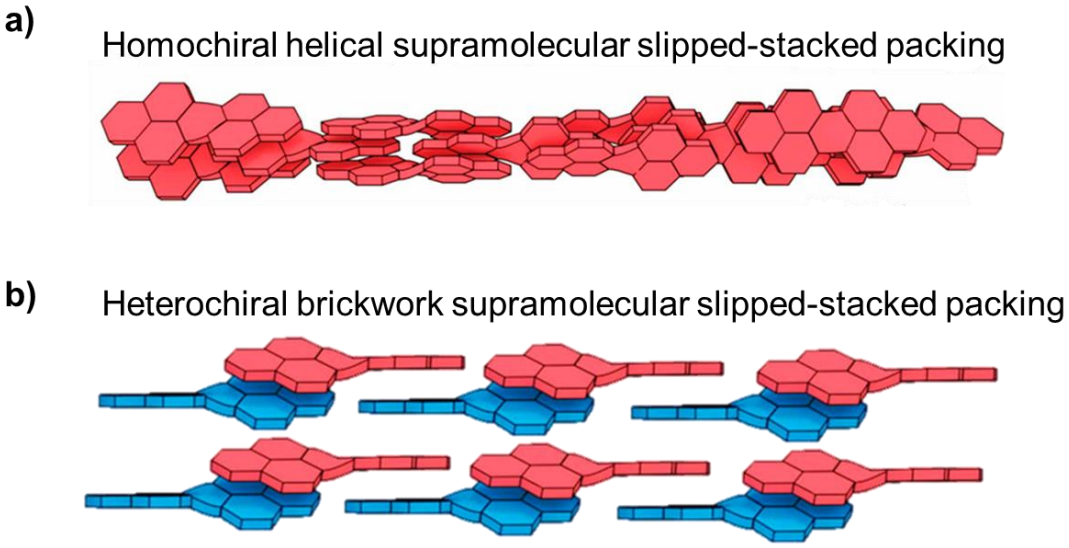

Figure 1.27: a) Cartoon depiction of a homochiral helical slipped-stack packing. **b)** Cartoon depiction of a heterochiral brickwork-like packing. Adapted with permission from ref. 182. Copyright 2020 American Chemical Society

Heterochiral brickwork packing is particularly common in the solid state, where the optimisation of molecular interactions in all directions is usually achieved by the densest 3D packing arrangement. For example, 1,2,5,6,7,8,11,12-octachloro-PDI with NH H-bonding imide groups adopts a brickwork-type packing in the crystal state driven by complementary H-bonding and π–π stacking where the π-contact between adjacent PDI cores is heterochiral (**Figure 1.28**).[183] The continuous π-overlap present throughout the assembly creates electron transport paths that make this material an excellent organic semiconductor.

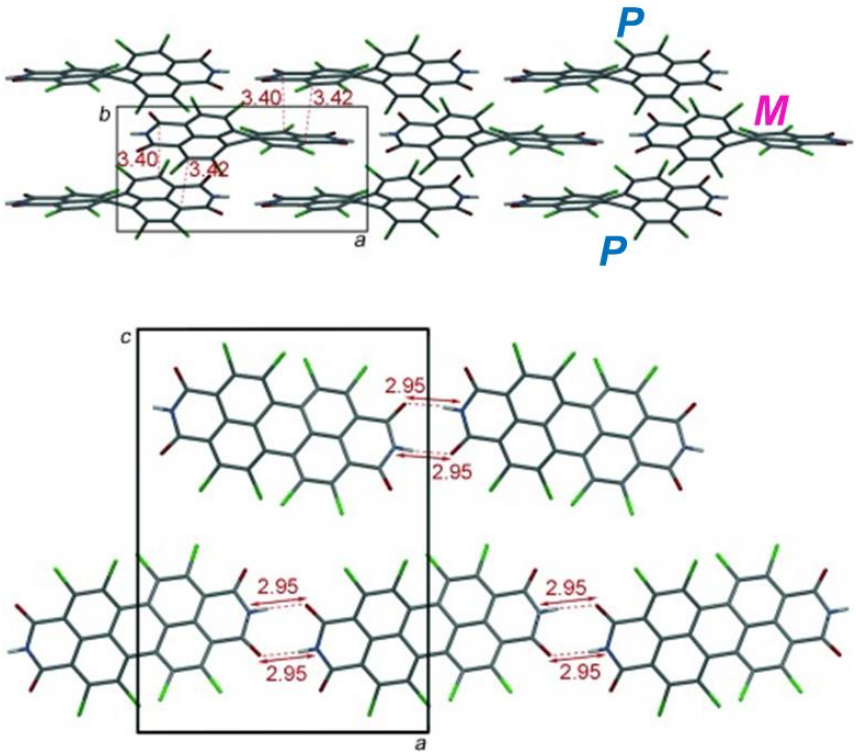

Figure 1.28: Crystal structure of 1,2,5,6,7,8,11,12-octachloro-PDI with free NH imide groups, which adopts a brickwork-type packing in the crystal state driven by complementary H-bonding between imide NH groups and π–π stacking between the PDI cores, where the π-contact between adjacent PDIs is heterochiral.[183] Adapted with permission from ref. 183. Copyright 2023 The Authors. Angewandte Chemie International Edition published by Wiley-VCH GmbH.

In solution however, homochirally stacked J-aggregates appear to be more common. The Würthner group has been the most prolific at studying PDI J-aggregates in solution. A particularly interesting design for a supramolecularly-engineered PDI J aggregate in solution is shown in **Figure 1.29**, where the PDI imide N-H groups are available for hydrogen bonding, while the extremely bulky bay substituents "shield" the PDIs from aggregation beyond a single J-aggregated strand, leading to the formation of a "rope-like" supramolecular polymer as confirmed by NMR spectroscopy and atomic force microscopy (AFM).[149] Concentration-dependent UV-vis spectroscopy shows an impressive red-shift in the absorption maximum from 570 nm for the monomer to 640 nm in the aggregate.

Interestingly, the self-assembly of the PDIs proceeds via a cooperative nucleation–elongation mechanism as opposed to an isodesmic model (**Figure 1.29b**). With systems bearing chiral R groups at the bay positions, the effects of chirality on self-assembly were impossible

to determine. However, the introduction of chiral R groups led to amplification of the observed CD signal upon self-assembly into the J-aggregate, suggesting strong homochirality in these aggregates.[184] This was observed even in mixtures of PDI compounds bearing achiral and homochiral R groups demonstrating so-called "sergeants and soldiers" behaviour.

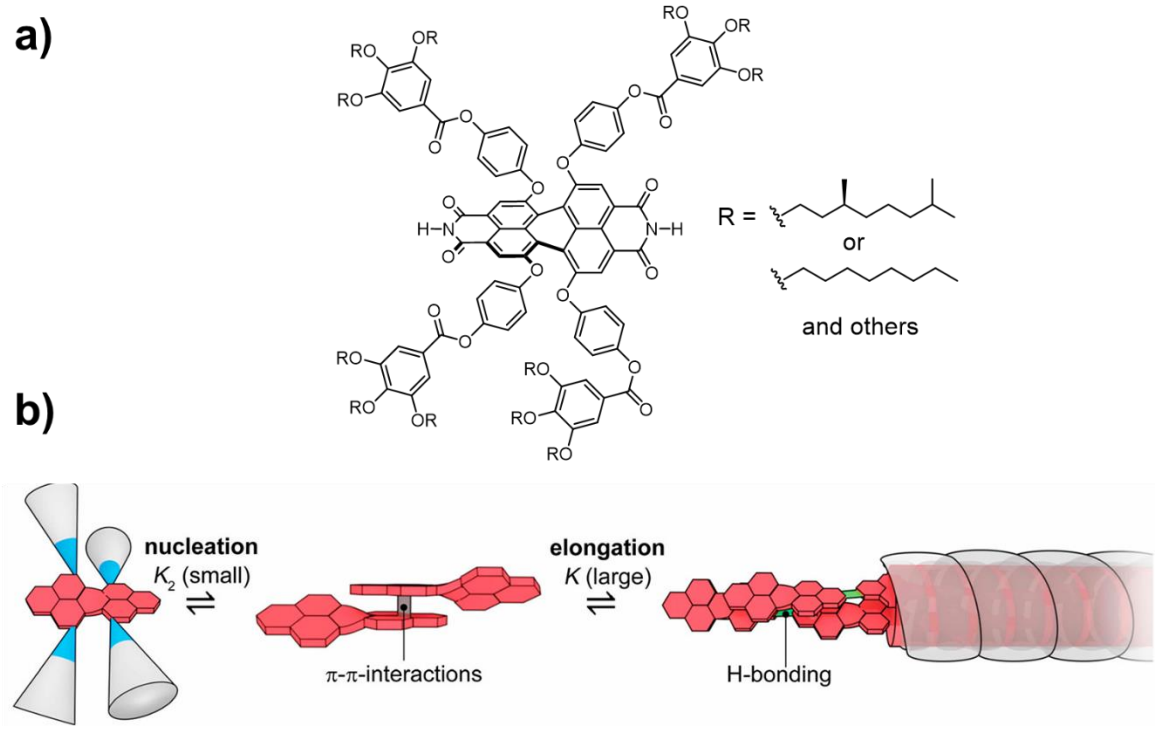

Figure 1.29: a) Structure of a PDI motif reported by the Würthner group which forms homochiral J-type "coiled rope" aggregates in solution. [149, 184] **b)** Cartoon depiction of the non-isodesmic "cooperative nucleation–elongation" mechanism for the formation of these aggregates in solution. Adapted with permission from ref 184. Copyright 2009 American Chemical Society

Whilst the systems shown in **Figure 1.29** exhibit dynamically chiral PDI cores, these can be modified to make the PDI cores chirally-locked by the introduction of a 2,2'-biphenoxy bridge at the 1,12-positions as shown in **Figure 1.30**, allowing resolution of the enantiomers by chiral HPLC. Enantiopure self-assemblies of this compound also lead to coiled rope chiral supramolecular polymers like that seen in **Figure 1.29**, but racemic mixtures instead form nanoparticles.[185]

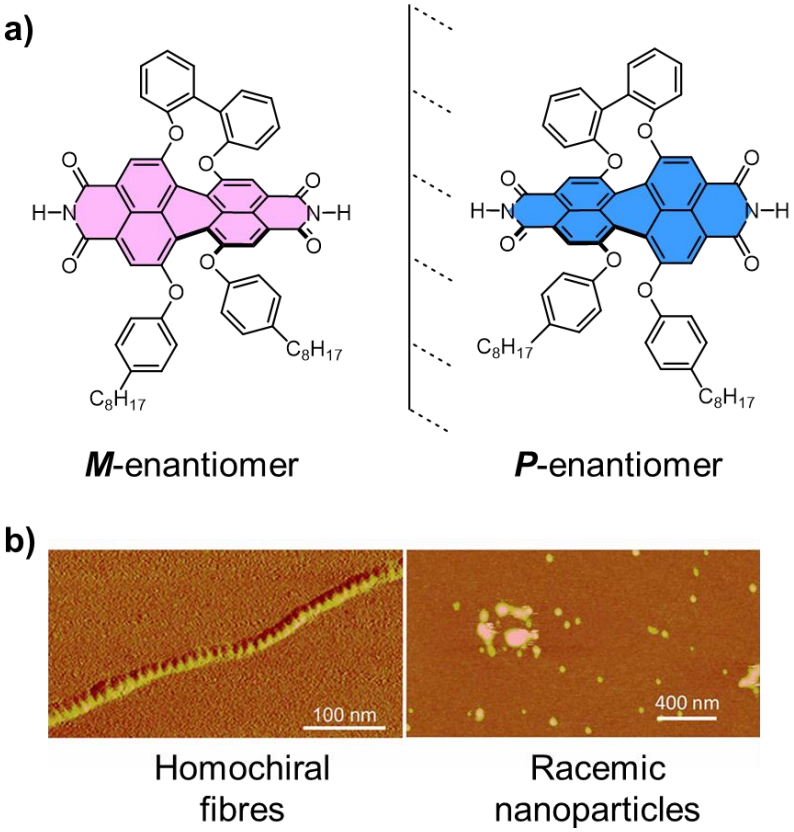

Figure 1.30: a) Structure of Chirally-locked PDI system reported by the Würthner group [185] which **b)** forms homochiral fibres when enantiopure but racemic mixtures form nanoparticles instead, as seen by AFM imaging. Adapted with permission from ref. 185 Copyright 2012 The Authors. Chemistry A European Journal published by Wiley-VCH GmbH.

The design principles outlined above (twisted PDI core, bulky bay substituents, and hydrogen bonding via free imide positions) have also been used to rationally design J-aggregates that form liquid crystals, gels,[186] and even supramolecular assemblies in water.[187] Furthermore, variation of the bay substituents to amino groups led to J aggregates with strong absorption deep into the NIR, with absorption maxima at up to 822 nm (**Figure 1.31**).[188]

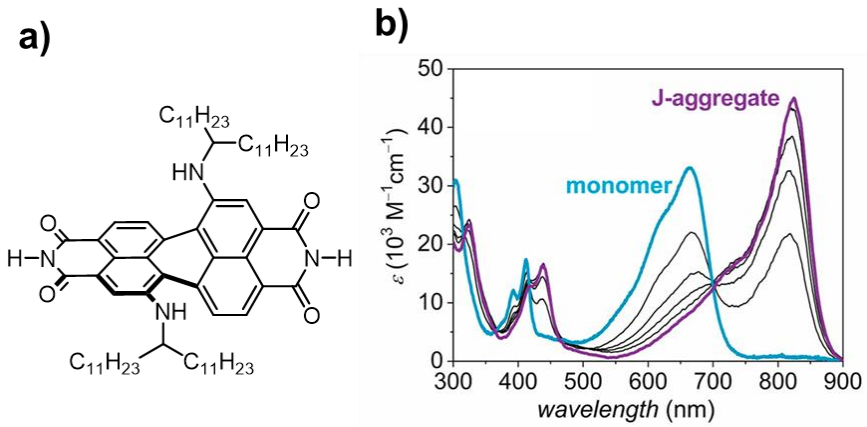

Figure 1.31: a) Structure and **b)** Concentration-dependent UV-vis-NIR absorption spectra of a PDI reported by the Würthner group which forms J-aggregates with absorption deep into the NIR. [188] Adapted from ref. 188 with permission from the Royal Society of Chemistry.

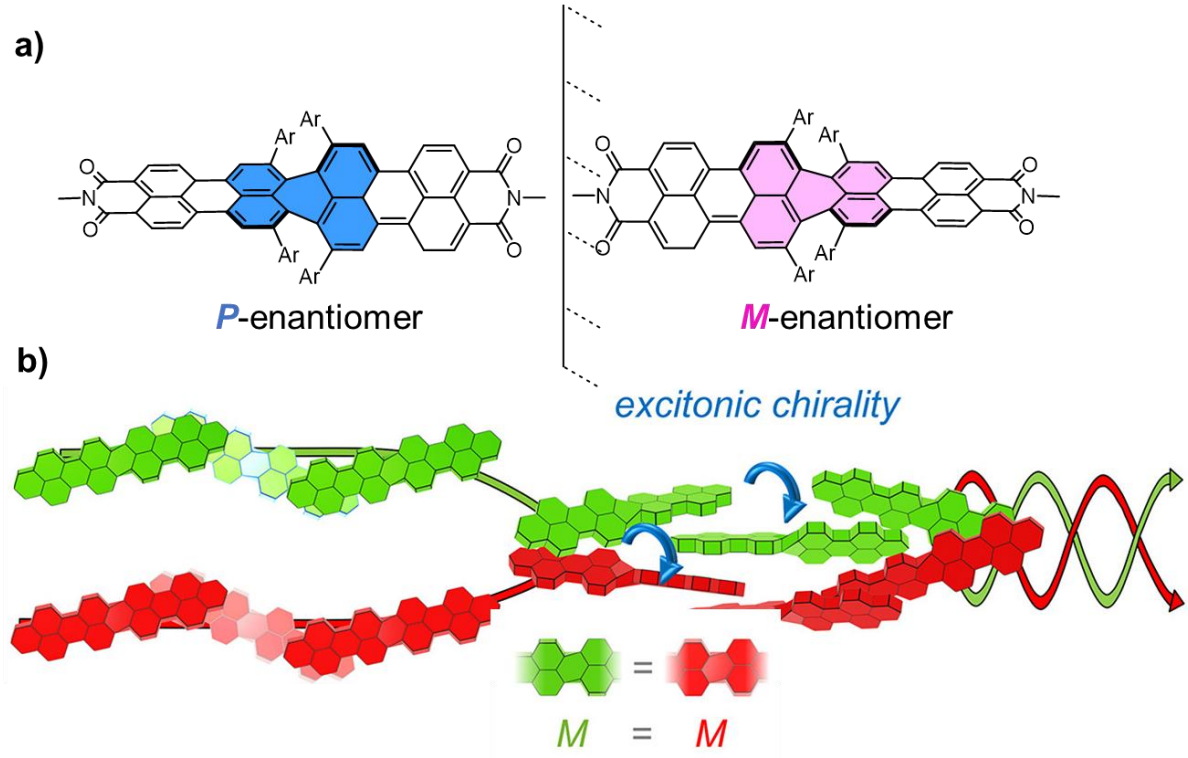

Figure 1.32: a) Structure of the enantiomers of a chirally-locked quaterrylene diimide. **b)** Enantiopure J-aggregate of a quaterrylene diimide reported by the Würthner group. [189] Adapted with permission from ref. 189 Copyright 2022 American Chemical Society.

Building on the above work, exciting advances in the rational design of chiral J-aggregates continue to be made. In 2023, Mahlmeister, Würthner and coworkers reported an enantiopure J-aggregate of quaterrylene diimides. [189] Quaterrylene diimides are structurally

similar to PDIs but with an extended π-system that allows them to absorb and emit light in the NIR region (Figure 1.32a).[144, 190, 191] Chirally locked versions of quaterrylene diimides were recently achieved by tetrasubstitution at the central perylene bay position with aryl groups (much like for tetraarylated PDIs, Figure 1.32a).[189] Self-assembly of chirally locked quaterrylene diimides with methyl groups at the imide positions leads to helical J-aggregates (Figure 1.32b) with deeply red-shifted absorption (897 nm) and emission (912 nm) maxima far into the NIR and $|g_{\mathrm{abs}}|$ values of up to 1.1×10^{-2} at 935 nm which is the highest reported dissymmetry factor in the NIR for an organic molecule.

1.12 Bis-PDI macrocycles

So far, we have explored chiral supramolecular assemblies of PDIs held together by non-covalent forces such as π–π stacking and H-bonding and directed by the chirality of the twisted PDI core. However, a further and very effective way to study PDI-PDI interactions is to strap two (or more) PDIs together using covalent bonds to form a macrocycle. A macrocycle containing two PDI cores is known as a bis-PDI macrocycle or bis-PDI cyclophane.

There are many motivations for studying bis-PDI macrocycles. Firstly, the preorganised macrocyclic architecture can hold the PDIs in close proximity, forming an *intra*molecular PDI dimer that can be studied at much lower concentrations than *inter*molecular PDI dimers. The dimer interaction in a macrocycle is therefore significantly stronger and more robust. Furthermore, the relative distance and orientation between the PDI cores, as well as their number (two), can be controlled by the macrocyclic architecture with much greater precision than in intermolecular assemblies, allowing for various geometries of π–π interactions to be studied in order to tune photophysical and electronic properties. Macrocyclic straps can also be used to conjugate the π-systems of the PDI cores via through-bond conjugation.[158] Additionally, macrocycles contain a cavity which if, large enough, can be used for the encapsulation of guest molecules,[192, 193] which has application in a diverse range of fields including sensing,[194] catalysis,[195] and organic electronic materials.[196, 197] Finally, from a chirality perspective, macrocycles containing chiral organic dyes have recently been driving the development of new chiroptical materials,[198, 199] including those that exhibit CPL.[33, 53, 200] In this section, we will cover a selection of the bis-PDI macrocycles most relevant to this thesis.

1.12.1 Imide-linked Bis-PDI macrocycles with planar PDI cores

In bis-PDI macrocycles, the PDI cores are most commonly linked together via the imide or bay positions. The earliest PDI macrocycles to be developed were cyclised via the imide positions due to the relative synthetic ease of functionalisation at these positions. The first PDI macrocycle to be developed was reported in 1998 by Langhals.[201] This cyclophane was prepared through the condensation reaction of PTCDA with 1,12-diaminododecane under high dilution conditions to avoid polymerisation. UV-vis spectroscopy revealed a blue-shifted absorption band relative to the PDI monomers, characteristic of H-type face-to-face stacking of the PDIs. Interestingly, the fluorescence spectrum reveals a strongly red-shifted emission band with a quantum yield of 40 %, which is relatively high for aggregated PDIs. Langhals attributes this to a slippage of the PDIs to form a J-type stack in the excited state, facilitated by the flexibility of the dodecyl chain. However, later work by Würthner suggests that, due to the broadness and lack of vibrational structure of the emission spectrum, this may instead be attributed to the formation of an emissive excimer state.[74, 202, 203] Calculations also suggest that this cyclophane is chiral in its lowest-energy conformations due to the torsional angle between the N-N longitudinal axes of the two stacked PDIs. This was demonstrated through CD spectroscopy, which showed a signal in the PDI region when the cyclophane was dissolved in the chiral solvent 1-phenylethylamine which biases the population towards one of the helical enantiomeric conformations.

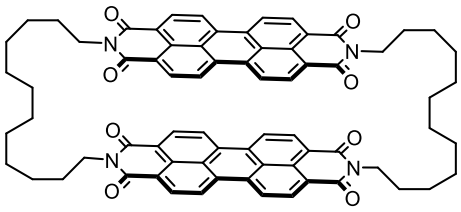

Figure 1.33: The first reported Bis-PDI macrocycle, reported by Langhals in 1998.[201]

Wasielewski and co-workers reported the macrocycle in **Figure 1.34**,[204] which was designed as a way to probe the proposed PDI dimer excimer state. The PDI units are forcibly held close together in an H-type stack by highly rigid linkers that prevent slippage of the PDIs to a J-type conformation, as could be envisaged for the more flexible cyclophane reported by Langhals (**Figure 1.33**). This was confirmed by UV-vis absorption spectroscopy. However, the emission spectrum was weak but strongly red-shifted to 790 nm, compared to 533 nm for the equivalent monomer PDI. This is attributed to mixing of the excitonically-split S_1 state with a

higher energy charge transfer (CT) state upon excimer formation.[205] This CT state is energetically available for mixing due to the short distance between the PDI cores (calculations suggest that the average distance between the planes of the PDI cores is 3.8 Å).

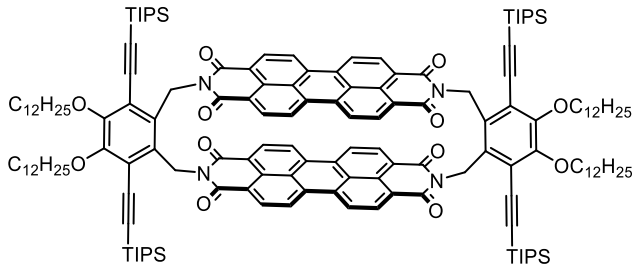

Figure 1.34: Bis-PDI macrocycle reported by Wasielewski and co-workers [204].

In 2012 Würthner and co-workers reported a bis-PDI cyclophane that can be used to study the impact of PDI redox states on the PDI-PDI interaction (**Figure 1.35**).[206] Each PDI core can be successively and reversibly reduced to the radical anion and dianion. In the neutral state, the emission and absorption spectra reveal clear signs of H-type cofacial stacking, with an increase in the 0-1 vibronic peak intensity relative to that of the 0-0 band. However, successive reduction of the PDIs causes the PDIs to repel each other electrostatically, expanding the size of the macrocyclic cavity. This is evidenced by spectroelectrochemistry, with the mono-reduced (PDI-$PDI^{\bullet -}$) and di-reduced ($PDI^{\bullet -}$- $PDI^{\bullet -}$) species showing CT bands in their UV/vis/NIR spectra which requires close spatial proximity between the PDI cores. In contrast the fully tetra-reduced species (PDI^{2-}- PDI^{2-}) shows no such CT bands, indicating a longer PDI-PDI distance.

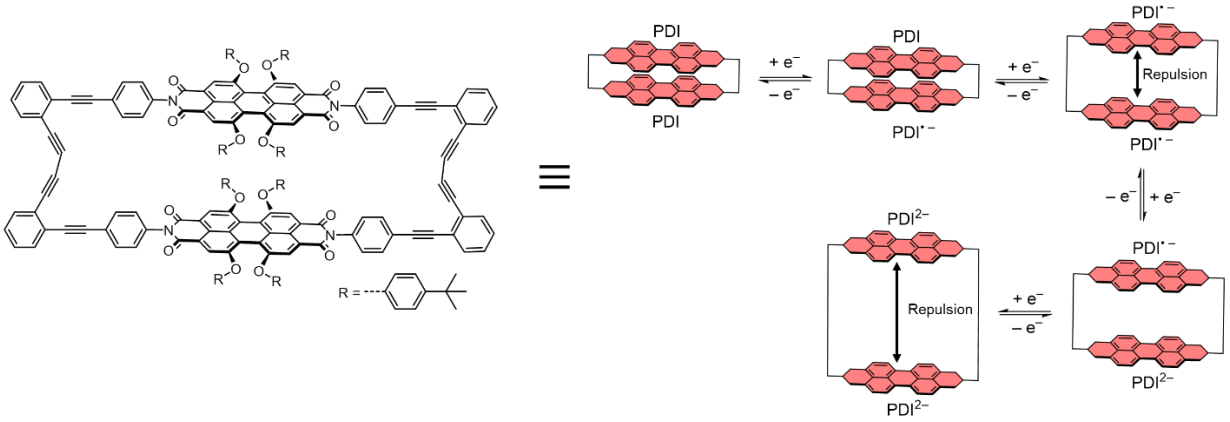

Figure 1.35: Bis-PDI cyclophane used Würthner and co-workers to study the impact of PDI redox states on the PDI-PDI interaction. [206]

More recently, similar redox behaviour was observed by the Champness group in a mechanically-interlocked "molecular handcuff " bis-PDI system (**Figure 1.36**).[207] While strictly speaking it is not a bis-PDI macrocycle, the similarity with other systems described here is clear. In this handcuff, H-aggregation and excimer emission is also observed in the neutral state. Upon mono-reduction to the (PDI-PDI$^{\bullet\,-}$) state, full delocalisation of the additional electron between the two PDI chromophores is observed by electron paramagnetic resonance (EPR) spectroscopy. Electronic communication is also observed in the spectroscopic features of the (PDI$^{\bullet-}$-PDI$^{\bullet\,-}$) species, which as seen by spectroelectrochemistry displays broad, redshifted absorption that is not usually observed in mono or di-reduced PDI monomers. However, the fully-reduced (PDI$^{2\,-}$- PDI$^{2\,-}$) species shows the same spectroscopic features as a non-interacting monomeric $(PDI)^{2-}$ species.

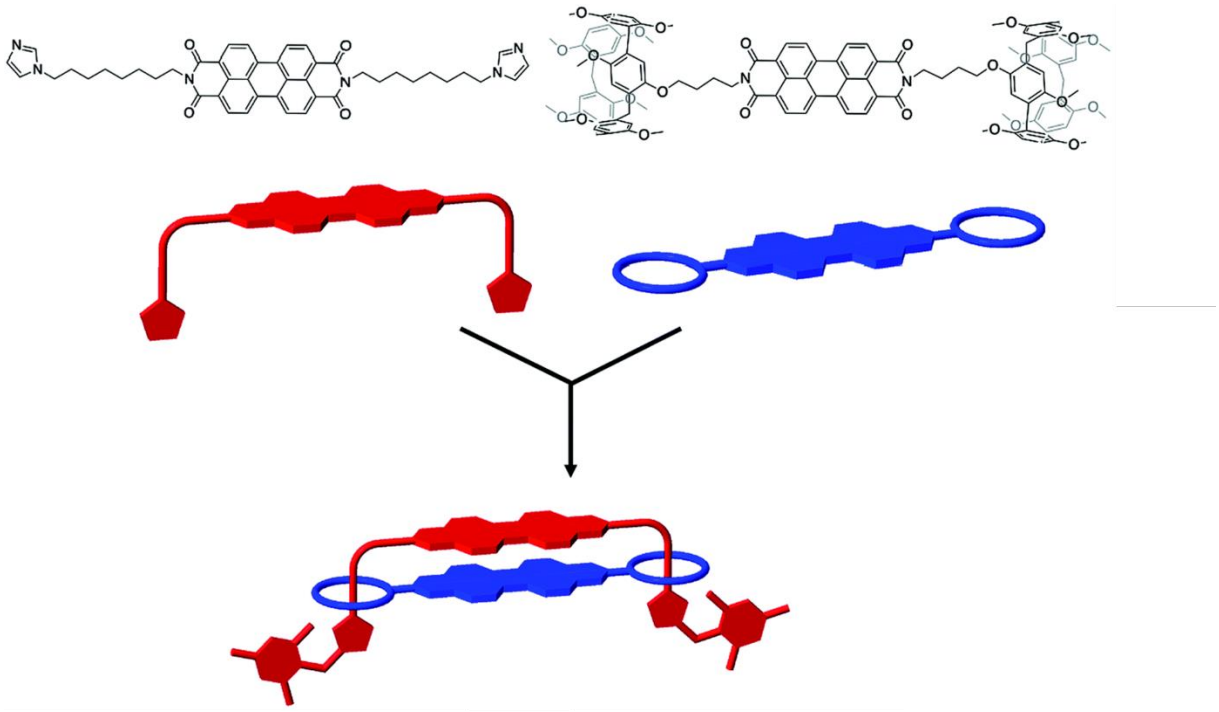

Figure 1.36: "Molecular handcuff" bis-PDI system reported by Champness and co-workers. [207] Adapted from ref. 207 with permission from the Royal Society of Chemistry.

1.12.2 Imide-linked Bis-PDI macrocycles with twisted PDI cores

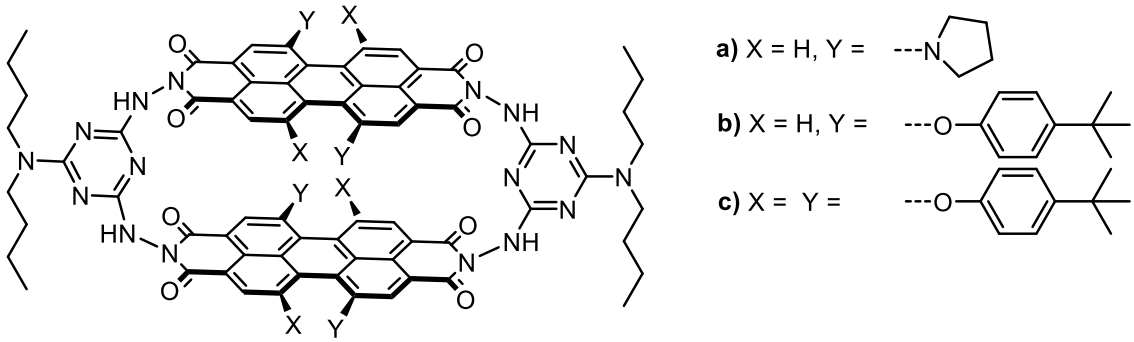

Figure 1.37: Structure of the cyclophanes with twisted PDI cores reported by Jiang and Li in 2008. [208]

The cyclophanes in **Figure 1.37** with twisted PDI cores reported by Jiang and Li, were designed in order to probe the effects of different bay substituents on PDI-PDI interactions.[208] The bay tetrasubstituted cyclophane **(Figure 1.37c**) formed in a very low yield of only ~ 3 %, presumably due to the high steric repulsion between the PDIs afforded by the bulky bay groups preventing H-aggregate templation as a prior step to macrocyclisation. Most interestingly, bay-disubstituted cyclophanes **(Figure 1.37a-b**) both formed as mixtures of two isomers, indicating

that the PDI cores cannot rotate about the imide bonds due to steric congestion. These isomers were successfully isolated for the di-pyrrolidine analogue (**Figure 1.37a**) through preparative TLC. These were characterised by COSY and ROESY NMR and were determined to be *trans* and *cis* configurations of the bay substituents on each PDI (**Figure 1.38**). These isomers have small differences in their absorption spectra, with the *cis* isomer exhibiting a greater blue-shift than the *trans* isomer in the main absorption band, relative to a control monomer PDI. This is attributed to a smaller PDI-PDI distance and a smaller torsion angle between the N,N axes in the *cis* isomer, facilitated by less steric repulsion between the bay substituents than in the trans isomer.

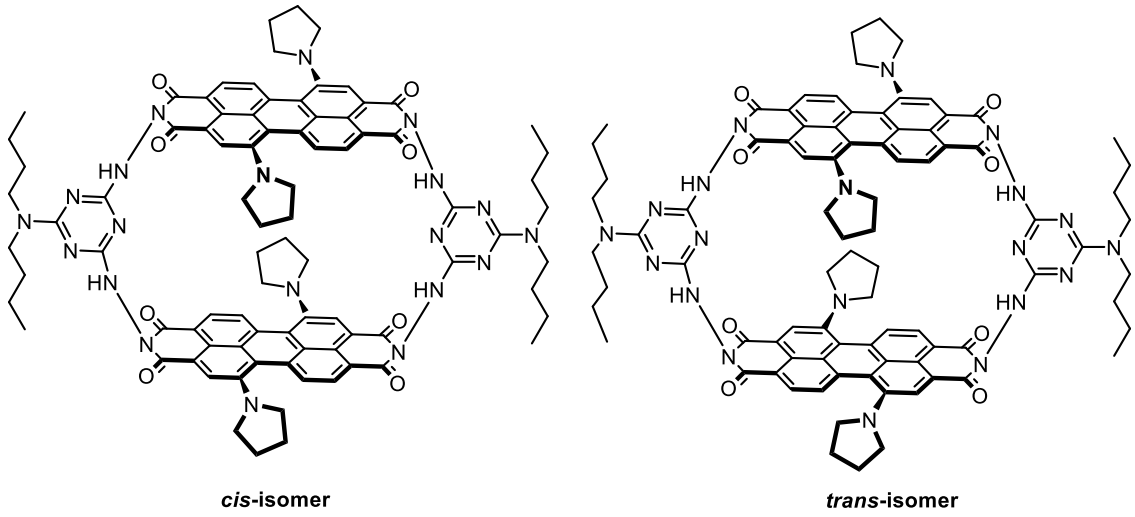

Figure 1.38: Structures of the *trans*- and *cis*- isomers of a 1,7-dipyrolidine bis-PDI cyclophane. [208]

The para-xylene bridged cyclophane scaffold in **Figure 1.39** originally reported by Spenst and Würthner in 2015, has been used extensively for a variety of guest-sensing applications.[194] This scaffold has a PDI-PDI distance of ~ 6.5 Å and is highly rigid, forming an ideal cavity for the encapsulation of aromatic guests. This cyclophane was initially developed as a sensor capable of distinguishing π-electron-rich from π-electron-poor aromatic molecules. For electron-poor guests such as 9-fluorenone, biphenyl and naphthalene, a noticeable increase in the fluorescence quantum yield of the cyclophane is detected upon binding of the guest. This is postulated to arise from the guest disrupting electronic coupling between the PDI chromophores. In contrast a dramatic quenching of fluorescence is observed upon encapsulation of electron-rich guests such as perylene, anthracene, carbazole and pyrene. This is attributed to the formation of less emissive CT states. A red-shift of the emission maximum is also observed

due to emissions originating from these CT states. Interestingly, binding studies revealed a selectivity towards more flexible guest molecules. For example, the binding constant K_a is 100 times greater for phenylnaphthalene than for pyrene. It is proposed that the cyclophane has a distorted cavity due to the twist in the PDI cores induced by the four bulky bay substituents, and so more flexible guests can adapt to the distorted geometry of the cavity more easily.

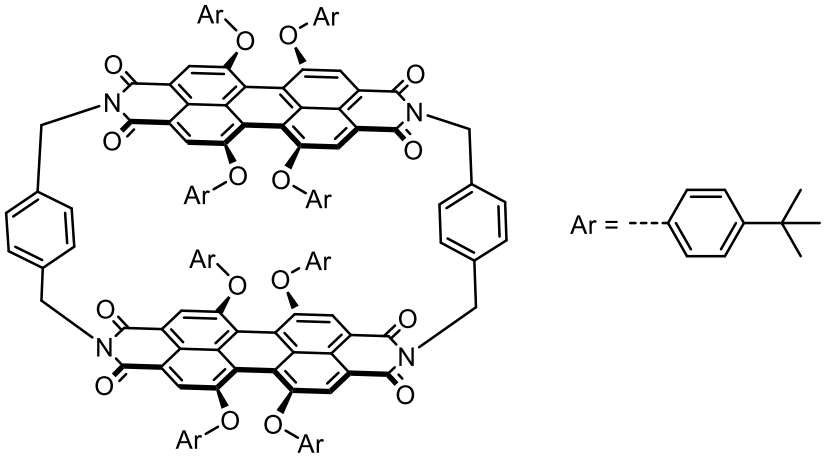

Figure 1.39: Structure of the para-xylene-bridged cyclophane reported by Spenst and Würthner in 2015.[209]

A further study was published by the Würthner group exploring the photophysical properties of this cyclophane in more detail (**Figure 1.40**).[209] The fluorescence emission spectrum exhibits no signs of excimer formation, in contrast to other reported bis-PDI macrocycles. This is attributed to the relatively large PDI-PDI distance in the para-xylyl-spaced cyclophane. Cyclic voltammetry and transient absorption spectroscopy experiments revealed that, in polar solvents such as CH_2Cl_2, the photoexcited singlet state of the PDI core instead decays via symmetry-breaking charge separation (SB-CS), with an electron being transferred from one PDI core to the other. The charges can then recombine slowly to form a PDI excited triplet state, which can subsequently decay to the PDI ground state by reacting with any oxygen present in the vicinity to generate singlet oxygen in up to 27% quantum yield. Quantum yields for triplet generation in PDIs are typically very low (< 1%), so these findings represent an exciting development in the field. SB-CS is prevented in non-polar solvents like toluene, while binding electron-rich guests such as anthracene leads to intermolecular CT between the cyclophane and the guest. A recent study has shown that SB-CS can occur in other cyclophanes with longer PDI-PDI distances, but with the rate of SB-CS decreasing as the PDI-PDI distance is increased.[210]

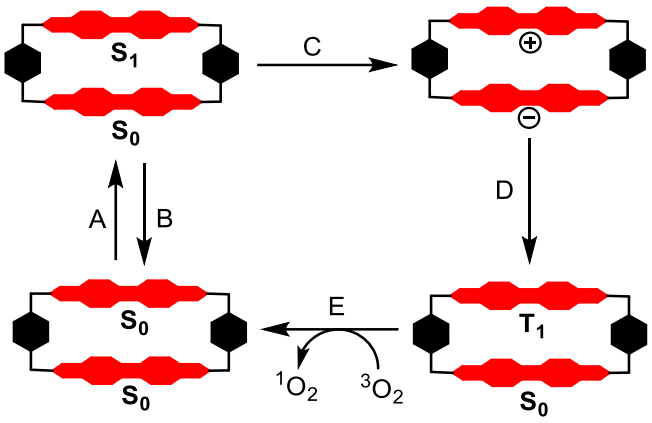

Figure 1.40: Cartoon depiction of the excited state photochemistry of the para-xylene-spaced cyclophane originally reported by Spenst and Würthner**.** [194, 209] **A)** Photon absorption leading to $S_0 \rightarrow S_1$ excitation in one of the PDI chromophores. **B)** Emission in toluene. **C)** Symmetry-breaking charge separation in CH_2Cl_2. **D**) Recombination to the PDI triplet state. **E)** Decay of triplet state to ground state via reaction with triplet oxygen to generate singlet oxygen.

1.12.3 Chirality in imide-linked Bis-PDI macrocycles with twisted PDI cores

Dynamically-chiral imide-connected bis-PDI macrocycles

The dynamic chirality of the para-xylene-spaced cyclophane reported by Spenst and Würthner has also been investigated.[211] Due to the twist in the PDI structure induced by the bulky bay substituents, each PDI core can locally be an ***M*** or ***P*** enantiomer (**Figure 1.42**). Hence the cyclophane can exist as three stereoisomers: the (***M***,***M***) and (***P***,***P***) enantiomers and the (***M***,***P***)/(***P***,***M***) meso isomer (**Figure 1.41**). These stereoisomers exist in a rapidly-exchanging dynamic equilibrium, so at room temperature only one set of proton signals is observed in the ^{1}H NMR spectrum. However, at a lower temperature (260 K) two sets of peaks are observed in a signal ratio of 2:1 for (***M***,***M***)/(***P***,***P***) : (***M***,***P***)/(***P***,***M***) instead of the statistically-expected 1:1 ratio. This is attributed to intramolecular homochiral recognition between the PDI cores in the cyclophane, such that the enantiomeric (***M***,***M***) and (***P***,***P***) stereoisomers are stabilised relative to the meso isomer. The chiral guest recognition properties of **6a** were investigated by circular dichroism (CD) spectroscopy. A large CD signal in the PDI region was detected upon encapsulation of several different chiral guests, indicating that chiral guests can induce a shift in the conformational equilibrium of the cyclophane stereoisomers by binding preferentially to one of the enantiomers of the cyclophane.

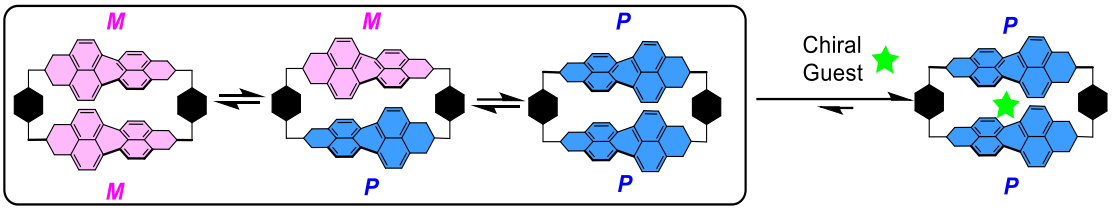

Figure 1.41: Cartoon depiction of the conformational equilibrium between the (*M*,*M*), (*P*,*M*)/(*M*,*P*) and (*P*,*P*) stereoisomers of a para-xylene spaced bis-PDI cyclophane, along with induction of chirality in the cyclophane upon chiral guest encapsulation (a bias towards (*P*,*P*) is shown here arbitrarily, but the favoured cyclophane enantiomer will depend upon the chirality of the guest). Heteroatoms and core substituents have been removed for clarity.[211]

Homochiral recognition has been observed in other PDI macrocycles. For example, in a study by Li, it was shown that the macrocycle in **Figure 1.42** forms exclusively as the homochiral (***M***,***M***) and (***P***,***P***) isomers, with no heterochiral (***M***,***P***)/(***P***,***M***) forming.[212] The homochiral macrocycles remain isomerically pure at 278K, but slowly equilibrate at room temperature to form a 1:1 mixture of homochiral and heterochiral stereoisomers. This implies that homochiral macrocycle formation is faster than heterochiral macrocycle formation, but once the macrocycle is formed there is no preference for the homochiral isomers. This may be due to the bulky tetra-chloro PDI cores disfavouring PDI-PDI π–π contacts.

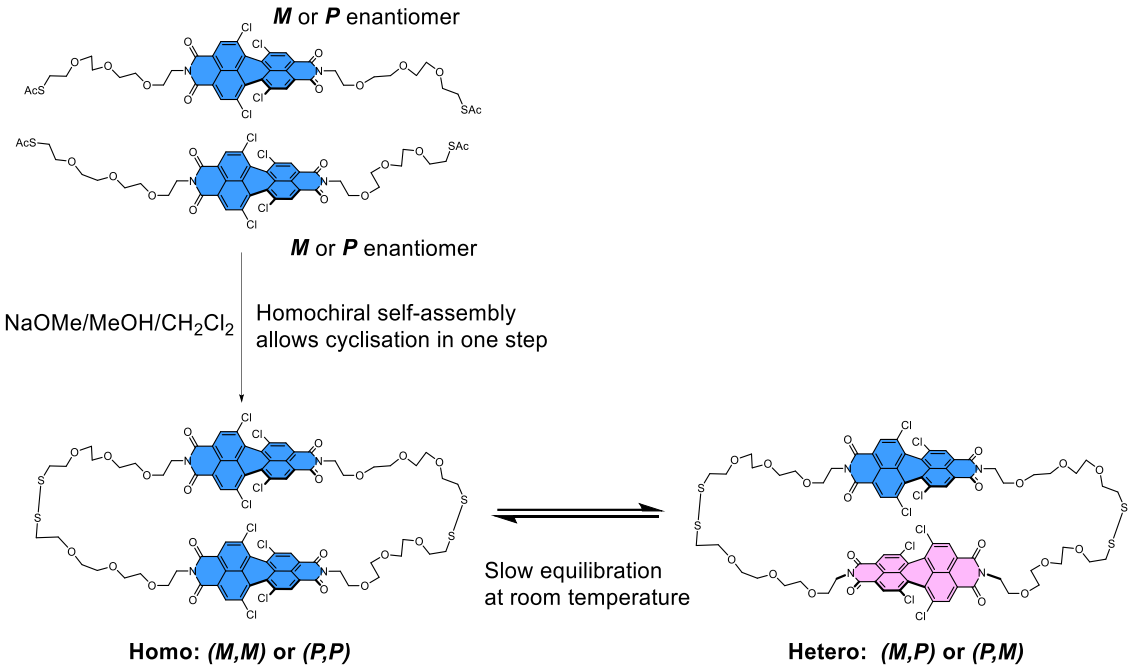

Figure 1.42: Synthesis of the macrocycle reported by Li, where cyclisation in one step is facilitated by homochiral self-assembly prior to cyclisation.[212]

More recently, Solymosi, Pérez-Ojeda, Hirsch and co-workers reported a bis-PDI macrocycle where the ***MM/PP*** and ***MP*** stereoisomers exist in a dynamic equilibrium in a 10:1 ratio as observed by ^{1}H NMR in deuterated 1,1,2,2-tetrachloroethane solvent (**Figure 1.43**), with complete diastereoselectivity for the ***MM/PP*** enantiomer pair observed in deuterated dichloromethane.[213] This strong selectivity for the homochiral pair may be attributed to a stronger cofacial homochiral π–π interaction facilitated by the more flexible bay-phenoxy substituents that can get out of the way upon aggregation, in contrast to the bay-chloro substituents in the macrocycle reported by Li.

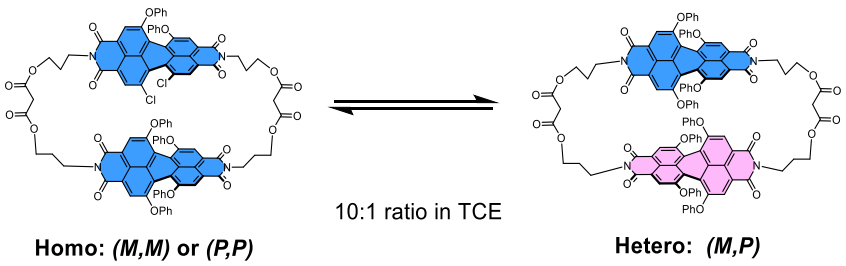

Figure 1.43: Dynamically-chiral bis-PDI macrocycle reported by Solymosi, Pérez-Ojeda, Hirsch and co-workers, which exhibits strong diastereoselectivity for the homochiral enantiomer pair over the heterochiral diastereomer.[213]

Interestingly, whilst this dynamically-chiral macrocycle displays strong selectivity for the homochiral pair of enantiomers in solution, in the crystalline state it adopts a heterochiral conformation in order to maximise the strength of both inter- and intra-molecular π–π interactions and crystal density (**Figure 1.44**).[214]

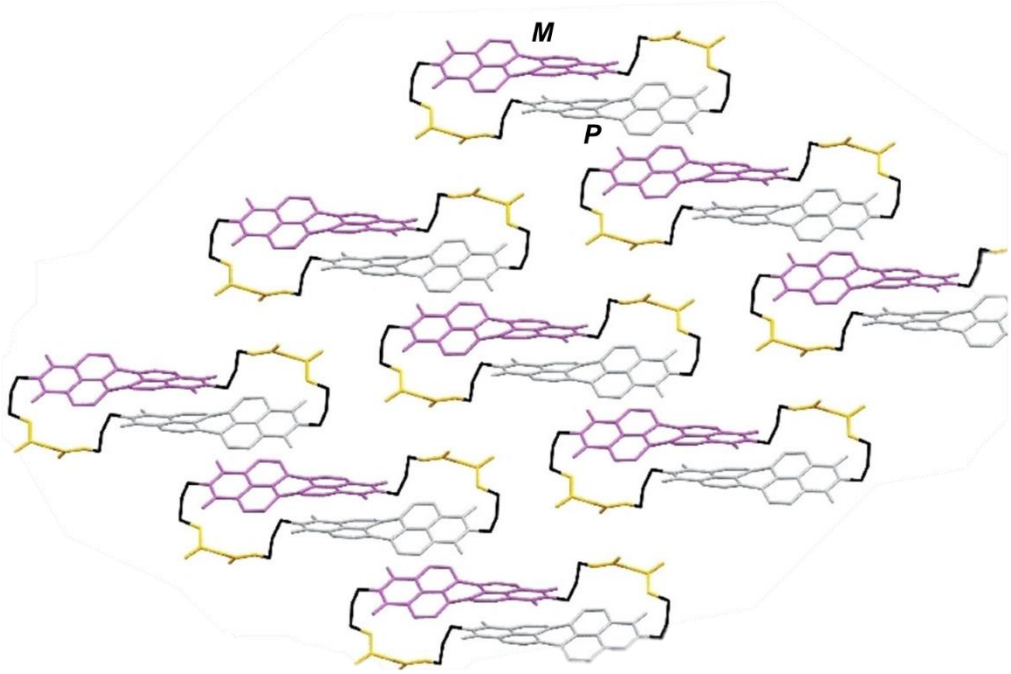

Figure 1.44: Heterochiral conformation adopted by Solymosi's macrocycle in the crystalline state, in order to maximise both inter- and intra-molecular π–π interactions and crystal density. Figure adapted from ref. 214 with permission from ChemistrySelect. Copyright 2023 The Authors. ChemistrySelect published by Wiley-VCH GmbH.

Chirally-locked imide-connected bis-PDI macrocycles

Very recently, the Würthner group has been developing chirally-locked versions of the same para-xylene spaced bis-PDI cyclophane scaffold. In 2021 they reported a version of this cyclophane scaffold with macrocyclic straps connecting the 1,7 positions of each PDI in order to lock the chirality, making the stereoisomers stable and separable by chiral HPLC (**Figure 1.45**).[198]

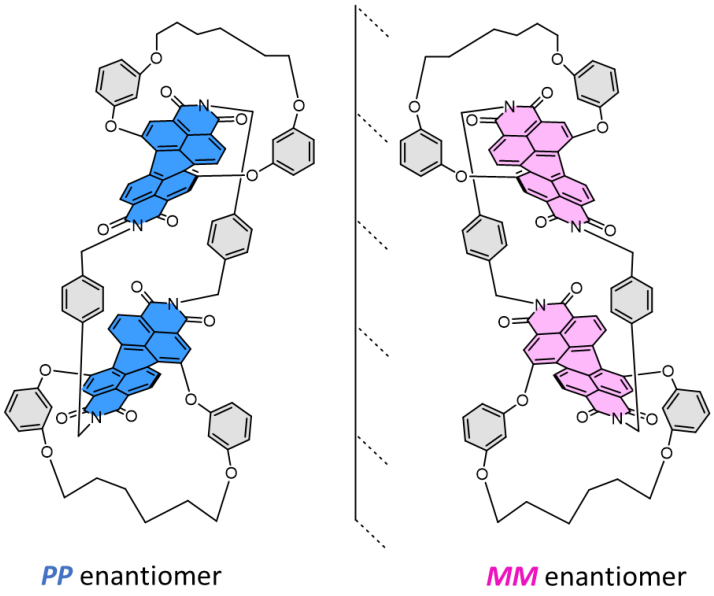

Figure 1.45: Chirally-locked version of the para-xylene spaced bis-PDI cyclophane scaffold, achieved by strapping each PDI more with itself via the 1,7 positions to maintain the core twist. [198]

These systems were used to investigate the chiral molecular recognition properties of these macrocycles. The guest molecules [4]helicene and [5]helicene were chosen as they exist as two enantiomers but with a low energy barrier for interconversion, so are not chirally locked, with the enantiomers of [5]helicene interconverting significantly more slowly than for [4] helicene. Through UV-vis titration experiments, involving enantiopure cyclophane and initially-enantiopure [5]helicene, it was found that homochiral binding is stronger, with the ***PP*** enantiomer of the cyclophane preferentially binding ***P***-[5]helicene, and vice-versa. Additionally, through crystallography, 2D NMR studies, and CD binding titrations, it was shown that the preferential homochiral binding of these guests to helicenes can de-racemise an initially racemic mixture of helicene guests (**Figure 1.46**). Additionally, recent studies have also explored how the rigid, curved chiral π-surfaces of the macrocyclic cavity catalyses the enantiomerisation of enantiopure 5[helicene],[215] as well the inversion of the bowl-conformation of corannulene.[216]

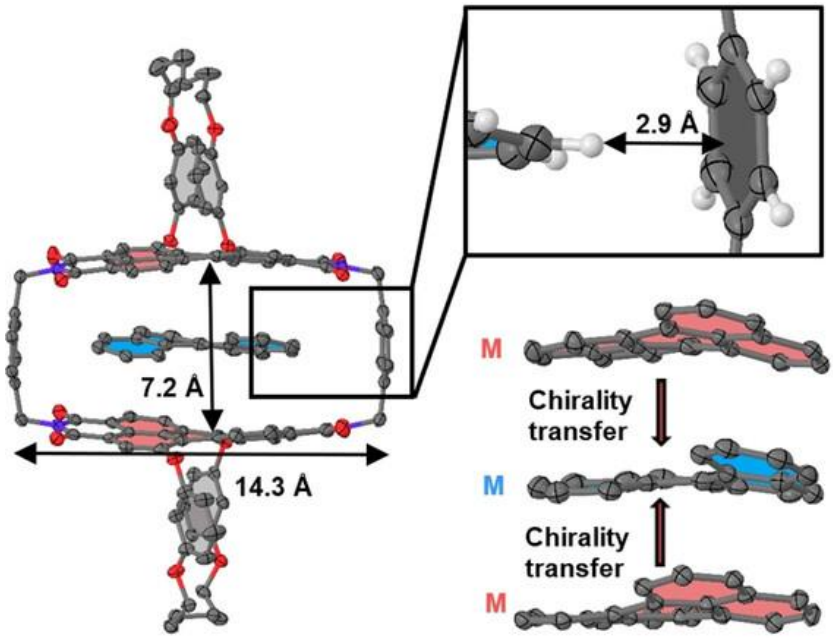

Figure 1.46: Crystal structure of the cyclophane depicted in **Figure 1.45**, showing transfer of chirality from the homochiral cyclophane to a dynamically-chiral co-crystallised guest molecule. Figure adapted with permission from ref. 198. Copyright 2021 The Authors. Angewandte Chemie International Edition published by Wiley-VCH GmbH.

In 2023 the Würthner group reported another xylene-spaced bis-PDI cyclophane which was chirally-locked through a different strategy using tetrasubstitution with bulky groups at the bay positions of the PDIs (**Figure 1.47a**).[199] Interestingly, these systems showed preferential heterochiral rather than homochiral guest recognition. For example, the ***PP*** enantiomer of this cyclophane preferentially binds ***M***-5[helicene]. This was attributed to additional interactions between the helicene guests and the phenyl bay substituents (**Figure 1.47b**).

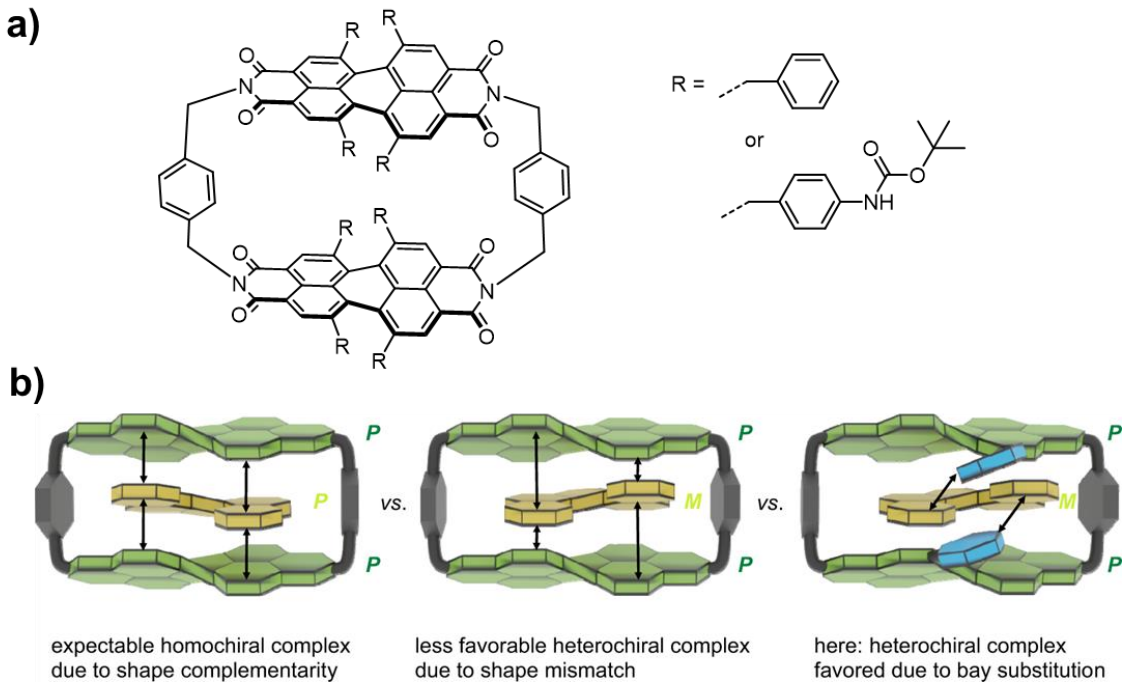

Figure 1.47: a) Para-xylene-spaced bis-PDI cyclophane reported by the Würthner group where chiral locking is achieved through tetrasubstitution with bulky groups at the bay positions of the PDIs. [199] **b)** Cartoon outlining why this cyclophane exhibits preferential heterochiral guest recognition. Figure adapted from ref 199 with permission with permission from Springer Nature.

1.12.4 Bay-strapped bis-PDI macrocycles

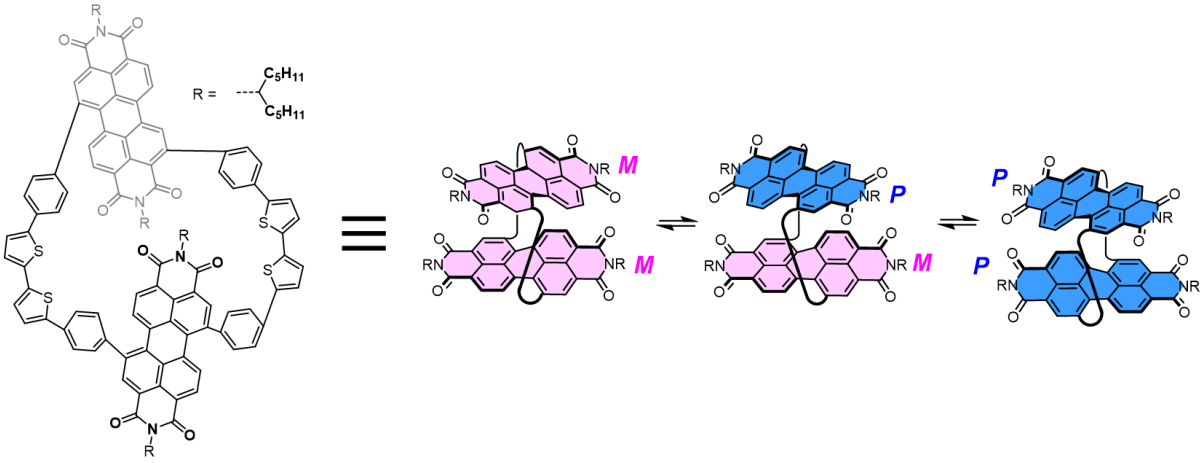

Figure 1.48: "Chiral conjugated corral" bay-connected bis-PDI macrocycle reported by the Nuckolls group.[158]

An alternative strategy for generating bis-PDI macrocycles is to strap the two PDIs together via the bay positions. For example, the Nuckolls group has reported the rather remarkable "conjugated corral" macrocycle in **Figure 1.48** that is both fully conjugated and chiral.[158] The macrocycle is comprised of two PDI cores bridged together with dithiophene linkers. This results in a conjugated system with an elliptical cavity. Due to the twisting of the PDI cores induced by bay-strapping, the macrocycle exists as three different stereoisomers: the enantiomers *MM* and *PP* and the meso isomer *MP*. These stereoisomers were separated by chiral HPLC. Although they interconvert at room temperature, they do so slowly enough to be analysed by CD spectroscopy, allowing the stereoisomers to be assigned as above. Subsequent iterative HPLC analysis of an initially pure sample of *MM* showed that the meso isomer *MP* appears before the other enantiomer *PP*, suggesting that the meso isomer is an intermediate in the interconversion between the two enantiomers. However, the fact that the stereoisomers interconvert was unexpected. Indeed, bay strapping of the PDIs in this macrocycle does not allow interconversion by axial twisting of the PDIs, as this would induce too much strain in the macrocycle.[156] Therefore, the mechanism of interconversion must occur through a "somersault" motion, with one of the PDI imide heads passing through the centre of the cavity (**Figure 1.49**).

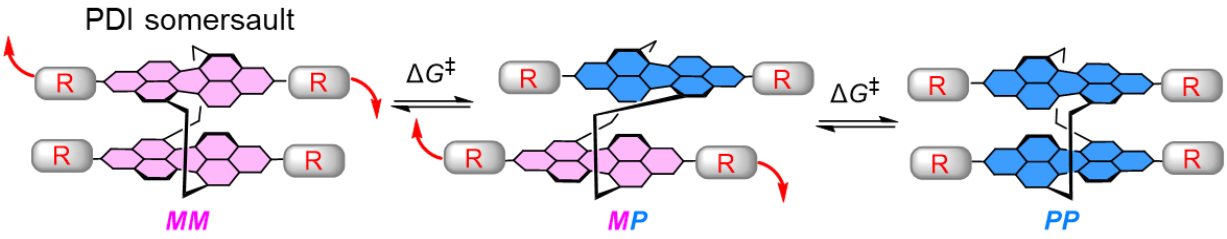

Figure 1.49: Intramolecular "somersault" motion of the PDI imide heads through the centre of the macrocyclic cavity, necessary for stereoisomer interconversion in bay-strapped bis-PDI macrocycles.

The corral macrocycle also has a very large, curved cavity with a PDI distance of ~ 16 Å (**Figure 1.50a**). The cavity is lined with the large π surfaces of the PDIs and the Lewis-basic sulphur atom lone pair, making it an ideal host for binding fullerenes through π-π and n-π interactions. This was explored by Barendt, Nuckolls and co-workers, who reported binding of various fullerenes including C_{60} and C_{70}, and used the host-guest complexes to build OFET devices (**Figure 1.50b**) that performed better than either the macrocycle or the fullerene on their own.[217]

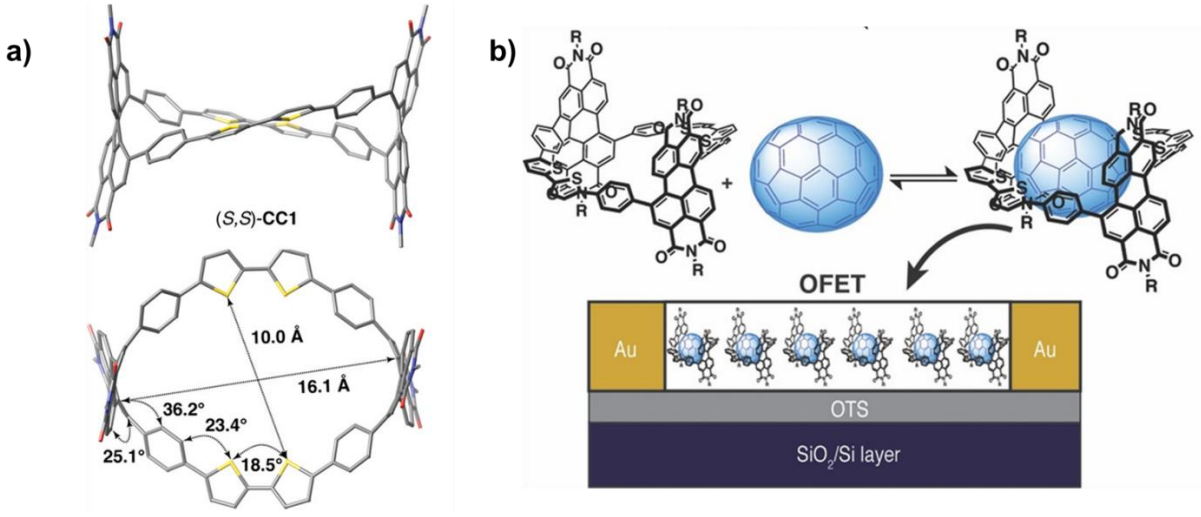

Figure 1.50: a) DFT-minimised model of the "chiral conjugated corral" macrocycle. [217] **b)** Cartoon depiction of this macrocycle being used to bind fullerene, and the resulting complex being used in an OFET. Figure adapted from ref. 217 with permission. Copyright 2020 Wiley-VCH Verlag GmbH & Co. KGaA, Weinheim

In a similar vein, the group of Valiyaveettil reported a bay-strapped bis-PDI macrocycle with meta-diphenoxy linkers capable of binding selectively the *Z*-isomer of azobenzenes in its tubular cavity in preference to the *E*-isomer.[218] Alongside the "corrals" macrocycle, these were

the only two bay-strapped bis-PDI macrocycles reported before the work described in **Chapter 2** was published.

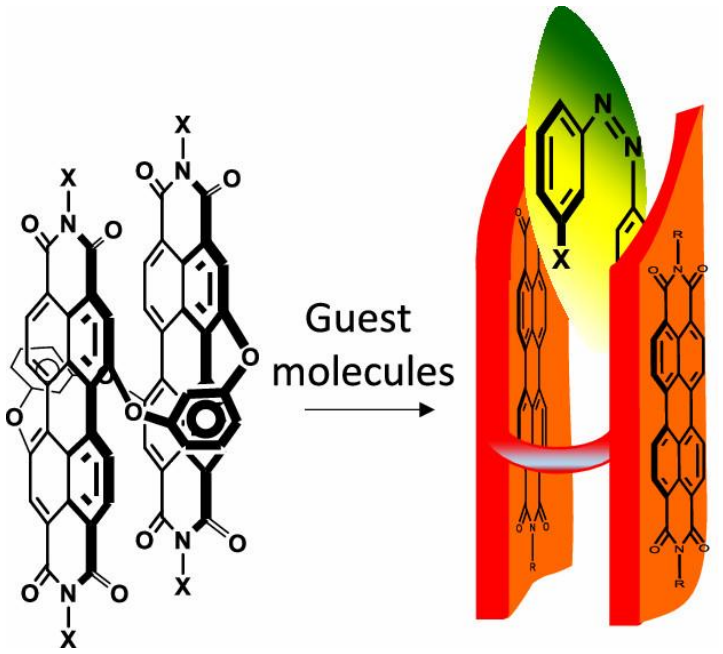

Figure 1.51: Bay-strapped bis-PDI macrocycle reported by the Valiyaveettil group, capable of selectively binding the *Z*-isomer of azobenzenes in its tubular cavity in preference to the *E*-isomer. [218] Figure adapted from ref. 218 with permission from the Royal Society of Chemistry.

1.13 Thesis aims

As discussed in the above section, several chiral bis-PDI macrocycles have been reported in the literature. However, all these systems have one or both of the following drawbacks:

a) They have large intramolecular PDI-PDI distances, which results in very little chiral excitonic coupling between the PDIs.

b) They are often dynamically chiral with rapidly-interconverting stereoisomers, such that the enantiomers cannot be isolated.

This thesis aims to explore the intramolecular and intermolecular interactions between chiral core-twisted PDIs in a novel bis-PDI macrocyclic scaffold (nicknamed the "Pink Box" due to its colour in solution) that is optimised for intramolecular PDI-PDI close contact π–π interactions, with a view towards using these as organic chiroptical materials.

Close contact between the PDI cores is achieved by connecting the two PDIs via the bay positions using short, rigid para-xylene linkers. Bay-connection is a superior strategy here because it automatically enforces a twist in the PDI cores resulting in chirality, while imide-connected macrocycles require bulky substituents at the bay positions which hinder the PDI-PDI interactions.[159] Additionally, the imide positions are free to be varied to tune aggregation properties and to investigate dynamic vs locked chirality.[158] The macrocycle can be synthesised relatively easily via "click chemistry" (hence the presence of the triazoles), allowing the linker groups to be also varied easily to examine the nature of the PDI-PDI interaction. Varying the linker groups could also give access to a cavity large enough to explore guest binding. The relative orientation and accessibility of the PDI chiral π–surfaces suggests that the *intra*molecular PDI-PDI dimer should be preferentially homochiral and co-facial, i.e. an H-type intramolecular dimer. This will enable new understanding of how this geometry impacts chiral, photophysical and electrochemical properties. In addition, there is also potential for *inter*molecular PDI-PDI contacts, to explore chirality-dependent supramolecular self-assembly.

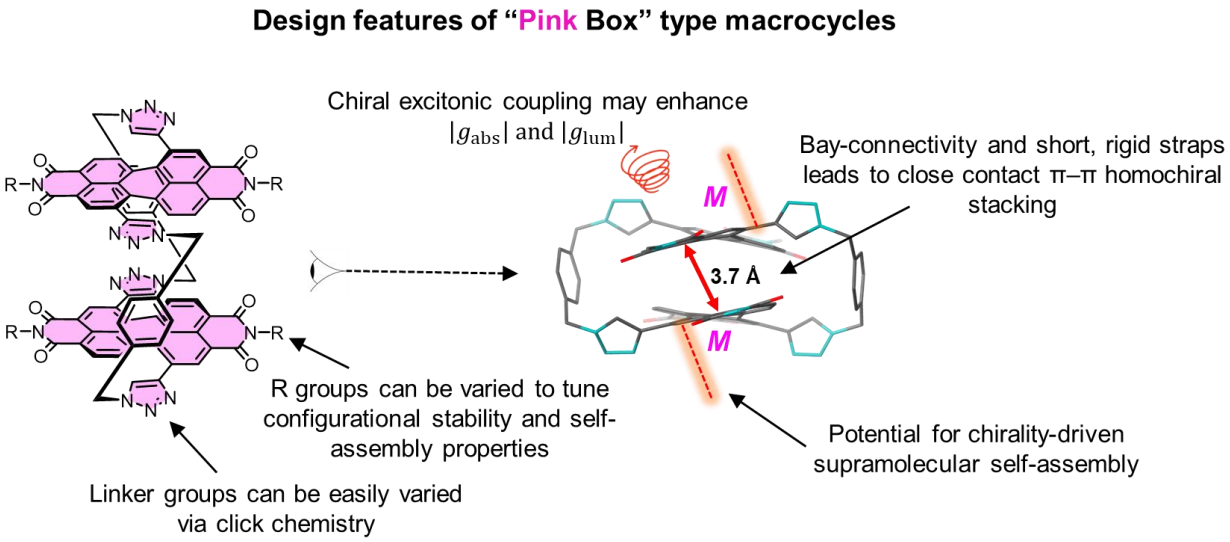

Figure 1.52: Summary of the key design features of "Pink Box" type macrocycles.

1.14 References

1. W. T. B. Kelvin, *The Molecular Tactics of a Crystal, Second Robert Boyle Lecture*, Oxford University Junior Scientific Club, 1894.
2. G. Darvas, *Symmetry: Cultural-historical and Ontological Aspects of Science-Arts Relations; the Natural and Man-made World in an Interdisciplinary Approach*, Birkhäuser Basel, 2007.
3. M. Liu, L. Zhang and T. Wang, *Chemical Reviews*, 2015, **115**, 7304-7397.
4. S. Capozziello and A. Lattanzi, *Astrophysics and Space Science*, 2006, **301**, 189-193.
5. L. D. Barron, *Israel Journal of Chemistry*, 2021, **61**, 517-529.
6. G. H. Wagnière, *On chirality and the universal asymmetry: reflections on image and mirror image*, John Wiley & Sons, 2007.
7. M. Cox and D. Nelson, *Lehninger Principles of Biochemistry*, 2000.
8. N. E. Shepherd, H. N. Hoang, G. Abbenante and D. P. Fairlie, *Journal of the American Chemical Society*, 2009, **131**, 15877-15886.
9. L. Pauling, R. B. Corey and H. R. Branson, *Proceedings of the National Academy of Sciences*, 1951, **37**, 205-211.
10. J. S. Richardson, *Advances in Protein Chemistry*, eds. C. B. Anfinsen, J. T. Edsall and F. M. Richards, Academic Press, 1981, vol. 34, pp. 167-339.
11. J. D. Watson and F. H. C. Crick, *Nature*, 1953, **171**, 737-738.
12. J. D. Carroll, *Chirality*, 2009, **21**, 354-358.
13. R. R. Julian, S. Myung and D. E. Clemmer, *The Journal of Physical Chemistry B*, 2005, **109**, 440-444.
14. S. F. Mason, *Nature*, 1984, **311**, 19-23.
15. J. Podlech, *Cellular and Molecular Life Sciences CMLS*, 2001, **58**, 44-60.
16. F. C. Frank, *Biochimica et Biophysica Acta*, 1953, **11**, 459-463.
17. N. Globus and R. D. Blandford, *The Astrophysical Journal Letters*, 2020, **895**, L11.

18. L. D. Barron, *Journal of the American Chemical Society*, 1986, **108**, 5539-5542.
19. S. F. Ozturk and D. D. Sasselov, *Proceedings of the National Academy of Sciences*, 2022, **119**, e2204765119.
20. C. Meinert, S. V. Hoffmann, P. Cassam-Chenaï, A. C. Evans, C. Giri, L. Nahon and U. J. Meierhenrich, *Angewandte Chemie International Edition*, 2014, **53**, 210-214.
21. R. D. Richardson, M. G. J. Baud, C. E. Weston, H. S. Rzepa, M. K. Kuimova and M. J. Fuchter, *Chemical Science*, 2015, **6**, 3853-3862.
22. J. L. Greenfield, J. Wade, J. R. Brandt, X. Shi, T. J. Penfold and M. J. Fuchter, *Chemical Science*, 2021, **12**, 8589-8602.
23. T. Fujisawa and M. Unno, in *Molecular and Laser Spectroscopy*, eds. V. P. Gupta and Y. Ozaki, Elsevier, 2020, DOI: https://doi.org/10.1016/B978-0-12-818870-5.00002-2, pp. 41-82.
24. R. Kuroda and T. Harada, in *Comprehensive Chiroptical Spectroscopy*, 2011, DOI: https://doi.org/10.1002/9781118120187.ch4, pp. 91-113.
25. A. Fresnel, *Memoir on the double refraction that light rays undergo in traversing the needles of quartz in the directions parallel to the axis*, 1822, DOI: https://doi.org/10.5281/zenodo.5079513
26. International Union of Pure and Applied Chemistry (IUPAC) Gold Book, 3.0.1 edn., 2019, DOI: doi:10.1351/goldbook.O04303.
27. L. Arrico, L. Di Bari and F. Zinna, *Chemistry – A European Journal*, 2021, **27**, 2920-2934.
28. T. Mori, in *Circularly Polarized Luminescence of Isolated Small Organic Molecules*, ed. T. Mori, Springer Singapore, Singapore, 2020, DOI: 10.1007/978-981-15-2309-0_1, pp. 1-10.
29. Y. Nagata and T. Mori, *Frontiers in Chemistry*, 2020, **8**.
30. L. Rosenfeld, *Zeitschrift für Physik*, 1929, **52**, 161-174.
31. N. H. List, J. Kauczor, T. Saue, H. J. A. Jensen and P. Norman, *The Journal of Chemical Physics*, 2015, **142**.
32. E. M. Sánchez-Carnerero, A. R. Agarrabeitia, F. Moreno, B. L. Maroto, G. Muller, M. J. Ortiz and S. de la Moya, *Chemistry – A European Journal*, 2015, **21**, 13488-13500.
33. M. Hasegawa, Y. Nojima and Y. Mazaki, *ChemPhotoChem*, 2021, **5**, 1042-1058.
34. J.-L. Ma, Q. Peng and C.-H. Zhao, *Chemistry – A European Journal*, 2019, **25**, 15441-15454.
35. J. Zhao and P. Xing, *ChemPhotoChem*, 2022, **6**, e202100124.
36. H. Tanaka, Y. Inoue and T. Mori, *ChemPhotoChem*, 2018, **2**, 386-402.
37. M. Wakabayashi, S. Yokojima, T. Fukaminato, K.-i. Shiino, M. Irie and S. Nakamura, *The Journal of Physical Chemistry A*, 2014, **118**, 5046-5057.
38. H. Tanaka, M. Ikenosako, Y. Kato, M. Fujiki, Y. Inoue and T. Mori, *Communications Chemistry*, 2018, **1**, 38.
39. X. Xiao, S. K. Pedersen, D. Aranda, J. Yang, R. A. Wiscons, M. Pittelkow, M. L. Steigerwald, F. Santoro, N. J. Schuster and C. Nuckolls, *Journal of the American Chemical Society*, 2021, **143**, 983-991.
40. Y. Nakai, T. Mori and Y. Inoue, *The Journal of Physical Chemistry A*, 2012, **116**, 7372-7385.
41. R. G. Uceda, C. M. Cruz, S. Míguez-Lago, L. Á. de Cienfuegos, G. Longhi, D. A. Pelta, P. Novoa, A. J. Mota, J. M. Cuerva and D. Miguel, *Angewandte Chemie International Edition*, 2024, **63**, e202316696.

42. J. Wade, J. N. Hilfiker, J. R. Brandt, L. Liirò-Peluso, L. Wan, X. Shi, F. Salerno, S. T. J. Ryan, S. Schöche, O. Arteaga, T. Jávorfi, G. Siligardi, C. Wang, D. B. Amabilino, P. H. Beton, A. J. Campbell and M. J. Fuchter, *Nature Communications*, 2020, **11**, 6137.
43. J. Kumar, B. Marydasan, T. Nakashima, T. Kawai and J. Yuasa, *Chemical Communications*, 2016, **52**, 9885-9888.
44. F. Zinna and L. Di Bari, *Chirality*, 2015, **27**, 1-13.
45. Y. Zhong, Z. Wu, Y. Zhang, B. Dong and X. Bai, *InfoMat*, 2023, **5**, e12392.
46. P. W. Atkins, J. De Paula and J. Keeler, *Atkins' Physical chemistry*, Oxford University Press, Oxford, United Kingdom ;, Eleventh edition. edn., 2018.
47. S. Cotton, *Lanthanide and actinide chemistry*, John Wiley & Sons, 2024.
48. N. C. Martinez-Gomez, H. N. Vu and E. Skovran, *Inorganic Chemistry*, 2016, **55**, 10083-10089.
49. J.-C. G. Bünzli and C. Piguet, *Chemical Society Reviews*, 2005, **34**, 1048-1077.
50. J. L. Lunkley, D. Shirotani, K. Yamanari, S. Kaizaki and G. Muller, *Inorganic Chemistry*, 2011, **50**, 12724-12732.
51. F. Zinna, U. Giovanella and L. D. Bari, *Advanced Materials*, 2015, **27**, 1791-1795.
52. J. Yuasa, T. Ohno, K. Miyata, H. Tsumatori, Y. Hasegawa and T. Kawai, *Journal of the American Chemical Society*, 2011, **133**, 9892-9902.
53. S. Sato, A. Yoshii, S. Takahashi, S. Furumi, M. Takeuchi and H. Isobe, *Proceedings of the National Academy of Sciences*, 2017, **114**, 13097-13101.
54. J. Kumar, T. Nakashima, H. Tsumatori, M. Mori, M. Naito and T. Kawai, *Chemistry – A European Journal*, 2013, **19**, 14090-14097.
55. S. C. J. Meskers, *ChemPhysChem*, 2023, **24**, e202300666.
56. J. Frenkel, *Physical Review*, 1931, **37**, 17-44.
57. J. G. Kirkwood, *Journal of Chemical Physics*, 1937, **5**, 479-491.
58. W. Kuhn, *Hand- u. Jahrb. Chem. Phys.*, 1932, **8**.
59. A. S. Davydov and E. F. Sheka, *physica status solidi (b)*, 1965, **11**, 877-890.
60. A. S. Davydov, *Theory of Molecular Excitons*, Springer New York, NY, 1 edn., 1971.
61. J. A. Schellman, *Accounts of Chemical Research*, 1968, **1**, 144-151.
62. R. M. Hochstrasser and M. Kasha, *Photochemistry and Photobiology*, 1964, **3**, 317-331.
63. M. Kasha, H. R. Rawls and M. A. El-Bayoumi, *Pure and Applied Chemistry*, 1965, **11**, 371-392.
64. M. Kasha, *Radiation Research*, 1963, **20**, 55-70.
65. E. G. McRae and M. Kasha, *The Journal of Chemical Physics*, 1958, **28**, 721-722.
66. N. J. Hestand and F. C. Spano, *Chemical Reviews*, 2018, **118**, 7069-7163.
67. E. E. Jelley, *Nature*, 1936, **138**, 1009-1010.
68. E. E. Jelley, *Nature*, 1937, **139**, 631-631.
69. N. S. S. Nizar, M. Sujith, K. Swathi, C. Sissa, A. Painelli and K. G. Thomas, *Chemical Society Reviews*, 2021, **50**, 11208-11226.
70. International Union of Pure and Applied Chemistry (IUPAC) Gold Book, 3.0.1 edn., 2019, DOI: doi:10.1351/goldbook.D01526.
71. M. Kasha, *Discussions of the Faraday Society*, 1950, **9**, 14-19.
72. F. Würthner, T. E. Kaiser and C. R. Saha-Möller, *Angewandte Chemie International Edition*, 2011, **50**, 3376-3410.
73. J. L. Bricks, Y. L. Slominskii, I. D. Panas and A. P. Demchenko, *Methods and Applications in Fluorescence*, 2018, **6**, 012001.
74. F. Wurthner, C. R. Saha-Moller, B. Fimmel, S. Ogi, P. Leowanawat and D. Schmidt, *Chem Rev*, 2016, **116**, 962-1052.

75. C. Kaufmann, D. Bialas, M. Stolte and F. Würthner, *Journal of the American Chemical Society*, 2018, **140**, 9986-9995.
76. N. J. Hestand and F. C. Spano, *The Journal of Chemical Physics*, 2015, **143**.
77. E. Sebastian, A. M. Philip, A. Benny and M. Hariharan, *Angewandte Chemie International Edition*, 2018, **57**, 15696-15701.
78. F. C. Spano, *Accounts of Chemical Research*, 2010, **43**, 429-439.
79. N. Harada and K. Nakanishi, *Accounts of Chemical Research*, 1972, **5**, 257-263.
80. N. Harada, S.-M. L. Chen and K. Nakanishi, *Journal of the American Chemical Society*, 1975, **97**, 5345-5352.
81. P. M. Bayley, *Progress in Biophysics and Molecular Biology*, 1973, **27**, 1-76.
82. G. Pescitelli, *Chirality*, 2022, **34**, 333-363.
83. K. Swathi, C. Sissa, A. Painelli and K. George Thomas, *Chemical Communications*, 2020, **56**, 8281-8284.
84. F. Bertocchi, C. Sissa and A. Painelli, *Chirality*, 2023, **35**, 681-691.
85. T. Bruhn, G. Pescitelli, S. Jurinovich, A. Schaumlöffel, F. Witterauf, J. Ahrens, M. Bröring and G. Bringmann, *Angewandte Chemie International Edition*, 2014, **53**, 14592-14595.
86. A. J. Miles, R. W. Janes and B. A. Wallace, *Chemical Society Reviews*, 2021, **50**, 8400-8413.
87. A. Rodger, R. Marrington, D. Roper and S. Windsor, in *Protein-Ligand Interactions: Methods and Applications*, ed. G. Ulrich Nienhaus, Humana Press, Totowa, NJ, 2005, DOI: 10.1385/1-59259-912-5:343, pp. 343-363.
88. L. E. MacKenzie, L.-O. Pålsson, D. Parker, A. Beeby and R. Pal, *Nature Communications*, 2020, **11**, 1676.
89. P. Stachelek, L. MacKenzie, D. Parker and R. Pal, *Nature Communications*, 2022, **13**, 553.
90. D. F. De Rosa, P. Stachelek, D. J. Black and R. Pal, *Nature Communications*, 2023, **14**, 1537.
91. Y. Gao, C. Ren, X. Lin and T. He, *Frontiers in Chemistry*, 2020, **8**.
92. S.-J. Zou, Y. Shen, F.-M. Xie, J.-D. Chen, Y.-Q. Li and J.-X. Tang, *Materials Chemistry Frontiers*, 2020, **4**, 788-820.
93. Y. Deng, M. Wang, Y. Zhuang, S. Liu, W. Huang and Q. Zhao, *Light: Science & Applications*, 2021, **10**, 76.
94. J. R. Brandt, F. Salerno and M. J. Fuchter, *Nature Reviews Chemistry*, 2017, **1**, 0045.
95. D.-W. Zhang, M. Li and C.-F. Chen, *Chemical Society Reviews*, 2020, **49**, 1331-1343.
96. K. Baek, D.-M. Lee, Y.-J. Lee, H. Choi, J. Seo, I. Kang, C.-J. Yu and J.-H. Kim, *Light: Science & Applications*, 2019, **8**, 120.
97. E. Peeters, M. P. T. Christiaans, R. A. J. Janssen, H. F. M. Schoo, H. P. J. M. Dekkers and E. W. Meijer, *Journal of the American Chemical Society*, 1997, **119**, 9909-9910.
98. D.-M. Lee, J.-W. Song, Y.-J. Lee, C.-J. Yu and J.-H. Kim, *Advanced Materials*, 2017, **29**, 1700907.
99. J. R. Brandt, X. Wang, Y. Yang, A. J. Campbell and M. J. Fuchter, *Journal of the American Chemical Society*, 2016, **138**, 9743-9746.
100. K. Liu, B. Ouyang, X. Guo, Y. Guo and Y. Liu, *npj Flexible Electronics*, 2022, **6**, 1.
101. Y. Yang, R. C. da Costa, M. J. Fuchter and A. J. Campbell, *Nature Photonics*, 2013, **7**, 634-638.
102. D. Zhu, W. Jiang, Z. Ma, J. Feng, X. Zhan, C. Lu, J. Liu, J. Liu, Y. Hu, D. Wang, Y. S. Zhao, J. Wang, Z. Wang and L. Jiang, *Nature Communications*, 2022, **13**, 3454.

103. Z. Ma, T. Winands, N. Liang, D. Meng, W. Jiang, N. L. Doltsinis and Z. Wang, *Science China Chemistry*, 2020, **63**, 208-214.
104. L. Zhang, I. Song, J. Ahn, M. Han, M. Linares, M. Surin, H.-J. Zhang, J. H. Oh and J. Lin, *Nature Communications*, 2021, **12**, 142.
105. A. G. Griesbeck and U. J. Meierhenrich, *Angewandte Chemie International Edition*, 2002, **41**, 3147-3154.
106. G. Volonakis and S. Logothetidis, in *Handbook of Flexible Organic Electronics*, ed. S. Logothetidis, Woodhead Publishing, Oxford, 2015, DOI: https://doi.org/10.1016/B978-1-78242-035-4.00002-6, pp. 37-56.
107. M. R. Chetyrkina, F. S. Talalaev, L. V. Kameneva, S. V. Kostyuk and P. A. Troshin, *Journal of Materials Chemistry C*, 2022, **10**, 3224-3231.
108. S. E. Penty, G. R. F. Orton, D. J. Black, R. Pal, M. A. Zwijnenburg and T. A. Barendt, *Journal of the American Chemical Society*, 2024, DOI: 10.1021/jacs.3c13191.
109. Y. Yang, B. Rice, X. Shi, J. R. Brandt, R. Correa da Costa, G. J. Hedley, D.-M. Smilgies, J. M. Frost, I. D. W. Samuel, A. Otero-de-la-Roza, E. R. Johnson, K. E. Jelfs, J. Nelson, A. J. Campbell and M. J. Fuchter, *ACS Nano*, 2017, **11**, 8329-8338.
110. H. Zollinger, *Color Chemistry: Syntheses, Properties, and Applications of Organic Dyes and Pigments*, Wiley, 2003.
111. M. Kardos, *German Patent, DE*, 1913, **276357**.
112. M. Greene, in *High Performance Pigments*, ed. H. M. Smith, Wiley, 2001, DOI: https://doi.org/10.1002/3527600493.ch16, ch. 16, pp. 249-261.
113. F. Würthner, *Chemical Communications*, 2004, DOI: 10.1039/B401630K, 1564-1579.
114. H. Langhals, *Heterocycles*, 1995, **1**, 477-500.
115. A. Nowak-Król and F. Würthner, *Organic Chemistry Frontiers*, 2019, **6**, 1272-1318.
116. F. Süßmeier and H. Langhals, *European Journal of Organic Chemistry*, 2001, **2001**, 607-610.
117. M. G. Ramírez, M. Morales-Vidal, V. Navarro-Fuster, P. G. Boj, J. A. Quintana, J. M. Villalvilla, A. Retolaza, S. Merino and M. A. Díaz-García, *Journal of Materials Chemistry C*, 2013, **1**, 1182-1191.
118. S. Wirsing, M. Hänsel, V. Belova, F. Schreiber, K. Broch, B. Engels and P. Tegeder, *Journal of Physical Chemistry C*, 2019, **123**, 27561-27572.
119. S. Toffanin, V. Benfenati, A. Pistone, S. Bonetti, W. Koopman, T. Posati, A. Sagnella, M. Natali, R. Zamboni, G. Ruani and M. Muccini, *Journal of Materials Chemistry B*, 2013, **1**, 3850-3859.
120. X. Shang, I. Song, H. Ohtsu, Y. H. Lee, T. Zhao, T. Kojima, J. H. Jung, M. Kawano and J. H. Oh, *Advanced Materials*, 2017, **29**, 1605828.
121. C. W. Struijk, A. B. Sieval, J. E. J. Dakhorst, M. van Dijk, P. Kimkes, R. B. M. Koehorst, H. Donker, T. J. Schaafsma, S. J. Picken, A. M. van de Craats, J. M. Warman, H. Zuilhof and E. J. R. Sudhölter, *Journal of the American Chemical Society*, 2000, **122**, 11057-11066.
122. D. Schmidt, D. Bialas and F. Würthner, *Angewandte Chemie International Edition*, 2015, **54**, 3611-3614.
123. J. Cann, B. S. Gelfand and G. C. Welch, *Molecular Systems Design & Engineering*, 2020, **5**, 1181-1185.
124. Q. Li, W. Hou, F. Peng, H. Wang, S. Zhang, D. Dong, S. Wu and H. Zhang, *Journal of Materials Science*, 2019, **54**, 217-227.
125. B. Lu, Y. Chen, P. Li, B. Wang, K. Mullen and M. Yin, *Nat Commun*, 2019, **10**, 767.
126. B. Tang, J. Zhao, J.-F. Xu and X. Zhang, *Chemical Science)*, 2020, **11**, 1192-1204.

127. Y. Geng, H.-B. Li, S.-X. Wu and Z.-M. Su, *Journal of Materials Chemistry*, 2012, **22**, 20840-20851.
128. C. Huang, S. Barlow and S. R. Marder, *Journal of Organic Chemistry*, 2011, **76**, 2386-2407.
129. X. Zhan, A. Facchetti, S. Barlow, T. J. Marks, M. A. Ratner, M. R. Wasielewski and S. R. Marder, *Advanced Materials*, 2011, **23**, 268-284.
130. F. Würthner and M. Stolte, *Chemical Communications*, 2011, **47**, 5109-5115.
131. T. Weil, T. Vosch, J. Hofkens, K. Peneva and K. Müllen, *Angewandte Chemie International Edition*, 2010, **49**, 9068-9093.
132. M. Mitsui, H. Fukui, R. Takahashi, Y. Takakura and T. Mizukami, *Journal of Physical Chemistry A*, 2017, **121**, 1577-1586.
133. R. Gronheid, A. Stefan, M. Cotlet, J. Hofkens, J. Qu, K. Müllen, M. Van der Auweraer, J. W. Verhoeven and F. C. De Schryver, *Angewandte Chemie International Edition*, 2003, **42**, 4209-4214.
134. P. Tinnefeld, J. Hofkens, D.-P. Herten, S. Masuo, T. Vosch, M. Cotlet, S. Habuchi, K. Müllen, F. C. De Schryver and M. Sauer, *ChemPhysChem*, 2004, **5**, 1786-1790.
135. T. Seki, X. Lin and S. Yagai, *Asian Journal of Organic Chemistry*, 2013, **2**, 708-724.
136. D. Görl, X. Zhang and F. Würthner, *Angewandte Chemie International Edition*, 2012, **51**, 6328-6348.
137. M. Sun, K. Müllen and M. Yin, *Chemical Society Reviews*, 2016, **45**, 1513-1528.
138. F. Kong, M. Lin and T. Qiu, *Luminescence*, 2018, **33**, 1209-1216.
139. E. H. A. Beckers, S. C. J. Meskers, A. P. H. J. Schenning, Z. Chen, F. Würthner and R. A. J. Janssen, *Journal of Physical Chemistry A*, 2004, **108**, 6933-6937.
140. C. Hippius, I. H. M. van Stokkum, E. Zangrando, R. M. Williams and F. Würthner, *Journal of Physical Chemistry C*, 2007, **111**, 13988-13996.
141. F. Zhang, Y. Ma, Y. Chi, H. Yu, Y. Li, T. Jiang, X. Wei and J. Shi, *Scientific Reports*, 2018, **8**, 8208.
142. W. E. Ford and P. V. Kamat, *Journal of Physical Chemistry*, 1987, **91**, 6373-6380.
143. R. Englman and J. Jortner, *Journal of Luminescence*, 1970, **1-2**, 134-142.
144. S. K. Lee, Y. Zu, A. Herrmann, Y. Geerts, K. Müllen and A. J. Bard, *Journal of the American Chemical Society*, 1999, **121**, 3513-3520.
145. R. O. Marcon and S. Brochsztain, *Langmuir*, 2007, **23**, 11972-11976.
146. A. Zhang, W. Jiang and Z. Wang, *Angewandte Chemie International Edition*, 2020, **59**, 752-757.
147. E. He, J. Wang, H. Liu, Z. He, H. Zhao, W. Bao, R. Zhang and H. Zhang, *Journal of Materials Science*, 2016, **51**, 9229-9238.
148. M. A. Iron, R. Cohen and B. Rybtchinski, *Journal of Physical Chemistry A*, 2011, **115**, 2047-2056.
149. T. E. Kaiser, H. Wang, V. Stepanenko and F. Würthner, *Angewandte Chemie International Edition*, 2007, **46**, 5541-5544.
150. Z. Chen, U. Baumeister, C. Tschierske and F. Würthner, *Chemistry – A European Journal*, 2007, **13**, 450-465.
151. Z. Chen, V. Stepanenko, V. Dehm, P. Prins, L. D. A. Siebbeles, J. Seibt, P. Marquetand, V. Engel and F. Würthner, *Chemistry – A European Journal*, 2007, **13**, 436-449.
152. B. Pagoaga, L. Giraudet and N. Hoffmann, *European Journal of Organic Chemistry*, 2014, **2014**, 5178-5195.
153. P. Osswald and F. Wuerthner, *Journal of the American Chemical Society*, 2007, **129**, 14319-14326.

154. G. Echue, I. Hamley, G. C. Lloyd Jones and C. F. J. Faul, *Langmuir*, 2016, **32**, 9023-9032.
155. L. Wan, J. Wade, X. Shi, S. Xu, M. J. Fuchter and A. J. Campbell, *ACS Applied Materials & Interfaces*, 2020, **12**, 39471-39478.
156. P. Osswald, M. Reichert, G. Bringmann and F. Wuerthner, *J. Org. Chem.*, 2007, **72**, 3403-3411.
157. B. Mahlmeister, 2023.
158. M. Ball, B. Fowler, P. Li, L. A. Joyce, F. Li, T. Liu, D. Paley, Y. Zhong, H. Li, S. Xiao, F. Ng, M. L. Steigerwald and C. Nuckolls, *Journal of the American Chemical Society*, 2015, **137**, 9982-9987.
159. S. E. Penty, M. A. Zwijnenburg, G. R. F. Orton, P. Stachelek, R. Pal, Y. Xie, S. L. Griffin and T. A. Barendt, *Journal of the American Chemical Society*, 2022, **144**, 12290-12298.
160. R. S. Cahn, C. Ingold and V. Prelog, *Angewandte Chemie International Edition in English*, 1966, **5**, 385-415.
161. S. E. Penty, G. R. F. Orton, D. J. Black, R. Pal, M. A. Zwijnenburg and T. A. Barendt, *Journal of the American Chemical Society*, 2024, **146**, 5470-5479.
162. P. Osswald, D. Leusser, D. Stalke and F. Würthner, *Angewandte Chemie International Edition*, 2005, **44**, 250-253.
163. S. R. LaPlante, L. D. Fader, K. R. Fandrick, D. R. Fandrick, O. Hucke, R. Kemper, S. P. F. Miller and P. J. Edwards, *Journal of Medicinal Chemistry*, 2011, **54**, 7005-7022.
164. W. Qiu, S. Chen, X. Sun, Y. Liu and D. Zhu, *Organic Letters*, 2006, **8**, 867-870.
165. R. Renner, B. Mahlmeister, O. Anhalt, M. Stolte and F. Würthner, *Chemistry – A European Journal*, 2021, **27**, 11997-12006.
166. B. Liu, M. Böckmann, W. Jiang, N. L. Doltsinis and Z. Wang, *Journal of the American Chemical Society*, 2020, **142**, 7092-7099.
167. N. J. Schuster, R. Hernández Sánchez, D. Bukharina, N. A. Kotov, N. Berova, F. Ng, M. L. Steigerwald and C. Nuckolls, *Journal of the American Chemical Society*, 2018, **140**, 6235-6239.
168. N. J. Schuster, D. W. Paley, S. Jockusch, F. Ng, M. L. Steigerwald and C. Nuckolls, *Angewandte Chemie International Edition*, 2016, **55**, 13519-13523.
169. D. Aranda, N. J. Schuster, X. Xiao, F. J. Ávila Ferrer, F. Santoro and C. Nuckolls, *The Journal of Physical Chemistry C*, 2021, **125**, 2554-2564.
170. R. F. Fink, J. Seibt, V. Engel, M. Renz, M. Kaupp, S. Lochbrunner, H.-M. Zhao, J. Pfister, F. Würthner and B. Engels, *Journal of the American Chemical Society*, 2008, **130**, 12858-12859.
171. Z. Chen, A. Lohr, C. R. Saha-Möller and F. Würthner, *Chemical Society Reviews*, 2009, **38**, 564-584.
172. J. Li, P. Li, M. Fan, X. Zheng, J. Guan and M. Yin, *Angewandte Chemie International Edition*, 2022, **61**, e202202532.
173. C. D. Schmidt, C. Böttcher and A. Hirsch, *European Journal of Organic Chemistry*, 2009, **2009**, 5337-5349.
174. D. Wei, Y. Yu, L. Ge, Z. Wang, C. Chen and R. Guo, *Langmuir*, 2021, **37**, 9232-9243.
175. J. Hu, W. Kuang, K. Deng, W. Zou, Y. Huang, Z. Wei and C. F. J. Faul, *Advanced Functional Materials*, 2012, **22**, 4149-4158.
176. X. Liu, Z. Huang, Y. Huang, L. Zhu and J. Fu, *The Journal of Physical Chemistry C*, 2017, **121**, 7558-7563.

177. Y. Huang, J. Hu, W. Kuang, Z. Wei and C. F. J. Faul, *Chemical Communications*, 2011, **47**, 5554-5556.
178. K.-R. Wang, H.-W. An, L. Wu, J.-C. Zhang and X.-L. Li, *Chemical Communications*, 2012, **48**, 5644-5646.
179. M. M. Safont-Sempere, P. Osswald, K. Radacki and F. Würthner, *Chemistry – A European Journal*, 2010, **16**, 7380-7384.
180. M. M. Safont-Sempere, P. Osswald, M. Stolte, M. Grüne, M. Renz, M. Kaupp, K. Radacki, H. Braunschweig and F. Würthner, *Journal of the American Chemical Society*, 2011, **133**, 9580-9591.
181. M. M. Safont-Sempere, V. Stepanenko, M. Lehmann and F. Würthner, *Journal of Materials Chemistry*, 2011, **21**, 7201-7209.
182. M. Hecht and F. Würthner, *Accounts of Chemical Research*, 2021, **54**, 642-653.
183. M. Gsänger, J. H. Oh, M. Könemann, H. W. Höffken, A.-M. Krause, Z. Bao and F. Würthner, *Angewandte Chemie International Edition*, 2010, **49**, 740-743.
184. T. E. Kaiser, V. Stepanenko and F. Würthner, *Journal of the American Chemical Society*, 2009, **131**, 6719-6732.
185. Z. Xie, V. Stepanenko, K. Radacki and F. Würthner, *Chemistry – A European Journal*, 2012, **18**, 7060-7070.
186. Z. Xie, V. Stepanenko, B. Fimmel and F. Würthner, *Materials Horizons*, 2014, **1**, 355-359.
187. V. Grande, B. Soberats, S. Herbst, V. Stepanenko and F. Würthner, *Chemical Science*, 2018, **9**, 6904-6911.
188. H. Wang, T. E. Kaiser, S. Uemura and F. Würthner, *Chemical Communications*, 2008, DOI: 10.1039/B717407A, 1181-1183.
189. B. Mahlmeister, M. Mahl, H. Reichelt, K. Shoyama, M. Stolte and F. Würthner, *Journal of the American Chemical Society*, 2022, **144**, 10507-10514.
190. Y. Geerts, H. Quante, H. Platz, R. Mahrt, M. Hopmeier, A. Böhm and K. Müllen, *Journal of Materials Chemistry*, 1998, **8**, 2357-2369.
191. H. Quante and K. Müllen, *Angewandte Chemie International Edition in English*, 1995, **34**, 1323-1325.
192. C. J. Pedersen, *Journal of the American Chemical Society*, 1967, **89**, 2495-2496.
193. D. J. Cram, *Angewandte Chemie International Edition in English*, 1988, **27**, 1009-1020.
194. P. Spenst and F. Würthner, *Angewandte Chemie International Edition*, 2015, **54**, 10165-10168.
195. J.-M. Yang, Y. Yu and J. Rebek, Jr., *Journal of the American Chemical Society*, 2021, **143**, 2190-2193.
196. E. J. Leonhardt and R. Jasti, *Nature Reviews Chemistry*, 2019, **3**, 672-686.
197. E. M. Pérez, *Chemistry – A European Journal*, 2017, **23**, 12681-12689.
198. M. Weh, J. Rühe, B. Herbert, A.-M. Krause and F. Würthner, *Angewandte Chemie International Edition*, 2021, **60**, 15323-15327.
199. M. Weh, K. Shoyama and F. Würthner, *Nature Communications*, 2023, **14**, 243.
200. J.-Q. Wang, X.-N. Han, Y. Han and C.-F. Chen, *Chemical Communications*, 2023, DOI: 10.1039/D3CC04187E.
201. H. Langhals and R. Ismael, *Eur. J. Org. Chem.*, 1998, 1915-1917.
202. M. Son, K. H. Park, C. Shao, F. Würthner and D. Kim, *Journal of Physical Chemistry Letters*, 2014, **5**, 3601-3607.
203. J. M. Lim, P. Kim, M.-C. Yoon, J. Sung, V. Dehm, Z. Chen, F. Würthner and D. Kim, *Chemical Science*, 2013, **4**, 388-397.

204. K. E. Brown, W. A. Salamant, L. E. Shoer, R. M. Young and M. R. Wasielewski, *Journal of Physical Chemistry Letters*, 2014, **5**, 2588-2593.
205. F. Gao, Y. Zhao and W. Liang, *Journal of Physical Chemistry B*, 2011, **115**, 2699-2708.
206. F. Schlosser, M. Moos, C. Lambert and F. Wurthner, *Adv Mater*, 2013, **25**, 410-414.
207. L. Yang, P. Langer, E. S. Davies, M. Baldoni, K. Wickham, N. A. Besley, E. Besley and N. R. Champness, *Chemical Science*, 2019, **10**, 3723-3732.
208. J. Feng, Y. Zhang, C. Zhao, R. Li, W. Xu, X. Li and J. Jiang, *Chemistry – A European Journal*, 2008, **14**, 7000-7010.
209. P. Spenst, R. M. Young, M. R. Wasielewski and F. Würthner, *Chemical Science*, 2016, **7**, 5428-5434.
210. A. F. Coleman, M. Chen, J. Zhou, J. Y. Shin, Y. Wu, R. M. Young and M. R. Wasielewski, *Journal of Physical Chemistry C*, 2020, **124**, 10408-10419.
211. M. Sapotta, P. Spenst, C. R. Saha-Moeller and F. Wuerthner, *Organic Chemistry Frontiers*, 2019, **6**, 892-899.
212. W. Wang, A. D. Shaller and A. D. Q. Li, *Journal of the American Chemical Society*, 2008, **130**, 8271 - 8279.
213. I. Solymosi, S. Krishna, E. Nuin, H. Maid, B. Scholz, D. M. Guldi, M. E. Pérez-Ojeda and A. Hirsch, *Chemical Science*, 2021, **12**, 15491-15502.
214. I. Solymosi, C. Neiß, H. Maid, F. Hampel, T. Solymosi, A. Görling, A. Hirsch and M. E. Pérez-Ojeda, *ChemistrySelect*, 2023, **8**, e202300523.
215. M. Weh, A. A. Kroeger, K. Shoyama, M. Grüne, A. Karton and F. Würthner, *Angewandte Chemie International Edition*, 2023, **62**, e202301301.
216. M. Weh, A. A. Kroeger, O. Anhalt, A. Karton and F. Würthner, *Chemical Science*, 2024, **15**, 609-617.
217. T. A. Barendt, M. L. Ball, Q. Xu, B. Zhang, B. Fowler, A. Schattman, V. C. Ritter, M. L. Steigerwald and C. Nuckolls, *Chemistry – A European Journal*, 2020, **26**, 3744-3748.
218. T. Türel, S. Bhargava and S. Valiyaveettil, *The Journal of Organic Chemistry*, 2020, **85**, 3092-3100.

Chapter 2: The Pink Box: exclusive homochiral π-π stacking in a bis-PDI macrocycle

The work described in this chapter has been published in: Samuel E. Penty, Martijn A. Zwijnenburg, Georgia R. F. Orton, Patrycja Stachelek, Robert Pal, Yujie Xie, Sarah L. Griffin, and Timothy A. Barendt, *J. Am. Chem. Soc.* **2022**, 144, 27, 12290–12298

Text and figures in this chapter have been reprinted and/or adapted with permission from this reference.

I thank all co-authors of the above paper for their contributions to this chapter. Martijn A. Zwijnenburg carried out computational modelling. Georgia R. F. Orton and Sarah L. Griffin collected and solved the single crystal X-ray diffraction data. Georgia R.F. Orton also helped me with electrochemistry. Yujie Xie helped me with quantum yield measurements, and Patrycja Stachelek and Robert Pal carried out CPL measurements.

2. The Pink Box: Exclusive homochiral π-π stacking in a bis-PDI macrocycle

2.1 Introduction and chapter objectives

As outlined in the previous chapter, the chiroptical properties of small organic molecules, including most PDIs, are overall rather poor, with dissymmetry factors typically ~ 10^{-3} or lower.[1, 2] However, chiral exitonic coupling can provide a means to amplifying their interaction with chiral light. One possible way of harnessing this is through the self-assembly of small organic molecules via chiral π–π interactions, which may result in materials with superior chiroptical properties combined with other desirable optical and electronic properties as a result of the interaction between π–systems.[3-5]

One excellent type of system for studying chiral π–π interactions is a bis-PDI macrocycle. As previously discussed, several chiral bis-PDI macrocycles have been reported in the literature. In these macrocycles, the PDI units can be connected by either the imide[6-10] or bay[11, 12] positions. Many of the imide-connected macrocycles, such as that reported by Weh *et al*.[9] (**Figure 2.1a**), have relatively large intramolecular PDI-PDI distances, which provides them with a cavity ideal for guest binding, but also results in weaker excitonic coupling between the PDIs. In addition, imide-linking often leads to the PDIs being held in an almost linear arrangement, which further reduces any chiral excitonic contribution to the chiroptical response. Bay-linking of the PDIs has the potential of favouring the rotational displacement of PDIs, which will amplify excitonic chirality. Furthermore, as the twist of the PDI chromophores is enforced by the linkers, there is no need for additional bay-substituents that would further hinder the PDI-PDI interaction. However, all the bay-linked bis-PDI macrocycles reported so far have either used long, rigid linkers (such as that reported by Ball *et al*.,[11] **Figure 2.1b**), or have not explored the chirality of these systems.[12]

This chapter describes the design, synthesis and characterisation of a new bis-PDI macrocycle, nicknamed the "Pink Box" due to its colour, that is optimised for close-contact (3.7 Å) intramolecular homochiral π-π stacking, allowing the photophysical, electrochemical and chiroptical properties of a closely-stacked twisted bis-PDI dimer to be explored (**Figure 2.1c**).[13]

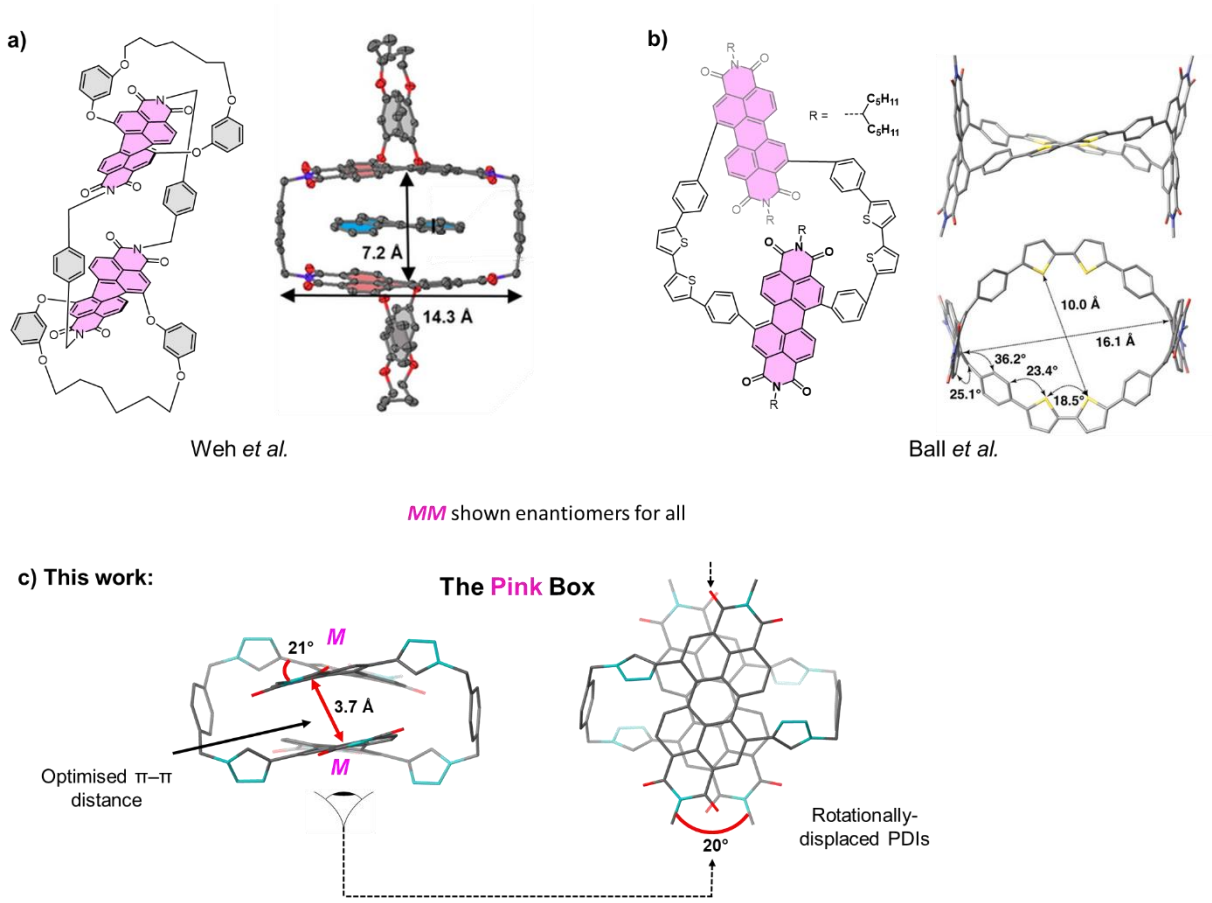

Figure 2.1: a) Imide-linked bis-PDI macrocycle reported by Weh *et al*. Figure adapted with permission with permission from ref [9]. Copyright 2021. **b**) Bay-linked bis-PDI macrocycle reported by Ball *et al*. Figure adapted with permission from ref [11]. Copyright 2015. **c)** Crystal structure of the main macrocycle studied in this chapter, the "Pink Box", with an optimised π–π distance (3.7 Å) and good rotational displacement (20°).

2.2 Design and synthesis of the Pink Box macrocycle 1

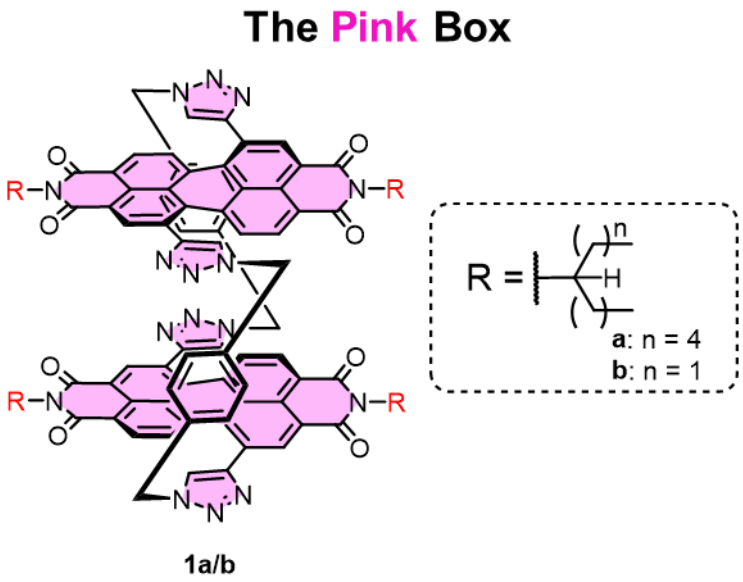

Figure 2.2: Structure of the target "Pink Box" macrocycle **1a/b**.

The structure of target macrocycle **1** is shown in **Figure 2.2**. The macrocycle consists of two 1,7-bistriazole PDI cores linked together by xylene spacers. The xylene linkers were chosen due to their rigidity and relatively short length (a xylene unit is approximately 5.8 Å in length).[14] This design enables the PDI cores to be held close together in space, preorganising them to interact electronically via π-π interactions. As discussed in the previous chapter, macrocyclic strapping of the 1,7 bay positions induces a twist in the PDI cores that results in atropisomerism. Therefore, macrocycle **1** may in principle exist as three different stereoisomers: the enantiomers **1**-***MM*** and **1**-***PP***; and the meso isomer **1**-***MP*** (**Figure 2.3**).

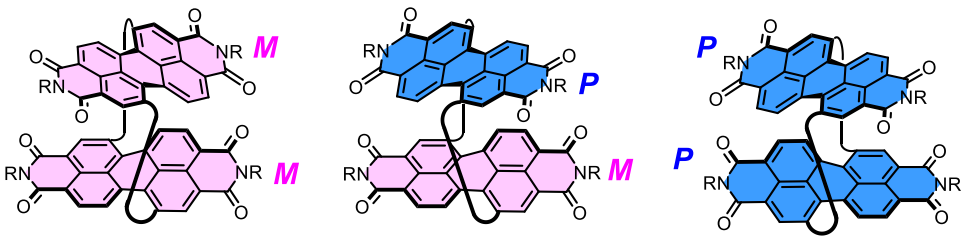

Figure 2.3: The ***MM***, ***MP*** and ***PP*** stereoisomers in a bay-connected bis-PDI macrocycle.

Two analogues of macrocycle **1** with different imide groups were synthesised: **1a**, bearing highly solubilising branched $C_{11}H_{23}$ imide groups was synthesised and studied first; macrocycle **1b**, bearing shorter branched C_5H_{11} imide groups was synthesised later to obtain a

crystal structure (**Figure 2.2**). Apart from their imide side chains, it should be noted that the bis-PDI macrocycles **1a** and **1b** are structurally identical due to matching ^{1}H NMR and UV–vis spectra, as shown later in this chapter.

The synthesis of macrocycles **1a/b** is summarised in **Scheme 2.1**. Compounds **4b**[15] and **2a**[16] had been previously prepared following literature procedures. Compounds **2a/b**, **3a/b** and **4a/b** were isolated as a mixture of 1,6 and 1,7 PDI regioisomers (1:4, see experimental section 2.9.3). Although it was possible to isolate the pure 1,7 isomer of compound **2b** by crystallisation (see experimental section 1.1.4), this was too time-consuming, and the yield was too low (< 25% pure 1,7-isomer) for it to be worthwhile to pursue. Both macrocycles **1a** and **1b** were isolated as the pure 1,7 regioisomer since removal of the 1,6 regioisomer was possible by silica gel column chromatography at this stage. Further experimental details are provided in experimental section 2.9.2.

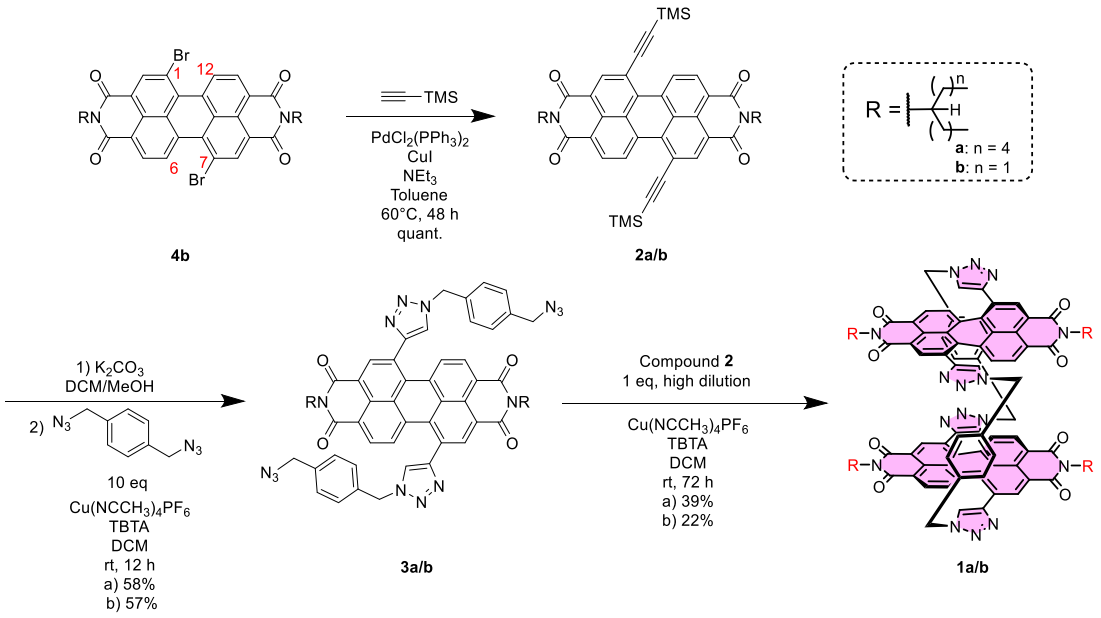

Scheme 2.1 Multistep synthesis of bis-PDI macrocycles **1a** and **1b**.

The synthesis capitalises on robust copper(I)-catalysed azide–alkyne cycloaddition (CuAAC) "click" chemistry for the final macrocyclisation step. Here, stoichiometric amounts of bis-alkyne PDI **2a/b** and bis-azide PDI **3a/b** were reacted under relatively high-dilution conditions (0.3 mM), to favour macrocyclisation.[15] Attempts at making macrocycle **1a** using a one-pot strategy by directly reacting compound **2a** with one equivalent of the *para*-xylyl bisazide linker[17] (see experimental section 2.9.2 for further synthetic details and a **safety**

discussion) under high dilution resulted in very low yields (< 1%) of macrocycle. The desired [1 + 1] macrocycle **1a** was isolated in 39% yield following purification by preparative silica thin layer chromatography, with key side products identified as the larger [2 + 2] and [3 + 3] macrocycles. This macrocyclization yield is over four times larger than previous bay connected bis-PDI macrocycles.[11, 12]

2.3 Characterisation of the Pink Box macrocycle

2.3.1 Initial characterisation

Macrocycle **1a** was characterized using ^{1}H and ^{13}C NMR spectroscopy, which, alongside high-resolution mass spectrometry, confirmed a [1 + 1] macrocyclic product (see experimental 2.9.2). The ^{1}H NMR spectrum in toluene-d_8 at room temperature was broad but dramatically sharpened at 100 °C (**Figure 2.4**). This has been observed before in other bay-connected bis-PDI macrocycles, and is attributed to restricted molecular motion at room temperature.[11]

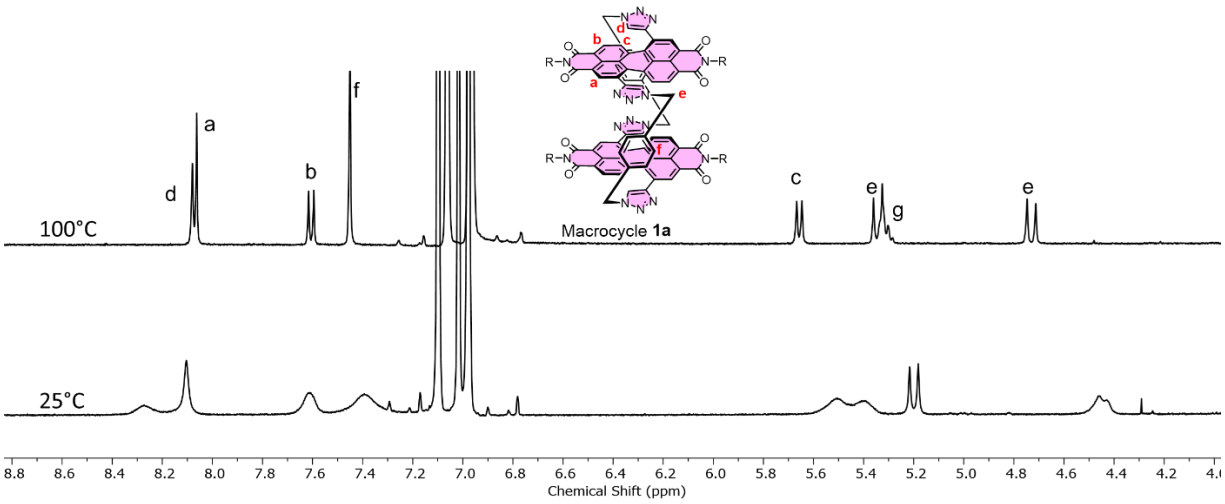

Figure 2.4: Comparison of the ^{1}H NMR spectra of macrocycle **1a** at 25°C and 100°C (toluene-d_8, 400 MHz).

The cyclic framework of macrocycle **1** affords diastereotopic splitting of the methylene protons labelled H_e in the *para*-xylyl linker (**Figure 2.5b)**,[18] which is not observed in the acyclic precursor bis-triazole PDI **3a**. Interestingly, relative to bis-triazole PDI **3a**, the ^{1}H NMR spectrum of macrocycle **1a** in toluene exhibits large upfield shifts of aromatic protons $H_{a–c}$, which is diagnostic of closely stacked π surfaces, while the downfield shift of the triazole proton H_d may be attributed to hydrogen bonding.[19]

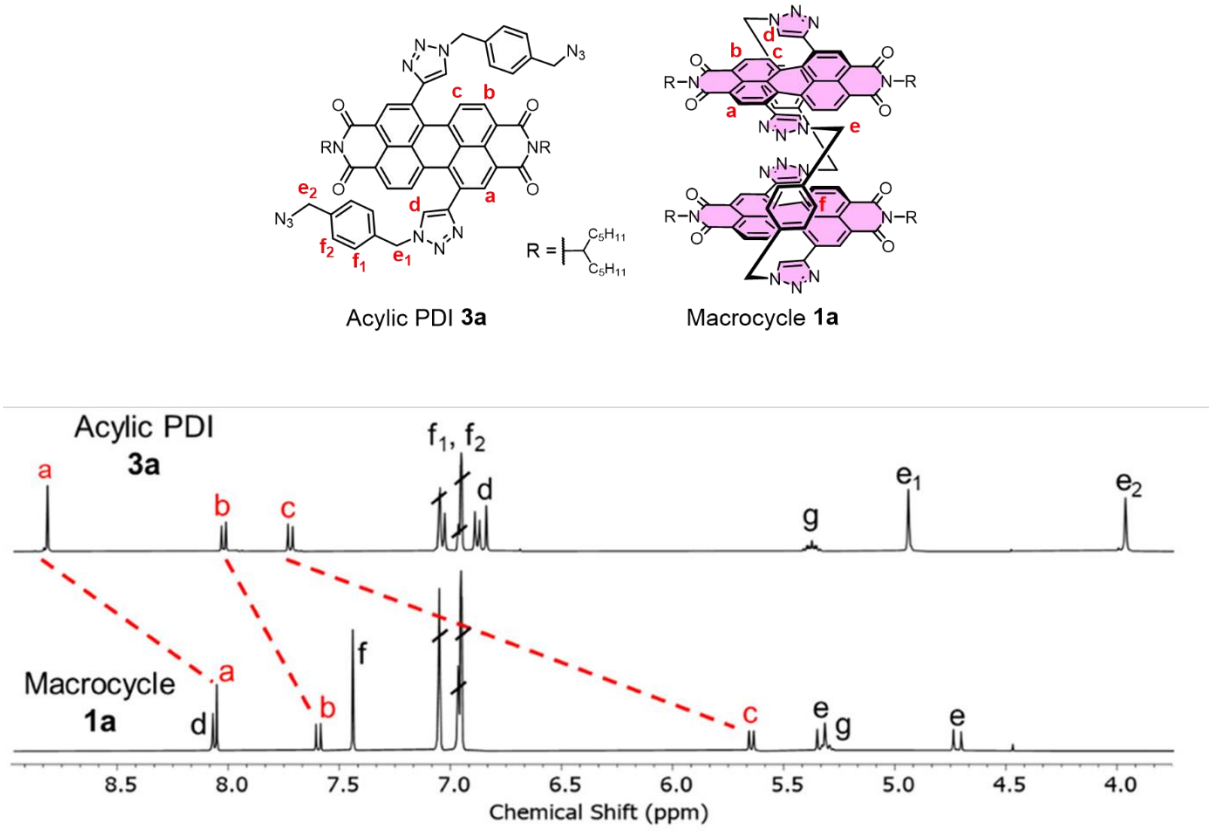

Figure 2.5 a) Final macrocyclisation step in the synthesis of bis-PDI macrocycles 1a/b. **b)** Comparison of the ^{1}H NMR spectra of macrocycle **1a** and acyclic PDI 3a (toluene-d_8, 373 K, 400 MHz).

Furthermore, from the NOESY NMR spectrum, a new through-space nuclear Overhauser effect (NOE) is observed due to the close proximity between the PDI H_c and triazole H_d signals in **1a (Figure 2.6)**. This is in agreement with the crystal structure of the macrocycle, as outlined in the next section.

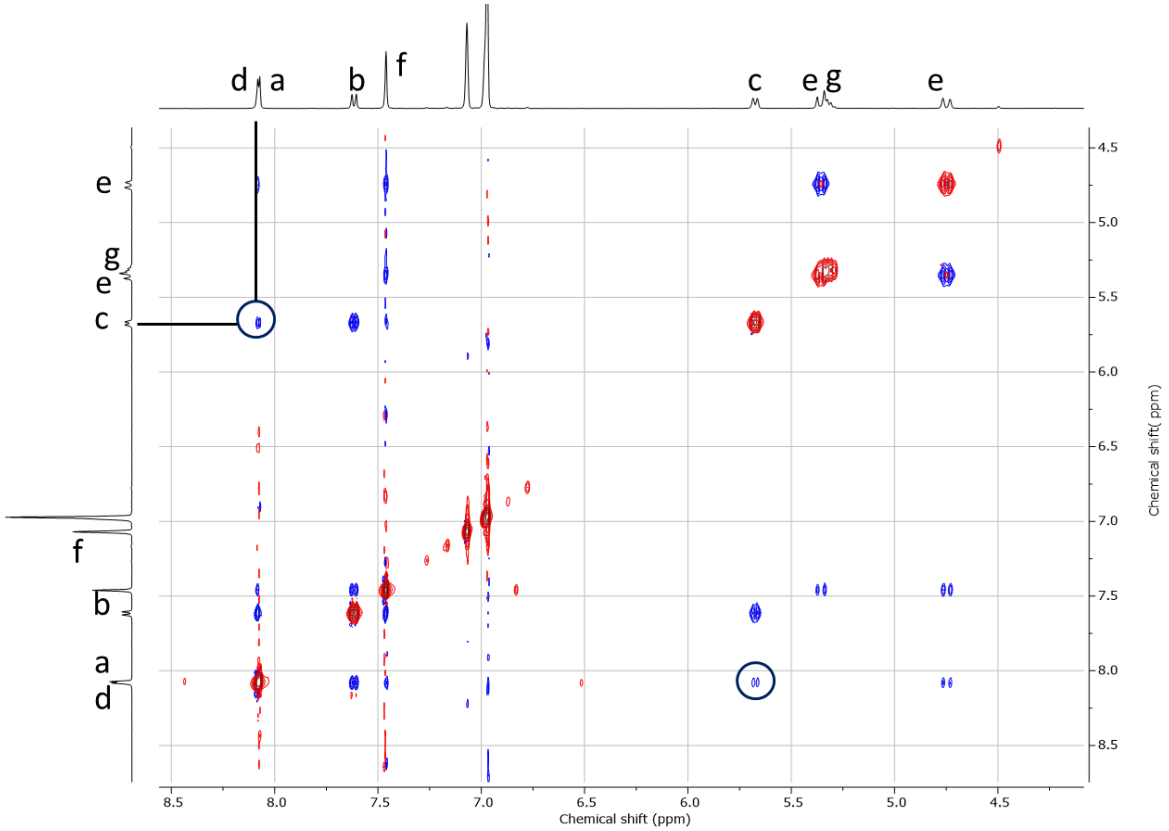

Figure 2.6 Partial ^{1}H-^{1}H NOESY NMR spectrum of macrocycle **1a** (toluene-d_8, 373 K, 400 MHz). Signals with phase shown in blue are NOESY signals. In toluene-d_8 a NOE between the protons H_c and H_d is observed.

2.3.2 Single crystal X-ray crystallography

While attempts to grow crystals of **1a** were unsuccessful, the otherwise identical macrocycle **1b**, bearing shorter C_5H_{11} chains at the imide positions, was successfully used to grow crystals. Slow diffusion of methanol into a chloroform solution of a racemic sample of **1b** afforded purple needle-like crystals. Single crystal diffraction data was collected at a synchrotron.

The crystal structure of **1b** (**Figure 2.7**) reveals that the relative rotation of the PDI units is 20°, enabling close contacts between them (3.7 Å), characteristic of strong intramolecular π–π stacking. The NOE effect between the PDI H_c and triazole H_d signals (**Figure 2.6**) is consistent with the close proximity of these protons in the crystal structure. Interestingly, a hydrogen bond can be observed between the triazole proton on one PDI and the imide carbonyl group on the other PDI (2.5 Å). Whilst a triazole-carbonyl hydrogen bond may be quite weak,[20] here its formation is aided by the preorganised scaffold of the macrocycle.

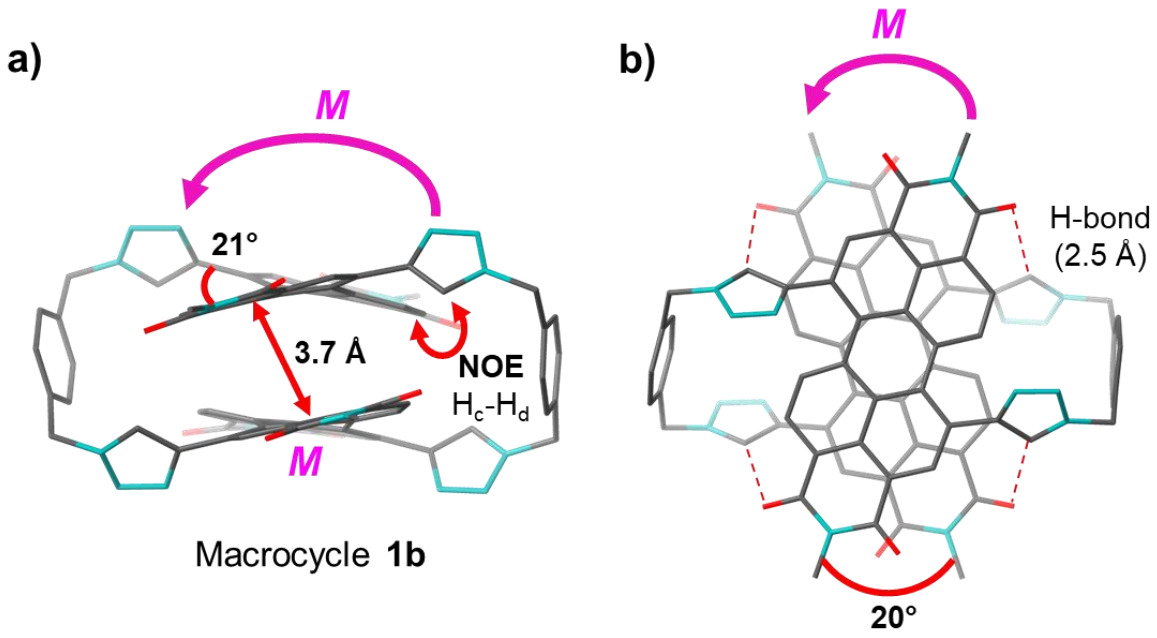

Figure 2.7: X-ray crystal structure of macrocycle **1b** (***MM*** enantiomer, assigned according to the rules of axial chirality), viewed from **(a)** the side and **(b)** the top (alkyl side chains, hydrogens, and cocrystallised solvent molecules are omitted for clarity). From the side view, ***MM*** axial chirality of the PDIs can be appreciated, while from the top one can also see that the PDIs form an ***M***-helically chiral co-facial π-stacked dimer. The NOE observed between PDI H_c and triazole H_d signals in NMR experiments (**Figure 2.6**) is consistent with their close proximity in the crystal structure.

The crystal structure of macrocycle **1b** reveals the atropisomerism[21] (i.e., axial chirality) exhibited by each PDI unit, arising from its twisted aromatic framework (dihedral angle = 21°, **Figure 2.7**). The intramolecular π–π stacking is complementary, occurring exclusively between PDIs of the same chirality, such that the unit cell contains only the enantiomers of the macrocycle ***MM*** and ***PP***.[22] In the ***MM*** macrocycle, the two ***M***-axially chiral twisted PDIs form an ***M***-helically chiral co-facial π-stacked dimer. Likewise, the ***PP*** macrocycle forms a ***P***-chiral dimer. No close-contact PDI-PDI interactions are observed between macrocycles in crystal packing, and the meso isomer ***MP*** is not observed (**Figure 2.8**). This is also the case in toluene solution because the ^{1}H NMR spectrum of macrocycle **1a** contains only a single set of peaks corresponding to the enantiomers ***MM*** and ***PP*** at 373 K. Whilst a preference for PDI-PDI homochiral aggregation had been reported previously,[8, 23, 24] this was the first time that exclusive formation of homochiral dimers was observed in a bay-connected bis-PDI macrocycle.[11, 12]

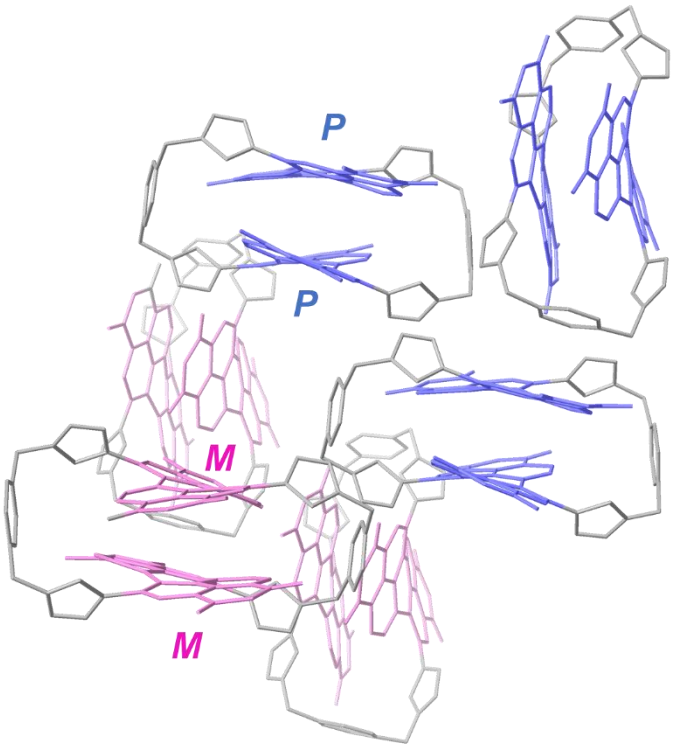

Figure 2.8: Packing of macrocycle **1b** in the crystal structure. Only the ***MM*** **and** ***PP*** enantiomers are observed. No close-contact PDI-PDI interactions are observed between macrocycles, and the diastereomer ***MP*** is not observed.

2.4 Chirality studies

2.4.1 Resolution of enantiomers by chiral HPLC

The next aim was to resolve the enantiomers of macrocycle **1a** by chiral high-performance liquid chromatography (HPLC). With toluene as the major eluent, the chromatogram of **1a** contained two peaks of equal integration, corresponding to the ***MM*** and ***PP*** enantiomers. The identity of these enantiomers is confirmed in the next section by comparison of their experimental and computationally predicted CD spectra.

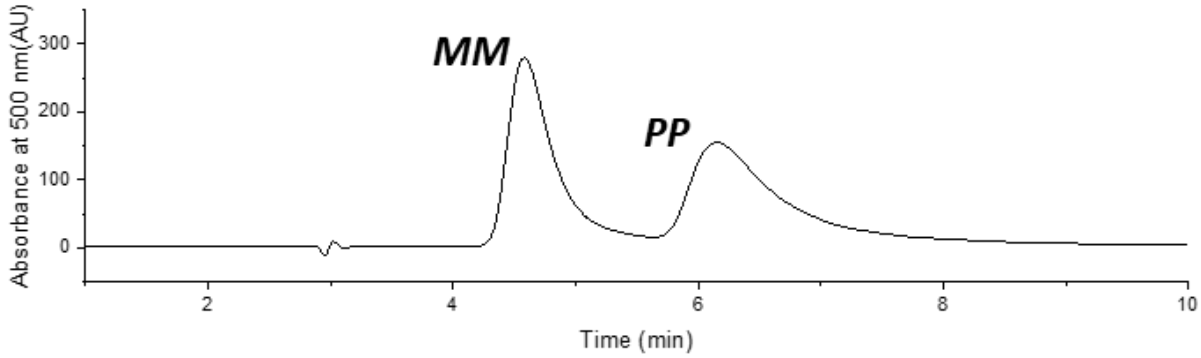

Figure 2.9: Chiral HPLC chromatogram (Phenomenex i-Amylose-1, 250 x 4.6 mm) of macrocycle **1a** dissolved in toluene and eluted with 4:1 (v/v) toluene:*n*-hexane. Using a combination of CD spectroscopy (Section 2.4.2) and computational modelling (Appendix A), the first peak is assigned as the ***MM*** enantiomer and second peak is assigned as the ***PP*** enantiomer. Peak integral ratio (***MM***:***PP***) = 1:1.

Interestingly, when macrocycle **1a** was eluted with DCM as the major eluent, a third peak could be observed, which was hypothesised to be the ***MP*** heterochiral diastereomer. This conclusion was confirmed by further ^{1}H NMR spectroscopic studies of macrocycle **1a** in chlorinated solvents (Section 2.5.1). However, it was found that due to poor resolution on the HPLC column and fast interconversion between stereoisomers in chlorinated solvents, it was not possible to isolate the ***MP*** heterochiral diastereomer for macrocycle **1a**.

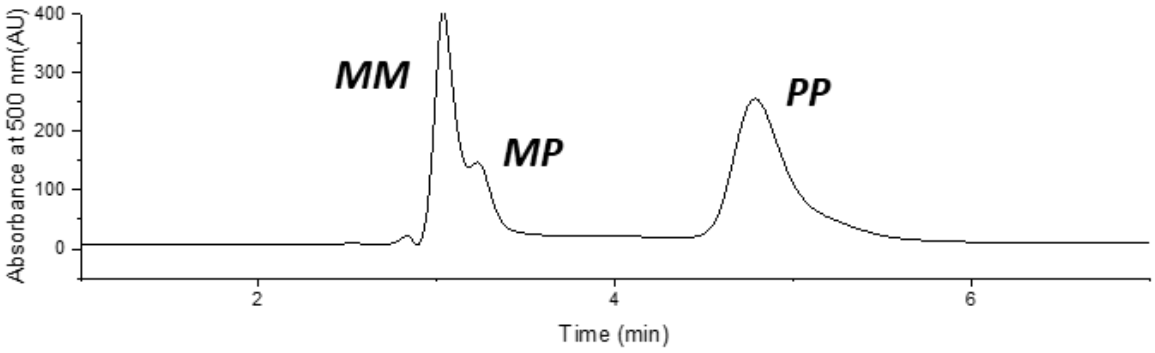

Figure 2.10: Chiral HPLC chromatogram (Phenomenex i-Amylose-1, 250 x 4.6 mm) of compound **1a** dissolved in DCM and eluted with 7:3 (v/v) DCM:n-hexane eluent. From ^{1}H NMR spectroscopy in chlorinated solvents (section 2.5.1), the peaks are assigned to the enantiomers (***PP,MM***) and the diastereomer (***MP***). Peak integral ratio (***MM***:***MP***:***PP***) ~ 4:1:4, although it is challenging to accurately decouple the integrals of ***MM*** and ***MP***.

2.4.2 Chiroptical studies

The enantiomers of macrocycle **1a** were analysed using CD and CPL spectroscopy. The CD and CPL spectra of the ***MM*** and ***PP*** enantiomers of macrocycle **1a** in toluene are shown in

Figure 2.11. The enantiomers were assigned to the spectra by comparison of the experimental CD spectra with time-dependent density functional theory predicted CD spectra of the enantiomers of an analogue of macrocycle **1** in which all the imide substituents are simplified as methyl groups (**Figure 2.12** and Appendix A).

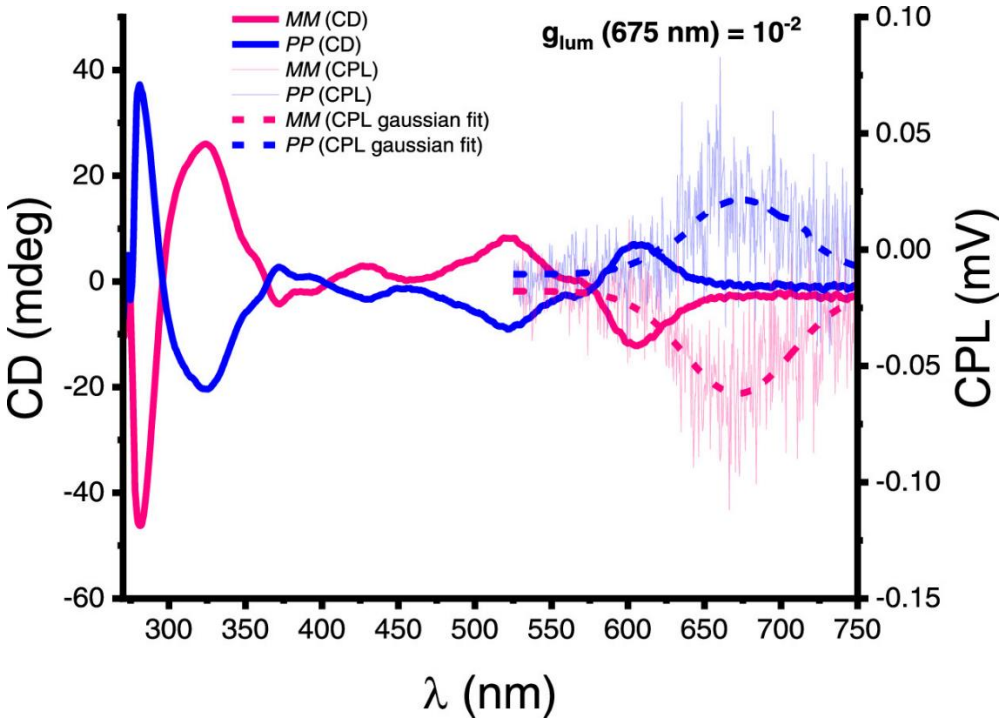

Figure 2.11: Circular dichroism (CD) and circularly polarized luminescence (CPL) spectra of macrocycle **1a** enantiomers ***MM*** and ***PP*** (toluene, 10 μM). Full experimental details are given in section 2.9.7.

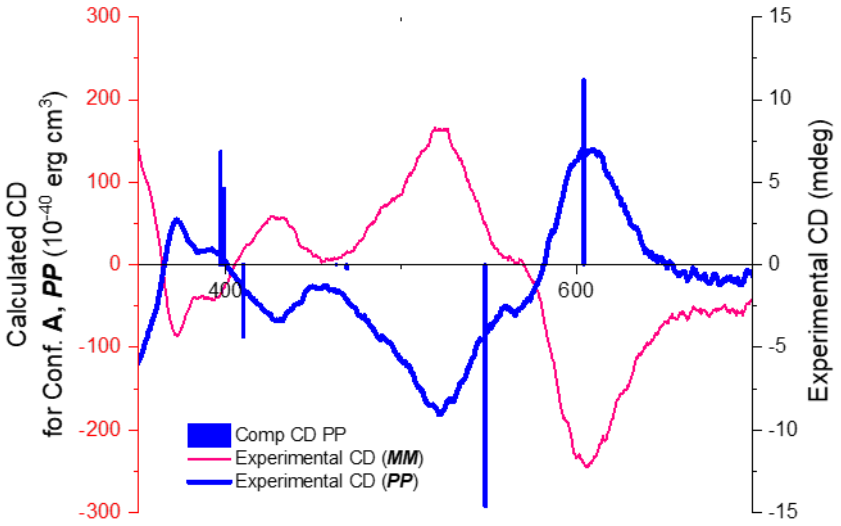

Figure 2.12: Comparison of the experimental CD spectra of macrocycle **1a** with the computationally-predicted CD spectrum (with a red-shift correction of 71 nm) of the ***PP*** enantiomer of a simplified version of macrocycle with methyl imide groups. See Appendix A for full details.

Due to relatively fast racemisation, it was not possible to accurately determine the concentration of the enantiomers (although this was estimated to be ~ 10 μM). Therefore, the molar circular dichroism $\Delta\varepsilon$ and the absorption dissymmetry factor $|g_{abs}|$ for macrocycle **1a** are not reported. However, for CPL measurements, the luminescence dissymmetry factor $|g_{lum}|$ can be determined independently of concentration (section 2.9.7). Excitingly, macrocycle **1a** exhibits one of the highest luminescence dissymmetry factors for a small organic molecule in solution ($|g_{lum}| = 10^{-2}$),[1, 25-28] and at wavelengths approaching the infrared (λ = 675 nm), useful for advanced security inks[29] and multiphoton imaging.[30] The sign of the CPL matches that of the lowest-energy transition in the CD spectrum, implying that the chirality of the emissive excited state matches that of the ground state.[31]

By referring to the UV-vis absorption spectra (**Figure 2.13a**), we can see that the 450-650 nm region in the CD spectra corresponds to the typical PDI $S_0 \rightarrow S_1$ transition. In toluene solvent, this region in the CD spectrum exhibits a Cotton effect, a characteristic feature of chiral excitonic coupling. The sign of this CD couplet is consistent with an ***MM***-axially chiral macrocycle forming an ***M***-helically chiral cofacial H-type dimer (as discussed in the introduction to this thesis) consistent with the crystal structure (and likewise the ***PP***-macrocycle forms a ***P***-helically chiral H-type dimer). The UV-vis spectrum also supports this: the 0–1

vibronic peak is significantly larger than the 0–0 peak ($\varepsilon_{0-0}/\varepsilon_{0-1}$ = 0.58), characteristic of an H-type aggregate.[3]

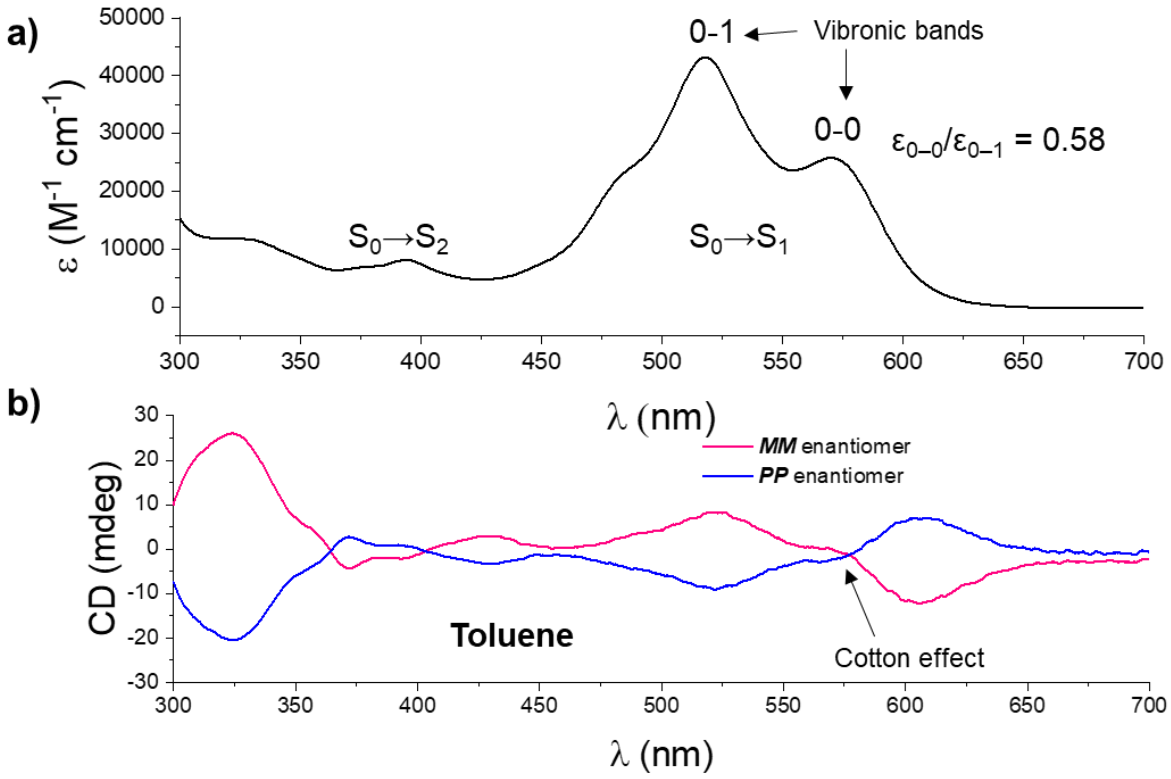

Figure 2.13: a) UV-vis absorption spectrum of macrocycle **1** in toluene (10 μM). **b)** CD spectra of the ***MM*** and ***PP*** enantiomers of macrocycle **1** in toluene (~ 10 μM).

Interestingly, in dichloromethane, the CD spectra are significantly different (**Figure 2.14b**), showing no signs of PDI–PDI chiral excitonic coupling, with the 450-650 nm region that corresponds to the PDI $S_0 \rightarrow S_1$ transition being entirely monosignate, without the Cotton effect observed in toluene. This implies that the H-type cofacial π–π stacking and subsequent excitonic coupling observed in the crystal structure and in toluene is somehow disrupted in dichloromethane. Indeed, the vibronic peak ratio in in the UV-vis spectrum in dichloromethane ($\varepsilon_{0-0}/\varepsilon_{0-1}$ = 0.99) is higher than in toluene, implying that the intramolecular H-aggregate is partially disrupted in dichloromethane (**Figure 2.14a**).

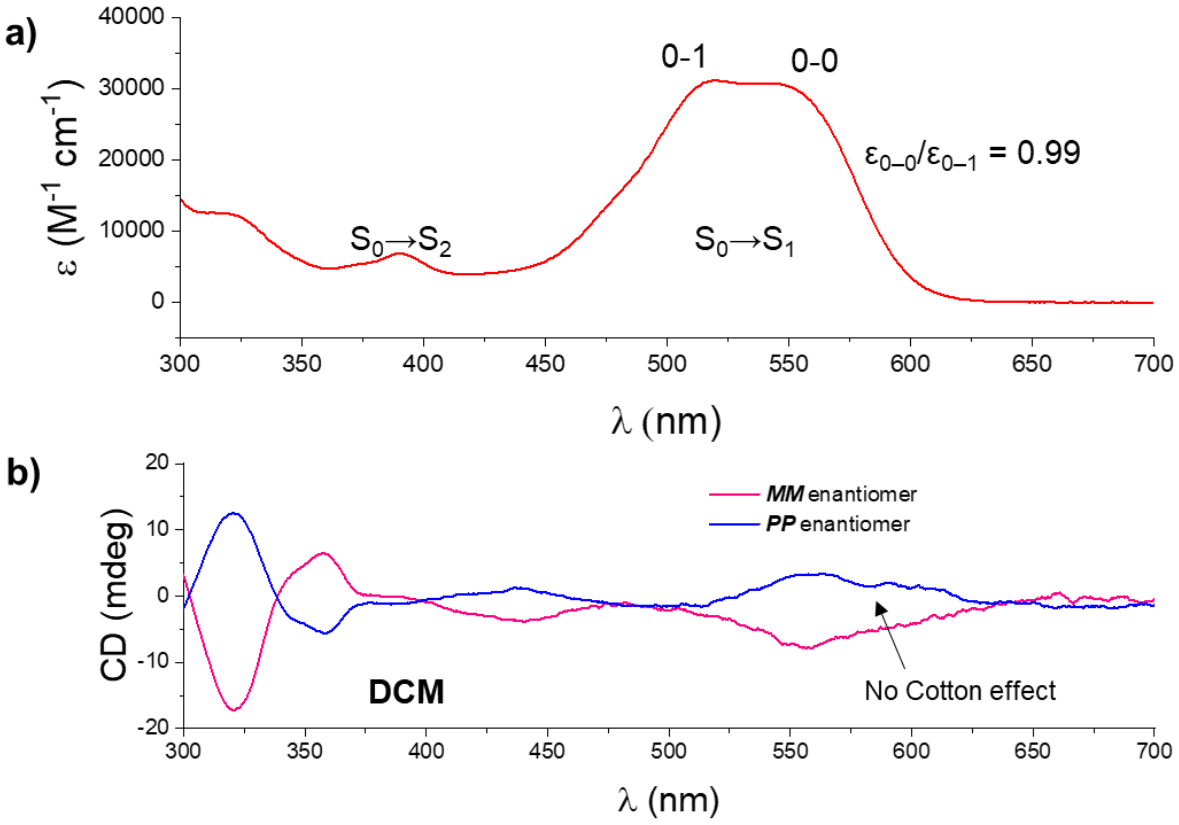

Figure 2.14: a) UV-vis absorption spectrum of macrocycle **1** in DCM (10 μM). **b)** CD spectra of the ***MM*** and ***PP*** enantiomers of macrocycle **1** in DCM (~ 10 μM).

The CD spectra of the same enantiomer **1-*MM*** in DCM and toluene are overlayed in **Figure 2.15a**. Strikingly, if we disregard the Cotton effect in toluene which arises from chiral excitonic coupling (at the red end of the spectrum), the remainder of the CD spectrum is reversed in sign in DCM compared to toluene. This feature is discussed in greater detail in Chapter 4.

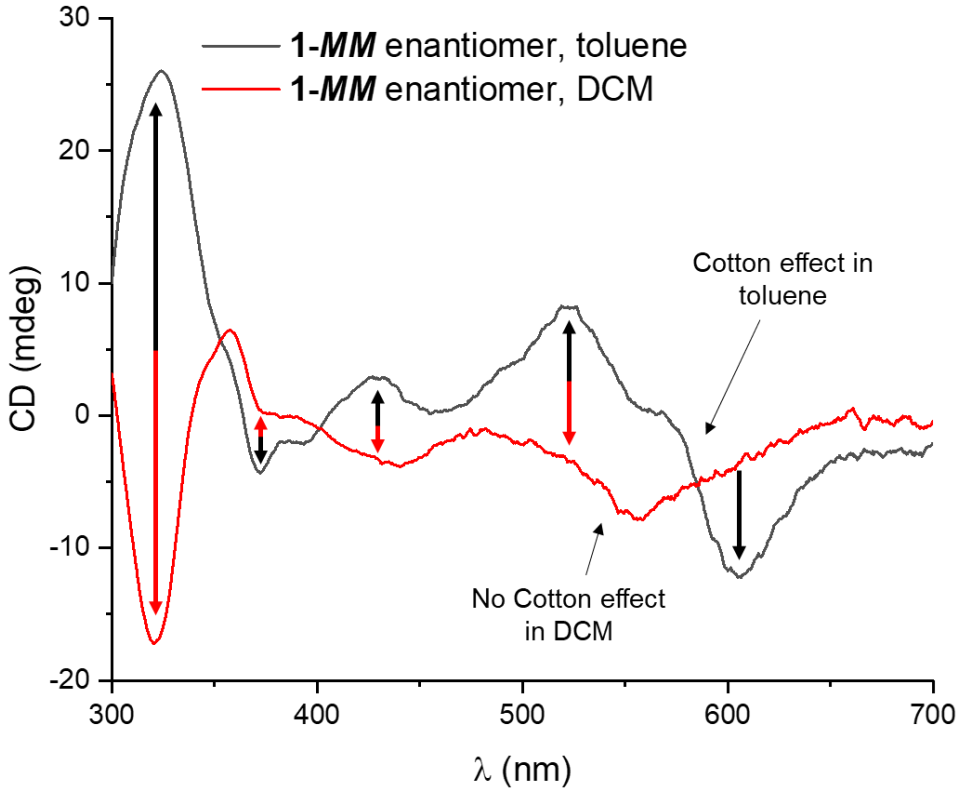

Figure 2.15: CD spectra of the same enantiomer **1-*MM*** in toluene (black trace) and DCM (red trace). **a)** CD spectra of the same enantiomer **1-*MM*** in toluene (black trace) and DCM (red trace).

2.4.3 Racemisation kinetics from chiral HPLC

The enantiomers of macrocycle **1** were found to interconvert and racemise slowly in toluene, and much faster in dichloromethane. Attempts were made to measure the rate of racemisation of the enantiomers in both dichloromethane and toluene using chiral HPLC, although the racemisation rate in dichloromethane was too fast to accurately measure with this method. To measure the rate of racemisation in toluene, a pure fraction of peak **1**-***MM*** was obtained by running macrocycle **1a** through the chiral HPLC column in 80:20 toluene-hexane eluent. The pure fraction of peak A was dried and re-dissolved in toluene. The sample was kept in toluene, and aliquots of it were re-injected into the column once a day for five days, allowing the growth of the **1**-***PP*** peak to be monitored (**Figure 2.16**).

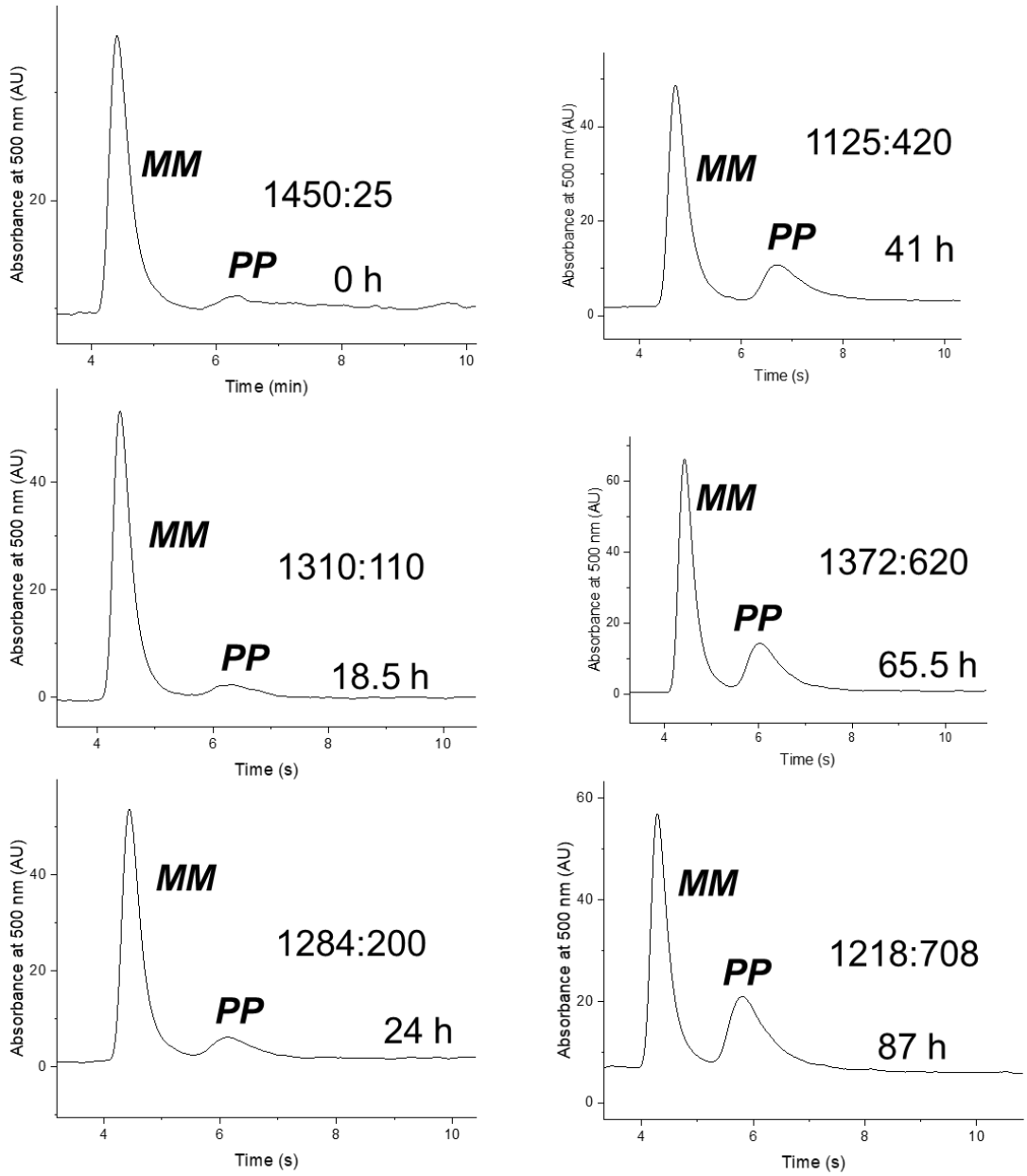

Figure 2.16: Change in the chiral HPLC chromatogram over time of an enantiopure sample of **1a**-***MM*** (***MM:PP*** > 99:1 mol%) kept in toluene at room temperature. The chromatograms were run in 80:20 (v/v) toluene:*n*-hexane eluent. The ***MM***:***PP*** peak integral ratios are given in each chromatogram.

By measuring the ratio of the integrals of the peaks an enantiomeric excess ee_t can be calculated at a given time t. The resulting data can then be fitted to the equation:

$$\ln\left({}^{ee_0}/_{ee_t}\right) = 2kt \qquad (2.1)$$

Where ee_0 is the enantiomeric excess at $t = 0$ and k is the enantiomerisation rate constant. The racemisation rate constant $k_{rac} = 2k$.[32]

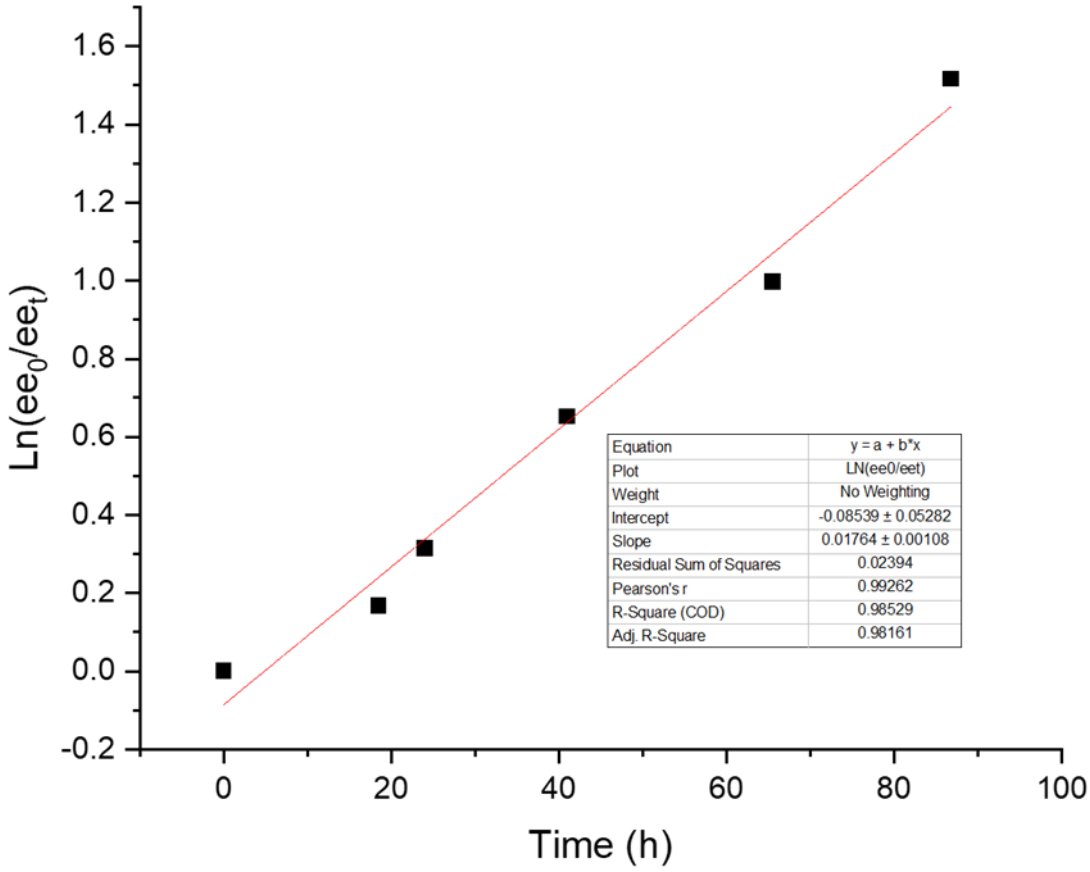

Figure 2.17: Plot and linear fit of $\mathbf{ln}\left(^{ee_0}/_{ee_t}\right)$ against $\boldsymbol{t}$.

The fitting of this data is shown in **Figure 2.17** and results in a rate constant of enantiomerisation $k = 8.82 \times 10^{-3}$ h^{-1} = 2.45×10^{-6} s^{-1} and hence a racemisation rate constant k_{rac} = 4.90×10^{-6} s^{-1} for toluene at room temperature. A free energy of activation for the racemisation process $\Delta G^{\ddagger}$ = 105 kJ mol^{-1} was determined for toluene at room temperature according to the Eyring equation. Interestingly, a sample kept as a solid for several months showed a small degree of racemisation, hence the enantiomer half-life is $t_{1/2}$ ~ years in the solid state (**Figure 2.18**).

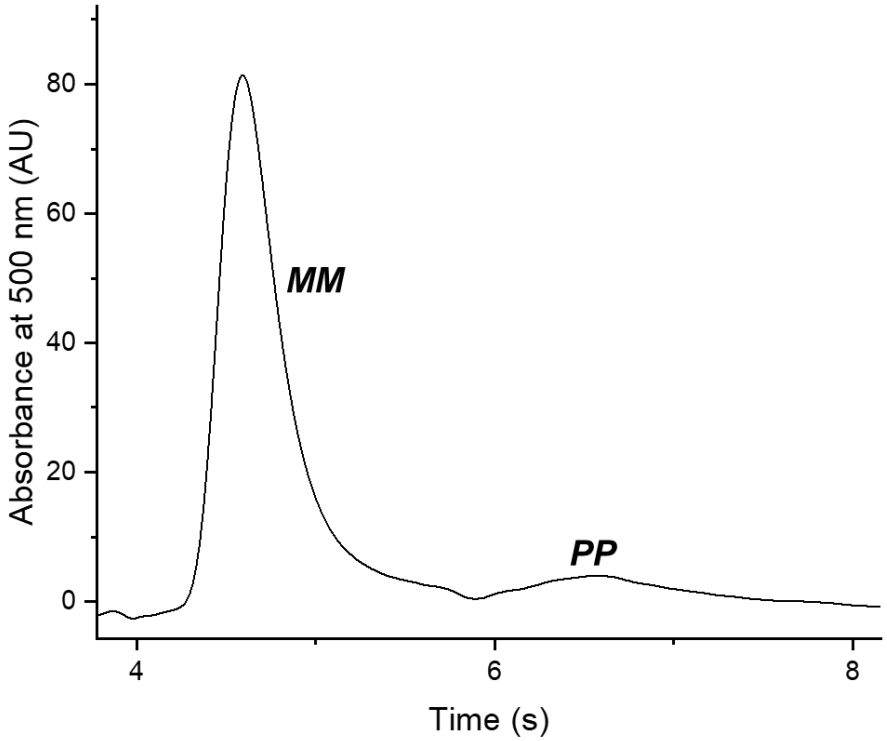

Figure 2.18: Chiral HPLC chromatogram run in 4:1 (v/v) toluene:n-hexane of a sample of **1-*MM*** kept as a dry solid for approximately 3 months (*MM:PP* = 95:5 mol% by peak integration).

2.4.4 Racemisation kinetics from time-course CD spectroscopy

As it was not possible to measure the rate of racemisation in dichloromethane using chiral HPLC, time-course CD spectroscopy was used to determine the rate of racemisation in DCM and verify the rate of racemisation previously obtained in toluene using chiral HPLC. To determine the racemisation rate constants, an enantiopure sample of **1a-*MM*** (10 μM, ***MM*:*PP*** > 99:1 mol%) was dissolved in the solvent being tested (toluene or dichloromethane) and kept in a sealed cuvette at 25 °C. The CD spectrum was recorded at regular time intervals. The decay in intensity of the strongest peaks between λ = 250 - 400 nm was monitored over time and the resulting data was fitted to the following equation:

$$\ln\left({}^{CD_0}/_{CD_t}\right) = 2kt \qquad (2.2)$$

Where CD_0 is the CD signal intensity at $t = 0$ for a given peak, CD_t is the CD signal intensity at time t for a given peak and k is the enantiomerisation rate constant.

For dichloromethane, a CD spectrum was recorded every three minutes, with full racemisation occurring within approximately one hour (**Figure 2.19-20**). For toluene, the spectrum was recorded at various times over the course of five days (**Figure 2.21-22**).

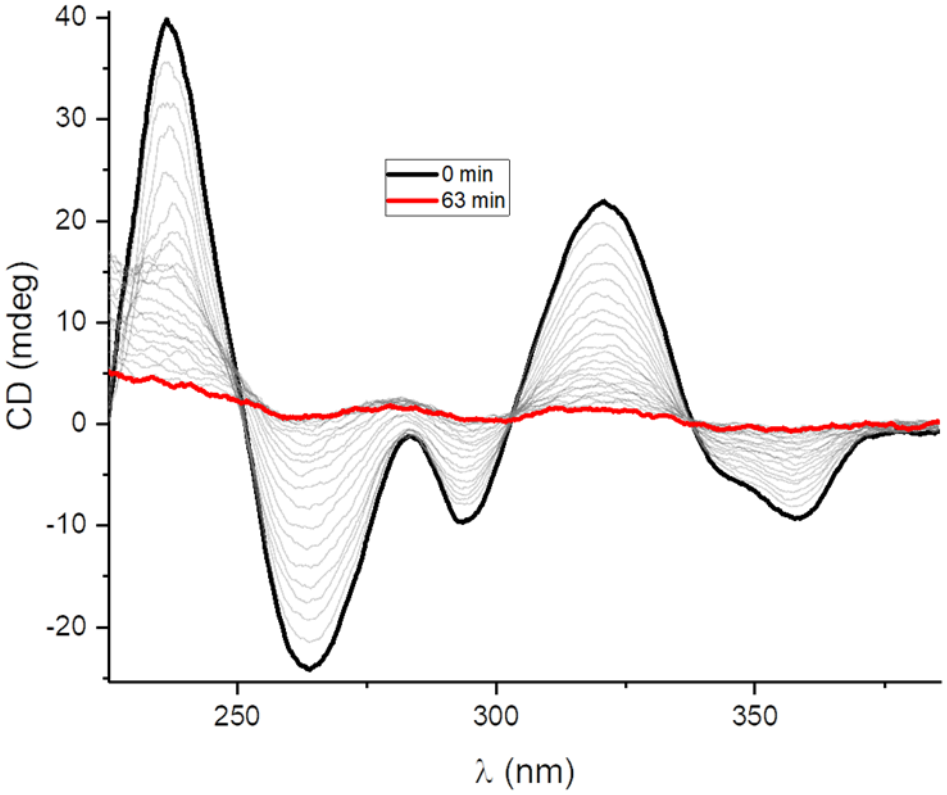

Figure 2.19: Time-course CD spectra for an enantiopure sample of **1a-*MM*** (10 μM, *MM*:*PP* > 99:1 mol%) in DCM.

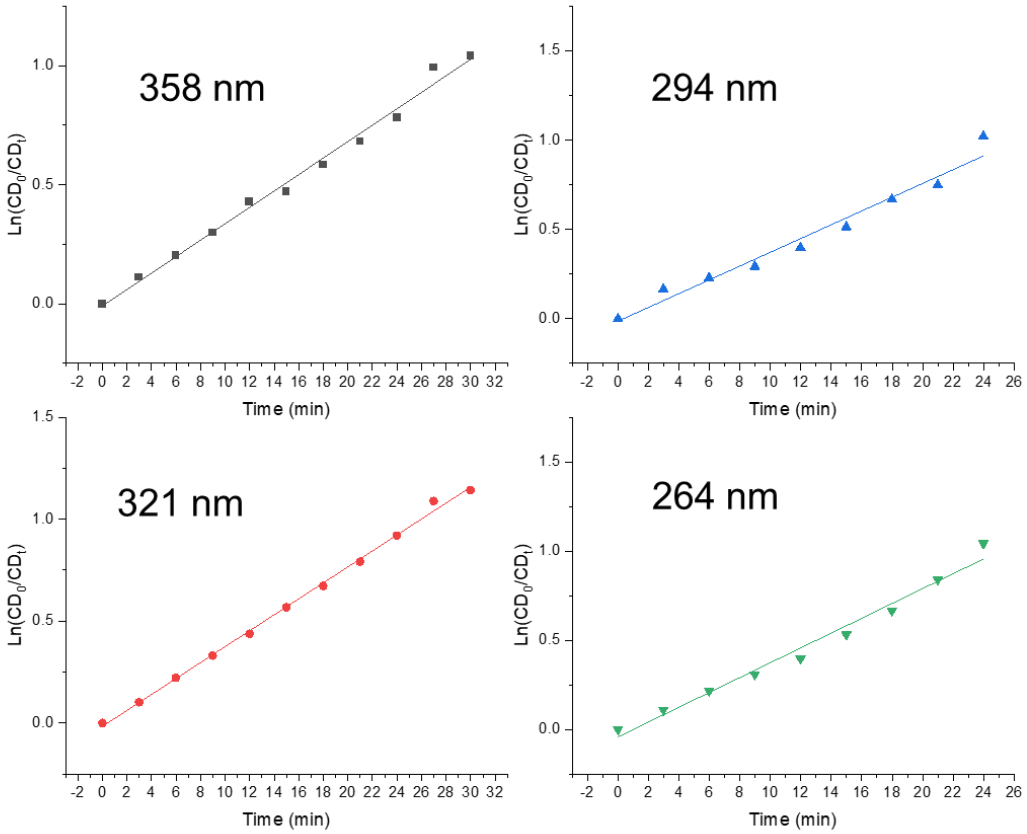

Wavelength	Slope (h^{-1})
358 nm	0.0345
321 nm	0.03914
294 nm	0.03855
264 nm	0.0416

Average slope (h^{-1})
0.0384

Figure 2.20: Plot and linear fit of $\mathbf{ln}\left(^{CD_0}/_{CD_t}\right)$ against $\boldsymbol{t}$ at 358, 321, 294 and 264 nm for the time-course CD experiment measuring the rate of racemisation of macrocycle **1a** in DCM.

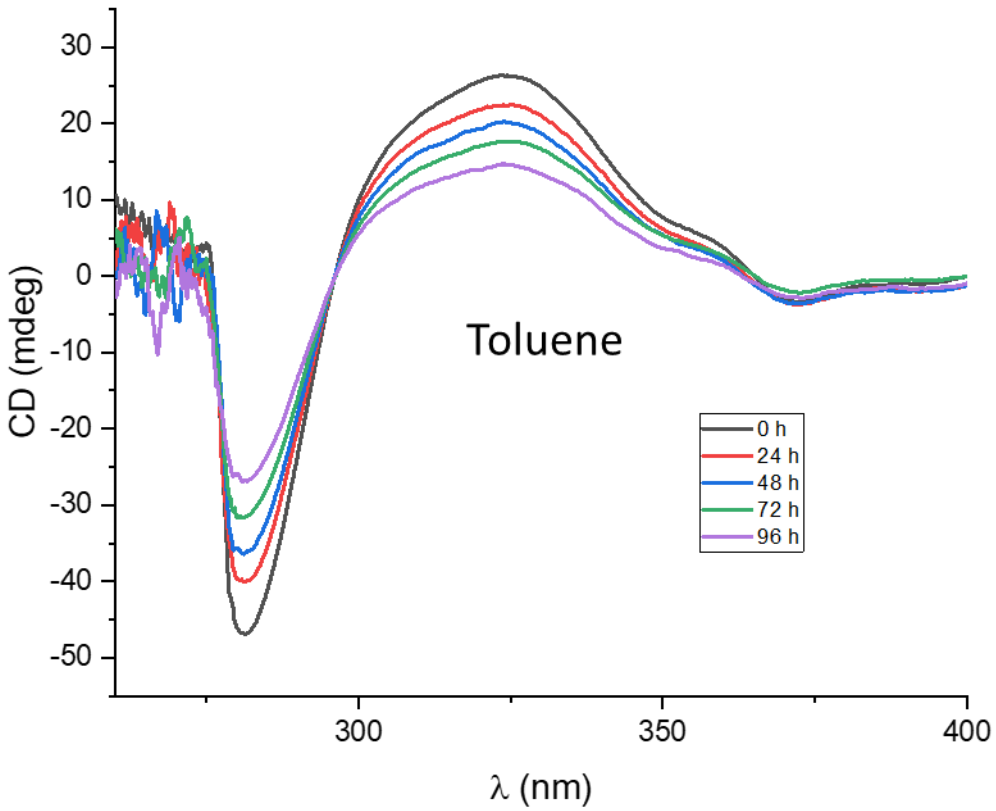

Figure 2.21 Time-course CD spectra for an enantiopure sample of **1a-*MM*** (10 μM, MM:PP > 99:1 mol%) in toluene.

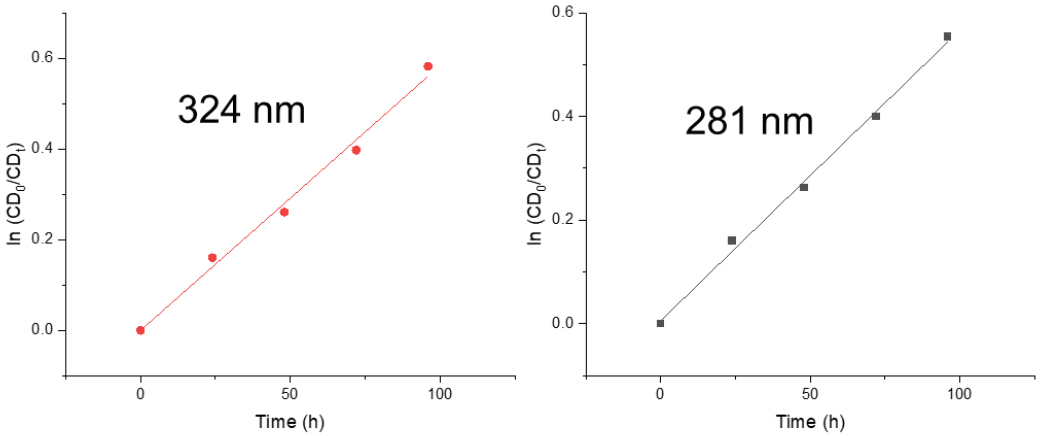

Wavelength	Slope (h^{-1})
324 nm	0.00584
281 nm	0.00561

Average slope (h^{-1})
0.005725

Figure 2.22: Plot and linear fit of $\ln\left(CD_0/CD_t\right)$ against t at 281 nm and 324 nm for the time-course CD experiment measuring the rate of racemisation of macrocycle **1a** in toluene.

The obtained kinetic parameters of racemisation of an initially enantiopure sample of **1a**-***MM*** are given in **Table 2.1**. The rate of racemisation k_{rac} obtained in toluene by CD signal decay is in agreement with the rate of racemisation obtained by chiral HPLC (~ 10^{-6} s^{-1}). Remarkably, the racemization rate in toluene is more than 400 times slower than in dichloromethane due to a significantly larger interconversion barrier ($\Delta\Delta G^{\ddagger}$ = 15 kJ mol^{-1}). Therefore, the ***MM***/***PP*** enantiomer half-life is increased from minutes in chlorinated solvent ($t_{1/2}$ = 18 min) to days in toluene ($t_{1/2}$ = five days), requiring nearly a month to racemize. To put this in further context, the interconversion barrier of **1a** in toluene ($\Delta G^{\ddagger}$ = 108 kJ mol^{-1}) is

significantly larger than previous dynamically chiral bis-PDI macrocycles employing imide- (53–69 kJ mol^{-1})[8, 33] or bay connectivity (86 kJ mol^{-1}).[11] Indeed, the barrier is the same as some tetra-*ortho*-substituted biaryls used for enantioselective catalysis and approaching that required for configurationally stable drugs ($\Delta G^{\ddagger}$ = 114 kJ mol^{-1}). [34-37]

Table 2.1: Kinetic parameters for the racemisation of an initially pure sample of **1**-***MM*** in toluene and DCM (298 K) as determined by time-course CD spectroscopy.

Solvent	***k*** **(s^{-1})**	***k*$_{rac}$ (s^{-1})**	***t*$_{1/2}$ (hours)**	**$\Delta G^{\ddagger}$ (kJ mol^{-1}, 298 K)**
Toluene	$7.95 \times 10^{-7} \pm 7.4 \times 10^{-8}$	$1.59 \times 10^{-6} \pm 1.5 \times 10^{-7}$	121 ± 10	107.8 ± 0.2
DCM	$3.20 \times 10^{-4} \pm 1.4 \times 10^{-5}$	$6.40 \times 10^{-4} \pm 2.3 \times 10^{-5}$	0.3 ± 0.01	92.9 ± 0.1

So far the experimental evidence indicate that macrocycle **1** behaves very differently in toluene compared to chlorinated solvents: the CD and UV-vis spectra in section 2.4.2 suggest that the macrocycle forms an intramolecular H-type aggregate in toluene, while in DCM this H-type aggregate is disrupted. Additionally, as shown by the above racemisation studies, in toluene the enantiomers appear to be relatively stable while in chlorinated solvents the barrier to racemisation is much lower. It is hypothesised that in toluene, strong intramolecular π–π interactions between the two PDIs "anchor" the PDI units into place, slowing down racemisation, while in DCM these intramolecular π–π interactions are much weaker due to improved solvation of the PDI units, [38] which allows the PDI imide heads to "somersault" though the centre of the cavity more easily (this "somersault" motion is a requirement for racemisation of bay-connected bis-PDI macrocycles).[11] The following sections will focus on exploring the contrasting solvent-dependent properties of macrocycle **1** to shed further light on the nature of these conformations and of the chiral PDI-PDI π–π interaction

2.5 Solvent-dependent conformational studies

2.5.1 Solvent-dependent NMR studies

In order to understand the striking differences in chiroptical properties and enantiomer stabilities of macrocycle **1a** in different solvents, ^{1}H NMR spectroscopy was carried out in different toluene-d_8:1,1,2,2-tetrachloroethane-d_2 (TCE-d_2) ratios (**Figure 2.23a**). TCE-d_2 was used instead of DCM-d_2 or chloroform-d to allow heating to 100°C, which is necessary for sharp ^{1}H NMR spectra with this macrocycle.

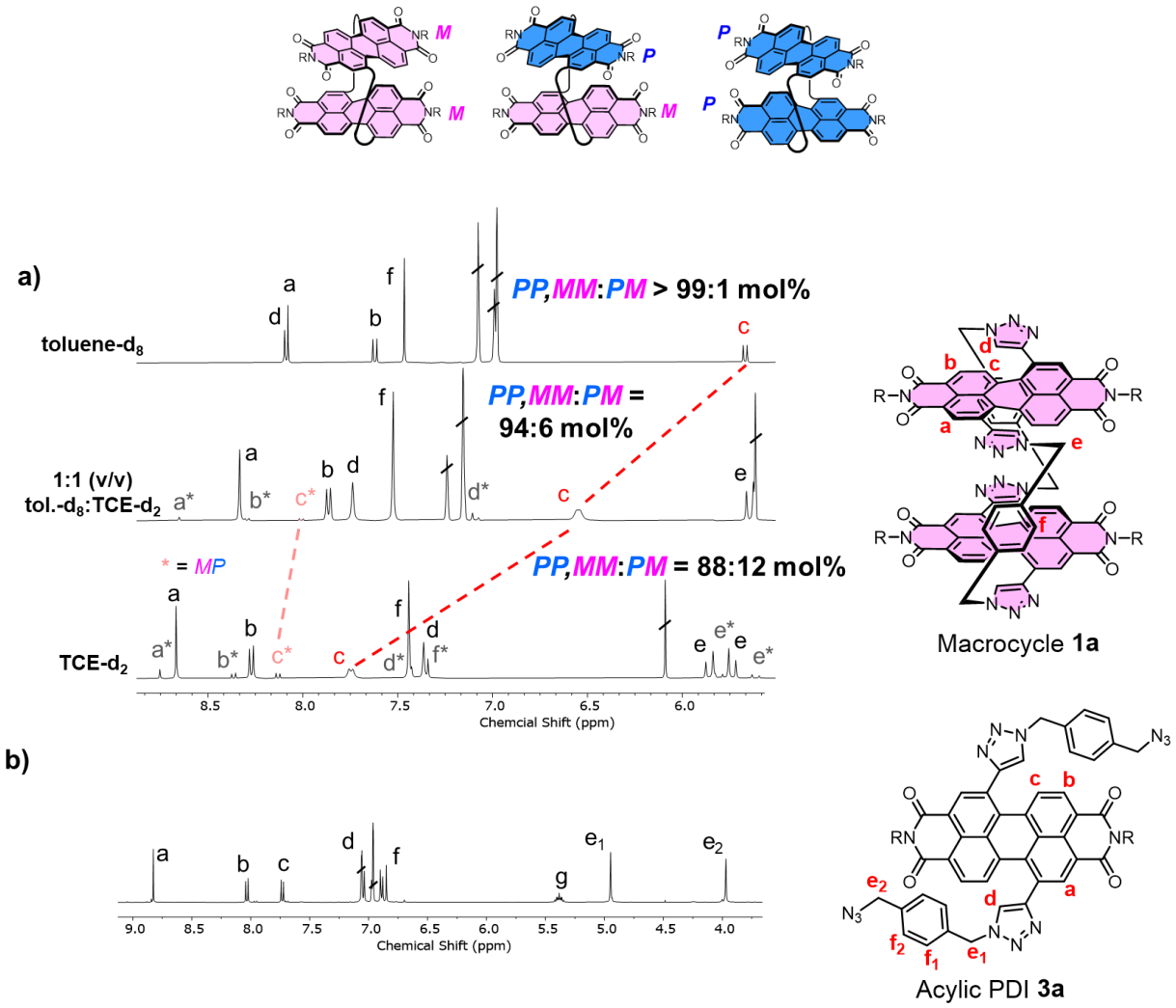

Figure 2.23: a) Stacked ^{1}H NMR spectra of macrocycle **1a** in different toluene-d_8:1,1,2,2-tetrachloroethane-d_2 (TCE-d_2) ratios (373 K, 400 MHz, each referenced to the same internal standard, full experimental details are in section 2.9.4). **b)** ^{1}H NMR spectrum of acyclic PDI **3a** in toluene-d_8 (373 K, 400 MHz).

In toluene-d_8, the upfield shifts of protons $H_{a–c}$ in the spectrum of **1a** are characteristic of closely stacked π surfaces, while the downfield shift of the triazole proton H_d may be

attributed to hydrogen bonding,[19] or may be indicative of the positioning of proton H_d with respect to the PDI aromatic ring currents in this closely π-stacked macrocycle conformation. In contrast, the chlorinated solvent TCE-d_2 disrupts PDI–PDI interactions since $H_{a–c}$ are shifted downfield (Δδ = 0.7–2.1 ppm) and H_d upfield (0.8 ppm), giving a ^{1}H NMR spectrum that more closely resembles the monomeric bis-triazole PDI **3a** (**Figure 2.23b**).

Interestingly, the ^{1}H NMR spectrum in TCE-d_2 also reveals two sets of signals corresponding to two distinct isomers in an 8:1 ratio at 100 °C (**Figure 2.23**), which were shown to be exchanging by ^{1}H–^{1}H EXSY NMR spectroscopy (**Figure 2.24**).

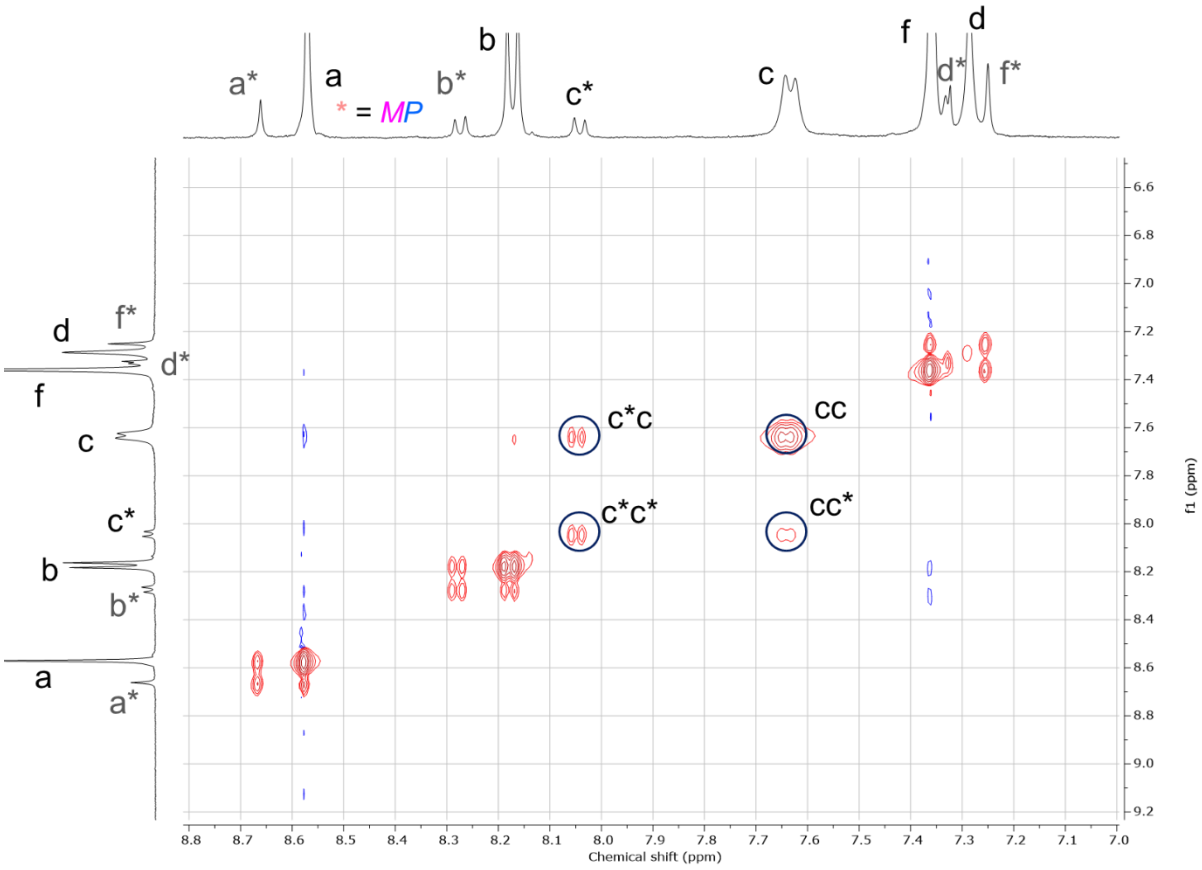

Figure 2.24: Partial ^{1}H-^{1}H EXSY NMR spectrum of macrocycle **1a** (TCE-d_2, 373 K, 400 MHz). Signals with phase shown in red are EXSY signals which show which ^{1}H NMR signals are under chemical exchange, via interconversion of *MM*,*PP* enantiomers with the *MP* diastereomer. The EXSY signal set for the exchange of H_c (*MM*,*PP* enantiomer species) and H_{c*} (*MP* diastereomer) is highlighted as an example.

In agreement with previous bis-PDI macrocycles,[8, 11, 39, 40] this strongly suggests the existence of the diastereomer ***MP***, alongside enantiomers ***MM*** and ***PP***. Upon increasing the

proportion of toluene-d_8, the mole fraction of the major component ***MM/PP*** increases, and its ^{1}H NMR signals converge on the single set of peaks observed in pure toluene-d_8 (**Figure 2.23a**). Interestingly, the solvent-induced perturbations are much larger for the homochiral ***MM/PP*** stereoisomers ($\Delta\delta$ = 2.1 ppm for H_c) than for the heterochiral ***MP*** diastereomer ($\Delta\delta$ = 0.1 ppm for H_{c*}), suggesting that the PDI–PDI π–π interactions are stronger in homochiral conformations compared to heterochiral conformations. In addition, the NOE observed in toluene-d_8 between protons H_c and H_d is not observed in TCE-d_2, which shows that these protons are further apart in space when the macrocycle adopts a different conformation in chlorinated solvents (**Figure 2.25**).

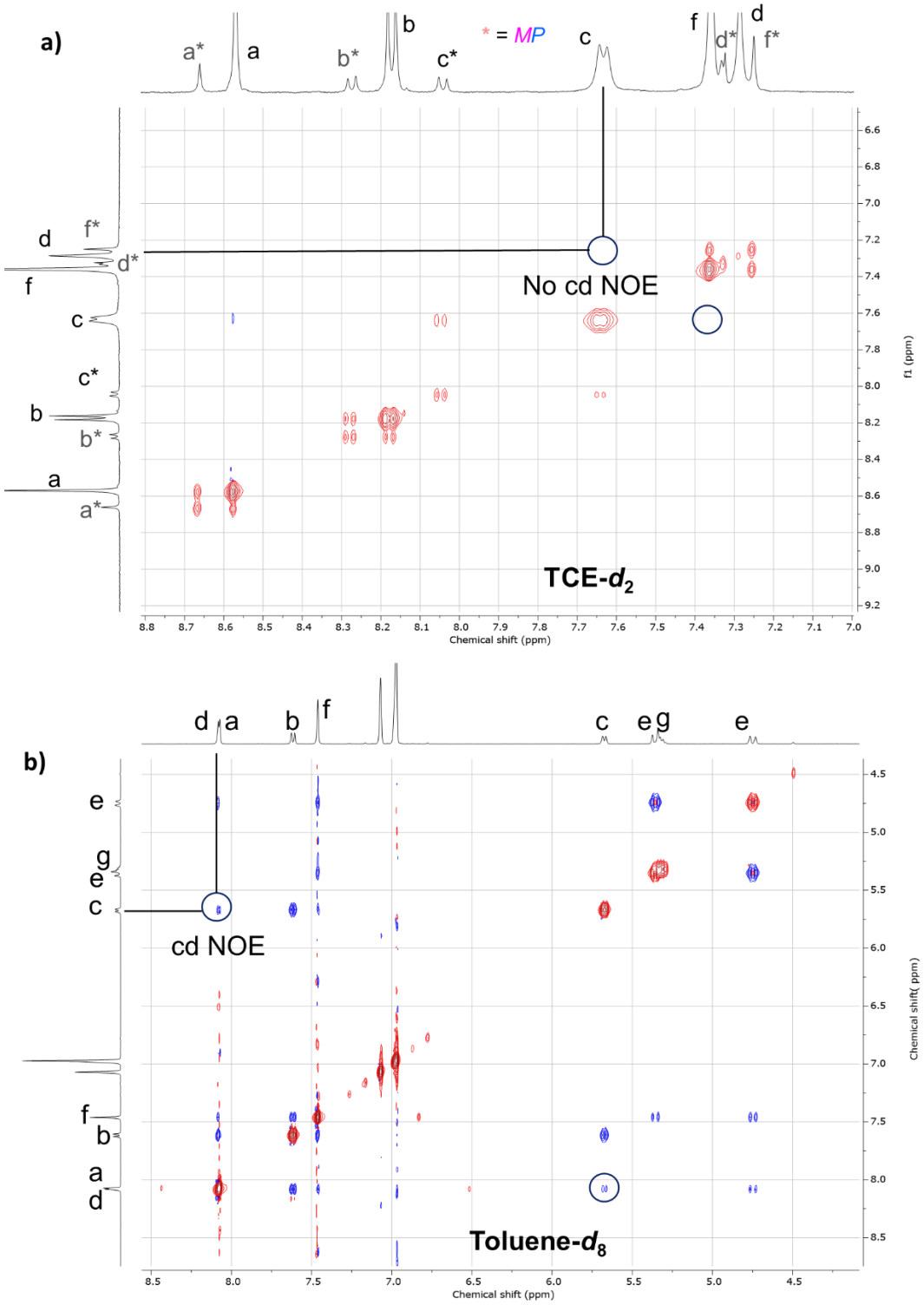

Figure 2.25 Partial ^{1}H-^{1}H EXSY/NOESY NMR spectrum of macrocycle **1a** (373 K, 400 MHz). In **(a)** TCE-d_2 and **(b)** toluene-d_8. Signals with phase shown in red are EXSY signals and signals with phase shown in blue are NOESY signals. Unlike in toluene no NOE is seen between the H_c and H_d protons in TCE-d_2.

To summarise, the results from these NMR experiments show that in toluene, macrocycle **1a** is in a conformation where there is a strong PDI-PDI π–π interaction that leads to exclusive homochirality (i.e. only the ***MM*** and ***PP*** enantiomers are present, with no ***MP*** being observed). In contrast, in the chlorinated solvent TCE, the PDI-PDI π–π interactions appear to be largely switched off, and some ***MP*** diastereomer is observed. This suggests that the π–π interactions themselves are preferentially homochiral, and when these interactions are switched on they lead to a stabilisation of the homochiral ***MM*** and ***PP*** enantiomers over the heterochiral ***MP*** meso isomer. These NMR results are therefore in agreement with the results from crystallography, CD and UV-vis spectroscopies, racemisation studies and chiral HPLC discussed in the previous sections. The following sections will further explore this preference for homochiral intramolecular PDI-PDI π–π stacking, the potential mechanism of racemisation, and how different solvents are able to switch the PDI-PDI π–π interactions on and off.

2.5.2 Kinetics of diastereomer interconversion by EXSY NMR

Having established that in TCE-d_2 both the ***MM/PP*** enantiomers and the ***MP*** meso isomer can be observed for macrocycle **1a** (and indeed also for **1b**, see experimental section 2.9), and that these are interconverting, it was assumed, based on previous work by Ball et al.,[11] that the ***MP*** meso isomer is an intermediate in the interconversion between the ***MM*** and ***PP*** enantiomers (**Figure 2.26**).

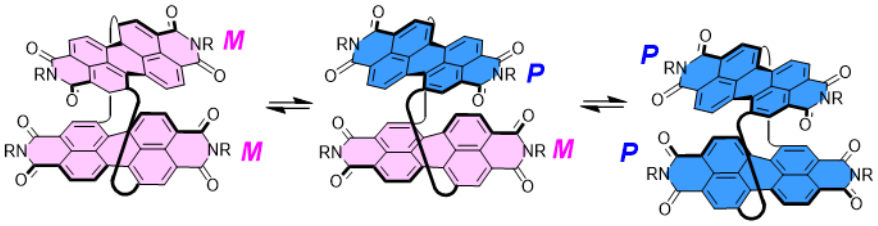

Figure 2.26: Proposed interconversion between the ***MM*** and ***PP*** enantiomers of macrocycle **1** via the ***MP*** meso isomer.

^{1}H-^{1}H EXSY spectra were carried out at different temperatures in order to obtain kinetic and thermodynamic information about the interconversion between the stereoisomers. In particular, by measuring the rates of interconversion between the ***MM/PP*** enantiomers and the ***MP*** meso isomer, an energy barrier for the interconversion process can be measured. These experiments were carried out in TCE-d_2 as well as 1:1 toluene-d_8:TCE-d_2 to see what effect the addition of toluene has on the kinetics of interconversion. Of course, in pure toluene-d_8 no ***MP*** can be observed.

By measuring the diagonal and cross peak intensities for each pair of exchanging signals in a ^{1}H-^{1}H EXSY spectrum at different mixing times, the forwards and backwards rates of ***MM/PP*↔*MP*** interconversion can be determined.[41-44] Full experimental details are given in section 2.9.4. The results are summarised in **Table 2.2**.

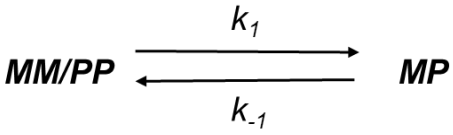

Table 2.2: Rates (k_1 and k_{-1}) and corresponding free energies of activation ($\Delta G^{\ddagger}_1$ and $\Delta G^{\ddagger}_{-1}$) for the interconversion between enantiomers *MM/PP* and diastereomer *MP* of macrocycle **1a**, determined by ^{1}H-^{1}H EXSY NMR spectroscopy at different temperatures and in different solvents.

Solvent	Temp. (K)	k_1 (s^{-1})	$\Delta G^{\ddagger}_1$ (kJ mol^{-1})	k_{-1} (s^{-1})	$\Delta G^{\ddagger}_{-1}$ (kJ mol^{-1})
TCE-d_2	353	0.023	103.8	0.086	99.7
	358	0.031	102.9	0.159	97.8
	363	0.043	101.8	0.206	97.0
	368	0.071	100.2	0.372	95.1
	373	0.103	99.1	0.574	93.8
1:1 (v/v) tol.-d_8:TCE-d_2	373	0.090	99.5	1.05	91.9

To obtain the thermodynamic parameters for the transition state for ***MM/PP*** ⇄ ***MP*** interconversion, the data in pure TCE-d_2 can be fitted to the linear form of the Eyring equation: [45]

$$\ln\frac{k}{T} = \frac{-\Delta H^{\neq}}{R}\frac{1}{T} + \ln\frac{k_B}{h} + \frac{\Delta S^{\neq}}{R} \qquad (2.3)$$

Where k_B is the Boltzmann constant, R is the gas constant and h is Planck's constant. The fittings for the forwards and backwards reactions are shown in **Figure 2.27-2.28.**

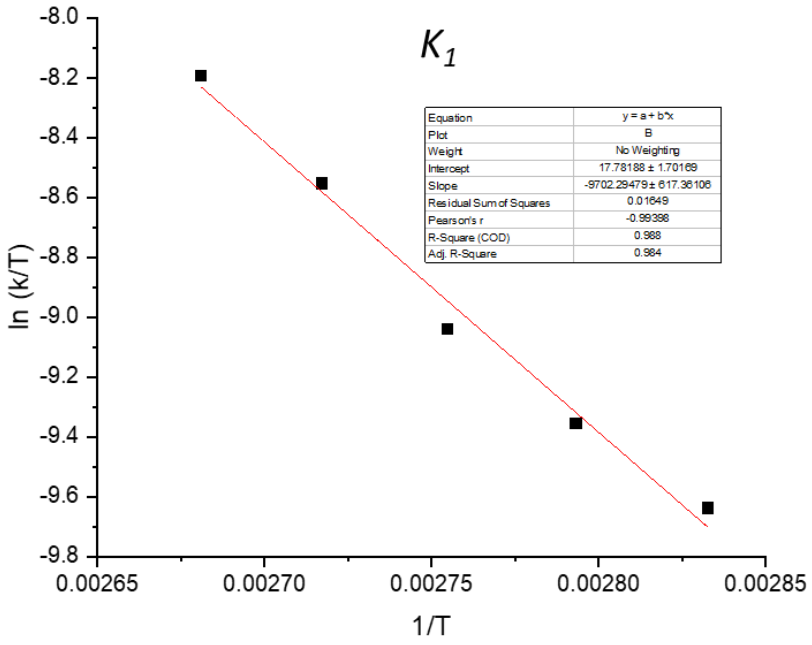

Figure 2.27: Van 't Hoff plot for the forwards rate constant (k_1) of interconversion between the enantiomer ***MM/PP*** and the diastereomer ***MP*** of macrocycle **1a**, obtained from ^{1}H-^{1}H EXSY NMR experiments at different temperatures.

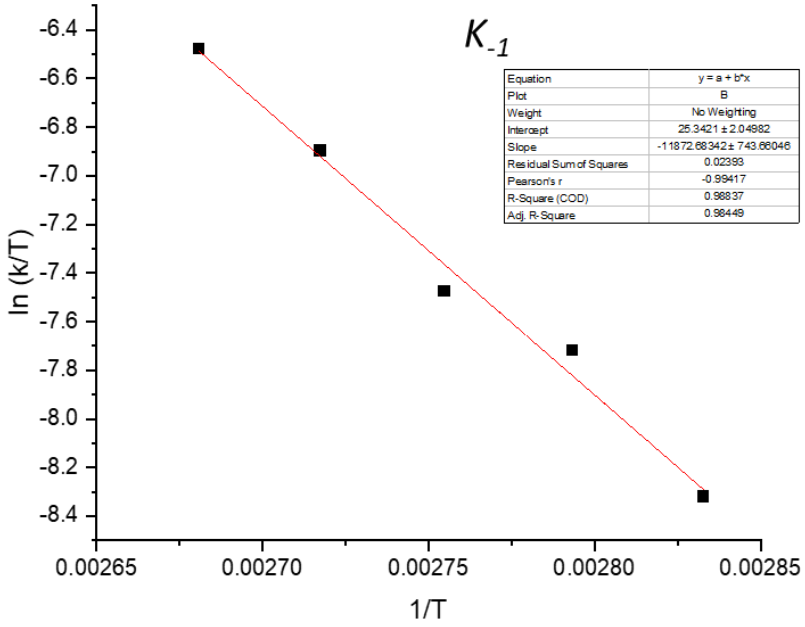

Figure 2.28: Van 't Hoff plot for the backwards rate constant (k_{-1}) of interconversion between the enantiomer ***MM/PP*** and the diastereomer ***MP*** of macrocycle **1a**, obtained from ^{1}H-^{1}H EXSY NMR experiments at different temperatures.

These fittings yield $\Delta H^{\ddagger}$ = 80.7 ± 5.7 kJ mol^{-1} and $\Delta S^{\ddagger}$ = – 49.7 ± 14.1 J K^{-1} mol^{-1} for the forwards ***MM/PP*** → ***MP*** process and $\Delta H^{\ddagger}$ = 98.7 ± 6.2 kJ mol^{-1} and $\Delta S^{\ddagger}$ = + 13.0 ± 17.0 J K^{-1} mol^{-1} for the backwards ***MP*** → ***MM/PP*** process, in pure TCE-d_2. From here, $\Delta G^{\ddagger}$ in pure TCE-d_2 can be calculated at 298 K: $\Delta G^{\ddagger}_{1}$ (298 K) = 95.5 kJ mol^{-1} for the forwards ***MM/PP*** → ***MP*** process and $\Delta G^{\ddagger}_{-1}$ (298 K) = 94.8 kJ mol^{-1} for the backwards ***MP*** → ***MM/PP*** process.

Interestingly, this barrier for interconversion between stereoisomers in TCE-d_2 at 298 K (~ 95 kJ mol^{-1}) is very close to the racemisation barrier determined in DCM by time-course CD spectroscopy (~ 93 kJ mol^{-1}), which is consistent with the ***MP*** stereoisomer being an intermediate in the interconversion between ***MM*** and ***PP***.

Additionally, as seen in **Table 2.2**, the addition of toluene-d_8 decreases the rate of ***MM***/***PP*** loss (Δk = −0.02 s^{-1}) and increases the rate of ***MP*** loss ($\Delta k'$ = 0.49 s^{-1}). This also agrees with ^{1}H NMR spectroscopic and chiral HPLC experiments outlined in previous sections which show that toluene stabilises the ***MM***/***PP*** enantiomers over the heterochiral ***MP*** meso isomer.

2.5.3 Absorption and emission spectroscopy

With ^{1}H NMR spectroscopy studies indicating that toluene switches on intramolecular PDI-PDI π–π interactions while chlorinated solvents switch them off, it was decided to study these interactions through UV–vis absorption and fluorescence emission spectroscopy, to gain a deeper insight into the switchable homochiral conformation of macrocycle **1**. The UV-vis absorption and fluorescence emission spectra of macrocycle **1a** are given in **Figure 2.29**.

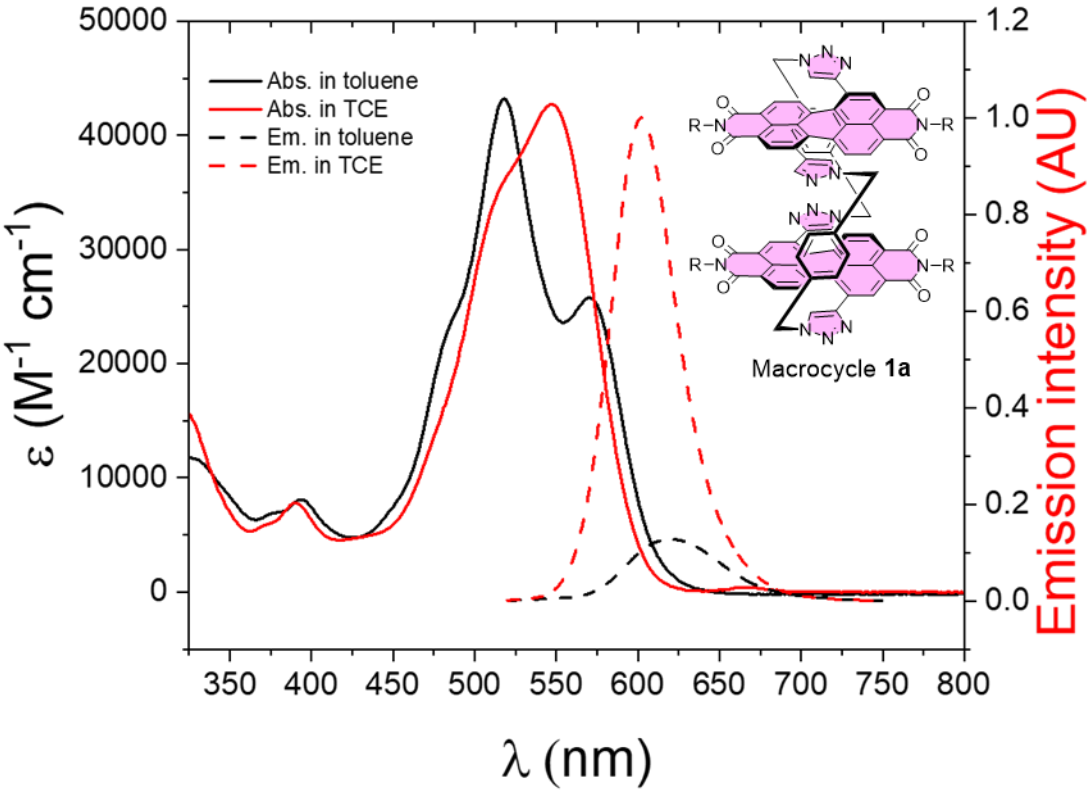

Figure 2.29: UV-vis absorption and fluorescence emission spectra of macrocycle **1a** in toluene and TCE (10 μM). Intramolecular H-type agreggation in toluene results in a reversal in the 0-0 and 0-1 vibronic peak intensities in the UV-vis spectrum, and in quenching of fluorescence emission.

The main PDI absorption band of **1a** in toluene has a 0–1 vibronic peak that is significantly larger than the 0–0 peak ($\varepsilon_{0-0}/\varepsilon_{0-1}$ = 0.58), characteristic of an H-type aggregate (**Figure 2.29**).[3] Indeed, this $\varepsilon_{0-0}/\varepsilon_{0-1}$ ratio is one of the lowest of any PDI dimer[46-48] indicative of strong PDI–PDI electronic coupling in macrocycle **1a**. It was hypothesised here that this is key to the macrocycle's high $|g_{\mathrm{lum}}|$, since the aggregation of chiral monomers is known to amplify their dissymmetry.[26, 49] This hypothesis is confirmed through further studies in **Chapter 3**. This finding also supports the theory that strong PDI–PDI π–π stacking is responsible for raising the barrier to macrocycle racemisation in toluene and in the solid state.

In contrast, the UV–vis spectrum of **1a** in TCE resembles that of the monomeric bis-triazole PDI **3a** ($\varepsilon_{0-0}/\varepsilon_{0-1}$ = 1.19, **Figure 2.30**), consistent with a weakly coupled conformation in which H-type aggregation is disrupted.[50] The fluorescence spectrum of macrocycle **1a** in toluene is indicative of a PDI–PDI excimer,[51] since relative to **1a** in TCE and acyclic control **3a**, the emission becomes weaker (quantum yield $\Phi_{\mathbf{1a}}$ = 0.42 in toluene, $\Phi_{\mathbf{1a}}$ = 0.9 in TCE), broader (Δ[FWHM] = 19 nm), and bathochromically shifted (Δλ = 20 nm), with a large Stokes shift (λ = 102 nm). The UV–vis spectra of **1a** follow the Beer–Lambert law in both toluene and TCE, demonstrating that the solvent-mediated π–π stacking observed is intramolecular in origin (**Figure 2.31**).

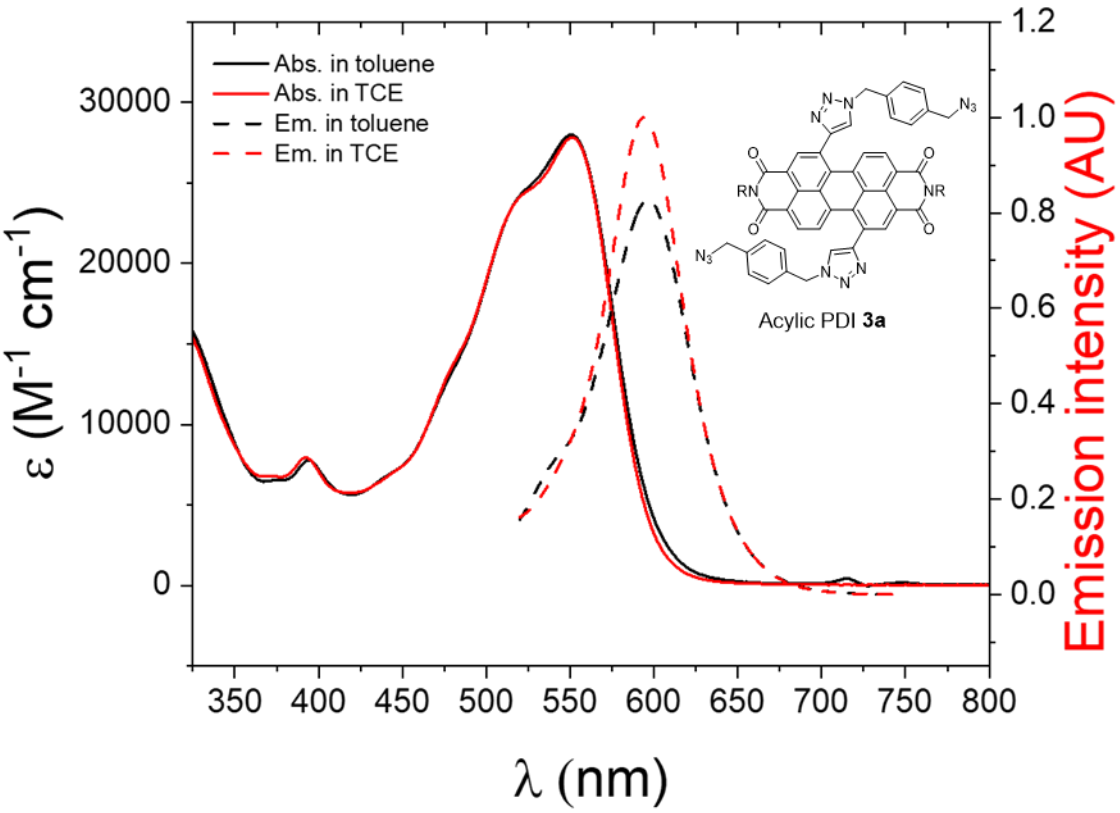

Figure 2.30: UV-vis absorption and fluorescence emission spectra of acyclic bis-triazole PDI **3a** in toluene and TCE (10 μM). The UV-vis spectra of 3a have no solvent dependence, in contrast to macrocycle **1a**.

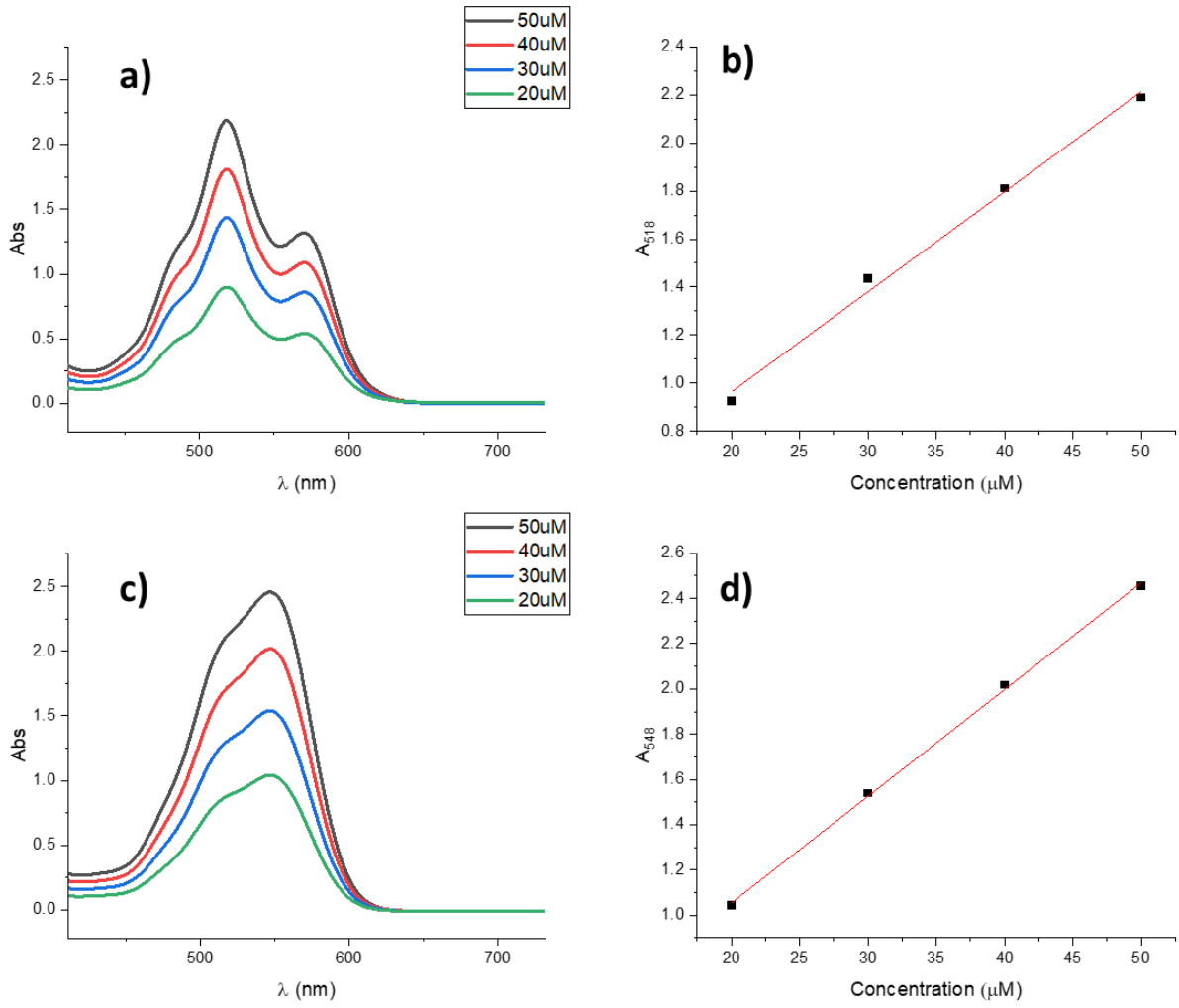

Figure 2.31 a) Absorption spectrum of macrocycle **1a** in toluene at different concentrations, up to Abs_{max} for the instrument. b) The dependence of absorption (518 nm) on concentration for macrocycle **1a** in toluene is linear, showing Beer-Lambert behaviour. c) Absorption spectrum of macrocycle **1a** in TCE at different concentrations. d) The dependence of absorption (548 nm) on concentration for macrocycle **1a** in TCE is linear, showing Beer-Lambert behaviour.

To summarise these results, toluene induces the formation of an intramolecular H-type aggregate in the ground state and a PDI excimer in the excited state of **1a**, while in TCE, the PDI–PDI excitonic coupling is significantly weaker.[52]

2.5.4 Further exploration of the solvent-dependent intramolecular π–π interaction

To gain a deeper insight into the macrocycle-solvent interactions that promote intramolecular H-type aggregation, the UV-vis absorption spectrum of **1a** was recorded in a wide range of solvents. The ratio of the 0-0 and 0-1 vibronic bands ($A_{0\text{-}0}$ / $A_{0\text{-}1}$) in the main PDI transition ($S_0 \rightarrow S_1$) was recorded for each solvent.

For a quantitative analysis, a Gibbs free energy of intramolecular H-type aggregation (ΔG_{agg}) was determined for each solvent, following an adapted method used by Würthner and co-workers.[53] In this method, the following assumptions are made:

1) The $A_{0\text{-}0}$ / $A_{0\text{-}1}$ ratio in toluene (0.58) corresponds to all molecules of macrocycle **1a** being in a state of full intramolecular H-type aggregation.

2) The $A_{0\text{-}0}$ / $A_{0\text{-}1}$ ratio in TCE (1.19) corresponds to all molecules of macrocycle **1a** being in a state where there is no H-type aggregation.

These assumptions are validated by the fact the $A_{0\text{-}0}$ / $A_{0\text{-}1}$ ratio for macrocycle **1a** is minimised in toluene (0.58), while the ratio is maximised in TCE (1.19) and is the same as that of the monomeric PDI **3a** in either solvent. The ***MP*** diastereomer, which is unlikely to be an H-type aggregate (**Appendix A** and **Chapter 4**), is disregarded in this analysis, since it is present as a minor species in chlorinated solvents (~10 mol%).

From the above assumptions, the mole fraction α_u of fully unaggregated molecules can be estimated according to the following equation:

$$\alpha_u = \frac{\rho_a - \rho_{obs}}{\rho_a - \rho_u} \qquad (2.4)$$

Where ρ_a is the $A_{0\text{-}0}$ / $A_{0\text{-}1}$ ratio of the fully H-type aggregated macrocycle in toluene, ρ_u is the $A_{0\text{-}0}$ / $A_{0\text{-}1}$ ratio of the non H-type aggregated macrocycle in TCE and ρ_{obs} is the observed $A_{0\text{-}0}$ / $A_{0\text{-}1}$ for a given solvent being investigated.[53]

From this, an equilibrium constant K_{eq} can be calculated as follows:

$$K_{eq} = \frac{C_a}{C_u} = \frac{1 - \alpha_u}{\alpha_u} \qquad (2.5)$$

Where C_a and C_u are the concentrations of H-type aggregated and non H-type aggregated macrocycles respectively. Hence, a Gibbs free energy of intramolecular H-type aggregation (ΔG_{agg}) can be determined for each solvent according to:

$$\Delta G_{\text{agg}} = -RT \ln K_{eq}$$

As toluene and TCE are the reference solvents for fully H-type aggregated and non-H-type aggregated species respectively, they cannot be included in the ΔG plots as they represent asymptotes in the model.

Table 2.3: $A_{0\text{-}0}$ / $A_{0\text{-}1}$ ratios and corresponding ΔG_{agg} values for macrocycle **1a** in different solvents.

Solvent	**$A_{0\text{-}0}$ / $A_{0\text{-}1}$**	**ΔG_{agg} (kJ mol^{-1})**
Benzene	0.58	n/a
Toluene	0.58	n/a
tert-Butylbenzene	0.58	n/a
α,α,α-trifluorotoluene	0.59	-11.37
m-Xylene	0.62	-6.94
Fluorobenzene	0.62	-6.53
p-Xylene	0.62	-6.51
1:1 Chloroform:n-hexane	0.64	-5.76
o-Xylene	0.65	-5.22
Chlorobenzene	0.65	-5.12
Bromobenzene	0.73	-2.73
Acetonitrile	0.75	-2.39
Benzyl alcohol	0.78	-2.73
Chloroform	0.80	-1.40
Iodobenzene	0.82	-1.02
Trifluoroethanol	0.89	-0.035
Acetone	0.91	0.43
DCM	0.99	1.82
1,2-Dichlorobenzene	1.07	3.68
Benzonitrile	1.09	4.21
Benzaldehyde	1.09	4.47
DMSO	1.13	5.98
Nitrobenzene	1.16	8.00
TCE	1.19	n/a

The ΔG_{agg} of macrocycle **1a** for different solvents were plotted against various solvent scales (**Figures 2.32-2.39**). Good correlations are observed against scales that account for solvent polarity (ε, μ_a, Kirkwood-Onsager) or solvent polarity and polarizability (π^*, Catalán SPP, χ_R), where Pearson's r = 0.8-0.9.[54] There is no correlation with solvent polarizability (α) on its own or hydrogen bonding (β).

Based on these results, it is proposed that both high solvent polarity and high solvent polarizability promote favourable interactions between the solvent molecules and the PDI units of **1a**, interacting with the solvent in preference to with each other, inhibiting intramolecular H-agreggation. In solvents with lower polarity and lower polarizability, the PDI cores within the macrocycle will interact with each other in preference to with the solvent, leading to intramolecular H-aggregation.

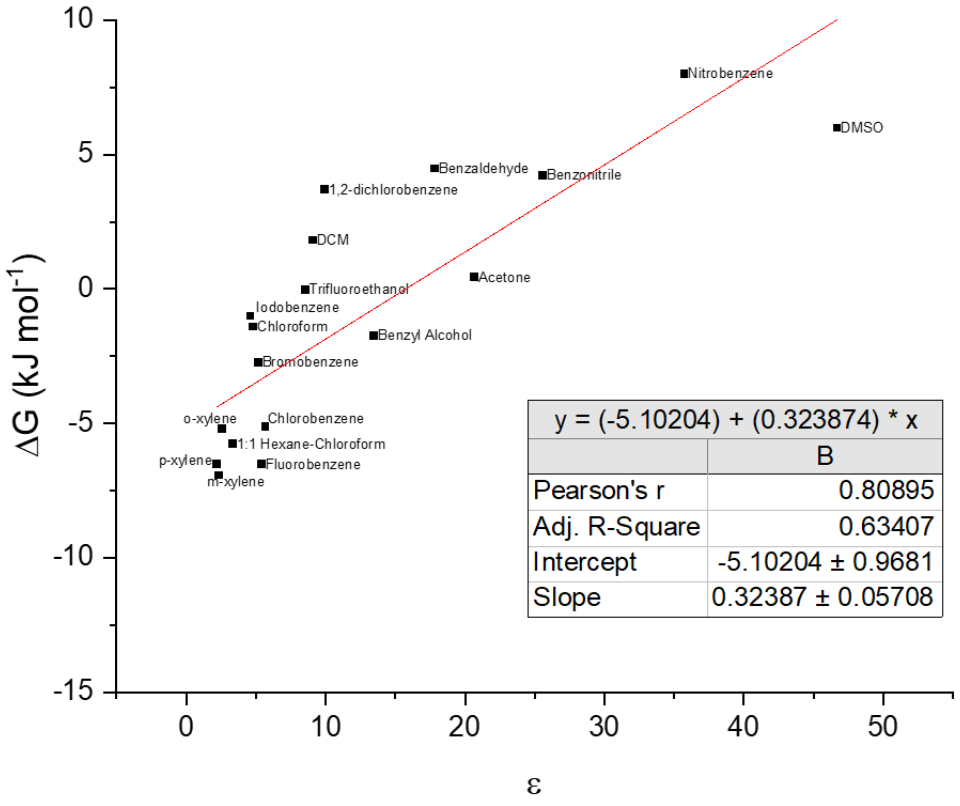

Figure 2.32 Plot of ΔG_{agg} against dielectric constant ε of each solvent. The red line represents the linear regression fitting of the data.

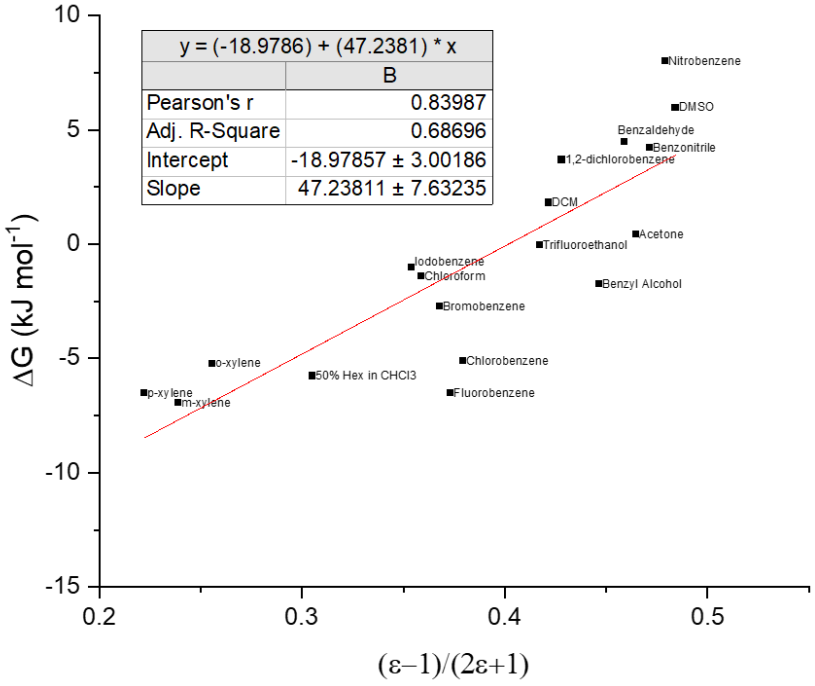

Figure 2.33: Plot of ΔG_{agg} against the Kirkwood-Onsager function $(\varepsilon - 1)(2\varepsilon + 1)$ for each solvent. The red line represents the linear regression fitting of the data.

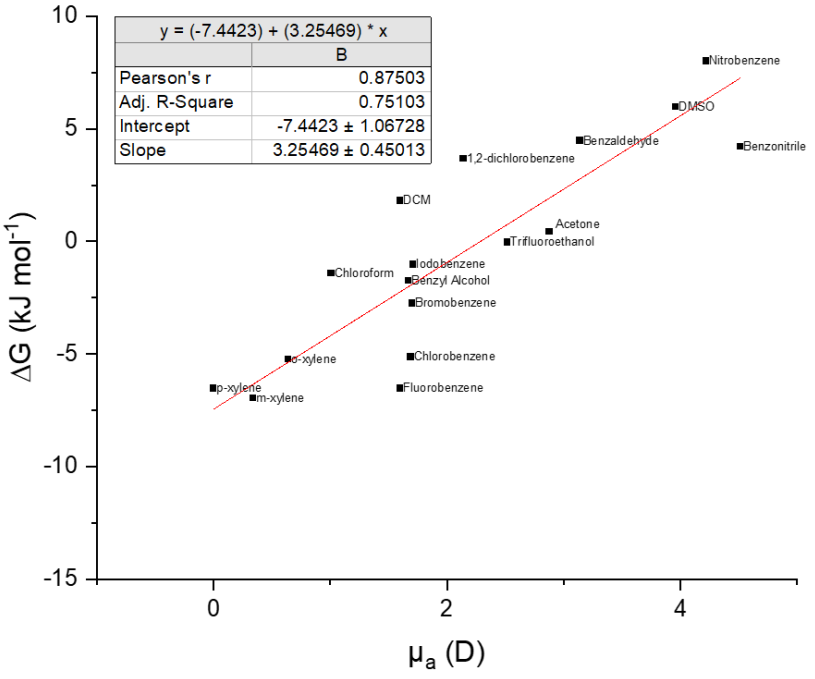

Figure 2.34: Plot of ΔG_{agg} against dipole moment μ_a of each solvent. The red line represents the linear regression fitting of the data.

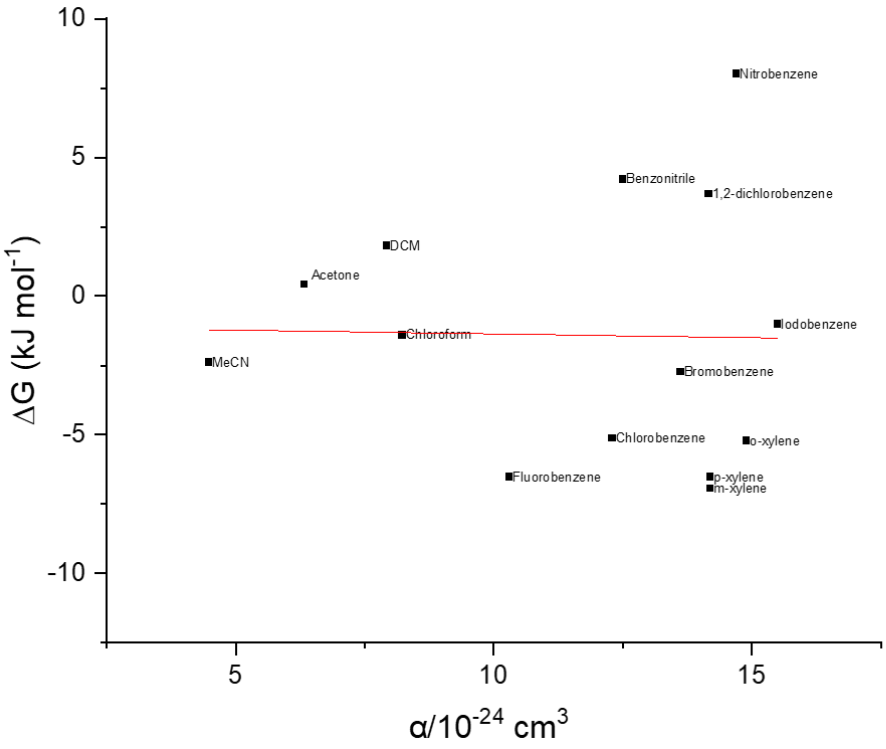

Figure 2.35: Plot of ΔG_{agg} against polarizability α of each solvent, showing no correlation.

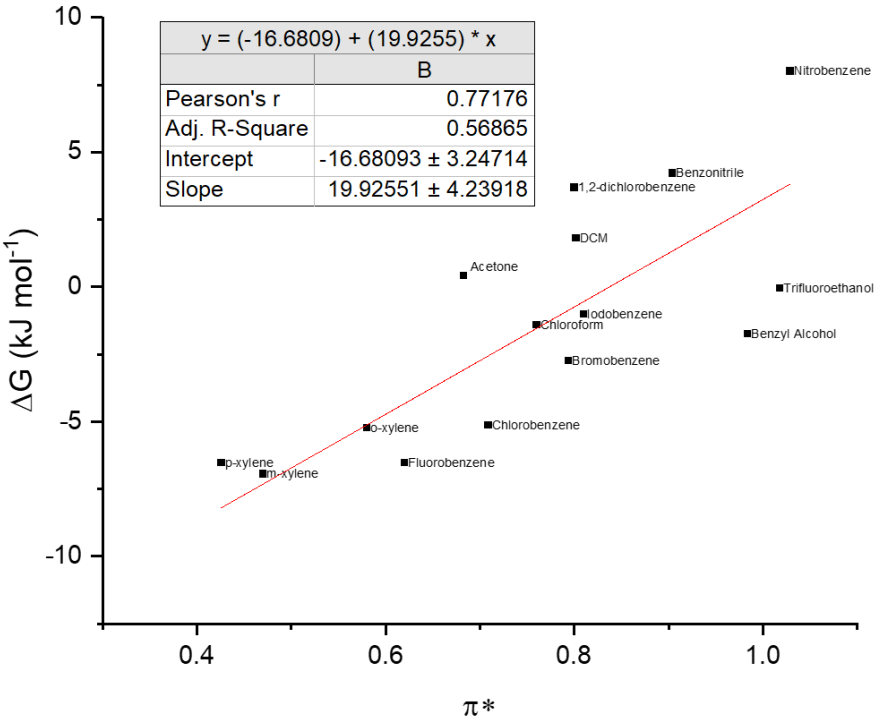

Figure 2.36: Plot of ΔG_{agg} against the empirical Kamlet-Taft π^*scale of solvent polarity/polarizability. [55] The red line represents the linear regression fitting of the data.

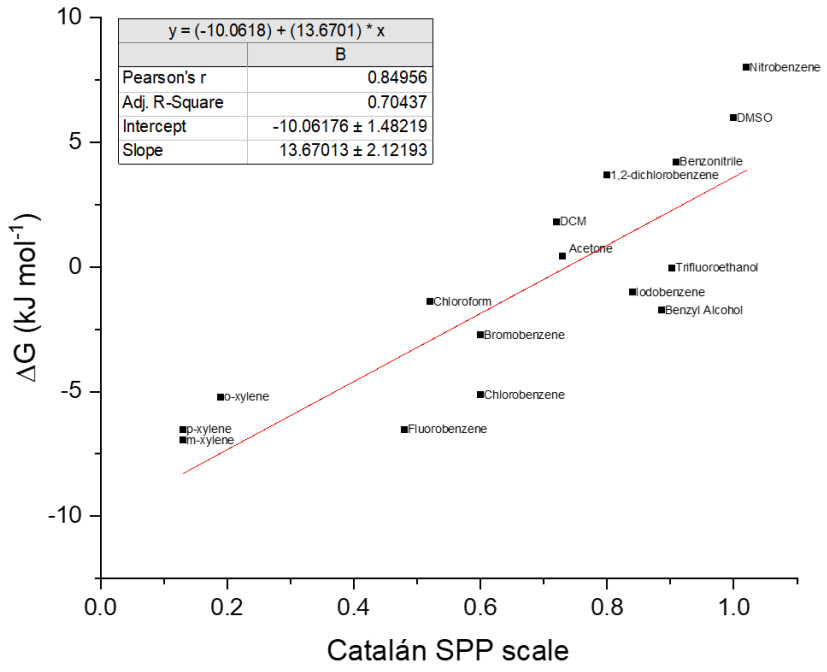

Figure 2.37: Plot of ΔG_{agg} against the empirical Catalán SPP scale of solvent polarity/polarizability. [56] The red line represents the linear regression fitting of the data.

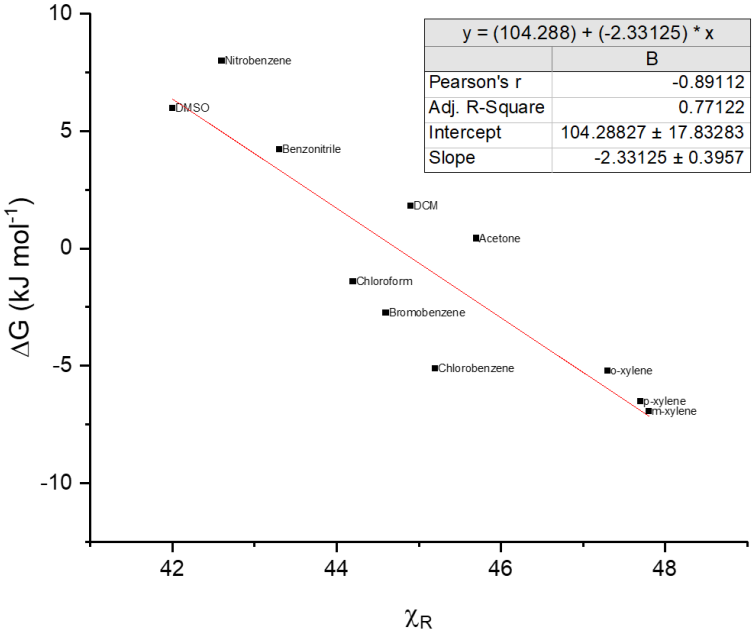

Figure 2.38: Plot of ΔG_{agg} against the empirical χ_R scale of solvent polarity/polarizability.[57] The red line represents the linear regression fitting of the data.

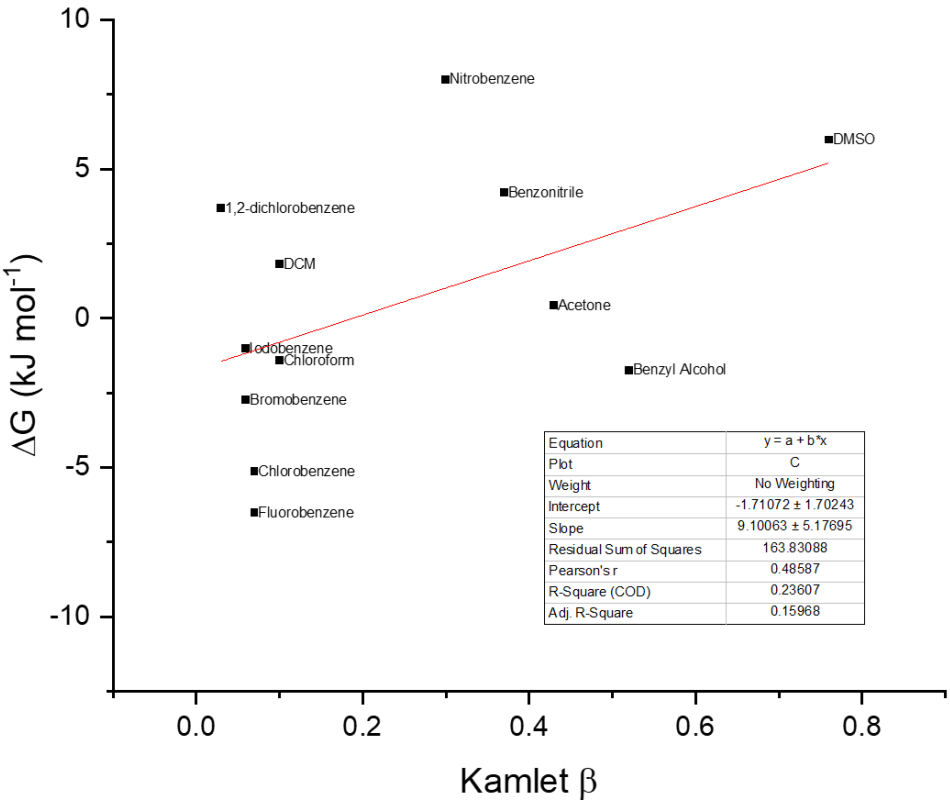

Figure 2.39: Plot of $\Delta \boldsymbol{G}_{\mathbf{agg}}$ against the Kamlet-Taft β scale of hydrogen bond acceptor strength.[58] No correlation is observed against β.

2.5.5 Quantification of intramolecular π-π stacking strength in toluene and TCE

As previously discussed, the distinct UV–vis absorption spectra of macrocycle **1a** in polar, polarizable chlorinated solvents and less polar aromatic solvents allows the strength of intramolecular PDI–PDI π–π interactions to be estimated. However, because toluene and TCE were assumed to lead to the "fully H-aggregated" and "fully non-H-aggregated" states of macrocycle **1a**, they represent asymptotes in the model described in the previous section, such that ΔG_{agg} in these solvents cannot be determined by this method. Instead, the method of Moore and Ray (explained below),[53, 59] previously used for measuring the solvent-induced folding of aromatic oligomers, was used to estimate the free energy of PDI–PDI H-type aggregation for **1a** in toluene. For this, TCE was titrated into a solution of **1a** in toluene (at constant concentration), which led to the formation of isosbestic points (λ = 505, 523, 577 nm), indicative of conformations that are in equilibrium (**Figure 2.40**).

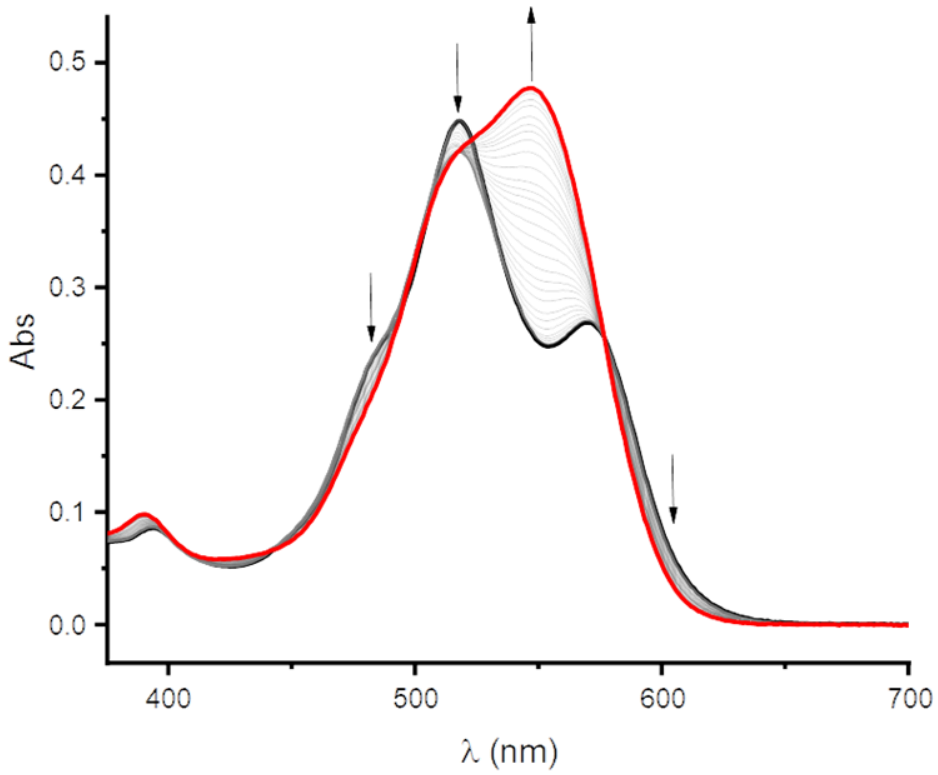

Figure 2.40: Change in the UV-vis absorption spectrum of a 10 μmol solution of macrocycle **1a** in toluene:TCE solvent mixtures (grey) going from pure toluene (black) to 97:3 (v/v) toluene:TCE (red). The arrows denote the direction of change as the proportion of TCE is increased.

By monitoring the $A_{0\text{-}0}$ / $A_{0\text{-}1}$ ratio for each solvent composition (**Figure 2.41**), the free energy of intramolecular H-type aggregation (ΔG_{agg}) can be determined for different toluene:TCE solvent mixtures (**Figure 2.42**).

The model used to calculate ΔG_{agg} results in asymptotes at 0 % and 100 % TCE. However, plotting of the ΔG in the transition region against % TCE gives a straight-line relationship that can be extrapolated to obtain an estimate ΔG_{agg} for full intramolecular H-type aggregation in pure toluene (i.e., at 0% TCE) according to the equation:

$$\Delta G_{agg} = \Delta G(\text{Tol}) + m[\text{TCE}]$$

Where $\Delta G(\text{Tol})$ is the free energy for full intramolecular H-type agreggation in pure toluene, [TCE] is the concentration of TCE in the solvent mixture, and m is the gradient of the

plot. From **Figure 2.42**, this gives $\Delta G(\mathrm{Tol})$ = -11.1 ± 0.1 kJ mol^{-1}, which represents an estimate for the strength of the homochiral π–π interaction in toluene.

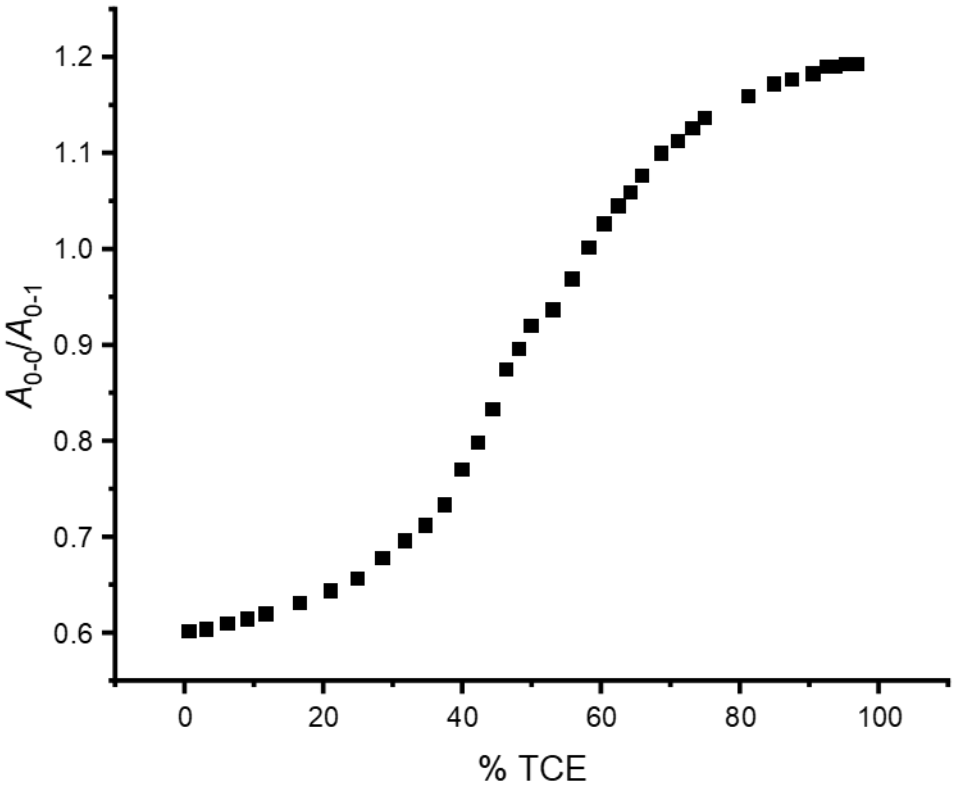

Figure 2.41: Change in $A_{0\text{-}0}$ / $A_{0\text{-}1}$ ratio in the absorption spectrum of compound **1a** in toluene:TCE mixture as the volume % of TCE is increased**.**

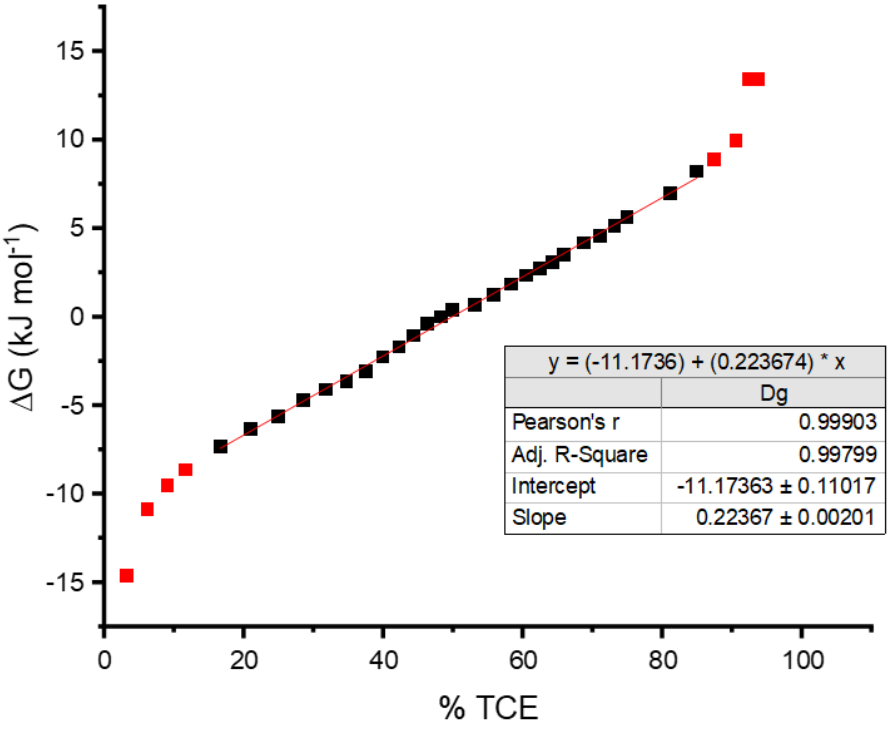

Figure 2.42: Plot of ΔG_{agg} of macrocycle 1a (derived from the $A_{0\text{-}0}$ / $A_{0\text{-}1}$ ratio) for different toluene:TCE solvent mixtures. Data points in red are excluded from the linear regression fitting.

In summary, this work enabled an estimation of the strength of the homochiral intramolecular PDI-PDI π–π interaction in toluene, -11 kJ mol^{-1}. This is over twice as strong as the aggregation of PDIs functionalized with four bulky 4-*tert*-butylphenoxy groups at the bay positions, as reported using a recent PDI-based macrocycle in toluene.[53] The following section will attempt to bring together the experimental results so far in order to construct "conformational energy landscapes" for the ***MM/PP*** and ***MP*** macrocycle stereoisomers in toluene and chlorinated solvents.

2.6 Conformational energy landscape of macrocycle 1

This section will use the experimental results obtained so far to build a solvent-dependent "energy landscape" for the conformations of the ***MM/PP*** enantiomers and ***MP*** diastereomer of macrocycles **1a/b**.

The experimental evidence obtained so far points towards macrocycle **1a/b** having distinct conformations in toluene and chlorinated solvents (**Figure 2.43**).

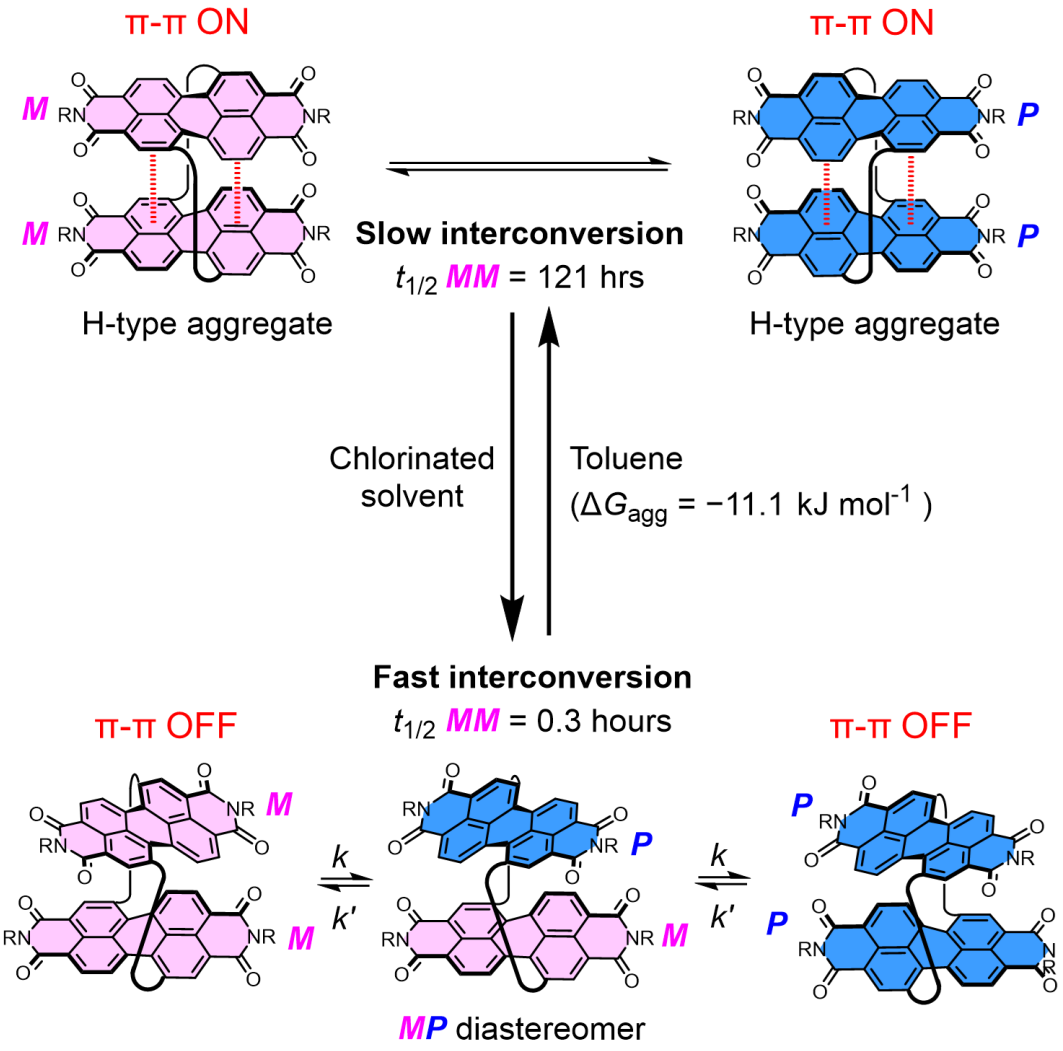

Figure 2.43: Proposed solvent dependence of conformations and stereoisomer interconversion for macrocycle **1a**.

In toluene, UV-vis absorption and CD spectroscopy both indicate that the macrocycle exhibits H-type excitonic coupling between its two PDI cores (**Sections 2.4.2 and 2.5.3**). This is also consistent with NMR spectroscopic studies which point towards closely stacked π–surfaces in the macrocycle (**Section 2.3** and **2.5**). From NMR, chiral HPLC and CD spectroscopy it can also be deduced that this intramolecular H-type dimer must be exclusively homochiral, occurring only as the ***MM*** and ***PP*** stereoisomers (**Section 2.4**). Therefore, the conformation in toluene is consistent with the exclusively homochiral π-stacked intramolecular dimer conformation observed in the crystal structure of **1b** (**Section 2.3.1**). From chiral HPLC studies and time-course CD measurements it was also shown that enantiomer interconversion is relatively slow in toluene, with an enantiomer half-life of 121 h (**Sections 2.5.3 and 2.5.4**). It is hypothesised that the π-stacking between the PDI cores helps to "anchor" them in position,

thus preventing enantiomerisation via an "intramolecular somersault".[11] The strength of the π-π interaction in toluene, relative to a non-π-stacked conformation, was measured as ΔG_{agg} = −11.1 kJ mol^{-1} (**Section 2.5.5**).

In contrast, chlorinated solvents like dichloromethane and TCE can disrupt the intramolecular π-π interaction, leading to a non-π-stacked conformation being dominant, as evidenced by UV-vis, NMR and CD spectroscopy (**Sections 2.4.2 and 2.5**). The preference for homochirality is less strong in this non-π-stacked conformation. This is evidenced by the presence of a second set of signals, corresponding to the ***MP*** stereoisomer in the ^{1}H NMR spectrum of macrocycle **1a** in TCE and the presence of an extra peak in the chiral HPLC chromatogram when run in dichloromethane as the major eluent. The lack of strong π-π interactions in chlorinated solvents also leads to a faster rate of enantiomerisation, with an enantiomer half-life of only 0.3 hours (**Sections 2.4.3** and **2.4.4**).

The experimental results are summarised as conformation–energy diagrams in different solvents, as shown in **Figure 2.44**. There are three experimentally observable conformations in a racemic sample of macrocycle **1a/b**: two homochiral conformations, with intramolecular π-π interactions switched on and off respectively, and a heterochiral ***MP*** conformation, which from NMR studies (**Section 2.5.1**) appears to have weaker π-π interactions.

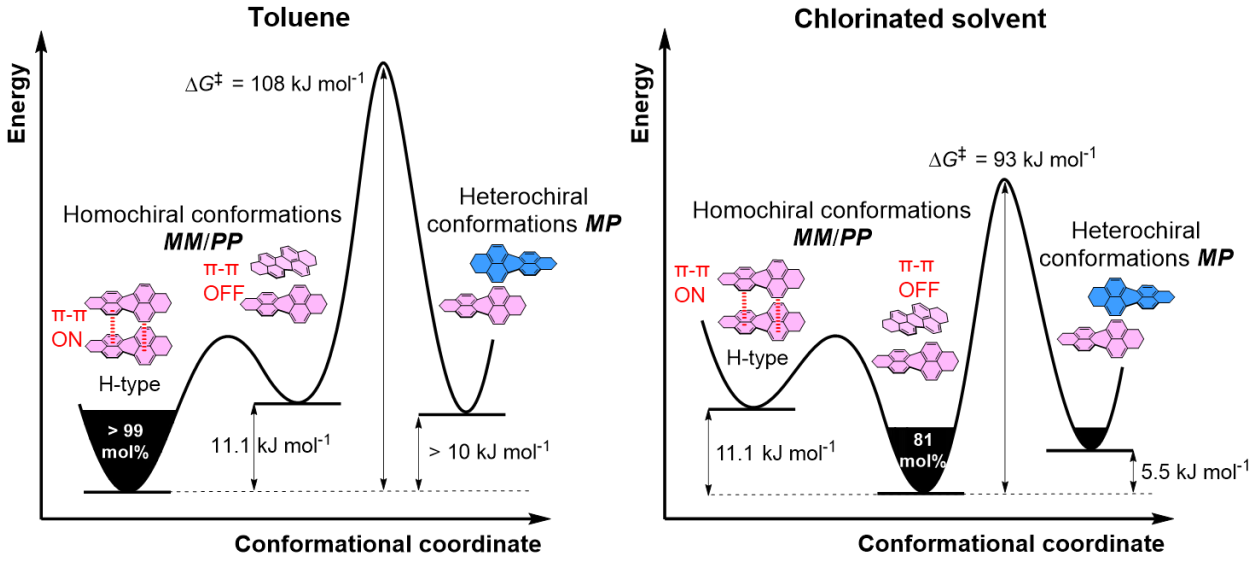

Figure 2.44: Proposed conformation–energy diagrams for macrocycle **1a** in toluene (left) and chlorinated solvent (right) using experimental data. All values are at 298 K, except for the populations and free energy difference between ***MM*/*PP*** and ***MP***, which are estimated at 373 K, by ^{1}H NMR spectroscopy.

In toluene, the homochiral conformation with π-π interactions switched on is observed exclusively. This is because in toluene this stereoisomer is stabilised relative to the heterochiral stereoisomer by at least 10 kJ mol^{-1}, as estimated from the fact that only the(π-stacked) ***MM***/***PP*** are observed by ^{1}H NMR spectroscopy in toluene. The energy barrier for racemisation, which likely goes via the ***MP*** heterochiral conformation as an intermediate, was determined to be $\Delta G^{\ddagger}$ = 108 kJ mol^{-1} in toluene (**Section 2.4.4**).

In contrast, in chlorinated solvents the non-π-stacked conformations are observed exclusively, with a homochiral:heterochiral ratio of 81:19 as determined by ^{1}H NMR spectroscopy in TCE (section 2.5.1). An energy difference between the non-π-stacked homochiral ***MM***/***PP*** enantiomers and the heterochiral ***MP*** can be estimated as 5.5 kJ mol^{-1} from this population ratio. As before, the racemisation barrier corresponds to the barrier between the homochiral ***MM***/***PP*** and the heterochiral ***MP*** and was measured as $\Delta G^{\ddagger}$ = 93 kJ mol^{-1} in DCM (section 2.5.2). The experiment described in Section 2.5.5 which measured the strength of the π-π interaction in toluene relative to a non-π-stacked conformation, also implies that in TCE the non-π-stacked homochiral conformation is stabilised relative to the π-stacked homochiral conformation by 11.1 kJ mol^{-1}. Interestingly, the strength of this π-π interaction measured in toluene is similar to the difference in racemisation energy barriers in toluene and DCM ($\Delta\Delta G^{\ddagger}$ = 15 kJ mol^{-1}), which supports the hypothesis that it is the intramolecular π-π interaction that "anchors" the PDI units and slows down enantiomerisation.

2.7 Electrochemical studies

As established in the previous sections, macrocycle **1a/b** is notable for exhibiting solvent-switchable intramolecular PDI-PDI π–π stacking, which provides switchable chiroptical and photophysical properties. Following on from this, it was hypothesised that this may also result in switchable electrochemical properties. This would be interesting because through-space π-orbital overlap and redox stability are critical for advancing the charge carrier mobility and air/photo-stability of PDI-based (chiral) optoelectronic materials.[60, 61] To probe this, cyclic voltammetry measurements were carried out on macrocycle **1a** (**Figure 2.45**).

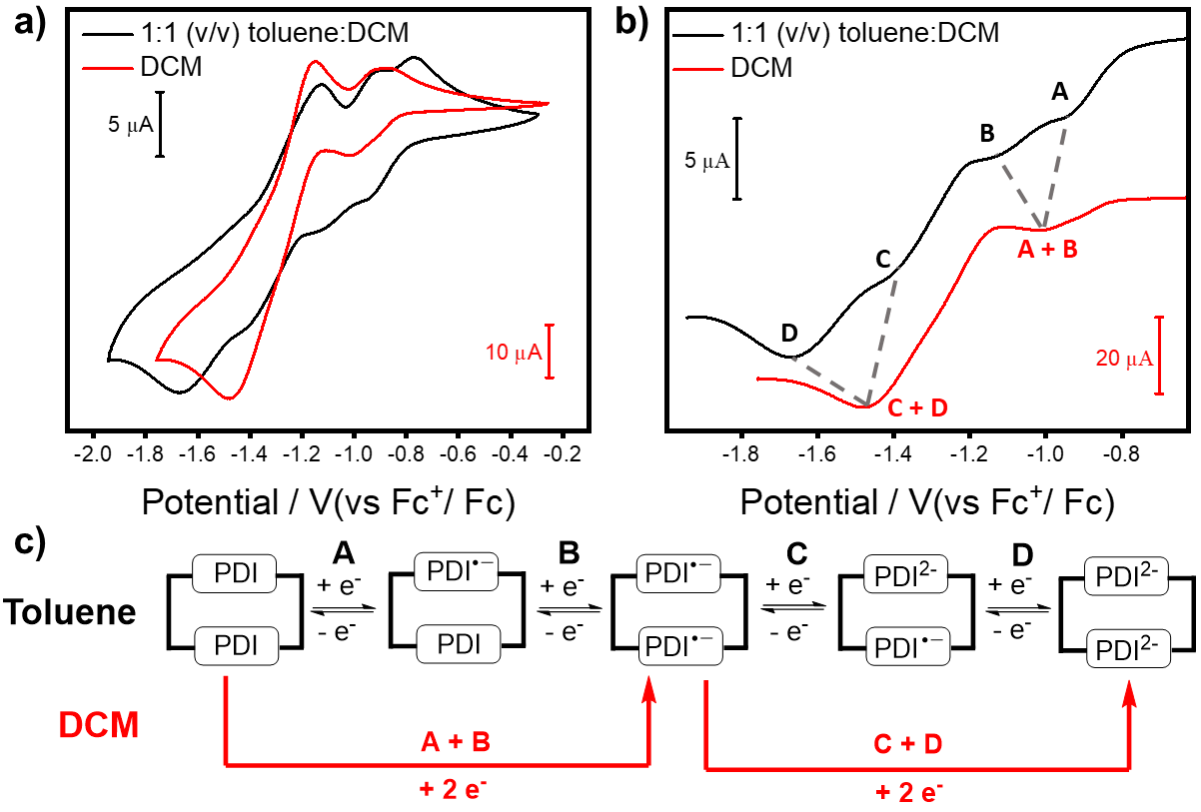

Figure 2.45: a) Full and **b)** zoomed-in region of the cyclic voltammograms of macrocycle **1a** recorded in dichloromethane and 1:1 (v/v) toluene:dichloromethane (each containing 0.4 M [nBu_4N][BF4]). **c)** Schematic of the redox processes of macrocycle 1a in each solvent.

In dichloromethane, cyclic voltammetry of **1a** revealed two typical chemically reversible two-electron reduction processes (**Figure 2.45b-c)**.[3] This implies that the reduction of one PDI in the macrocycle does not affect the reduction of the other PDI.

In contrast, the addition of toluene splits these peaks into a series of four distinct one-electron reductions. This demonstrates that homochiral intramolecular π–π stacking between

the two PDI units facilitates their through-space electronic communication,[48, 62] which is solvent-switchable. It should be noted here that the 4e$^-$ reduction of **1a** in 1:1 (v/v) toluene:dichloromethane‡ is chemically reversible, yet the CV wave appears different on the reverse sweep, likely because in **1a**$^{4-}$ the PDI units repel each other and lose through-space communication.[48, 62]

It is clear that the H-type aggregate in 1:1 (v/v) toluene:dichloromethane also significantly stabilises the first reduced PDI state (**1a**$^{\bullet-}$, $E_{1/2}$ = −0.84 V) relative to the corresponding species in neat dichloromethane or the acyclic PDI control **3a**$^{\bullet-}$ ($E_{1/2}$ = −0.94 V for both, **Table 2.4** and **Figure 2.46**). Since it is an acyclic monomer, the electrochemistry of **3a** is much less dependent on solvent.

It is also interesting to consider the difference between the reduction and oxidation peak potentials for each redox process (ΔE_p). In general, the closer ΔE_p is to 57 mV, the more reversible the redox process is.[63] The first redox process **A** is relatively close to being fully reversible in macrocycle **1a** in DCM and in acyclic PDI **3a** in both solvents (ΔE_p =68-89 mV, **Table 2.4**), but is significantly higher for **1a** in 1:1 (v/v) toluene:DCM (136 mV) which indicates a greater conformational change upon reduction. It is also worth noting that while ΔE_p increases for each subsequent redox process as a result of repulsion between the added electrons, the increase in ΔE_p for **1a** is greater in 1:1 (v/v) toluene:DCM than in DCM. This may be because the addition of toluene favours PDI aggregation, thereby leading to a greater conformational change upon PDI reduction as the chromophores are repelled.

‡ The H-type aggregate in 1:1 (v/v/) toluene:dichloromethane was characterised using UV-vis spectroscopy. It was not possible to measure the cyclic voltammogram in toluene due to the poor solubilities of the reduced species in toluene.

Table 2.4: Cyclic voltammetry data for macrocycle **1a** and acyclic PDI **3a**[a].

		Redox Process, $E_{1/2}$ / V, [ΔE_p,mV]			
	Solvent	**A**	**B**	**C**	**D**
Macrocycle **1a**	1:1 (v/v) toluene:DCM	−0.84 [136]	−1.02 [206]	−1.18 [300]	−1.70[b]
	DCM	−0.94 [89]		−1.31 [325]	
Acyclic PDI **3a**	1:1 (v/v) toluene:DCM	−0.94 [82]		−1.20 [138]	
	DCM	−0.94 [68]		−1.18 [279]	

[a]Recorded in the stated solvents containing 0.4 M [^{n}Bu$_4$N][BF$_4$] as supporting electrolyte at ambient temperature, with potentials quoted at 0.10 V s^{-1} against $E_{1/2}$ Fc$^+$/Fc. [b]$E_{1/2}$ value could not be calculated so E_{ca} is given instead.

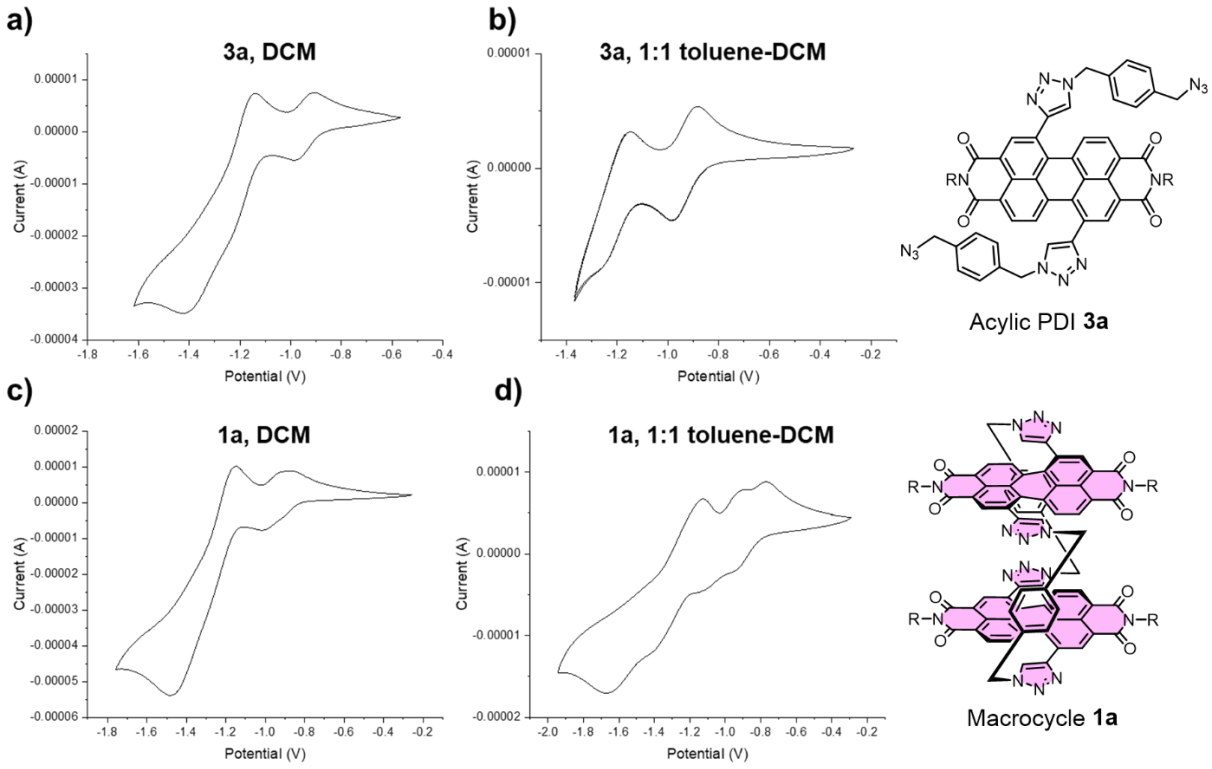

Figure 2.46: Cyclic voltammograms of **a)** Acyclic bis-triazole PDI **3a** in DCM, **b)** Acyclic bis-triazole PDI **3a** in 1:1 (v/v) toluene:DCM, **c)** macrocycle 1a in DCM, d) macrocycle **1a** in 1:1 (v/v) toluene:DCM.

Overall, these results imply that H-type homochiral π−π stacking, which is a through-space interaction, leads to solvent switchable stabilization of the PDI radical anion **1a**$^{\bullet-}$ (by 0.1 V in 1:1 (v/v) toluene:dichloromethane, likely more in neat toluene). Thus, PDI-PDI electronic

communication in this system leads to an enhancement in electron accepting power superior to the covalent addition of two *ortho*-cyanophenyl electron withdrawing groups to the perylene core.[64] Additionally, the electron deficiency of macrocycle **1a** ($E_{1/2}$ = −0.84 V) is in line with a tetrachloro-substituted PDI ($E_{1/2}$ = −0.87 V),[65] which has already been used as a good n-type semiconducting material.

2.8 Summary and conclusions

This chapter has explored the design, synthesis and characterisation of a new bis-PDI macrocycle, the "Pink Box" macrocycle **1a/b**. The PDI chromophores in **1** are optimised for close-contact (3.7 Å) intramolecular homochiral π-π stacking, allowing the optical, electronic and chiroptical properties of a closely-stacked twisted bis-PDI dimer to be explored by a wide range of experimental techniques.

In toluene and in the solid state, the macrocycle **1a/b** exists as an exclusively homochiral PDI-PDI intramolecular dimer with strong H-type excitonic coupling. This through-space π–π electronic communication of two chiral PDI units leads to an enhancement of their enantiomeric stability ($t_{1/2}$ = days vs. minutes) and electron-accepting ability ($\Delta E_{1/2}$ = 0.1 V). Macrocycle **1a** therefore matches the electron-accepting power of a tetrachloro-substituted PDI semiconducting material[65] but with a notably higher barrier to stereoisomer interconversion ($\Delta G^{\ddagger}$ = 108 vs 97 kJ mol^{-1}).[66] Excitingly, this homochiral π–π interaction also results in the enantiomers of **1a** having the highest circularly polarized luminescence dissymmetry factor of any discrete PDI dye in solution (g_{lum} = 10^{-2} vs 10^{-3}).[67] In comparison to other organic molecules, the CPL is amongst the most red-shifted (675 nm) and has one the highest dissymmetry factors.[1, 25-28]

Interestingly, the conformation of macrocycle **1a/b** is solvent-dependent, resulting in switchable photophysical, electrochemical and chiroptical properties. Since the writing of this chapter, collaborators have used femtosecond transient absorption (fsTA) and two-dimensional electronic spectroscopy to conclusively show that in toluene there is strong excitonic coupling and emission from an excimer, while in chlorinated solvents the PDIs behave monomerically as a result of a conformational change which switches off excitonic coupling.[68] This solvent dependent conformational change is discussed in detail in Chapter 4.

Overall, the work described in this chapter highlights how through-space π–π electronic communication of two PDI units can be optimised by tuning their relative chirality (homochiral), orientation (H-type aggregate), and distance (3.7 Å) using a preorganised macrocyclic architecture to enhance their chiroptical, photophysical and electrochemical properties. Work in the next chapters will explore how variation of this "Pink Box" macrocyclic architecture, via changing the imide or linker groups, can be used to achieve indefinitely stable enantiomers (chiral locking), to direct the self-assembly of PDI H- and J-aggregates (via chiral

π–π interactions), and to isolate and study the various chiral conformers that can exist in these macrocycles, including the ***MP*** heterochiral diastereomer.

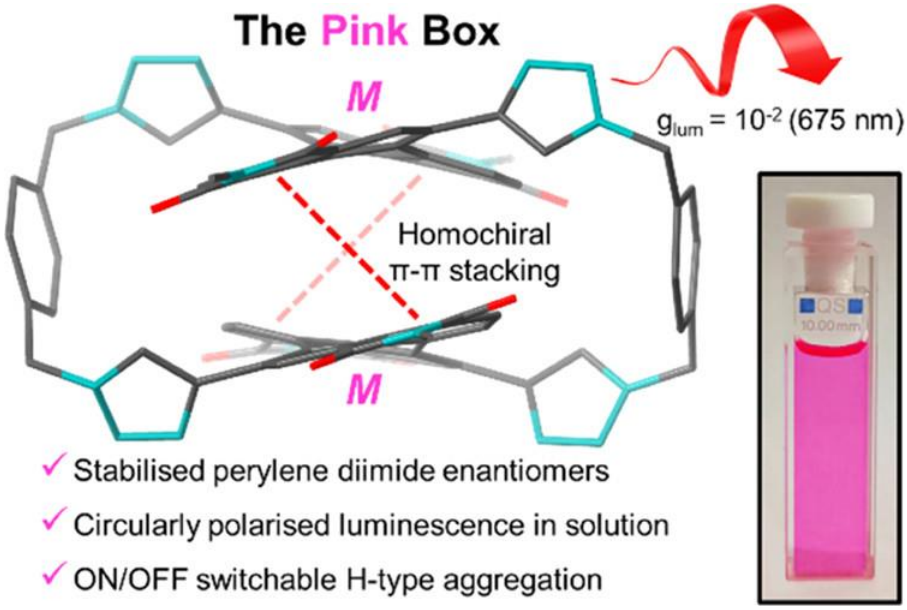

Figure 2.47: Summary of results for **Chapter 2**.

2.9 Experimental

2.9.1 Materials and methods

All commercial solvents and reagents were used as purchased, unless otherwise stated. Anhydrous solvents were degassed with N_2 and dried using an Innovative Technology PureSolv MD 5 solvent purification system. $Cu(MeCN)_4 \cdot PF_6$ was stored in a desiccator. TBTA was prepared following a literature procedure.[69] Water was distilled and microfiltered using an ELGA DV 35 Purelab water purification system. Chromatography was undertaken using silica gel (particle size: 40-63 μm) or preparative TLC plates (20 × 20 cm, 1 cm silica thickness). ^{1}H and ^{13}C NMR spectra were recorded using Bruker AVIII400 (400 MHz), Bruker AV NEO 400 (400 MHz), Bruker AV NEO 500 (500 MHz, with cryoprobe). Mass spectra were recorded using a Bruker UltrafleXtreme MALDI-TOF mass spectrometer or a Waters Synapt G2-S mass spectrometer for high resolution MS-ESI. Details of equipment used for other analytical techniques (photophysics, electrochemistry, HPLC etc.) are provided in their appropriate sections in this supporting information. All analytical experiments were performed with bis-perylene diimide (PDI) macrocycle **1a** and acyclic bis-triazole PDI control **3a**. Only single crystal X-ray diffraction was performed with macrocycle **1b**, for which shorter alkyl chains enabled the growth of useable crystals. Apart from their side chains, macrocycles **1a** and **1b** are structurally identical, as evidenced by their matching ^{1}H NMR (aromatic signals, see below) and solvent-dependent UV-vis spectra (**Figures 2.64-2.65**).

2.9.2 Synthesis and characterisation

The synthesis of macrocycles **1a** and **1b** was carried out according to **Scheme 2.2**. Compounds **4b**[15] and **2a**[16] were prepared following literature procedures. Compounds **2a/b**, **3a/b** and **4a/b** were isolated as a mixture of 1,6 and 1,7 PDI regioisomers. Both macrocycles **1a** and **1b** were isolated as the pure 1,7 regioisomer since removal of the 1,6 regioisomer was possible by silica gel column chromatography at this stage.

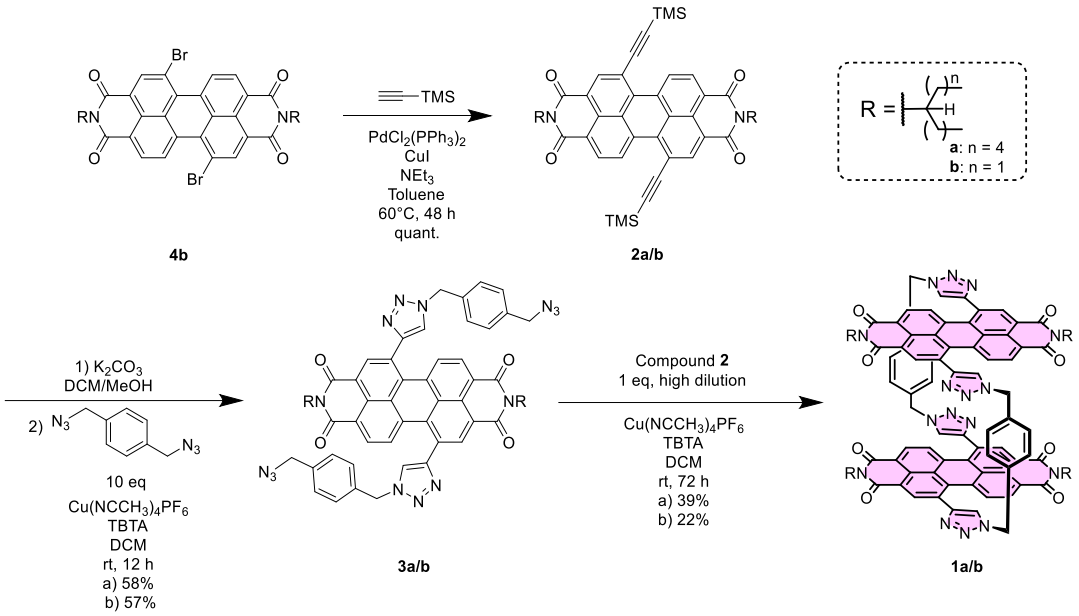

Scheme 2.2: Multistep synthesis of bis-PDI macrocycles **1a** and **1b**.

A note on the safe use of 1,4-bis(azidomethyl)benzene and other bisazides

1,4-bis(azidomethyl)benzene was kindly synthesised by Angus Yeung according to a literature procedure.[17] 1,4-bis(azidomethyl)benzene and other organic bisazide compounds are used as synthetic reagents throughout this thesis. Whilst in the Barendt group we have thus far not encountered any problems with the azide compounds we have used, working with these can be dangerous as organic azides can be unstable and explosive if there are fewer than six carbon atoms per azide group in the molecule. Additionally, synthesising these involves the use of sodium azide which is highly toxic and can lead to the formation of other explosive products. A good assessment method for determining whether a chemical reaction is potentially explosive is the O.R.E.O.S. assessment[70] (*O*xygen balance calculations, the *R*ule of six, explosive functional group list, *O*nset of decomposition determined by differential scanning calorimetry, *S*cale). The 1,4-bis(azidomethyl)benzene and other bis-azides used in this thesis fail this assessment simply thorough the consideration of the rule of six and the presence of two explosive azide groups per molecule before the other tests are even taken into account. **Therefore, the following precautions must be taken when working with these compounds**:
71

- Do not use halogenated solvents (e.g. DCM or chloroform) in the presence of sodium azide, as this can lead to the formation of explosive compounds such as diazidomethane and triazidomethane.

- Avoid using acids in the presence of sodium azide as this can produce the toxic gas hydrogen azide.

- Do not handle sodium azide with metal spatulas as this can catalyse the formation of hydrogen azide.

- Avoid working on large scales (work with < 1 g or less ideally). For example, if 1,4-bis(azidomethyl)benzene fully decomposes, it can theoretically release 3 moles of N_2 per mole of compound. Therefore, 1 g of 1,4-bis(azidomethyl)benzene can release ~ 16 mmol of N_2 gas, which would occupy 384 cm^3 at room temperature and pressure. Therefore, sub-gram amounts of 1,4-bis(azidomethyl)benzene can be handled relatively safely as long as the other precautions below are followed.

- Avoid using sealed flasks. Always use an escape needle/balloon when using septum seals on glassware.

- Avoid concentrating organic azides in large quantities through rotary evaporation or distillation. If absolutely necessary to do so, then it is essential to use large enough round bottom flasks and a blast shield.

- Do not heat sodium azide or organic azides.

Acyclic bis-triazole PDI 3a

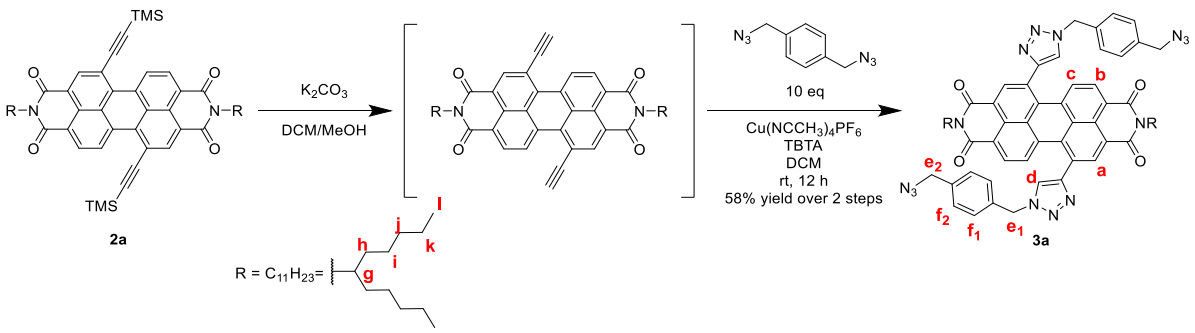

To a solution of TMS-protected bisalkyne PDI **2a**[15] (150 mg, 168 µmol) in DCM (20 ml) was added K_2CO_3 (85 mg, 616 µmol, 3.6 equiv) in MeOH (10 ml). The mixture was stirred at rt for 3 min, and completion of the reaction was confirmed by TLC. A further 20 mL of DCM was added to the mixture. The mixture was then washed with 1 M HCl (2 x 30 mL), water (2 x 30 mL) and brine (30 ml). The mixture was then dried over anhydrous $MgSO_4$ and concentrated to dryness *in vacuo* to afford the PDI bis-alkyne, which was used immediately without further purification. To a solution of this PDI bis-alkyne in dry DCM (20 ml) was added 1,4-bis(azidomethyl)benzene (316 mg, 1.68 mmol, 10 equiv) and Tris((1-benzyl-4-triazolyl)methyl)amine (TBTA) (17.86 mg, 34 µmol, 0.2 equiv). The solution was then de-gassed with argon. The copper (I) catalyst $Cu(CH_3CN)_4PF_6$ (12.5 mg, 34 µmol, 0.2 equiv) was then added and the solution was once again de-gassed with argon. The reaction was stirred at rt for 12 h. The solvent was then removed *in vacuo*. The resulting residue was purified by silica gel flash column chromatography (1:99 MeOH-DCM) affording the title compound as a purple solid (110 mg, 98 µmol, 58%).

^{1}H NMR (500 MHz, Chloroform-*d*, 1,7-regiosiomer) δ 8.63 (d, *J* = 26.4 Hz, $2H_b$), 8.12 (s, $2H_a$), 7.83 (d, *J* = 8.1 Hz, $2H_c$), 7.66 (s, $2H_d$), 7.43 – 7.36 (m, $8H_f$), 5.67 (s, $2H_{e1}$), 5.15 (p, $2H_g$), 4.42 (s, $4H_{e2}$), 2.27 – 2.16 (m, $4H_h$), 1.87 – 1.77 (m, $4H_h$), 1.43 – 1.15 (m, $24H_{i-k}$), 0.89 – 0.78 (m, $12H_l$).

^{13}C NMR (126 MHz, $CDCl_3$) δ 164.57, 163.45, 148.63, 136.88, 135.46, 134.60, 133.54, 130.37, 129.65, 129.25, 129.10, 128.96, 128.66, 128.62, 128.55, 123.30, 123.18, 122.61, 122.44, 121.96, 54.40, 54.37, 32.43, 31.88, 26.70, 22.73, 22.70, 14.19.

HRMS ESI (m/z) calculated for $C_{66}H_{71}N_{14}O_4^+$ $[M+H]^+$ 1123.5782, found 1123.5765.

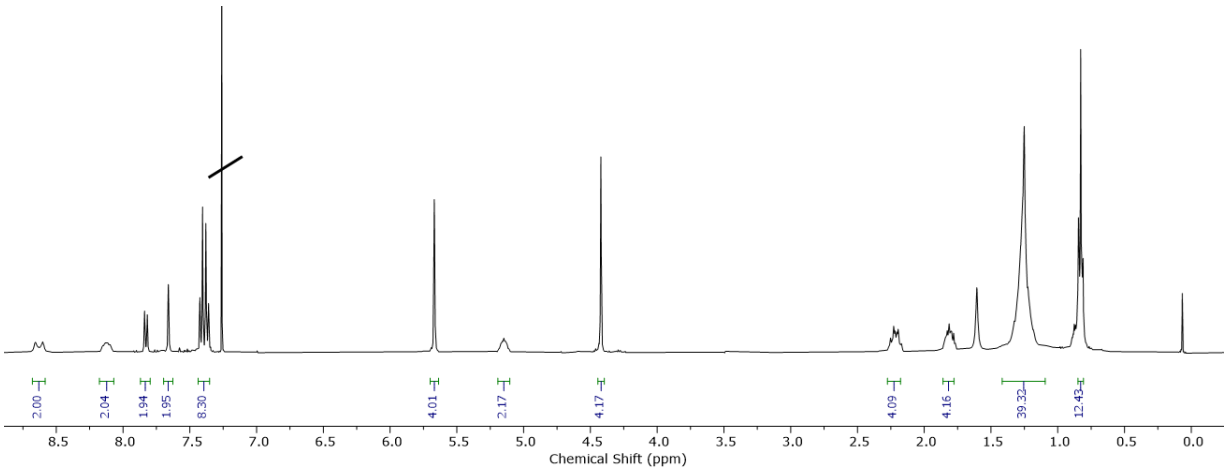

^{1}H NMR spectrum of **3a** (Chloroform-*d*, 298 K, 500 MHz).

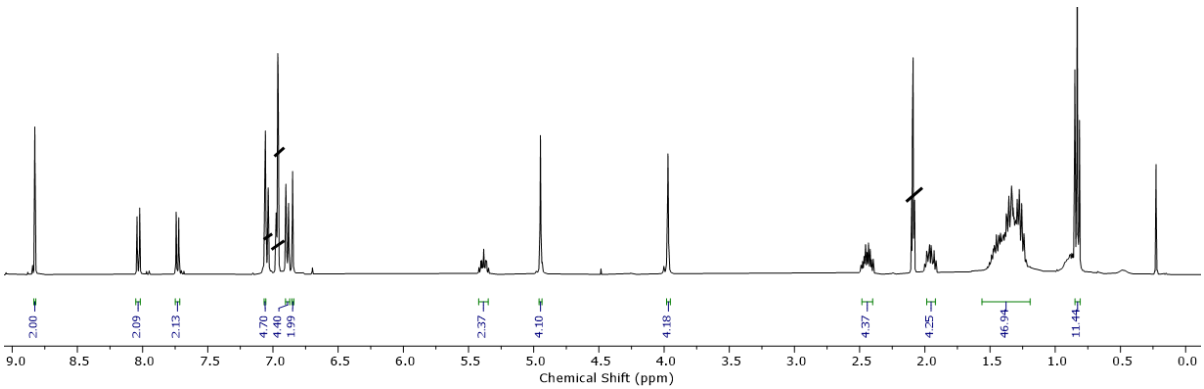

^{1}H NMR spectrum of **3a** (Toluene-d_8, 298 K, 500 MHz).

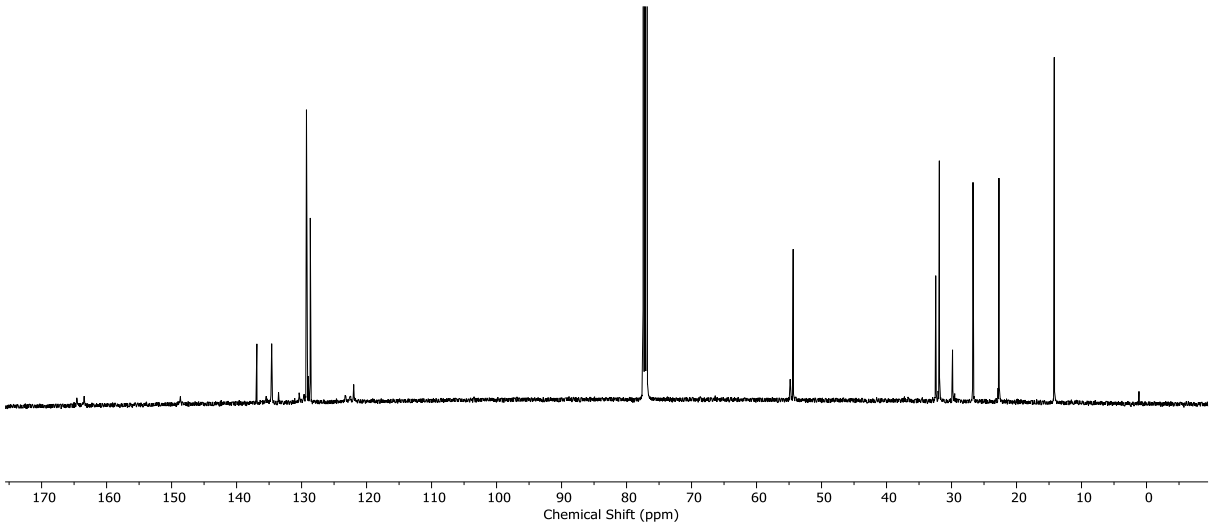

^{13}C NMR spectrum of **3a** (Chloroform-*d*, 298 K, 101 MHz).

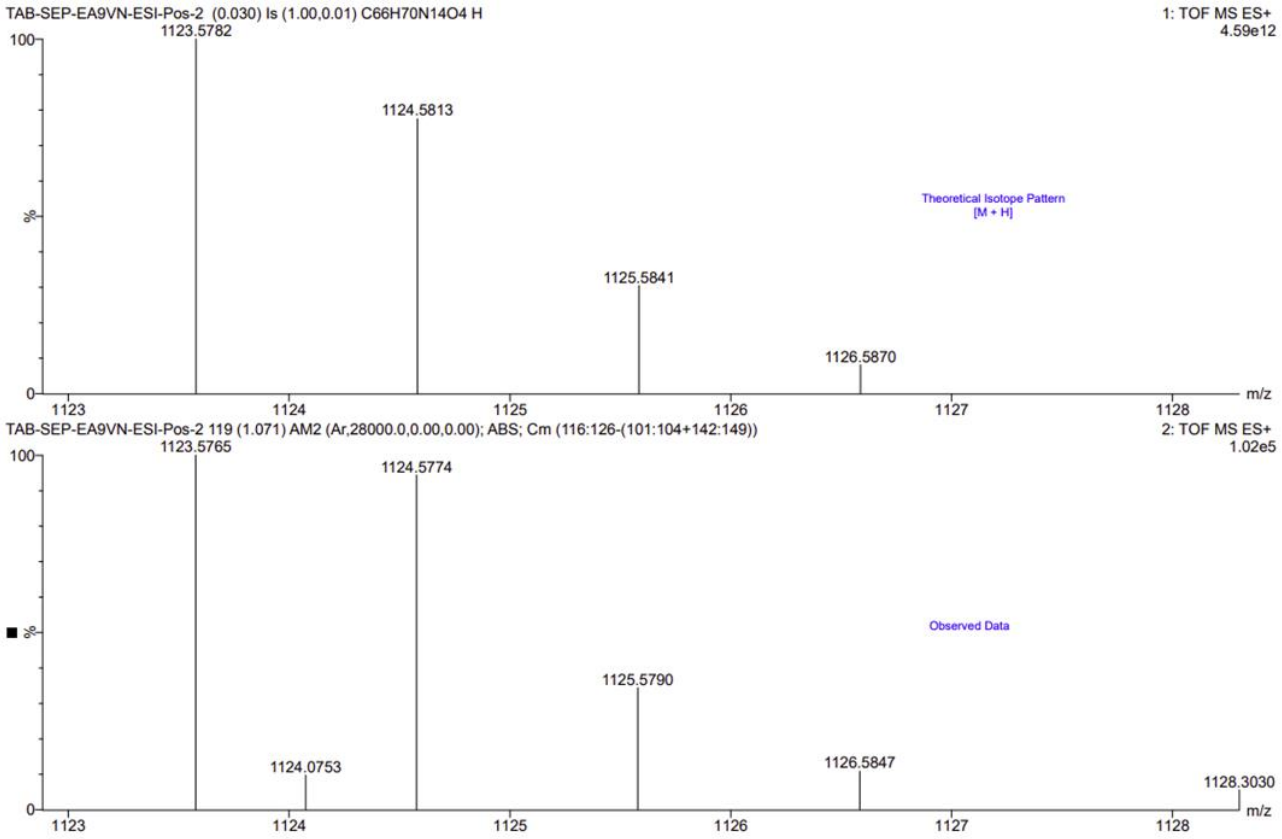

Calculated (top) and observed (bottom) ESI MS data for compound **3a**.

Bis-PDI macrocycle 1a

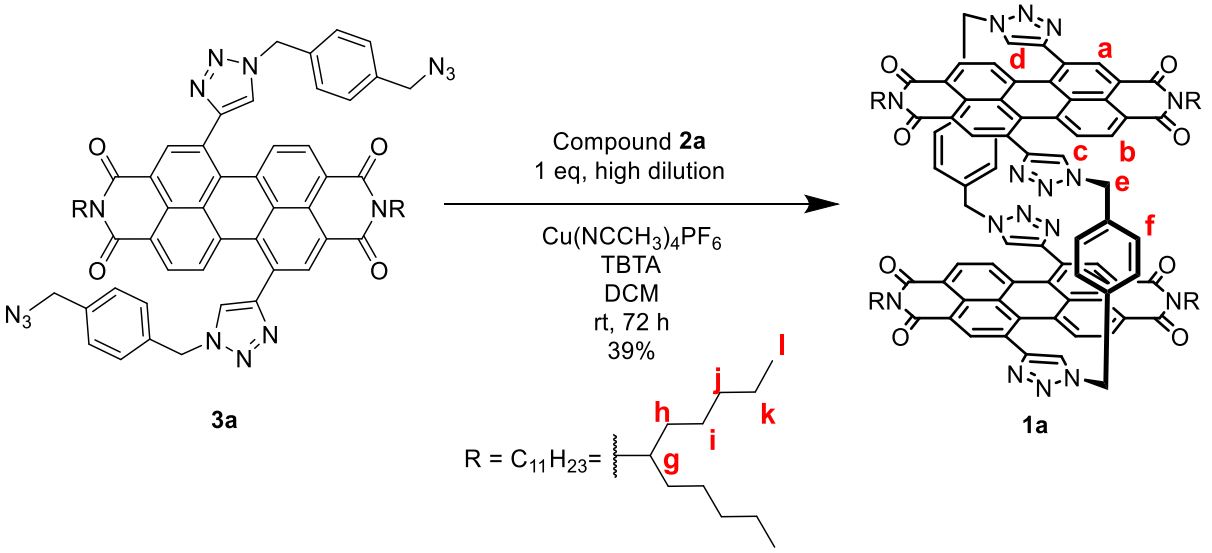

To a solution of compound **3a** (110 mg, 98 µmol) in DCM (250 mL) was added compound **2a** (73 mg, 98 µmol, 1 equiv) and Tris((1-benzyl-4-triazolyl)methyl)amine (TBTA) (21mg, 39 µmol, 0.4 equiv). The solution was then de-gassed with argon. The copper catalyst $Cu(CH_3CN)_4PF_6$ (14 mg, 39 µmol, 0.4 equiv) was then added and the solution was once again de-gassed with argon. The reaction was stirred at rt for 36 h and monitored by TLC (1:99 MeOH-DCM). The solvent was then removed *in vacuo*. The resulting residue was purified by silica gel flash column chromatography (1:99 MeOH-DCM) followed by preparative silica TLC (0.5:99.5 MeOH-DCM), affording the title compound (as the pure 1,7-regioisomer) as a purple solid (70.8 mg, 38 µmol, 39%).

^{1}H NMR (400 MHz, TCE-d_2, 373K, the major species are the enantiomers, i.e. ***MM*,*PP*:*PM*** = 88:12 mol%) δ 8.58 (s, 4H$_a$), 8.18 (d, J = 8.1 Hz, 4H$_b$), 7.66 (d, J = 8.1 Hz, 4H$_c$), 7.35 (s, 8H$_f$), 7.27 (s, 4H$_d$), 5.77 (d, J = 15.2 Hz, 4H$_e$), 5.65 (d, J = 15.1 Hz, 4H$_e$), 5.10 (p, J = 8.4, 6.3 Hz, 4H$_g$), 2.27 – 2.06 (m, 8H$_h$), 2.05 – 1.83 (m, 8H$_h$), 1.32 – 1.24 (m, 48H$_{i\text{-}k}$), 0.93 – 0.83 (m, 24H$_l$).

^{13}C NMR (101 MHz, TCE, 373K) δ 163.48, 162.81, 148.02, 136.10, 134.87, 134.34, 133.53, 132.59, 129.43, 128.98, 128.27, 128.12, 127.76, 122.74, 121.01, 54.90, 53.84, 31.36, 29.40, 26.45, 22.18, 13.62.

HRMS (ESI) (m/z) calculated for $C_{116}H_{125}N_{16}O_8^+$ $[M+H]^+$ 1869.9866, found 1869.9879.

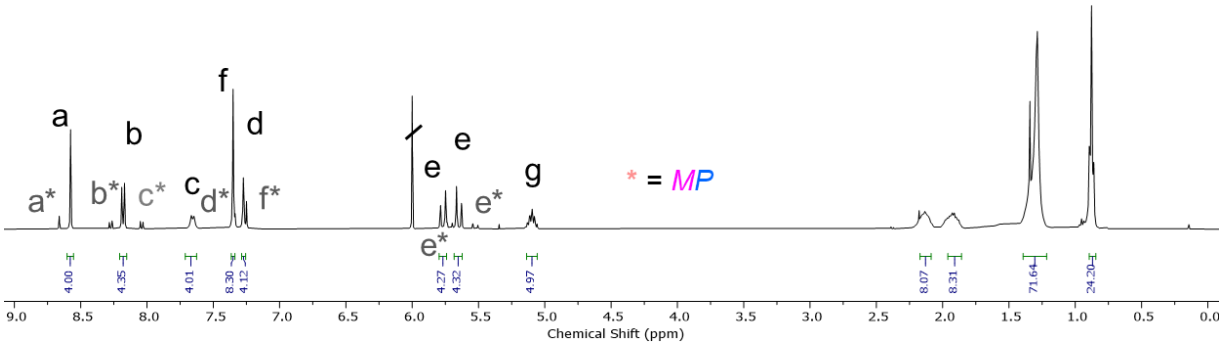

^{1}H NMR spectrum of **1a** (TCE-d_2, 373K, 400 MHz). Peaks are assigned in the 5-9 ppm region. Peaks labelled with an asterisk correspond to the minor species (***MP*** diastereomer), while those without an asterisk correspond to the major species (***MM***/***PP*** enantiomers).

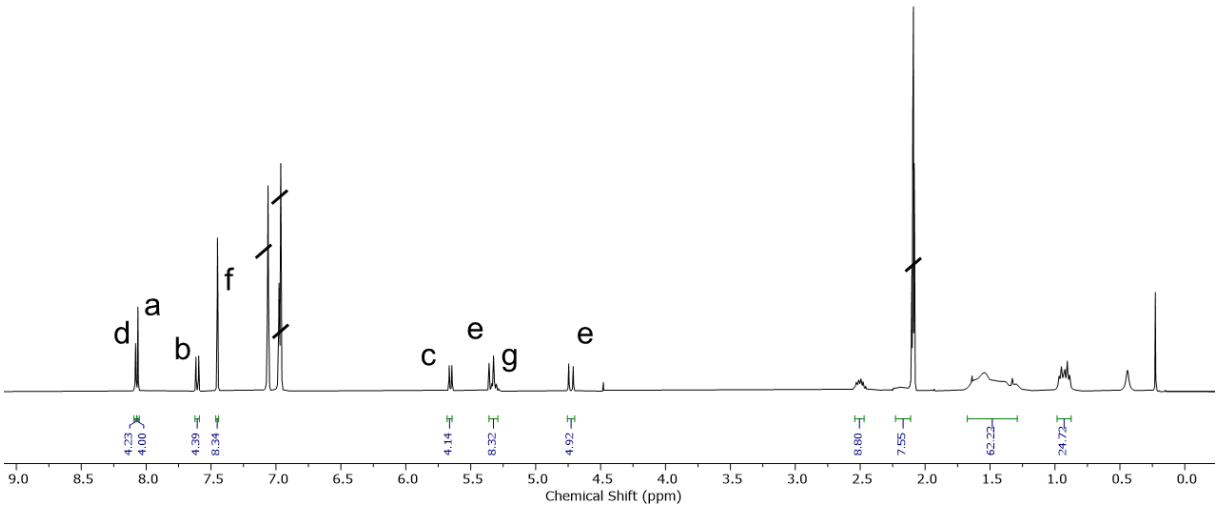

^{1}H NMR spectrum of **1a** (toluene-d_8, 373 K, 400 MHz, *MM,PP:PM* > 99:1 mol%).

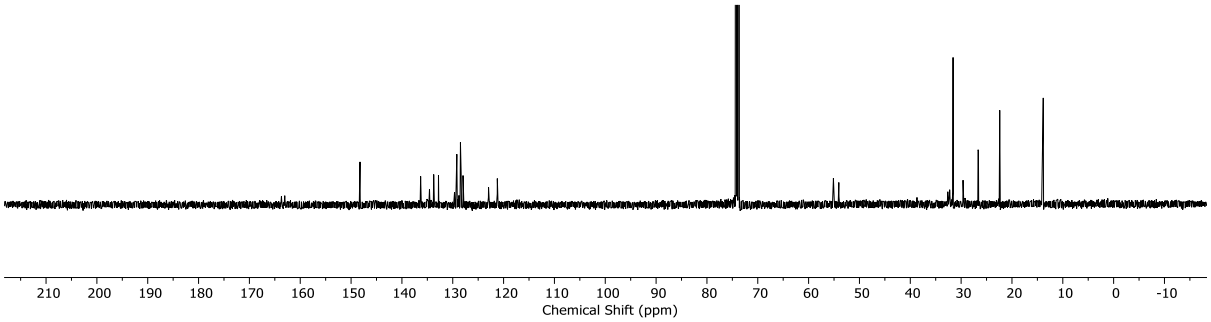

^{13}C NMR spectrum of **1a** (TCE-d_2, 373 K, 101 MHz).

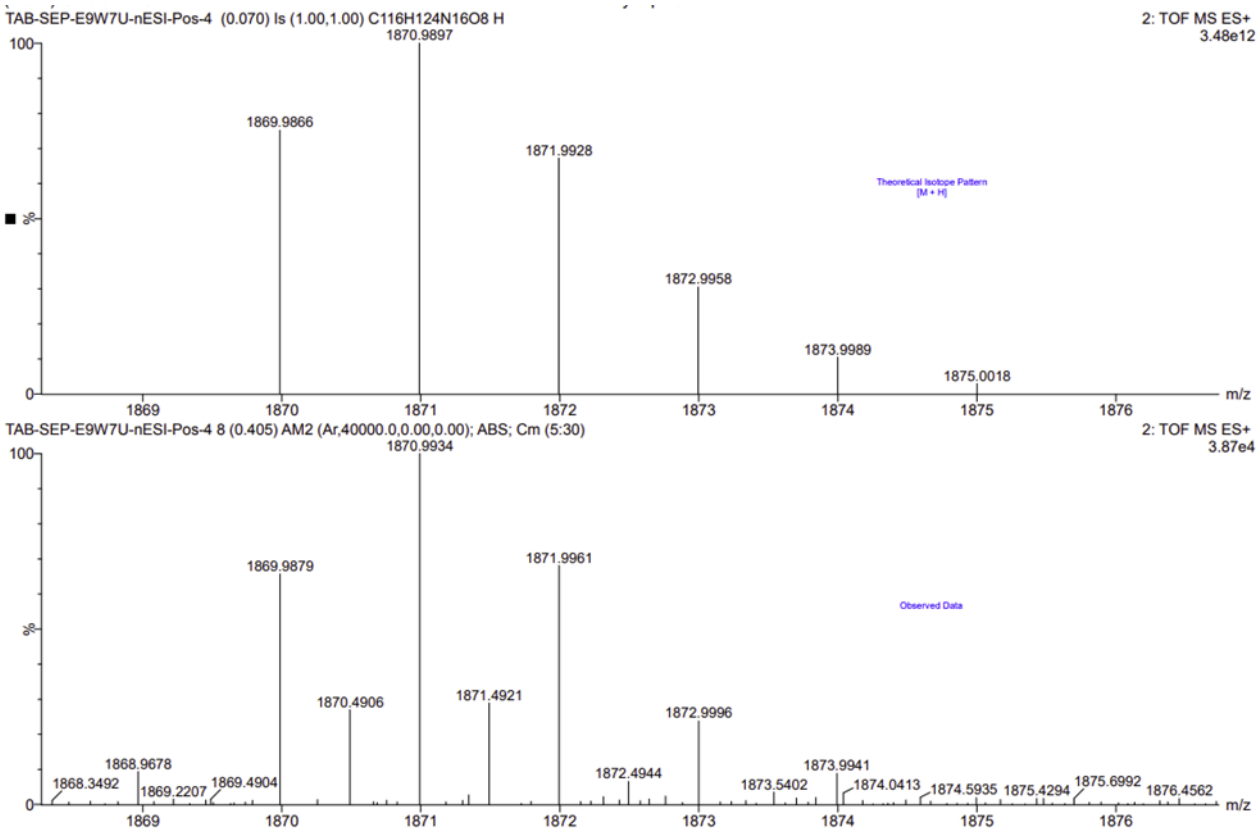

Calculated (top) and observed (bottom) ESI MS data for compound **1a**.

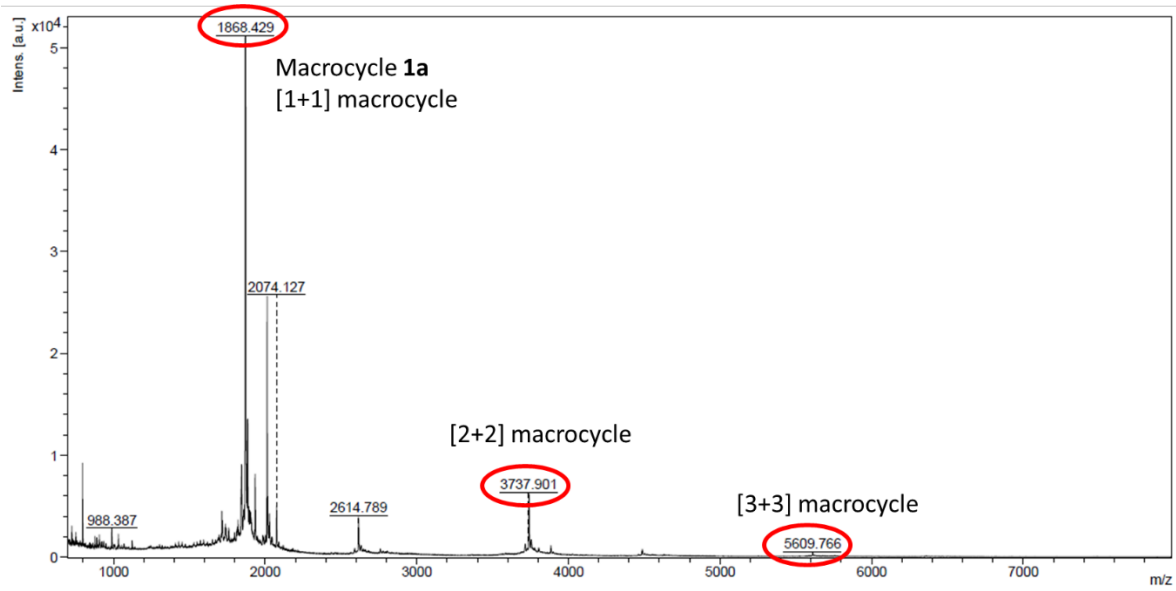

MALDI (TOF) mass spectrum of a crude reaction mixture of **1a**. This shows the formation of larger macrocyclic [2+2] and [3+3] side products, alongside the target [1+1] macrocycle **1a**.

Acyclic bis-triazole PDI 3b

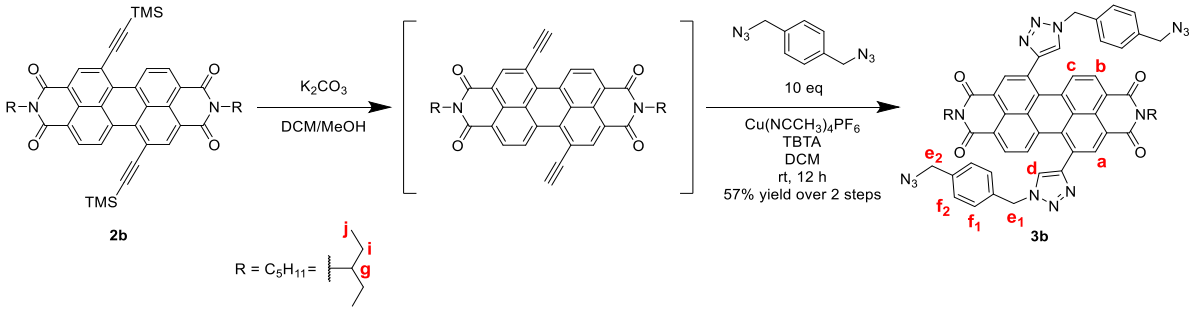

To a solution of TMS-protected bis-alkyne PDI **2b** (85 mg, 118 µmol) in DCM (20 ml) was added K_2CO_3 (50 mg) in MeOH (10 ml). The mixture was stirred at rt for 3 min, and completion of the reaction was confirmed by TLC. A further 20 mL of DCM was added to the solution. The solution was then washed with 1 M HCl (2 x 30 mL), water (2 x 30 mL) and brine (30 ml). The organic layer was then dried over anhydrous $MgSO_4$ and concentrated to dryness *in vacuo* to afford the deprotected PDI bis-alkyne which was used immediately without further purification. This PDI bis-alkyne was immediately re-dissolved in dry DCM (25 mL). To this was added 1,4-bis(azidomethyl)benzene (220 mg, 1.18 mmol, 10 equiv) and Tris((1-benzyl-4-triazolyl)methyl)amine (TBTA) (12 mg, 24 µmol, 0.2 equiv). The solution was then de-gassed with argon. The copper (I) catalyst $Cu(CH_3CN)_4PF_6$ (9 mg, 24 µmol, 0.2 equiv) was then added and the solution was once again de-gassed with argon. The reaction was stirred at rt for 12 h. The solvent was then removed *in vacuo*. The resulting residue was purified by silica gel flash column chromatography (1:99 MeOH-DCM) affording the title compound (as the pure 1,7-regioisomer) as a purple solid (63 mg, 66 µmol, 57%).

^{1}H NMR (500 MHz, Chloroform-*d*) δ 8.64 (s, 2H$_a$), 8.11 (d, *J* = 8.0 Hz, 2H$_b$), 7.82 (d, *J* = 8.1 Hz, 2H$_c$), 7.65 (s, 2H$_d$), 7.41 – 7.34 (m, 8H$_f$), 5.66 (s, 4H$_{e1}$), 5.02 (m, 2H$_g$), 4.41 (s, 4H$_{e1}$), 2.28 – 2.16 (m, 4H$_i$), 1.94 – 1.85 (m, 4H$_i$), 0.88 (t, *J* = 7.5, 1.3 Hz, 12H$_j$).

^{13}C NMR (126 MHz, $CDCl_3$) δ 163.81, 148.51, 136.81, 135.00, 134.58, 134.48, 134.18, 133.49, 129.87, 129.20, 129.18, 129.04, 128.96, 128.59, 128.55, 128.52, 122.81, 121.96, 57.74, 54.34, 54.30, 25.08, 11.36.

HRMS (ESI) (m/z) calculated for $C_{54}H_{47}N_{14}O_4^+$ [M+H$^+$] 955.3904, found 955.3885

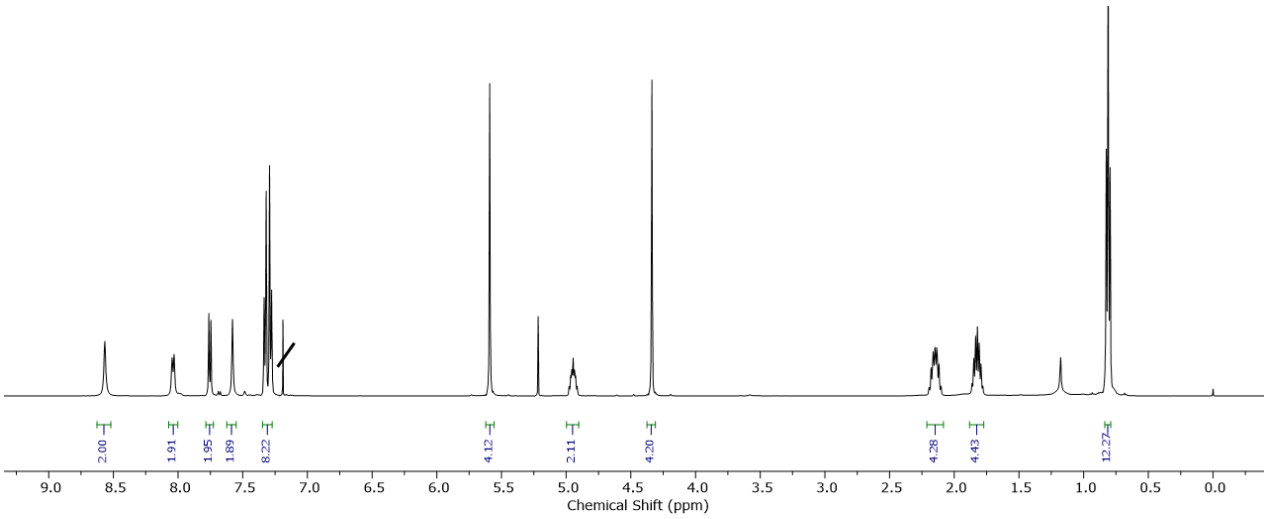

^{1}H NMR spectrum of **3b** (Chloroform-*d*, 298 K, 500 MHz).

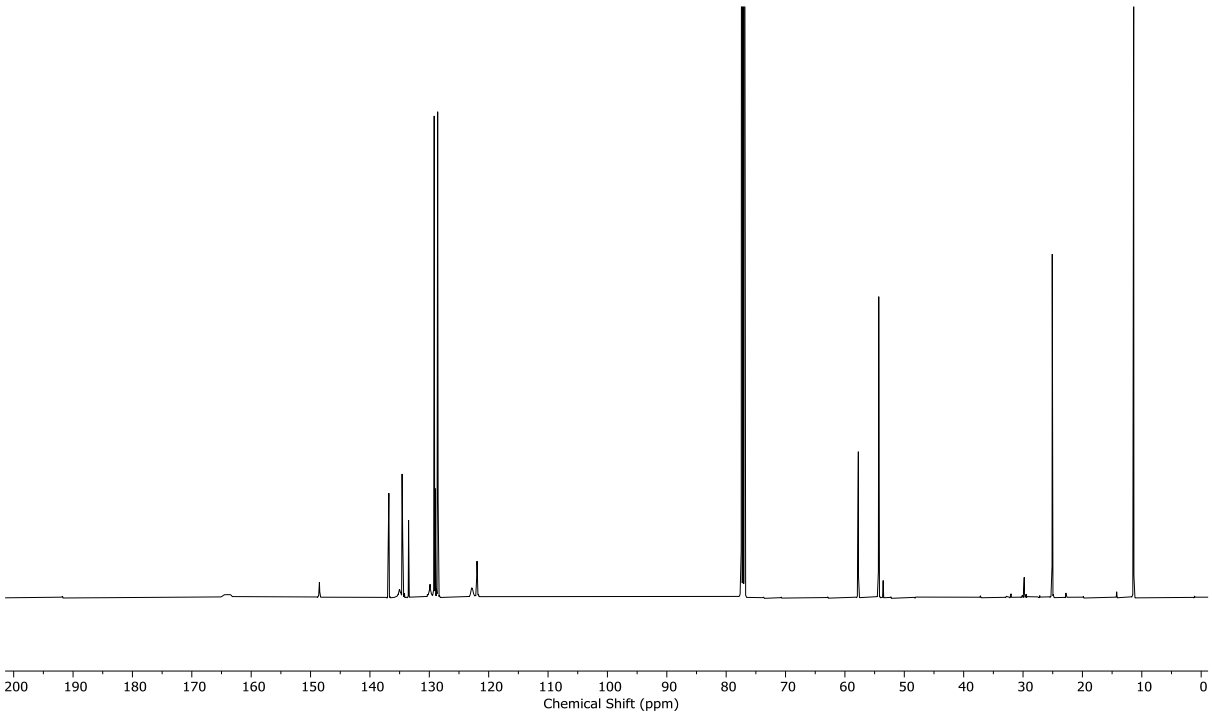

^{13}C NMR spectrum of **3b** (Chloroform-*d*, 298 K, 101 MHz).

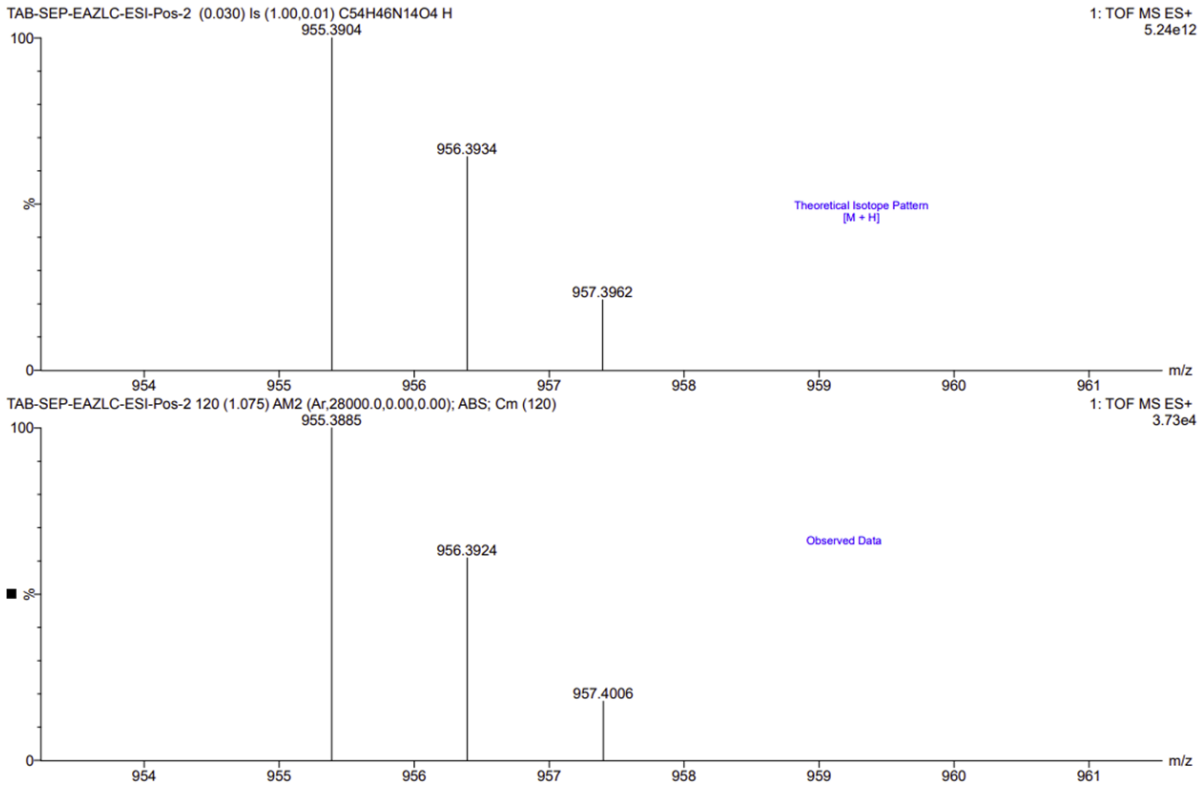

Calculated (top) and observed (bottom) ESI MS data for compound **3b**.

Bis-PDI macrocycle 1b

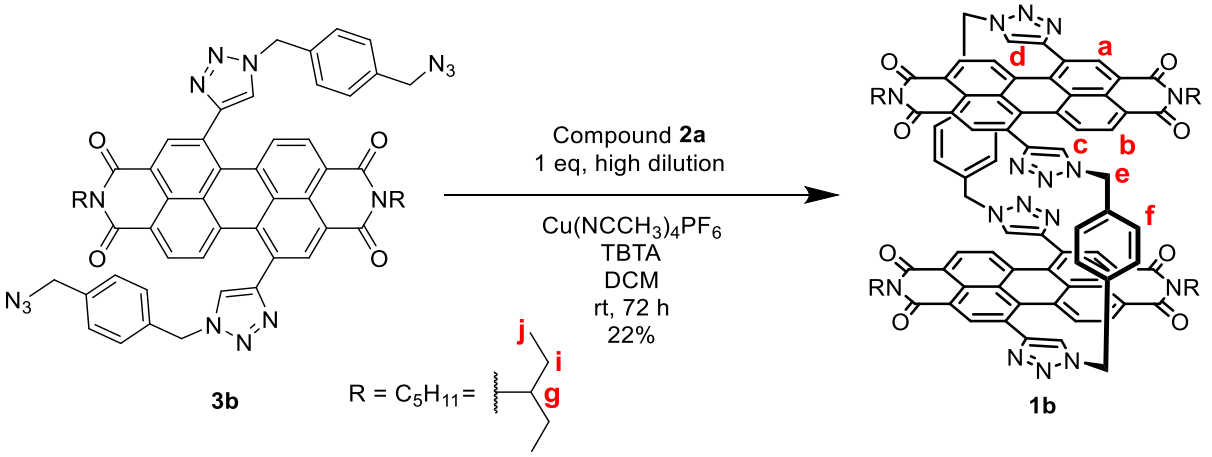

To a solution of compound **3b** (63 mg, 66 µmol) and freshly-prepared compound **2a** (38 mg, 66 µmol, 1 equiv) in DCM (250 mL) was added Tris((1-benzyl-4-triazolyl)methyl)amine (TBTA) (14 mg, 26 µmol, 0.4 equiv). The solution was then de-gassed with argon. The copper catalyst $Cu(CH_3CN)_4PF_6$ (10 mg, 26 µmol, 0.4 equiv) was then added and the solution was once again de-gassed with argon. The reaction was stirred at rt for 36 h and monitored by TLC (1:99 MeOH-DCM). The solvent was then removed *in vacuo*. The resulting residue was purified by silica gel flash column chromatography (1:99 MeOH-DCM) followed by preparative silica TLC (0.5:99.5 MeOH-DCM), affording the title compound (as the pure 1,7-regioisomer) as a purple solid (22.7 mg, 15 µmol, 22%).

^{1}H NMR (400 MHz, TCE-d_2, 373K, the major species are the enantiomers, i.e. ***MM*,*PP*:*PM*** = 81:19 mol%) δ 8.63 (s, 4H$_a$), 8.23 (d, J = 8.1 Hz, 4H$_b$), 7.79 (d, J = 8.1 Hz, 4H$_c$), 7.31 (s, 8H$_f$), 7.20 (s, 4H$_d$), 5.74 (d, J = 15.2 Hz, 4H$_e$), 5.64 (d, J = 15.2 Hz, 4H$_e$), 5.02 – 4.95 (m, 4H$_g$), 2.18 (m, 8H$_i$), 1.98 (m, 8H$_i$), 0.90 (q, J = 7.2 Hz, 24H$_j$).

^{13}C NMR (101 MHz, TCE, 373K) δ 164.53, 163.49, 148.29, 136.30, 134.87, 134.02, 133.08, 129.91, 129.49, 129.37, 128.62, 128.25, 123.15, 121.25, 58.74, 54.18, 29.78, 25.43, 25.22, 11.53.

HRMS (ESI) (m/z) calculated for $C_{92}H_{76}N_{16}O_8$ $[M]^+$ 1533.6111, found 1533.6090.

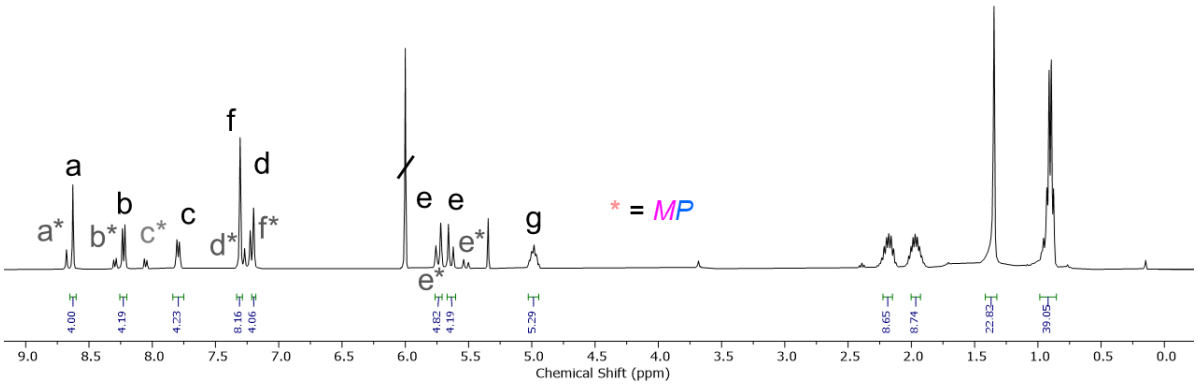

^{1}H NMR spectrum of **1b** (TCE-d_2, 373K, 400 MHz). The δ = 5-9 ppm region of this spectrum is near identical (Δδ = 0.05 - 0.1 ppm) to that of macrocycle **1a**. Peaks labelled with an asterisk correspond to the minor species (***MP*** diastereomer), while those without an asterisk correspond to the major species (***MM***,***PP*** enantiomers).

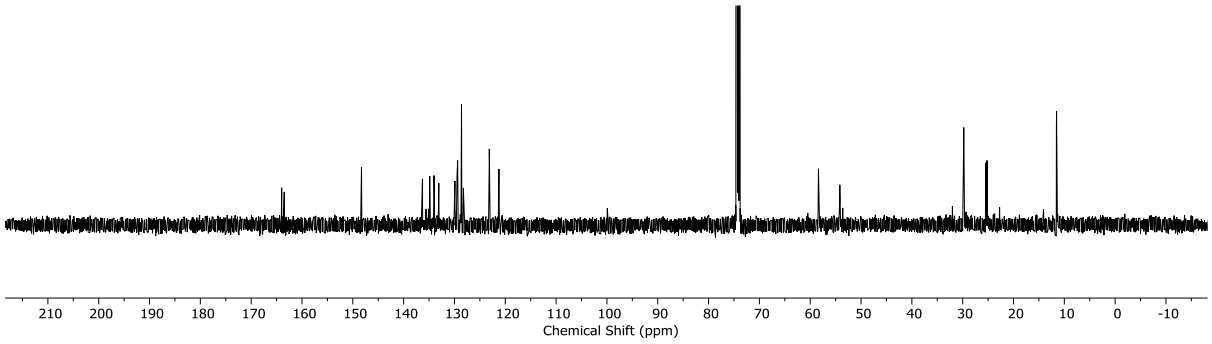

^{13}C NMR spectrum of **1b** (TCE-d_2, 373 K, 101 MHz).

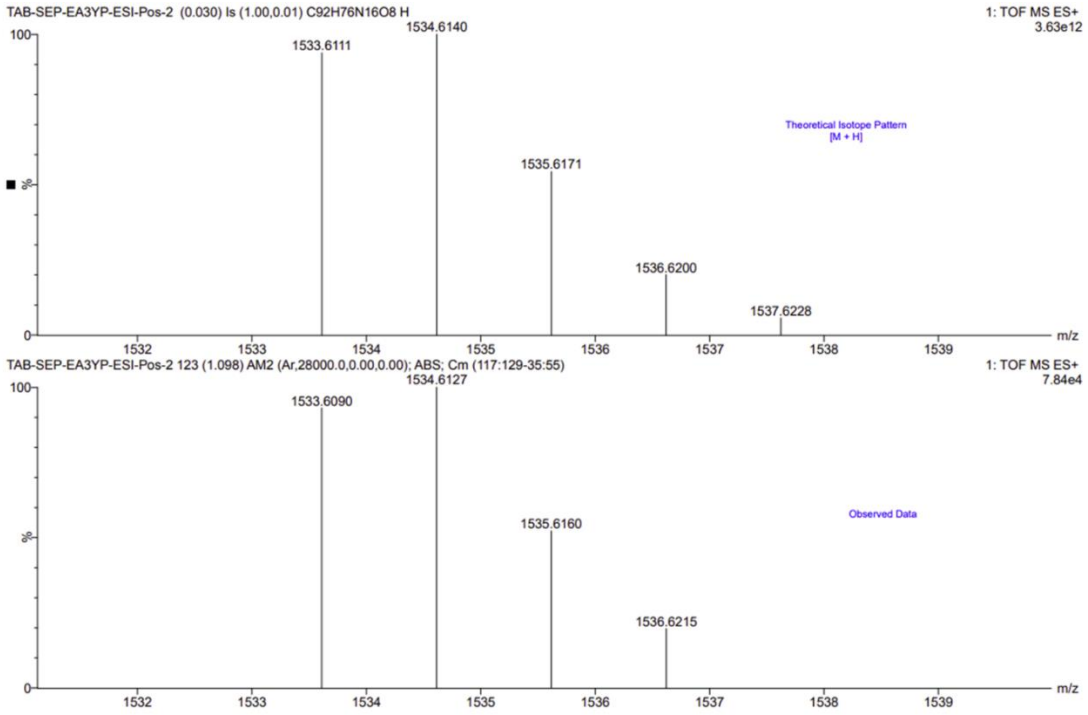

Calculated (top) and observed (bottom) ESI MS data for compound **1b**.

1,7-TMS-protected bis-alkyne PDI 2b.

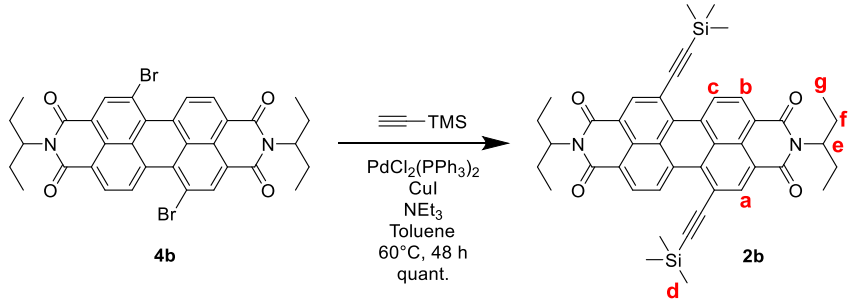

To a solution of dibromo PDI **4b**[16] (200 mg, 290 µmol) in 1:1 dry NEt_3-toluene (30mL) under a nitrogen atmosphere was added $Pd(PPh_3)_2Cl_2$ (12.94 mg, 17 µmol, 0.06 equiv), CuI (6.09 mg, 32 µmol, 0.11 equiv) and trimethylsilylacetylene (142 mg, 207 µL, 1.45 mmol, 5 equiv). The mixture was thoroughly de-gassed with nitrogen and stirred at 60 °C for 48 h. The solvent mixture was then removed *in vacuo*. The resulting residue was then re-dissolved in DCM (30 mL) and washed with 1M HCl (50 mL) and water (3 x 50 mL); dried over anhydrous $MgSO_4$ and concentrated to dryness *in vacuo*. The resulting residue was purified by silica gel flash column chromatography (1:1 n-hexane:DCM) affording the title compound as a red solid (210mg, 290 µmol, 100%).

^{1}H NMR (400 MHz, Chloroform-*d*) δ 10.22 (d, *J* = 8.2 Hz, $2H_c$), 8.82 (s, $2H_a$), 8.65 (d, *J* = 8.2 Hz, $2H_b$), 5.11 – 5.02 (m, $2H_e$), 2.33 – 2.19 (m, $4H_f$), 2.02 – 1.81 (m, $4H_f$), 0.93 (t, *J* = 7.5 Hz, $12H_g$), 0.39 (s, $18H_d$).

^{13}C NMR (101 MHz, $CDCl_3$) δ 134.49, 134.21, 128.13, 127.83, 127.66, 120.02, 106.19, 105.81, 77.48, 77.16, 76.84, 57.94, 25.17, 11.44, -0.23

MS (MALDI-TOF) (m/z) calculated for $C_{44}H_{46}N_2O_4Si_2$ [M]: 722.2996, found 722.3007

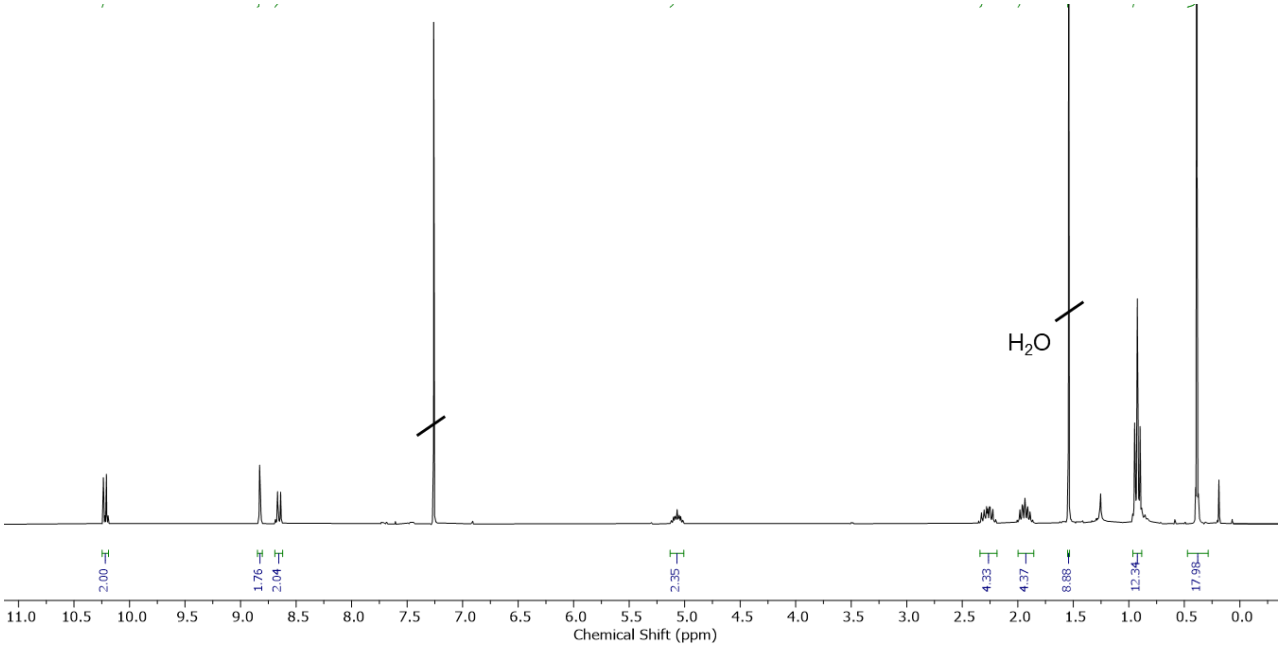

^{1}H NMR spectrum of **5b** (Chloroform-*d*, 298 K, 400 MHz).

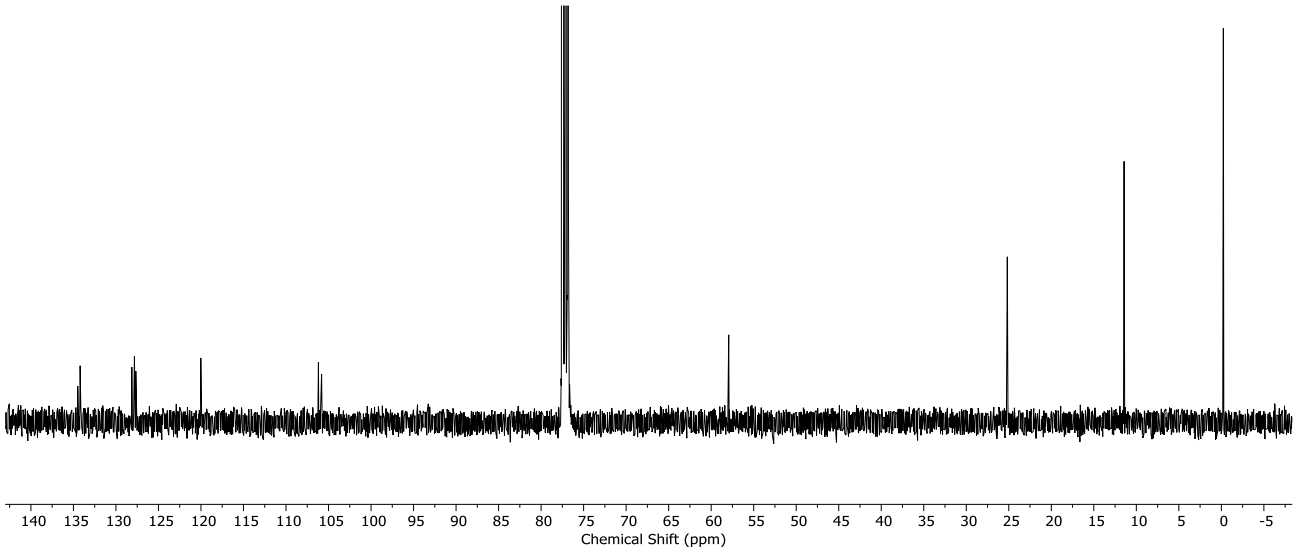

^{13}C NMR spectrum of **5b** (Chloroform-*d*, 298 K, 400 MHz).

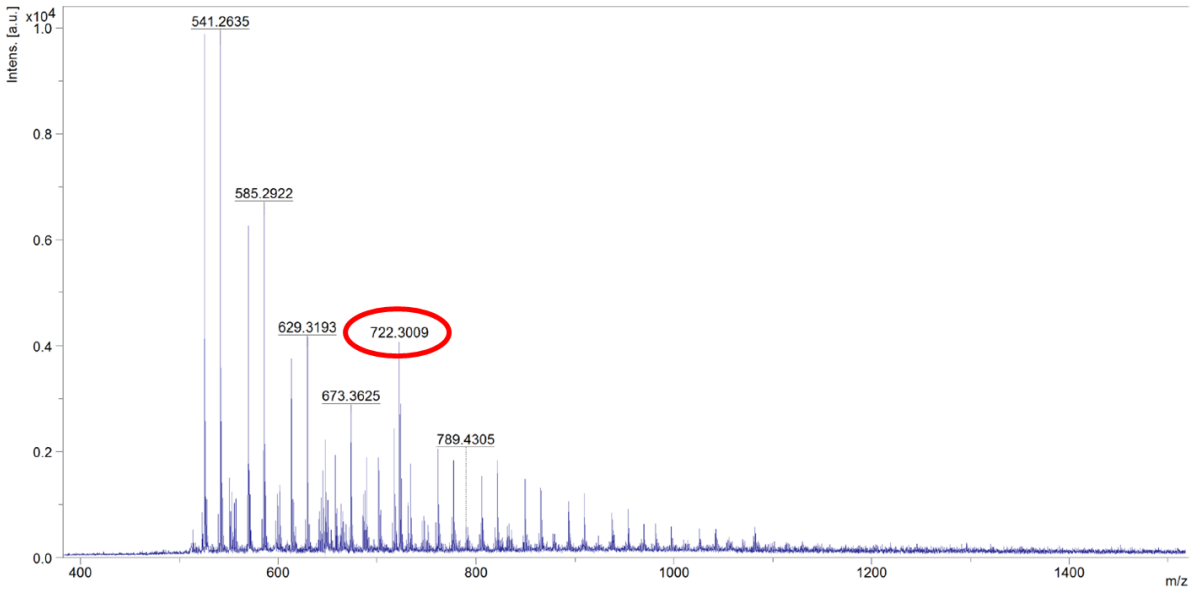

MALDI (TOF) mass spectrum for compound **5b**. An accurate mass was obtained by calibration to polyethylene glycol chains that were co-spotted with the sample and therefore also observed in the mass spectrum

2.9.3 Separation of 1,6- and 1,7- stereoisomers by crystallisation

It was found that it is possible to separate the 1,7- and 1,6-regioisomers of bis-bromo PDI **4b** through recrystallisation. In a typical procedure, 500 mg of **4b** (as a mix of 1,7- and 1,6-regioisomers) was dissolved in 200 mL of chloroform and placed in a 500 mL measuring cylinder. On top of this was layered 200 mL of hexane. The cylinder was sealed with parafilm and left overnight. The next day, the mixture was filtered, yielding crystals enriched in the 1,7 isomer. Multiple recrystallisations allowed the pure 1,7-isomer to be isolated. However, the yield for this was only ~ 25 % pure 1,7-isomer, and as this was also quite time consuming, it was decided that pursuing this method was not worthwhile. Instead, it was later found that the 1,6 and 1,7 isomers can be separated by column chromatography at the macrocyclisation stage.

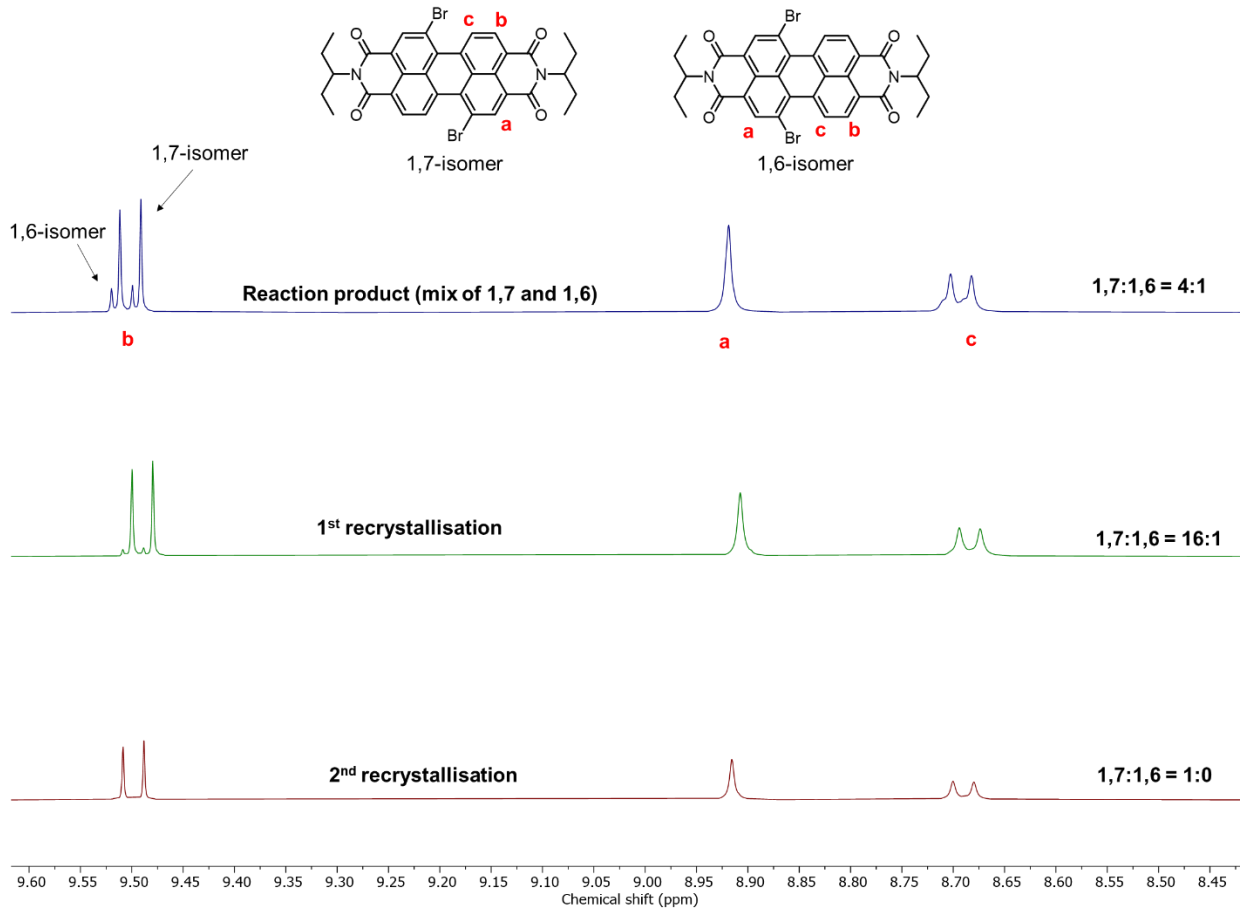

Figure 2.48: ^{1}H NMR spectrum (Chloroform-*d*, 298 K, 500 MHz) of compound **4b** after successive recrystallizations.

2.9.4 Further NMR spectroscopy experiments

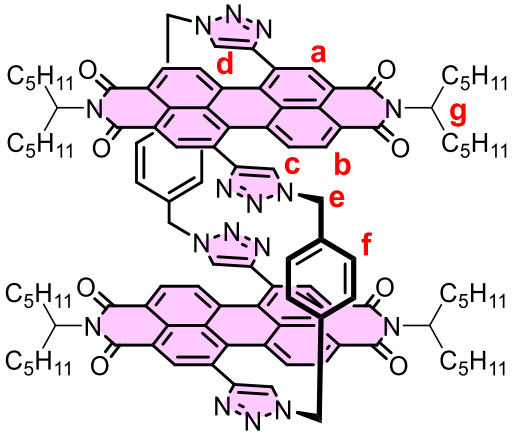

Macrocycle **1a**

a) Variable temperature ^{1}H NMR spectroscopy experiments

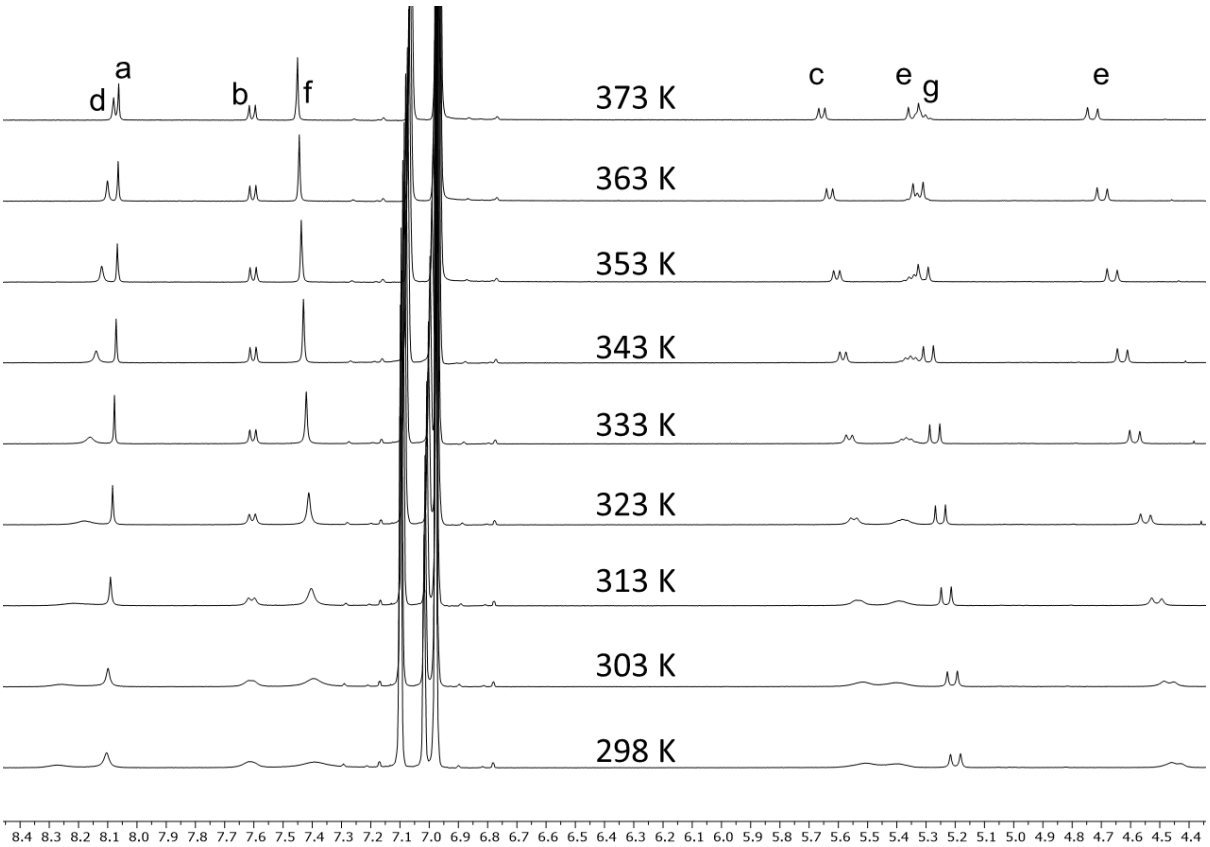

Figure 2.49: Truncated ^{1}H NMR spectra of **1a** (Toluene-d_8, 400 MHz) at various temperatures ranging from 298 K (bottom spectrum) to 373 K (top spectrum), showing how the spectrum is too broad to assign at room temperature (298K) but sharpens as the temperature is increased.

b) Solvent dependent ^{1}H NMR spectroscopy of macrocycle 1a

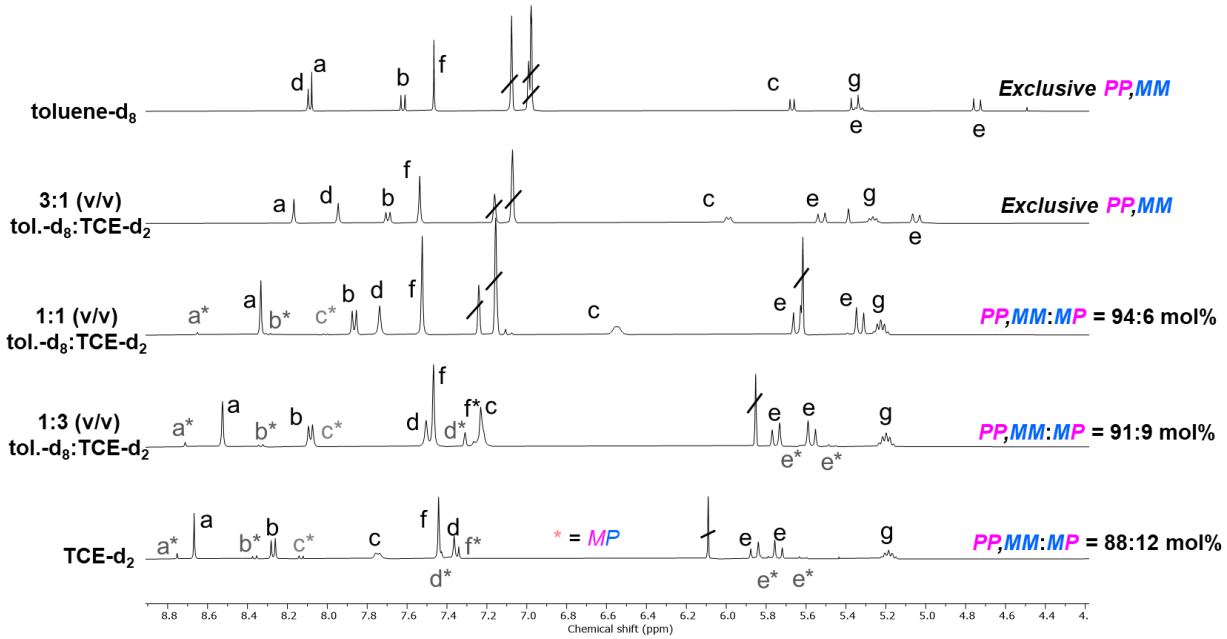

Figure 2.50: Partial ^{1}H NMR spectra of macrocycle **1a** in different toluene-d_8:TCE-d_2 solvent mixtures (373K, 400 MHz). The spectra are aligned using an internal reference standard, poly(dimethylsiloxane), added to each sample. Peaks labelled with an asterisk correspond to the minor species (***MP*** diastereomer), while those without an asterisk correspond to the major species (***MM,PP*** enantiomers). The ***MM,PP*:*MP*** ratios are shown for each spectrum.

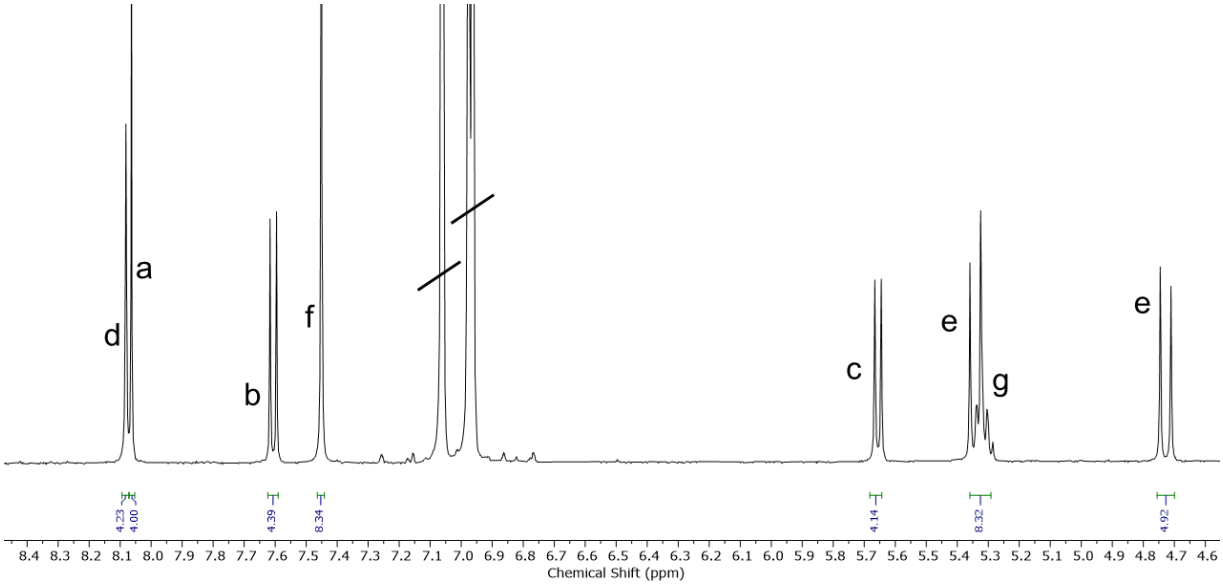

Figure 2.51: Zoomed in region of the ^{1}H NMR spectrum of macrocycle **1a** in toluene-d_8 (373 K, 400 MHz, ***MM,PP:PM*** > 99:1 mol%) to show that no ***MP*** diastereomer (i.e. minor species) is detectable by ^{1}H NMR spectroscopy.

c) ^{1}H-^{1}H EXSY/NOE NMR Spectroscopy

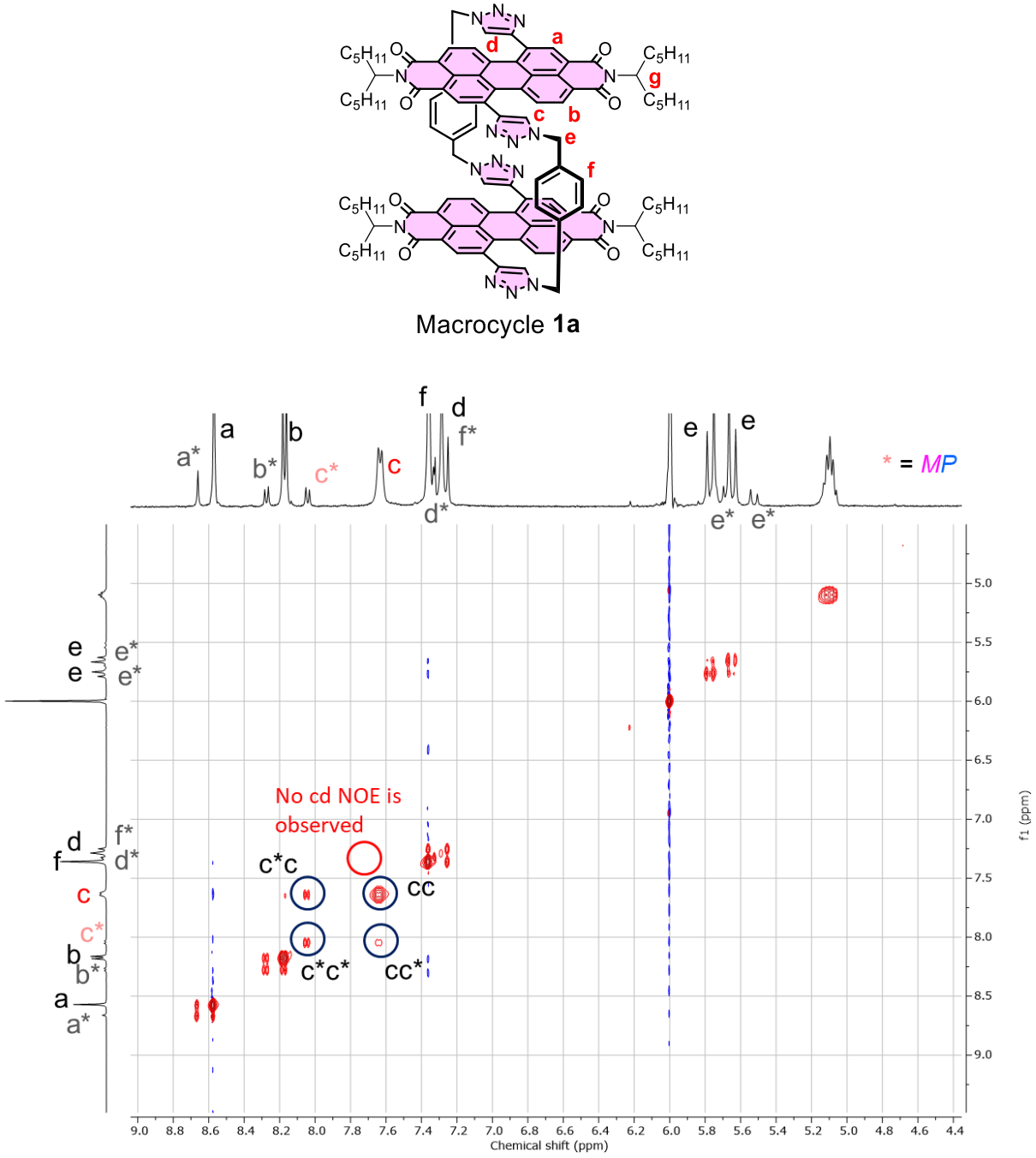

Figure 2.52: Partial ^{1}H-^{1}H EXSY/NOESY NMR spectrum of macrocycle **1a** (TCE-d_2, 373 K, 400 MHz). Signals with phase shown in red are EXSY signals and signals with phase shown in blue are NOESY signals. Unlike in toluene (**Figure 2.53**), no NOE is seen between the H_c and H_d protons in TCE-d_2. EXSY signals show which ^{1}H NMR signals are under chemical exchange, via interconversion of ***MM,PP*** enantiomers with the ***MP*** diastereomer. The EXSY signal set for the exchange of H_c (***MM,PP*** enantiomer species) and H_{c*} (***MP*** diastereomer) is highlighted as an example.

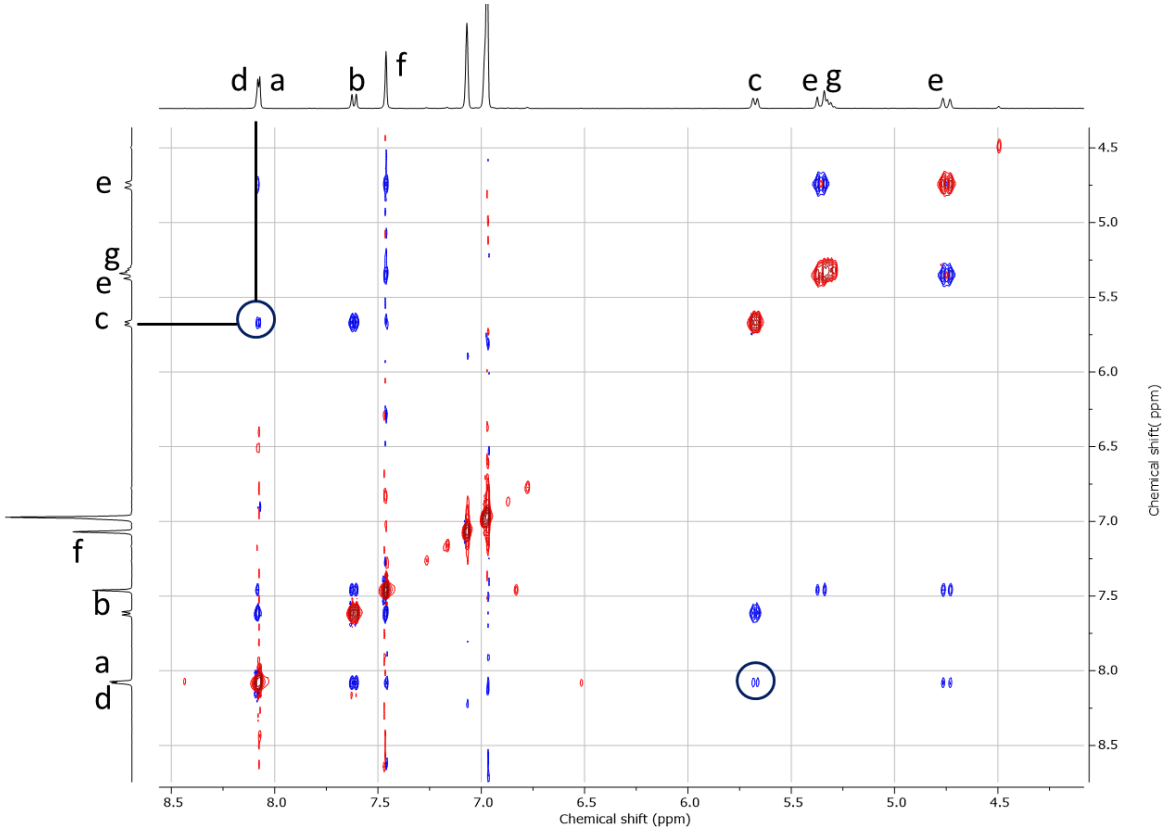

Figure 2.53: Partial ^{1}H-^{1}H EXSY/NOESY NMR spectrum of macrocycle **1a** (toluene-d_8, 373 K, 400 MHz). Signals with phase shown in red are EXSY signals and signals with phase shown in blue are NOESY signals. In toluene-d_8 a NOE between the protons H_c and H_d is observed, in contrast to TCE-d_2 (**Figure 2.52**).

d) Determination of rate constants of *MM/PP*↔*MP* interconversion by ^{1}H-^{1}H EXSY NMR spectroscopy

Quantitative ^{1}H-^{1}H EXSY NMR spectroscopy can be used to obtain rate constants for the interconversion between different species.[41] This has been used to quantify the exchange kinetics in supramolecular systems where the exchanging species have different energies and populations.[43] An adapted version of this method has been used here.

All 2D-EXSY NMR spectra were recorded on a Bruker AV NEO 400 (400 MHz) NMR spectrometer. Exchange rates were calculated using the program EXSY CALC.[44] To calculate the exchange rates between two species, diagonal and cross-peak intensities for the exchanging NMR resonances are required from two EXSY NMR experiments at different mixing times. For each data point, one EXSY NMR experiment was carried out with a mixing time of 900 ms and another was carried out with a very short mixing time of 5 ms. The same major and minor exchanging proton signals were used for every EXSY experiment. Here, we used H_c and H_{c*} in the ^{1}H NMR spectrum of **1a** (section 2.5.1), as the large chemical shift difference between these signals allowed easy and reliable integration ($\Delta\delta$ = 0.5 ppm).

The exchange matrix is as follows:

$$\begin{vmatrix} -R_1 - k_1 & k_{-1} \\ k1 & -R_2 - k_{-1} \end{vmatrix}$$

Where k_1 and k_{-1} are exchange rates and R_1 and R_2 are the longitudinal relaxation rates.

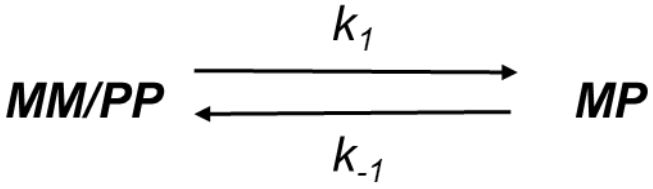

Table 5: Rates (k_1 and k_{-1}) and corresponding free energies of activation ($\Delta G^{\ddagger}_1$ and $\Delta G^{\ddagger}_{-1}$) for the interconversion between enantiomer ***MM/PP*** and diastereomer ***MP*** of macrocycle **1a**, determined by ^{1}H-^{1}H EXSY NMR spectroscopy at different temperatures and in different solvents.

Solvent	Temp. (K)	k_1 (s^{-1})	$\Delta G^{\ddagger}_1$ (kJ mol^{-1})	k_{-1} (s^{-1})	$\Delta G^{\ddagger}_{-1}$ (kJ mol^{-1})
TCE-d_2	353	0.023	103.8	0.086	99.7
	358	0.031	102.9	0.159	97.8
	363	0.043	101.8	0.206	97.0
	368	0.071	100.2	0.372	95.1
	373	0.103	99.1	0.574	93.8
1:1 (v/v) tol.-d_8:TCE-d_2	373	0.090	99.5	1.05	91.9

This data in pure TCE-d_2 can be fitted to the linear form of the Eyring equation: [45]

$$\ln\frac{k}{T} = \frac{-\Delta H^{\neq}}{R}\frac{1}{T} + \ln\frac{k_B}{h} + \frac{\Delta S^{\neq}}{R}$$

Where k_B is the Boltzmann constant, R is the gas constant and h is Planck's constant.

This fitting yields $\Delta H^{\ddagger}$ = 80.7 ± 5.7 kJ mol^{-1} and $\Delta S^{\ddagger}$ = – 49.7 ± 14.1 J K^{-1} mol^{-1} for the forwards MM/PP → MP process and $\Delta H^{\ddagger}$ = 98.7 ± 6.2 kJ mol-1 and $\Delta S^{\ddagger}$ = + 13.0 ± 17.0 J K^{-1} mol^{-1} for the backwards MP → MM/PP process, in pure TCE-d2.

From here, $\Delta G^{\ddagger}$ in pure TCE-d_2 can be calculated at 298 K: $\Delta G^{\ddagger}_1$ (298 K) = 95.5 kJ mol-1 for the forwards MM/PP → MP process and $\Delta G^{\ddagger}_{-1}$ (298 K) = 94.8 kJ mol^{-1} for the backwards MP → MM/PP process. Therefore, the barrier in TCE-d_2 at 298 K is close to that in dichloromethane at 298 K, as determined by CD spectroscopy in section 2.4.4.

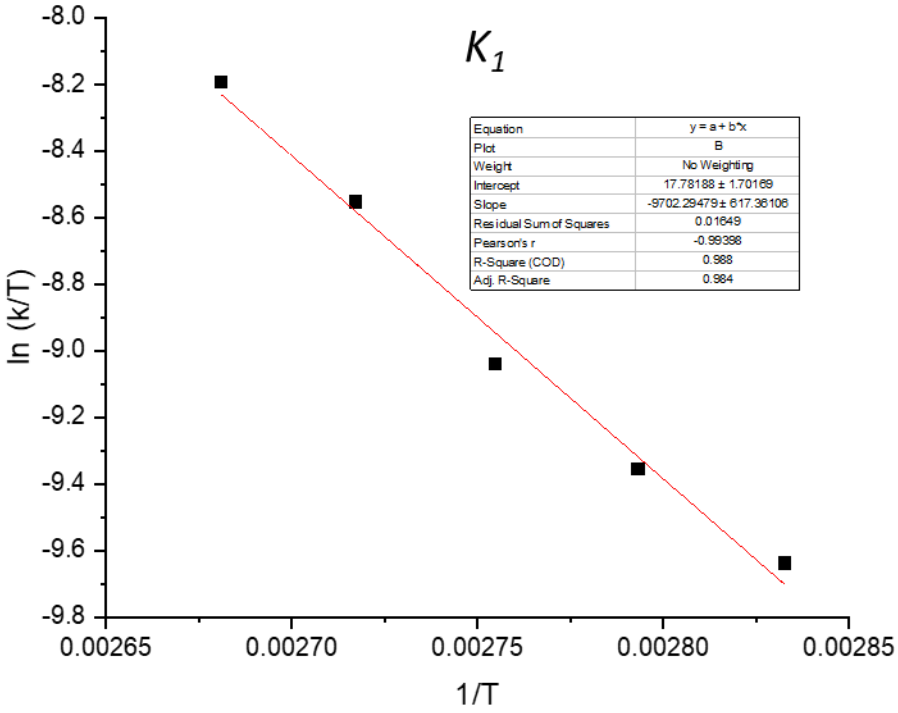

Figure 2.54: Van 't Hoff plot for the forwards rate constant (k_1) of interconversion between the enantiomer ***MM/PP*** and the diastereomer ***MP*** of macrocycle **1a**, obtained from ^{1}H-^{1}H EXSY NMR experiments at different temperatures.

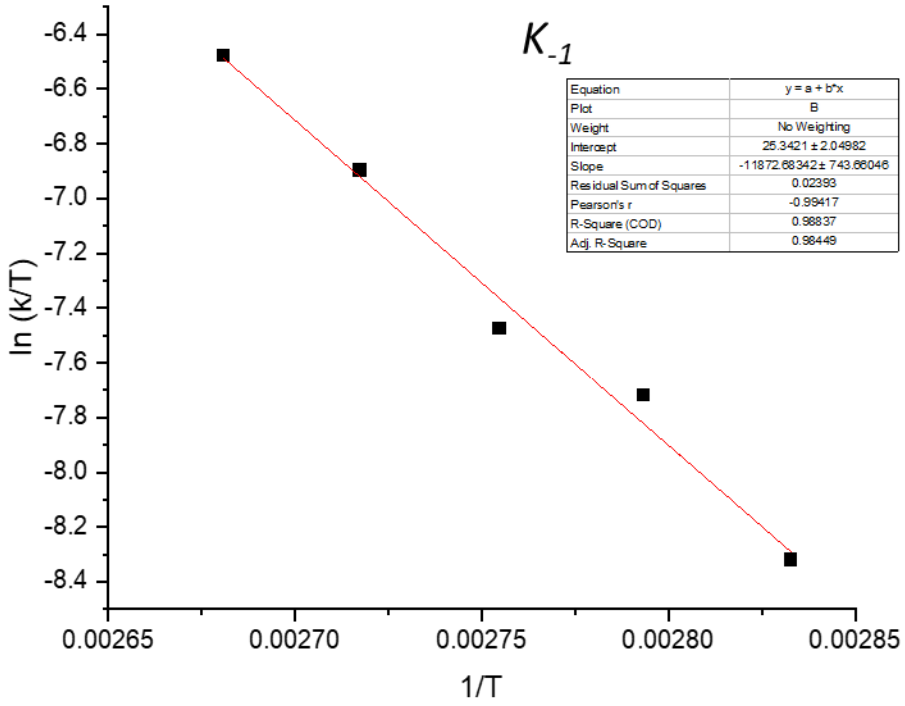

Figure 2.55: Van 't Hoff plot for the backwards rate constant (k_{-1}) of interconversion between the enantiomer ***MM/PP*** and the diastereomer ***MP*** of macrocycle **1a**, obtained from ^{1}H-^{1}H EXSY NMR experiments at different temperatures.

2.9.5 Crystallography

*The single crystal X-ray diffraction data for macrocycle **1b** was collected and solved by Dr Georgia Orton and Dr Sarah Griffin.*

Purple, needle-like crystals of macrocycle **1b**, suitable for single crystal X-ray diffraction, were grown from a racemic mixture of **1b** dissolved in chloroform, with slow diffusion of methanol (antisolvent).

Single crystal X-ray diffraction experiments were performed at the UK Diamond Light Source I19-1 3-circle diffractometer (λ = 0.6889 Å).[72-74] A suitable single crystal was selected and mounted using fomblin film on a micromount. Data were collected on a dectris-CrysAlisPro-abstract goniometer imported dectris images diffractometer. The crystals were kept at 100(2) K during data collection (single omega sweep). The structures were solved by direct methods using ShelXT[75] and refined with ShelXL using a least squares method. Olex2 software was used as the solution, refinement and analysis program.[76] The crystal diffracted weakly despite the use of synchrotron radiation and numerous attempts at growing better diffracting crystals. The data used in the refinement was truncated to a resolution of 0.84 Å which reduced completeness but improved signal to noise. Overall the data to parameter ratio is 11.5.A completeness of 83% did not support meaningful modelling of most of the disordered solvent. Instead, the olex solvent mask function was used which found 672 electrons in a volume of 2296 Å^3 in 2 voids per unit cell. This is consistent with the presence of 0.625[$CHCl_3$], 2.625[COH_4] per asymmetric unit which account for 668 electrons per unit cell. Hydrogen atoms were placed in geometrically calculated positions; non-hydrogen atoms were refined with anisotropic displacement parameters. Methyl hydrogens were refined as idealized CH_3 groups with tetrahedral angles. ADPs of atoms on the PDI core were restrained to be similar (SIMU). Figures were produced using CrystalMakerX.

Crystal Data for Macrocycle **1b** $C_{93}H_{80}N_{16}O_9$(*M* = 1565.73 g/mol): monoclinic, space group C2/c, *a* = 42.6612(4) Å, *b* =12.02180(10) Å, *c* = 34.4752(3) Å, α = 90°, β = 109.6030(10)°, γ = 90°, *V* = 16656.3(3) Å^3, *Z* = 8, *T* = 100(2) K, μ(Synchrotron) = 0.078 mm^{-1}, D_{calc} = 1.245, 35021 reflections collected (3.428° ≤ 2Θ ≤ 48.406°), 12270 unique [R_{int} = 0.0521, R_{sigma} = 0.0852] which were all used in the calculations. The final R_1 was 0.1629 (I > 2σ(I)) and wR_2 was 0.4597 (all data). Deposited cif number: 2157213.

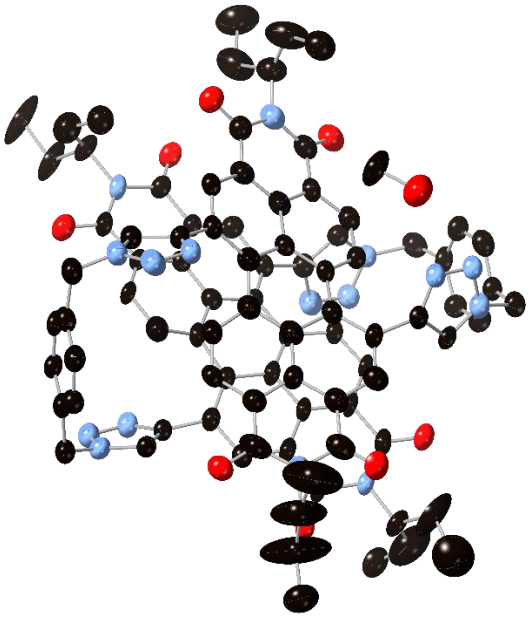

Figure 2.56: Asymmetric unit of macrocycle **1b** with all non-hydrogen atoms represented by ellipsoids at the 50% probability level. Hydrogen atoms omitted for clarity (C, black; O, red; N, blue)

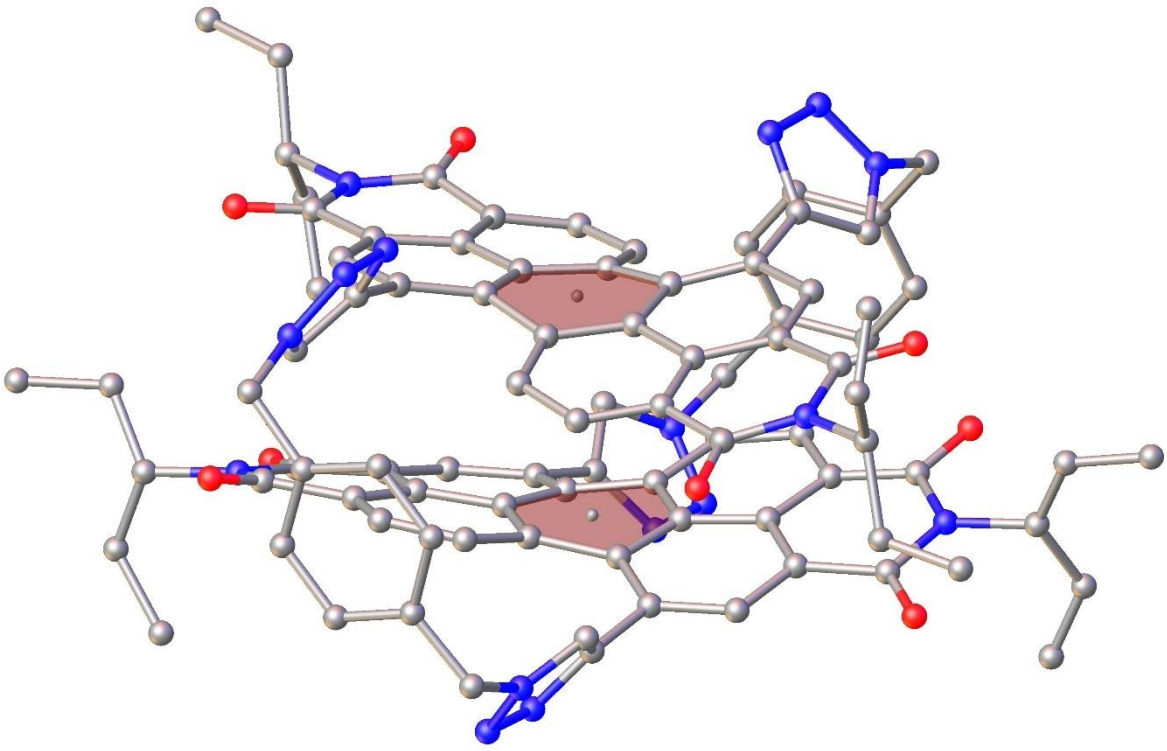

Figure 2.57: PDI–PDI plane to plane centroid = 3.7 Å, calculated using Olex2 software.

2.9.6 Chiral HPLC

Chiral chromatographic studies were performed using a Phenomenex i-Amylose-1 chiral column on an Agilent 1290 Infinity analytical HPLC instrument. The flow rate was 1 mL/minute and the detection wavelength was 500 nm. The eluents and injection volumes for each chromatogram are specified in the figure captions. To separate the enantiomers for chiroptical studies, the system was set up to run automatedly and the enantiomers were collected using an automated fraction collector. For this purification the eluent system was 4:1 toluene:n-hexane and the injection volume was 20 µL.

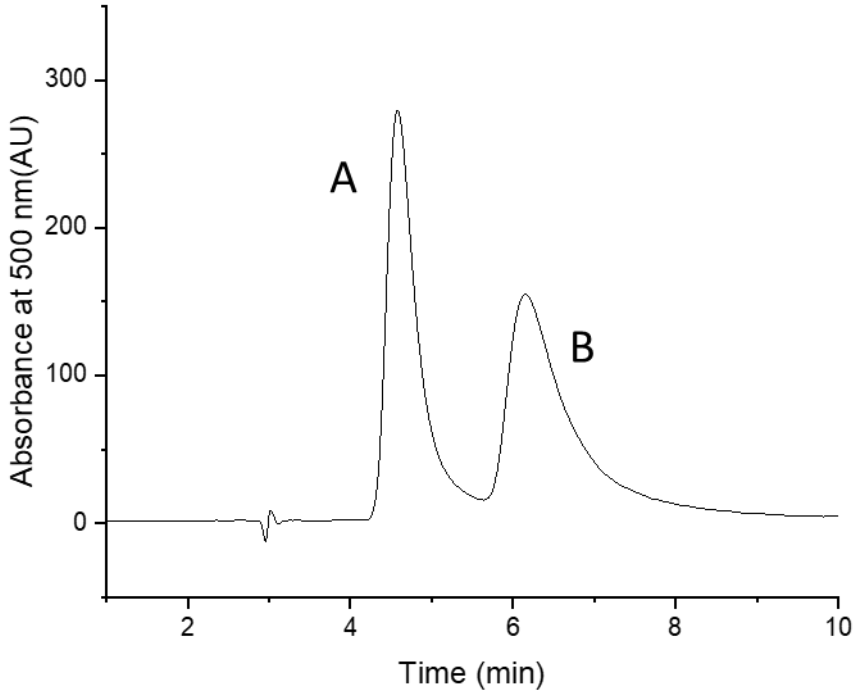

Figure 2.58: Chiral HPLC chromatogram of compound **1a** dissolved in toluene (injection volume 50 µL, ~ 2 mg/mL) and eluted with 4:1 (v/v) toluene:n-hexane. Using a combination of CD spectroscopy (**Section 2.9.7**) and computational modelling (**Appendix A**), peak A is assigned as the ***MM*** enantiomer and peak B is assigned as the ***PP*** enantiomer.

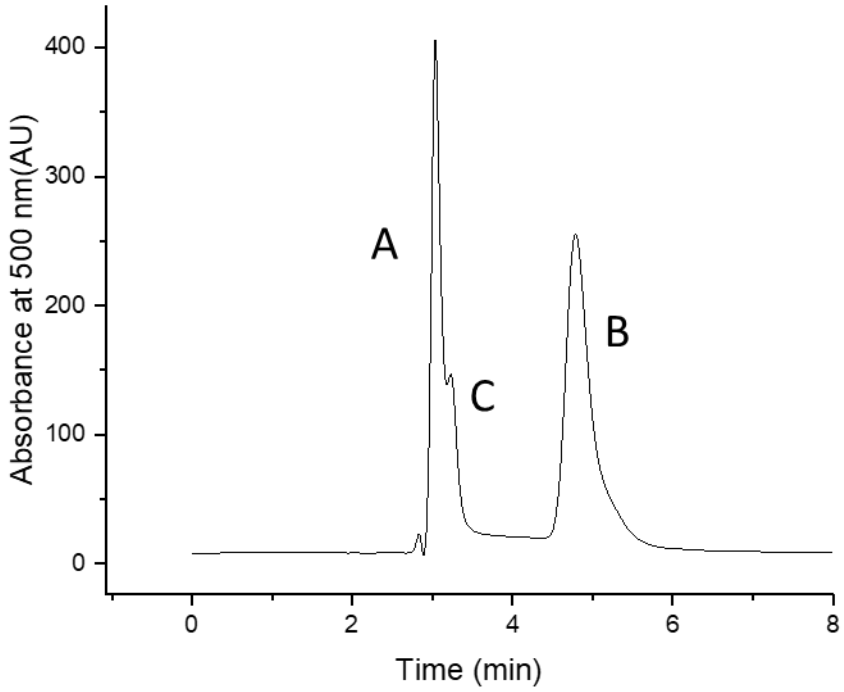

Figure 2.59: Chiral HPLC chromatogram of compound **1a** dissolved in DCM and eluted with 7:3 (v/v) DCM:n-hexane eluent (injection volume 50 µL, ~ 2 mg/mL). From ^{1}H NMR spectroscopy, peaks A and B are assigned to the enantiomers (***PP***,***MM***) and peak C is the diastereomer (***MP***).

2.9.7 Chiroptical studies

a) Circular dichroism studies

Circular dichroism (CD) spectra were recorded on a Jasco J-1500 CD spectrophotometer with a wavelength accuracy ± 0.2 nm (250 to 500 nm), ± 0.5 nm (500 to 800 nm) and a CD root mean square noise < 0.007 mdeg (500 nm). A quartz cuvette with 0.5 mm path length was used. The spectra were recorded at a concentration of 10 µM. The enantiomers were assigned by comparison of their CD spectra in toluene (**Figure 2.60**) with the computationally calculated spectra of the enantiomers in toluene (**Appendix A**).

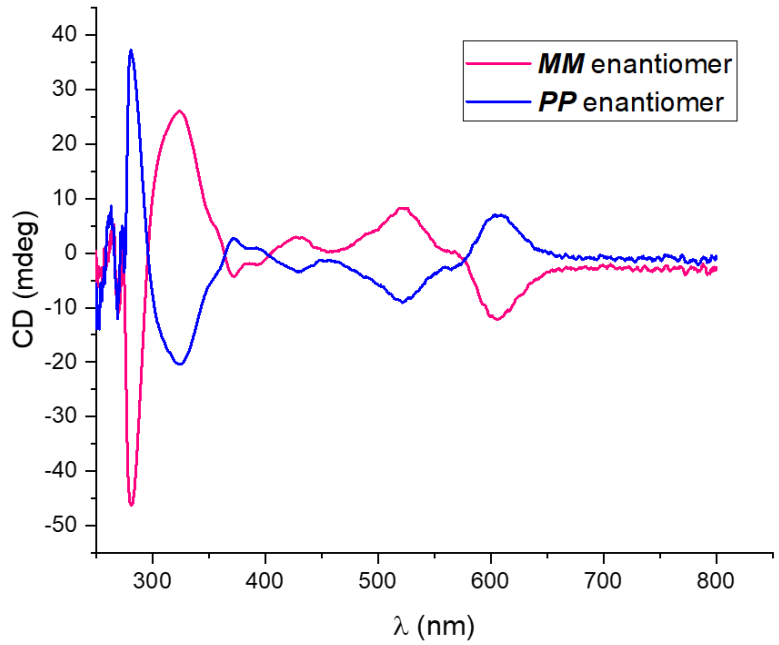

Figure 2.60: CD spectra for the ***MM*** (***MM***:***PP*** > 99:1 mol%) and ***PP*** (*MM*:*PP* = 12:88 mol%) enantiomers of macrocycle **1a** in toluene.

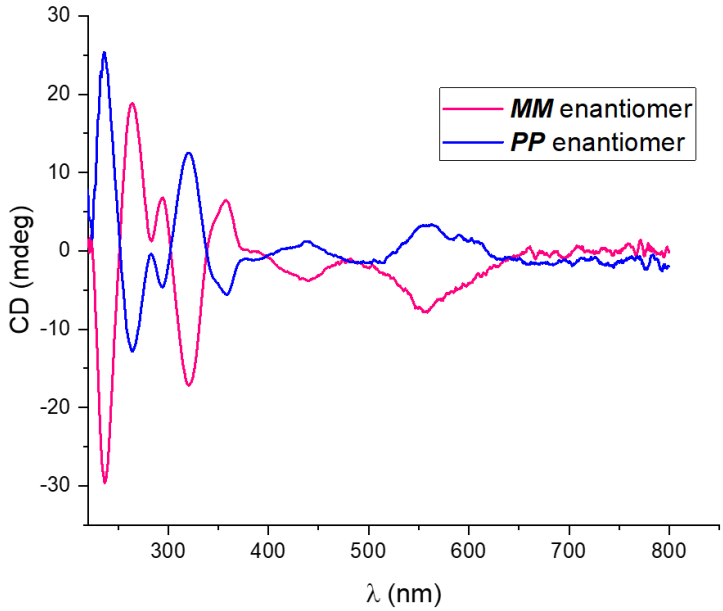

Figure 2.61: CD spectra for the ***MM*** (***MM***:***PP*** > 99:1 mol%) and ***PP*** (***MM***:***PP*** = 12:88 mol%) enantiomers of macrocycle **1a** in DCM. As the enantiomers racemise relatively quickly in chlorinated solvents ($t_{1/2}$ = 18 min), particular care was taken to record the spectra immediately after dissolving the samples in DCM.

b) Circularly polarised luminescence studies

The circularly polarised luminescence (CPL) data in this section was collected by Dr Patrycja Brook and Prof Robert Pal from Durham University.

CPL was measured with a home-built (modular) spectrometer. The excitation source was a broad band (200 – 1000 nm) laser- driven light source EQ 99 (Elliot Scientific). The excitation wavelength was selected by feeding the broadband light into an Acton SP-2155 monochromator (Princeton Instruments); the collimated light was focused into the sample cell (1 cm quartz cuvette). Sample PL emission was collected perpendicular to the excitation direction with a lens (f = 150 mm). The emission was fed through a photoelastic modulator (PEM) (Hinds Series II/FS42AA) and through a linear sheet polariser (Comar). The light was then focused into a second scanning monochromator (Acton SP- 2155) and subsequently on to a photomultiplier tube (PMT) (Hamamatsu H10723 series). The detection of the CPL signal was achieved using the field modulation lock-in technique. The electronic signal from the PMT was fed into a lock-in amplifier (Hinds Instruments Signaloc Model 2100). The reference signal for the lock-in detection was provided by the PEM control unit. The monchromators, PEM control unit and lock-in amplifier were interfaced to a desktop PC and controlled by a custom-written Labview graphic user interface. The lock-in amplifier provided two signals, an AC signal corresponding to (IL- IR) and a DC signal corresponding to (IL + IR) after background subtraction. The emission dissymmetry factor was therefore readily obtained from the experimental data, as 2 AC/DC.

Spectral calibration of the scanning monochromator was performed using a Hg-Ar calibration lamp (Ocean Optics). A correction factor for the wavelength dependence of the detection system was constructed using a calibrated lamp (Ocean Optics). The measured raw data was subsequently corrected using this correction factor. The validation of the CPL detection systems was achieved using light emitting diodes (LEDs) at various emission wavelengths. The LED was mounted in the sample holder and the light from the LED was fed through a broad band polarising filter and $\lambda/4$ plate (Ocean Optics) to generate circularly polarised light. Prior to all measurements, the $\lambda/4$ plate and a LED were used to set the phase of the lock-in amplifier correctly. The emission spectra were recorded with 0.5 nm step size and the slits of the detection monochromator were set to a slit width corresponding to a spectral

resolution of 0.25 nm. CPL spectra (as well as total emission spectra) were obtained through an averaging procedure of several scans. The CPL spectra were smoothed using a shape-preserving Savitzky-Golay smoothing (polynomial order 5, window size 9 with reflection at the boundaries) to reduce the influence of noise and enhance visual appearance; all calculations were carried out using raw spectral data. Analysis of smoothed vs raw data was used to help to estimate the uncertainty in the stated g_{lum} factors, which was ±10%.

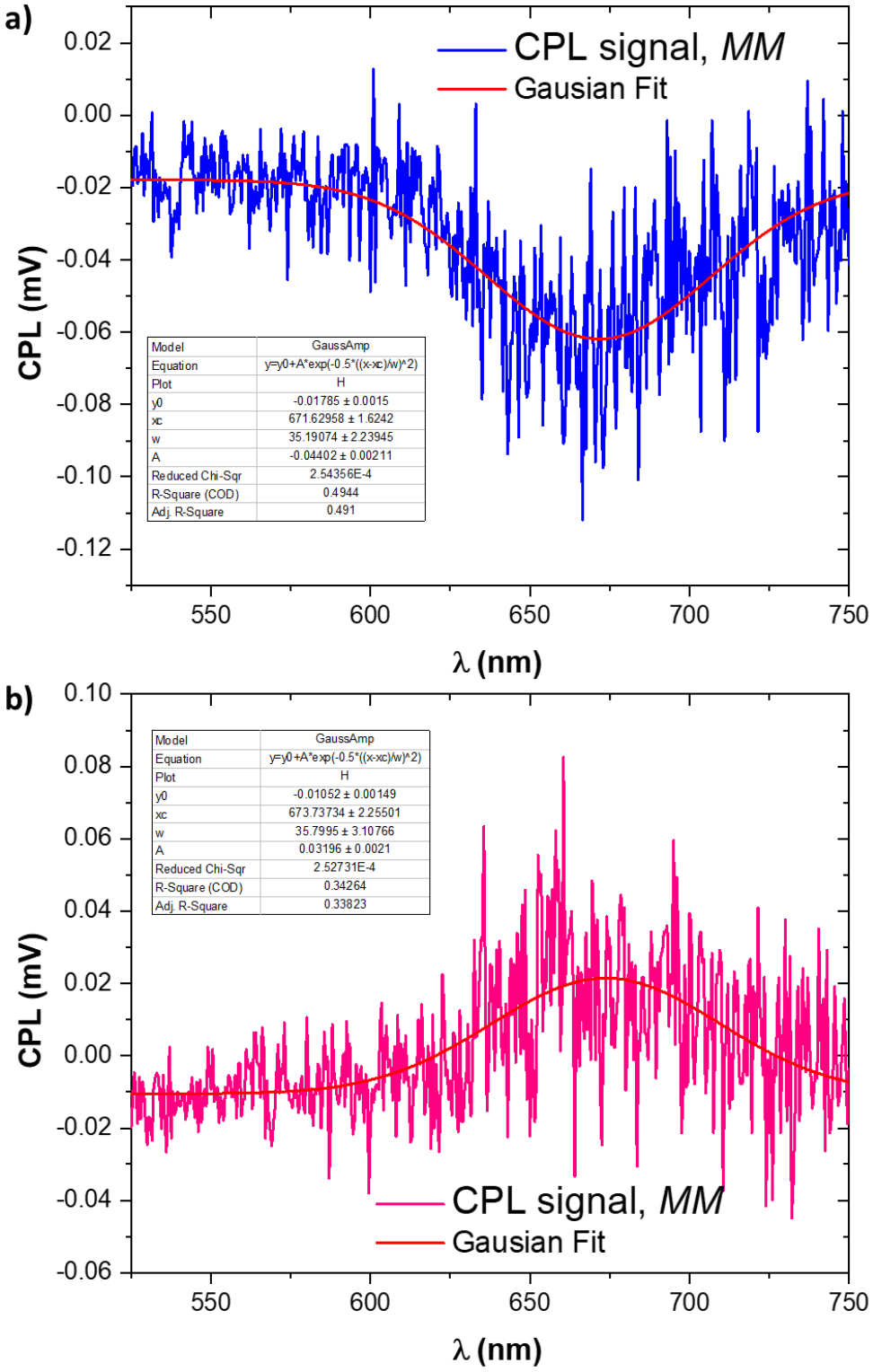

Figure 2.62: Raw and fitted CPL spectra of **a)** ***MM*** enantiomer (*MM*:*PP* > 99:1 mol%) and **b)** ***PP*** enantiomer (*MM*:*PP* = 12:88 mol%) of macrocycle **1a**.

2.9.8 Photophysics

All steady state electronic absorption and emission spectra were recorded at a concentration of 10 μM (unless otherwise stated) at 298 K. For UV-Vis-NIR spectroscopy a Cary 5000 spectrophotometer was used, with a wavelength accuracy ≤ 0.08 nm and absorbance accuracy ≤ 0.01 Abs. For fluorescence spectroscopy a Jasco FP-8500 was used with emission and excitation wavelength accuracies ± 1.0 nm. The detector base sensitivity is 8500:1. Quartz cuvettes with 1 cm path length were used.

a) UV-vis-NIR absorption and emission spectra

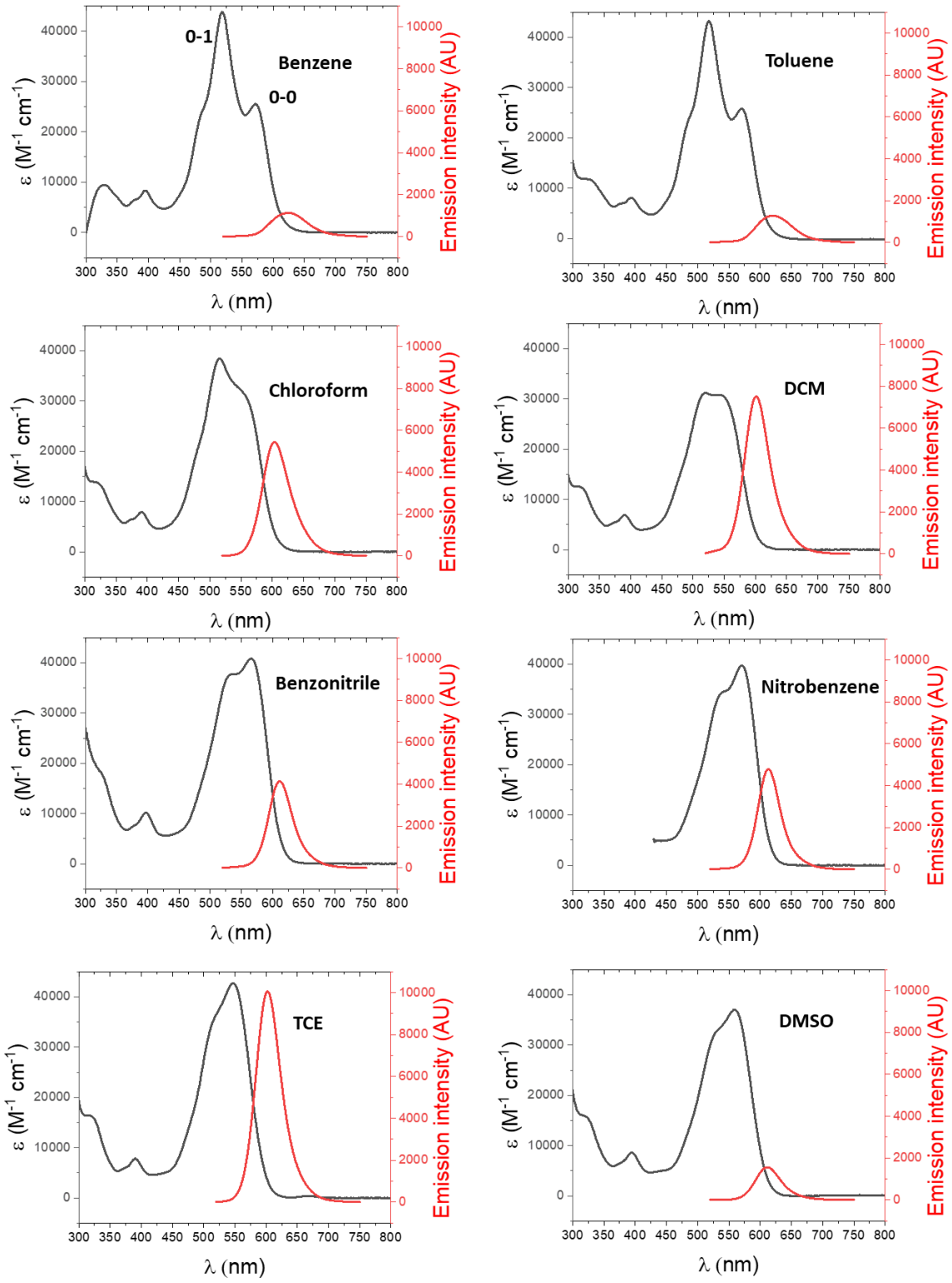

Figure 2.63: UV-vis absorption spectra and fluorescence emission spectra of macrocycle **1a** in selected solvents (10 μM). The 0-0 and 0-1 vibronic transition peaks are labelled in the absorption spectrum of benzene.

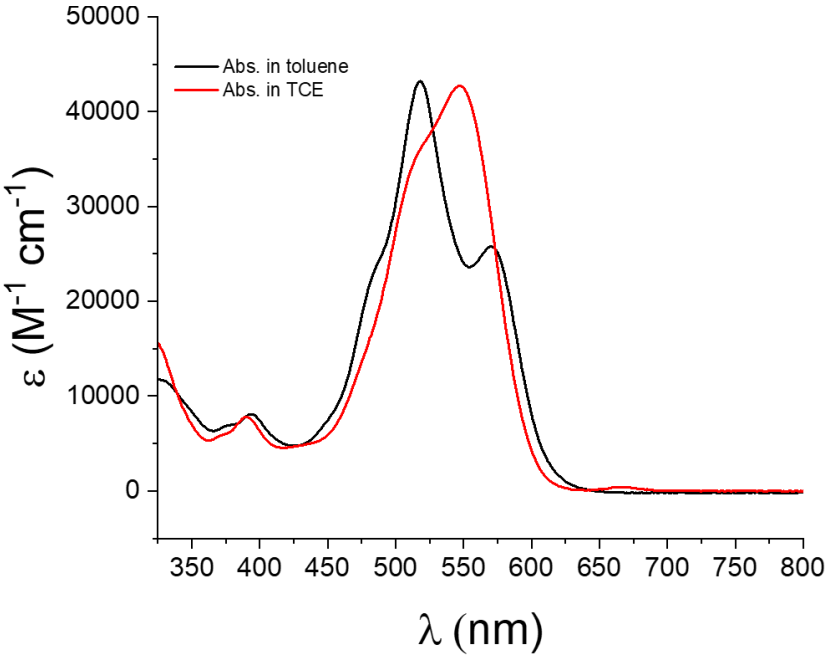

Figure 2.64: UV-vis absorption spectra of macrocycle **1a** in toluene and TCE (10 μM). Intramolecular H-type agreggation in toluene results in a reversal in the 0-0 and 0-1 vibronic peak intensities in the UV-vis spectrum.

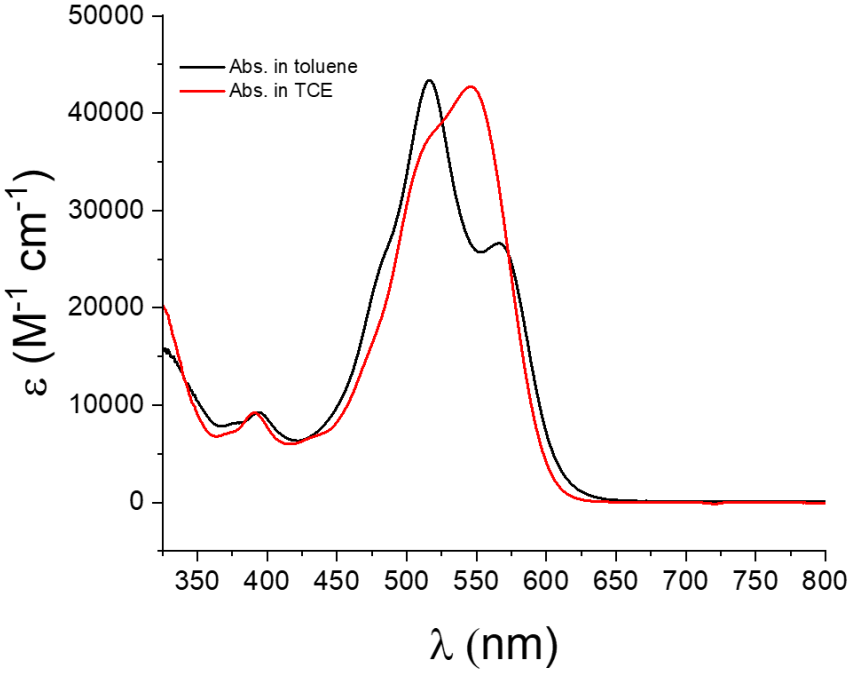

Figure 2.65: UV-vis absorption spectra of macrocycle **1b** in toluene and TCE (10 μM). These spectra are very similar to those of macrocycle **1a**.

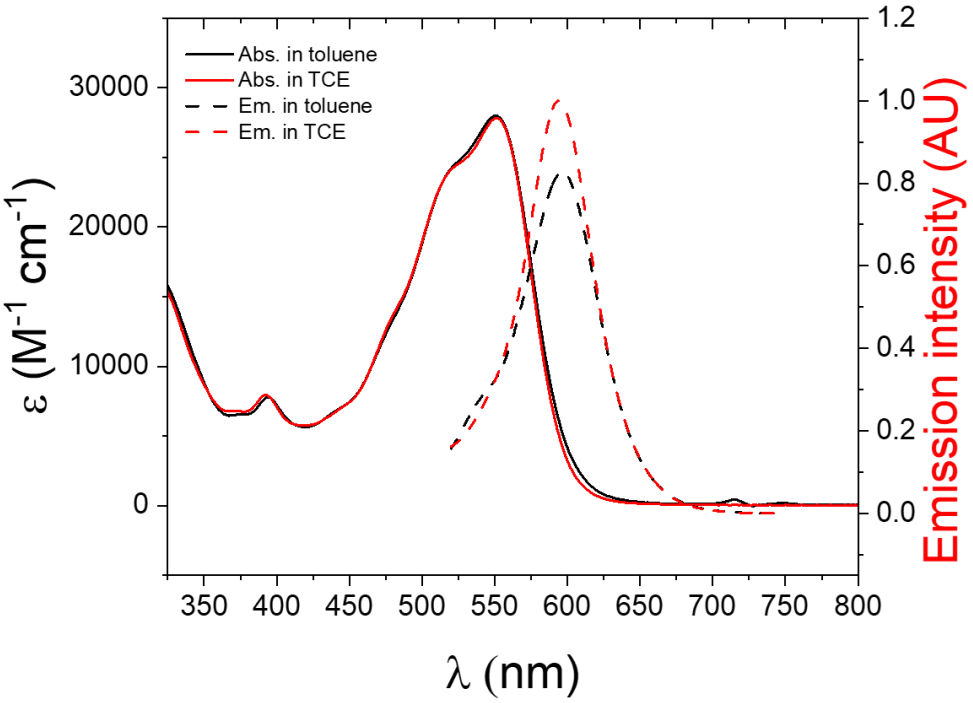

Figure 2.66: UV-vis absorption and fluorescence emission spectra of acyclic bis-triazole PDI 3a in toluene and TCE (10 µM). The UV-vis spectra of **3a** have no solvent dependence, in contrast to macrocycles **1a,b**.

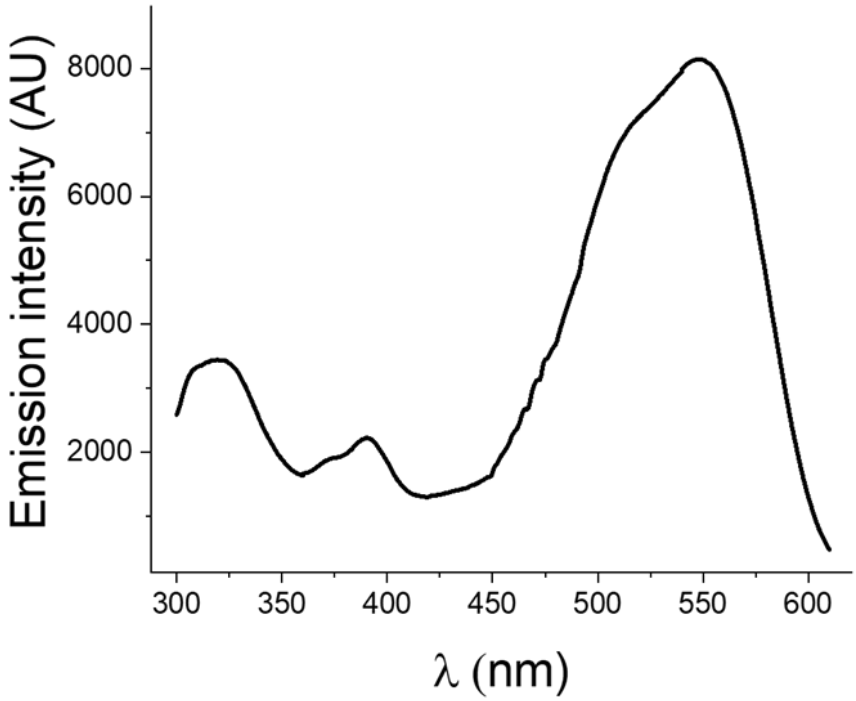

Figure 2.67: Excitation spectrum (λ_{em} = 620 nm) of macrocycle **1a** in TCE (10 µM).

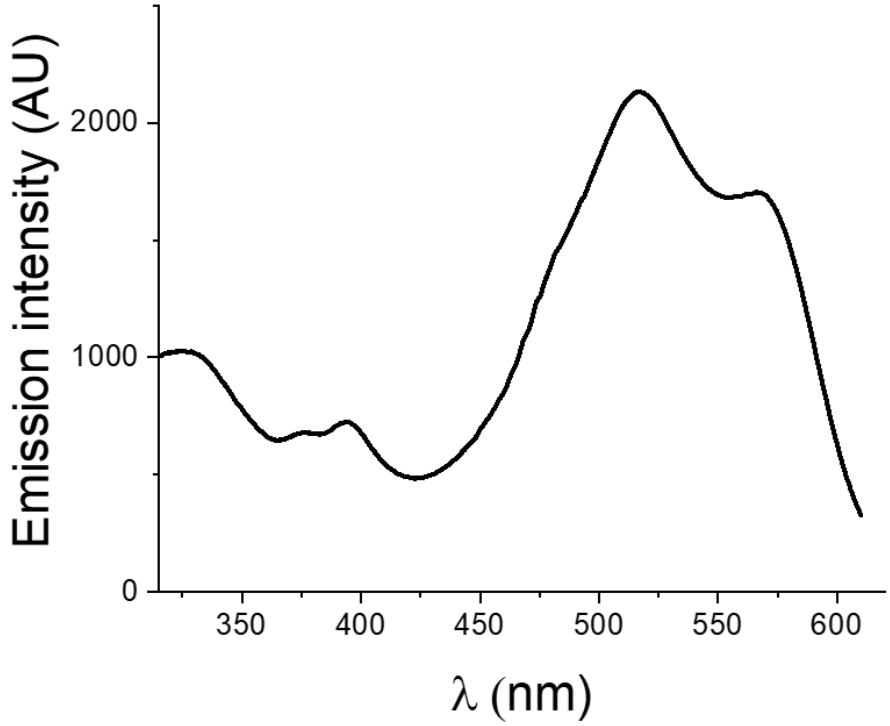

Figure 2.68: Excitation spectrum (λem = 620 nm) of macrocycle **1a** in toluene (10 μM).

b) Beer-lambert plots

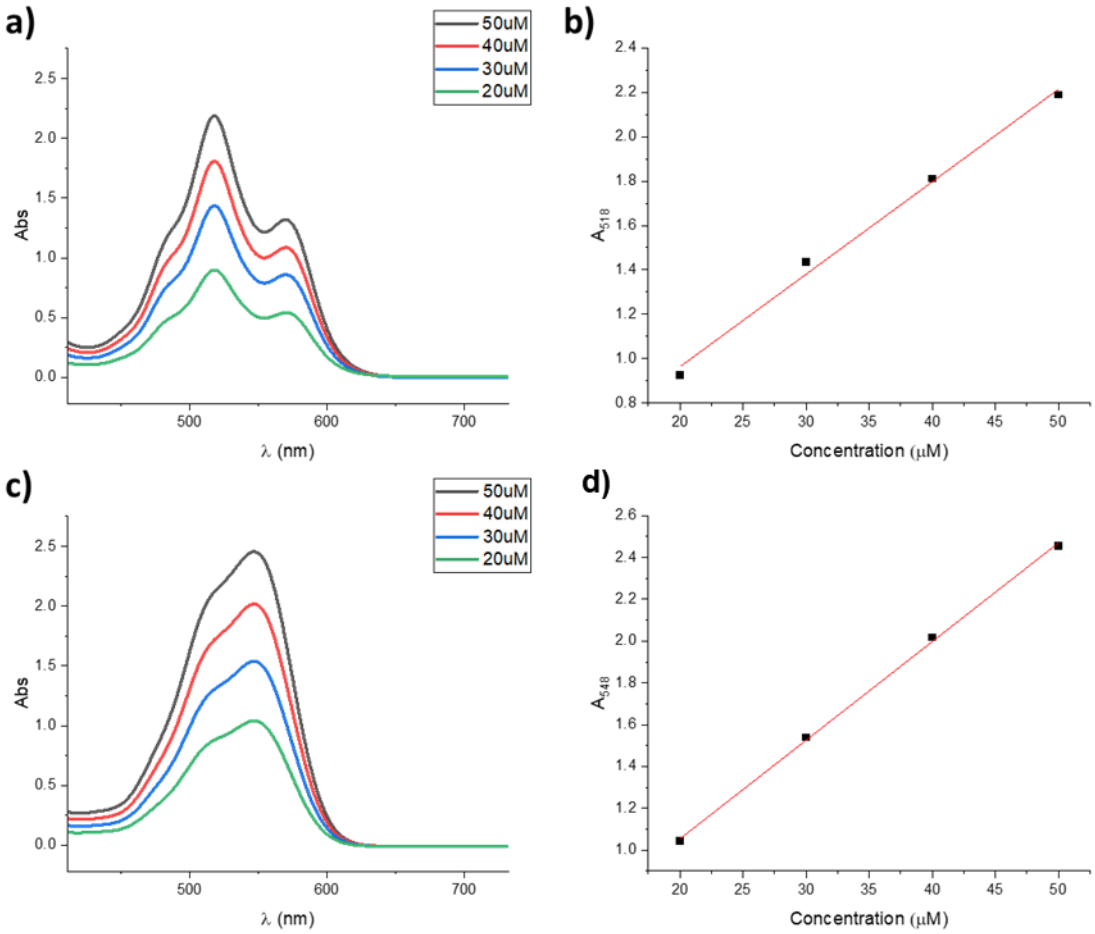

Figure 2.69: a) Absorption spectrum of macrocycle **1a** in toluene at different concentrations, up to Abs_{max} for the instrument. **b**) The dependence of absorption (518 nm) on concentration for macrocycle **1a** in toluene is linear, showing Beer-Lambert behaviour. **c)** Absorption spectrum of macrocycle **1a** in TCE at different concentrations. **d)** The dependence of absorption (548 nm) on concentration for macrocycle **1a** in TCE is linear, showing Beer-Lambert behaviour.

c) Quantum yields

Absolute fluorescence quantum yields were obtained on an Edinburgh Instruments FLS920 steady-state spectrometer fitted with an integrating sphere. All samples were recorded at a 1 µM with a 7 - 8 nm excitation slit and 0.1 - 0.2 nm emission slit width. Experiments were carried out in solution using 1 cm path length quartz cuvettes with four transparent polished faces.

Table 6: Quantum yields for compounds **1a** and **3a** in toluene and TCE.

Compound	Solvent	Quantum Yield
1a	Toluene	0.48
	TCE	0.90
3a	Toluene	> 0.99
	TCE	> 0.99

2.9.9 Electrochemistry

Electrochemical experiments were carried out in anhydrous degassed solvents (DCM or 1:1 toluene-DCM) using 0.1 M tetrabutylammonium tetrafluoroborate as the supporting electrolyte. The working electrode was a 3 mm glassy carbon electrode (polished with diamond slurry prior to use), a Pt counter electrode, and a Ag/AgCl reference. All cyclic voltammograms (CVs) were referenced to the Fc^{+}/Fc^{0} redox couple and recorded at a scan rate of 0.1 Vs^{-1}. An Autolab Interface 6 potentiostat was used for electrochemical measurements. The inherent instrument error is V: ± 0.2% (± 2 mV).

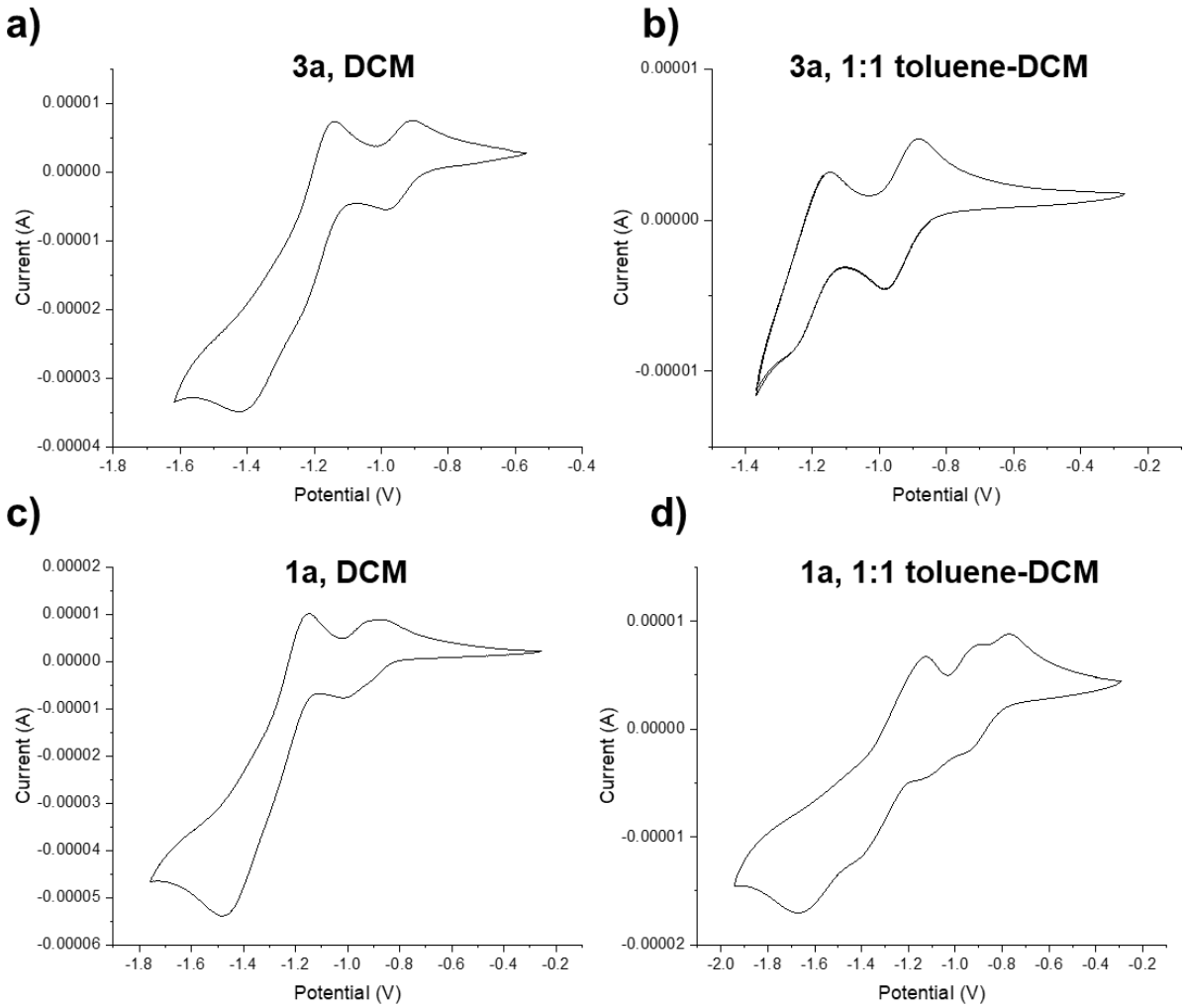

Figure 2.70: Cyclic voltammograms of **a)** Acyclic bis-triazole PDI **3a** in DCM, **b)** Acyclic bis-triazole PDI **3a** in 1:1 (v/v) toluene:DCM, **c)** macrocycle **1a** in DCM, **d)** macrocycle **1a** in 1:1 (v/v) toluene:DCM.

Table 7: Cyclic voltammetry data for macrocycle **1a** and acyclic PDI **3a**[a].

		Redox Process, $E_{1/2}$ / V, [ΔE_p,mV]			
	Solvent	**A**	**B**	**C**	**D**
Macrocycle **1a**	1:1 (v/v) toluene:DCM	−0.84 [136]	−1.02 [206]	−1.18 [300]	−1.70[b]
	DCM	−0.94 [89]		−1.31 [325]	
Acyclic PDI **3a**	1:1 (v/v) toluene:DCM	−0.94 [82]		−1.20 [138]	
	DCM	−0.94 [68]		−1.18 [279]	

[a]Recorded in the stated solvents containing 0.4 M [^{n}Bu$_4$N][BF$_4$] as supporting electrolyte at ambient temperature, with potentials quoted at 0.10 V s^{-1} against $E_{1/2}$ Fc$^+$/Fc. [b]$E_{1/2}$ value could not be calculated so E_{ca} is given instead.

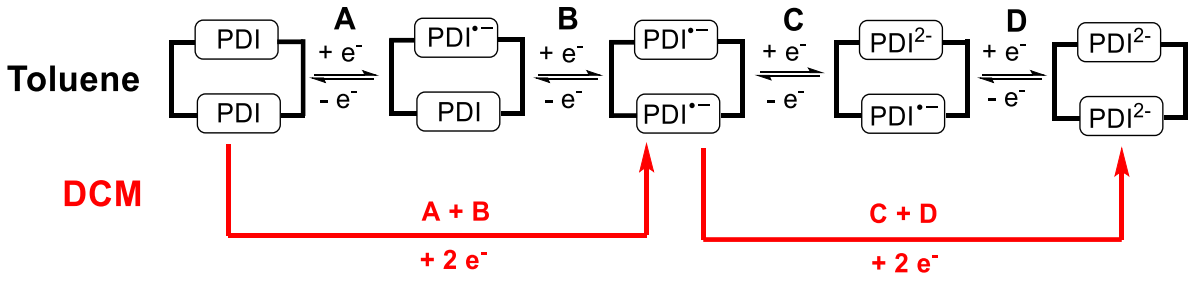

Figure 2.71: Proposed schematic of the redox processes of macrocycle **1a** in each solvent.

2.10 References

1. E. M. Sánchez-Carnerero, A. R. Agarrabeitia, F. Moreno, B. L. Maroto, G. Muller, M. J. Ortiz and S. de la Moya, *Chemistry – A European Journal*, 2015, **21**, 13488-13500.
2. J. L. Greenfield, J. Wade, J. R. Brandt, X. Shi, T. J. Penfold and M. J. Fuchter, *Chemical Science*, 2021, **12**, 8589-8602.
3. F. Würthner, C. R. Saha-Möller, B. Fimmel, S. Ogi, P. Leowanawat and D. Schmidt, *Chemical Reviews*, 2016, **116**, 962-1052.
4. Y. Yang, B. Rice, X. Shi, J. R. Brandt, R. Correa da Costa, G. J. Hedley, D.-M. Smilgies, J. M. Frost, I. D. W. Samuel, A. Otero-de-la-Roza, E. R. Johnson, K. E. Jelfs, J. Nelson, A. J. Campbell and M. J. Fuchter, *ACS Nano*, 2017, **11**, 8329-8338.
5. Y. Yang, L. Liu and Z. Wei, *Accounts of Materials Research*, 2024, **5**, 329-346.
6. M. Sapotta, P. Spenst, C. R. Saha-Moeller and F. Wuerthner, *Organic Chemistry Frontiers*, 2019, **6**, 892-899.
7. W. Wang, A. D. Shaller and A. D. Q. Li, *Journal of the American Chemical Society*, 2008, **130**, 8271 - 8279.
8. I. Solymosi, S. Krishna, E. Nuin, H. Maid, B. Scholz, D. M. Guldi, M. E. Pérez-Ojeda and A. Hirsch, *Chemical Science*, 2021, **12**, 15491-15502.
9. M. Weh, J. Rühe, B. Herbert, A.-M. Krause and F. Würthner, *Angewandte Chemie International Edition*, 2021, **60**, 15323-15327.

10. M. Weh, K. Shoyama and F. Würthner, *Nature Communications*, 2023, **14**, 243.
11. M. Ball, B. Fowler, P. Li, L. A. Joyce, F. Li, T. Liu, D. Paley, Y. Zhong, H. Li, S. Xiao, F. Ng, M. L. Steigerwald and C. Nuckolls, *Journal of the American Chemical Society*, 2015, **137**, 9982-9987.
12. T. Türel, S. Bhargava and S. Valiyaveettil, *The Journal of Organic Chemistry*, 2020, **85**, 3092-3100.
13. S. E. Penty, M. A. Zwijnenburg, G. R. F. Orton, P. Stachelek, R. Pal, Y. Xie, S. L. Griffin and T. A. Barendt, *Journal of the American Chemical Society*, 2022, **144**, 12290-12298.
14. R. M. Ibberson, W. I. F. David, S. Parsons, M. Prager and K. Shankland, *Journal of Molecular Structure*, 2000, **524**, 121-128.
15. C. D. Schmidt, N. Lang, N. Jux and A. Hirsch, *Chemistry – A European Journal*, 2011, **17**, 5289-5299.
16. P. Rajasingh, R. Cohen, E. Shirman, L. J. W. Shimon and B. Rybtchinski, *The Journal of Organic Chemistry*, 2007, **72**, 5973-5979.
17. E. J. O'Neil, K. M. DiVittorio and B. D. Smith, *Organic Letters*, 2007, **9**, 199-202.
18. O. Anamimoghadam, L. O. Jones, J. A. Cooper, Y. Beldjoudi, M. T. Nguyen, W. Liu, M. D. Krzyaniak, C. Pezzato, C. L. Stern, H. A. Patel, M. R. Wasielewski, G. C. Schatz and J. F. Stoddart, *Journal of the American Chemical Society*, 2021, **143**, 163-175.
19. C. Shao, M. Grüne, M. Stolte and F. Würthner, *Chemistry – A European Journal*, 2012, **18**, 13665-13677.
20. N. Chopra, D. Kaur and G. Chopra, *ACS Omega*, 2018, **3**, 12688-12702.
21. P. Osswald, M. Reichert, G. Bringmann and F. Würthner, *The Journal of Organic Chemistry*, 2007, **72**, 3403-3411.
22. G. P. Moss, *Pure and Applied Chemistry*, 1996, **68**, 2193-2222.
23. M. M. Safont-Sempere, P. Osswald, K. Radacki and F. Würthner, *Chemistry – A European Journal*, 2010, **16**, 7380-7384.
24. M. M. Safont-Sempere, P. Osswald, M. Stolte, M. Grüne, M. Renz, M. Kaupp, K. Radacki, H. Braunschweig and F. Würthner, *Journal of the American Chemical Society*, 2011, **133**, 9580-9591.
25. M. Hasegawa, Y. Nojima and Y. Mazaki, *ChemPhotoChem*, 2021, **5**, 1042-1058.
26. J. Zhao and P. Xing, *ChemPhotoChem*, 2022, **6**, e202100124.
27. J.-L. Ma, Q. Peng and C.-H. Zhao, *Chemistry – A European Journal*, 2019, **25**, 15441-15454.
28. J.-Q. Wang, X.-N. Han, Y. Han and C.-F. Chen, *Chemical Communications*, 2023, DOI: 10.1039/D3CC04187E.
29. L. E. MacKenzie and R. Pal, *Nature Reviews Chemistry*, 2021, **5**, 109-124.
30. P. Stachelek, L. MacKenzie, D. Parker and R. Pal, *Nature Communications*, 2022, **13**, 553.
31. K. Kumaranchira Ramankutty, *Nanoscale*, 2024, DOI: 10.1039/D4NR01232A.
32. M. Rickhaus, L. Jundt and M. Mayor, *CHIMIA*, 2016, **70**, 192.
33. M. Sapotta, P. Spenst, C. R. Saha-Möller and F. Würthner, *Organic Chemistry Frontiers*, 2019, **6**, 892-899.
34. S. R. LaPlante, P. J. Edwards, L. D. Fader, A. Jakalian and O. Hucke, *ChemMedChem*, 2011, **6**, 505-513.
35. S. R. LaPlante, L. D. Fader, K. R. Fandrick, D. R. Fandrick, O. Hucke, R. Kemper, S. P. F. Miller and P. J. Edwards, *Journal of Medicinal Chemistry*, 2011, **54**, 7005-7022.

36. A. Ahmed, R. A. Bragg, J. Clayden, L. W. Lai, C. McCarthy, J. H. Pink, N. Westlund and S. A. Yasin, *Tetrahedron*, 1998, **54**, 13277-13294.
37. F. Leroux, *ChemBioChem*, 2004, **5**, 644-649.
38. F. Würthner, *The Journal of Organic Chemistry*, 2022, **87**, 1602-1615.
39. I. Solymosi, C. Neiß, H. Maid, F. Hampel, T. Solymosi, A. Görling, A. Hirsch and M. E. Pérez-Ojeda, *ChemistrySelect*, 2023, **8**, e202300523.
40. W. Wang, A. D. Shaller and A. D. Q. Li, *Journal of the American Chemical Society*, 2008, **130**, 8271-8279.
41. C. L. Perrin and T. J. Dwyer, *Chemical Reviews*, 1990, **90**, 935-967.
42. K. Zhu, V. N. Vukotic and S. J. Loeb, *Chemistry – An Asian Journal*, 2016, **11**, 3258-3266.
43. N. Farahani, K. Zhu and S. J. Loeb, *ChemPhysChem*, 2016, **17**, 1875-1880.
44. J. C. Cobas and M. Martin-Pastor, *EXSYCalc Ver 1.0; Mestrelab Research, Coruña, Spain*, 2007.
45. P. W. Atkins and J. De Paula, *Atkins' Physical chemistry*, Oxford University Press, Oxford, 10th ed. edn., 2014.
46. J. Rühe, D. Bialas, P. Spenst, A.-M. Krause and F. Würthner, *Organic Materials*, 2020, **02**, 149-158.
47. H. Langhals and R. Ismael, *European Journal of Organic Chemistry*, 1998, **1998**, 1915-1917.
48. F. Schlosser, M. Moos, C. Lambert and F. Würthner, *Advanced Materials*, 2013, **25**, 410-414.
49. J. Kumar, T. Nakashima, H. Tsumatori, M. Mori, M. Naito and T. Kawai, *Chemistry – A European Journal*, 2013, **19**, 14090-14097.
50. E. Sebastian, A. M. Philip, A. Benny and M. Hariharan, *Angewandte Chemie International Edition*, 2018, **57**, 15696-15701.
51. W. Kim, A. Nowak-Król, Y. Hong, F. Schlosser, F. Würthner and D. Kim, *The Journal of Physical Chemistry Letters*, 2019, **10**, 1919-1927.
52. M. Kasha, H. R. Rawls and M. A. El-Bayoumi, *Pure and Applied Chemistry*, 1965, **11**, 371-392.
53. P. Spenst, R. M. Young, B. T. Phelan, M. Keller, J. Dostál, T. Brixner, M. R. Wasielewski and F. Würthner, *Journal of the American Chemical Society*, 2017, **139**, 2014-2021.
54. Y. Lan, M. G. Corradini, X. Liu, T. E. May, F. Borondics, R. G. Weiss and M. A. Rogers, *Langmuir*, 2014, **30**, 14128-14142.
55. M. J. Kamlet, J. L. Abboud and R. W. Taft, *Journal of the American Chemical Society*, 1977, **99**, 6027-6038.
56. J. Catalán, V. López, P. Pérez, R. Martin-Villamil and J.-G. Rodríguez, *Liebigs Annalen*, 1995, **1995**, 241-252.
57. L. G. S. Brooker, A. C. Craig, D. W. Heseltine, P. W. Jenkins and L. L. Lincoln, *Journal of the American Chemical Society*, 1965, **87**, 2443-2450.
58. M. J. Kamlet and R. W. Taft, *Journal of the American Chemical Society*, 1976, **98**, 377-383.
59. J. S. Moore and C. R. Ray, in *Poly(arylene etynylene)s: From Synthesis to Application*, ed. C. Weder, Springer Berlin Heidelberg, Berlin, Heidelberg, 2005, DOI: 10.1007/b101380, pp. 91-149.

60. I. Giri, S. Chhetri, J. John P, M. Mondal, A. B. Dey and R. K. Vijayaraghavan, *Chemical Science*, 2024, **15**, 9630-9640.
61. T. A. Barendt, M. L. Ball, Q. Xu, B. Zhang, B. Fowler, A. Schattman, V. C. Ritter, M. L. Steigerwald and C. Nuckolls, *Chemistry – A European Journal*, 2020, **26**, 3744-3748.
62. L. Yang, P. Langer, E. S. Davies, M. Baldoni, K. Wickham, N. A. Besley, E. Besley and N. R. Champness, *Chemical Science*, 2019, **10**, 3723-3732.
63. N. Elgrishi, K. J. Rountree, B. D. McCarthy, E. S. Rountree, T. T. Eisenhart and J. L. Dempsey, *Journal of Chemical Education*, 2018, **95**, 197-206.
64. S. Dey, A. Efimov and H. Lemmetyinen, *European Journal of Organic Chemistry*, 2012, **2012**, 2367-2374.
65. Z. Chen, M. G. Debije, T. Debaerdemaeker, P. Osswald and F. Würthner, *ChemPhysChem*, 2004, **5**, 137-140.
66. P. Osswald and F. Würthner, *Journal of the American Chemical Society*, 2007, **129**, 14319-14326.
67. R. Renner, B. Mahlmeister, O. Anhalt, M. Stolte and F. Würthner, *Chemistry – A European Journal*, 2021, **27**, 11997-12006.
68. G. Bressan, S. E. Penty, D. Green, I. Heisler, G. Jones, T. A. Barendt and S. Meech, *Angewandte Chemie International Edition*, 2024, **63**, e202407242.
69. T. R. Chan, R. Hilgraf, K. B. Sharpless and V. V. Fokin, *Organic Letters*, 2004, **6**, 2853-2855.
70. J. B. Sperry, M. Azuma and S. Stone, *Organic Process Research & Development*, 2021, **25**, 212-224.
71. https://ehs.stanford.edu/reference/information-azide-compounds, (accessed 07/10, 2024).
72. J. Beilsten-Edmands, G. Winter, R. Gildea, J. Parkhurst, D. Waterman and G. Evans, *Acta Crystallographica Section D*, 2020, **76**, 385-399.
73. G. Winter, *Journal of Applied Crystallography*, 2010, **43**, 186-190.
74. G. Winter, D. G. Waterman, J. M. Parkhurst, A. S. Brewster, R. J. Gildea, M. Gerstel, L. Fuentes-Montero, M. Vollmar, T. Michels-Clark, I. D. Young, N. K. Sauter and G. Evans, *Acta Crystallographica Section D*, 2018, **74**, 85-97.
75. G. Sheldrick, *Acta Crystallographica Section A*, 2015, **71**, 3-8.
76. O. V. Dolomanov, L. J. Bourhis, R. J. Gildea, J. A. K. Howard and H. Puschmann, *Journal of Applied Crystallography*, 2009, **42**, 339-341.

Chapter 3: A chirally-locked bis-PDI macrocycle: consequences for chiral self-assembly and circularly polarised luminescence

The work described in this chapter has been published in:

Samuel E. Penty, Georgia R. F. Orton, Dominic J. Black, Robert Pal, Martijn A. Zwijnenburg, and Timothy A. Barendt, *J. Am. Chem. Soc.* **2024**, 146, 8, 5470–5479

Text and figures in this chapter have been reprinted and/or adapted with permission from this reference.

I thank all co-authors of the above paper for their contributions to this chapter. Georgia R. F. Orton and I collected the single crystal X-ray diffraction data at the synchrotron at Diamond light source. Dominic J. Black and Robert Pal carried out CPL measurements and CPL-LSCM microscopy. Martijn A. Zwijnenburg carried out computational modelling.

3. A chirally-locked bis-PDI macrocycle: consequences for chiral self-assembly and circularly polarised luminescence

3.1 Introduction

As discussed in the introduction to this thesis, in 1,7-disubsituted PDIs, the substituents are directed towards the same face of the PDI (**Figure 3.1a**).[1] Therefore, 1,7-disubstituted PDIs possess two different π-surfaces, one more sterically hindered than the other. These π-surfaces would be expected to exhibit distinct π–π interactions and thus different π–π self-assembly properties. However, for the handful of configurationally stable 1,7-disubstituted PDIs reported so far ($\Delta G^{\ddagger} > 117$ kJ mol^{-1}),[2-4] π–π self-assembly is limited to the formation of H-type cofacial dimers.[4, 5] This is because macrocyclic strapping via the 1,7 bay positions, which is necessary for preventing atropisomer interconversion, restricts π–π interactions to only one of the π-surfaces of the mono-PDI macrocycle (**Figure 3.1b**). However, it was noticed that a promising strategy for extending π–π self-assembly would be to strap the PDI core with a second PDI unit, yielding a bay-connected bis-PDI macrocycle[6-8] with accessible π-surfaces[9] on both the interior and exterior of the macrocycle, for *intra*- and *inter*-molecular π–π interactions respectively (**Figure 3.1c**). Indeed, the "Pink Box" macrocyclic scaffold discussed in the previous chapter is an ideal candidate for achieving this.

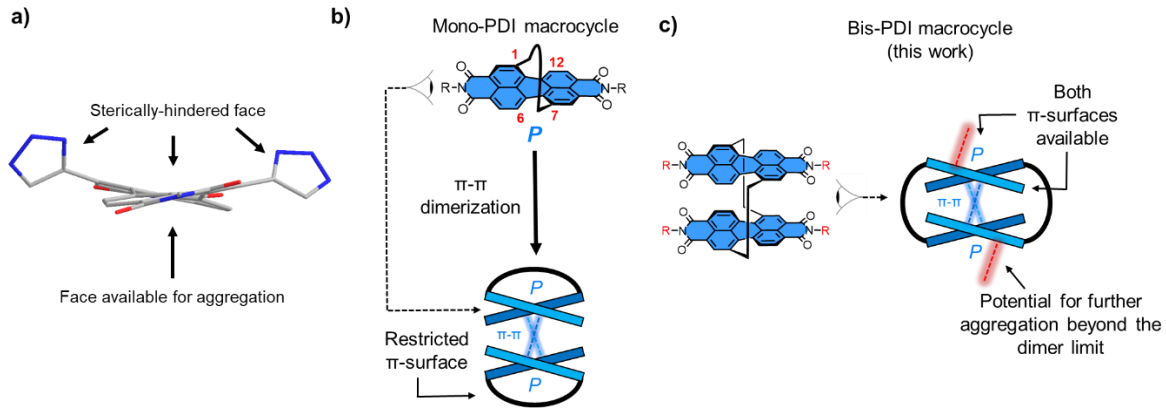

Figure 3.1: a) Illustration of the two distinct π-surfaces in a 1,7-disubstituted PDI. **b)** Cartoon of a 1,7-strapped mono-PDI macrocycle [4, 5] and its preference for homochiral dimerization. **c)** Cartoon depiction of a "Pink Box" bis-PDI macrocycle with available π-surfaces on the exterior of the macrocycle for intermolecular self-assembly.

The previous chapter explored the design, synthesis and characterisation of a novel bis-PDI macrocycle, the "Pink Box" macrocycle **1**, that is optimised for a close-contact (3.7 Å) intramolecular π–π interaction between the two PDI cores. The H-type π–π stacking was found to be exclusively homochiral, occurring between PDIs of the same axial chirality (i.e. ***MM*** or ***PP*** but not ***MP***). However, macrocycle **1** did not exhibit any further self-assembly via π–π interactions beyond this intramolecular PDI dimer limit, as evidenced by its crystal structure and Beer-Lambert behaviour. It was hypothesised that the branched alkyl imide groups in macrocycle **1** prevent these *inter*molecular PDI-PDI interactions, and that a different, less bulky, imide group might therefore be more conducive to intermolecular self-assembly. Additionally, the enantiomers of macrocycle **1** are not configurationally stable. Chirally-locked enantiomers are a requirement for studying the impact of optical purity on π–π directed self-assembly (i.e., comparing racemic and enantiopure materials). As suggested by Nuckolls and co-workers,[7] and proven conclusively by the work described in this chapter,[10] interconversion between the ***MM***, ***PP***, and ***MP*** stereoisomers in a bay-connected bis-PDI macrocycle requires a "somersault" motion where one of the PDI imide heads passes through the centre of the macrocyclic cavity (**Figure 3.2**). As such, in addition to aiding intermolecular self-assembly, a careful choice of imide group would also prevent racemisation of the macrocycle.

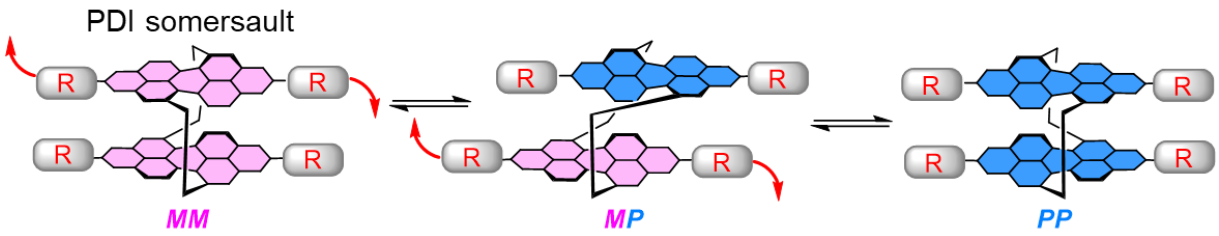

Figure 3.2: Cartoon of the "intramolecular somersault" mechanism[7] for the interconversion of bis-PDI macrocycle stereoisomers.

This chapter outlines the development, synthesis, and characterisation of a 2nd generation "Pink Box" type bis-PDI macrocycle that is chirally locked (macrocycle **5**, **Figure 3.3**). This was achieved by replacing the branched alkyl imide groups in macrocycle **1** with long, rigid *tert*-butyl benzoate imide groups which prevent racemisation via a PDI "intramolecular somersault" motion. This imide group also makes the outer π-surfaces of the macrocycle more accessible, allowing the self-assembly of macrocycle **5** via *inter*molecular chiral π–π interactions to be studied in racemic and enantiopure samples.

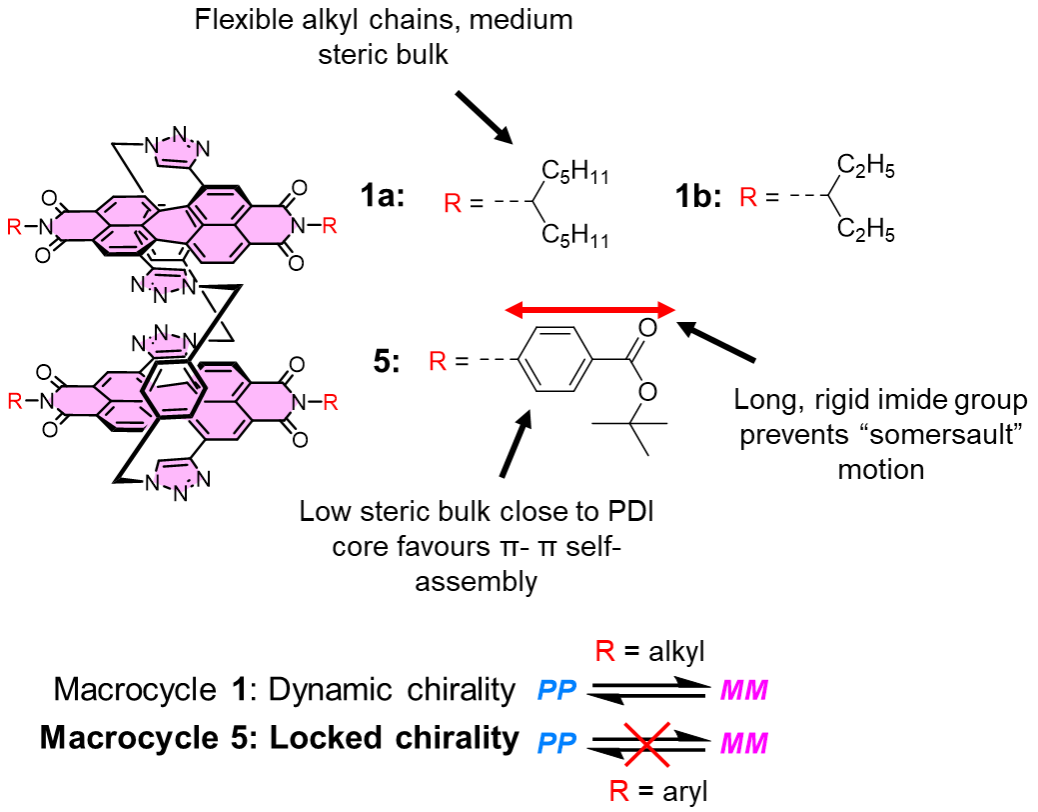

Figure 3.3: Comparison of the structures of macrocycle **1a/b** and of target chirally-locked macrocycle **5**.

3.2 Macrocycle design and synthesis

The feature that sets macrocycle **5** apart from the previous 1st generation "Pink Box" macrocycle **1** is the use of *tert*-butyl benzoate substituents at the imide termini of the PDI units (**Figure 3.4**). It was envisaged that these substituents would enforce configurational stability on the macrocycle because, from the initial molecular modelling studies **(Figure 3.5**, see appendix A for further details), these rigid substituents elongate the PDIs by ~ 8 Å, thereby potentially preventing them from somersaulting through the macrocycle cavity (PDI-PDI distance = 3.7 Å). Furthermore, the absence of ortho substituents on the phenyl rings is designed to facilitate strong π–π stacking between PDI units, essential for supramolecular self-assembly.

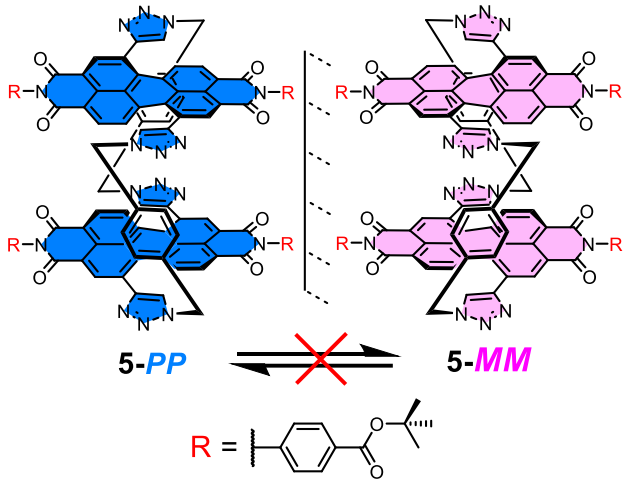

Figure 3.4: Structures of the enantiomers of chirally-locked target macrocycle **5**.

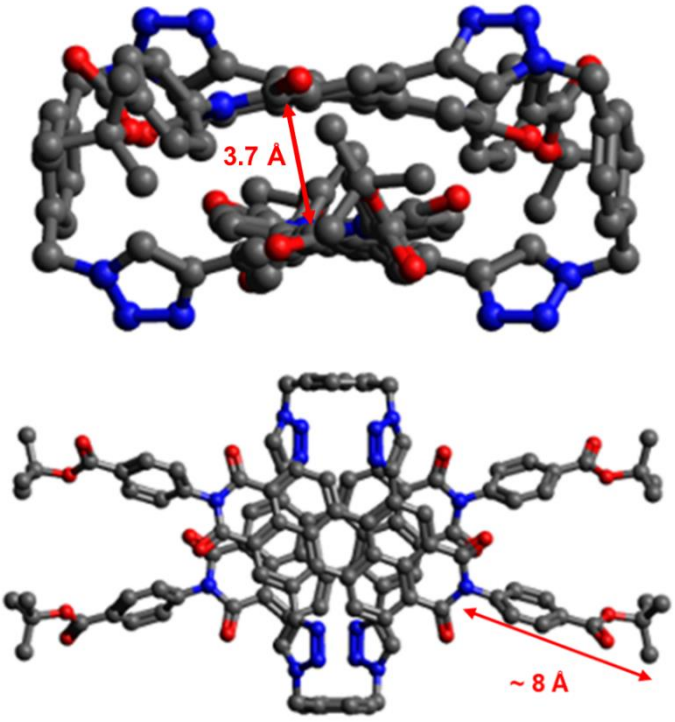

Figure 3.5: DFT-predicted structure of the ***MM*** stereoisomer of the lowest energy conformer of macrocycle **5** (hydrogens omitted for clarity). See Appendix A for further details.

The synthesis of macrocycle **5** is outlined in **Scheme 3.1**. The synthetic strategy is related to that of "Pink Box" macrocycle **1**. However, the key difference is that the aromatic *tert*-butyl benzoate imide group is not compatible with bromination conditions, hence bromination of the perylene core must be carried out prior to imidisation. Furthermore, the

reduced steric bulk of this imide group close to the PDI core favours aggregation of the PDI cores which, while desirable for studying self-assembly, also makes these PDI derivatives more challenging to work with due to poorer solubility. Further details about the synthesis of macrocycle **5** are given in experimental **Section 3.11.1**.

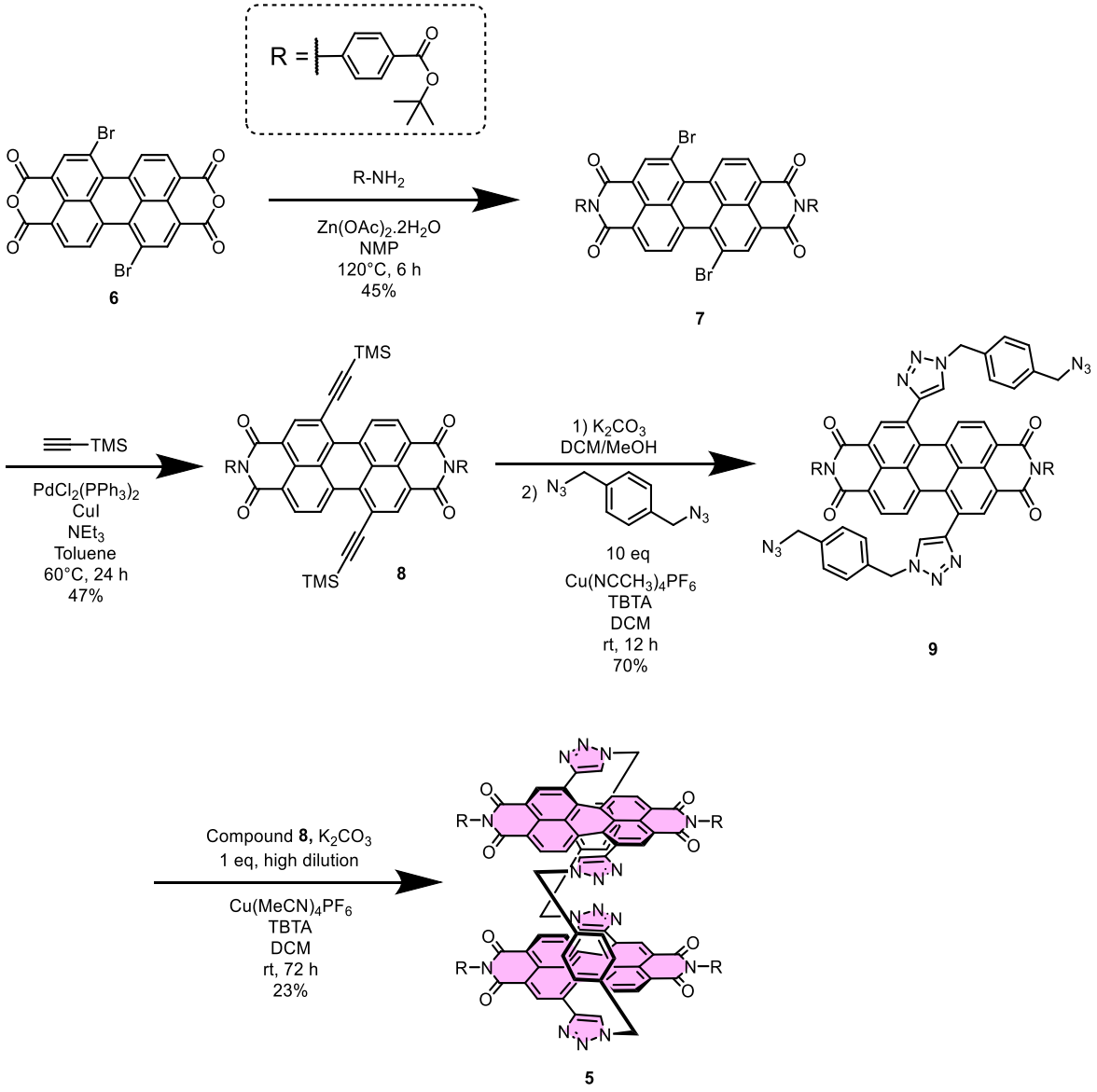

Scheme 3.1: Multistep synthesis of bis-PDI macrocycle **5.**

3.3 Evidence for diastereoselective macrocyclisation

After the final macrocyclisation step, which once again capitalised on copper(I)-catalysed azide–alkyne cycloaddition (CuAAC) "click" chemistry, macrocycle **5** was purified by preparatory thin-layer chromatography (TLC). Since the chirality of this macrocycle is locked (Section 3.4), it would be reasonable to expect to obtain all macrocycle stereoisomers from the TLC plate, namely the pair of enantiomers (**5-*MM*/*PP***) and the heterochiral diastereomer (**5-*MP***). However, only **5-*MM*** and **5-*PP*** were isolated (*vide infra*), which is intriguing because this means that the macrocyclization reaction is diastereoselective. This implies that homochiral templation between the two PDI cores must occur prior to the ring-closing step that forms the macrocycle.

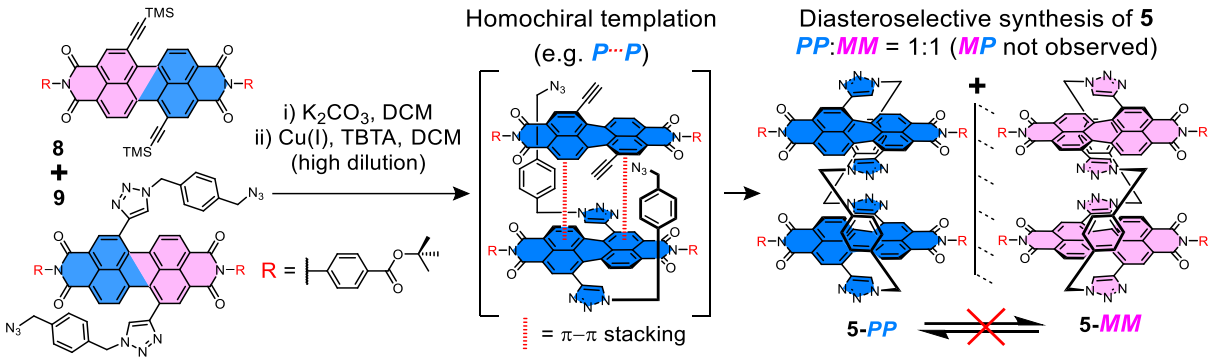

Figure 3.6: The diastereoselective synthesis of macrocycle **5**.

The exclusive formation of homochiral macrocycles was confirmed by (chiral and achiral) HPLC analysis of the crude reaction mixture. For these experiments, samples of the crude reaction mixture were microfiltered prior to injection into the HPLC column to remove insoluble oligomeric side-products, but no other purification was carried out prior to injection. Normal phase achiral HPLC revealed only one peak that contained the mass of the macrocycle (as determined by ESI-MS) while chiral HPLC revealed two macrocycle peaks of equal intensity corresponding to **5-*MM*** and **5-*PP*** (**Figure 3.7a-b**). The other peaks in these chromatograms are likely to be shorter PDI oligomers.

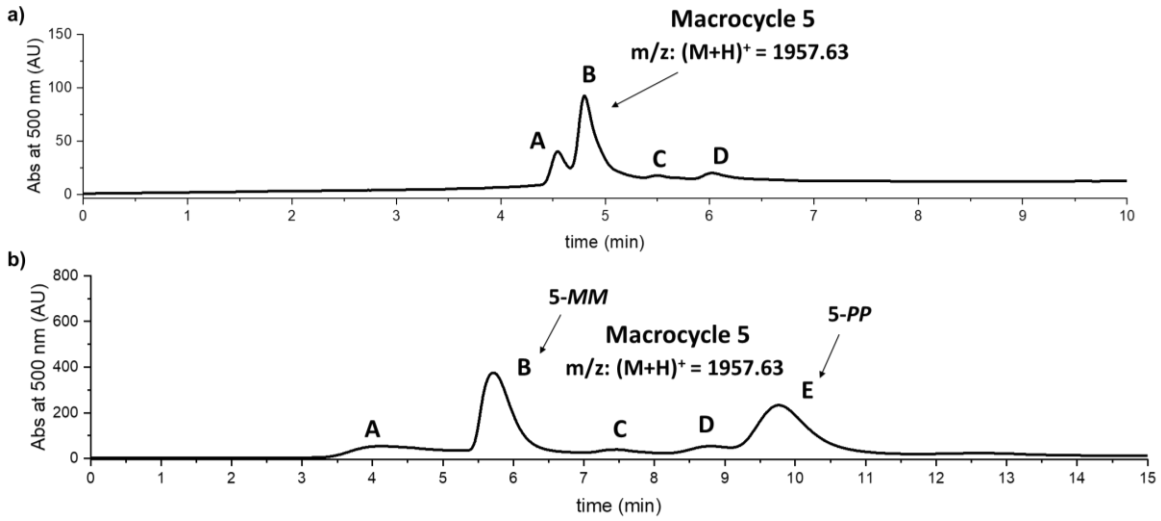

Figure 3.7: a) HPLC chromatogram (COSMOSIL Buckyprep 250 x 10 mm, injection volume 50 µL, ~ 2 mg/mL, eluted with 9:1 (v/v) DCM:methanol) of the crude reaction mixture of macrocycle **5**. Peaks A-D were collected and analysed by ESI-MS. Macrocycle **5** was only present in peak B (m/z = 1958) which, when resolved by chiral HPLC, contains only the enantiomers **5**-***MM*** and **5**-***PP***. Peak integral ratio (A:B:C:D) = 8:24:6:6. **b)** Chiral HPLC chromatogram (Phenomenex i-Amylose-1, 250 x 10 mm, injection volume 100 µL, ~ 2 mg/mL, eluted with 9:1 (v/v) DCM:methanol) of the crude reaction mixture of macrocycle **5**. Peaks A-E were collected and analysed by ESI-MS. Macrocycle **5** was only present in peaks B and E (m/z = 1958) which, as identified by CD-spectroscopy, are **5**-***MM*** and **5**-***PP*** respectively. Peak integral ratio (A:B:C:D:E) = 7:21:3:4:21.

As for macrocycle **1**, upon their resolution by chiral HPLC, the enantiomers of macrocycle **5** exhibit mirror image CD spectra (**Figure 3.8**). The enantiomers were assigned by X-ray crystallography of enantiopure samples (**Section 3.8.3**) and by comparing the experimental and computationally predicted (by TD-DFT) CD spectra (**Appendix A**).

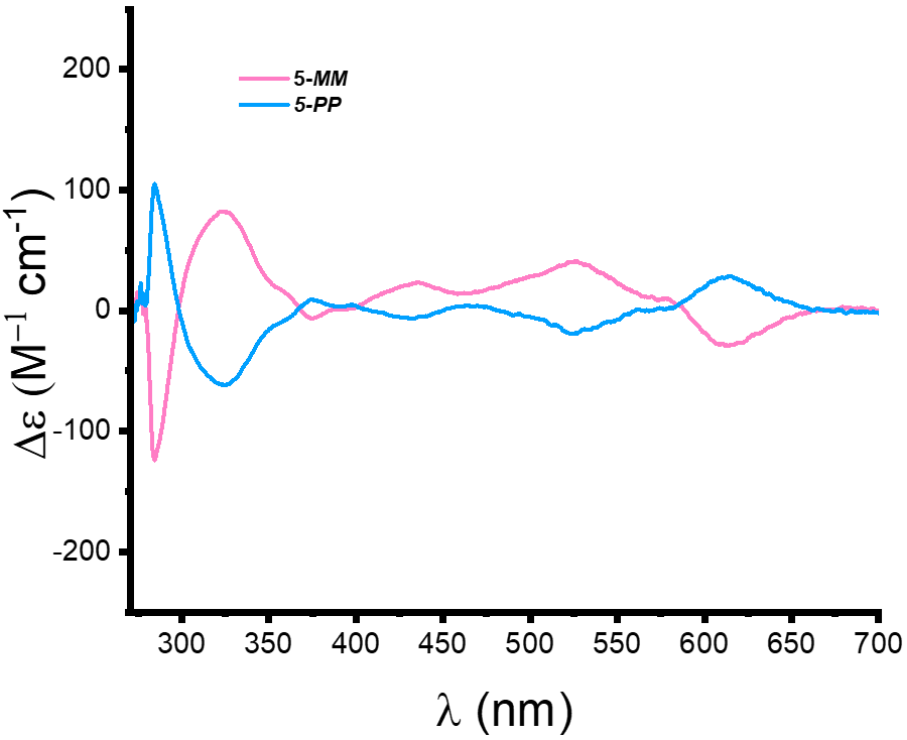

Figure 3.8: CD spectra for the **5-*MM*** (100% ee) and **5-*PP*** (90% ee) enantiomers of macrocycle **5** in toluene. Enantiomeric excesses were determined from chiral HPLC (**Figure 3.33**).

3.4 Investigation of configurational stability

In order to establish whether macrocycle **5** is chirally locked, the enantiomers of a pure sample of racemic macrocycle **5** (**5-*rac***) were isolated using chiral HPLC and an enantiopure sample of **5-*MM*** enantiomer was then heated at 180 °C for 24 h. This sample was reinjected into the chiral HPLC column, which showed no trace of the other enantiomer, **5-*PP***. Therefore, the enantiomers of macrocycle **5** can be said to be chirally stable at temperatures at least as high as 180 °C.

As no chiral interconversion was detected at 180 °C in 24 h, the racemization lifetime τ is much greater than 24 h. To obtain a lower bound for the free energy barrier for stereoisomer interconversion, the Eyring equation was used with a racemization lifetime τ = 24 h at 180 °C (453 K). This yields a free energy barrier $\Delta G^{\ddagger} > 155$ kJ mol^{-1} with a racemisation half-life ($t_{rac}^{1/2}$) of more than 10^5 years at room temperature.[11] This $\Delta G^{\ddagger}$ is significantly higher than for all previously reported bay-connected bis-PDI macrocycles ($\Delta G^{\ddagger} < 108$ kJ mol $^{-1}$), including the previous "Pink Box" macrocycle **1**, which have $t_{rac}^{1/2}$ values ranging from minutes to days.[6, 7]

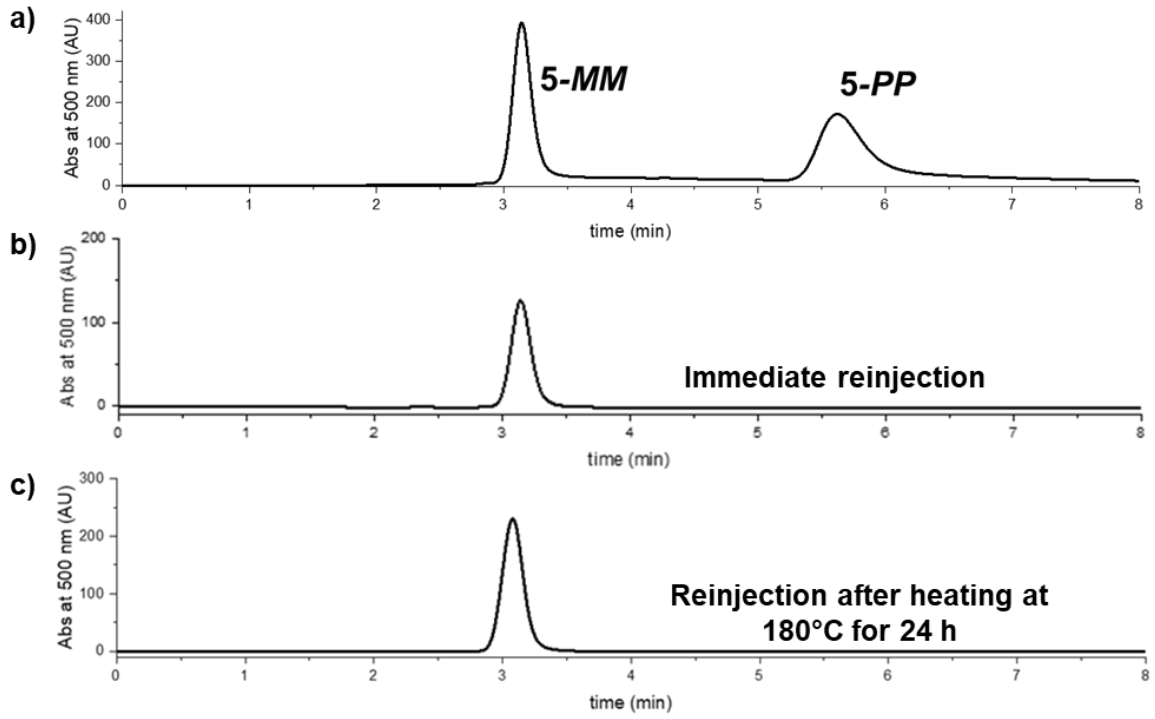

Figure 3.9: Chiral HPLC chromatograms (Phenomenex i-Amylose-1, 250 x 4.6 mm, eluted with 9:1 (v/v) DCM:methanol) of **a)** pure racemic macrocycle **5-*rac***, **b)** a sample of enantiomer **5-*MM***, reinjected immediately after isolation by chiral HPLC, and **c)** a sample of enantiomer **5-*MM***, heated at 180°C for 24 h and then reinjected into the chiral HPLC column.

The configurational stability of macrocycle **5** provides excellent evidence for the "intramolecular somersault" mechanism originally postulated by Nuckolls and co-workers,[7] since the PDI cores with the long, rigid *tert*-butyl benzoate imide groups are now too long to "somersault" through the cavity (**Figure 3.10a**), as seen from the crystal structure (**Figure 3.10b**).

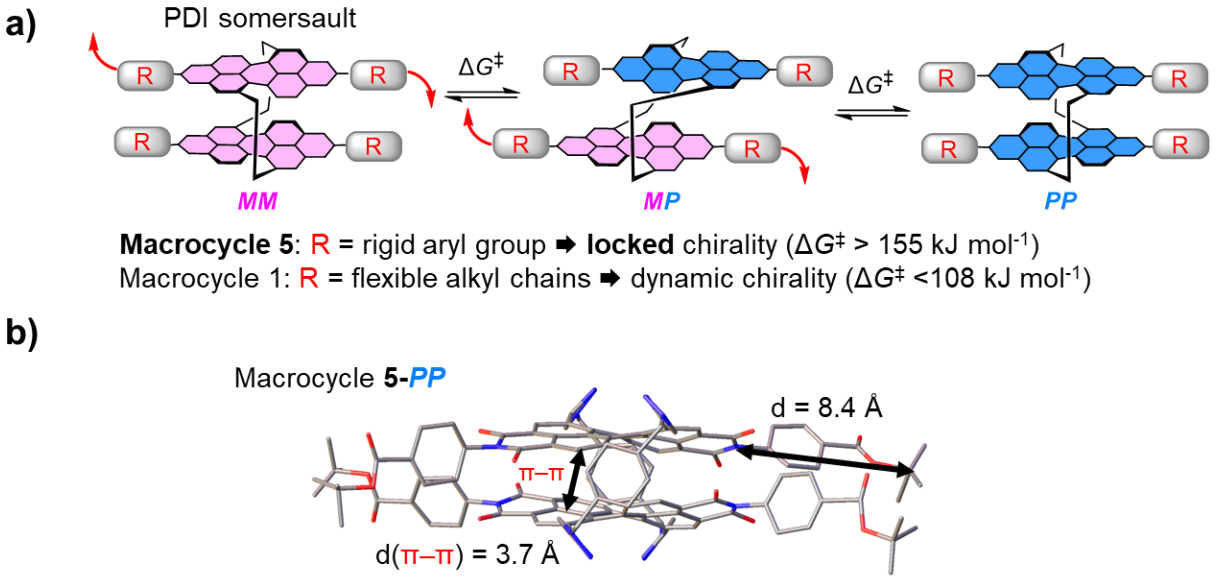

Figure 3.10: a) Cartoon of the 'intramolecular somersault' mechanism for the interconversion of bis-PDI macrocycle stereoisomers,[7] which is inhibited in **5**. b) X-ray crystal structure of macrocycle **5-*PP***.

3.5 Characterisation of the intramolecular PDI-PDI dimer

With stable enantiomers in hand, there is an opportunity to study the intermolecular self-assembly of enantiopure and racemic samples of macrocycle **5**. However, in order to be able to do so it was first necessary to characterise any *intra*molecular PDI-PDI π–π interactions within the macrocycle. It should be noted that the analysis in this section concerns *intra*molecular interactions only because the bis-PDI macrocycle is found to be monomeric in solution at concentrations below 10μM.

3.5.1 X-ray crystallography

Single crystals of racemic macrocycle (**5-*rac***) were grown by slow diffusion of methanol into a chloroform solution, allowing an X-ray crystal structure to be obtained for macrocycle **5**. The crystal structure of **5** is remarkably similar to that of macrocycle **1**, with both exhibiting a clear intramolecular homochiral face-to-face π–π interaction between the two PDI cores (**Figure 3.11**), with a centroid-centroid distance of 3.7 Å in both.

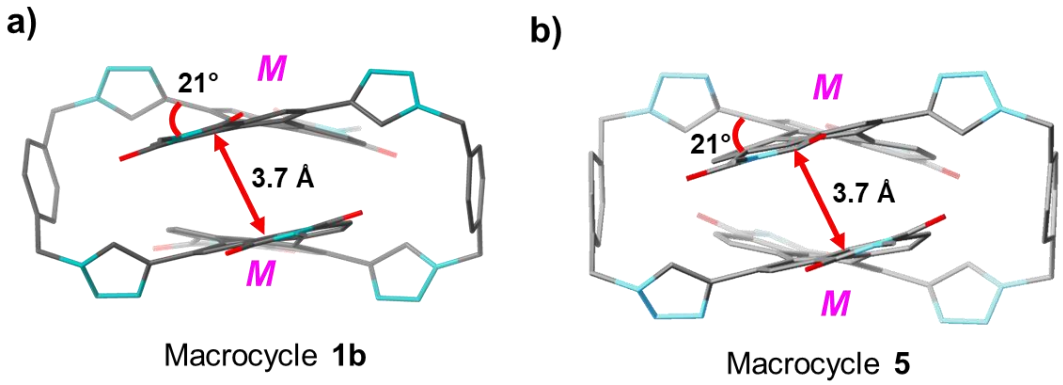

Figure 3.11: X-ray crystal structures (showing only the *MM* enantiomer) in racemic crystals of **(a)** macrocycle **1b** and **(b)** macrocycle **5**. Imide substituents and hydrogens have been removed for clarity.

3.5.2 ^{1}H NMR spectroscopy

As discussed in the previous chapter, "Pink Box" macrocycle **1** exhibits a switchable conformation with intramolecular homochiral H-type π–π stacking in toluene that is switched off in chlorinated solvents. Therefore, it was decided to investigate whether macrocycle **5** exhibits similar behaviour. This was initially probed by ^{1}H NMR spectroscopy (**Figure 3.12** and **Figure 3.13**).

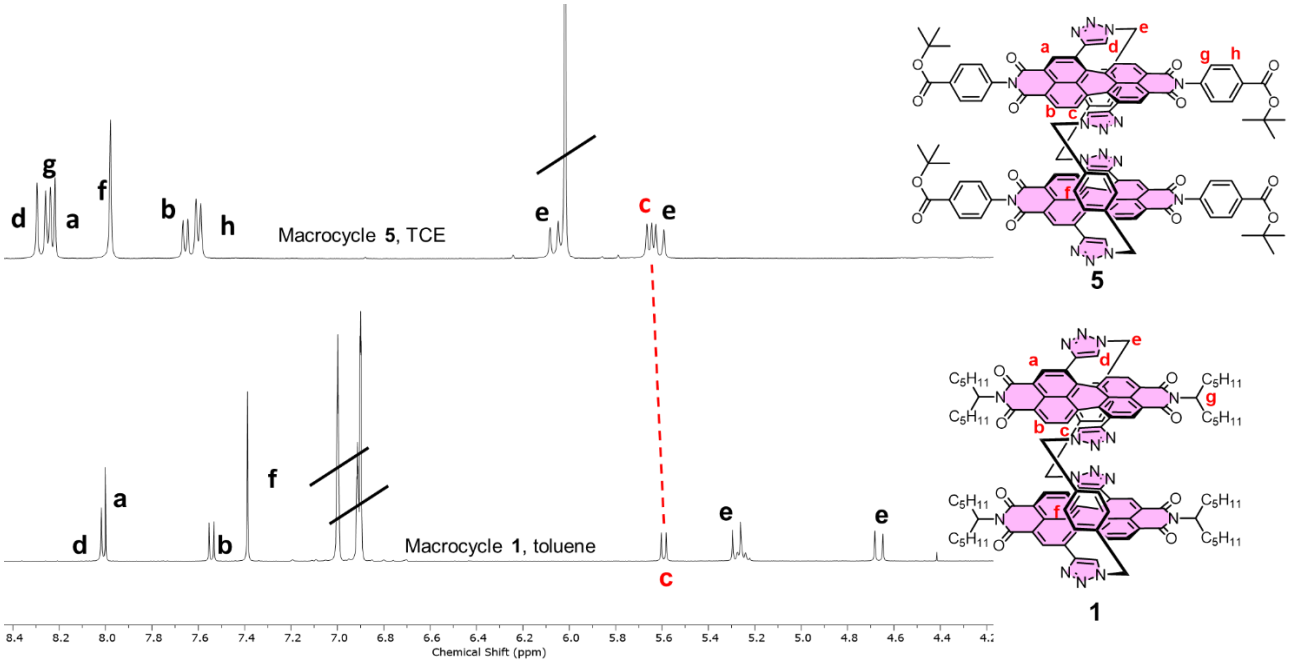

Figure 3.12: ^{1}H NMR (400 MHz, 373K) spectra of macrocycle **5** (top, TCE-d_2) and macrocycle **1** (bottom, toluene-d_8).

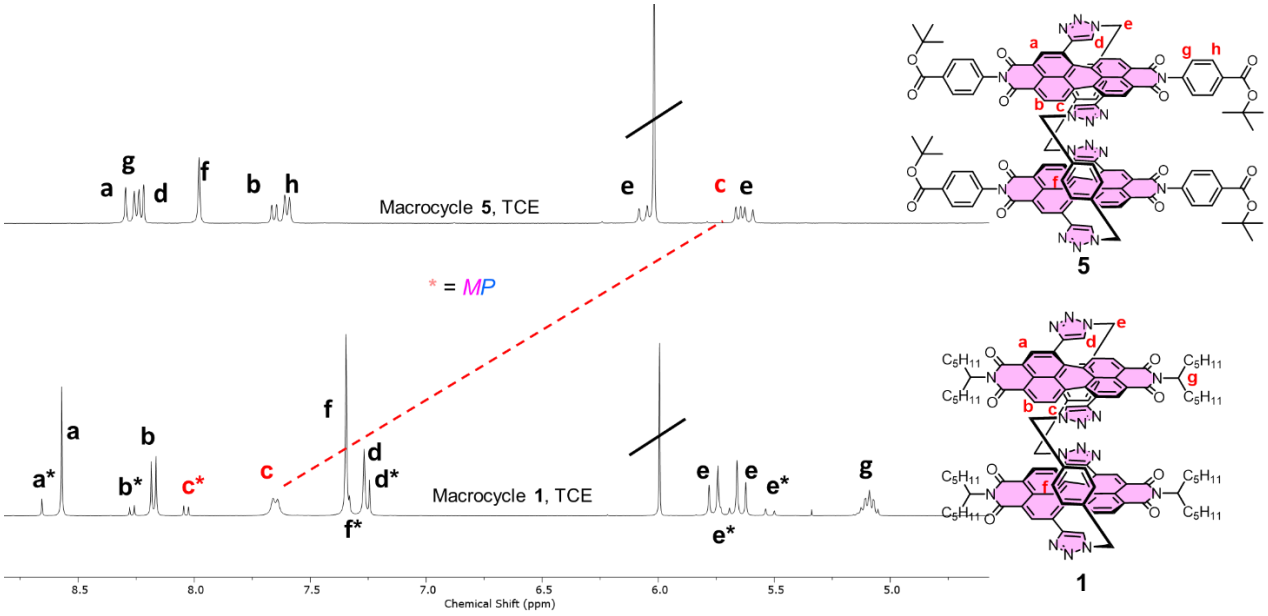

Figure 3.13: ^{1}H NMR (400 MHz, 373K) spectra of macrocycle **5** (top) and macrocycle **1** (bottom), both in TCE-d_2.

Interestingly, the ^{1}H NMR spectrum of macrocycle **5** in TCE-d_2 is very different to that of macrocycle **1** in TCE-d_2 (**Figure 3.13**) but is quite similar to that of macrocycle **1** in toluene-d_8 (**Figure 3.12**). As established in the previous chapter, macrocycle **1** displays an upfield shift

of protons $H_{a–c}$ in toluene-d_8 relative to the spectrum in TCE-d_2. Once again, proton H_c appears to be particularly diagnostic of closely stacked π-surfaces, presumably because of its proximity to the triazole and perylene aromatic ring systems. Proton H_c has a similar chemical shift for macrocycle **5** in TCE-d_2 and macrocycle **1** in toluene-d_8 (~ 5.6 ppm for both). In contrast, for macrocycle **1** in TCE-d_2, proton H_c is shifted dramatically downfield (~ 7.7 ppm). This suggests that for macrocycle **5** the intramolecular H-type dimer persists in chlorinated solvents, in stark contrast to macrocycle **1** for which chlorinated solvents disrupt the intramolecular H-type dimer. It is also worth noting that the ***MP*** heterochiral stereoisomer observed for macrocycle **1** in TCE-d_2 is not observed for macrocycle **5**, because as established in the previous sections it is chirally locked and forms exclusively homochiral stereoisomers.

3.5.3 UV-vis absorption spectroscopy

UV-vis absorption spectroscopy was performed to obtain further insight into the effects of solvent on the intramolecular PDI-PDI dimer in macrocycle **5**. The UV-vis spectra of **5**-***rac*** in toluene and TCE are virtually identical, with both displaying clear evidence of excitonic coupling between the PDIs as result of the intramolecular PDI-PDI H-type interaction ($\varepsilon_{0-0}/\varepsilon_{0-1}$ = 0.54, for both solvents, **Figure 3.14**). In contrast, as established in the previous chapter, the UV-vis spectra of macrocycle **1** show that it exhibits H-type excitonic coupling in toluene which is switched off in TCE ($\varepsilon_{0-0}/\varepsilon_{0-1}$ = 0.58 (toluene), 1.19 (TCE), **Figure 3.14**). Therefore, the UV-vis spectra of macrocycle **5** in toluene and TCE are consistent with the intramolecular H-type dimer persisting in chlorinated solvents.

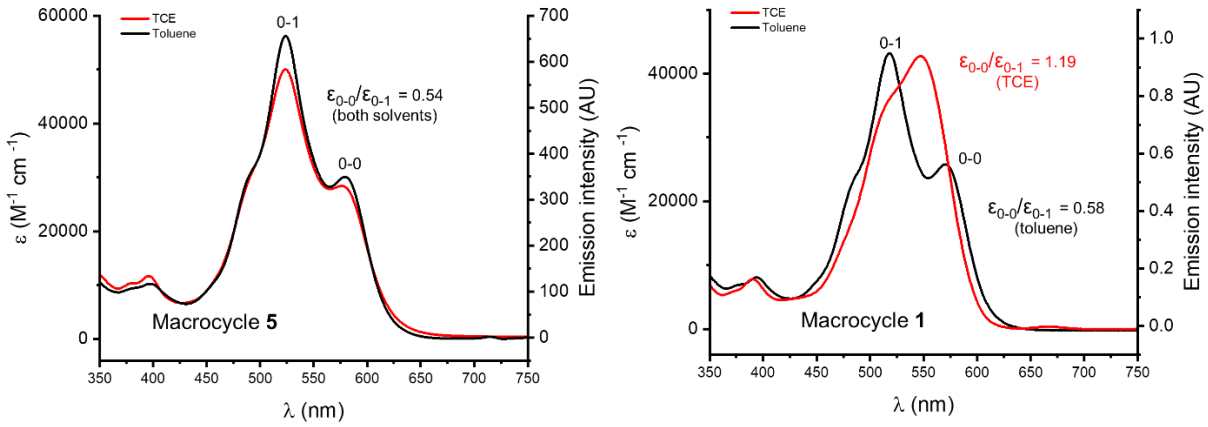

Figure 3.14: Normalised UV-vis absorption and fluorescence emission spectra of macrocycle **5** (left) and macrocycle **1** (right) in toluene and TCE (10 μM), showing that the intramolecular H-type dimer is persists in chlorinated solvents for macrocycle **5** but is disrupted by chlorinated solvents in macrocycle **1**.

3.5.4 Emission spectroscopy

Emission spectroscopy was carried out to study the PDI-PDI π–π dimer in macrocycle **5** in the excited state. The fluorescence spectra of macrocycle **5** and of acyclic PDI monomer **9** in toluene are shown in **Figure 3.15**. The fluorescence of macrocycle **5** appears typical of excimer emission because, compared to the PDI monomer **9**, it is red-shifted (by 35 nm) and quenched (quantum yield Φ = 35% *vs.* 70%).

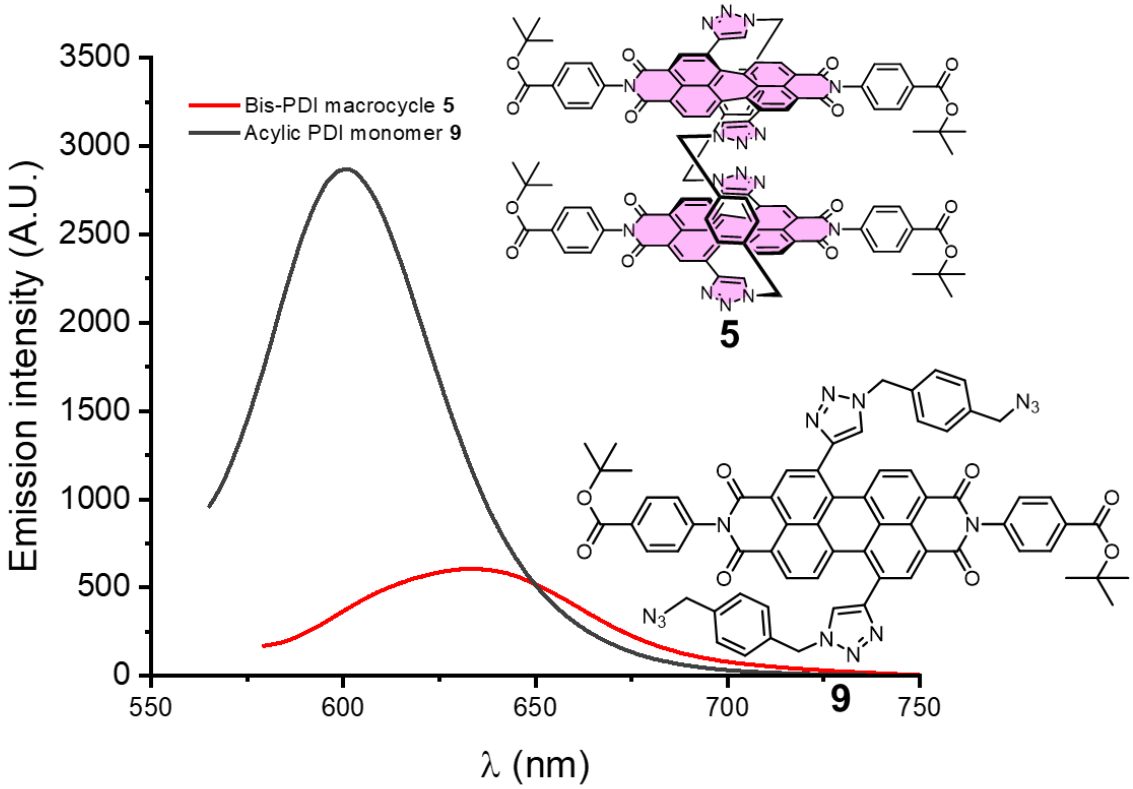

Figure 3.15: Emission spectra of acyclic PDI **9** and macrocycle **5** in toluene (λ_{ex} = 520 nm, 10 μM).

To further probe this excimer state in **5**, the fluorescence lifetimes of macrocycle **5** and PDI monomer **9** were measured. Macrocycle **5** exhibits a significantly longer lifetime compared to PDI monomer **9** (τ = 36 *vs.* 8 ns), consistent with excimer emission in **5**.[12]

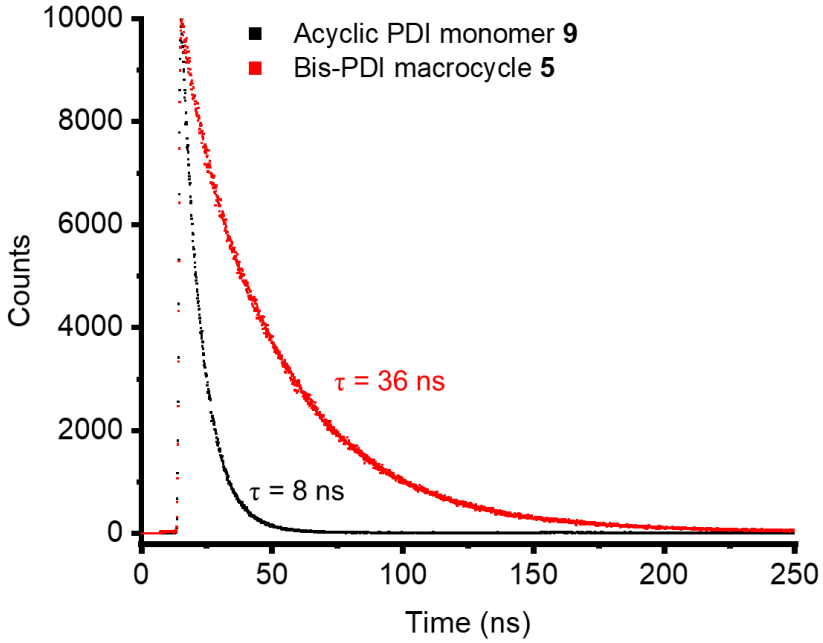

Figure 3.16: Time-resolved fluorescence decay profiles of macrocycle **5** and PDI monomer **9** (toluene, 5 μmol, λ_{ex} = 373 nm, λ_{em} = 635 nm for **5**, and λ_{em} = 604 nm for **9**).

3.6 Chiroptical properties in solution

3.6.1 CD spectroscopy

In addition to the experiments described above, the CD spectra of the enantiomers of macrocycle **5** in TCE and toluene also confirm that the intramolecular H-type dimer is present in both toluene and chlorinated solvents. This is because the CD spectra are identical in both solvents (**Figure 3.17**)with clear evidence of H-type excitonic coupling from the Cotton effect at ~ 573 nm.

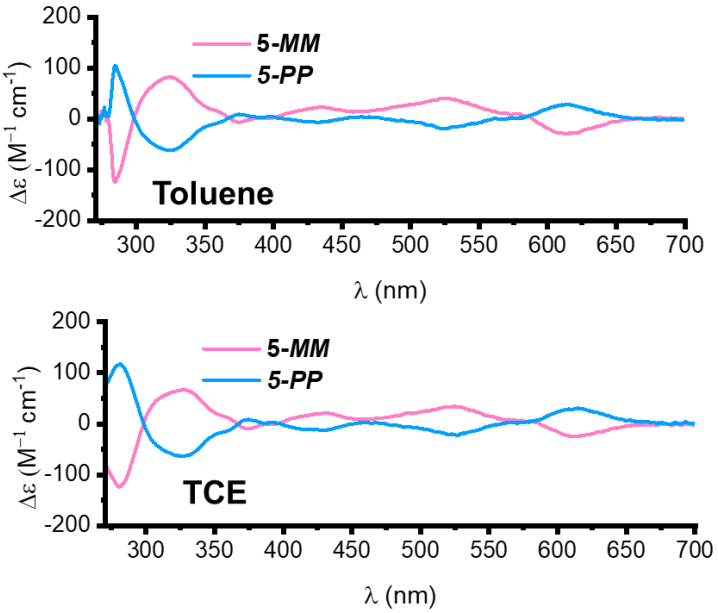

Figure 3.17: CD spectra (10 µM) of the enantiomers **5-*MM*** and **5-*PP*** of macrocycle **5**, in toluene (top) and TCE (bottom).

Stable macrocycle enantiomers ensure that the concentration of enantiomers and thus chiroptical parameters, such as the absorption dissymmetry factor $|g_{abs}|$, may be measured accurately. Indeed, for the previous "Pink Box" macrocycle **1,** which is dynamically chiral, $|g_{abs}|$ could not be measured from the CD spectra as there was too much uncertainty in the concentration of the enantiomers. Therefore, using macrocycle **5**, accurate $|g_{abs}|$ values from the CD spectra in toluene and in chlorinated solvent gave $|g_{abs}| \sim 2.7 \times 10^{-3}$ in both solvents, which is in line with other reported twisted PDI systems.[13, 14]

3.6.2 CPL spectroscopy

CPL spectroscopy was also carried out on the enantiomers of macrocycle **5** in both TCE and toluene, from which a $|g_{lum}| \sim 2 \times 10^{-2}$ at λ_{em} = 675 nm in both solvents (**Figure 3.18)**. The $|g_{abs}|$ and $|g_{lum}|$ values for the enantiomers in both solvents are summarised in **Table 3.1**.

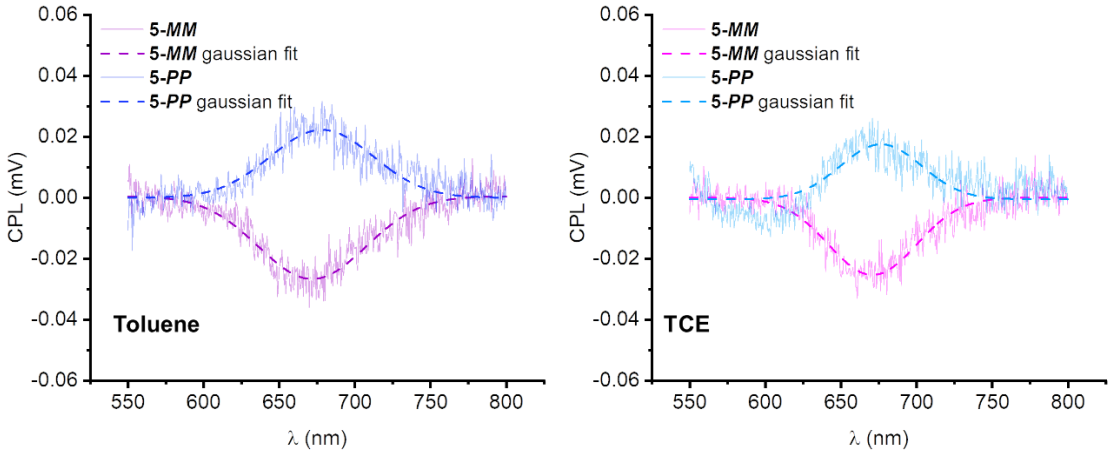

Figure 3.18: CPL spectra for the **5-*MM*** and **5-*PP*** enantiomers of macrocycle **5** in toluene and TCE (10 μM, 298 K, λ_{ex} = 520 nm).

Table 3.1: Absorption and emission dissymmetry factors $\boldsymbol{g_{abs}}$ and $\boldsymbol{g_{lum}}$ for macrocycle **5** enantiomers in toluene and TCE (both at 10 μM).

Enantiomer	Solvent	g_{abs} (at 610 nm)	g_{lum} [nm]
MM	Toluene	- 2.7 × 10^{-3}	- 1.8 × 10^{-2} [672]
PP	Toluene	+ 2.8 × 10^{-3}	+ 1.7 × 10^{-2} [678]
MM	TCE	- 2.5 × 10^{-3}	- 1.6 × 10^{-2} [671]
PP	TCE	+ 2.8 × 10^{-3}	+ 1.5 × 10^{-2} [676]

Interestingly, the $|g_{lum}| = 2 \times 10^{-2}$ (675 nm) is an order of magnitude larger than the equivalent dissymmetry factor for absorption, $|g_{abs}| = 3 \times 10^{-3}$ (λ = 610 nm, **Table 3.1**), a characteristic feature of CPL emission from a chiral intramolecular excimer state which arises from the excitonic coupling of two chromophores in rigid systems such as macrocycles.[15-17] Indeed, as discussed in **Section 3.5.4**, the fluorescence of macrocycle **5** is typical of excimer emission. As for the "Pink Box" macrocycle **1** in the previous chapter, the strict homochirality of the intramolecular π–π dimer is thought to be key to the high $|g_{lum}|$ of macrocycle **5**. Macrocycle **5** has a higher CPL dissymmetry factor than the majority of chirally locked small organic molecules in solution that emit in the red region of the spectrum.[14, 18-27] Therefore, the π–π homochiral preorganisation of chromophores, as evidenced from absorption and CD spectra, provides an effective strategy for amplifying $|g_{lum}|$ in organic materials.

3.7 Estimation of the intramolecular PDI-PDI dimer strength

Having characterised the nature of the intramolecular PDI-PDI interaction in macrocycle **5**, it was then decided to estimate the strength of the dimer. However, since the intramolecular π–π dimer in macrocycle **5** could not be disrupted by changing the solvent, it was not possible to measure the strength of this interaction in the way that it was done for macrocycle **1** in the previous chapter.

Instead, acyclic bis-triazole PDI **9** was used to estimate the binding strength of the PDI dimer (K_d). Of course, the K_d measured with **9** provides a lower estimate of K_d in **5**, since the former is an *inter*molecular system (i.e., $K_{d\text{-inter}}$) which is less preorganized than macrocycle **5** (i.e., $K_{d\text{-intra}}$). Upon concentration of acyclic PDI **9** up to 418 μM in 3:2 (v/v) DCM:*n*-hexane (**Figure 3.19)** the monomeric UV-vis spectrum evolves into one characteristic of H-type aggregation ($\varepsilon_{0\text{-}0}/\varepsilon_{0\text{-}1}$ decreases from 1.14 to 0.74), from which a $K_{d\text{-inter}}$ = 1,677 M^{-1} was calculated by non-linear curve fitting to the monomer–dimer model (**Figure 3.20**).[28] It is noted that the error in this $K_{d\text{-inter}}$ value (± 19%) arises from further changes to the UV-vis spectrum at higher concentrations of **9**, which are indicative of the formation of larger aggregates than dimers.

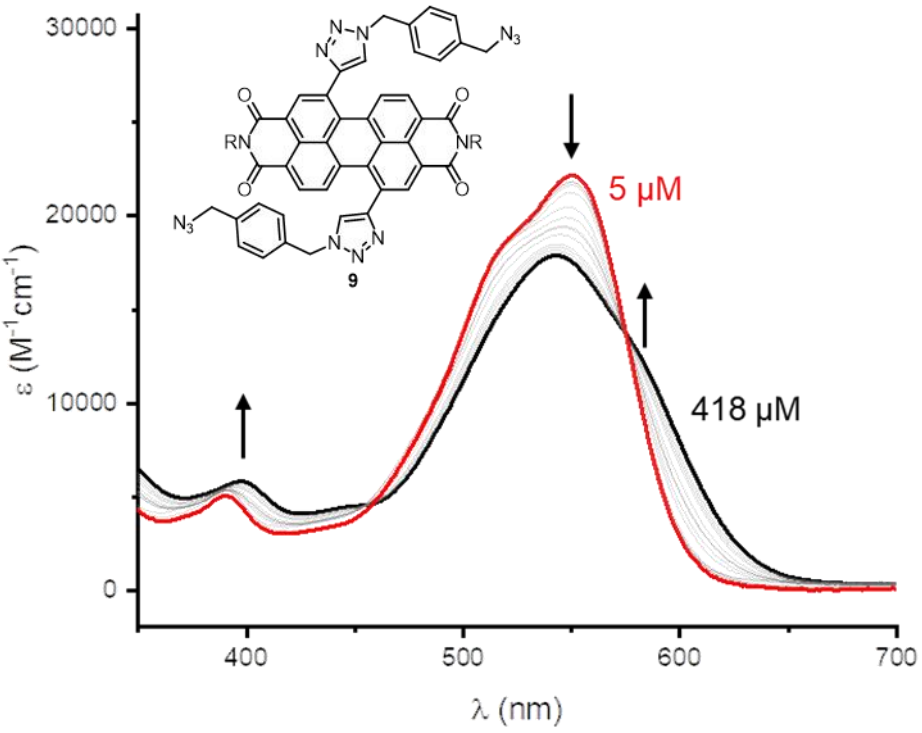

Figure 3.19: Change in UV-vis absorption spectrum of acyclic PDI **9** upon concentration from 5 μM (red trace) to 418 μM (black trace) in 3:2 (v/v) DCM:*n*-hexane.

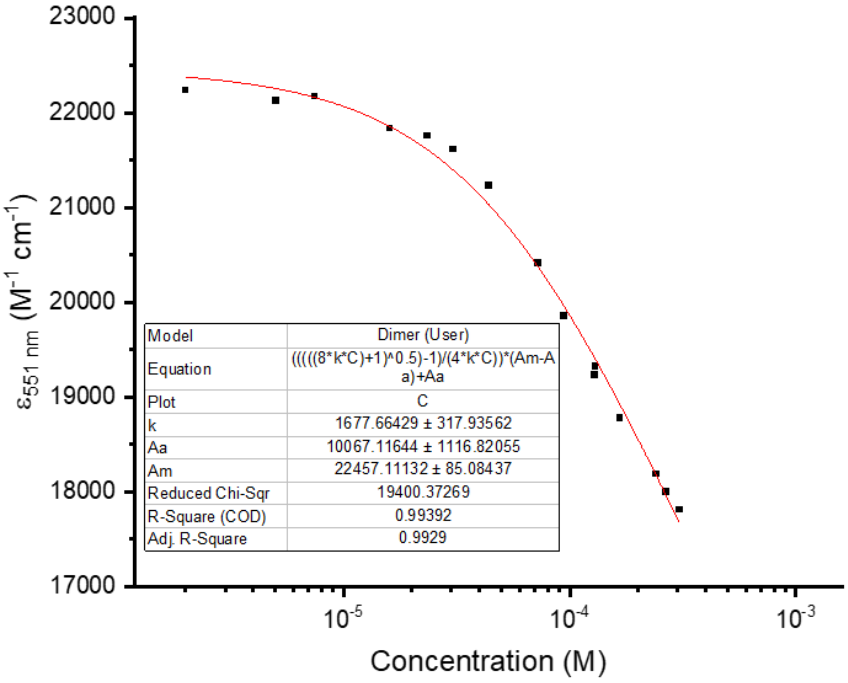

Figure 3.20: Change in extinction coefficient of acyclic PDI **9** at 551 nm upon concentration from 5 μM to 418 μM in 3:2 (v/v) DCM:*n*-hexane, fitted to the monomer-dimer model, giving a dimerization constant K_d = 1678 ± 318 M^{-1}.

3.8 Chirality-dependent supramolecular self-assembly

Whilst PDI homochiral dimerization could not be decoupled from subsequent binding events using acyclic PDI **9**, bis-PDI macrocycle **5** is ideally suited to investigating chiral π–π self-assembly beyond the dimer limit. This is because macrocycle **5** is preorganized into an intramolecular H-type dimer and has two accessible π-surfaces on its exterior. The work described in this section attempts to capitalise on the chiral stability of the enantiomers of macrocycle **5** to study the chirality-dependent supramolecular self-assembly of racemic and enantiopure samples of the macrocycle.

3.8.1 Concentration-dependent UV-vis spectroscopy of **5-*rac***

The supramolecular self-assembly of a racemic sample of the macrocycle (**5-*rac***) was first studied by concentration-dependent UV-vis spectroscopy in 3:2 dichloromethane:*n*-hexane. This solvent system was chosen because it facilitates self-assembly at lower concentrations than in neat dichloromethane.

Whilst **5-*rac*** exhibits Beer-Lambert behaviour at low concentrations, the UV-vis spectrum shows significant deviations above 10 μM (**Figure 3.21**). Upon concentration, a new PDI absorption band at λ = 596 nm appears with isosbestic points (λ = 472, 545, 571, 582 nm) indicating the macrocycle "monomer", in fact an intramolecular dimer, is in equilibrium with a new aggregated species (**Figure 3.21**). That this absorption band is significantly red-shifted relative to the monomer of acyclic PDI **9** (Δλ = 46 nm) suggests the self-assembly of macrocycle **5-*rac*** into a slipped-stacked J-type aggregate.

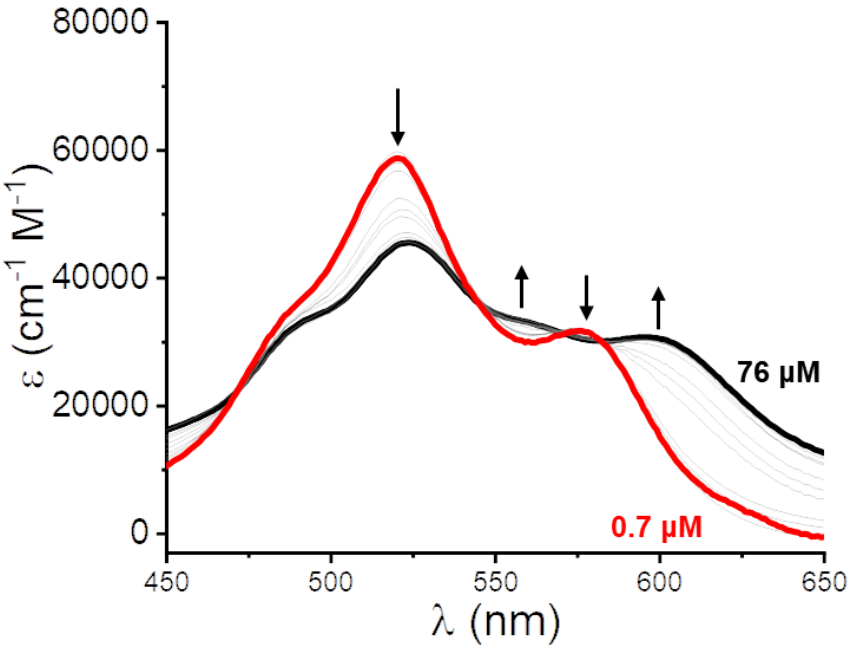

Figure 3.21: Change in UV-vis absorption spectrum of macrocycle **5-*rac*** upon concentration from 0.7 μM (red trace) to 76 μM (black trace) in 3:2 (v/v) DCM:*n*-hexane.

To estimate the binding constant(s) *K* for macrocycle self-assembly, the data from the concentration-dependent UV-vis spectra was fitted to several binding models suited to the aggregation of π-conjugated molecules.[28] As well as the dimer model (**Section 3.7**), this included a model for the formation of larger aggregates, namely the isodesmic model, in which all binding events have the same *K* value.

Interestingly, fits to both the dimer and isodesmic models were poor (**Figure 3.22** and **Figure 3.23)** suggesting the aggregate formed by **5-*rac*** is distinct to an H-type dimer[1] or co-facial columnar stack,[29] common assemblies for PDIs.[30]

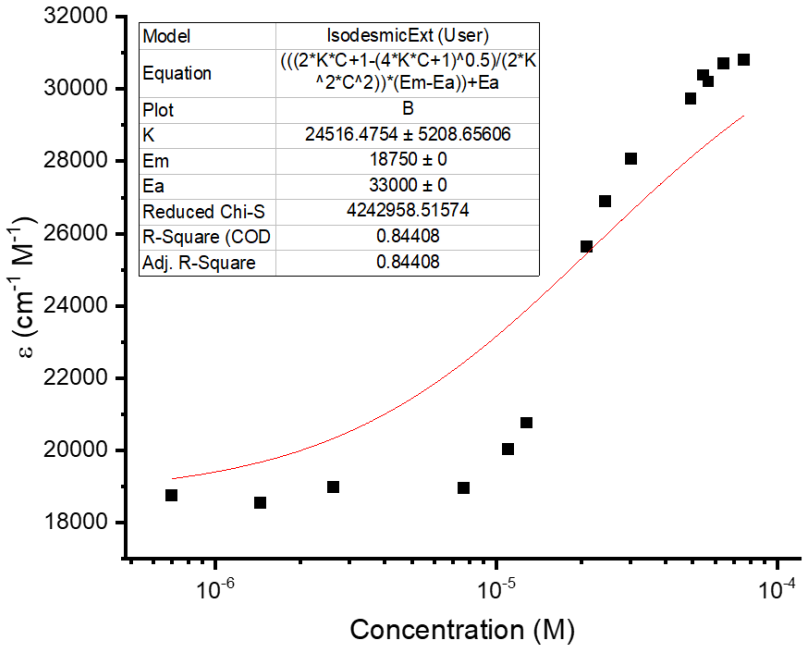

Figure 3.22: Change in extinction coefficient ε at 596 nm of macrocycle **5-*rac*** upon concentration from 0.7 μM to 76 μM in 3:2 (v/v) DCM:*n*-hexane, fitted to the isodesmic model by non-linear regression analysis, with fixed ε_{agg} = 33,000 cm^{-1} M^{-1} and ε_{mon} = 18750 cm^{-1} M^{-1}. The fit is very poor, yielding K ~ 25000 with a large error (~ 20%). The sudden, steep rise in ε at 10^{-5} M suggests that aggregate formation is non-isodesmic and cooperative. Beer-lambert behaviour is observed below 10^{-5} M.

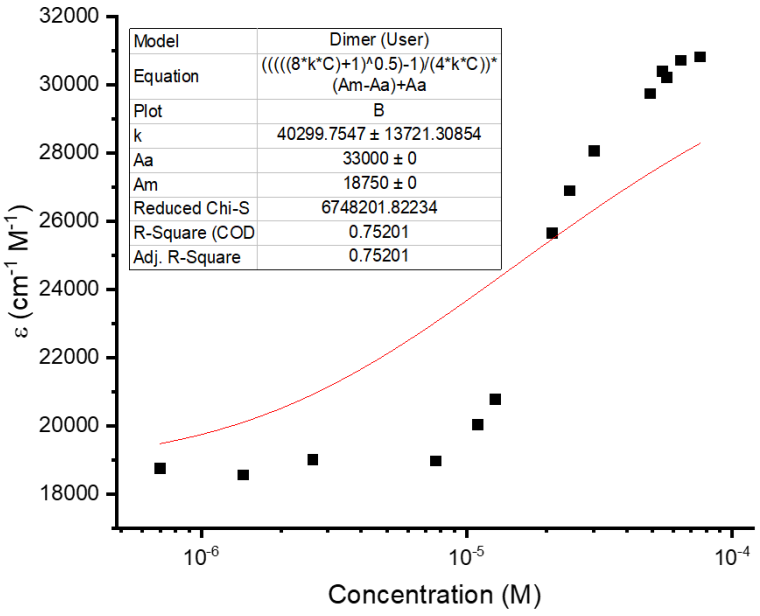

Figure 3.23: Change in extinction coefficient ε at 596 nm of macrocycle **5-*rac*** upon concentration from 0.7 μM to 76 μM in 3:2 (v/v) DCM:*n*-hexane, fitted to the monomer-dimer mode by non-linear regression analysis, with fixed ε_{agg} = 33,000 cm^{-1} M^{-1} and ε_{mon} = 18750 cm^{-1} M^{-1}. The fit is very poor, yielding K = 40,000 with a large error (~ 35%). The sudden, steep rise in ε at 10^{-5} M suggests that aggregate formation is non-isodesmic and cooperative. Beer-lambert behaviour is observed below 10^{-5} M

Instead, the fact that spectral changes occur over a narrower concentration range indicates a non-isodesmic aggregation process.[28, 31] Indeed, a "nucleation-elongation" mechanism is characteristic of slipped-stack J-type aggregates of PDIs.[31] In the modified isodesmic (nucleation-elongation) model, dimerisation (with a distinct dimerisation constant $K_d = K_2$) is followed by isodesmic aggregation, such that $K_2 \neq K_3 = K_4 ... = K_i ... = K$. This can be described by the cubic equation:

$$\alpha_{\mathrm{mon}}{}^3(KC_{\mathrm{T}})^2(\mathrm{p}-1) + \alpha_{\mathrm{mon}}{}^2 KC_{\mathrm{T}}\big(KC_{\mathrm{T}} - 2(\mathrm{p}-1)\big) - \alpha_{\mathrm{mon}}(2KC_{\mathrm{T}}+1) + 1 = 0 \quad (3.1)$$

Where $\mathrm{p} = K_2/K$. Therefore, $\mathrm{p} < 1$ implies cooperative binding when the aggregate forms after the initial dimerization nucleation event. α_{mon} is the mole fraction of the monomer (i.e., the unaggregated macrocycle) and C_T is the total concentration of the sample. This equation cannot be solved for α_{mon} analytically for general cases. However, it is possible to calculate KC_{T} as a function of KC_{mon} for specific values of p using the equation:

$$KC_T = (1-\mathrm{p})\,KC_{\mathrm{mon}} + \frac{\mathrm{p}KC_{\mathrm{mon}}}{(1-KC_{\mathrm{mon}})^2} \quad (3.2)$$

α_{agg} is related to the extinction coefficients of the aggregate ($\varepsilon_{\mathrm{agg}}$), monomer ($\varepsilon_{\mathrm{mon}}$) and intermediate state ($\varepsilon(C_{\mathrm{T}})$) by the equation:

$$\alpha_{\mathrm{agg}} = 1 - \frac{\varepsilon(C_{\mathrm{T}}) - \varepsilon_{\mathrm{agg}}}{\varepsilon_{\mathrm{mon}} - \varepsilon_{\mathrm{agg}}} \quad (3.3)$$

Hence,

$$\varepsilon(C_{\mathrm{T}}) = \frac{KC_{\mathrm{mon}}}{KC_{\mathrm{T}}}\big(\varepsilon_{\mathrm{mon}} - \varepsilon_{\mathrm{agg}}\big) + \varepsilon_{\mathrm{agg}} \quad (3.4)$$

Hence the data $\varepsilon(C_{\mathrm{T}})$ can be plotted against KC_{T} and fitted manually to the parameters K, $\varepsilon_{\mathrm{mon}}$, $\varepsilon_{\mathrm{agg}}$ and p. As such, the best fit was achieved with a cooperative nucleation-elongation model in which a weaker dimerization, $K_d = 90\ \mathrm{M}^{-1}$, is followed by a stronger isodesmic extension of the aggregate, $K = 90{,}000\ \mathrm{M}^{-1}$ (**Figure 3.24**).

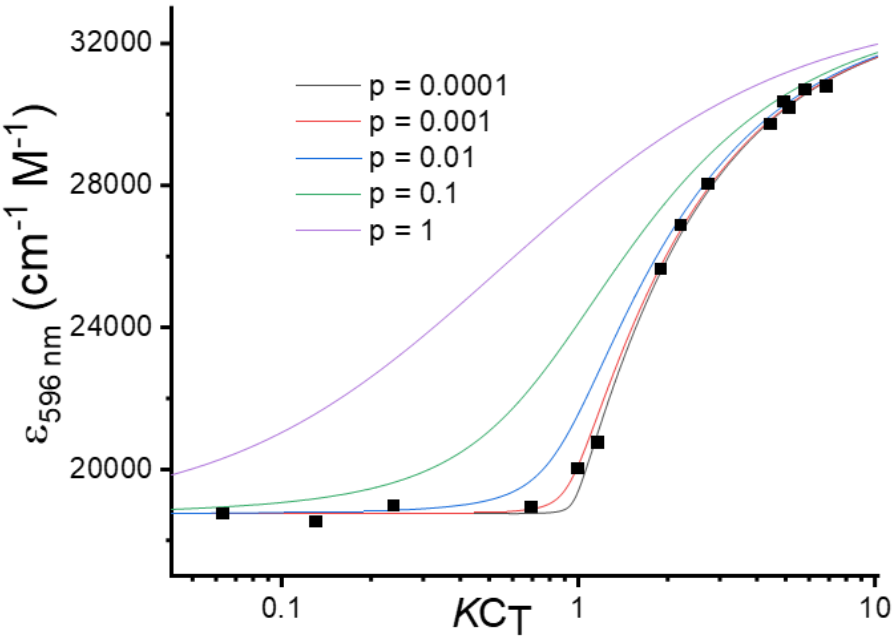

Figure 3.24: Change in extinction coefficient at 596 nm of macrocycle **5-*rac*** upon concentration from 0.7 μM to 76 μM in 3:2 (v/v) DCM:*n*-hexane, manually fitted to the modified isodesmic (nucleation-elongation) model for various values of p = K_2/K. The best manual fit (red trace) was obtained for K = 90,000 M^{-1}, p = 0.001, ε_{agg} = 33,000 cm^{-1} M^{-1} and ε_{mon} =18,750 cm^{-1} M^{-1}. From this we can deduce K_2 = 90 M^{-1}. An error of < 10% is estimated based on the quality of other fits that were tested.

Interestingly the H-type dimer formed by the acylic bis-triazole PDI **9** ($K_{d\text{-inter}}$ = 1,677 M^{-1} for acyclic PDI **9**, see previous **Section 3.7**) is much stronger than the analogous intermolecular J-type dimer observed for the bis-PDI macrocycle (K_d = 90 M^{-1} for **5**). This is likely because, as evident from the crystal structure of macrocycle **5** (**Figure 3.25**), the PDI's bay triazole groups point away from the internal π-surfaces, thereby favouring a face-to-face H-type dimerization within the macrocycle. The positioning of these heterocycles towards the outer π-surfaces of the dimer provides steric hindrance that directs subsequent self-assembly through slipped-stack J-type π–π stacking (**Figure 3.25**). This difference in K_d for H- and J-type aggregates is expected to be even larger in **5-*rac*** since the macrocycle preorganizes the H-type dimer to make it *intra*molecular (so $K_{d\text{-intra}}$ >> 1,677 M^{-1}), while the J-type dimer is *inter*molecular (K_d = 90 M^{-1}).

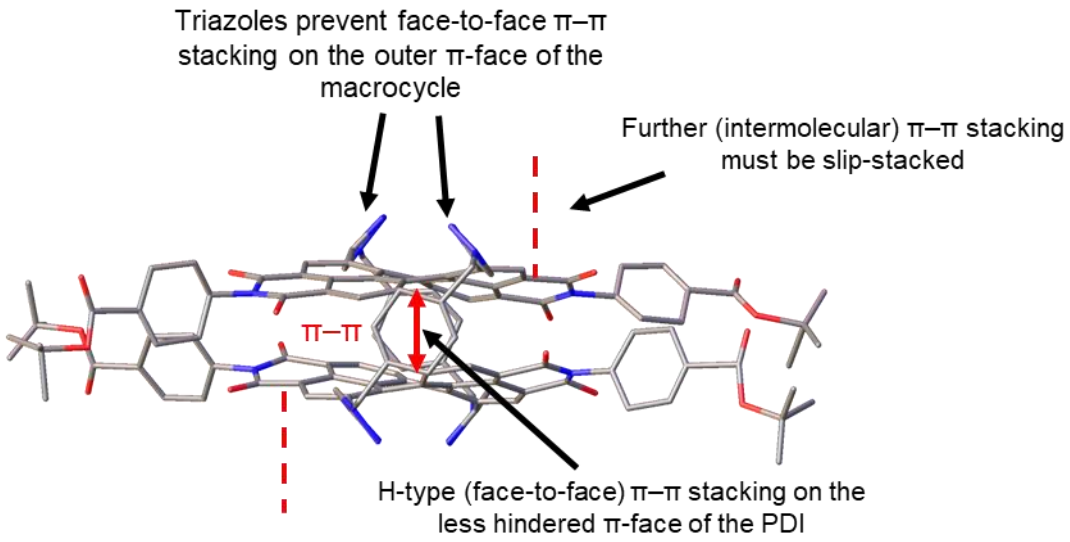

Figure 3.25: X-ray crystal structure of macrocycle **5**, showing the self-assembly properties of its inner and outer π-faces.

3.8.2 Concentration-dependent UV-vis spectroscopy of enantiopure **5-*PP***

The supramolecular self-assembly of an enantiopure sample of the macrocycle (**5-*PP***) was also probed by concentration-dependent UV-vis spectroscopy in 3:2 dichloromethane:*n*-hexane (**Figure 3.26b**). In contrast to the racemate **5-*rac*** which exhibits clear evidence of aggregation as the concentration is increased (**Figure 3.26a**), enantiopure **5-*PP*** continues to obey the Beer-Lambert law at higher concentrations. This indicates the absence of higher order (intermolecular) π–π aggregates in enantiopure **5-*PP***. This implies that the *inter*molecular π–π J-type (slipped-stack) aggregation seen in **5-*rac*** must be occurring between PDIs of opposite chirality.

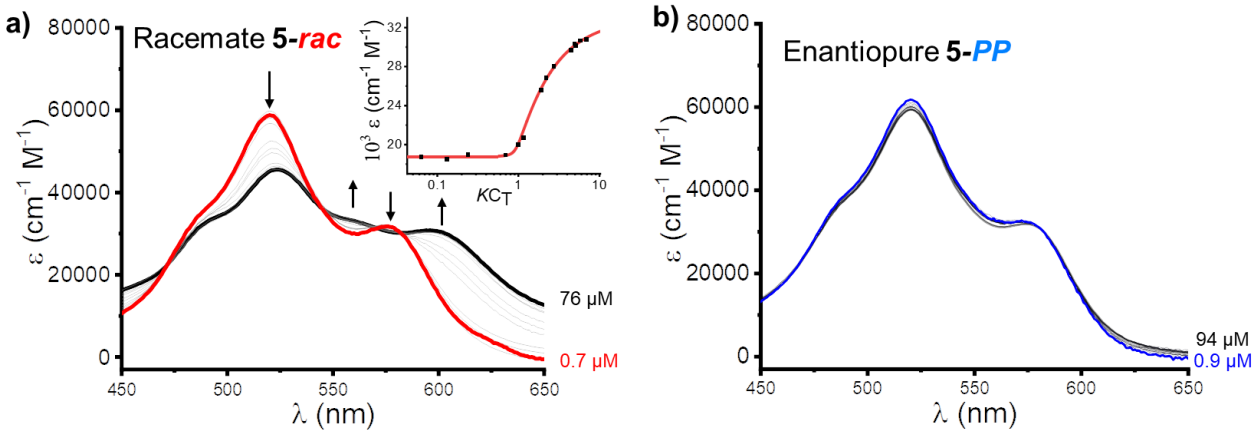

Figure 3.26: UV–vis spectra of **(a) 5-*rac*** and **(b) 5-*PP*** upon increasing the concentration (3:2 CH_2Cl_2:*n*-hexane, 298 K).

Therefore, in stark contrast to *intra*molecular π–π stacking between PDIs, which was shown to be exclusively homochiral and H-type, the *inter*molecular π–π stacking of macrocycle **5** must be heterochiral and J-type. In other words, the studies with **5-*rac*** and **5-*PP*** indicate that, when both π-surfaces of this twisted 1,7-disubstituted PDI are available for π–π self-assembly, homochiral H-type dimerization on the less sterically hindered face is followed by heterochiral J-type stacking on the remaining π-surface (**Figure 3.27a-b**). As such, the aggregate formed by **5-*rac*** may be described as an extended J-type aggregate of H-type dimers (**Figure 3.27c**).

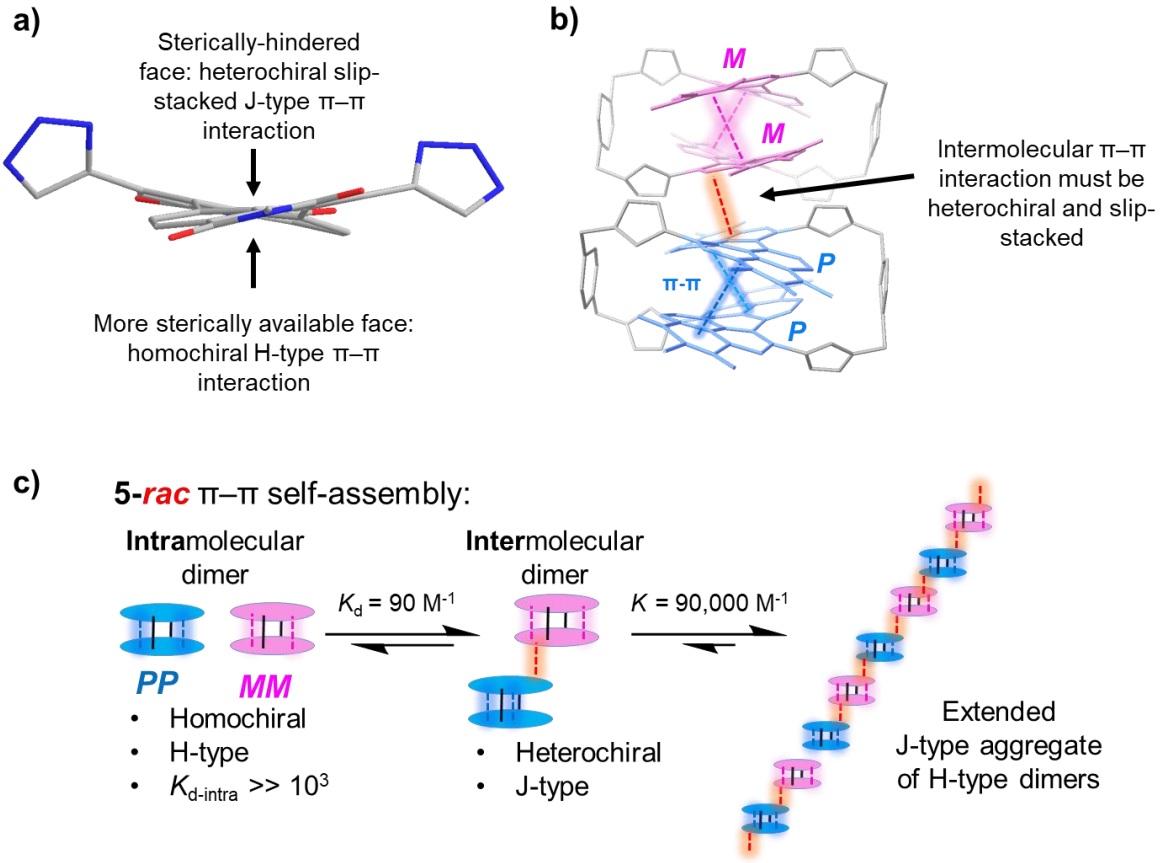

Figure 3.27: a) Depiction of the two distinct π-surfaces in a 1,7-disubstituted bistriazole PDI and their chiral requirements for self-assembly. **b)** Depiction of the slip-stacked heterochiral interaction required for self-assembly of macrocycle **5** via π-π on its outer π-surfaces (adapted from the X-ray crystal structure in section 3.8.4). **c**) Schematic of the π–π self-assembly of **5-*rac***.

3.8.3 Crystallography of **5-*rac*** and **5-*PP***

The configurational stability of macrocycle **5** also enables enantiopure single crystals of the **5-*PP*** and **5-*MM*** enantiomers to be grown in addition to crystals of the racemate without the risk of forming scalemic or racemic mixtures during the crystallisation process. Single crystals of **5-*rac*** were grown by slow diffusion of methanol into a chloroform solution, while the growth of **5-*PP*** and **5-*MM*** crystals required the slow diffusion of hexane into a 1:1 chloroform:1,2-dicholobenzene solution. With enantiopure and racemic crystals in hand, the chirality-dependent supramolecular self-assembly of macrocycles in these crystals was analysed by X-ray crystallography in order to validate the findings from the self-assembly studies in solutions described in the previous sections. The packing of macrocycles in the crystal structures of **5-*rac*** and **5-*PP*** is shown in **Figure 3.28**.

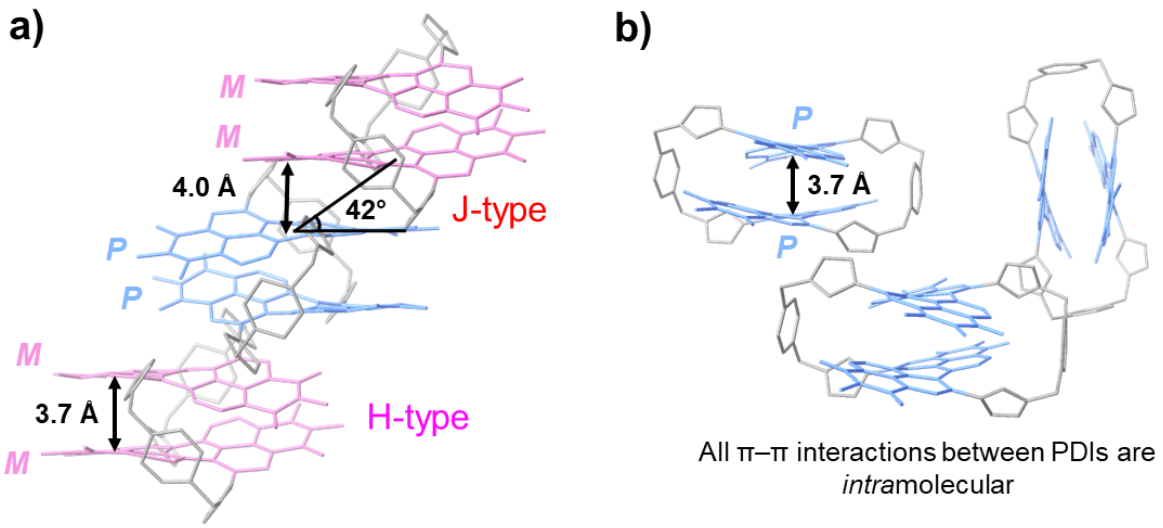

Figure 3.28: Supramolecular packing in the crystal structures of **(a) 5-*rac*** and **(b) 5-*PP***.

While both enantiopure and racemic crystals exhibit *intra*molecular H-type π–π stacking between the macrocycle's two PDI units (d = 3.7 Å), only **5-*rac*** exhibits *inter*molecular J-type π–π stacking (d = 4.0 Å, centroid-centroid slip-angle = 42°) between the PDI macrocycles themselves. Furthermore, this intermolecular π–π stacking in **5-*rac*** is exclusively heterochiral, occurring between the ***M***-PDI unit of one macrocycle and the ***P***-PDI unit of a neighbour. No *inter*molecular π–π PDI-PDI interactions are observed in the crystal structure of **5-*PP***. Overall, the crystal packing shows how a mismatch in PDI chirality goes hand-in-hand with a slipped-stacked J-type arrangement, since the intermolecular π–π stacking can only occur between naphthalene sub-units on adjacent macrocycles of opposite chirality. These observations are consistent with the self-assembly studies in solution described previously.

3.8.4 Photophysical properties of 5-*rac* and 5-*PP* crystals

To provide further evidence that the self-assembled structure of **5-*rac*** in solution matches that in the single crystal, the UV-vis absorption spectra of **5-*rac*** and **5-*PP*** crystals were measured and compared to the absorption spectra of these samples in solution (**Figure 3.29**).

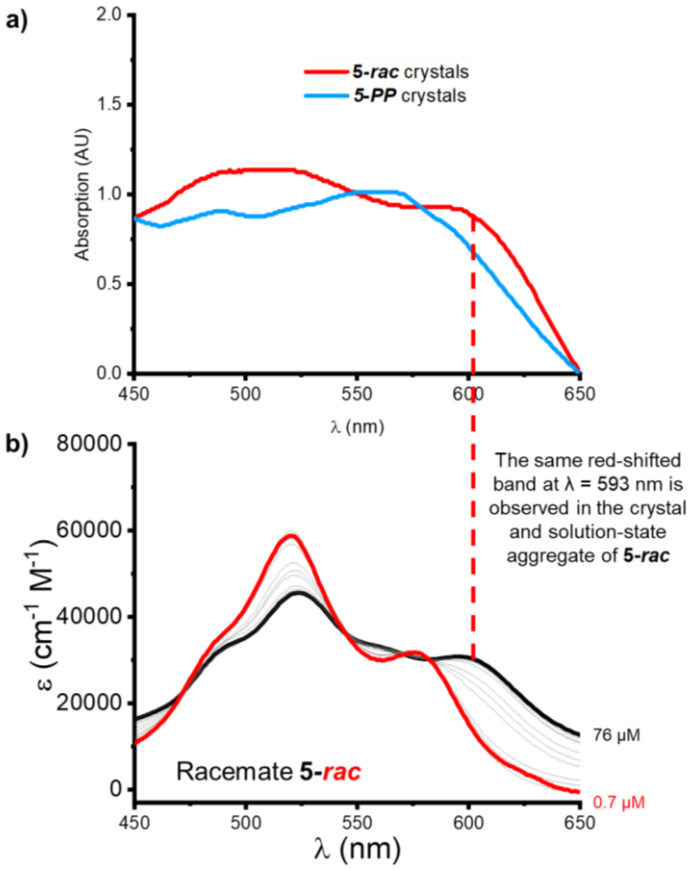

Figure 3.29: a) Solid state UV-vis absorption spectra for crystals of **5-*rac*** and **5-*PP***. See section 3.11 for further details. **b)** UV–vis absorption spectra of **5-*rac*** upon increasing the concentration (3:2 CH_2Cl_2:*n*-hexane).

For **5-*rac*** there is good agreement between solution spectra and solid-state UV-vis spectra, most notably the presence of the same, red-shifted absorption band seen upon aggregation in solution ($\lambda = 593$ nm), a feature not observed in the crystals or in the concentrated solution of **5-*PP***.

Additionally, the emission spectra of the crystals of **5-*rac*** and **5-*PP*** were recorded (**Figure 3.30**). Whilst the fluoresence emission of both is red-shifted relative to their spectra in toluene, the fluorescence emission in **5-*rac*** crystals is red-shifted relative to the **5-*PP*** crystals ($\Delta\lambda = 23$ nm). This is attributed to the additional intermolecular slipped-stack π–π interactions present in **5-*rac***.

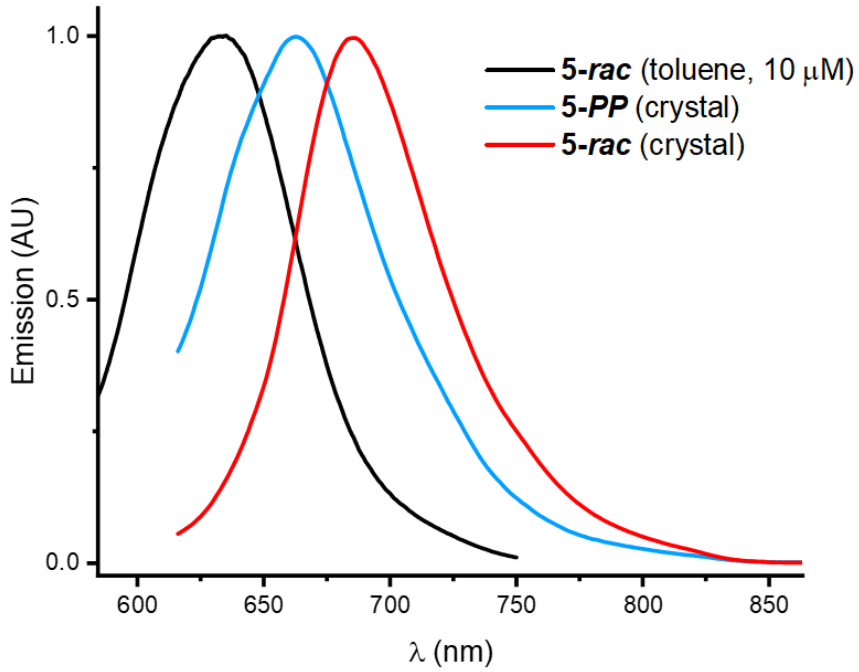

Figure 3.30: Normalised emission spectra for crystals of **5-*rac*** and **5-*PP*** as well as **5-*rac*** in toluene solution (10 μM, λ_{ex} = 520 nm).

3.9 Enantioselective Differential Chiral Contrast (EDCC) imaging of single crystals

Having established the chiroptical properties of macrocycle **5** and its chirality-dependent supramolecular organisation, the next aim was to understand how the structure impacts chiroptical properties in the solid state.

For this, Enantioselective Differential Chiral Contrast (EDCC) imaging of single crystals of **5-*rac***, **5-*PP***, and **5-*MM*** was performed using CPL Laser Scanning Confocal Microscopy (CPL-LSCM).[32] In CPL-LSCM, right- and left-handed left-circularly polarized photons are collected simultaneously from the sample, generating independent right and left CPL images rapidly. To ascertain the difference between the degree of left-handed- and right-handed-circularly polarized luminescence dominance, one of these images is subtracted from the other to generate an EDCC image. As such, it is possible to perform EDCC imaging of **5-*MM*** and **5-*PP*** crystals because they emit equal and opposite CPL. Importantly, while the **5-*rac*** and **5-*MM/PP*** crystals show emission in both the right- and left-handed CPL channels, only the enantiopure crystals exhibit a difference between the right and left CPL emission intensities (**Figure 3.31**). These are the first reported CPL-LSCM EDCC images of single crystals.

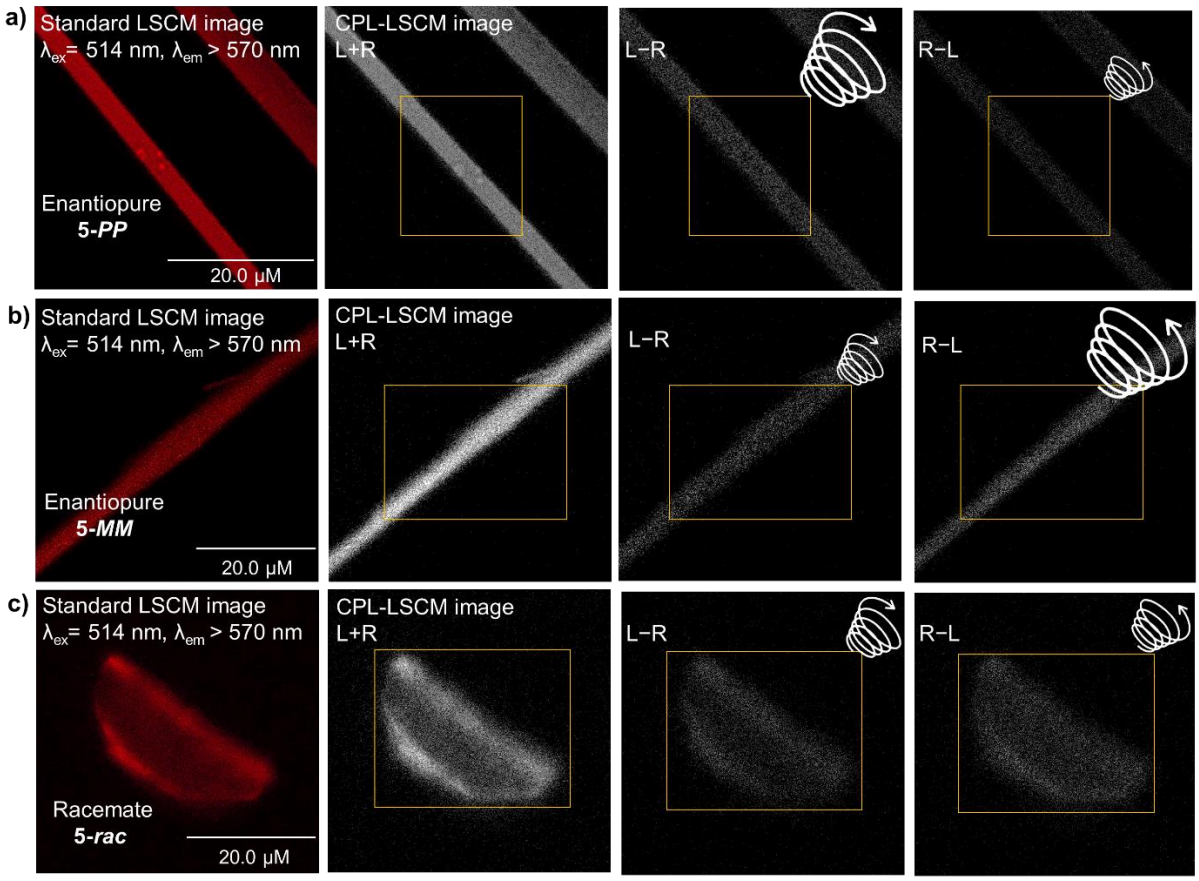

Figure 3.31: Standard and CPL-LSCM images (λ_{em} = 514 nm, Ar-laser, 2 mW) of single crystals of **a) 5-*PP***, (b) **5-*MM*** and (c) **1-*rac***. The yellow squares denote the area where the image brightness was measured.

Having distinct enantiopure and racemic single crystals provides the opportunity to quantify the degree of circularly polarized emitted light from single crystals for the first-time using CPL-LSCM, by calculating an EDCC dissymmetry factor (g_{EDCC}), which is analogous to the luminescence dissymmetry factor obtained by CPL spectroscopy (g_{lum}). In doing so, it is critical to correct for the inherent CPL bias arising from orientation induced reflection and subsequent partial helicity inversion of emitted circularly polarized light. Therefore, a bias factor ($B = 8 \times 10^{-3}$) was introduced, which is subtracted from the uncorrected (raw) EDCC values of the enantiopure crystals (Section 3.11.7). Importantly, this bias factor could be easily determined using the enantiopure **5-*MM*** and **5-*PP*** single crystal EDCC values. However, it is the **5-*rac*** racemic crystals that enable the validation of this system-specific bias factor as no overall CPL should be observed from **5-*rac*** since it is a racemic material. Incorporating the bias factor leads to **equation 3.5**:

$$g_{EDCC} = \frac{I_{(L-R)} - I_{(R-L)}}{2I_{(L+R)}} - B \qquad (3.5)$$

where g_{EDDC} is the enantioselective differential chiral contrast (EDCC) dissymmetry factor, $I_{(L-R)}$ is the left handed EDCC average 8-bit (0-255 greyscale) pixel value[32] (i.e., Left CPL − Right CPL), $I_{(L+R)}$ is the right handed EDCC average 8-bit pixel value (i.e., Right CPL − Left CPL), $I_{(L+R)}$ is the total image average 8-bit pixel value (Left CPL + Right CPL) and B is the bias factor (8×10^{-3}). Further details are given in section 3.11.7.

Equation 3.5 was then used to calculate a $|g_{\mathrm{EDCC}}|$ of 6×10^{-2} at $\lambda_{em} > 570$ nm for **5-*MM*** and **5-*PP*** single crystals (see section 3.11.7). Interestingly, the degree of emitted light circular polarization is three times higher in the crystalline state than in solution, most likely due to restricted molecular dynamics in the solid-state.[33-35] This includes rigidification of the homochiral intramolecular π–π dimer which, as found from self-assembly studies, is the primary PDI–PDI interaction in **5-*MM*/*PP***.

3.10 Summary and conclusions

This chapter has explored the development, synthesis, and characterisation of a 2nd generation "Pink Box" type bis-PDI macrocycle that is chirally locked (macrocycle **5**). Configurational stability was achieved by introduction of long, rigid imide groups (*tert*-butyl benzoate) that prevent the "intramolecular somersault" mechanism for stereoisomer interconversion, allowing stable enantiomers to be isolated. An advantage of configurationally stable enantiomers is that their chiroptical properties will persist over time, potentially making these materials solution-processable or possible to sublime at elevated temperatures. Solution processability is often required in many industrial processes for the manufacture of organic electronic devices.[36]

Interestingly, configurational stability allowed the discovery that the synthesis of macrocycle **5** is diastereoselective, forming exclusively as the pair of enantiomers **5**-***MM*** and **5**-***PP***, with no **5**-***MP*** diastereomer being observed. As such, homochiral templation must be occurring as part of the macrocyclisation process.

In terms of photophysical and chiroptical properties, chirally-locked macrocycle **5** behaves similarly to macrocycle **1**. However, the intramolecular homochiral dimer appears to be stronger in **5** because it could not be disrupted in chlorinated solvents, a feature which is likely responsible for stronger chiroptical properties ($|g_{\mathrm{lum}}| = 2 \times 10^{-2}$ for **5** and 1×10^{-2} for **1**). Macrocycle **5** enabled the calculation of $|g_{\mathrm{abs}}|$, which is an order of magnitude lower than $|g_{\mathrm{lum}}|$, demonstrating the importance of a chiral excimer state with excitonic coupling between the two chromophores for boosting CPL emission.[15-17] Notably, the degree of emitted light circular polarization is further amplified in single crystals of **5**-***MM/PP***, as shown by their enantioselective differential chiral contrast dissymmetry factor ($|g_{\mathrm{EDCC}}| = 6 \times 10^{-2}$), a value akin to a g_{lum} and calculated here for the first-time using CPL-Laser Scanning Confocal Microscopy. The ability to grow emissive racemic and enantiopure crystals was a requirement for this.

The *tert*-butyl benzoate imide groups also make the outer π-surfaces of the macrocycle more accessible, allowing the self-assembly of macrocycle **5** via *inter*molecular π–π interactions to be explored in both enantiopure and racemic mixtures. As for macrocycle **1** in the previous chapter, the *intra*molecular PDI-PDI interaction is exclusively cofacial (H-type) and homochiral, but further *inter*molecular self-assembly beyond the dimer limit is exclusively

slipped-stacked (J-type) and heterochiral. This is because the interior and exterior π-surfaces of the macrocycle are distinct as a result of the geometry of 1,7-disubstituted PDIs. From this, a general prediction can be made: when both π-surfaces of a twisted 1,7-disubstituted PDI are available for π–π self-assembly, homochiral H-type dimerization on the less sterically hindered face is followed by heterochiral J-type slipped-stacking on the remaining π-surface (**fig**). As such, racemic macrocycle **5-*rac*** self-assembles into an extended J-type aggregate of H-type dimers.

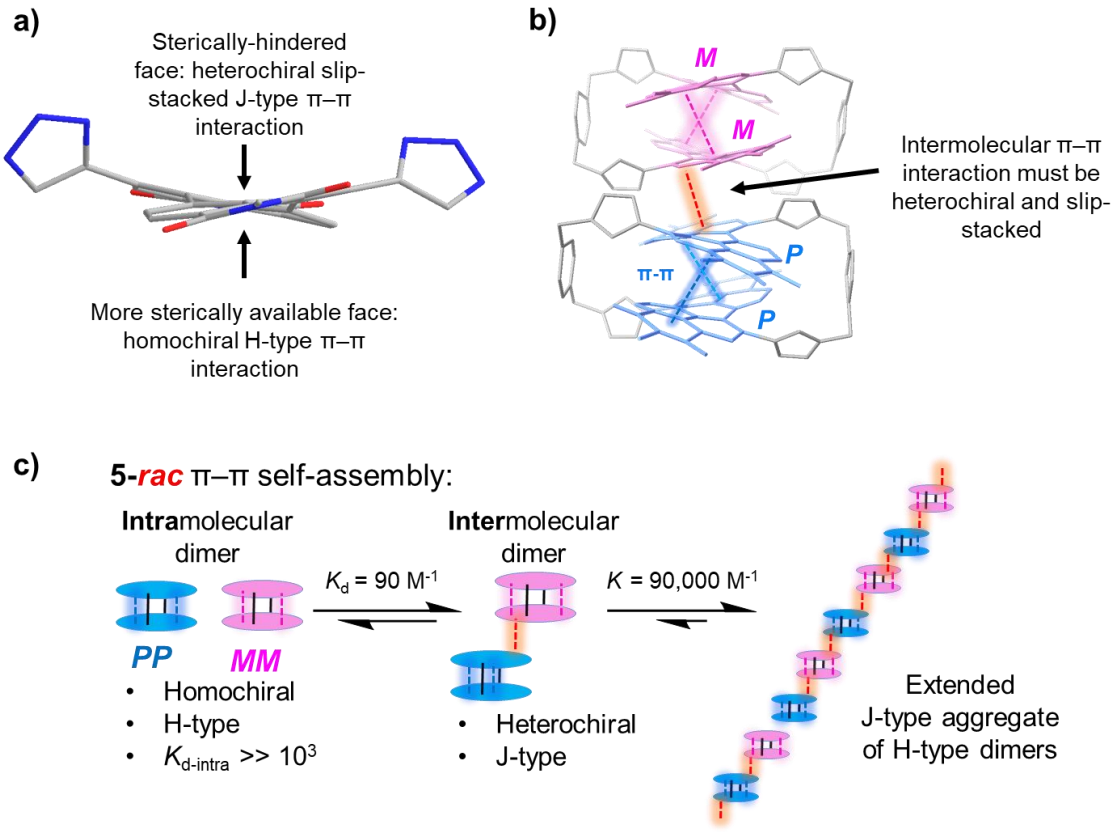

Figure 3.32: a) Depiction of the two distinct π-surfaces in a 1,7-disubstituted bistriazole PDI and their chiral requirements for self-assembly. **b)** Depiction of the slip-stacked heterochiral interaction required for self-assembly of macrocycle **5** via π-π on its outer π-surfaces. **c**) Schematic of the π–π self-assembly of **5-*rac***.

Therefore, this work shows that the chirality of the disubstituted PDI building block provides a rational route to designing H- and J-type aggregates as well as materials that simultaneously contain both H- and J-type aggregates, with **5-*rac*** providing a unique demonstration of the latter for twisted PDIs. This discovery seeds the possibility of scalemic materials[37] that synergise H- and J-type coupling between chiral chromophores to the mutual

benefit of photon polarisation and exciton transport, for the manipulation of circularly polarised light. The following chapter will seek to further explore the relationship between the chirality of PDI-PDI interactions and their photophysical properties.

3.11 Experimental

3.11.1 Materials and methods

All commercial solvents and reagents were used as purchased, unless otherwise stated. Anhydrous solvents were degassed with N_2 and dried using an Innovative Technology PureSolv MD 5 solvent purification system. $Cu(MeCN)_4 \cdot PF_6$ was stored in a desiccator. Tris((1-benzyl-4-triazolyl)methyl)amine (TBTA) was prepared following a literature procedure.[38] Water was distilled and microfiltered using an ELGA DV 35 Purelab water purification system. Chromatography was undertaken using silica gel (particle size: 40-63 μm) or preparative TLC plates (20 × 20 cm, 1 cm silica thickness).

^{1}H and ^{13}C NMR spectra were recorded using Bruker AVIII400 (400 MHz), Bruker AV NEO 400 (400 MHz) and Bruker AV NEO 500 (500 MHz, with cryoprobe). Mass spectra were recorded using a Bruker UltrafleXtreme MALDI-TOF mass spectrometer or a Waters Synapt G2-S mass spectrometer for high resolution MS-ESI. Details of equipment used for other analytical techniques (CPL-LSCM microscopy, CD and CPL spectroscopies, photophysics, HPLC etc.) are provided in their appropriate sub-sections in this experimental section.

Synthesis of macrocycle 1

The synthesis of bis-PDI macrocycle **5** was carried out as shown below. Compound **6** was previously prepared in-house by another lab member (Angus Yeung) according to a literature procedure[39] as a mixture of mono-, bis-, tris- and tetra-bromo isomers that could not be separated using chromatography at this stage due to poor solubility. Compounds **7**, **8** and **9** were isolated as a mixture of 1,6 and 1,7 PDI regioisomers. Macrocycle **5** was isolated as the pure 1,7 regioisomer since removal of the 1,6 regioisomer was possible by silica gel column chromatography at this stage. 1,4- bis(azidomethyl)benzene was prepared by Angus Yeung following the **safety precautions for the handling of organic azide compounds described in section 2.9.2**.

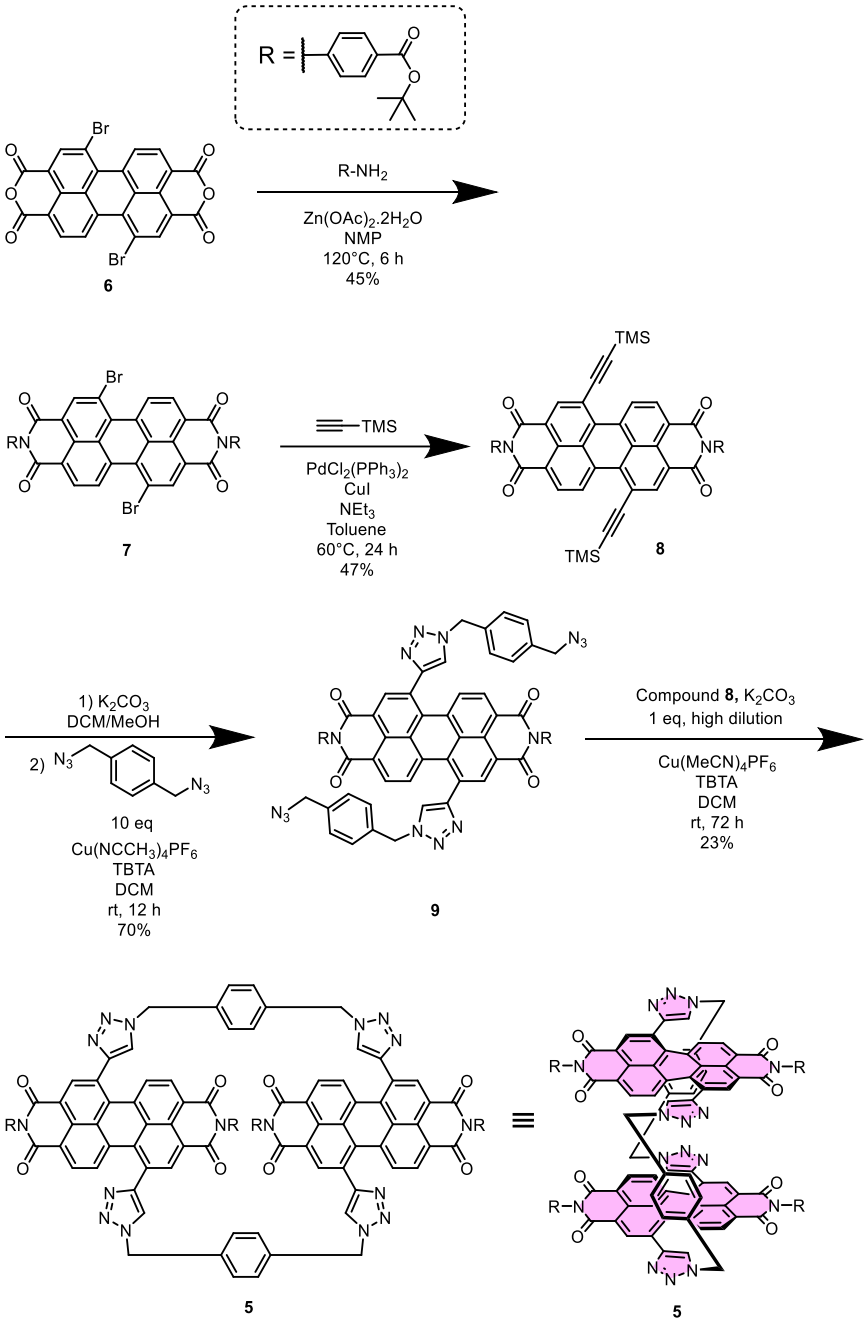

Multistep synthesis of bis-PDI macrocycle **5**.

Bis-bromo PDI 7

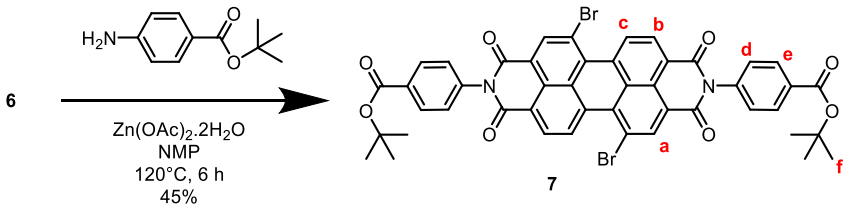

Compound **6** (a mixture of mono-, bis-, tris- and tetra-bromo perylenetetracarboxylic dianhydride, 1 g) was added to a flask containing N-Methyl-2-pyrrolidone (10 mL). To this was added tert-butyl 4-aminobenzoate (1.05 g, 5.45 mmol, 3 equiv) and $Zn(OAc)_2.2H_2O$ (678 mg, 3.09 mmol, 2 equiv). This mixture was purged with nitrogen and stirred at 120 °C for 6 hours. The reaction was then allowed to cool to rt, which yielded a red precipitate. The precipitate was collected by vacuum filtration, and thoroughly washed with water and then dried under vacuum. The resulting red residue was then purified by silica gel flash column chromatography (1:160 MeOH:$CHCl_3$), affording compound **7** as a mixture of 1,6 and 1,7 bis-bromo isomers (733 mg, 813 µmol, 45% yield if compound **6** was pure bis-bromo perylenetetracarboxylic dianhydride).

^{1}H NMR (500 MHz, Chloroform-*d*, 1,7-isomer) δ 9.58 (d, J = 8.1 Hz, $2H_b$), 9.01 (s, $2H_a$), 8.80 (d, J = 8.1 Hz, $2H_c$), 8.25 – 8.22 (m, $4H_d$), 7.44 – 7.42 (m, $4H_e$), 1.66 (s, $18H_f$).

^{13}C NMR (126 MHz, Chloroform-*d*) δ 164.89, 162.81, 162.29, 138.43, 138.33, 133.51, 133.30, 132.77, 130.73, 130.58, 129.52, 128.60, 127.37, 123.19, 122.78, 121.10, 81.49, 28.22.

HRMS (ESI) (m/z) calculated for $C_{46}H_{33}Br_2N_2O_8^+$ $[M+H]^+$ 899.0601, found 899.0604

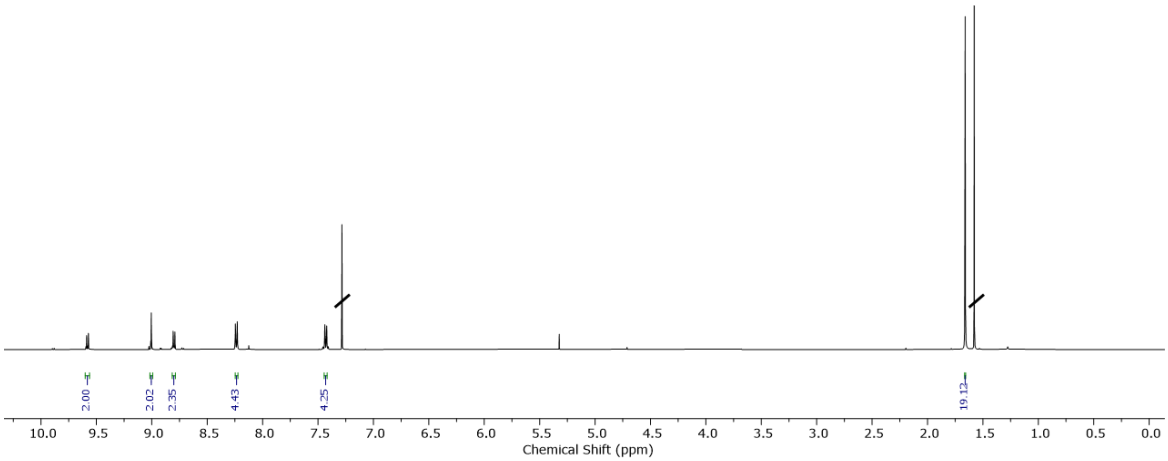

^{1}H NMR spectrum of compound **7** (chloroform-d, 298 K, 500 MHz)

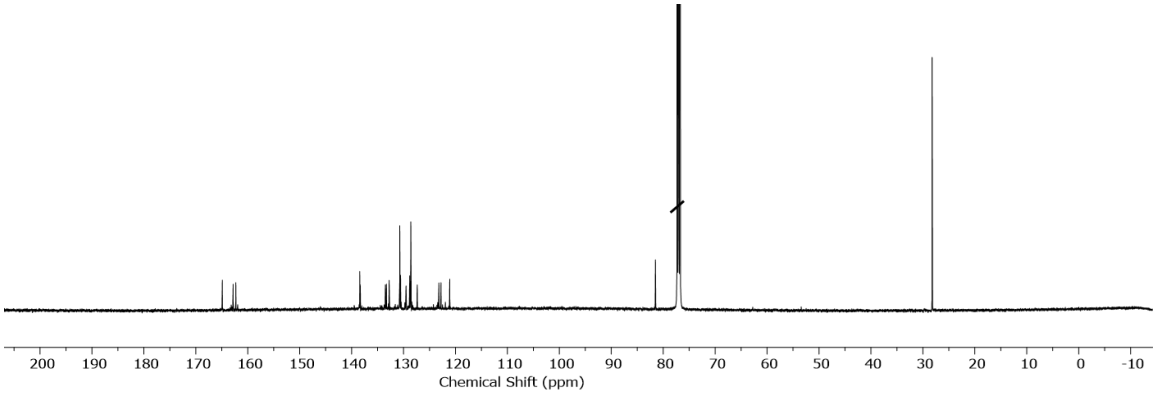

^{13}C NMR spectrum of compound **7** (chloroform-d, 298 K, 126 MHz)

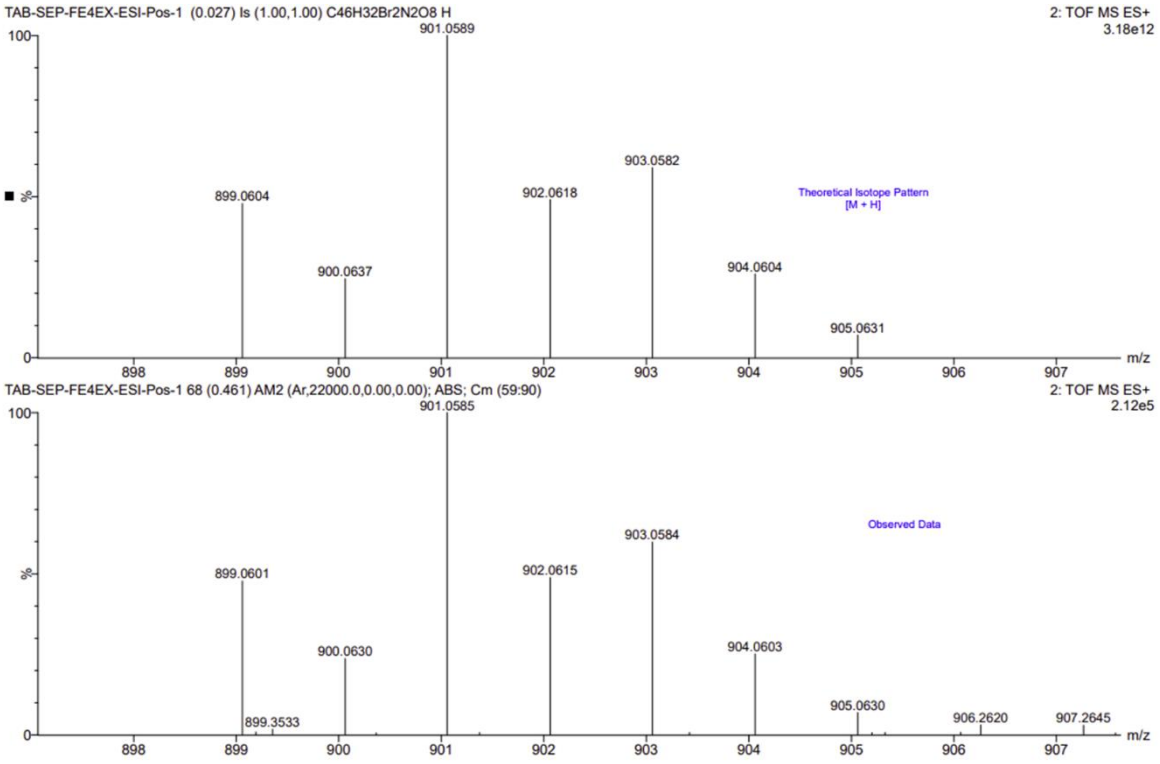

Calculated (top) and observed (bottom) ESI MS data for compound **7**.

TMS-protected bis-alkyne PDI 8

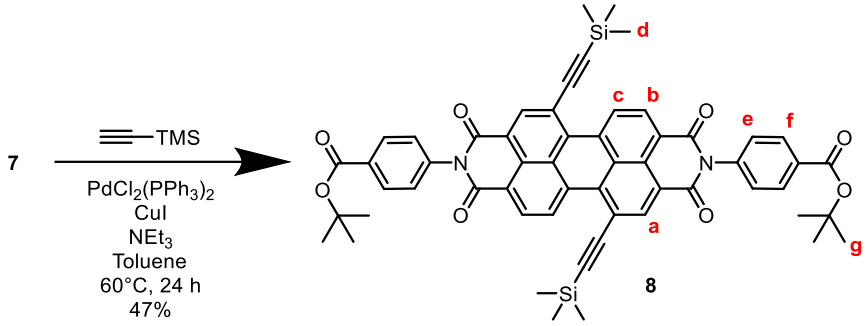

To a solution of bis-bromo PDI **7** (600 mg, 666 µmol) in 1:1 dry NEt_3-toluene (250mL) under a nitrogen atmosphere was added $Pd(PPh_3)_2Cl_2$ (28 mg, 40 µmol, 0.06 equiv), CuI (14 mg, 73 µmol, 0.11 equiv) and trimethylsilylacetylene (327 mg, 474 µL, 3.33 mmol, 5 equiv). The mixture was thoroughly de-gassed with nitrogen and stirred at 60 °C for 24 h. The solvent mixture was then removed in vacuo. The resulting residue was then re-dissolved in DCM (100 mL) and washed with 1 M HCl (50 mL) and water (3 x 50 mL); dried over anhydrous $MgSO_4$ and concentrated to dryness in vacuo. The resulting residue was purified by silica gel flash column chromatography (1:1 n-hexane:DCM) affording the title compound as a red solid as a mixture of 1,6 and 1,7-regiosiomers (297 mg, 318 µmol, 48%).

^{1}H NMR (500 MHz, Chloroform-*d*, 1,7 isomer) δ 10.20 (d, J = 8.2 Hz, $2H_b$), 8.83 (s, $2H_a$), 8.65 (d, J = 18.5 Hz, $2H_c$), 8.23 – 8.19 (m, $4H_e$), 7.45 – 7.41 (m, $4H_f$), 1.64 (s, $18H_g$), 0.40 (s, $18H_d$)

^{13}C NMR (126 MHz, Chloroform-*d*) δ 165.13, 163.16, 162.84, 138.85, 138.66, 138.53, 134.80, 134.48, 132.76, 131.06, 130.98, 130.80, 130.67, 128.98, 128.86, 128.82, 128.77, 128.08, 127.99, 127.73, 123.30, 122.19, 120.94, 120.36, 107.06, 106.75, 105.51, 105.45, 81.58, 29.85, 28.37, -0.23

HRMS (ESI) (m/z) calculated for $C_{56}H_{51}N_2O_8Si_2$ $[M+H]^+$ 935.3184, found 935.3182.

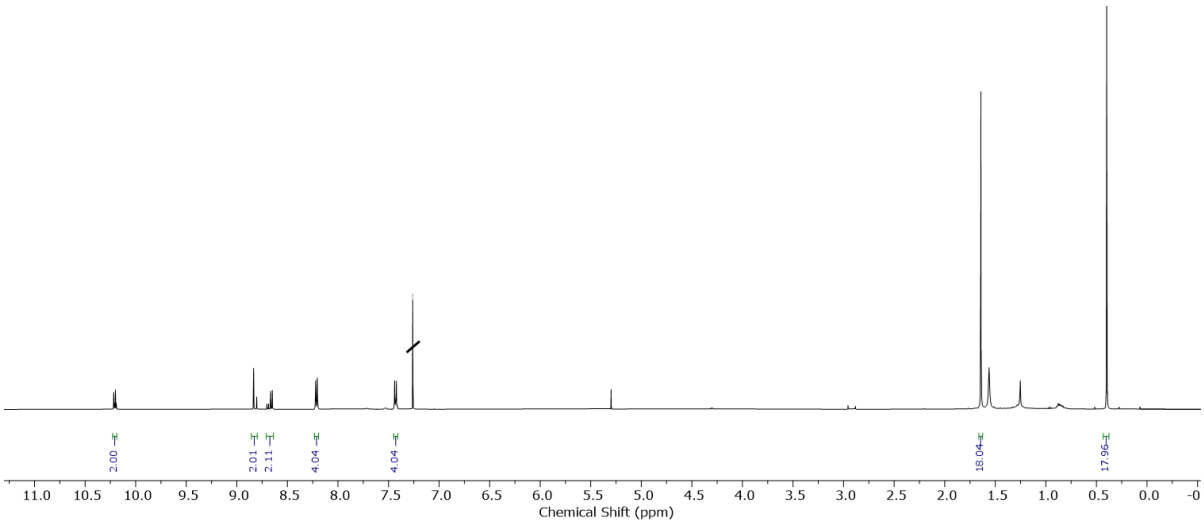

^{1}H NMR spectrum of compound **8** (chloroform-d, 298 K, 500 MHz).

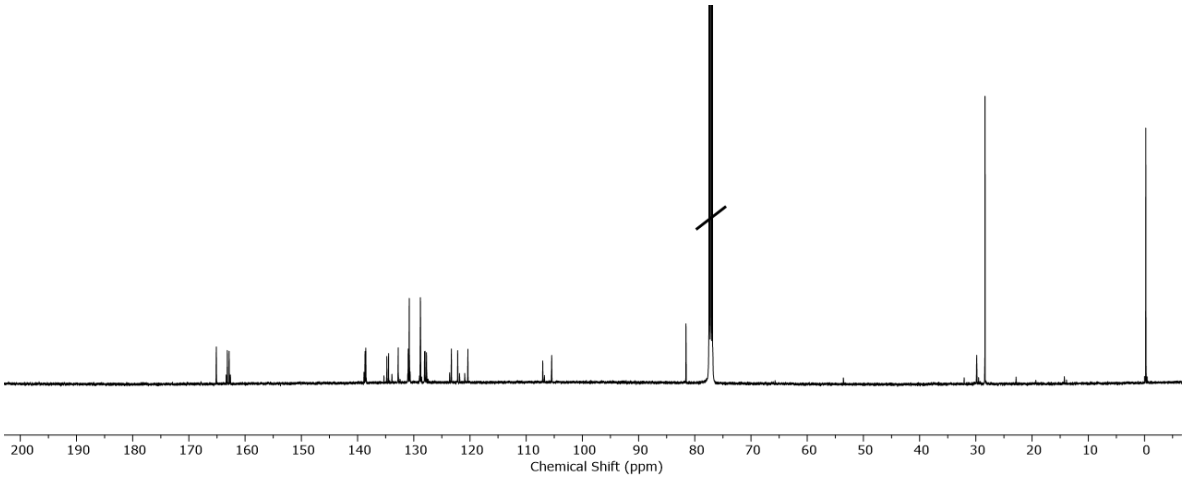

^{13}C NMR spectrum of compound **8** (chloroform-d, 298 K, 126 MHz)

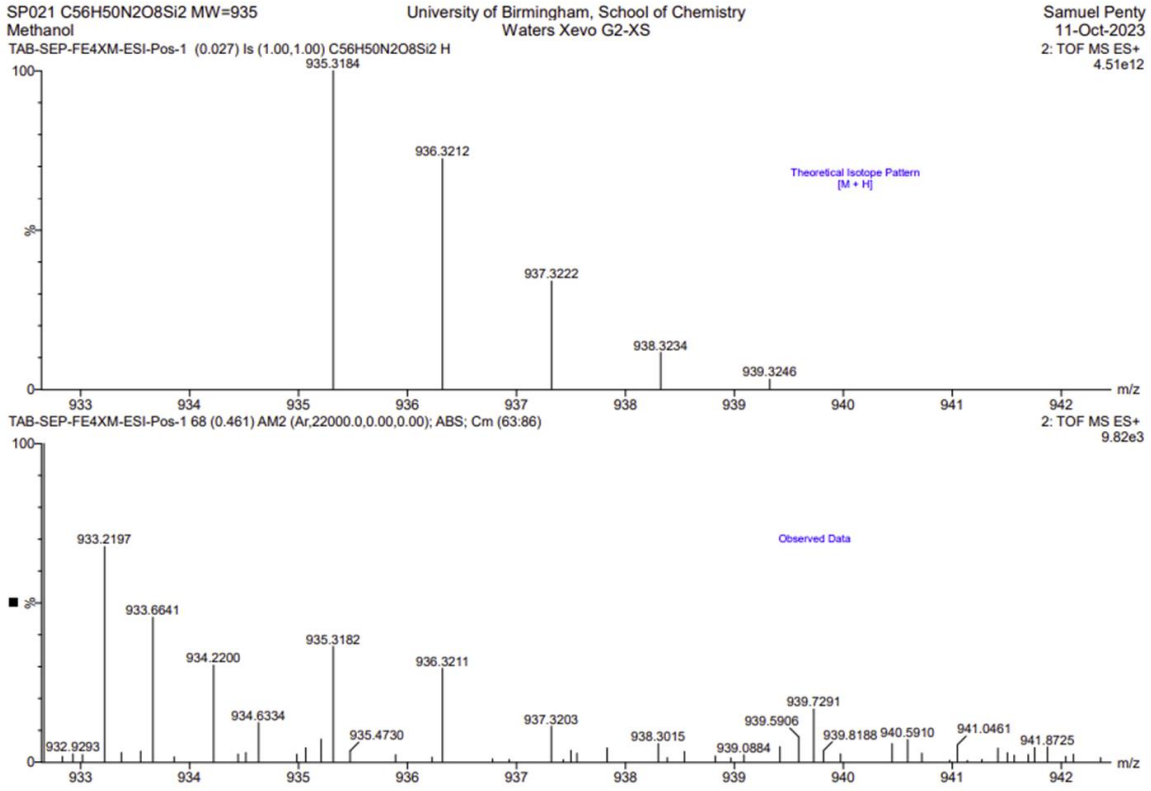

Calculated (top) and observed (bottom) ESI MS data for compound **8**.

Acyclic bis-triazole PDI 9

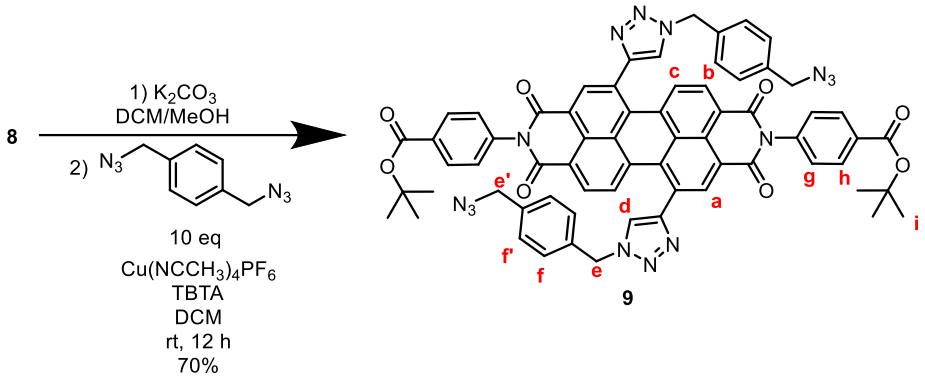

To a solution of TMS-protected bis-alkyne PDI **8** (70 mg, 75 µmol) in DCM (20 ml) was added K_2CO_3 (30 mg) in MeOH (10 ml). The mixture was stirred at rt for 3 min, and completion of the reaction was confirmed by TLC. The solution was then washed with water (2 x 30 mL) and brine (30 ml). The organic layer was then dried over anhydrous $MgSO_4$ and concentrated to dryness in vacuo to afford the deprotected PDI bis-alkyne which was used immediately without further purification. This PDI bis-alkyne was immediately re-dissolved in dry DCM (30 mL). To this was added 1,4- bis(azidomethyl)benzene (142 mg, 758 µmol, 10 equiv) and tris((1-benzyl-4- triazolyl)methyl)amine (TBTA) (16 mg, 30 µmol, 0.2 equiv). The solution was then de-gassed with argon. The copper (I) catalyst $Cu(CH_3CN)_4PF_6$ (11 mg, 30 µmol, 0.2 equiv) was then added and the solution was once again de-gassed with argon. The reaction was stirred at rt for 12 h. The solvent was then removed in vacuo. The resulting residue was purified by silica gel flash column chromatography (1:99 MeOH-DCM) affording the title compound as a purple solid as a mixture of 1,6 and 1,7-regiosiomers (62 mg, 53 µmol, 70%).

^{1}H NMR (500 MHz, Chloroform-*d*, 1,7 isomer) δ 8.67 (s, $2H_a$), 8.22 – 8.17 (m, $4H_g$), 8.15 (d, J = 8.1 Hz, $2H_b$), 7.84 (d, J = 8.0 Hz, $2H_c$), 7.63 (s, $2H_d$), 7.40 – 7.35 (m, $12H_{h,f,f'}$), 5.64 (s, $4H_e$), 4.36 (s, $4H_{e'}$), 1.63 (s, $18H_i$).

^{13}C NMR (126 MHz, Chloroform-*d*) δ 165.08, 163.15, 163.07, 148.12, 138.75, 136.86, 135.31, 135.01, 134.56, 133.97, 132.73, 130.79, 130.22, 129.99, 129.50, 129.43, 129.29, 129.22, 129.08, 128.78, 128.67, 128.64, 128.60, 122.69, 122.49, 122.11, 121.93, 81.57, 54.39, 54.28, 28.35.

HRMS (ESI) (m/z) calculated for $C_{66}H_{50}N_{14}O_8^+$ $[M+H]^+$ 1167.4015, found 1167.4026.

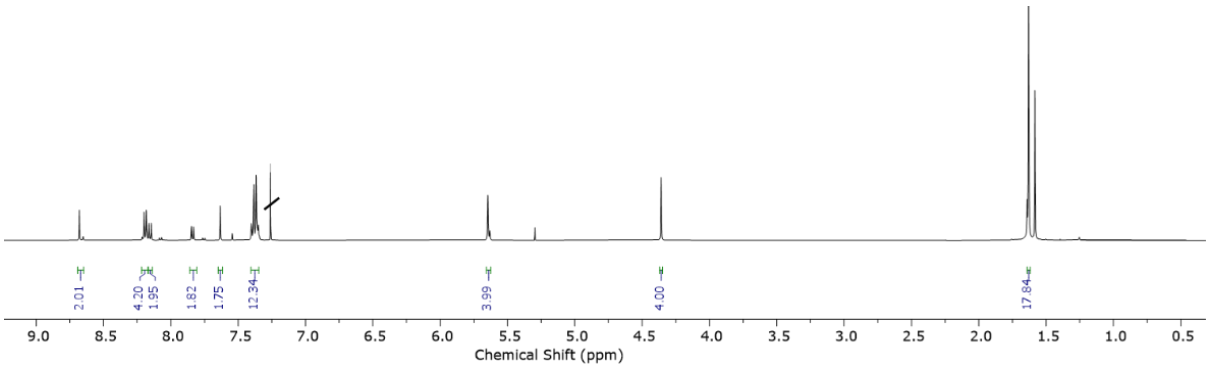

^{1}H NMR spectrum of compound **9** (chloroform-*d*, 298 K, 500 MHz).

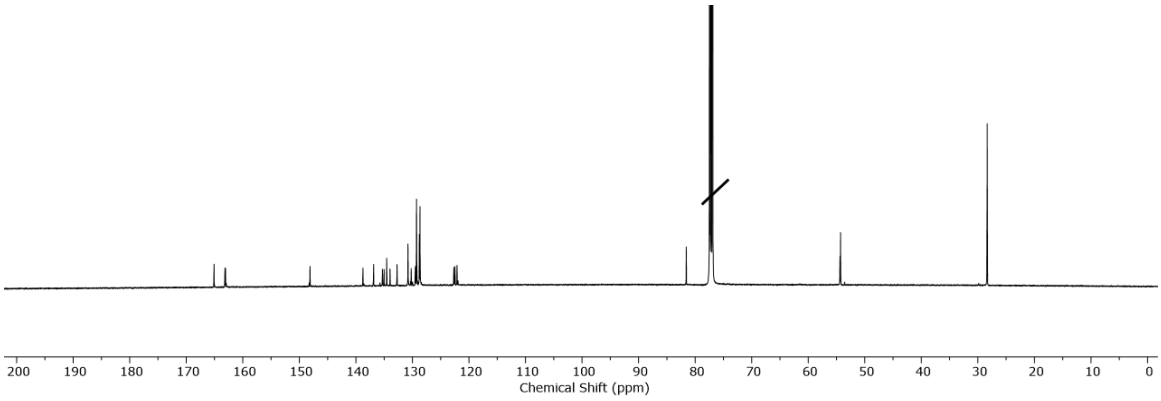

^{13}C NMR spectrum of compound **9** (chloroform-*d*, 298 K, 126 MHz).

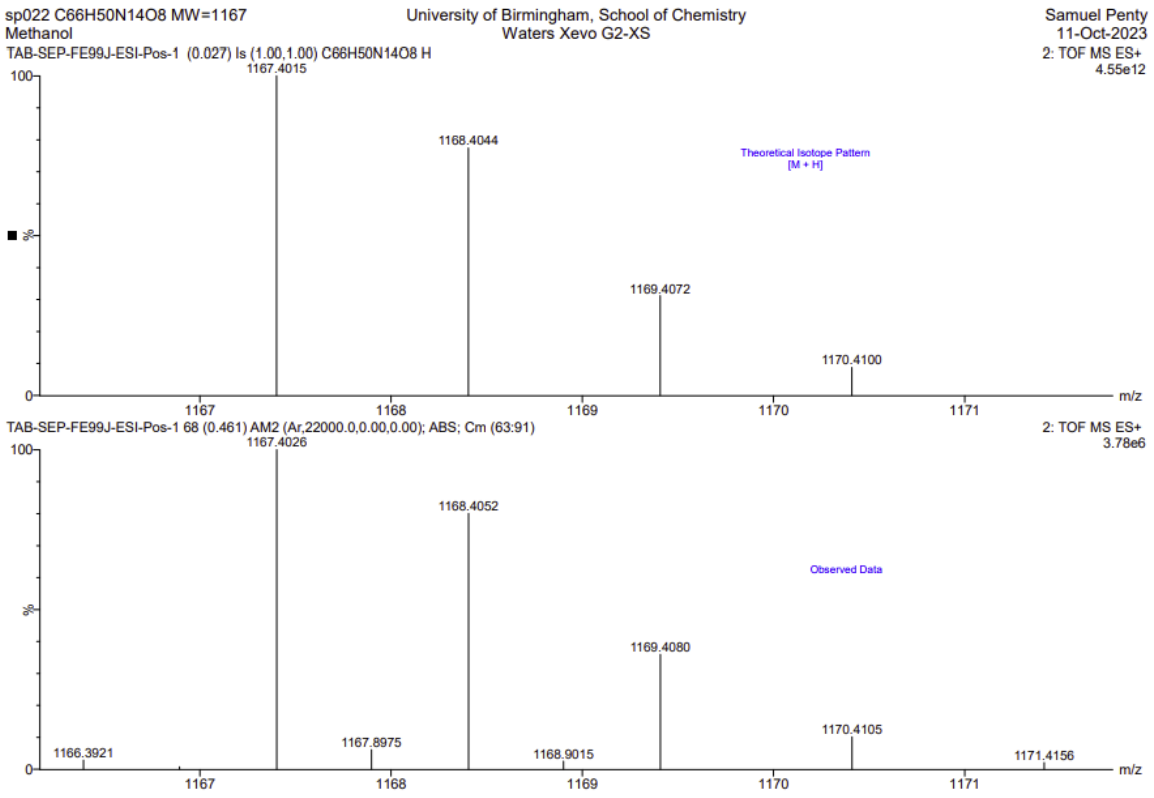

Calculated (top) and observed (bottom) ESI MS data for compound **9**.

Bis-PDI macrocycle 5

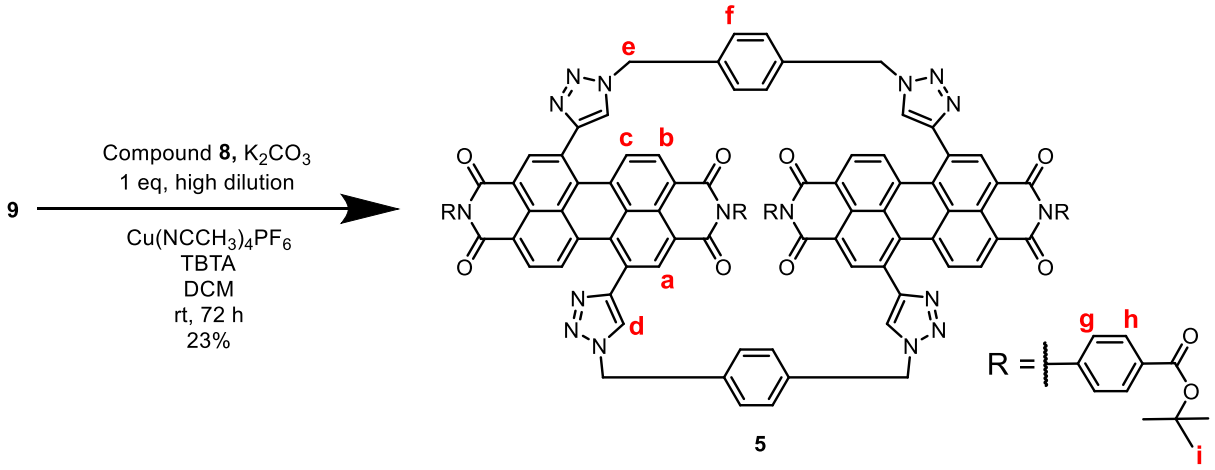

TMS-protected bis-alkyne PDI **8** (50 mg, 53 µmol) was dissolved in DCM (20 mL). To this was added K_2CO_3 (20 mg) in MeOH (10 mL). The reaction was monitored by TLC (1:99 MeOH:DCM). Upon completion the reaction mixture was thoroughly washed with water in a separating funnel (3 x 100 mL) and dried with $MgSO_4$ to yield crude deprotected bis-alkyne PDI in DCM, which was used immediately without further purification due to its tendency to aggregate and crash out of solution over time. This was added to a flask, along with acyclic bis-triazole PDI **9** (62 mg, 53 µmol, 1 equiv), tris((1-benzyl-4-triazolyl)methyl)amine (TBTA) (12 mg, 21 µmol, 0.4 eq) and a further 350 mL of DCM. The reaction mixture was thoroughly de-gassed with N_2. The copper catalyst $Cu(CH_3CN)_4PF_6$ (8 mg, 21 µmol, 0.4 equiv) was then added and the reaction mixture was thoroughly de-gassed again. The reaction was stirred at rt for 36 h and monitored by TLC (2:98 MeOH-DCM). The solvent was then removed *in vacuo*. The resulting residue was dissolved in DCM and filtered through cotton wool and the filtrate was then purified by preparative silica TLC (2:98 MeOH-DCM), affording the title compound (as the pure 1,7-regioisomer) as a purple solid (24 mg, 12 µmol, 23%).

^{1}H NMR (400 MHz, 373K, TCE-d_2) δ 8.28 (s, 4H$_d$), 8.23 (d, J = 8.2 Hz, 8H$_g$), 8.20 (s, 4H$_a$), 7.96 (s, 8H$_f$), 7.64 (d, J = 8.3 Hz, 4H$_b$), 7.58 (d, J = 8.2 Hz, 8H$_h$), 6.05 (d, J = 13.8 Hz, 4H$_e$), 5.64 (d, J = 8.3 Hz, 4H$_c$), 5.59 (d, J = 13.9 Hz, 4H$_e$), 1.72 (s, 36H$_i$).

^{13}C NMR (101 MHz, TCE-d_2) δ 165.13, 162.00, 138.35, 133.40, 130.70, 130.06, 129.44, 129.19, 121.53, 99.91, 81.88, 74.45, 74.17, 73.90, 32.03, 29.79, 29.41, 29.24, 28.52, 25.01, 22.75, 14.11.

HRMS (ESI) (m/z) calculated for $C_{116}H_{85}N_{16}O_{16}^{+}$ $[M+H]^{+}$ 1957.6329, found 1957.6272

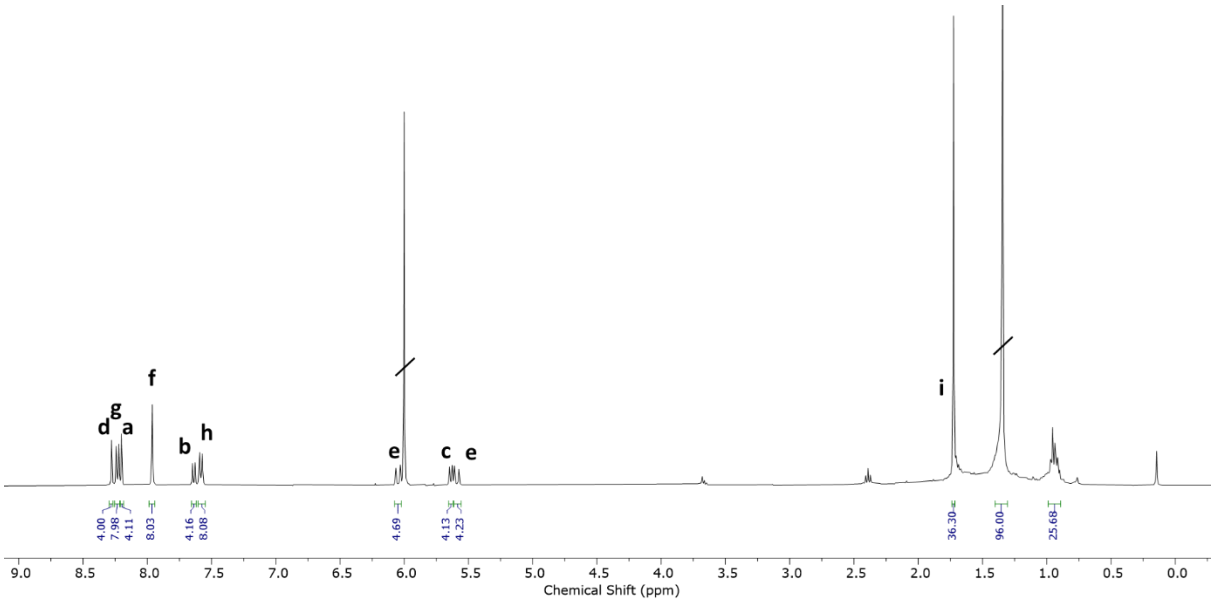

^{1}H NMR spectrum of macrocycle **5** (TCE-d_2, 373 K, 400 MHz).

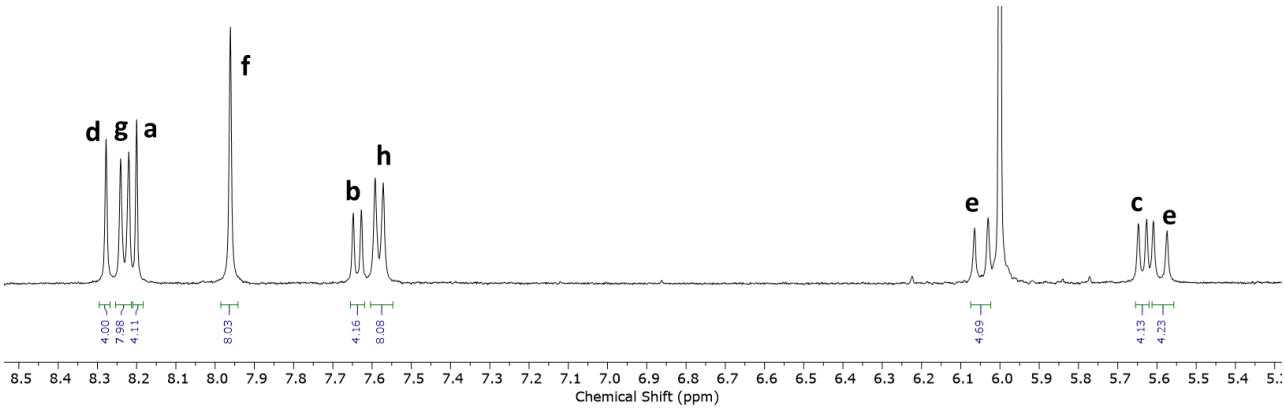

Aromatic region of the ^{1}H NMR spectrum of macrocycle **5** (TCE-d_2, 373 K, 400 MHz).

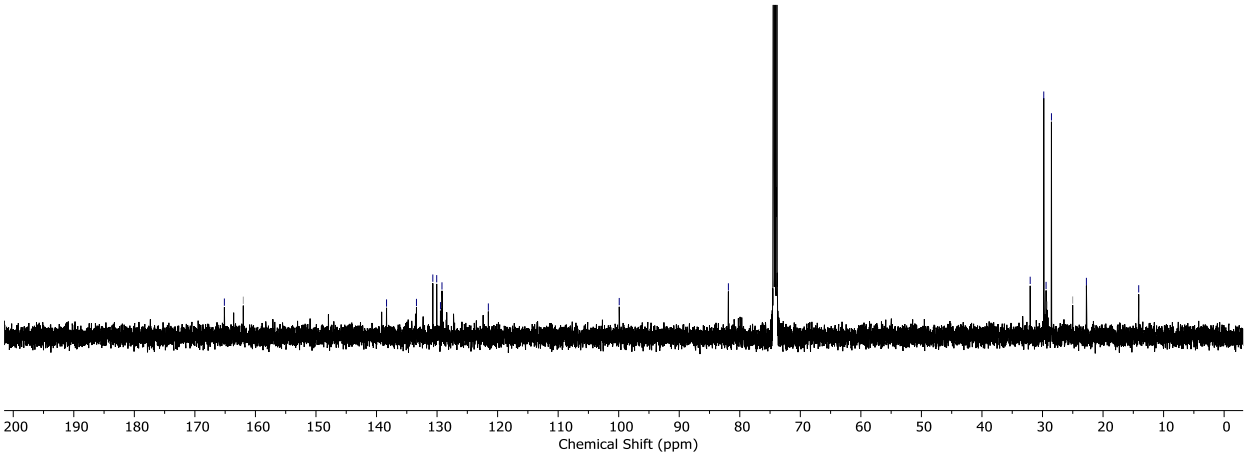

^{13}C NMR spectrum of macrocycle **5** (TCE-d_2, 373 K, 400 MHz). The poor signal to noise ratio is due to the large number of quaternary carbons and the somewhat low solubility of macrocycle **5**.

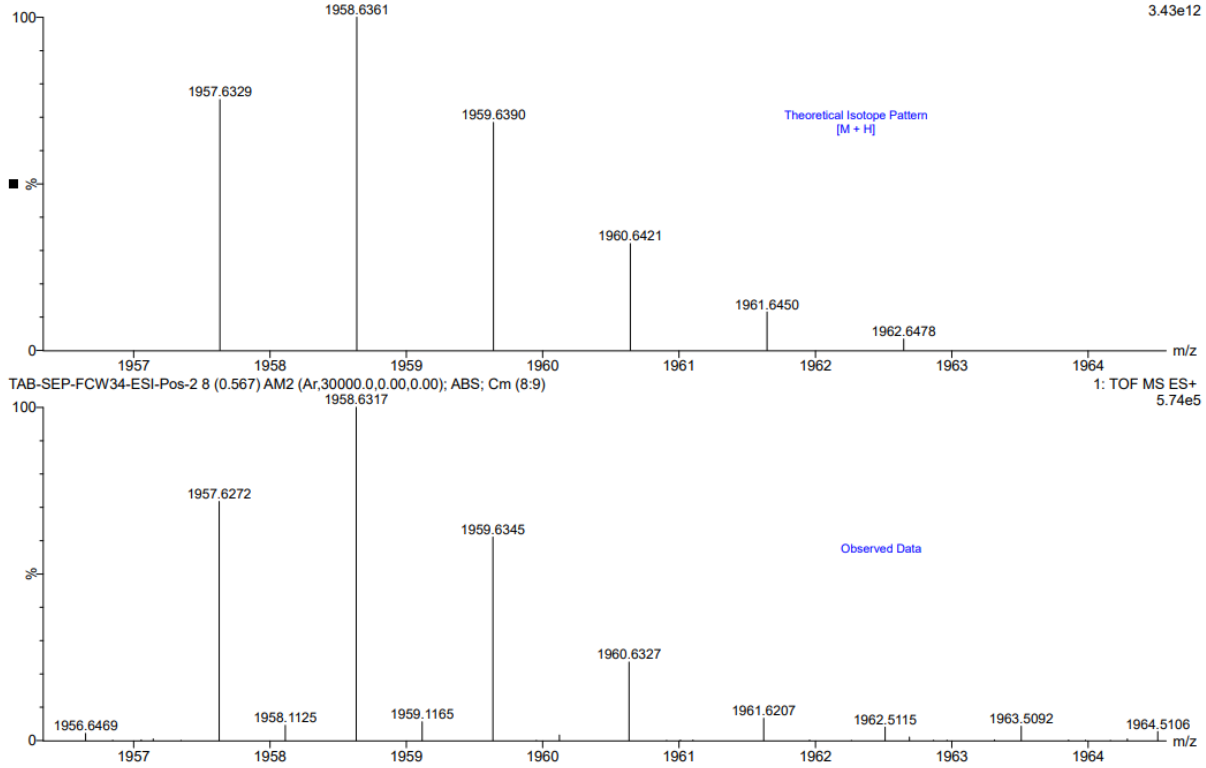

Calculated (top) and observed (bottom) ESI MS data for macrocycle **5**.

3.11.2 HPLC analysis

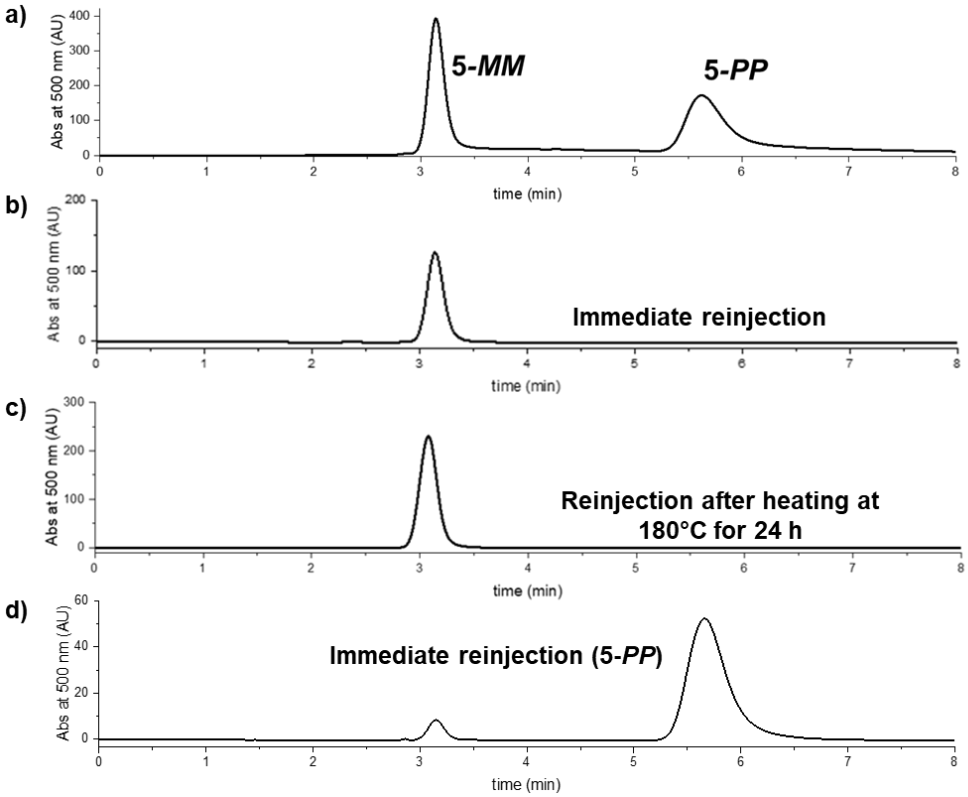

Figure 3.33: Chiral HPLC chromatograms (Phenomenex i-Amylose-1, 250 x 4.6 mm, injection volume 50 µL, ~ 2 mg/mL, eluted with 9:1 (v/v) DCM:methanol) of **a)** pure racemic macrocycle 5-rac, **b)** a sample of enantiomer 5-MM, reinjected immediately after isolation by chiral HPLC, **c)** a sample of enantiomer **5-*MM***, heated at 180°C for 24 h and then reinjected into the chiral HPLC column, and d) a sample of **5-*PP*** reinjected immediately after isolation by chiral HPLC, from which an enantiomeric excess (ee) of 90% can be determined for **5-*PP***.

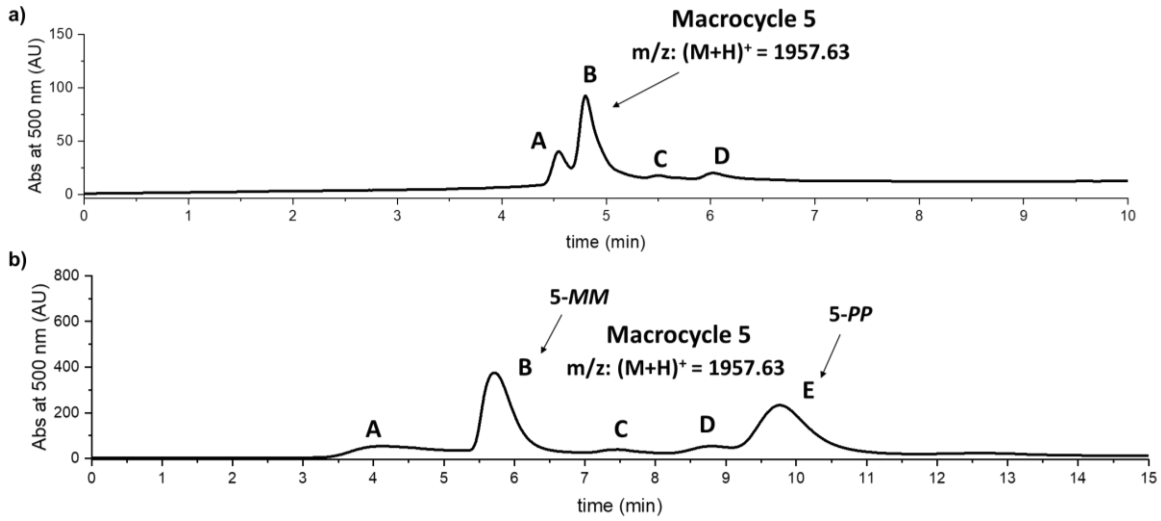

Figure 3.34: a) HPLC chromatogram (COSMOSIL Buckyprep 250 x 10 mm, injection volume 50 µL, ~ 2 mg/mL, eluted with 9:1 (v/v) DCM:methanol) of the crude reaction mixture of macrocycle **5**. Peaks A-D were collected and analysed by ESI-MS. Macrocycle **5** was only present in peak B (m/z = 1958) which, when resolved by chiral HPLC, contains only the enantiomers **5-*MM*** and **5-*PP***. Peak integral ratio (A:B:C:D) = 8:24:6:6. **b)** Chiral HPLC chromatogram (Phenomenex i-Amylose-1, 250 x 10 mm, injection volume 100 µL, ~ 2 mg/mL, eluted with 9:1 (v/v) DCM:methanol) of the crude reaction mixture of macrocycle **5**. Peaks A-E were collected and analysed by ESI-MS. Macrocycle **5** was only present in peaks B and E (m/z = 1958) which, as identified by CD-spectroscopy, are **5-*MM*** and **5-*PP*** respectively. Peak integral ratio (A:B:C:D:E) = 7:21:3:4:21.

3.11.3 X-ray crystallography

I thank Dr Georgia Orton for performing X-ray crystallography, including solving of the crystal structure.

Racemic macrocycle 5-*rac*

Purple, needle-like crystals of macrocycle **5-*rac***, suitable for single crystal X-ray diffraction, were grown by slow diffusion of methanol into a chloroform solution.

Single crystal X-ray diffraction experiments were performed by the UK National Crystallography Service on a Rigaku 007HF diffractometer with HF Varimax confocal mirrors, an UG2 goniometer and HyPix 6000HE detector.

The crystals were kept at 100(2) K during data collection. The structures were solved by direct methods using ShelXT[40] and refined with ShelXL[41] using a least squares method. Olex2 software was used as the solution, refinement and analysis program.[42]

The crystal diffracted weakly with a low-resolution diffraction limit; the data was truncated to a resolution of 1.00 A. Many attempts were made to grow stronger diffracting crystals, and this sample was sent to the synchrotron on several occasions. This dataset from the UK National Crystallography Service (NCS) gave the best refinement.

All non-hydrogen atoms were refined anisotropically. All hydrogen atoms were geometrically placed and refined using a riding model. Owing to the weak data, all methyl groups were placed in eclipsed conformations (AFIX 33) rather than having their torsion angles refined against a search of the Fourier map. This method aided convergence of the refinement. Restraints and constraints were applied to the structure to aid refinement. The anisotropic displacement parameters of tertiary carbon atoms C32, C43, C78, and C89 in the t-butyl ester groups were constrained to be identical (EADP). The anisotropic displacement parameters of carbon atoms C90, C91, and C92, which from a t-butyl group with tertiary carbon C86, were constrained to be identical (EADP) and the C-C bond lengths of the bonds carbon atoms C90, C91, C92 form with carbon atom C89 were restrained to have similar distances (SADI). The anisotropic displacement parameters of CH3 carbon atoms C35 C34 C33 C45 C44 C46 C79 C80 C81 of the remaining three t-butyl groups were restrained to be similar (SIMU). The anisotropic displacement parameters of oxygen atoms O1, O2, O3, O4, O9, O10, O11, and O12 were restrained to be similar (SIMU).

Due to poor data quality residual solvent could not be sensibly modelled. A solvent mask was calculated and 469 electrons were found in a volume of 1757 cubic angstrom in 1 void per unit cell. This is consistent with the presence of 13 methanol molecules per Asymmetric Unit which account for 468 electrons per unit cell.

Crystal Data for macrocycle **5-*rac***: $C_{116}H_{84}N_{16}O_{16}$ (M = 1958 g/mol): triclinic, space group P-1, a = 17.357(3) Å, b = 18.793(3) Å, c = 21.113(3) Å, α = 103.153(12)°, β = 94.994(11)°, γ = 115.198(16)°, V = 5934.2(17) $Å^3$, Z = 2, T = 100.15 K, μ(Cu Kα) = 0.784 mm^{-1}, *Dcalc* = 1.329 g/cm^3, 30226 reflections measured (5.436° ≤ 2Θ ≤ 100.868°), 11839 unique (R_{int} = 0.1886, R_{sigma} = 0.3929) which were used in all calculations. The final R_1 was 0.1226 (I > 2σ(I)) and wR_2 was 0.4448 (all data). Deposited cif number: 2308898

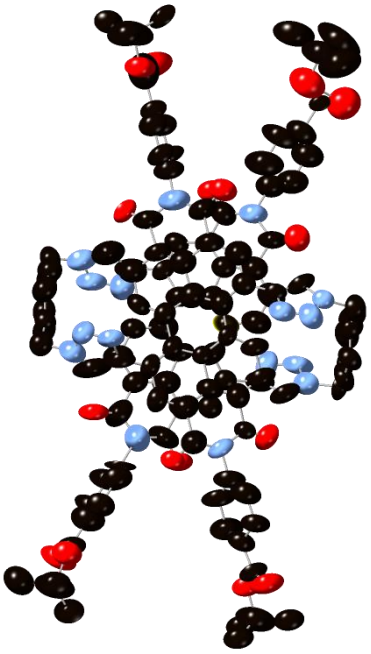

Figure 3.35: Molecular unit of macrocycle **5** from the **5-*rac*** crystal structure with all non-hydrogen atoms represented by ellipsoids at the 50% probability level. Hydrogen atoms omitted for clarity (C, black; O, red; N, blue).

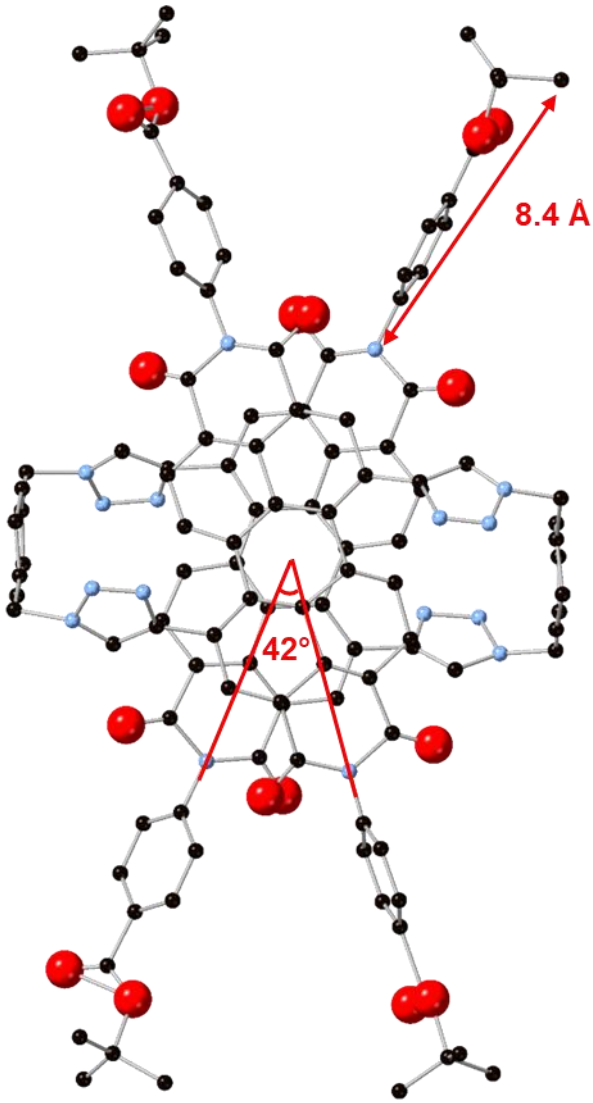

Figure 3.36: Crystal structure of macrocycle **5** from the **5-*rac*** crystal structure depicting the length of the imide groups and the rotational displacement of the PDI cores.

Enantiopure macrocycle 5-*PP*

Needle-like crystals of enantiopure macrocycle **5-*PP*** suitable for single crystal X-ray diffraction were grown from an enantiopure sample of **5-*PP*** by slow diffusion of hexane into a 1:1 chloroform:1,2-dicholobenzene solution.

Single crystal X-ray diffraction experiments were performed at the UK Diamond Light Source I19-1 3-circle diffractometer (λ = 0.6889 Å).[43-45] A suitable single crystal was selected and mounted using fomblin film on a micromount. Data were collected on a dectris-

CrysAlisProabstract goniometer imported dectris images diffractometer. The crystals were kept at 100(2) K during data collection. The structures were solved by direct methods using ShelXT,[40] and refined with ShelXL[41] using a least squares method. Olex2 software was used as the solution, refinement and analysis program.[42] Figures were produced using CrystalMakerX.

All non-hydrogen atoms were refined anisotropically. Positional disorder is modelled for carbon atoms C44A and C44B, C45A and C45B, C46A and C46B. The occupancies of the two sites were refined and constrained to sum to unity. Their occupancies refined to 0.5 so their occupancies were then set to 0.5. The anisotropic displacement parameters of carbon atoms C44A, C44B, C45A, C45B, C46A, and C46B were constrained to be similar (**SIMU**). The C-C bond lengths of the C43 with C44, C45, and C46 were restrained to be the same (**EADP**).

All hydrogen atoms were geometrically placed and refined using a riding model. Methyl hydrogens on carbon atoms C44A, C44B, C45A, C45B, C46A, and C46B were placed in eclipsed conformations (**AFIX 33**) rather than having their torsion angles refined against a search of the Fourier map. This method aided convergence of the refinement.

The majority of disordered solvent molecules could not be sensibly modelled. Carbon atom C117 is the pivot point (occupancy 1) for several possible orientations of one disordered chloroform model. Chlorine atoms Cl1, Cl2, and Cl3 are modelled with occupancy 0.5. Although further Cl orientations for this disordered molecule could be observed in the electron density map, they could not be sensibly modelled. A solvent mask was calculated using the Olex implementation of SQUEEZE and 394 electrons were found in a volume of 1218 cubic angstroms in 1 void per unit cell. This is consistent with the presence of 3.4[CCl3H] per Asymmetric Unit which account for 394 electrons per unit cell.

Crystal Data for **5-*PP*** : $C_{116}H_{84}N_{16}O_{16}$ (M = 1958 g/mol): monoclinic, space group $P2_1$ (no. 4), a = 12.2125(4) Å, b = 20.4026(4) Å, c = 23.5546(5) Å, β = 104.554(2)°, V = 5680.7(3) Å^3, Z = 2, T = 100 K, μ(Synchrotron) = 0.332 mm^{-1}, *Dcalc* = 1.421 g/cm^3, 96354 reflections measured (2.596° ≤ 2Θ ≤ 51.006°), 21937 unique (R_{int} = 0.0769, R_{sigma} = 0.0806) which were used in all calculations. The final R_1 was 0.0659 (I > 2σ(I)) and wR_2 was 0.1938 (all data). Deposited cif number: 2308894

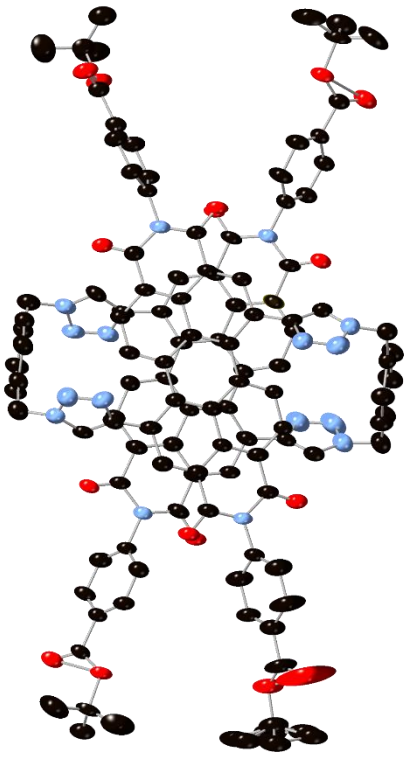

Figure 3.37: Molecular unit of macrocycle **5** from the **5-*PP*** crystal structure with all non-hydrogen atoms represented by ellipsoids at the 50% probability level. Hydrogen atoms omitted for clarity (C, black; O, red; N, blue).

3.11.4 Chiroptical studies

Circular dichroism

Circular dichroism (CD) spectra were recorded on a Jasco J-1500 CD spectrophotometer with a wavelength accuracy ± 0.2 nm (250 to 500 nm), ± 0.5 nm (500 to 800 nm) and a CD root mean square noise < 0.007 mdeg (500 nm). A quartz cuvette with 1 mm path length was used. The spectra were recorded at a concentration of 10 µM. The enantiomers were assigned by corroboration of the samples with the crystal structure of enantiopure **5-*PP***, as well as by comparison of their CD spectra to the computationally predicted CD spectra (see Appendix A for further details).

Circularly polarised luminescence

I thank Dr Dominic J. Black and Professor Robert Pal who carried out CPL measurements.

CPL was measured with a home-built (modular) spectrometer.[46] The excitation source was a broad band (200 – 1000 nm) laser- driven light source EQ 99 (Elliot Scientific). The excitation wavelength was selected by the incorporation of an Acton SP-2155 monochromator (Princeton Instruments); the collimated light was focused into the sample holder (1 cm quartz cuvette). Emission was collected perpendicular to the excitation direction with a lens (f = 150 mm). The emission was fed through a photoelastic modulator (PEM) (Hinds Series II/FS42AA) and through a linear sheet polariser (Comar Optics). The light was then focused into a second scanning monochromator (Acton SP-2155) and subsequently on to a photomultiplier tube (PMT) (Hamamatsu H10723 series). The detection of the CPL signal was achieved using the field modulation lock-in technique. The electronic signal from the PMT was fed into a lock-in amplifier (Hinds Instruments Signaloc Model 2100). The reference signal for the lock-in detection was provided by the PEM control unit. The monchromators, PEM control unit and lock-in amplifier were interfaced to a desktop PC and controlled by a custom-written Labview graphic user interface. The lock-in amplifier provided two signals, an AC signal corresponding to (I_L- I_R) and a DC signal corresponding to (I_L + I_R). Background subtraction was achieved post data collection The emission dissymmetry factor was, therefore, readily obtained from the experimental data as 2 AC/DC.

Spectral calibration of the scanning monochromator was performed using a Hg-Ar calibration lamp (Ocean Optics HL-3P-CAL). A correction factor for the wavelength dependence of the detection system was constructed using a calibrated lamp (Ocean Optics HL-3_CAL). The measured raw data was subsequently corrected using this correction factor. The validation of the CPL detection systems was achieved using light emitting diodes (LEDs) at various emission wavelengths. The LED was mounted in the sample holder and the light from the LED was fed through a broad band polarising filter and $\lambda/4$ plate (Comar Optics) to generate circularly polarised light. Prior to all measurements, the $\lambda/4$ plate and a LED were used to set the phase of the lock-in amplifier correctly. The emission spectra were recorded with 0.5 nm step size and the slits of the detection monochromator were set to a slit width corresponding to a spectral resolution of 0.25 nm. CPL spectra (as well as total emission spectra) were obtained through an averaging procedure of several scans.

3.11.5 Photophysics

UV-vis-NIR absorption and emission spectra in solution

All steady state electronic absorption and emission spectra were recorded at a concentration of 10 µM (unless otherwise stated) at 298 K. For UV-vis-NIR spectroscopy a Shimadzu UV-3600i Plus spectrophotometer was used, with a wavelength accuracy ± 0.2 nm in the UV-vis range and absorbance accuracy ± 0.002 Abs. For fluorescence spectroscopy a Jasco FP-8500 was used with emission and excitation wavelength accuracies ± 1.0 nm. The detector base sensitivity is 8500:1. Quartz cuvettes with 1 cm path length were used.

Calculation of the exciton coupling energy of macrocycle 5

The exciton coupling energy of macrocycle **5-*rac*** was calculated following the method originally reported by Spano,[47] and used by Würthner to investigate long- and short-range coupling in PDI dimers.[48]

For small rotational displacements of chromophores (< 45°, as seen in macrocycle **5** in the x-ray crystal structure in **Figure 3.36**) the rotational displacement of transition dipole moments of two chromophores can be neglected and the ratio of intensities of the 0–0 and 0–1 vibronic absorption bands of a dimer aggregate exhibiting exciton-vibrational coupling can be calculated using the equation:

$$\frac{I_{\mathrm{A}}^{(0-0)}}{I_{\mathrm{A}}^{(0-1)}} = \frac{1}{\lambda^2}\left[\frac{1 - G(0,\lambda^2)e^{-\lambda^2}J/\omega_0}{1 - G(1,\lambda^2)e^{-\lambda^2}J/\omega_0}\right], \quad \omega_0, J \ll |E_{\mathrm{CT}} - E_{\mathrm{S1}}| \quad (3.6)$$

where λ^2 is the Huang-Rhys factor, J is the exciton coupling energy, and ω_0 is the vibrational frequency.

The vibrational function $G(\nu_{\mathrm{t}}, \lambda^2)$ is given by:

$$G(\nu_{\mathrm{t}}, \lambda^2) = \sum_{\substack{u=0,1,\ldots \\ (\mathrm{u} \neq \nu_{\mathrm{t}})}} \frac{\lambda^{2u}}{u!\,(u - \nu_{\mathrm{t}})}. \; \nu_{\mathrm{t}} = 0,1,2,\ldots \quad (3.7)$$

From the UV-vis absorption spectrum of **5-*rac*** in toluene:

$$\frac{I_{\mathrm{A}}^{(0-0)}}{I_{\mathrm{A}}^{(0-1)}} = 0.567(3.8)$$

The Huang-Rhys factor was obtained by gaussian fitting of the vibronic peaks in the UV-vis spectrum of **5-*rac*** (**Figure 3.38**), considering only the area of the spectrum arising from the S_0–S_1 transition (< 23360 cm^{-1}). The Huang-Rhys factor was calculated as:

$$\lambda^2 = \frac{I_{\mathrm{Gaussian}}^{(0-1)}}{I_{\mathrm{Gaussian}}^{(0-0)}} = 1.598\ (3.9)$$

The frequency ω_0 was set as 1709 cm^{-1}, corresponding to the energy difference between the maxima of the Gaussian functions of the 0–0 and 0–1 absorption bands. The exciton coupling energy J was then calculated using equation 1. From this J = 420.4 cm^{-1} was obtained.

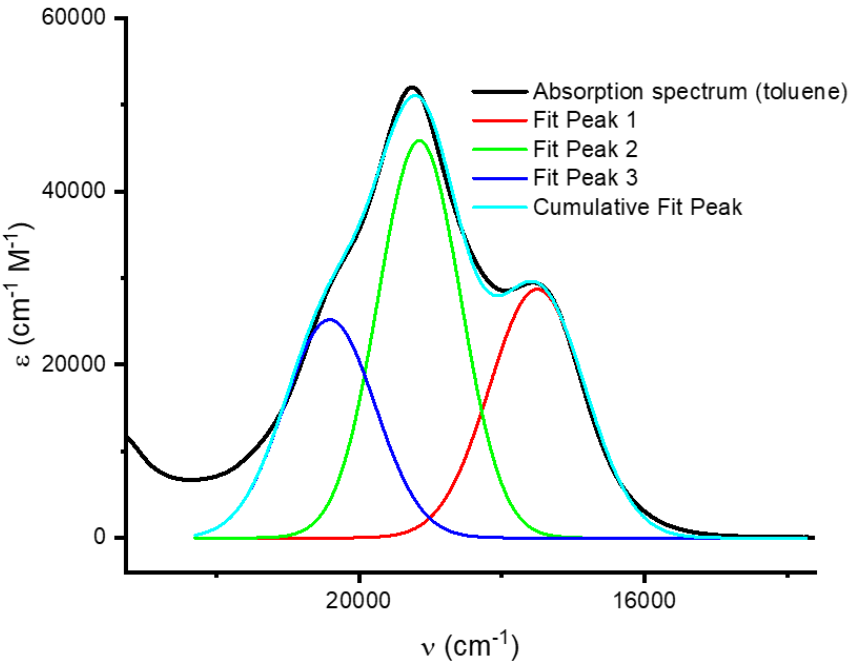

Figure 3.38: UV-vis absorption spectrum of macrocycle **5** in toluene (10 μM, black trace), along with the cumulative fit of the spectrum as the sum of three gaussian functions for the 0-0, 0-1 and 0-2 vibronic peaks.

Quantum yields

Absolute fluorescence quantum yields were obtained on an Edinburgh Instruments FLS1000 photoluminescence spectrometer fitted with an integrating sphere. All samples were recorded in toluene at a 1 μM with a 7 - 8 nm excitation slit and 0.1 - 0.2 nm emission slit width. Experiments were carried out in solution using 1 cm path length quartz cuvettes with four transparent polished faces.

Table 3.2: Quantum yields for compounds **5** and **9** in toluene.

Compound	Quantum yield
5-*rac*	0.35
9	0.70

Fluorescence lifetime measurements

Fluorescence lifetimes measurements were carried out on the emission band of compounds **1-*rac*** (635 nm) and **3** (604 nm) in toluene using a Horiba Fluorolog-3 Time Correlated Single Photon Counting (TCSPC) module controlled by Datastation software. The sample was excited using a 373-nm Delta Diode 373 nm laser attenuated with a neutral density filter and analysed using DAS6 software. Fluoresence lifetimes were obtained by fitting the resulting data to exponential decay curves.

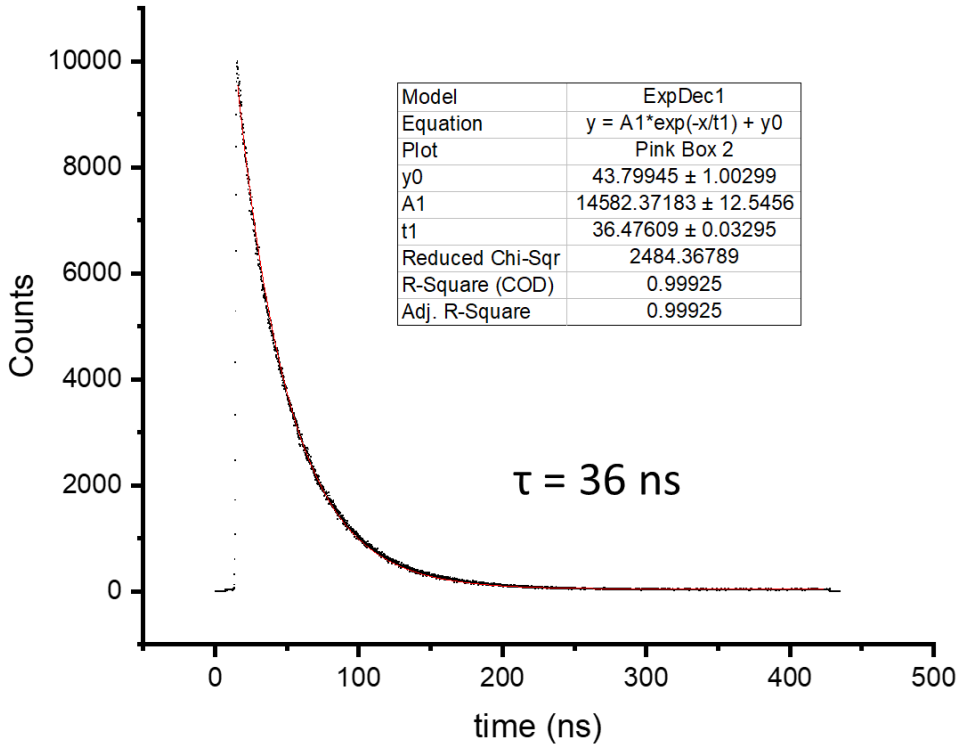

Figure 3.39: Exponential decay of emission for macrocycle **5-*rac*** (toluene, 5 μmol, λ_{ex} = 373 nm, λ_{em} = 635 nm) from which a fluoresence lifetime of 36 ns is obtained.

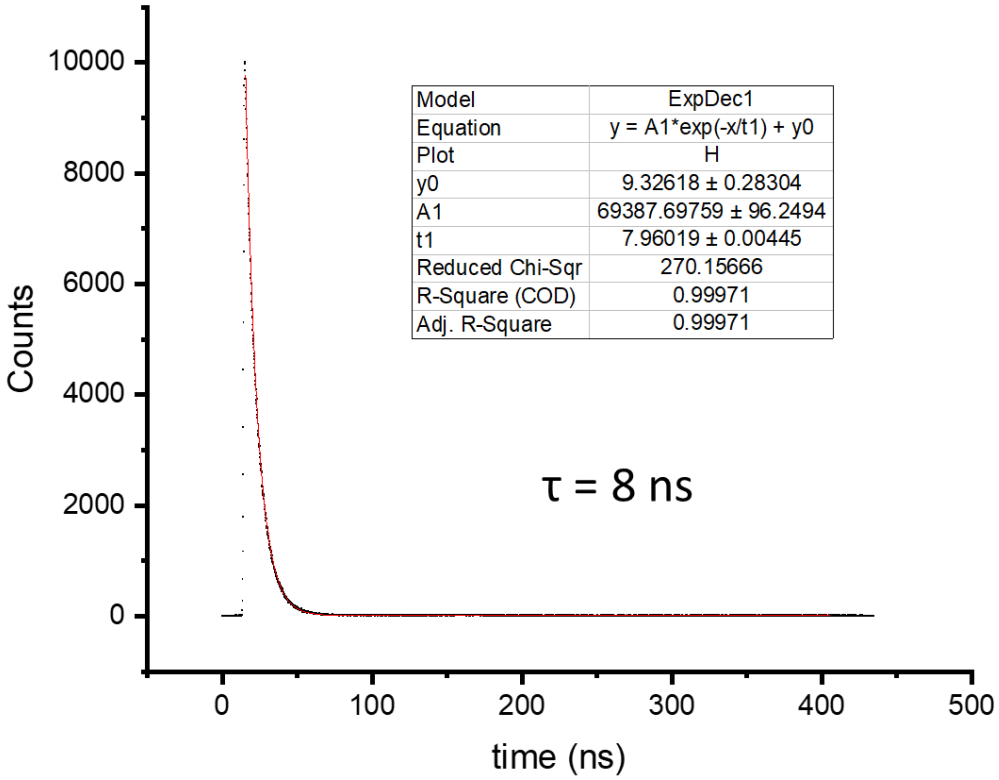

Figure 3.40: Exponential decay of emission for compound **9** (toluene, 5 μmol, λ_{ex} = 373 nm, λ_{em} = 604 nm) from which a fluoresence lifetime of 8 ns is obtained.

UV-vis-NIR absorption (reflectance) and emission spectra from crystals

UV-vis-NIR absorption (reflectance) spectra from crystals of **5-*rac*** and **5-*PP*** were measured on a Shimadzu UV3600i spectrometer fitted with a ISR-603 integrating sphere with a powder sample holder. Absorption spectra were calculated from the resulting reflectance spectra using the Kubelka-Munk function: Abs = $(1\text{-}R^2)/2R$ where R is reflectance.[49] The reflectance spectrum of $BaSO_4$ was measured as a baseline with 100% reflectance.

Emission spectra from crystals were measured on a Horiba Fluorolog-3 (L-configuration) equipped with a 450 W Xenon light source, R928P photomultiplier tube and double monochromators. The crystals were placed on a quartz slide on the instrument's slide-holder attachment.

Crystals of both **5-*rac*** and **5-*PP*** were approximately 100 µm × 20 µm as estimated by microscopy.

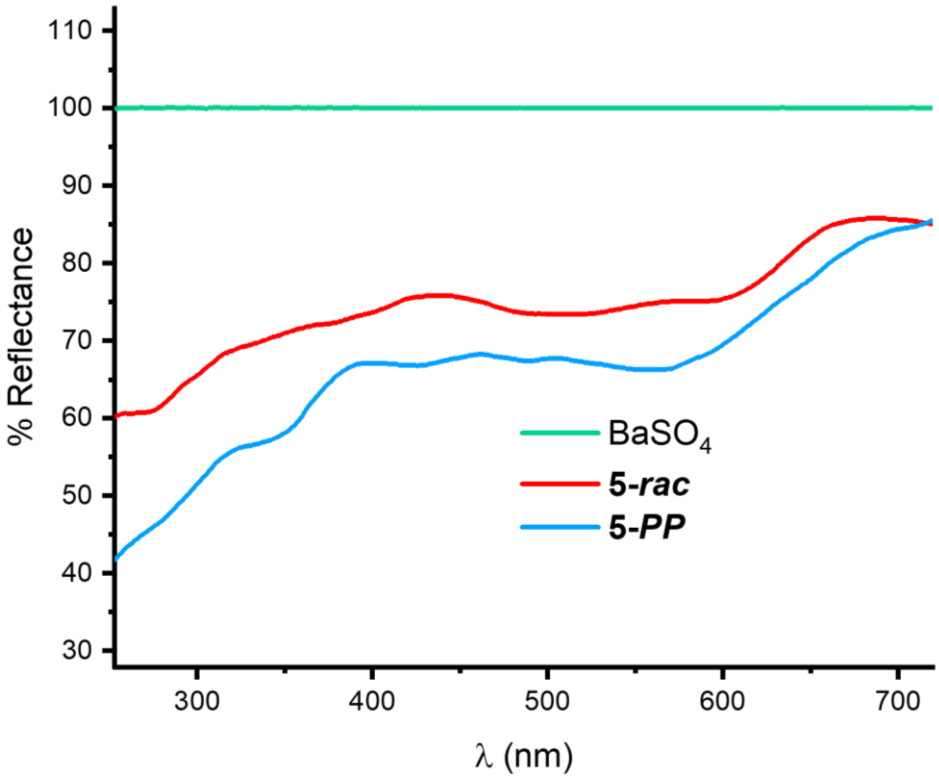

Figure 3.41: Solid state reflectance spectra for crystals of **5-*rac*** and **5-*PP*** as well as $BaSO_4$.

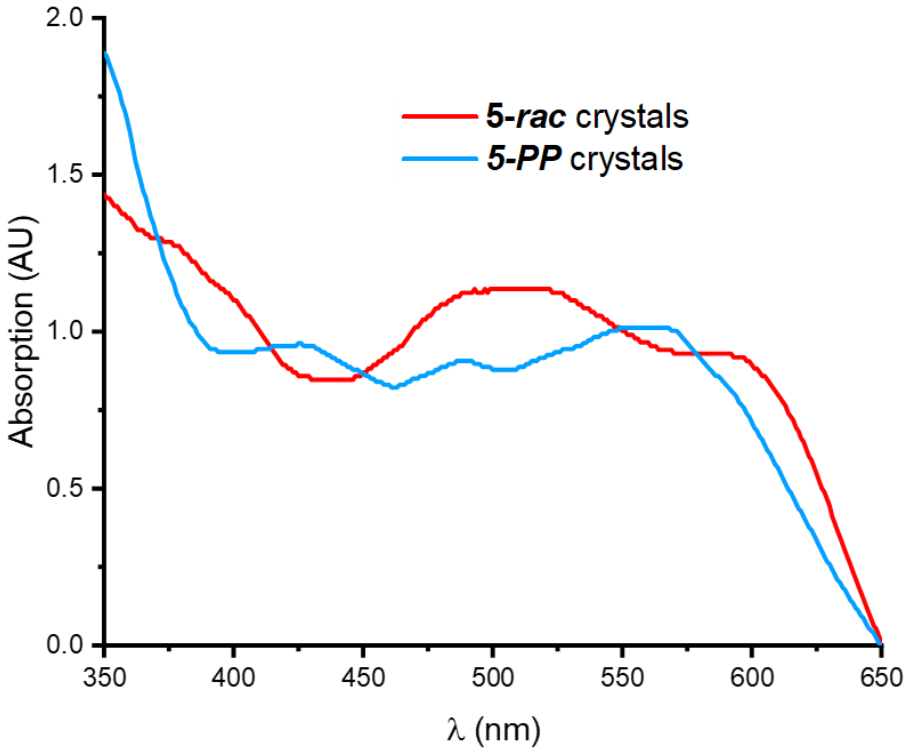

Figure 3.42: Solid state absorption spectra for crystals of **5-*rac*** and **5-*PP***. Spectra were calculated from raw reflectance spectra using the Kubelka-Munk formula: Abs = $(1-R^2)/2R$ where R is reflectance. The spectra were normalised to give an absorbance of 0 at 650 nm.

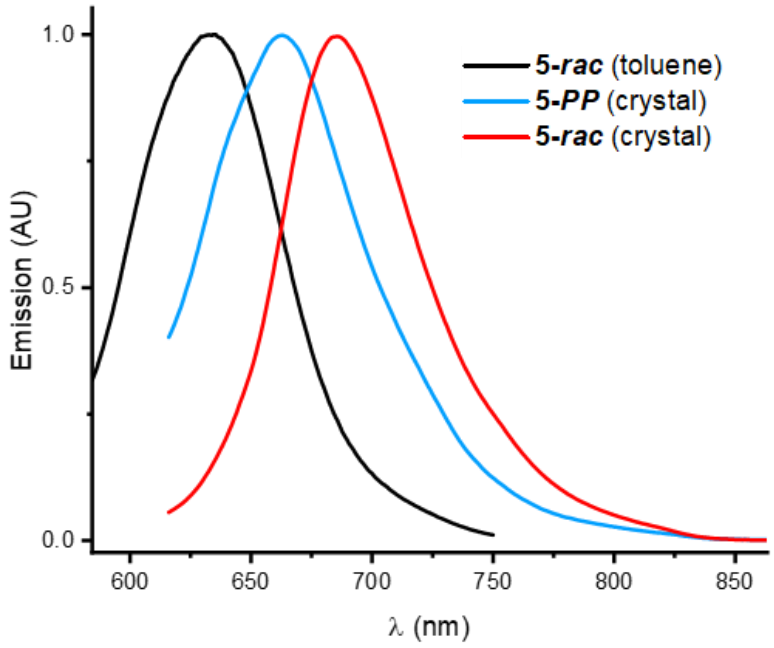

Figure 3.43: Normalised emission spectra for crystals of **5-*rac*** and **5-*PP*** as well as **5-*rac*** in toluene solution (10 μM).

3.11.6 Self-assembly studies through UV-vis spectroscopy

UV-vis spectra were measured as described in **section 3.9.5**. Quartz cuvettes with 0.1, 1 and 10 cm path lengths were used to enable accurate spectra to be measured over large concentration ranges.

Modified isodesmic model used for 5-*rac*

The UV-vis absorption spectrum of racemic macrocycle **5-*rac*** was measured as the sample was concentrated from 0.7 μM to 76 μM in 3:2 (v/v) DCM:*n*-hexane.

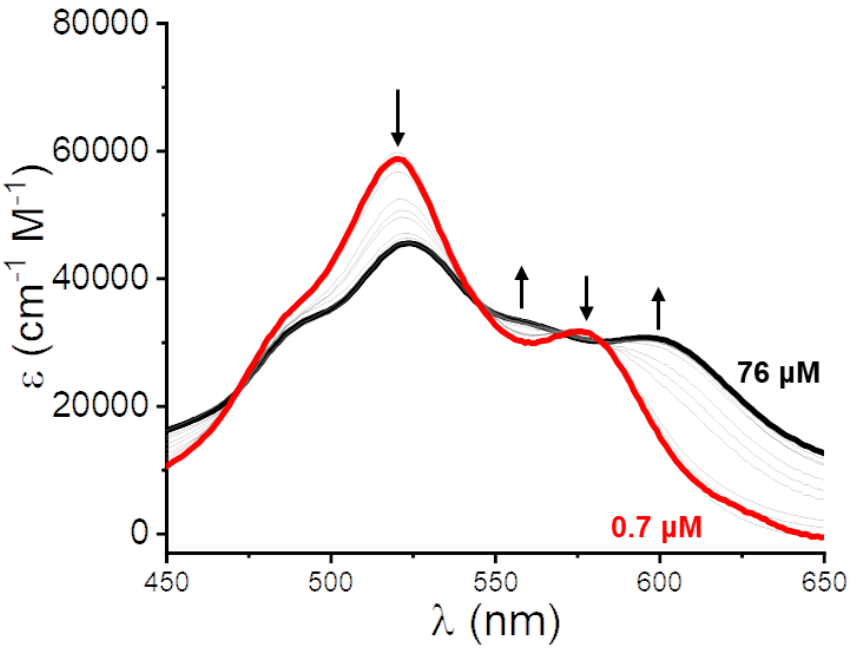

Figure 3.44: Change in UV-vis absorption spectrum of macrocycle **5-*rac*** upon concentration from 0.7 μM (red trace) to 76 μM (black trace) in 3:2 (v/v) DCM:*n*-hexane.

The change in extinction coefficient ε at 596 nm was fitted with various models including the monomer-dimer model), the isodesmic model, and the modified isodesmic (nucleation-elongation) model[28, 31] which gave the best fits.

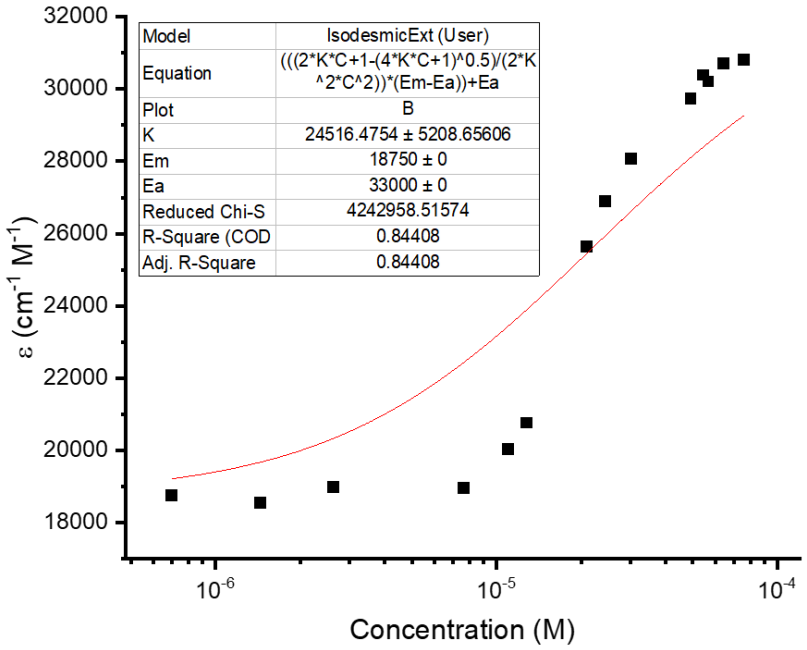

Figure 3.45: Change in extinction coefficient ε at 596 nm of macrocycle **5-*rac*** upon concentration from 0.7 μM to 76 μM in 3:2 (v/v) DCM:*n*-hexane, fitted to the isodesmic model by non-linear regression analysis, with fixed ε_{agg} = 33,000 $cm^{-1}\,M^{-1}$ and ε_{mon} = 18750 $cm^{-1}\,M^{-1}$. The fit is very poor, yielding K ~ 25000 with a large error (~ 20%). The sudden, steep rise in ε at 10^{-5} M suggests that aggregate formation is non-isodesmic and cooperative. Beer-lambert behaviour is observed below 10^{-5} M.

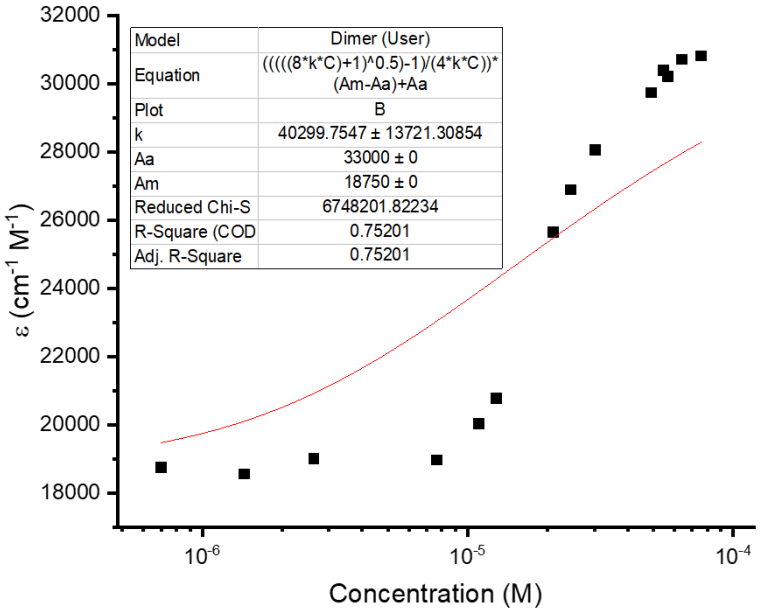

Figure 3.46: Change in extinction coefficient ε at 596 nm of macrocycle **5-*rac*** upon concentration from 0.7 μM to 76 μM in 3:2 (v/v) DCM:*n*-hexane, fitted to the monomer-dimer mode by linear regression analysis, with fixed ε_{agg} = 33,000 $cm^{-1}\,M^{-1}$ and ε_{mon} = 18750 $cm^{-1}\,M^{-1}$. The fit is very poor, yielding K = 40,000 with a large error (~ 35%). The sudden, steep rise in ε at 10^{-5} M suggests that aggregate formation is non-isodesmic and cooperative. Beer-lambert behaviour is observed below 10^{-5} M

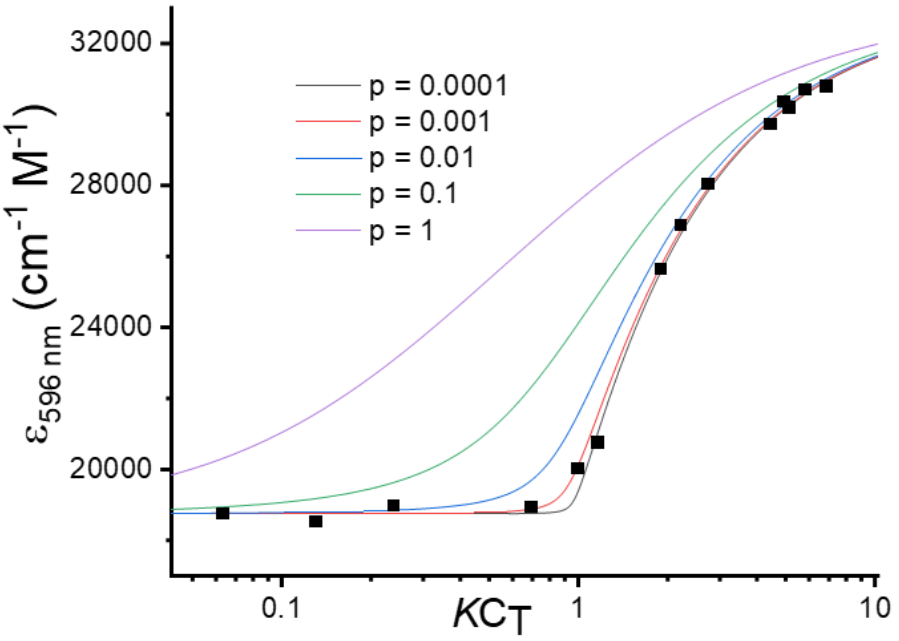

Figure 3.47: Change in extinction coefficient at 596 nm of macrocycle **5-*rac*** upon concentration from 0.7 μM to 76 μM in 3:2 (v/v) DCM:*n*-hexane, manually fitted to the modified isodesmic (nucleation-elongation) model for various values of p = K_2/K. The best manual fit (red trace) was obtained for K = 90,000 M^{-1}, p = 0.001, ε_{agg} = 33,000 cm^{-1} M^{-1} and ε_{mon} =18,750 cm^{-1} M^{-1}. From this we can deduce K_2 = 90 M^{-1}. An error of < 10% is estimated based on the quality of other fits that were tested.

In the modified isodesmic (nucleation-elongation), dimerization (with a distinct dimerization constant $K_d = K_2$) is followed by isodesmic aggregation, such that $K_2 \neq K_3 = K_4 \ldots = K_i \ldots = K$. This can be described by the cubic equation:

$$\alpha_{\mathrm{mon}}{}^{3}(KC_{\mathrm{T}})^{2}(\mathrm{p}-1)+\alpha_{\mathrm{mon}}{}^{2}KC_{\mathrm{T}}\left(KC_{\mathrm{T}}-2(\mathrm{p}-1)\right)-\alpha_{\mathrm{mon}}\left(2KC_{\mathrm{T}}+1\right)+1=0 \quad (3.10)$$

Where p = K_2/K. Therefore, p < 1 implies cooperative binding when the aggregate forms after the initial dimerization nucleation event. α_{mon} is the mole fraction of the monomer (i.e., the unaggregated macrocycle) and C_T is the total concentration of the sample. This equation cannot be solved for α_{mon} analytically for general cases. However, it is possible to calculate KC_{T} as a function of KC_{mon} for specific values of p using the equation:

$$KC_T=(1-\mathrm{p})\,KC_{\mathrm{mon}}+\frac{\mathrm{p}KC_{\mathrm{mon}}}{(1-KC_{\mathrm{mon}})^{2}} \quad (3.11)$$

α_{agg} is related to the extinction coefficients of the aggregate ($\varepsilon_{\mathrm{agg}}$), monomer ($\varepsilon_{\mathrm{mon}}$) and intermediate state ($\varepsilon(C_{\mathrm{T}})$) by the equation:

$$\alpha_{\mathrm{agg}} = 1 - \frac{\varepsilon(C_{\mathrm{T}}) - \varepsilon_{\mathrm{agg}}}{\varepsilon_{\mathrm{mon}} - \varepsilon_{\mathrm{agg}}} \quad (3.12)$$

Hence,

$$\varepsilon(C_{\mathrm{T}}) = \frac{KC_{\mathrm{mon}}}{KC_{\mathrm{T}}}\left(\varepsilon_{\mathrm{mon}} - \varepsilon_{\mathrm{agg}}\right) + \varepsilon_{\mathrm{agg}} \quad (3.13)$$

Hence the data $\varepsilon(C_{\mathrm{T}})$ can be plotted against KC_{T} and fitted manually to the parameters K, $\varepsilon_{\mathrm{mon}}$, $\varepsilon_{\mathrm{agg}}$ and p.

3.11.7 CPL microscopy

I thank Dr Dominic J. Black and Professor Robert Pal who carried out the EDCC imaging of crystals.

Circular Polarisation Luminescence Laser Scanning Confocal Microscope (CPL-LSCM)

CPL-LCSM[32] was enabled by adapting a commercial LSCM (SP5 II, Leica Microsystems) with excitation provided by a fibre coupled 80 mW variable power 355 nm Nd:YAG CW laser. The CPL analysis module was external to an output port and all elements were mounted in a 30 mm cage mount system for optimal alignment (assorted 30 mm components, Thorlabs). First, light from the sample focal plane excites the mirror controlled X1 emission port and passes through a selectable high transmission 570 nm longpass filter (FGL570, Thorlabs) mounted in a switchable filter selector apparatus (CFS1/M, Thorlabs). The circularly polarised emission is then converted to linearly polarised light by an achromatic quarter wave plate (AQWP05M-600, Thorlabs) and is separated into two detection arms by a simple 50/50 beam-splitter cube (BS013, Thorlabs). In each arm, the linearly polarised light is selectively analysed by linear polarisers (LPVISE100-A, Thorlabs) mounted within ultra-high precision computer-controlled rotation mounts with ± 60 µrad unidirectional repeatability (K10CR1/M, Thorlabs), orientated to select for left or right CPL states via computer control software (Kinesis, Thorlabs). The intensity of emission in each path was quantified by fibre-coupled (200 micron) high performance matched tandem avalanche photodiodes (Leica ADPs, Becker & Hickl ID-120). The two detection arms were aligned to achieve matched sensitivity to enable rapid simultaneous acquisition of left and right CPL images. Calibration of the linear polarisers for

enantioselective localisation was executed based upon the procedure reported by Mackenzie et. al.[50]

Enantioselective differential chiral contrast imaging

We performed enantioselective differential chiral contrast (EDCC) imaging of single crystals of **5-*rac*** and **5-*PP/MM*** using CPL-LSCM. In CPL-LSCM, right- and left-circularly polarised photons are collected simultaneously from the sample, generating independent right and left CPL images rapidly. EDDC is used to quantify the difference between the amount of left-handed- and right-handed-circularly polarised photons that are emitted, one of the two images can be subtracted from the other and the brightness of the resulting image determines the chirality-induced helicity dominance of each enantiomer.

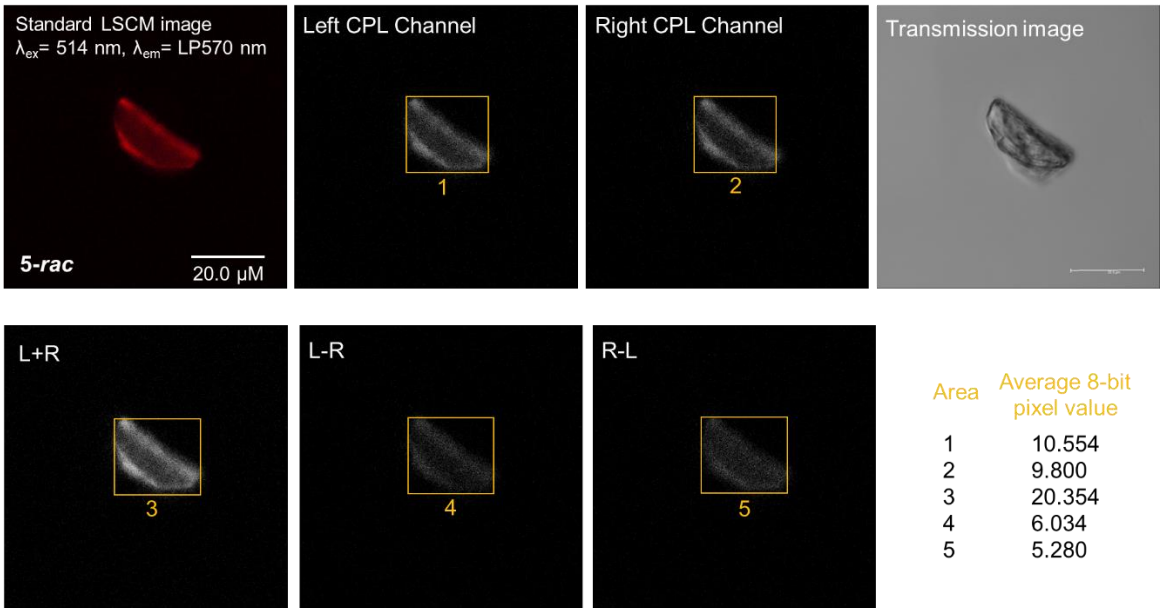

Figure 3.48: Enantioselective differential chiral contrast (EDCC) images for crystals of **5-*rac*** along with the average 8-bit pixel values for the highlighted areas in the images.

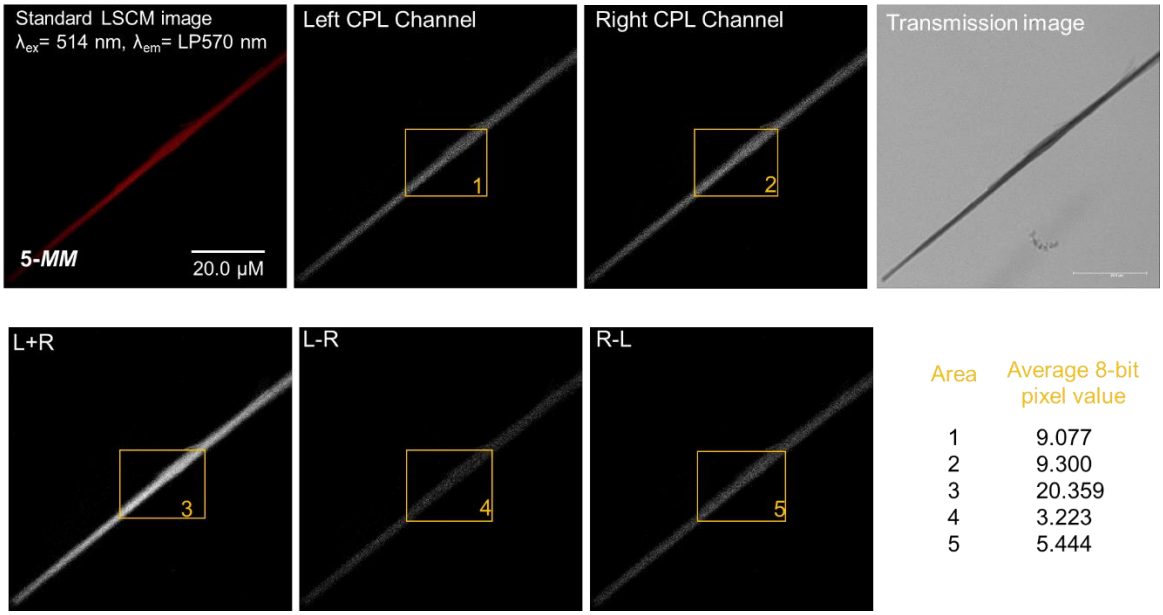

Area	Average 8-bit pixel value
1	9.077
2	9.300
3	20.359
4	3.223
5	5.444

Figure 3.49: Enantioselective differential chiral contrast (EDCC) images for crystals of **5-*MM*** along with the average 8-bit pixel values for the highlighted areas in the images.

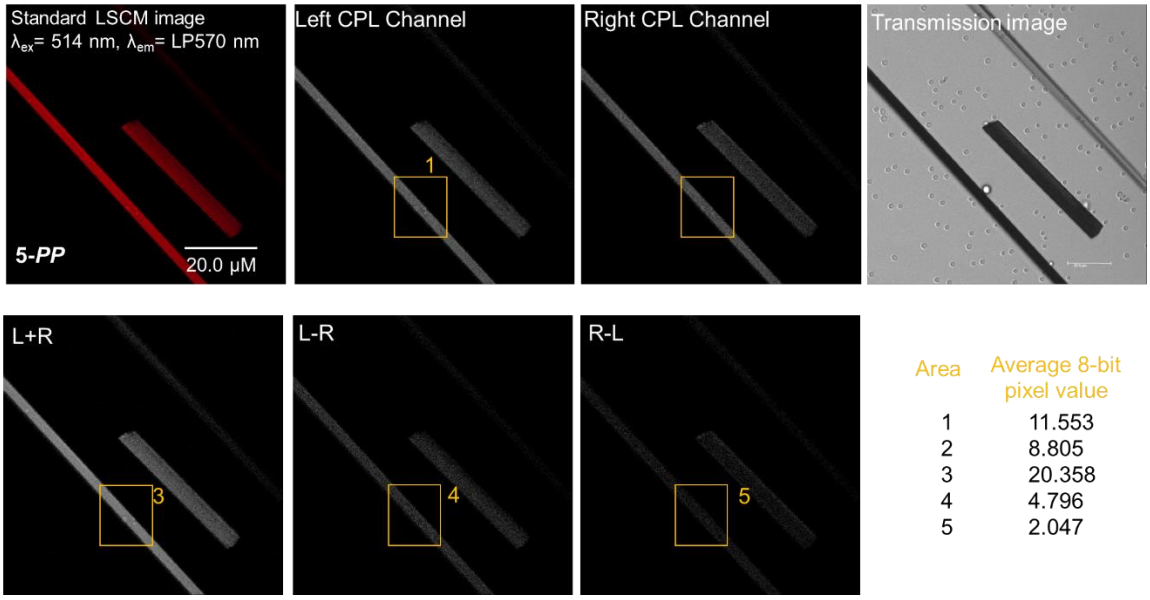

Area	Average 8-bit pixel value
1	11.553
2	8.805
3	20.358
4	4.796
5	2.047

Figure 3.50: Enantioselective differential chiral contrast (EDCC) images for crystals of **1-*PP*** along with the average 8-bit pixel values for the highlighted areas in the images.

Determination of enantioselective differential chiral contrast dissymmetry factors ($g_{\mathbf{EDCC}}$)

Having distinct enantiopure and racemic single crystals provides the opportunity to quantify the degree of circularly polarized emitted light from single crystals for the first time using CPL-

LSCM, by calculating an EDCC dissymmetry factor (g_{EDCC}), a value analogous to the luminescence dissymmetry factor obtained from CPL spectroscopy (g_{lum}). In doing so, it is critical to correct for the inherent CPL bias arising from orientation induced reflection and helicity inversion of light. Therefore, a bias factor B was calculated as follows:

From the EDCC images of **5-*rac*** we calculate a (left-handed) contrast transfer function (CTF):

$$\mathrm{CTF} = \frac{I_{(L-R)} - I_{(R-L)}}{2} = 0.0185 \quad (3.14)$$

where $I_{(L-R)}$ is the left-handed EDCC average 8-bit pixel value (Left CPL - Right CPL) and $I_{(R-L)}$ is the right-handed EDCC average 8-bit pixel value (Right CPL - Left CPL).

As **5-*rac*** is racemic, it will emit equal amounts of Left- and Right-handed light. From this, the bias factor B is half of the CTF as the bias is present equally in the Left and Right channels, so B = CTF (**5-*rac***) / 2 = 0.0093.

We then define g_{EDCC} as:

$$g_{\mathrm{EDCC}} = \frac{\mathrm{CTF}}{I_{(L+R)}} - \mathrm{B} = \frac{I_{(L-R)} - I_{(R-L)}}{2I_{(L+R)}} - \mathrm{B} \quad (3.15)$$

Where $I_{(L+R)}$ is the total image average 8-bit pixel value (Left CPL + Right CPL) and B is the calculated bias factor. From this we obtain g_{EDCC} values of +0.0582 and -0.0643 for the **5-*PP*** **5-*MM*** crystals respectively.

This analysis can be validated by also calculating the bias factor B from the uncorrected CTFs for the enantiomeric crystals **5-*PP*/*MM***:

$$\mathrm{B} = \frac{\frac{\mathrm{CTF}\ (\mathbf{5}\text{-}\boldsymbol{PP})}{I_{(L+R)}} + \frac{\mathrm{CTF}\ (\mathbf{5}\text{-}\boldsymbol{MM})}{I_{(L+R)}}}{\sqrt{2}}\ \mathrm{B} \quad (3.16)$$

From equation [3.15] we obtain a B value 0.0084, which is within 10% of the B value of 0.0093 calculated from equation [3.13].

3.12 References

1. Z. Chen, U. Baumeister, C. Tschierske and F. Würthner, *Chemistry – A European Journal*, 2007, **13**, 450-465.
2. A. Li, X. Zhang, S. Wang, K. Wei and P. Du, *Organic Letters*, 2023, **25**, 1183-1187.
3. S. Dnyaneshwar Veer, V. Chandrakant Wakchaure, K. Asokan, R. Dixit, T. Goswami, R. Saha, R. Gonnade, H. N. Ghosh and S. Santhosh Babu, *Angewandte Chemie International Edition*, 2023, **62**, e202212934.
4. M. M. Safont-Sempere, P. Osswald, K. Radacki and F. Würthner, *Chemistry – A European Journal*, 2010, **16**, 7380-7384.
5. M. M. Safont-Sempere, P. Osswald, M. Stolte, M. Grüne, M. Renz, M. Kaupp, K. Radacki, H. Braunschweig and F. Würthner, *Journal of the American Chemical Society*, 2011, **133**, 9580-9591.
6. S. E. Penty, M. A. Zwijnenburg, G. R. F. Orton, P. Stachelek, R. Pal, Y. Xie, S. L. Griffin and T. A. Barendt, *Journal of the American Chemical Society*, 2022, **144**, 12290-12298.
7. M. Ball, B. Fowler, P. Li, L. A. Joyce, F. Li, T. Liu, D. Paley, Y. Zhong, H. Li, S. Xiao, F. Ng, M. L. Steigerwald and C. Nuckolls, *Journal of the American Chemical Society*, 2015, **137**, 9982-9987.
8. T. Türel, S. Bhargava and S. Valiyaveettil, *The Journal of Organic Chemistry*, 2020, **85**, 3092-3100.
9. T. A. Barendt, M. L. Ball, Q. Xu, B. Zhang, B. Fowler, A. Schattman, V. C. Ritter, M. L. Steigerwald and C. Nuckolls, *Chemistry – A European Journal*, 2020, **26**, 3744-3748.
10. S. E. Penty, G. R. F. Orton, D. J. Black, R. Pal, M. A. Zwijnenburg and T. A. Barendt, *Journal of the American Chemical Society*, 2024, **146**, 5470-5479.
11. J.-P. Heeb, J. Clayden, M. D. Smith and R. J. Armstrong, *Nature Protocols*, 2023, **18**, 2745-2771.
12. J. Gorman, R. Pandya, J. R. Allardice, M. B. Price, T. W. Schmidt, R. H. Friend, A. Rao and N. J. L. K. Davis, *The Journal of Physical Chemistry C*, 2019, **123**, 3433-3440.
13. M. Weh, K. Shoyama and F. Würthner, *Nature Communications*, 2023, **14**, 243.
14. R. Renner, B. Mahlmeister, O. Anhalt, M. Stolte and F. Würthner, *Chemistry – A European Journal*, 2021, **27**, 11997-12006.
15. L. Arrico, L. Di Bari and F. Zinna, *Chemistry – A European Journal*, 2021, **27**, 2920-2934.
16. F. Zinna, E. Brun, A. Homberg and J. Lacour, in *Circularly Polarized Luminescence of Isolated Small Organic Molecules*, ed. T. Mori, Springer Singapore, Singapore, 2020, DOI: 10.1007/978-981-15-2309-0_12, pp. 273-292.
17. H. Tanaka, Y. Inoue and T. Mori, *ChemPhotoChem*, 2018, **2**, 386-402.
18. Z.-H. Zhao, X. Liang, M.-X. He, M.-Y. Zhang and C.-H. Zhao, *Organic Letters*, 2019, **21**, 9569-9573.
19. B. Liu, M. Böckmann, W. Jiang, N. L. Doltsinis and Z. Wang, *Journal of the American Chemical Society*, 2020, **142**, 7092-7099.
20. Y. Liu, Z. Ma, Z. Wang and W. Jiang, *Journal of the American Chemical Society*, 2022, **144**, 11397-11404.
21. J. Kumar, T. Nakashima, H. Tsumatori, M. Mori, M. Naito and T. Kawai, *Chemistry – A European Journal*, 2013, **19**, 14090-14097.

22. K. Dhbaibi, L. Favereau, M. Srebro-Hooper, M. Jean, N. Vanthuyne, F. Zinna, B. Jamoussi, L. Di Bari, J. Autschbach and J. Crassous, *Chemical Science*, 2018, **9**, 735-742.
23. S. Pascal, C. Besnard, F. Zinna, L. Di Bari, B. Le Guennic, D. Jacquemin and J. Lacour, *Organic & Biomolecular Chemistry*, 2016, **14**, 4590-4594.
24. J. Bosson, G. M. Labrador, S. Pascal, F.-A. Miannay, O. Yushchenko, H. Li, L. Bouffier, N. Sojic, R. C. Tovar, G. Muller, D. Jacquemin, A. D. Laurent, B. Le Guennic, E. Vauthey and J. Lacour, *Chemistry – A European Journal*, 2016, **22**, 18394-18403.
25. R. B. Alnoman, S. Rihn, D. C. O'Connor, F. A. Black, B. Costello, P. G. Waddell, W. Clegg, R. D. Peacock, W. Herrebout, J. G. Knight and M. J. Hall, *Chemistry – A European Journal*, 2016, **22**, 93-96.
26. M. Saikawa, T. Nakamura, J. Uchida, M. Yamamura and T. Nabeshima, *Chemical Communications*, 2016, **52**, 10727-10730.
27. F. Zhao, J. Zhao, H. Liu, Y. Wang, J. Duan, C. Li, J. Di, N. Zhang, X. Zheng and P. Chen, *Journal of the American Chemical Society*, 2023, **145**, 10092-10103.
28. Z. Chen, A. Lohr, C. R. Saha-Möller and F. Würthner, *Chemical Society Reviews*, 2009, **38**, 564-584.
29. Z. Chen, V. Stepanenko, V. Dehm, P. Prins, L. D. A. Siebbeles, J. Seibt, P. Marquetand, V. Engel and F. Würthner, *Chemistry – A European Journal*, 2007, **13**, 436-449.
30. F. Würthner, C. R. Saha-Möller, B. Fimmel, S. Ogi, P. Leowanawat and D. Schmidt, *Chemical Reviews*, 2016, **116**, 962-1052.
31. T. E. Kaiser, V. Stepanenko and F. Würthner, *Journal of the American Chemical Society*, 2009, **131**, 6719-6732.
32. P. Stachelek, L. MacKenzie, D. Parker and R. Pal, *Nature Communications*, 2022, **13**, 553.
33. O. El-Zubir, P. R. Martinez, G. Dura, L. L. G. Al-Mahamad, T. Pope, T. J. Penfold, L. E. Mackenzie, R. Pal, J. Mosely, F. Cucinotta, L. F. McGarry, B. R. Horrocks and A. Houlton, *Journal of Materials Chemistry C*, 2022, **10**, 7329-7335.
34. O. El-Zubir, P. Rojas Martinez, G. Dura, C. Doherty, F. Cucinotta, L. E. Mackenzie, R. Pal, B. R. Horrocks and A. Houlton, *Dalton Transactions*, 2023, **52**, 5545-5551.
35. Y. Kitagawa, S. Wada, M. D. J. Islam, K. Saita, M. Gon, K. Fushimi, K. Tanaka, S. Maeda and Y. Hasegawa, *Communications Chemistry*, 2020, **3**, 119.
36. A. Knebel, A. Bavykina, S. J. Datta, L. Sundermann, L. Garzon-Tovar, Y. Lebedev, S. Durini, R. Ahmad, S. M. Kozlov, G. Shterk, M. Karunakaran, I. D. Carja, D. Simic, I. Weilert, M. Klüppel, U. Giese, L. Cavallo, M. Rueping, M. Eddaoudi, J. Caro and J. Gascon, *Nature Materials*, 2020, **19**, 1346-1353.
37. Y. Yang, B. Rice, X. Shi, J. R. Brandt, R. Correa da Costa, G. J. Hedley, D.-M. Smilgies, J. M. Frost, I. D. W. Samuel, A. Otero-de-la-Roza, E. R. Johnson, K. E. Jelfs, J. Nelson, A. J. Campbell and M. J. Fuchter, *ACS Nano*, 2017, **11**, 8329-8338.
38. T. R. Chan, R. Hilgraf, K. B. Sharpless and V. V. Fokin, *Organic Letters*, 2004, **6**, 2853-2855.
39. M. Franceschin, A. Alvino, G. Ortaggi and A. Bianco, *Tetrahedron Letters*, 2004, **45**, 9015-9020.
40. G. M. Sheldrick, *Acta Crystallographica Section A: Foundations and Advances*, 2015, **71**, 3-8.
41. G. M. Sheldrick, *Acta Crystallographica Section C: Structural Chemistry*, 2015, **71**, 3-8.

42. O. V. Dolomanov, L. J. Bourhis, R. J. Gildea, J. A. Howard and H. Puschmann, *Journal of applied crystallography*, 2009, **42**, 339-341.
43. J. Beilsten-Edmands, G. Winter, R. Gildea, J. Parkhurst, D. Waterman and G. Evans, *Acta Crystallographica Section D: Structural Biology*, 2020, **76**, 385-399.
44. G. Winter, *Journal of applied crystallography*, 2010, **43**, 186-190.
45. G. Winter, D. G. Waterman, J. M. Parkhurst, A. S. Brewster, R. J. Gildea, M. Gerstel, L. Fuentes-Montero, M. Vollmar, T. Michels-Clark, I. D. Young, N. K. Sauter and G. Evans, *Acta Crystallogr D Struct Biol*, 2018, **74**, 85-97.
46. R. Carr, R. Puckrin, B. K. McMahon, R. Pal, D. Parker and L.-O. Pålsson, *Methods and Applications in Fluorescence*, 2014, **2**, 024007.
47. K. A. Kistler, C. M. Pochas, H. Yamagata, S. Matsika and F. C. Spano, *The Journal of Physical Chemistry B*, 2012, **116**, 77-86.
48. C. Kaufmann, D. Bialas, M. Stolte and F. Würthner, *Journal of the American Chemical Society*, 2018, **140**, 9986-9995.
49. P. Makuła, M. Pacia and W. Macyk, *The Journal of Physical Chemistry Letters*, 2018, **9**, 6814-6817.
50. L. E. MacKenzie, L.-O. Pålsson, D. Parker, A. Beeby and R. Pal, *Nature Communications*, 2020, **11**, 1676.

Chapter 4: Chiral conformations in Pink Box-type macrocycles

4. Chiral conformations in Pink Box-type macrocycles

4.1 Introduction

As discussed in the previous chapters, core-twisted PDIs can exist as two different enantiomers, ***M*** and ***P***. Therefore, "Pink Box" type bis-PDI macrocycles can exist as three stereoisomers: the ***MM*** and ***PP*** enantiomer pair, and the ***MP*** meso isomer (**Figure 4.1**). Indeed, these were experimentally observed as distinct species for macrocycle **1** in Chapter 2.

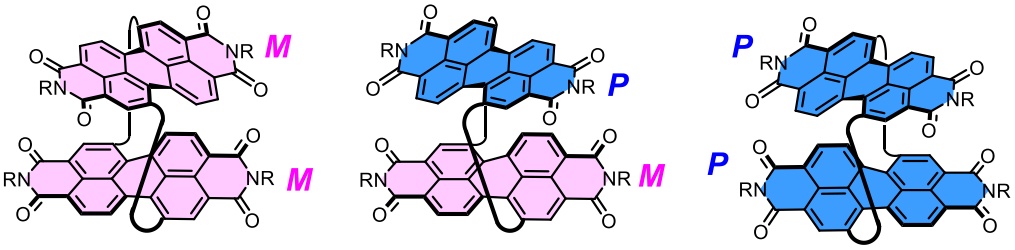

Figure 4.1: Stereoisomers in a bis-PDI macrocycle: the ***MM*** and ***PP*** enantiomer pair, and the ***MP*** meso isomer.

However, the results in Chapter 2 hint at a more complex picture because external stimuli may trigger these stereoisomers to adopt different conformations which will likely have consequences for their chiroptical properties. For example, the CD spectra of the enantiomers of Pink Box macrocycle **1** changed dramatically with solvent. The CD spectra of the *same enantiomer*, **1-*MM***, in DCM and toluene are shown in **Figure 4.2a**. Two main differences can be observed. Firstly, the Cotton effect in toluene due to chiral excitonic coupling (in the S_0-S_1 transition, ~ 570 nm) is not observed in DCM. Secondly, leaving aside the S_0-S_1 transition, the remainder of the CD spectrum appears to have the opposite sign in DCM compared to toluene. It was hypothesised that this is due to the macrocycle adopting a different conformation in DCM where: a) the H-type cofacial π–π stacking seen in toluene and in the crystal structure is disrupted, hence the loss of the Cotton effect, and b) the core-twist of the PDI cores is inverted, such that each PDI has the opposite axial chirality, yet *homochirality* is maintained, since this is a distinct process to macrocycle racemisation by PDI somersaulting. As a result of the change in PDI axial chirality, the triazole groups now point in towards the macrocycle's cavity (**Figure 4.2b**).

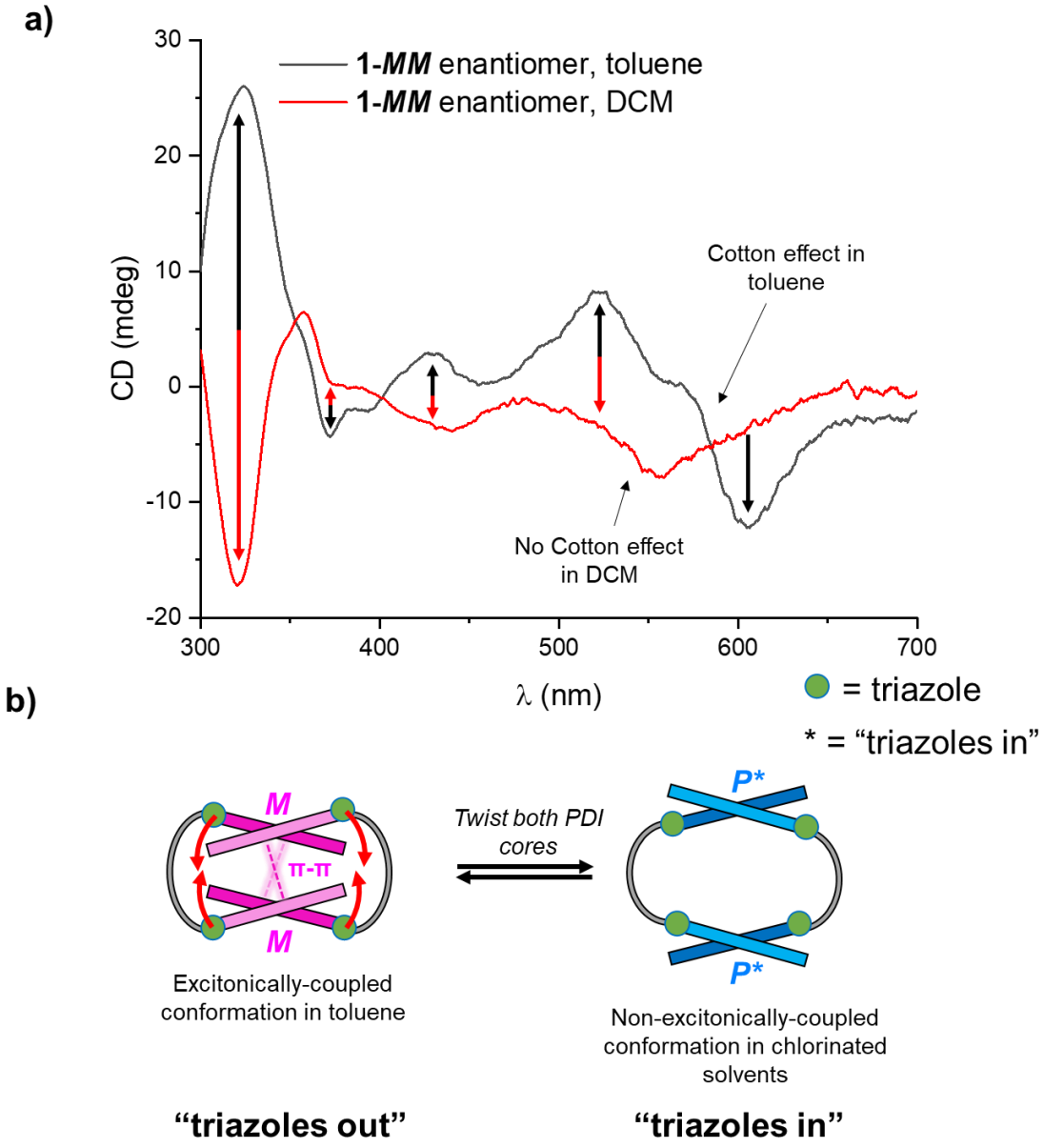

Figure 4.2: a) CD spectra of the same enantiomer (assigned as **1-*MM*** in Chapter 2) in toluene (black trace) and DCM (red trace). **b)** Proposed solvent-induced conformational change that may explain the inversion of the CD spectra in **(a)**, where the PDI cores "twist", resulting in an inversion of the local axial chirality of the PDI cores. In the "triazoles in" conformation, excitonic coupling between the two PDIs is proposed to be "switched off", such that no Cotton effect is seen in the $S_0 \rightarrow S_1$ transition.

It must be stressed that these "triazoles in" and "triazoles out" conformations in **Figure 4.2b** are not mirror images of each other, so while twisting of the PDI cores inverts their local axial chirality, it does not lead to racemisation of the macrocycle as seen for macrocycle **1** over

time in chlorinated solvents. Indeed, as theorised by Nuckolls and co-workers,[1] and proven by the work described in Chapter 3 of this thesis,[2] alongside PDI core twisting, racemisation requires an "intramolecular somersault" motion where one of the PDI imide heads passes through the centre of the cavity (**Figure 4.3**).

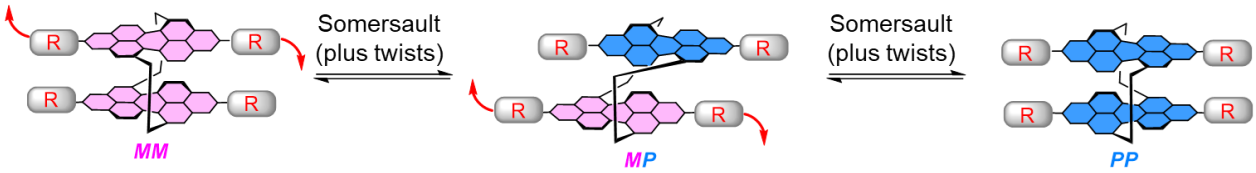

Figure 4.3: A cartoon of the "intramolecular somersault" mechanism for the interconversion of bis-PDI macrocycle stereoisomers.

Considering the PDI cores individually, a twist (**Figure 4.4a**) inverts the local axial chirality of the PDI core (i.e. ***P*** → ***M****, the asterisk [*] used henceforth denotes that the triazole groups now point *in* towards the cavity while no asterisk means the triazoles point *out*). A somersault (**Figure 4.4b**) leads to a reversal in the direction that the triazoles are pointing in, but without a change in local axial chirality (i.e. ***P*** → ***P****). Consideration of all the possible permutations of ***M*** and ***P*** core chirality with "triazoles in" and "triazoles out" conformations for two PDI cores results in 16 possible chiral conformations (**Figure 4.4c**). Of course, some of these conformations, e.g. ***M*P*** and ***MP****, are identical for bis-PDI macrocycles where the PDI units are identical, giving ten distinct conformations (**Figure 4.4c**). **Figure 4.4c** also shows how these chiral conformations can interconvert via PDI somersaults (S) or twists (T).

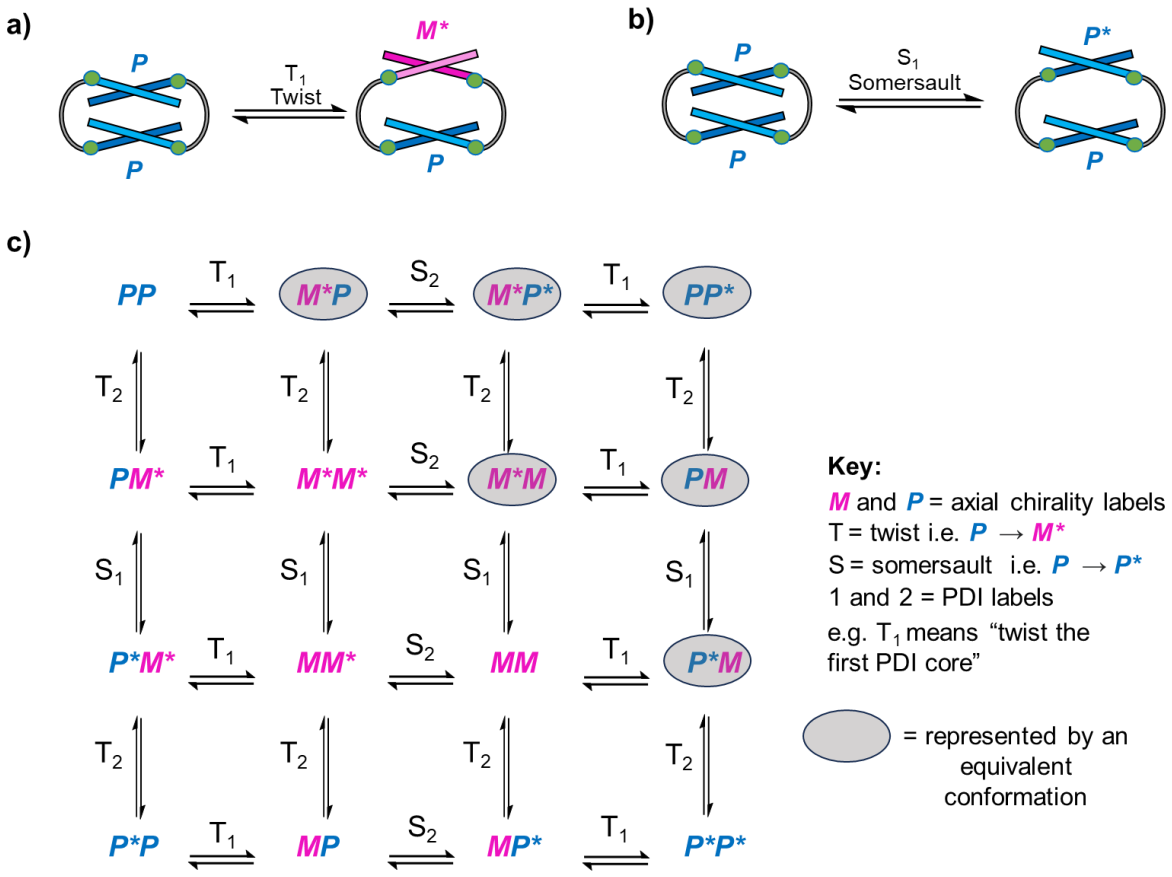

Figure 4.4: a) Cartoon depiction of a "twist" in one of the PDI cores in a bis-PDI macrocycle, resulting in inversion of the local axial chirality of the PDI core (i.e. ***P*** → ***M****). As a result of the twist, the bay substituents (triazoles) now point *in* towards the cavity. **b)** Cartoon depiction of a "somersault" of one of the PDI cores in a bis-PDI macrocycle. A somersault leads to a reversal in the direction that the triazoles are pointing in, but without a change in local axial chirality (i.e. ***P*** → ***P****). **c)** Map of all the possible permutations of ***M*** and ***P*** chirality and "triazoles in" and "triazoles out" conformations in each PDI core in a 1,7-bay-connected bis-PDI macrocycle. These conformations interconvert via "somersaults" (S) or "twists" (T).

Some interesting questions now arise, including: is it possible to control which chiral conformation a macrocycle adopts, what chiral conformational isomer(s) can be isolated, and what impact do these chiral conformations have on their (chir)optical and electronic properties? This Chapter aims to answer these questions by preparing and analysing a new bis-PDI macrocycle in combination with the results from related "Pink Box" type macrocycles reported in Chapters 2 and 3. The analysis in this Chapter is supported by computational studies carried out by Prof. Martijn Zwijnenburg to aid interpretation of the experimental work. These

computational studies are referred to throughout the chapter, and full details about these calculations are given in Appendix A.

4.2 Library of bis-PDI macrocycles

Building on the bis-PDI macrocycles described in Chapters 2 and 3 (**1** and **5**), this Chapter will add to (macrocycles **10** and **11**), and then study, a library of "Pink Box" type macrocycles featuring systematic variation of the imide groups (**Figure 4.5**). For this set of macrocycles, the linker group (para-xylene) is kept constant. Macrocycles **1a** and **1b**, which are discussed extensively in Chapter 2, bear flexible branched alkyl "C_{11}" and "C_5" imide groups. As a result of their flexibility, these groups do not strongly hinder intramolecular PDI–PDI interactions. Macrocycle **5**, which was the focus of Chapter 3, bears long, rigid, *tert*-butyl benzoate imide groups, which enforce chiral locking by preventing the "intramolecular somersault" motion. These groups also have low steric bulk near the PDI cores due to the absence of substituents at the *ortho* positions of the benzene rings, which means that this imide group facilitates PDI–PDI stacking interactions. In contrast to **5**, new macrocycles with *ortho* substituted aromatic imide groups (**10** and **11**) were designed in an attempt to disrupt *homochiral* PDI–PDI stacking interactions while still preventing the "intramolecular somersault" motion, with the aim of enabling further chiral conformers to be isolated and analysed.

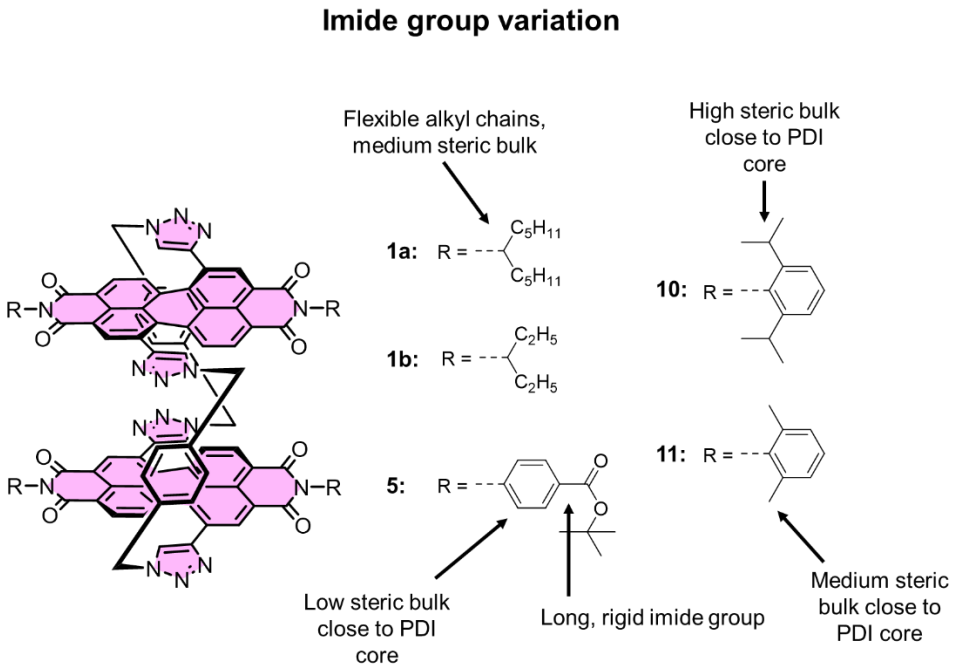

Figure 4.5: Structures of macrocycles **1**, **5**, **10** and **11**, designed to study the effects of imide group variation on the population, stability and properties of the various chiral conformations of "Pink Box" type macrocycles.

4.3 Conformational analysis: branched alkyl imide groups

4.3.1 Homochiral stereoisomers

Let us first consider the original Pink Box macrocycles with branched alkyl imide groups, macrocycles **1a** and **1b**, to identify which chiral conformations they can adopt. For macrocycle **1**, the enantiomers can be separated through chiral HPLC and, as shown in Chapter 2, these enantiomers are exclusively observed in *homochiral* "triazoles out" conformations (i.e. ***MM*** or ***PP***) in toluene and in the solid state. However, the results in Chapter 2 also show that these enantiomers can adopt a different conformation in chlorinated solvents, which is discussed in more detail below and summarised in **Figure 4.6**.

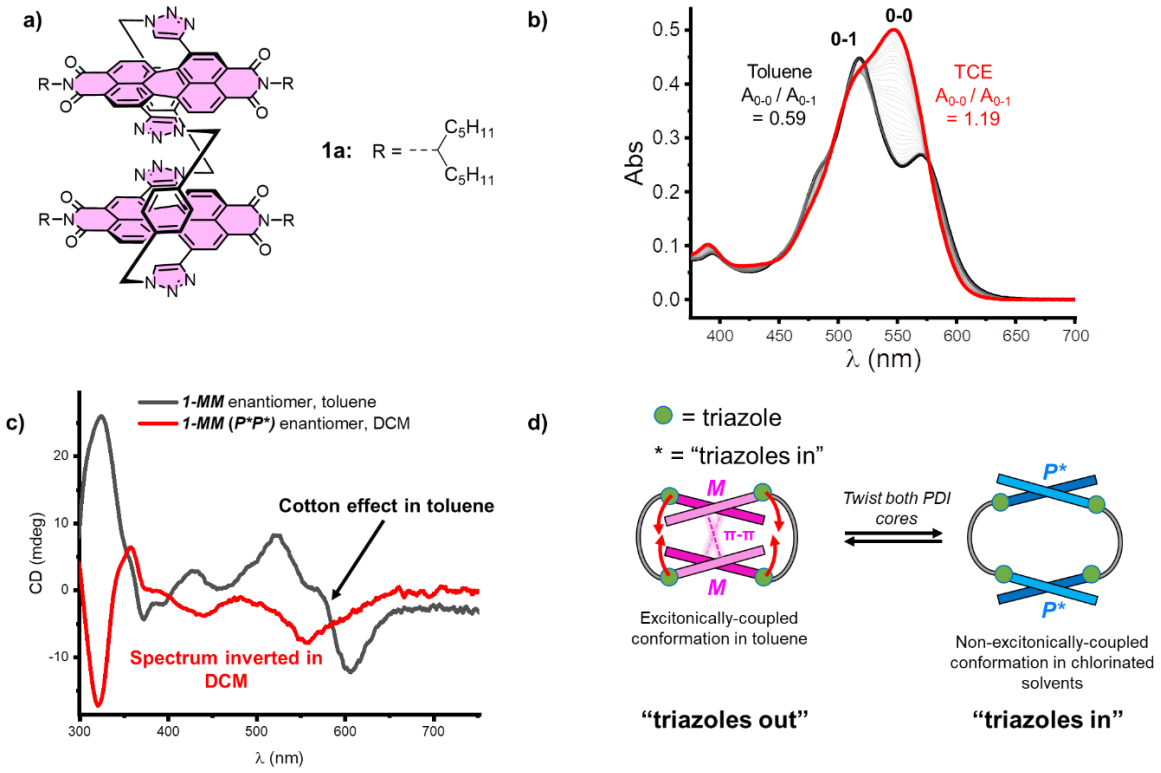

Figure 4.6: a) Structure of macrocycle **1a**. **b)** CD spectra of the same enantiomer (assigned as **1-*MM*** in Chapter 2) in toluene (black trace) and DCM (red trace). **c)** UV-vis absorption spectra of macrocycle **1a** in toluene and TCE, exhibiting solvent-dependent excitonic coupling. **d)** Proposed solvent-induced conformational change that explains the inversion of the CD spectra in **(c)**, where the PDI cores "twist", resulting in an inversion of the local axial chirality of the PDI cores. In the "triazoles in" conformation, excitonic coupling between the two PDIs is proposed to be "switched off", such that no Cotton effect is seen in the $S_0 \rightarrow S_1$ transition.

In particular, CD spectroscopy suggests that that the axial chirality of the PDI cores in the ***MM*** and ***PP*** stereoisomers is inverted in chlorinated solvents (i.e. ***PP*** → ***M*M**** and ***MM*** → ***P*P**, **Figure 4.6c** and **Figure 4.6d**). It must be stressed that this is achieved by a "twist" motion of the PDI cores. This conformational change occurs instantly when the macrocycles are re-dissolved in chlorinated solvents, in contrast with true enantiomerisation (i.e. ***PP*** ⇄ ***MM*** or ***P*P**** ⇄ ***M*M****), which occurs much more slowly (enantiomer half-life $t_{1/2}$ = 5 days in toluene or 18 mins in dichloromethane). This shows that for ***PP*** ⇄ ***MM*** enantiomerisation, it is the "somersault" motion that is the rate-determining step, rather than the twist motion, with the former having a larger energy barrier. This discussion is summarised in **Figure 4.7**, where the chiral conformations corresponding to each enantiomer are grouped together and labelled as "Enantiomer ***PP***" (***PP*** ⇄ ***M*M****) and "Enantiomer ***MM***" (***MM*** ⇄ ***P*P****).

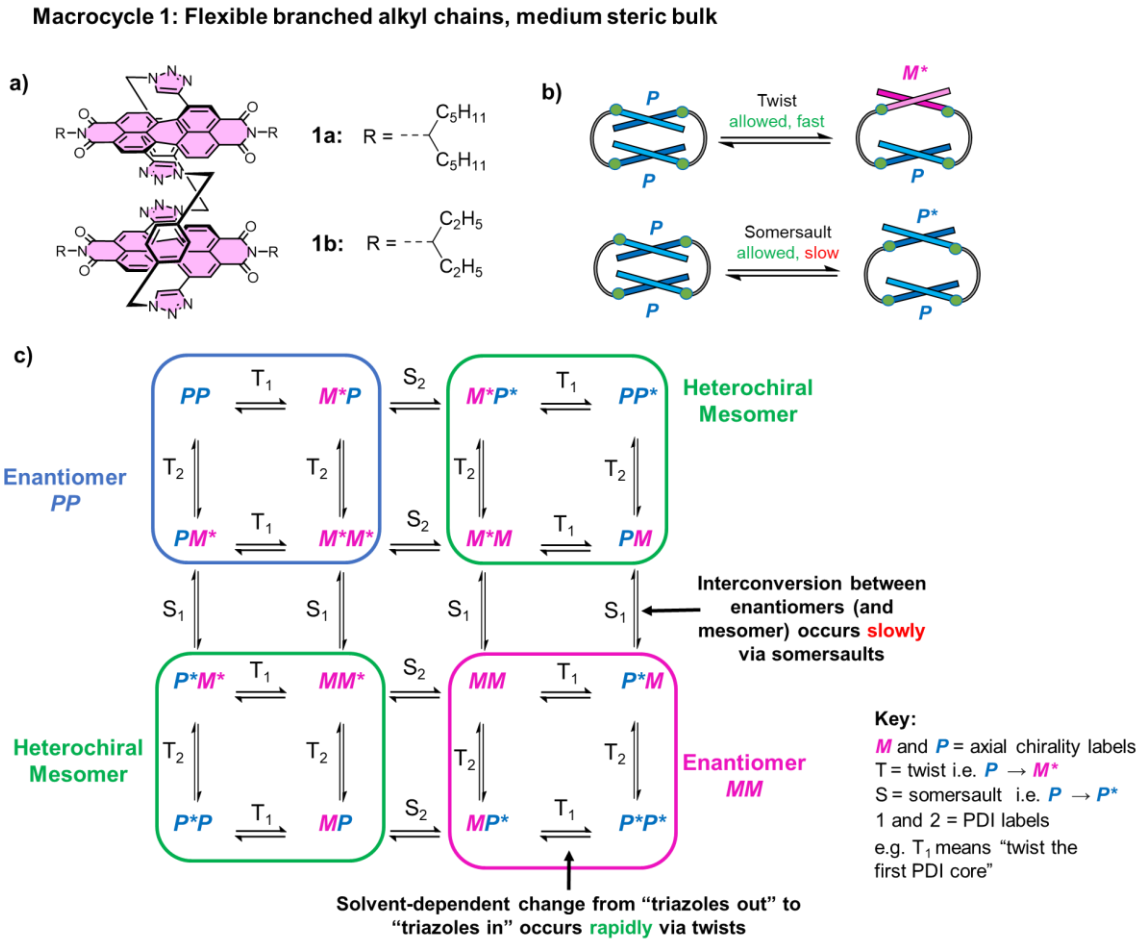

Figure 4.7: a) Structures of macrocycles **1a** and **1b**. **b)** Cartoon depiction of a "twist" and a "somersault" of one PDI core in a 1,7-bay-connected bis-PDI macrocycle. **c)** Annotated map of all the possible permutations of ***M*** and ***P*** chirality and "triazoles in" and "triazoles out" conformations in each PDI core in a 1,7-bay-connected bis-PDI macrocycle, showing which of these conformations correspond to the two isolated enantiomers and meso isomer of macrocycle **1a.** Stereoisomers that are the same (e.g. ***PM**** and ***M*P***) have also been left in for completeness.

4.3.2 Density Functional Theory (DFT) studies

In order to further investigate the "triazoles in" and "triazoles out" conformations, Density Functional Theory (DFT) calculations were carried out by Prof. Martijn Zwijnenburg, for which full details are given in Appendix A. An initial conformer search in the gas phase was carried out using a simplified model of macrocycle **1**, where the alkyl chains at the imide positions (R groups) were replaced with methyl groups. The lowest energy conformer, labelled **A** in **Figure 4.8**, was found to be a *homochiral* "triazoles out" conformer and is virtually identical to the single crystal X-ray crystal structure obtained for macrocycle **1b** (see Appendix A). The second lowest energy conformer (labelled **B**) is closely related to conformer **A**, the

difference being that the macrocycle now has a rotated triazole group. However, the third lowest energy conformation (labelled **C**) is substantially different and is a *homochiral* "triazoles in" conformation. The lowest energy heterochiral conformation was the eight-lowest energy conformation found (labelled conformer **H**) and is also shown in **Figure 4.8**.

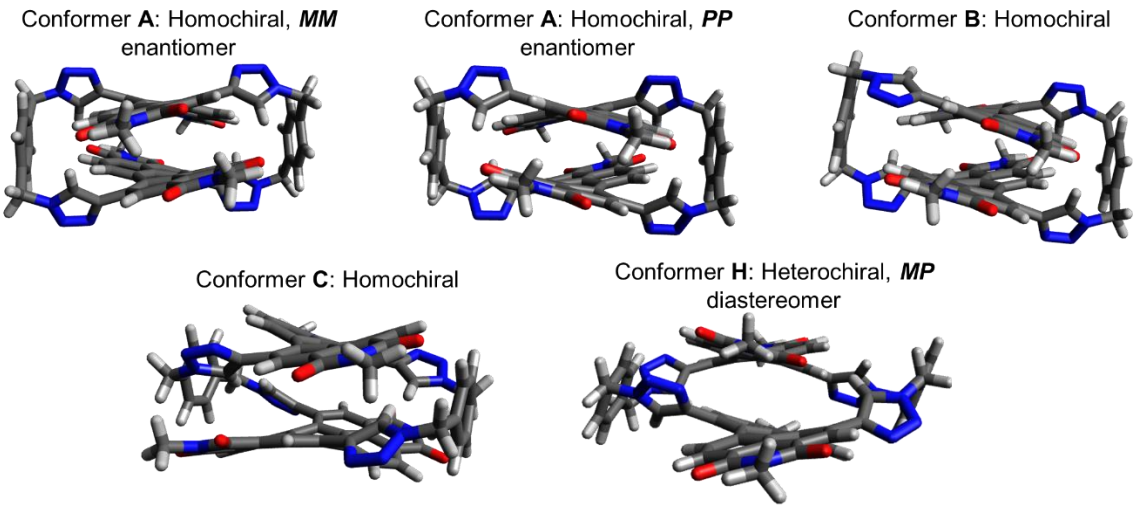

Figure 4.8: Selected DFT-predicted conformers of a simplified model "Pink Box" macrocycle where the imide group is simply a methyl group. The letter labels denote each conformer's position in the ordering of the conformers by energy, e.g. **A** is the lowest energy conformer, **B** is the second lowest, etc. Full details about the DFT calculations are given in Appendix A.

Conformer **A** can convert into conformer **C** most easily by two PDI twists, i.e. twisting the naphthalene units of both PDI units, such that the triazole groups, which point out of the macrocyclic cavity in conformer **A**, now point towards the cavity in conformer **C (Figure 4.9)**. This leads to a change in the PDI axial chirality labels such that conformer **A**, either ***PP*** or ***MM***, becomes ***M*M**** or ***P*P**** respectively, in conformer **C**, with homochirality being maintained. Crucially though, this does not equate to enantiomerisation, as conformer **A**-***PP*** is not a mirror image of conformer **C**-***M*M****. However, TD-DFT calculations (Appendix A) predict that **A→C** conformational change will invert the macrocycle's CD spectrum since the local chirality of the PDI cores has been inverted, which is consistent with the solvent-dependent CD spectrum of **1a** (**Figure 4.6c**).

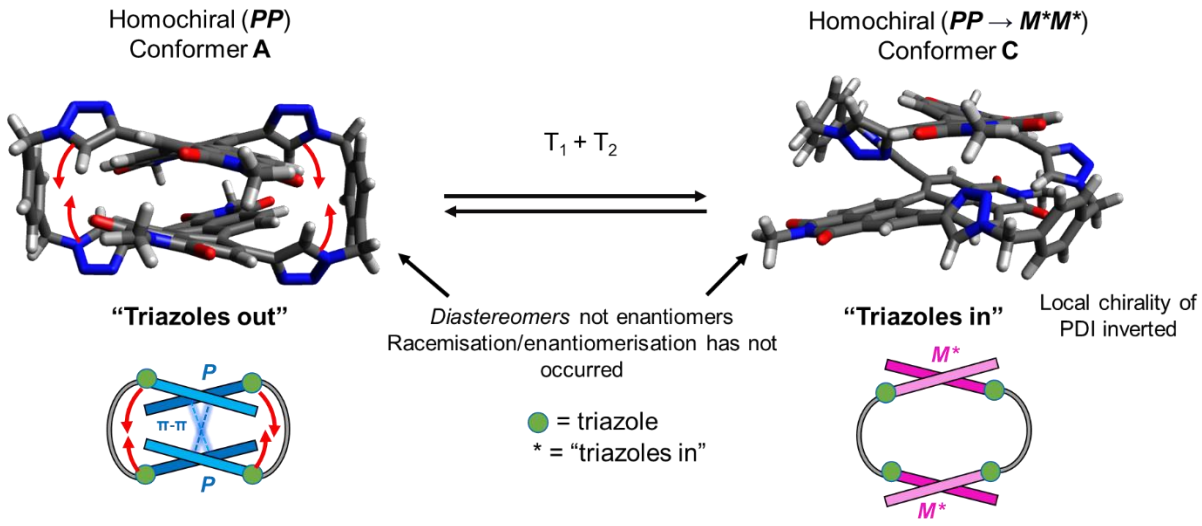

Figure 4.9: Interconversion between DFT-predicted conformers **A** and **C** via a "twist" of the PDI cores.

Confidence in the value of these computational studies was reinforced by comparisons between computationally predicted and experimental NMR, CD and UV-vis absorption spectra measured in toluene which showed excellent agreement for conformer **A** (homochiral enantiomers). Furthermore, the predicted UV-vis and NMR spectra for conformer **C** show good agreement with experimental spectra measured in chlorinated solvents (see appendix A for full details). Therefore, the dominant conformation in toluene of macrocycles **1a/b** is represented by DFT conformer **A**, while the dominant conformation in chlorinated solvents closely resembles that of conformer **C**.

Compared to conformer **A**, the PDIs in conformer **C** have a larger rotational displacement relative to each other. Specifically, the PDI's relative rotation angle is 70° in DFT conformer **C** and 20° in DFT conformer **A** as well as the X-ray crystal structure (**Figure 4.10**). There is no significant change in the PDI-PDI π–π distance in conformers **A** and **C** (3.7 Å), so it was proposed that it is the increase in relative rotation between the PDIs that switches off excitonic coupling between the PDIs upon going from conformer **A** to conformer **C**. This is because, as well as interchromophore distance, PDI-PDI excitonic coupling is extremely sensitive to rotational angle.[3, 4] Indeed, this has since been confirmed by recent calculations by Bressan, Meech and co-workers,[5] which showed that the population of conformer **C** explains the monomer-like absorption spectrum for macrocycle **1** in chlorinated solvents because this conformer leads to a cancelling out of the long- and short-range electronic coupling between the PDI units, resulting in a "null aggregate".[3]

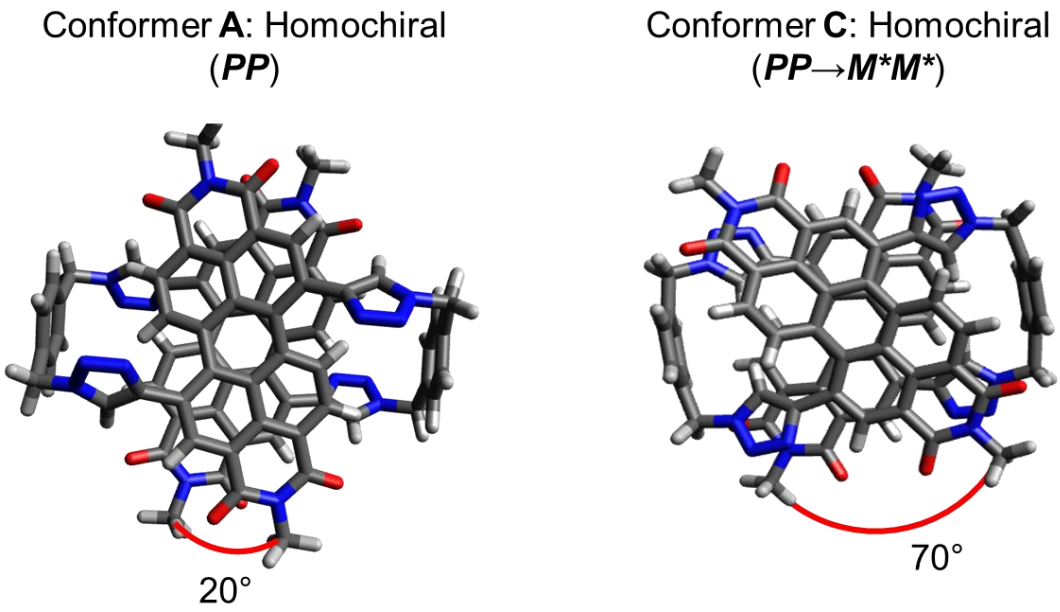

Figure 4.10: A top-down view of conformer **C** shows the PDI units are rotated by 70° relative to one another, which switches off PDI–PDI excitonic coupling. This contrasts with the 20° rotation in the H-type coupled conformer **A** as seen by DFT and X-ray crystallography.

4.3.3 Heterochiral conformer

Additionally, in chlorinated solvents a distinct macrocycle stereoisomer is observed by a second set of signals by ^{1}H NMR spectroscopy (**Figure 4.11a**) and as a separate peak in the chiral HPLC chromatogram (**Figure 4.11b**). This was assigned in Chapter 2 as the heterochiral meso isomer, ***MP***. This now poses a new question; how might this conformation be described in terms of "triazoles in" vs "triazoles out", i.e. is it ***MP*** or ***M*P****? The lowest energy heterochiral conformer found by DFT (conformer **H**) suggests that the triazoles point "in" as this conformation can geometrically facilitate a heterochiral slip-stack PDI-PDI contact where the naphthalene units in contact are parallel to each other, while likely minimises ring strain in the macrocycle as well (**Figure 4.11c**). However, as the stereoisomers of macrocycle **1** interconvert rapidly in chlorinated solvents, it proved impossible to isolate and study the heterochiral conformer. As such, the following sections detail efforts to stabilise and isolate the chiral conformers of bay-connected bis-PDI macrocycles, including this heterochiral conformer, "***MP***".

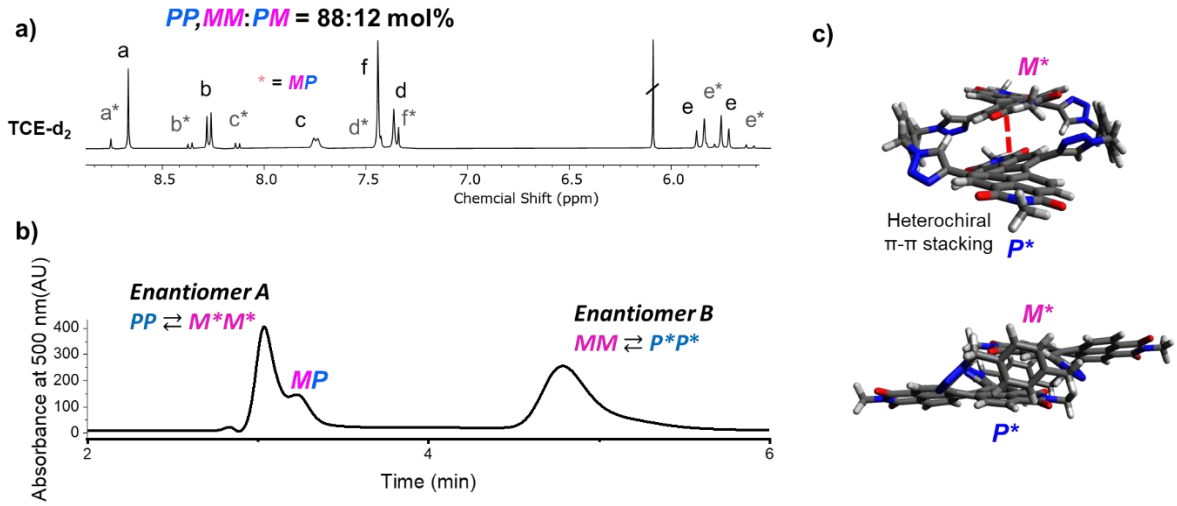

Figure 4.11: a) ^{1}H NMR spectrum of macrocycle **1a** in TCE-d_2, showing the presence of the heterochiral diastereomer as a separate set of signals. **b)** Chiral HPLC chromatogram of macrocycle **1a** dissolved in DCM and eluted with 7:3 (v/v) DCM:n-hexane eluent, showing a peak corresponding to the heterochiral diastereomer in addition to two peaks of equal integration corresponding to the pair of enantiomers. **c**) Lowest energy DFT-predicted heterochiral conformer of a "Pink Box" bis-PDI macrocycle (conformer **H**).

4.3.4 Summary

In summary, macrocycles **1a** and **1b** provide the first results to suggest it is possible to switch between "triazoles in" and "triazoles out" chiral conformations for each enantiomer via a "twist" motion of the PDI core by switching the solvent (***PP*** ⇄ ***M*M**** and ***MM*** ⇄ ***P*P****). True enantiomerisation (***PP*** ⇄ ***MM*** or ***P*P***** ⇄ ***M*M****) occurs more slowly and requires a "somersault" motion of the PDI cores. A heterochiral conformer is also observed in chlorinated solvents (but not in toluene and in the solid state), but at this stage it is challenging to establish whether it is ***MP*** or ***M*P****. Additionally, as these conformational-dynamic macrocycles allow both "somersaults" and "twists" it is possible that all of the chiral conformers shown in **Figure 4.4c** may exist as short-lived intermediates, although only ***MM***, ***PP***, ***M*M****, ***P*P****, and ***MP/M*P**** have been detected experimentally (**Figure 4.12**). It should be noted that "non-symmetric" conformations with one PDI with "triazoles in" and the other with "triazoles out" (e.g. ***MP****, ***PP***, **MM****) have not been observed experimentally, since this conformation would result in more complex ^{1}H NMR spectra arising from inequivalent PDI units.

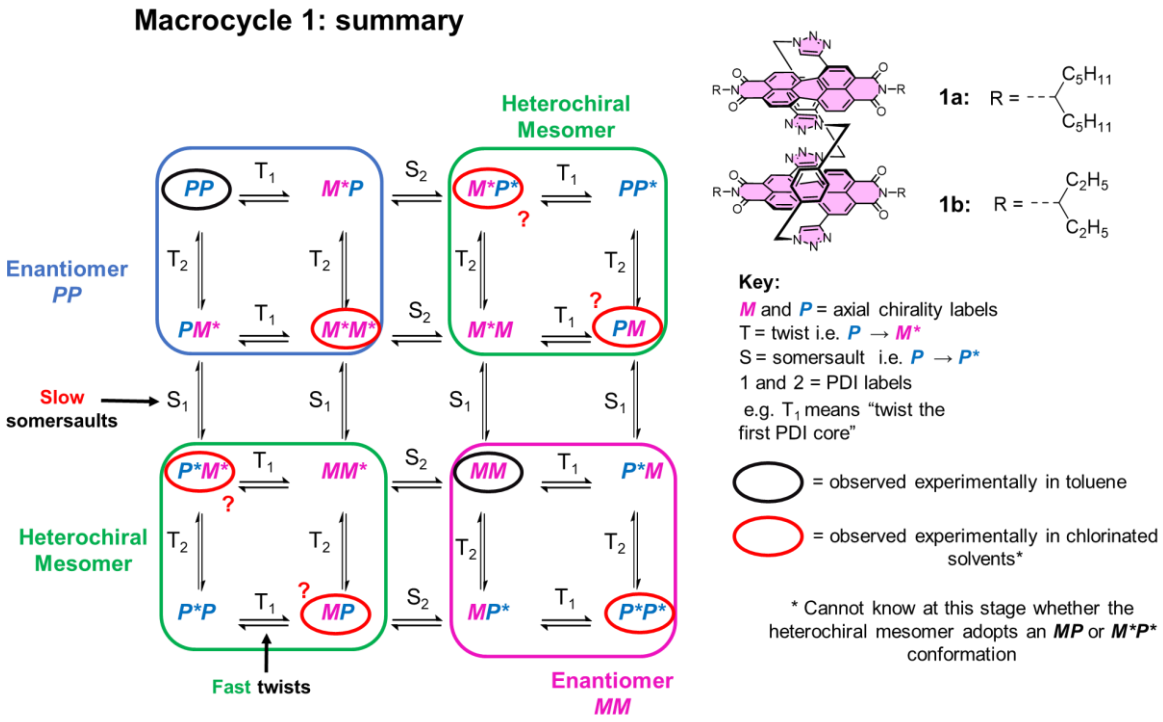

Figure 4.12: Annotated map of all the possible permutations of ***M*** and ***P*** chirality and "triazoles in" and "triazoles out" conformations in each PDI core in a 1,7-bay-connected bis-PDI macrocycle, showing which of these conformations have been observed experimentally in different solvents with macrocycle **1a/b**. Overall, macrocycle **1a/b** exhibits a dynamic conformation. In toluene conformers ***MM*** and ***PP*** are observed, while in chlorinated solvents ***M*M**** and ***P*P**** are observed in addition to the heterochiral diastereomer, which at this point cannot be assigned conclusively as either ***MP*** or ***M*P**.

4.4 Conformational analysis: *tert*-butyl benzoate imide groups (chirally locked)

As outlined in Chapter 3, macrocycle **5**, bearing long, rigid *tert*-butyl benzoate imide groups, was synthesised as an attempt to prevent racemisation by stopping the "intramolecular somersault" motion. This was successfully achieved, allowing stable enantiomers to be isolated and studied (**Figure 4.13a-b**). However, unlike macrocycle **1a/b**, macrocycle **5** does not exhibit any significant change in its CD and UV-vis absorption spectra upon changing the solvent from toluene to chlorinated solvents, implying that the macrocycle's conformation does not change with solvent (**Figure 4.13c-d**).

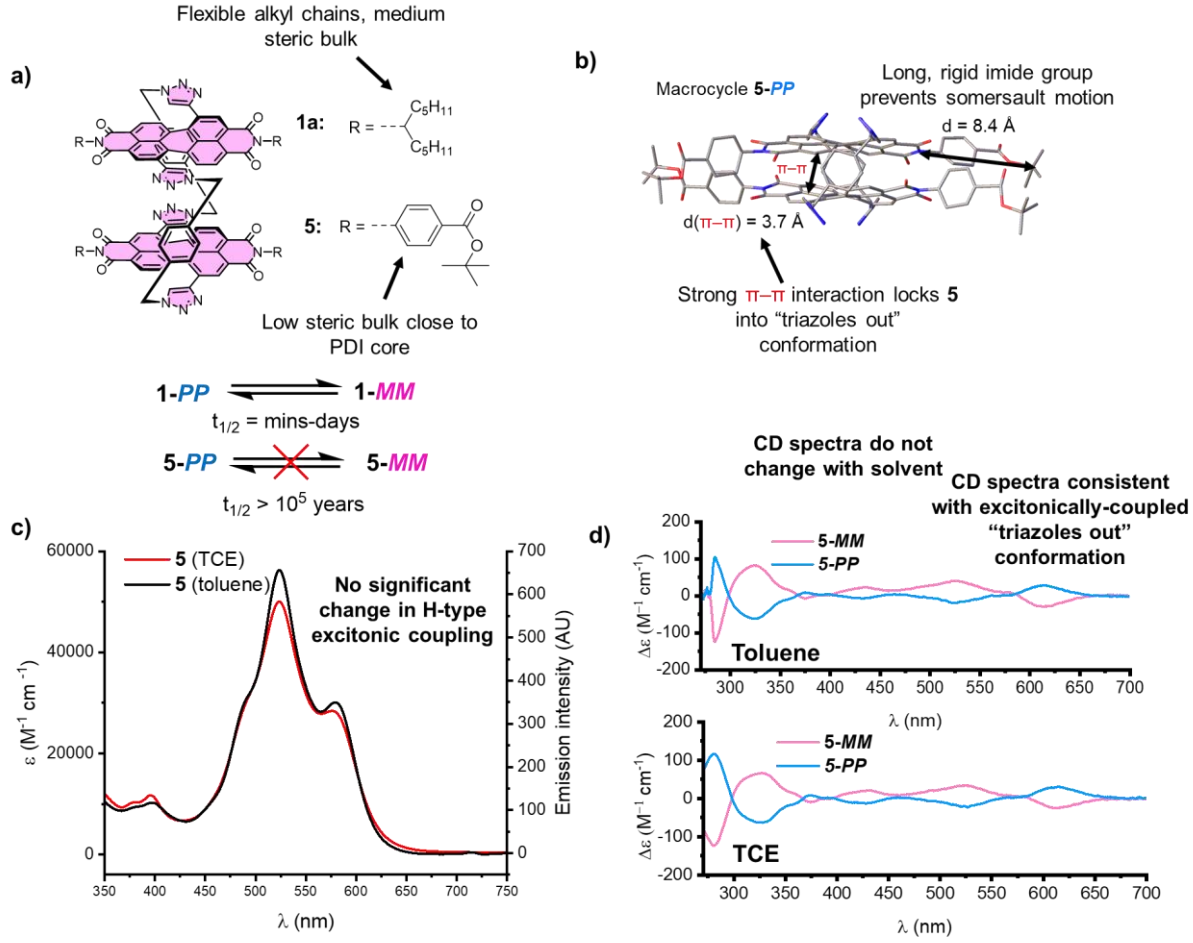

Figure 4.13: a) Structure of macrocycles **1a** and **5**, as well as the racemisation half-lives for both macrocycles. For macrocycle **5**, the enantiomers are stable with respect to racemisation because the long, rigid imide group successfully inhibits "intramolecular somersault" motions of the PDI imide heads through the centre of the macrocyclic cavity. **b)** X-ray crystal structure of macrocycle **5-*PP***, highlighting how the length and rigidity of the imide group prevents intramolecular somersaults. **c)** UV-vis absorption spectra of macrocycle **5** in TCE and

toluene, showing that intramolecular PDI-PDI H-type excitonic coupling is present in both solvents. **d)** CD spectra of the enantiomers of macrocycle **5** in toluene and TCE, which are essentially identical, suggesting that there is very little, if any, solvent-dependent conformational change in macrocycle **5**.

Therefore, macrocycle **5** appears to only ever populate the *homo*chiral, "triazoles out" conformations, i.e. ***MM*** or ***PP***. This is because the PDI–PDI π–π interactions, which are switched on in ***MM***/***PP*** conformations (but off in ***M*M***/ ***P*P****), are stronger in macrocycle **5** compared to **1** as a result of the lower steric bulk of the imide groups. As a result, the ***MM***/***PP*** conformations will be lower in energy than the ***M*M***/ ***P*P**** conformations for macrocycle **5** compared to macrocycle **1**. In addition, as discussed in Chapter 3, no heterochiral ***MP***/***M*P**** conformers could be observed or isolated.

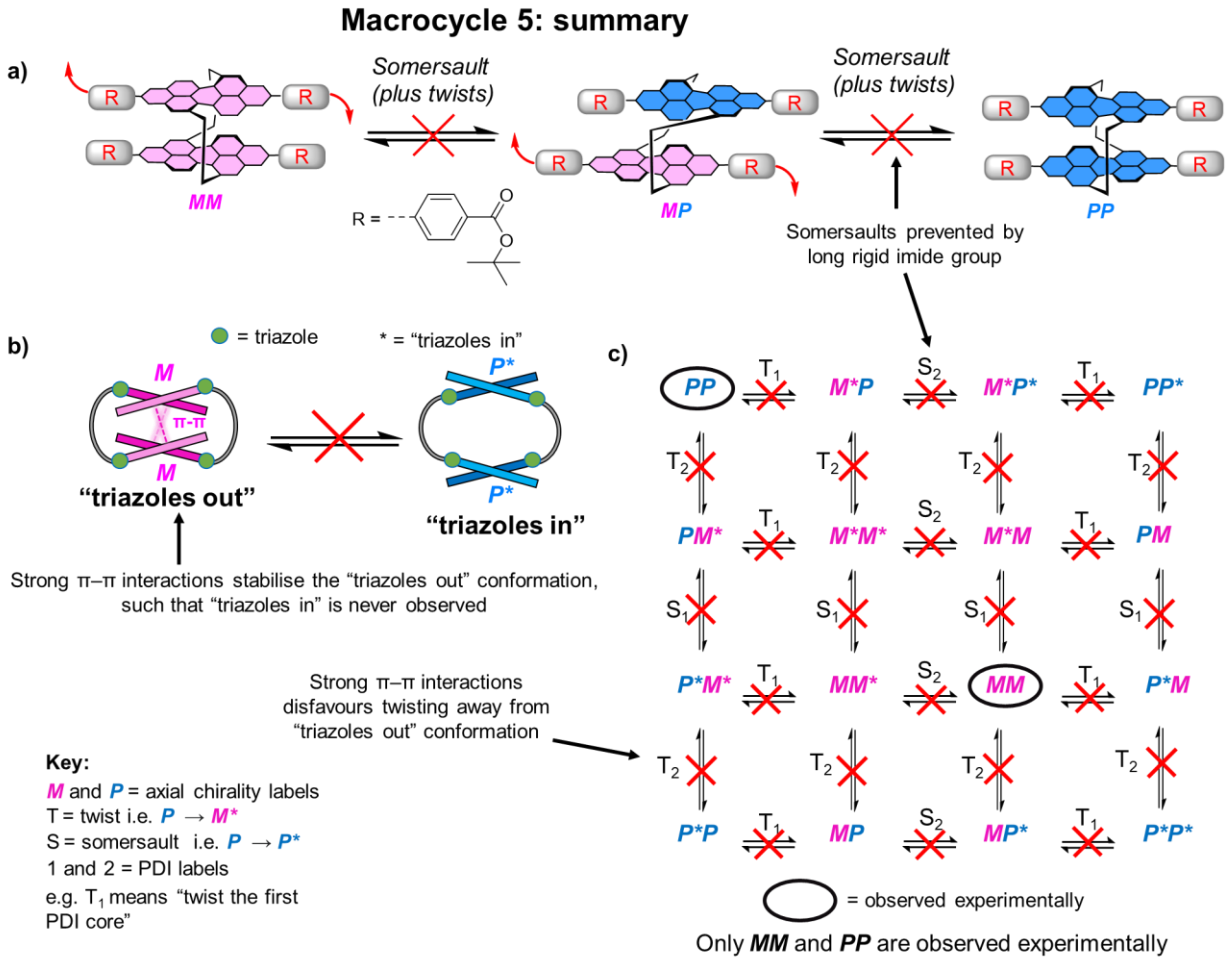

Figure 4.14: Summary of results for macrocycle **5**. **a)** Cartoon depiction of how the long, rigid, imide groups in macrocycle **5** prevent interconversion between stereoisomers by preventing "intramolecular somersaults" of the PDI imide heads through the centre of the macrocyclic cavity. **b)** Annotated map of all the possible permutations of ***M*** and ***P*** chirality and "triazoles in" and "triazoles out" conformations in each PDI core in a 1,7-bay-connected bis-PDI macrocycle, showing which of these conformations can be observed experimentally in different solvents for macrocycle **5**. The only conformers observed experimentally in any solvent for macrocycle **5** are ***MM*** and ***PP***.

In summary, macrocycle **5**, with long, rigid *tert*-butyl benzoate imide groups is not just chirally locked by preventing somersaults, it is also locked into the *homochiral*, "triazoles out" conformations ***MM***/***PP*** by preventing PDI twisting.

4.5 Conformational analysis: 2,6-dialkyl phenyl imide groups

4.5.1 Introduction

The results for macrocycle **1** show that it is possible to control the chiral conformation of Pink Box-type macrocycles using a stimulus (solvent), while the results for macrocycle **5**

show that the number of chiral conformers can be reduced via structural modification of the substituents on the macrocycle (elongation and rigidification of the imide group). This then presented a further challenge: the possibility to design and synthesise a 3rd generation bis-PDI macrocycle that combines both the chiral lock of macrocycle **5** (i.e. no racemisation) with the ability to switch between "triazoles in" and "triazoles out" conformers like macrocycle **1**. This is a worthwhile goal because this bis-PDI macrocycle would have separable and indefinitely stable enantiomers with chiral properties (PDI core local axial chirality, CD signal) that can be switched using an achiral stimulus such as solvent, without racemisation occurring. The switching of chiral properties using an achiral stimulus has been observed in only a small handful of molecular systems.[6-10] Furthermore, developing further chirally-locked macrocycles provides the exciting possibility of obtaining a stable sample of the heterochiral diastereomer (***MP***) for analysis (**Figure 4.15**).

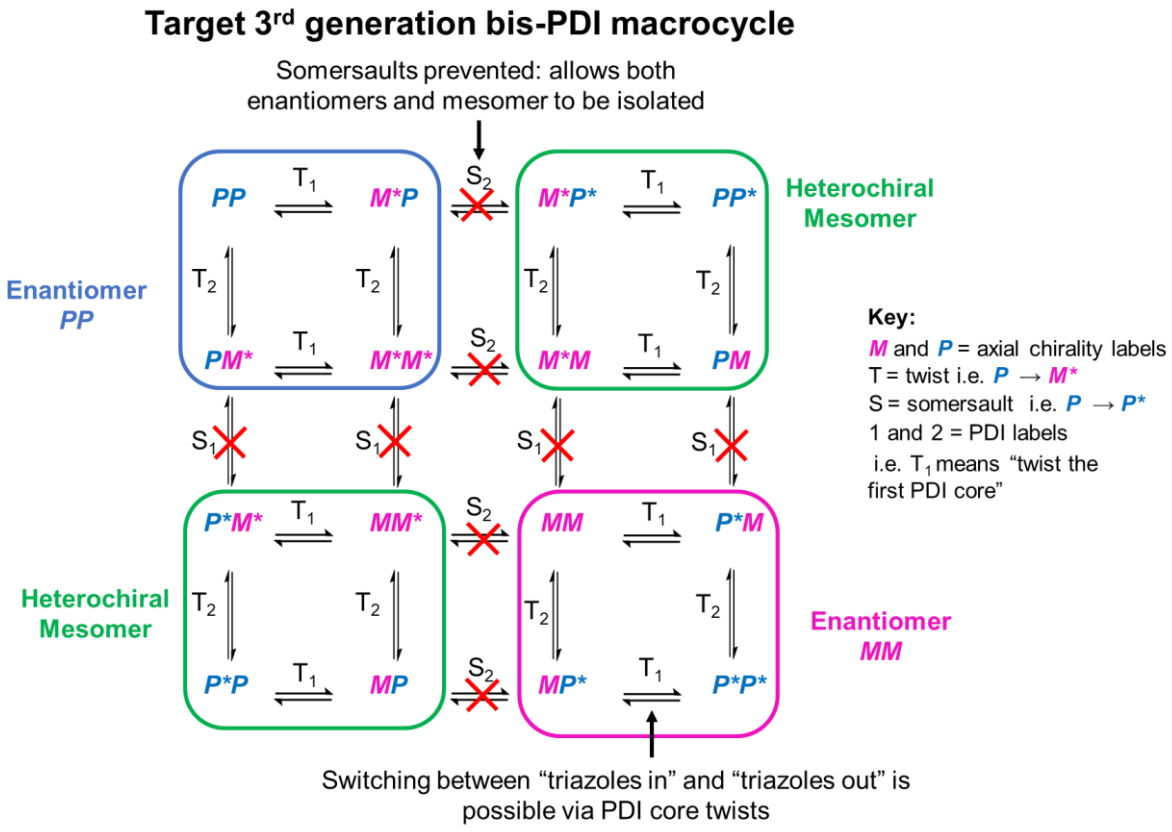

Figure 4.15: Target 3rd generation bis-PDI macrocycle, which aims to isolate both enantiomers and the heterochiral meso isomer in a "Pink Box" type macrocycle by preventing "intramolecular somersault" motions, while still allowing solvent-switching between "triazoles in" and "triazoles out" conformations.

4.5.2 Macrocycle design

With the above goals in mind, macrocycles **10** and **11** were designed as candidates for this 3rd generation bis-PDI macrocycle. The strategy here was to introduce imide groups that enforce chiral locking (such that enantiomerisation ***PP*** ⇄ ***MM*** cannot occur), but have added steric bulk so that they can temper PDI-PDI interactions, such that conformational changes through PDI core twist motions can still occur (i.e. ***PP*** ⇄ ***M*M**** and ***MM*** ⇄ ***P*P**** occurs without racemisation). The aromatic imide groups may temper intramolecular interactions because they are positioned perpendicular to the plane of the PDI cores to avoid steric clashing with the PDI carbonyl oxygens as shown by crystallography and computational modelling (**Figure 4.17**). In addition, it was hoped that the increased steric bulk of the imide groups will hinder *homochiral* templation as was seen in Chapter 3, such that the ***MP***/***M*P**** stereoisomer may be formed and isolated (**Figure 4.16**).

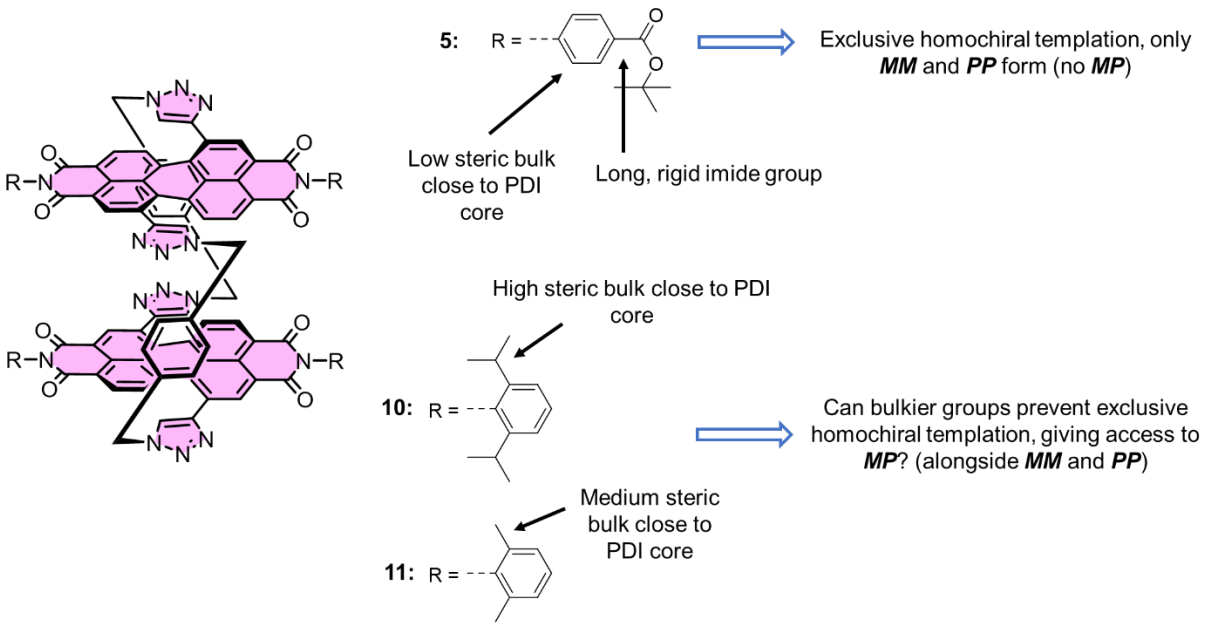

Figure 4.16: Structure of macrocycles **5**, **10**, and **11** highlighting the differences in steric bulk of their imide groups.

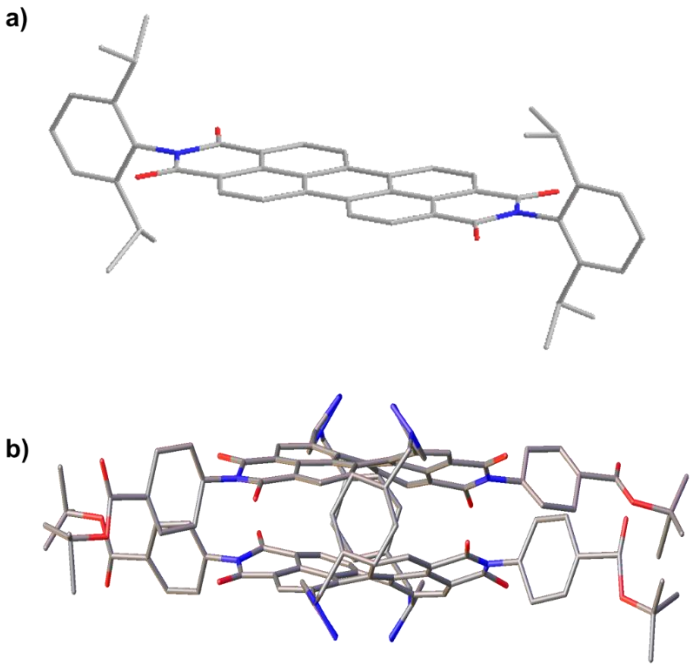

Figure 4.17: a) MM2-minimised structure of a bay-unsubstituted PDI with 2,6-diisopropylaniline imide groups. **b)** Crystal structure of macrocycle **5**. Note that in both cases the plane of the aromatic imide groups lies perpendicular to the plane of the PDI units.

4.5.3 Synthesis of 3rd generation macrocycles **10** and **11**

The synthesis of 3rd generation bis-PDI macrocycles was carried out using the same strategy as for macrocycles **1** and **5**, with a final macrocyclisation step where stoichiometric amounts of bis-alkyne PDI **12/15** and bis-azide PDI **13/16** are reacted under relatively high-dilution conditions (0.3 mM), to favour macrocyclisation.[11] Full details about the synthetic efforts to make macrocycles **10** and **11** are given in the experimental section 4.7.

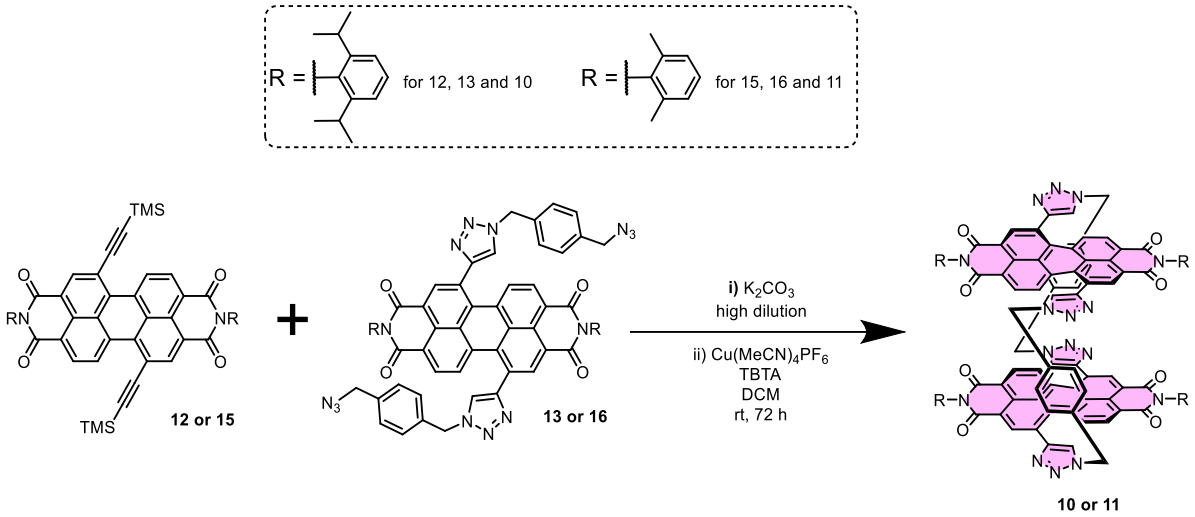

Figure 4.18: Final macrocyclization step in the synthesis of macrocycles **10** and **11**.

The synthesis of macrocycle **10** was attempted first. Unfortunately, macrocycle **10** could only be isolated in trace amounts (< 1 mg) and was only detectable by MALDI mass spectrometry. This is likely because the large steric bulk of the imide groups severely hinders the formation of the macrocycle. Indeed, MALDI mass spectrometry analysis of the crude reaction mixture appears to show the formation of a tris-PDI oligomer in preference to the macrocycle (**Figure 4.19**).

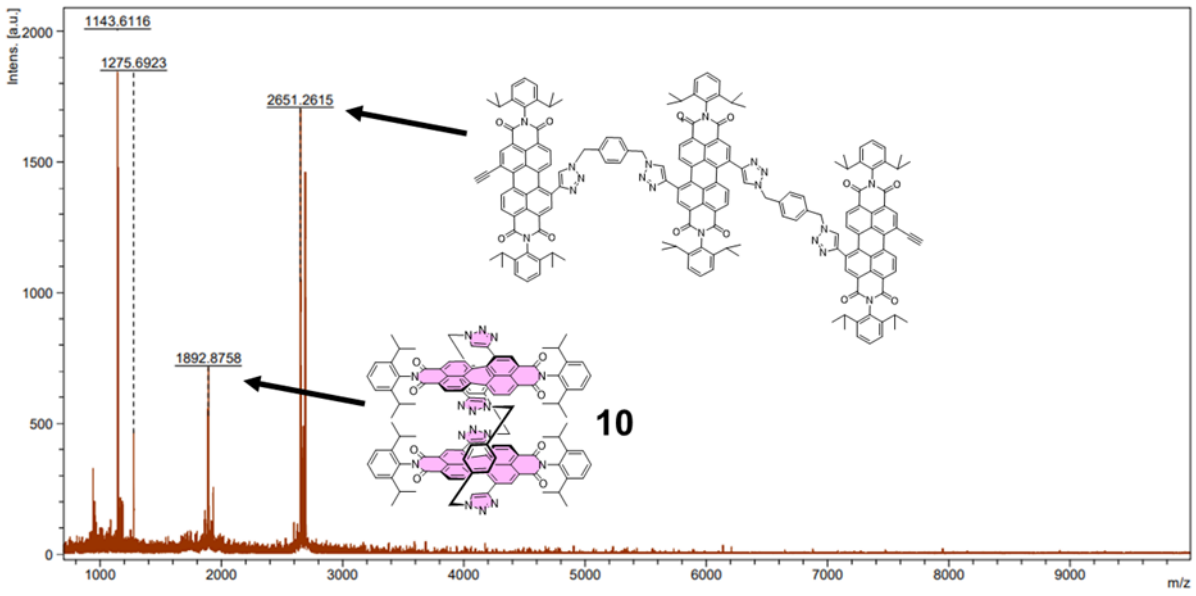

Figure 4.19: MALDI mass spectrum for the crude reaction mixture of the final macrocyclisation step in the synthesis of macrocycle **10**, after filtration to remove insoluble impurities (which are likely longer PDI oligomers).

Due to the failure to isolate macrocycle **10**, macrocycle **11** was designed with the same goals in mind but with somewhat reduced bulk at the *ortho* position on the imide groups, to aid macrocycle formation. Macrocycle **11** was prepared in an isolated yield of 9%, which included both the purified *homochiral* and heterochiral stereoisomers. In practice the yield of **11** was higher but was hampered by challenging purification which required the use of HPLC. Macrocycle **11** was fully characterised by ^{1}H NMR spectroscopy and high-resolution mass spectrometry (see section 4.7.3).

4.5.4 Isolation of stereoisomers of macrocycle **11**

Analytical HPLC analysis of the crude reaction mixture of macrocycle **11** revealed four peaks (**Figure 4.20**). MALDI mass spectrometry analysis of these fractions showed that two of them (A and C) contained the mass of the desired bis-PDI macrocycle. Peaks A and C were then isolated by preparative HPLC in a 3:2 ratio where, as shown from their analysis in the following sections, they correspond to thee configurationally stable homochiral and heterochiral stereoisomers of macrocycle **11**.

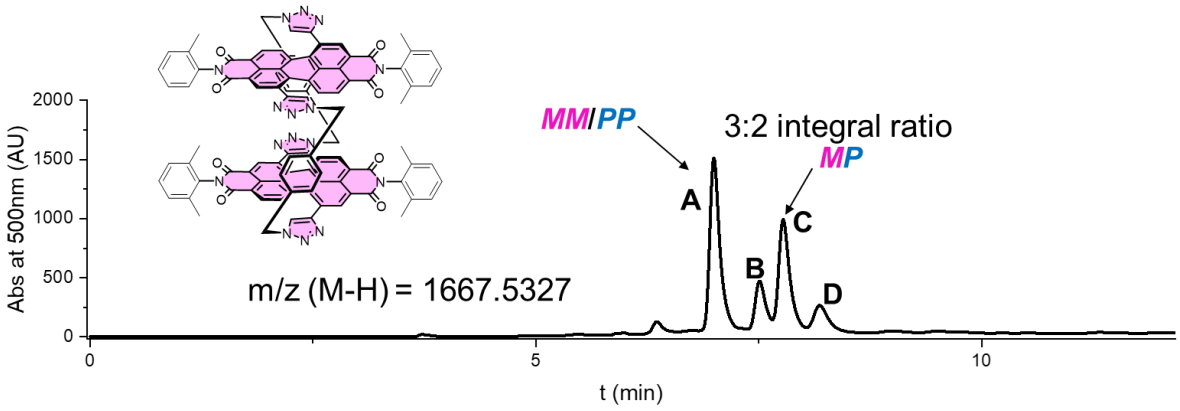

Figure 4.20: HPLC chromatogram of the crude reaction mixture (COSMOSIL Buckyprep 250 x 10 mm**,** eluted with a gradient going from 1:1 (v/v) DCM:n-hexane eluent to 7:3:1 (v/v/v) DCM:n-hexane:isopropanol) for the final macrocyclisation step in the synthesis of **11**, after filtration to remove insoluble impurities (likely longer PDI oligomers). Only peaks A and C contained the mass of macrocycle **11** upon analysis by MALDI mass spectrometry.

4.5.5 Analysis of the homochiral stereoisomers of macrocycle **11**

^{1}H NMR spectroscopy in TCE-d_2

Peak A in **Figure 4.20**, which corresponds to the homochiral stereoisomer **11-*homo*** (a racemic mixture of **11-*MM*** and **11-*PP*** enantiomers, *vide infra*), was isolated by preparatory

HPLC. Further details are given in experimental section 1.7.2. Macrocycle **11-*homo*** was first analysed by ^{1}H NMR spectroscopy in TCE-d_2 (**Figure 4.21**). At room temperature, the ^{1}H NMR spectrum is sharper than for macrocycle **1**, which potentially indicates a simpler conformational landscape. However, heating to 70 °C is required to observe the diastereotopic splitting of the methylene protons H_e in the *para*-xylyl linker.

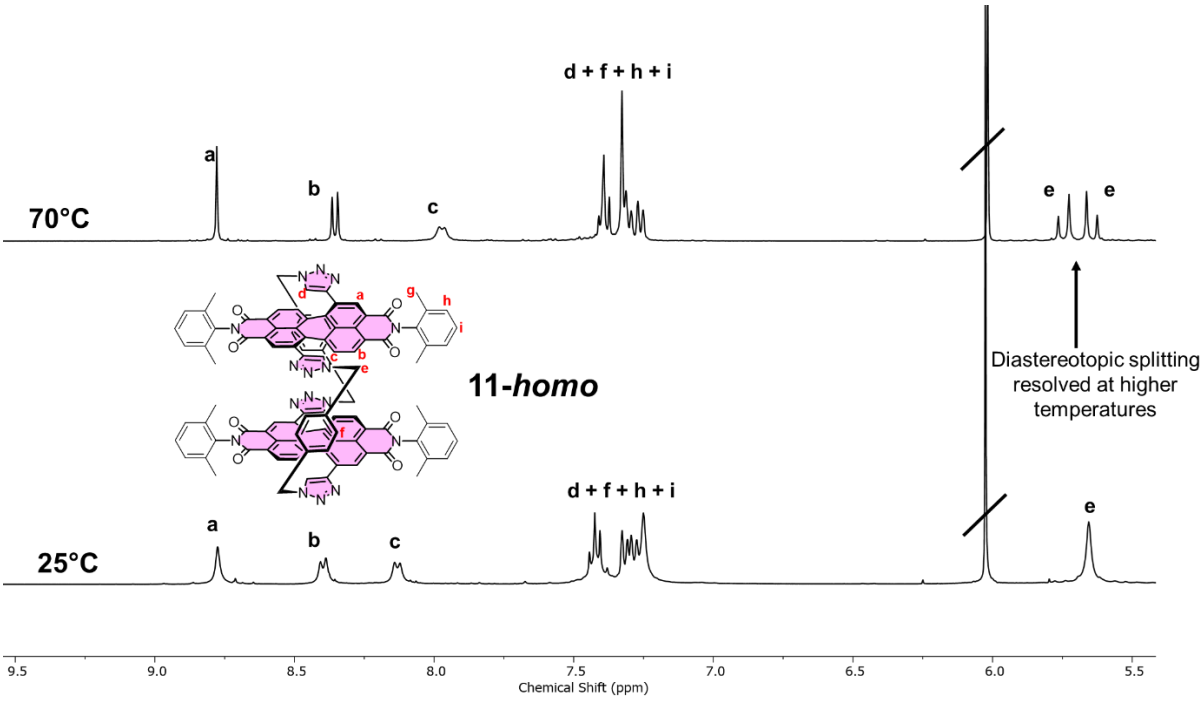

Figure 4.21: ^{1}H NMR spectra (TCE-d_2, 400 MHz) of macrocycle **11-*homo*** at 70°C (top) and 25°C (bottom).

At high temperature the ^{1}H NMR spectrum of macrocycle **11-*homo*** is remarkably similar to that of original macrocycle **1**, with the main being difference being that the second set of peaks corresponding to the heterochiral ***MP*** stereoisomer, as seen in macrocycle **1**, is not seen for macrocycle **11-*homo*** (**Figure 4.22**) This is consistent with chiral locking having been achieved in **11-*homo*** with the heterochiral stereoisomer having been separated by HPLC.

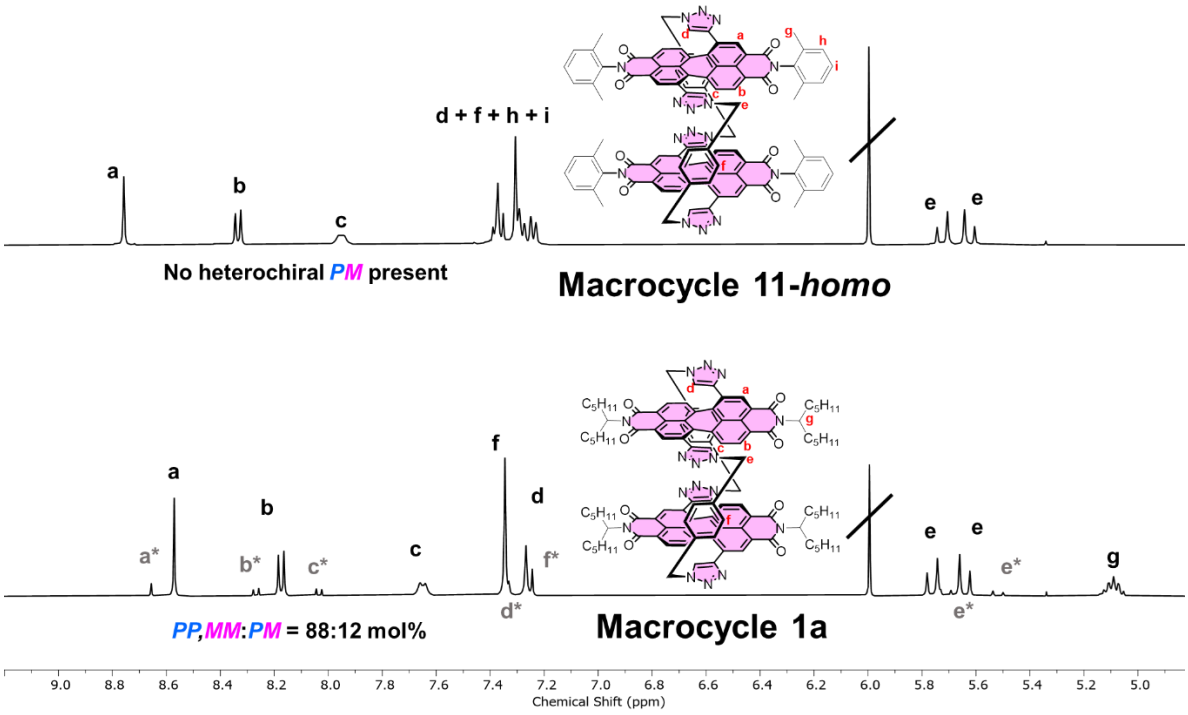

Figure 4.22: ^{1}H NMR spectra (TCE-d_2, 400 MHz) of macrocycle **11-*homo*** (70°C, top) and **1** (100°C, bottom).

Enantiomer resolution by chiral HPLC

The chiral HPLC chromatogram of **11-*homo*** revealed the presence of two peaks of equal integration (**Figure 4.23a**), corresponding to the pair of enantiomers **11-*MM*** and **11-*PP***, as confirmed by CD spectroscopy (**Figure 4.23c**). Semi-preparatory scale chiral HPLC allowed the enantiomers to be isolated. To prove that these are indeed chirally locked, a sample of **11-*PP*** was re-dissolved in 1,2-dichlorobenzene and heated at 180 °C overnight. Subsequent re-injection of this sample into the chiral HPLC column revealed that it remained enantiomerically pure (**Figure 4.23b**). Therefore, no racemisation via intramolecular somersaulting occurs for **11-*homo***.

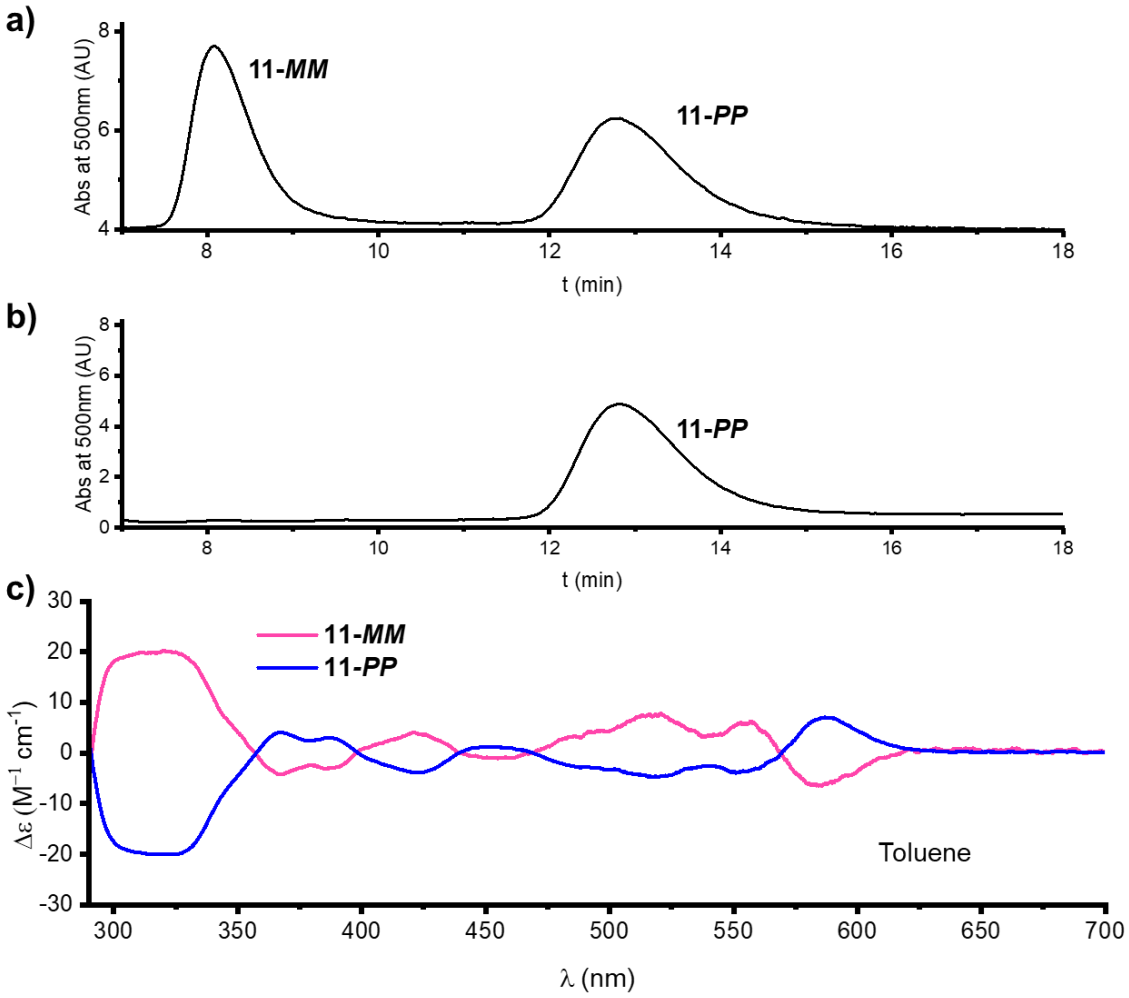

Figure 4.23: a) Chiral HPLC chromatogram of **11-*homo*** (Phenomenex i-Amylose-1, 250 x 10 mm, 7:3 (v/v) DCM:n-hexane eluent). Peak integral ratio (**11-*MM*:11-*PP***) = 1:1. **b)** Chiral HPLC chromatogram of the pure enantiomer **11-*PP*** that was heated at 180 °C for 24 h in 1,2-dicholorbenzene. After heating, the solvent was removed and the sample was re-dissolved in DCM and reinjected into the chiral HPLC column and eluted with 7:3 (v/v) DCM:n-hexane eluent. No formation of the opposite enantiomer **11-*PP*** can be detected in this chromatogram, proving that macrocycle **7** is chirally locked at temperatures at least as high as 180 °C. **c)** CD spectra of the enantiomers **11-*MM*** and **11-*PP*** (toluene, 10μM).

Chirally-locked conformational switching

As shown above, **11-*homo*** is chirally locked, as was the case for macrocycle **5**. However, with macrocycle **5** it was not possible to switch between "triazoles in" and "triazoles out" conformations by changing the solvent. Therefore, **11-*homo*** was investigated to see if conformational switching can be achieved by measuring the CD spectra of the enantiomers of

11-*homo* in toluene and TCE. The CD spectra for **11-*MM*** in these solvents are shown in **Figure 4.24**.

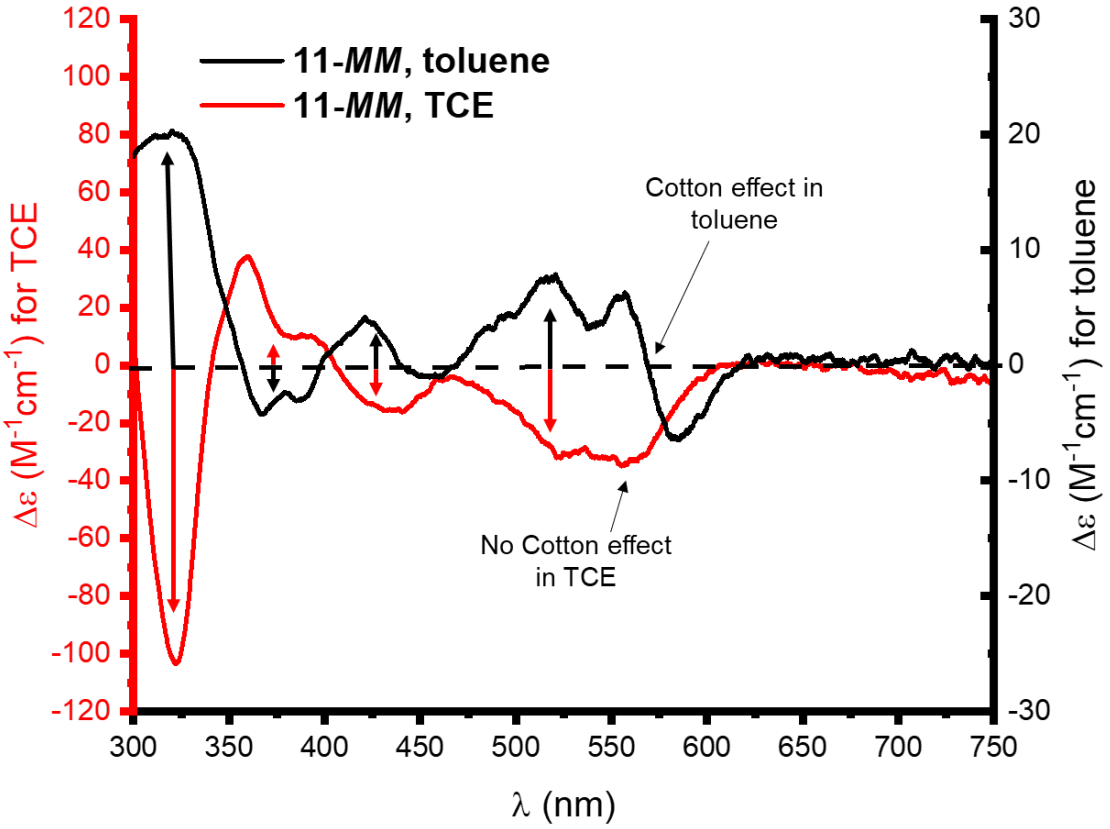

Figure 4.24: CD spectra (10 μM) of the same enantiomer **11-*MM*** in toluene (black trace) and TCE (red trace). Note the different scales for Δε in the two solvents to highlight the changes occurring.

Switching the solvent from toluene to TCE leads to a general reversal of the CD sign across the spectrum, consistent with a dominant "triazoles out" (***MM***) conformation in toluene and a dominant "triazoles in" (***P*P*****) conformation in TCE, as seen and discussed for macrocycle **1**. Likewise, chiral excitonic coupling is observed in toluene but not in TCE, as evidenced by the presence or absence of a Cotton effect for the S0→S1 transition. However, in comparison to macrocycle **1**, **11-*homo*** has the advantage of being chirally locked, such that the enantiomers do not racemise, making it a fully stable chiroptical switch (**Figure 4.25**).

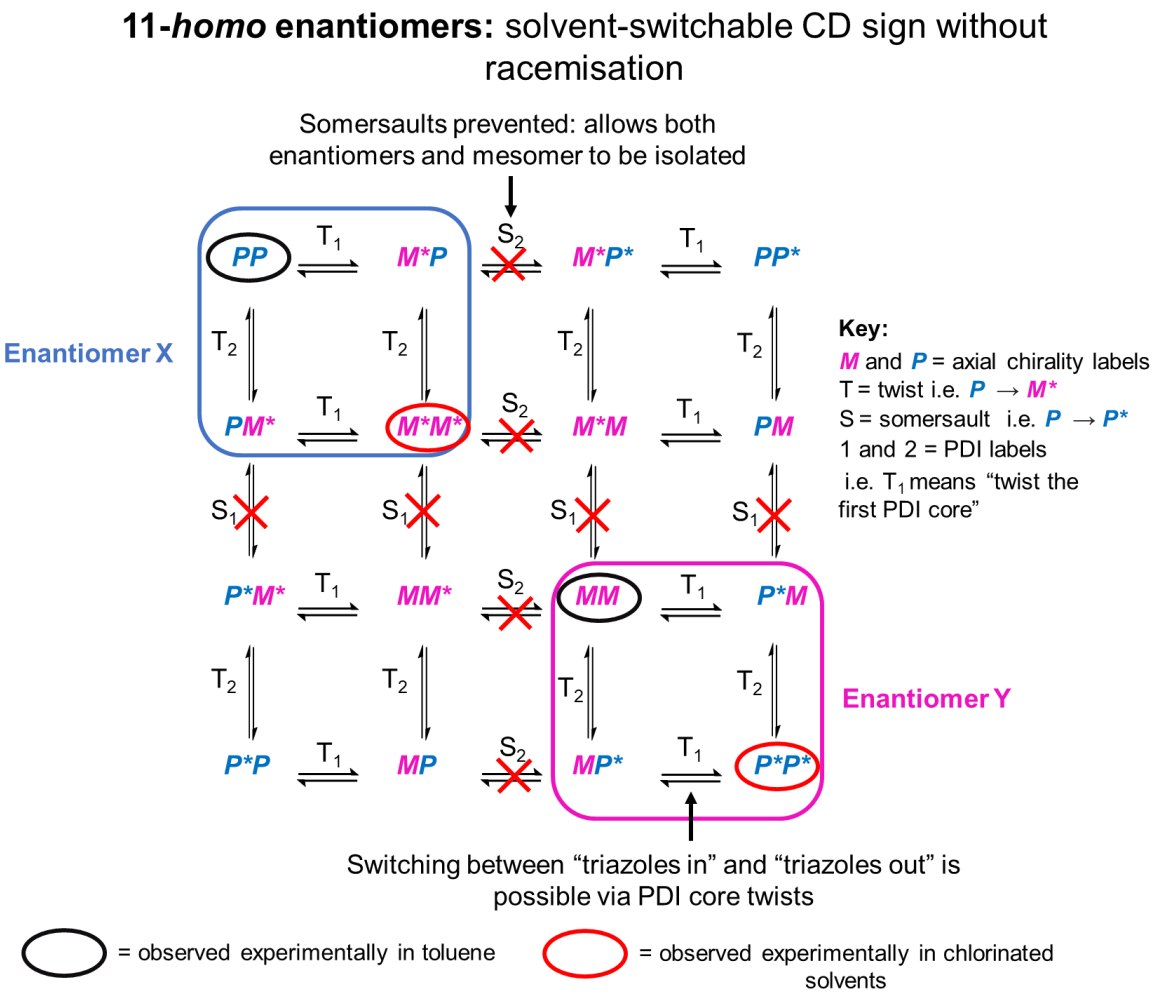

Figure 4.25: Annotated map of all the possible permutations of ***M*** and ***P*** chirality and "triazoles in" and "triazoles out" conformations for each PDI core in a 1,7-bay-connected bis-PDI macrocycle, showing which of these conformations can be observed experimentally in different solvents for macrocycle **11**. For this system, "intramolecular somersaults" are prevented by the bulky imide groups, but twists of the PDI cores can still occur. As such, enantiomerisation (i.e. ***PP*** ⇄ ***MM*** or ***P*P**** ⇄ ***M*M*****) does not occur, but inversion of local axial chirality in the PDI cores (i.e. ***PP*** ⇄ ***M*M***** or ***MM*** ⇄ ***P*P*****) can be achieved by changing the solvent.

It is worth noting here that in toluene the CD spectrum of **11-*MM*** is weaker than might be expected. Indeed, for macrocycle **1**, as seen in **Figure 4.26a**, the spectra in TCE and toluene have the opposite signs but have broadly similar intensities, but for macrocycle **11-*homo***, the spectrum in toluene is clearly weaker than in TCE (**Figure 4.26b**). This is also apparent from the $|g_{abs}|$ values for **11-*MM*** (5 x 10^{-4} in toluene vs 1 x 10^{-3} in TCE) seen in **Table 4.1**. Furthermore, comparison of the ***MM*** enantiomer CD spectra for macrocycles **11-*homo*** and **5** (**Figure 4.26b**) shows that the Cotton effect which arises from chiral excitonic coupling is less

redshifted (λ = 590 vs 570 nm) and has a less intense bisignate band in **11-*homo*** compared to macrocycle **5**. This is not surprising when considering the greater steric bulk of the 2,6-dimethylphenyl imide groups in **11-*homo*** will inhibit PDI-PDI intramolecular aggregation and thus excitonic coupling relatively to that observed in macrocycles **5** (in all solvents) and **1** (in toluene). Therefore, it is possible that the bulky imide groups in **11-*homo*** lead to sub-optimal excitonic coupling in toluene due to a larger PDI-PDI distance or different PDI-PDI rotational angle compared to the macrocycle **5** in toluene. An alternative explanation is that, for **11-*homo***, the "triazoles in" ***P*P**** conformation seen in TCE is still partially populated in toluene, which subtracts from the CD signal of the "triazoles out" ***MM*** conformation favoured in toluene.

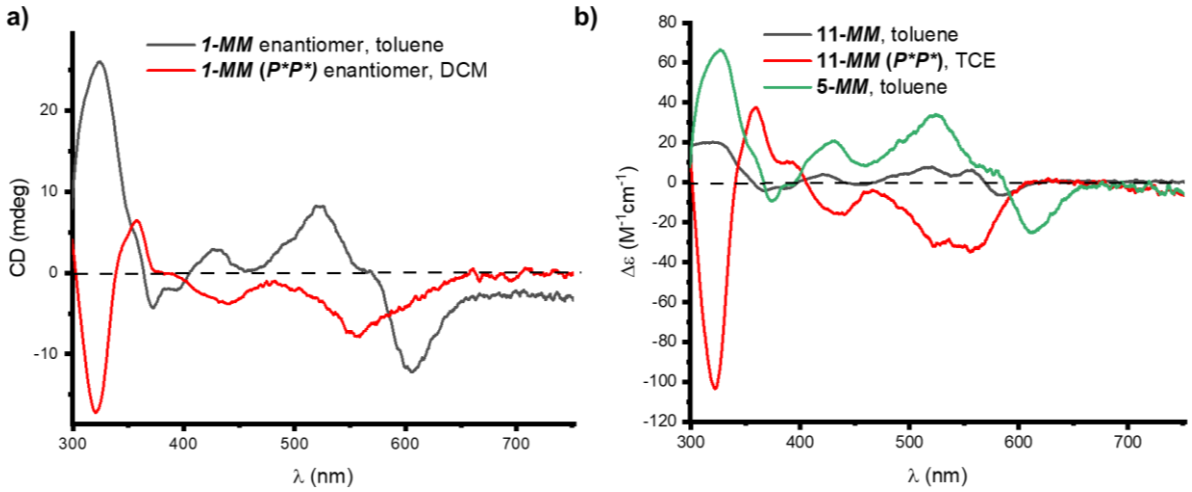

Figure 4.26: a) CD spectra (10 μM) of the same enantiomer **1-*MM*** in toluene (black trace) and TCE (red trace). **b**) CD spectra (10 μM) of the same enantiomer **11-*MM*** in toluene (black trace) and TCE (red trace) as well as the CD spectrum of **5-*MM*** in toluene (green trace).

The CPL spectra of both enantiomers of **11-*homo*** were also measured in TCE and toluene (**Figure 4.27**), which could not be achieved for macrocycle **1** due to its relatively rapid racemisation. Unlike the CD signal, which is generally inverted upon going from "triazoles out" ***MM/PP*** to "triazoles in" ***P*P*/M*M**, the CPL sign is the same in both solvents. As such, the sign of the CPL spectrum is found to match the sign of the lowest energy branch of the CD spectrum, which is unchanged between solvents due to the presence or absence of the Cotton effect in toluene and TCE respectively. Therefore, while the change in PDI local axial chirality impacts the CD spectra, the change in excitonic coupling is important in determining the sign of the CPL signal.

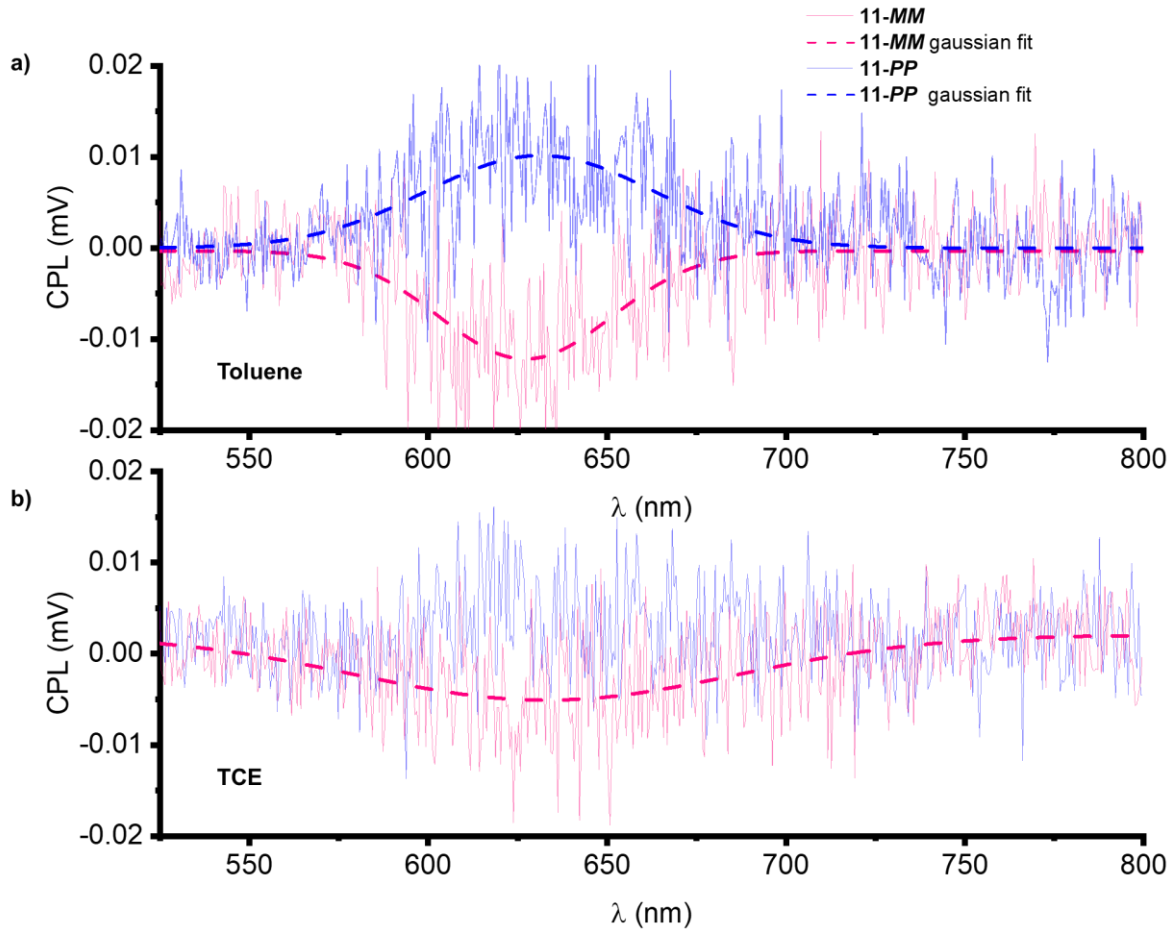

Figure 4.27: CPL spectra of the enantiomers of macrocycle **11-*homo*** in **(a)** toluene and **(b)** TCE. Note that the CPL spectra of **11-*MM*(*P**P**)** in TCE could not be fitted due to a poor signal:noise ratio.

The $|g_{\mathrm{lum}}|$ values recorded for **11-*homo*** in toluene and TCE are an order of magnitude lower than those recorded for macrocycles **1** and **5** (**Table 4.1**), which is consistent with the bulkier 2,6-dimethylphenyl imide groups in **11-*homo*** hindering chiral excitonic coupling which, as established in Chapters 2 and 3, will amplify $|g_{\mathrm{lum}}|$. In toluene, **11-*homo*** has a higher $|g_{\mathrm{lum}}|$ than in TCE (3×10^{-3} vs 1×10^{-3}), which is in line with an excitonic chirality contribution to the $|g_{\mathrm{lum}}|$, albeit with weaker coupling between the PDIs when compared to macrocycles **1** and **5**.

Table 4.1: Absorption dissymmetry factors $|g_{abs}|$ and luminescence dissymmetry factors $|g_{lum}|$ in toluene and TCE for macrocycles **1**, **5**, and **11**.

Macrocycle	**Solvent**	$\|g_{abs}\|$ **[nm]**	$\|g_{lum}\|$ **[nm]**
1	Toluene	-	1×10^{-2} [675]
5	Toluene	3×10^{-3} [610]	2×10^{-2} [675]
	TCE	3×10^{-3} [610]	2×10^{-2} [675]
11-*homo*	Toluene	5×10^{-4} [585]	3×10^{-3} [630]
	TCE	1×10^{-3} [558]	1×10^{-3} [630]

To further probe the excitonic coupling in toluene and TCE for macrocycle **11-*homo***, UV-vis spectroscopy was performed in both solvents (**Figure 4.28b**). In TCE, the UV-vis absorption spectrum shown no signs of excitonic coupling and resembles that of the acyclic precursor PDI **3a** (see Chapter 2). In contrast, the UV-vis absorption spectrum in toluene shows characteristic signs of H-type aggregation, namely, a blue-shift in the absorption maximum (42 nm) and a decrease in the intensity of the 0-0 vibronic peak intensity relative to the 0-1 peak in the region corresponding to the PDI $S_0 \rightarrow S_1$ transition ($\varepsilon_{0\text{-}0}/\ \varepsilon_{0\text{-}1}$ = 1.06 in TCE, 0.96 in toluene). However, in contrast to the behaviour observed for macrocycle **1** (**Figure 4.28a**), the excitonic coupling seen in **11-*homo*** in toluene ($\varepsilon_{0\text{-}0}/\ \varepsilon_{0\text{-}1}$ = 0.96) is clearly weaker than for macrocycle **1** in toluene ($\varepsilon_{0\text{-}0}/\ \varepsilon_{0\text{-}1}$ = 0.53). This is consistent with the behaviour seen by CD spectroscopy discussed above.

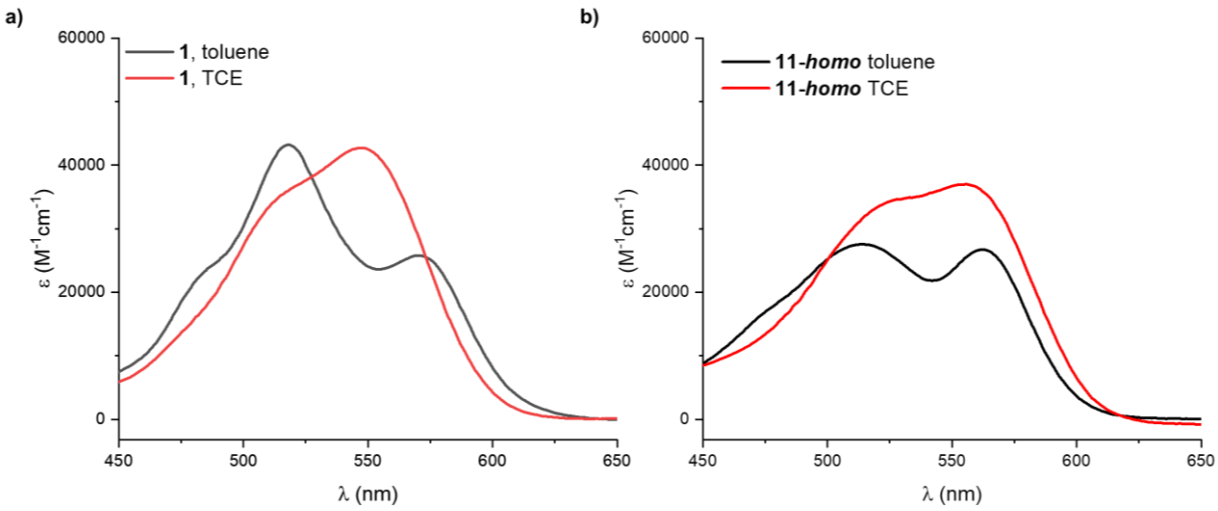

Figure 4.28: a) U-vis absorption spectrum (10 μM) of macrocycle **1** in toluene (black trace) and TCE (red trace). **b)** U-vis absorption spectrum (10 μM) of macrocycle **11-*homo*** in toluene (black trace) and TCE (red trace).

Taken together, the UV-vis absorption and CD spectra show that excitonic coupling in **11-*homo*** in toluene is weaker than in macrocycles **1** and **5** in toluene, due to the sterically bulkier imide groups in **11-*homo***. The effect of the bulky imide groups can be rationalised in three ways. Firstly, it could be that the non-excitonically coupled "triazoles in" conformation is still partially populated in toluene for **11-*homo***. Secondly, the PDIs may be forced further apart, weakening excitonic coupling by increasing the interchromophoric distance. Finally, the relative rotation of the PDIs might be larger than the ~ 20° seen in conformer **A** (and the X-ray crystal structures of **1** and **5**) to accommodate the larger steric bulk.

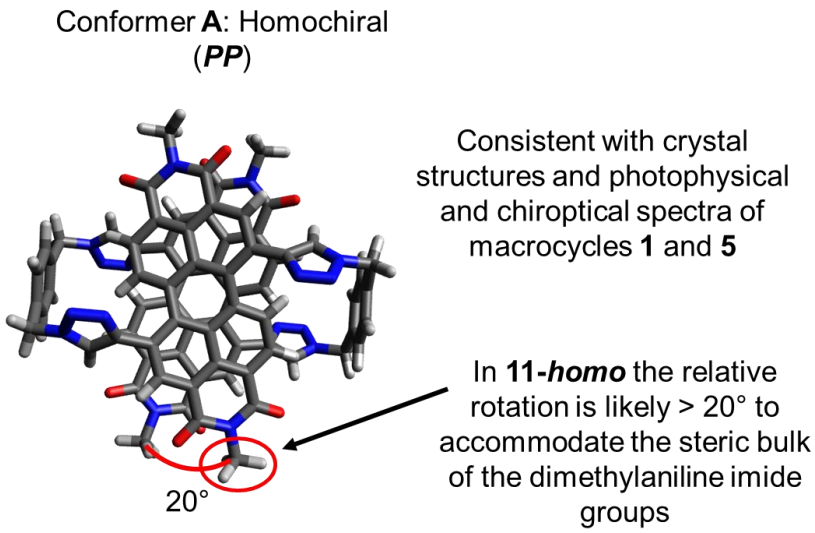

Figure 4.29: Illustration of the likely rotational displacement between the two PDI cores in toluene for macrocycles **1**, **5**, and **11-*homo***.

Interestingly, a linear correlation was found between the CD signal and the $\varepsilon_{0\text{-}0}/\varepsilon_{0\text{-}1}$ UV-vis vibronic peak ratio for the $S_0 \rightarrow S_1$ transition upon gradually changing the solvent from toluene to TCE, highlighting how changing relative populations of ***MM***/***PP*** and ***P*P*/M*M**** conformations impacts both photophysical and chiroptical properties (**Figure 4.30**). This may lend weight to the argument that the "triazoles in" ***P*P*/M*M**** is still partially populated in toluene.

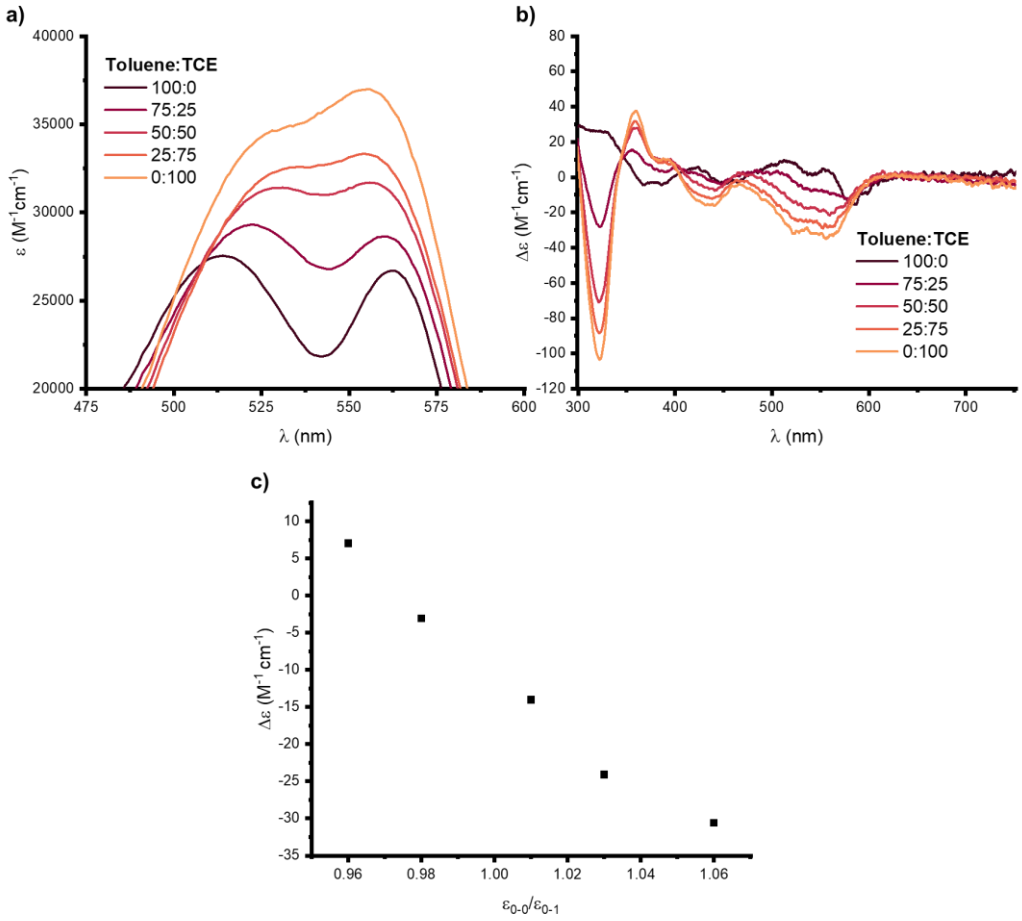

Figure 4.30: a) UV-vis absorption spectrum of macrocycle **11-*homo*** in different toluene:TCE mixtures. **b)** CD spectra of the same enantiomer **11-*MM*** in different toluene:TCE mixtures. **c**) Relationship between circular dichroism at 526 nm and vibronic peak ratio $\varepsilon_{0\text{-}0}/\ \varepsilon_{0\text{-}1}$ for the $S_0 \rightarrow S_1$ transition determined from the UV-vis absorption spectra in **(b)**.

The solvent-dependent conformational change was also studied by ^{1}H NMR spectroscopy (**Figure 4.31**). As for macrocycle **1**, considerable upfield shifts of the aromatic protons are observed in **11-*homo*** when toluene-d_8 is added to a solution in TCE-d_2, in particular proton H_c ($\Delta\delta$ = 1.5 ppm), which is consistent with intramolecular π–π interactions in toluene-d_8.

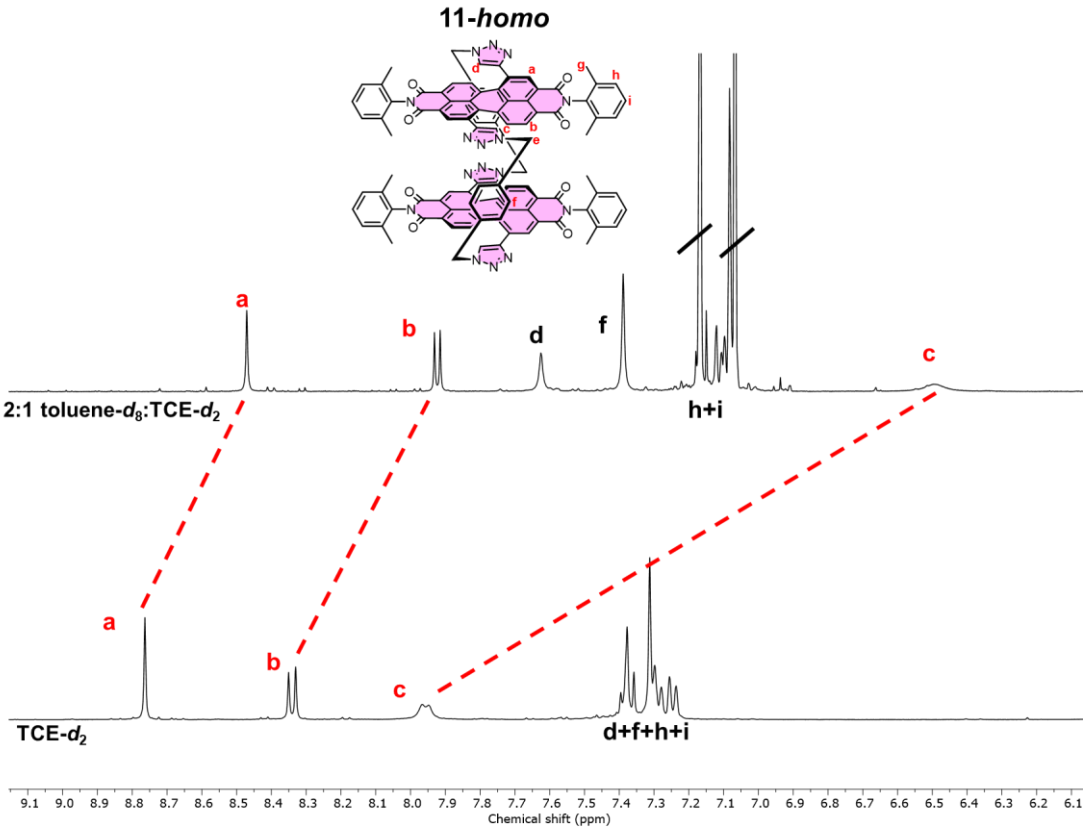

Figure 4.31: ^{1}H NMR spectra (70°C, 400 MHz, each referenced to the same internal standard, poly(dimethylsiloxane)) of macrocycle **11-*homo*** in 2:1 toluene-d_8:TCE-d_2 (top) and TCE-d_2 (bottom).

4.5.6 Analysis of the heterochiral stereoisomer

Initial characterisation

In addition to **11-*homo***, a further peak (C in **Figure 4.32**) corresponding to the heterochiral stereoisomer (**11-*hetero***) was isolated from the crude reaction mixture of macrocycle **11** by preparatory HPLC.

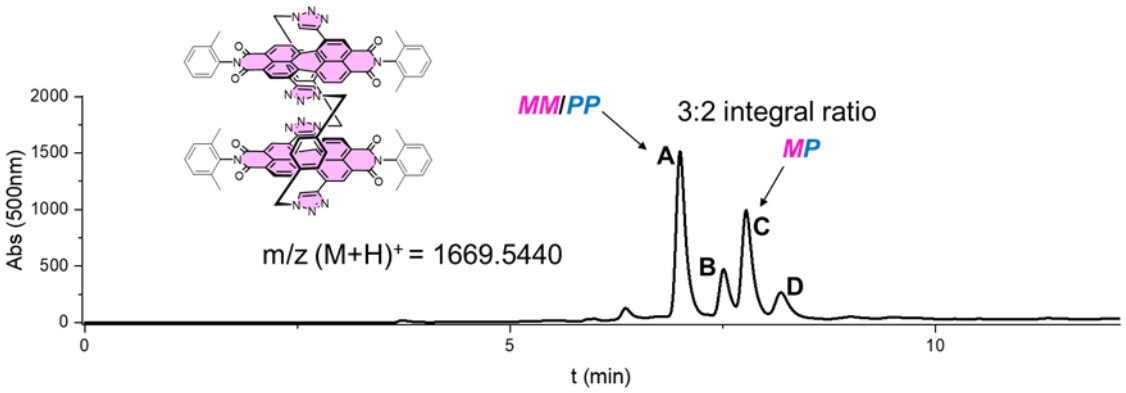

Figure 4.32: HPLC chromatogram of the crude reaction mixture of the final macrocyclisation step for macrocycle **11** (COSMOSIL Buckyprep 250 x 10 mm**,** eluted with a gradient going from 1:1 (v/v) DCM:n-hexane eluent to 7:3:1 (v/v/v) DCM:n-hexane:isopropanol), after filtration to remove insoluble impurities (likely longer PDI oligomers). Only peaks A and C contained the mass of macrocycle **11** upon analysis by mass spectrometry.

The ^{1}H NMR spectrum of **11-*hetero*** in TCE-d_2 looks broadly similar to that of **11-*homo***, with only small differences in chemical shifts for all the peaks in the aromatic region (**Figure 4.33a**).

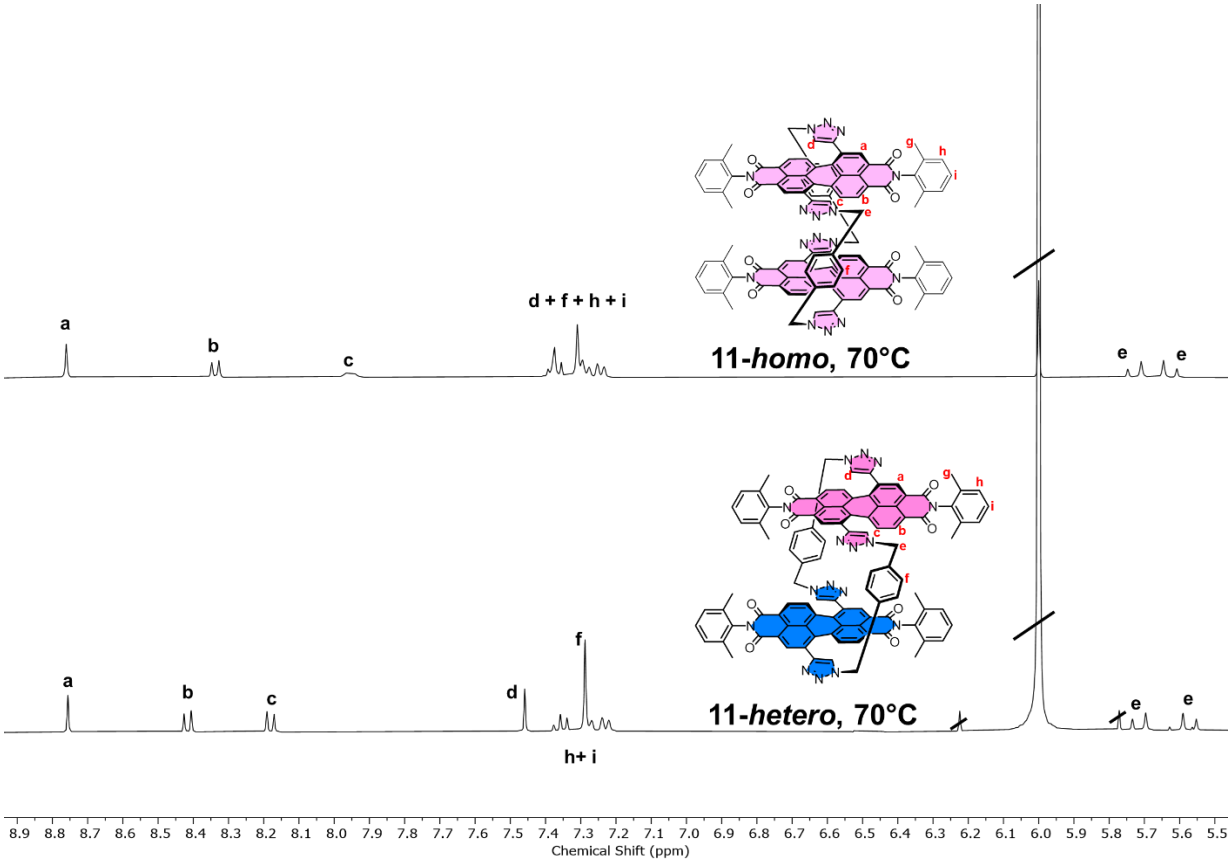

Figure 4.33: ^{1}H NMR spectra (TCE-d_2, 70°C, 400 MHz) of macrocycle **11-*homo*** (top) and **11-*hetero*** (bottom).

However, there is one striking difference, which is that for **11-*hetero*** the diastereotopic splitting of the methylene protons H_e in the *para*-xylyl linker can be observed at room temperature (25°C), while for **11-*homo***, heating to 70 °C was required to observe this diastereotopic splitting (**Figure 4.34**). It is proposed that broadness of NMR signals in bis-PDI macrocycles at room temperature is due to restricted molecular motion,[1] and as such heterochiral stereoisomer **11-*hetero*** may be more conformationally flexible than **11-*homo***, although both macrocycles are configurationally stable.

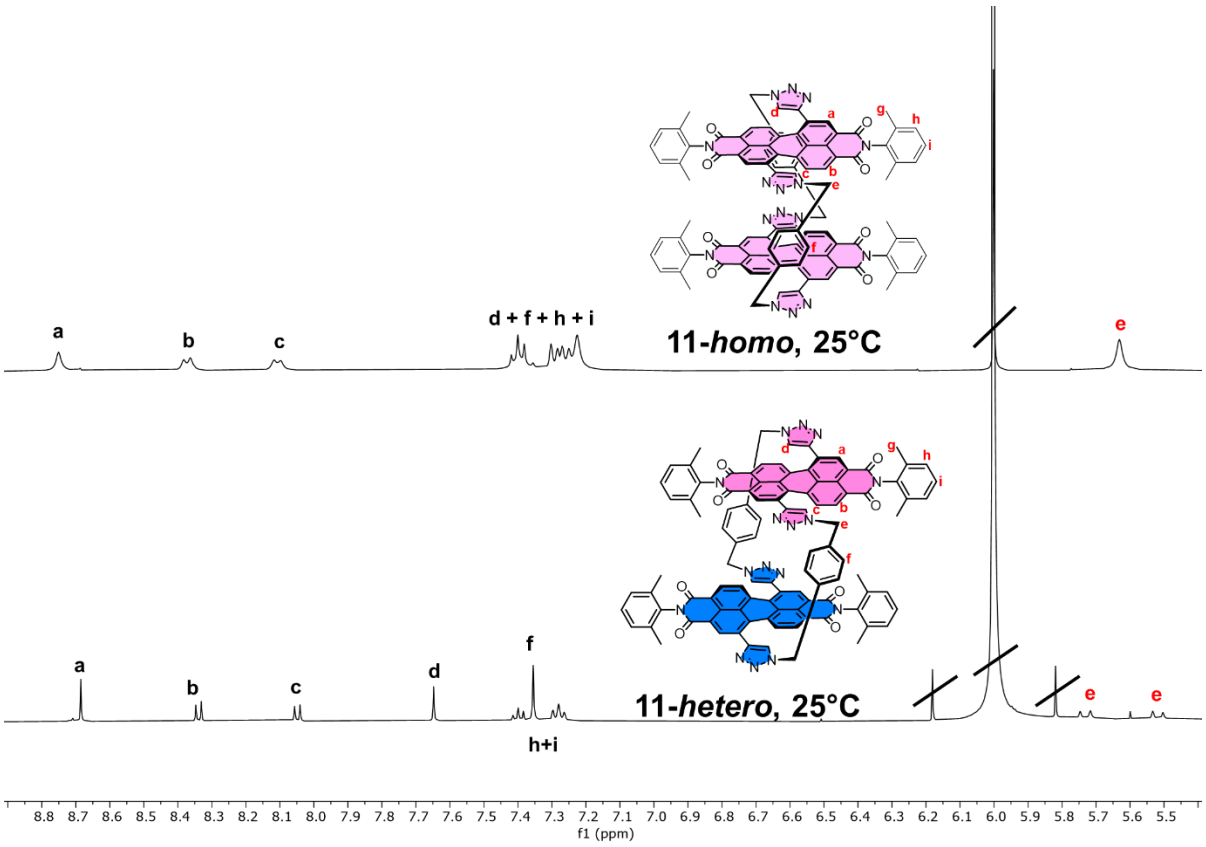

Figure 4.34: ^{1}H NMR spectra (TCE-d_2, 25°C, 400 MHz) of macrocycle **11-*homo*** (top) and **11-*hetero*** (bottom).

Confirmation of heterochirality

Several experiments were carried out to show that **11-*hetero*** is indeed a heterochiral (***MP***) stereoisomer of macrocycle **11**. Firstly, a sample of **11-*hetero***, previously purified by (achiral) HPLC, was injected into a chiral HPLC column. The resulting chromatogram only contained one peak (**Figure 4.35b**), unlike the chiral HPLC chromatogram of **11-*homo***, which contained two peaks of equal integration (**Figure 4.35a**). Subsequent re-injections into the chiral HPLC column after heating **11-*hetero*** overnight at 180 °C in 1,2-dichlorobenzene revealed no change in the chiral chromatogram, which was expected as the results for **11-*homo*** already showed that this system is chirally locked (i.e. no "somersault" motion is allowed), which prevents interconversion between **11-*hetero*** and **11-*homo*** (**Figure 4.35c**).

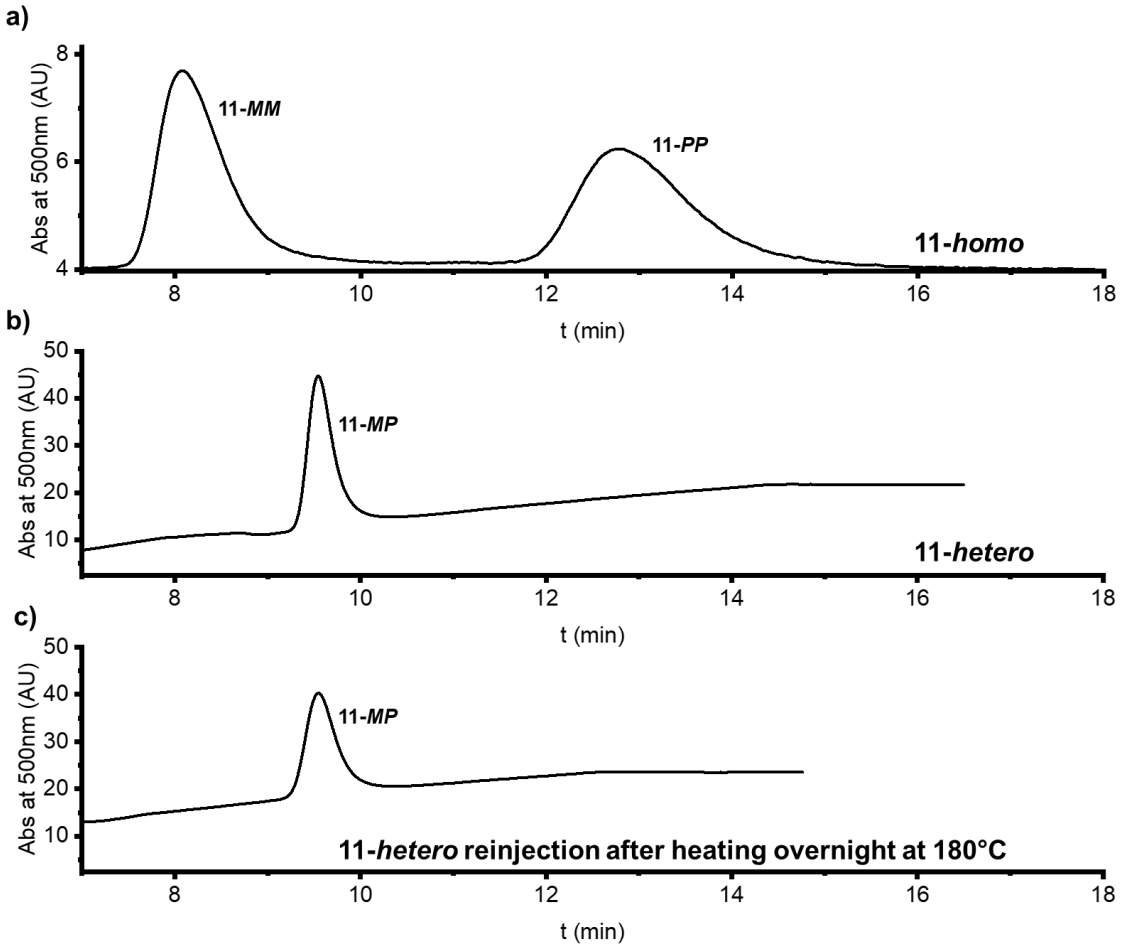

Figure 4.35: Chiral HPLC chromatograms (Phenomenex i-Amylose-1, 250 x 10 mm, 7:3 (v/v) DCM:n-hexane eluent) of **(a) 11-*homo***, **(b) 11-*hetero***, and **(c)** a sample of **11-*hetero*** that was heated at 180°C for 24 h in 1,2-dichlorobenzene. After heating, the solvent was removed, and the sample was re-dissolved in DCM and reinjected into the chiral HPLC column.

Additionally, a sample of **11-*hetero*** was studied by CD spectroscopy to show it exhibits no CD signal (**Figure 4.36**).

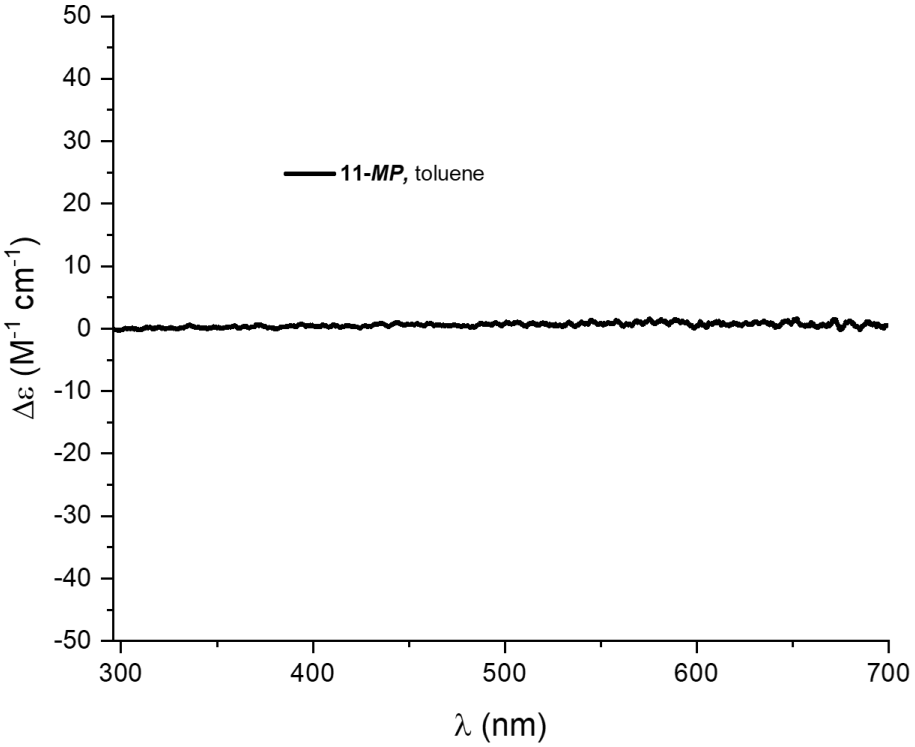

Figure 4.36: CD spectrum of **11-*hetero***. The lack of CD signal confirms the heterochiral nature of **11-*hetero***.

Solvent-dependent conformational switching

Naturally, the conformation of **11-*hetero*** in terms of "triazoles in" vs "triazoles out" cannot be studied by CD spectroscopy. However, the intramolecular PDI-PDI interaction is indicative of these conformations and can be analysed by UV-vis and NMR spectroscopy in different solvents.

In TCE, the UV-vis spectra of **11-*homo*** and **11-*hetero*** are very similar, with both displaying PDI monomer-like spectra (**Figure 4.37a**). However, in toluene, the UV-vis spectrum of **11-*hetero*** is markedly different to the spectrum of **11-*homo*** (**Figure 4.37b**). While **11-*homo*** shows typical signs of H-type PDI-PDI stacking in toluene (including a blue-shifted spectrum with $\Delta\lambda_{max} = -40$ nm, $\varepsilon_{0\text{-}0}/\varepsilon_{0\text{-}1} = 0.96$), **11-*hetero*** exhibits a new red-shifted shoulder in toluene. This spectral change is characteristic of J-type PDI-PDI stacking,[12-14] although it is smaller than for other PDIs that form J-aggregates (including macrocycle **5**), likely as a result of the bulk of the 2,6-dimethylphenyl imide groups which hinders aggregation. Indeed, this imide group is also partially hindering **11-*homo*** from forming an intramolecular H-aggregate

in toluene as discussed in the previous section, possibly by enforcing a larger relative rotation of the PDIs.

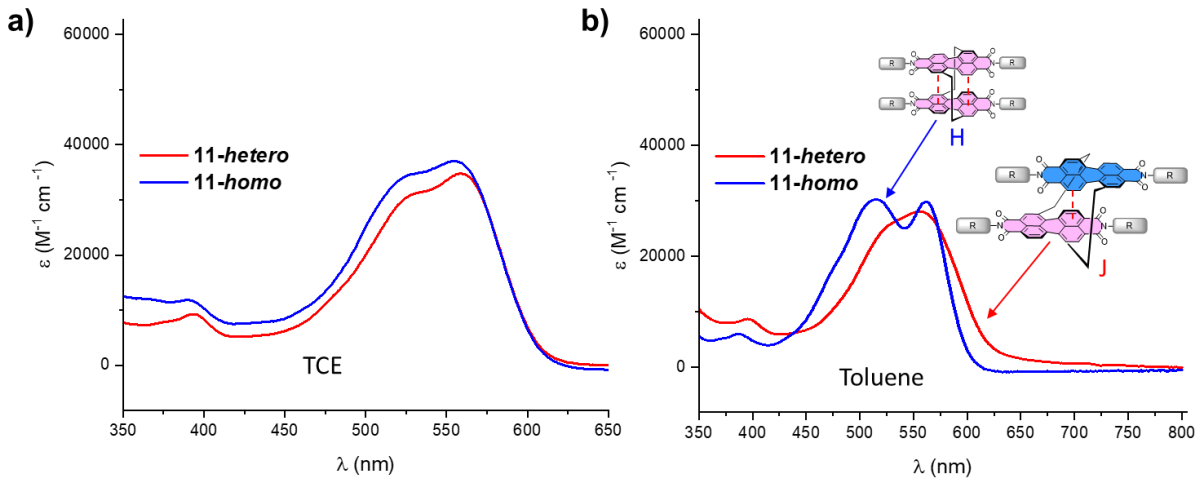

Figure 4.37: UV-vis absorption spectra of **11-*hetero*** (red trace) and **11-*homo*** (blue trace) in **(a)** TCE and **(b)** toluene.

As discussed above, the ^{1}H NMR spectra of **11-*hetero*** and **11-*homo*** are very similar in TCE-d_2. However, the addition of toluene-d_8 has an opposite effect on the ^{1}H NMR spectrum. For **11-*homo***, the PDI signals $H_{a\text{-}c}$ experience a significant upfield shift relative to the spectrum in TCE-d_2 ($\Delta\delta$ = 0.4–1.5 ppm, **Figure 4.38a**), mirroring the behaviour seen by the *homochiral* stereoisomer of macrocycle **1** upon changing the solvent from TCE to toluene (see **Figure 4.6b** and **Chapter 2**). In line with UV-vis and CD spectroscopic data, this is evidence for H-type intramolecular PDI-PDI aggregation in **11-*homo***. In contrast, for **11-*hetero***, the PDI signals $H_{a\text{-}c}$ shift moderately downfield ($\Delta\delta$ = 0.1-0.3 ppm) upon the addition of toluene (**Figure 4.38b**), indicating that a distinct conformation is now adopted.

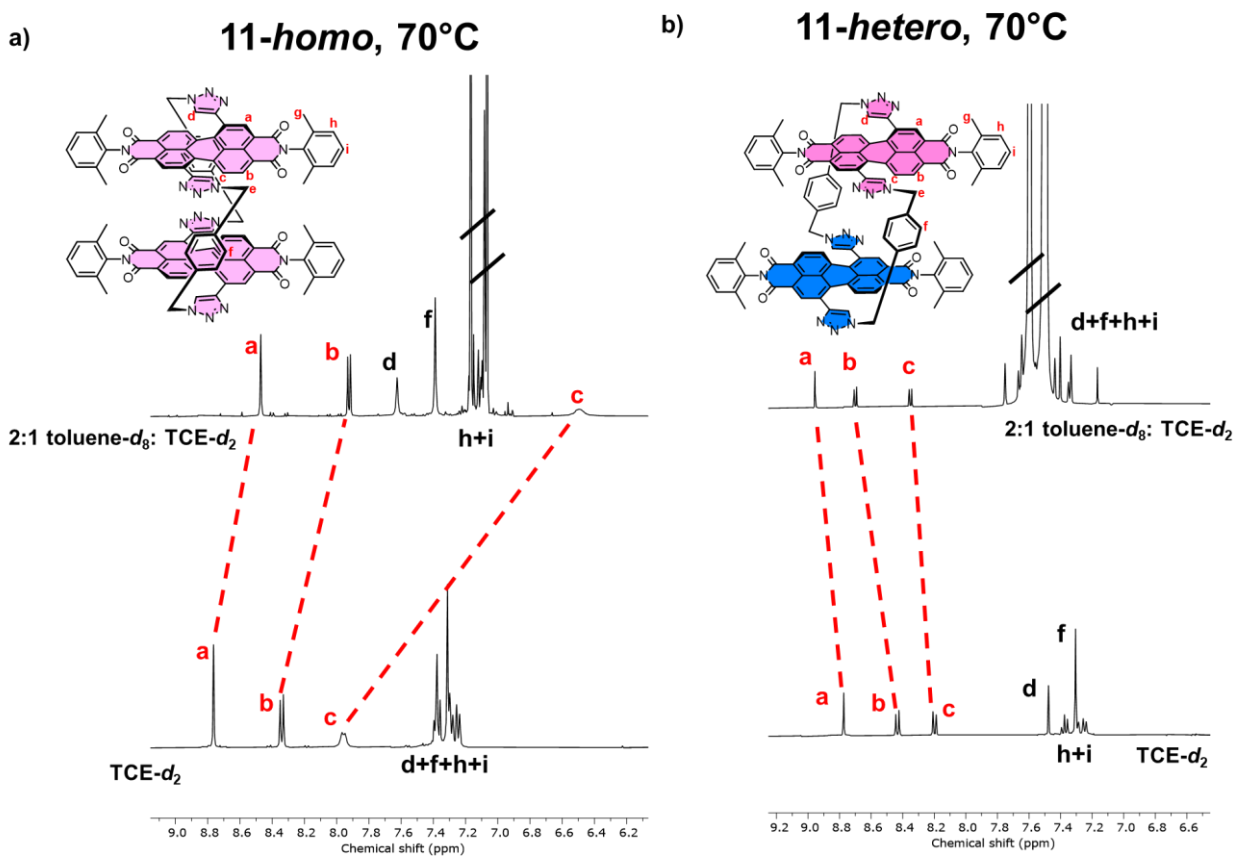

Figure 4.38: Stacked ^{1}H NMR spectra (75°C, 400 MHz) of macrocycle **(a) 11-*homo*** and **(b) 11-*hetero*** in TCE-d_2 and 2:1 toluene-d_8:TCE-d_2.

The above UV-vis and NMR spectroscopy results are consistent with **11-*hetero*** and **11-*homo*** adopting conformations in TCE where the two PDIs do not significantly interact, such that their photophysical and NMR spectra appear monomeric. However, upon addition of toluene, they both adopt conformations where intramolecular PDI-PDI stacking interactions are switched on, but distinct UV-vis and NMR spectra evidences the difference in *homochiral* vs heterochiral PDI-PDI stacking (**Figure 4.39a**). As established earlier, **11-*homo*** in toluene adopts a conformation featuring an H-type intramolecular PDI-PDI dimer. In contrast, the UV-vis spectrum in toluene of **11-*hetero*** suggests it may adopt a conformation featuring a J-type intramolecular PDI-PDI dimer. This is supported by DFT modelling of the heterochiral conformer of a macrocycle with methyl imide groups (**Figure 4.39b**), and also by the *inter*molecular heterochiral J-type PDI-PDI slip-stack seen in the crystal structure of **5-*rac*** (**Figure 4.39c**) as discussed in Chapter 3. It must be noted that the J-type interaction seen by UV-vis spectroscopy in toluene for **11-*hetero*** is quite weak. This is because, as for **11-*homo***,

the PDI-PDI interaction is hindered by the 2,6-dimethylphenyl imide groups, which provide more steric hinderance than the imide groups in **5-*rac*** (*tert*-butyl benzoate) and the DFT model (methyl).

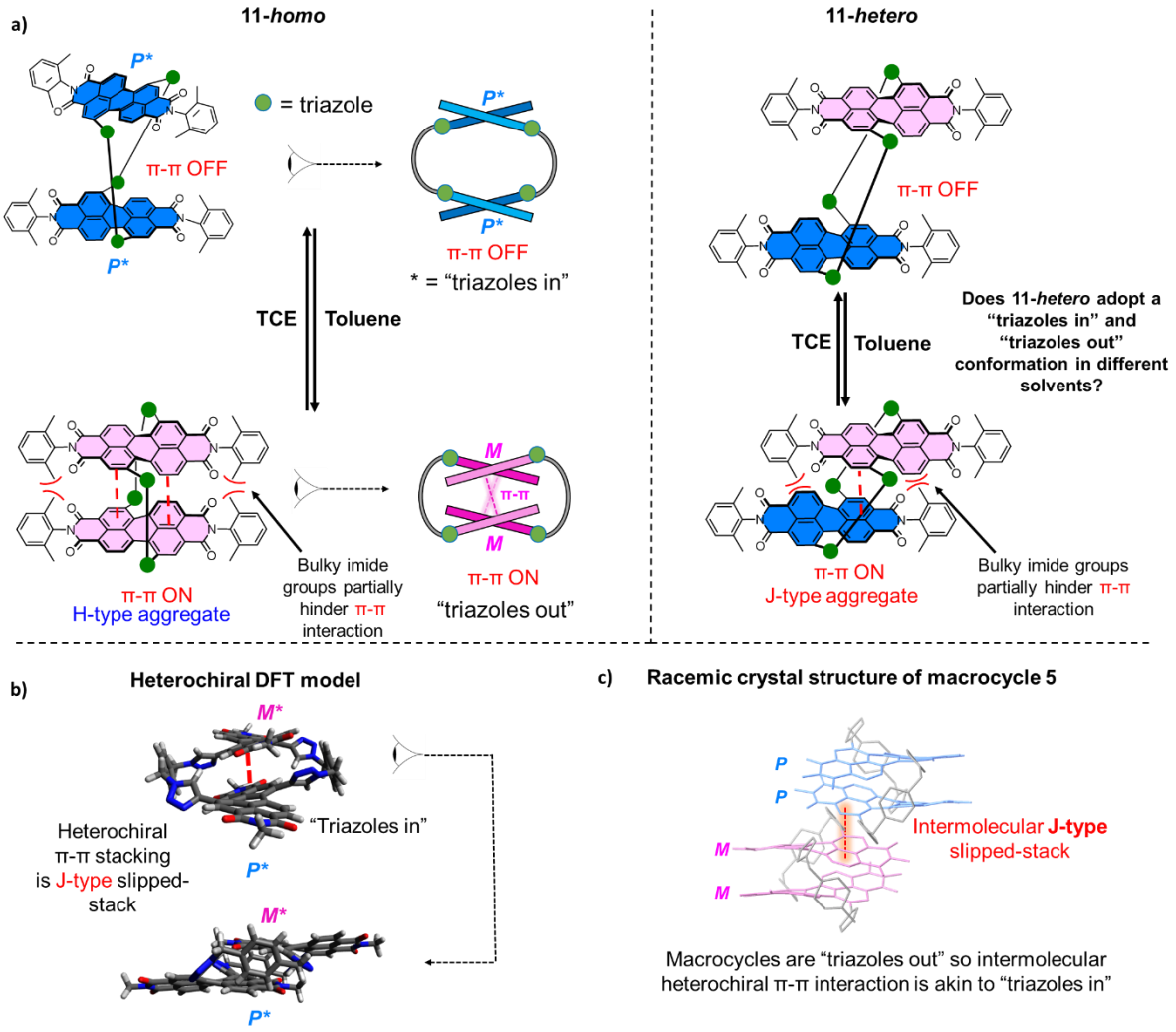

Figure 4.39: a) Cartoon depiction of the solvent-dependent conformational switching in **11-*homo*** (left) and **11-*hetero*** (right). **b)** Lowest energy DFT-predicted heterochiral structure of model "Pink Box" macrocycle with methyl imide groups (conformer **H**). **c**) X-ray crystal structure of a racemic sample of macrocycle **5**.

The DFT model (conformer **H**) and the crystal structure of **5-*rac*** suggest that a suitable arrangement for a close slip-stacked PDI-PDI J-type contact is "triazoles in". Hence, the conformation of **11-*hetero*** in toluene is proposed to be ***M*P***, although a crystal structure would be required to provide further support to this hypothesis. Unfortunately, single crystals of macrocycle **11** could not be grown to obtain an X-ray crystal structure.

4.5.7 Predictions on the self-assembly of bis-PDI macrocycle stereoisomers and chiral conformers

As discussed previously in Chapters 1 and 3, 1,7-disubsituted PDIs possess two distinct π-surfaces, one more sterically hindered than the other (**Figure 4.40a**). In Chapter 3 it was shown that for "triazoles out" *homo*chiral macrocycle **5**, *intra*molecular *homo*chiral H-type π–π stacking occurs on the less hindered face of the PDIs, while further *inter*molecular π–π stacking occurs on the more sterically hindered outer π-surfaces which requires a slipped-stack and heterochiral relationship between the PDI units (**Figure 4.40b**).

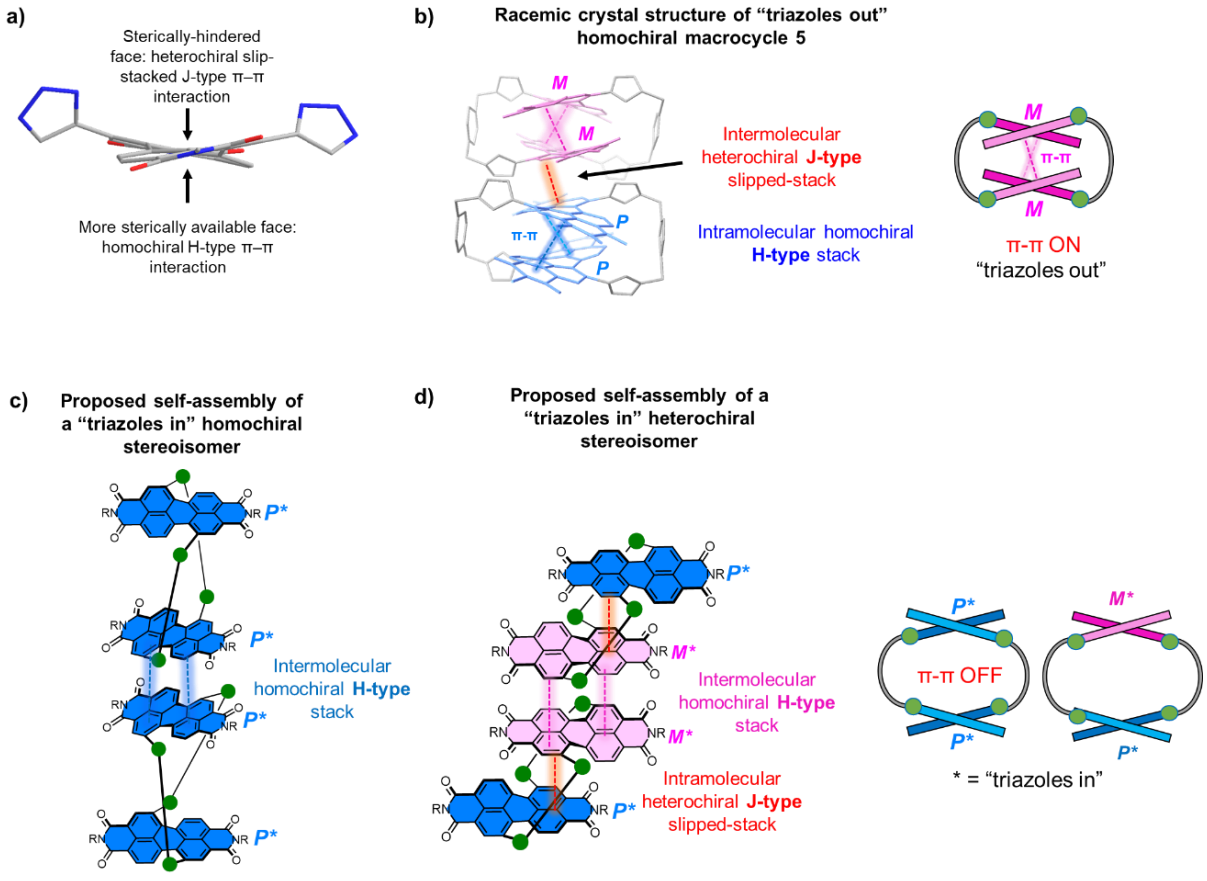

Figure 4.40: a) Structure of a 1,7-disubstituted PDI, showing its two distinct π-surfaces. **b)** Supramolecular packing in the racemic crystal structure of "triazoles out" *homo*chiral macrocycle **5**. **c**) Proposed self-assembly of a "Pink Box" type *homo*chiral macrocycle in a "triazoles in" conformation. **d**) Proposed self-assembly of a "Pink Box" type heterochiral macrocycle in a "triazoles in" conformation.

Overall, for 1,7-bistriazole PDIs, the face from which the triazole substituents are directed favours heterochiral, slip-stacked π–π stacking, while the other, less hindered, face

favours *homo*chiral face-to-face π–π stacking. The logical conclusion from this is that bis-PDI macrocycles populating a "triazoles in" conformation (***M*M***/***P*P***) should exhibit opposite self-assembly properties to "triazoles out" macrocycle **5** (***MM***/***PP***) since the less hindered faces of the PDIs are now the outer π-surfaces of the macrocycles.

For *homo*chiral macrocycles in a "triazoles in" conformation (***M*M**** and ***P*P****) we should therefore expect to see self-assembly of these macrocycles into fully *homo*chiral stacks via *homo*chiral intermolecular π–π stacking as shown in **Figure 4.40c**. One would also expect there to be an absence of *intra*molecular π–π stacking as "triazoles in" conformations disrupt this as seen for macrocycle **1** and **11-*homo*** in chlorinated solvents. Similarly, for heterochiral macrocycles in a "triazoles in" conformation (***M*P****) we would expect to see self-assembly with *homo*chiral intermolecular π–π contacts (**Figure 4.40d**). As discussed in the above section, *intra*molecular π–π stacking appears to be possible in "triazoles in" heterochiral macrocycles such as **11-*hetero***, so the overall structure of a self-assembly of "triazoles in" heterochiral macrocycles should be the "opposite" of that observed in the racemic crystal structure of macrocycle **5**, i.e. it will have heterochiral slipped-stack *intra*molecular and *homo*chiral face-to-face *inter*molecular π–π contacts. Unfortunately however, weaker PDI−PDI π–π interactions, due to sterically bulky imide groups and chlorinated solvents supressing these interactions, meant that neither macrocycles **11-*homo*** nor **11-*hetero*** underwent π–π self-assembly akin to macrocycle **5**.

4.5.8 Summary

In summary, this section has shown that while the *homo*chiral enantiomers of macrocycle **11** (**11-*homo***) are chirally-locked and so do not racemise via a PDI "somersault", the local axial chirality of the PDI cores can be inverted via a "twist motion" using a solvent stimulus. This leads to switching between ***PP*** ⇄ ***M*M**** and ***MM*** ⇄ ***P*P**** chiral conformers, where the asterisk (*) indicates a "triazoles in" conformation (**Figure 4.41**). As such, the enantiomers of **11-*homo*** act as a chiroptical switch, whereby changing the PDI's axial chirality in the ground state using an achiral stimulus (the solvent), leads to an inversion of the CD signal. Chiral locking also allows the heterochiral stereoisomer **11-*hetero*** to be isolated. This is the first time that a stable heterochiral stereoisomer has been isolated in a solely bay-connected bis-PDI macrocycle. Whilst **11-*homo*** adopts a "triazoles out" conformation in toluene with an intramolecular H-type PDI-PDI interaction, spectroscopic analysis suggests that in toluene **11-**

hetero instead adopts a "triazoles in" (i.e. ***M*P****) conformation with a slipped-stack J-type intramolecular PDI-PDI interaction.

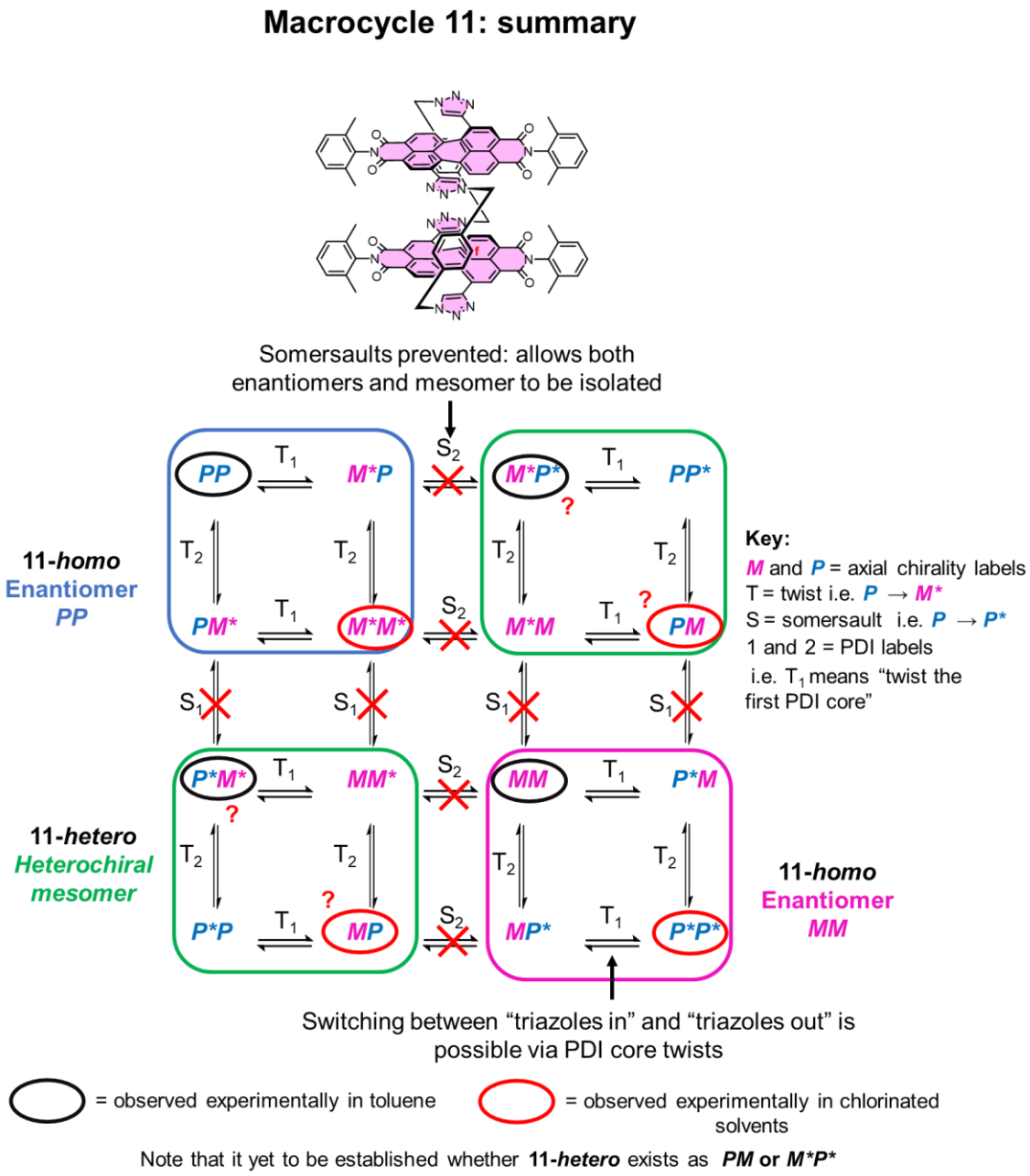

Figure 4.41: Annotated map of all the possible permutations of ***M*** and ***P*** chirality and "triazoles in" and "triazoles out" conformations in each PDI core in a 1,7-bay-connected bis-PDI macrocycle, showing which of these conformations can be observed experimentally in different solvents for macrocycle **11**. For **11-*hetero***, DFT studies suggest the "triazoles in" conformation (i.e. *M*P**) is lowest in energy.

4.6 Summary and future work

This chapter has sought to explore and categorise the wide range of chiral conformations of "Pink Box" type bis-PDI macrocycles, a necessary requirement to unlock their potential as switchable chiroptical materials.

The chapter began by identifying that, in addition to the ***M/P*** axial chirality of the PDI cores, the positioning of the bay substituents, namely "triazoles in" and "triazoles out" conformations, must also be considered. These "triazoles in" and "triazoles out" conformations can interconvert via "twisting" of the PDI cores, which additionally inverts the local axial chirality of the PDI cores, i.e. ***PP*** ⇄ ***M*M****, ***MM*** ⇄ ***P*P****, and ***MP*** ⇄ ***P*M**** where the asterisk indicates a "triazoles in" conformation. However, this does not equate to enantiomerisation, i.e. ***PP*** ⇄ ***MM***, which requires a "somersault" of one of the PDI imide heads through the centre of the macrocyclic cavity.

To provide evidence for this theory, the 1st generation dynamically chiral "Pink Box" macrocycle **1** presented in Chapter 2 has been systematically altered to isolate and analyse the various stereoisomers and conformers. The results in Chapter 3 using 2nd generation bis-PDI macrocycle **5** had already shown that it was possible to isolate the ***MM*** and ***PP*** enantiomers by using a long, rigid imide group that prevents the "somersault" motion of the PDI imide heads through the centre of the macrocyclic cavity, inhibiting racemisation. However, due to the low steric bulk of the imide group used for this (*tert*-butyl benzoate), PDI-PDI *homo*chiral π–π stacking interactions were very strong, which prevented access to the "triazoles in" conformations (where intramolecular π–π stacking is switched off) and resulted in no ***MP*** heterochiral meso isomer forming due to exclusive *homo*chiral templation during the macrocyclisation process.

Building on this, a 3rd generation bis-PDI macrocycle was developed with bulkier imide groups to partially disrupt the very strong PDI-PDI *homo*chiral π–π stacking interactions while also preventing interconversion between stereoisomers via "somersaults". This was successfully achieved with a macrocycle bearing 2,6-dimethylpehnyl imide groups (macrocycle **11**), which prevented stereoisomer interconversion while also disrupting exclusive *homo*chiral templation as part of the macrocyclisation process, allowing the ***MP*** heterochiral diastereomer to be isolated and studied. It was found that while the ***MM*** and ***PP*** enantiomers form *homo*chiral H-type cofacial intramolecular aggregates in toluene, the ***MP*** heterochiral diastereomer instead

forms a “slip-stack” with some J-aggregate characteristics. Furthermore, for the ***MM*** and ***PP*** enantiomers it was confirmed that they can be switched between “triazoles in” and “triazoles out” conformations using different solvents, which results in an inverted CD spectrum. As such, these systems act as a rare type of PDI-based chiroptical switch where the CD spectrum is inverted using an achiral stimulus (solvent) due to a change in PDI axial chirality.

As introduced in Section 1.5.7, further work may now seek to develop macrocycle **11** for self-assembly, with new arrangements arising from distinct chiral conformations. While in Chapter 3 it was shown that “triazoles out” ***MM*** and ***PP*** macrocycles stack with each other via heterochiral slip-stacked intermolecular π–π interactions, it is hoped that “triazoles in” ***M*M*****, ***P*P***** and ***M*P***** conformations will self-assemble via *homo*chiral cofacial intermolecular π–π interactions. As such, it will become possible to direct the self-assembly of organic materials into different structures via π–system chirality, with exciting applications in electronic and chiroptical materials.

Complementing this work on changing the imide functional groups, the next Chapter will explore the effects of varying the linker in bis-PDI macrocycles. These designs are also expected to influence the PDI-PDI distance and relative rotation and so tune π–π interaction and excitonic coupling strength.

4.7 Experimental

4.7.1 Materials and methods

All commercial solvents and reagents were used as purchased, unless otherwise stated. Anhydrous solvents were degassed with N_2 and dried using an Innovative Technology PureSolv MD 5 solvent purification system. $Cu(MeCN)_4 \cdot PF_6$ was stored in a desiccator. Tris((1-benzyl-4-triazolyl)methyl)amine (TBTA) was prepared following a literature procedure.[15] Water was distilled and microfiltered using an ELGA DV 35 Purelab water purification system. Chromatography was undertaken using silica gel (particle size: 40-63 μm) or preparative TLC plates (20 × 20 cm, 1 cm silica thickness).

^{1}H and ^{13}C NMR spectra were recorded using Bruker AVIII400 (400 MHz), Bruker AV NEO 400 (400 MHz) and Bruker AV NEO 500 (500 MHz, with cryoprobe). Mass spectra were recorded using a Bruker UltrafleXtreme MALDI-TOF mass spectrometer or a Waters Synapt G2-S mass spectrometer for high resolution MS-ESI. Details of equipment used for other analytical techniques (CD and CPL spectroscopies, photophysics, HPLC etc.) are provided in their appropriate sub-sections in this experimental section.

4.7.2 Synthesis of macrocycle 10

The synthesis of bis-PDI macrocycle **10** was carried out as shown below. Compound **12** was previously prepared in-house by group member Angus Yeung according to a literature procedure[16] as a mixture 1,6- and 1,7- regioisomers. Compounds **12** and **13** were isolated as a mixture of 1,6- and 1,7- regioisomers. 1,4- bis(azidomethyl)benzene was prepared by Angus Yeung following the **safety precautions for the handling of organic azide compounds described in section 2.9.2**.

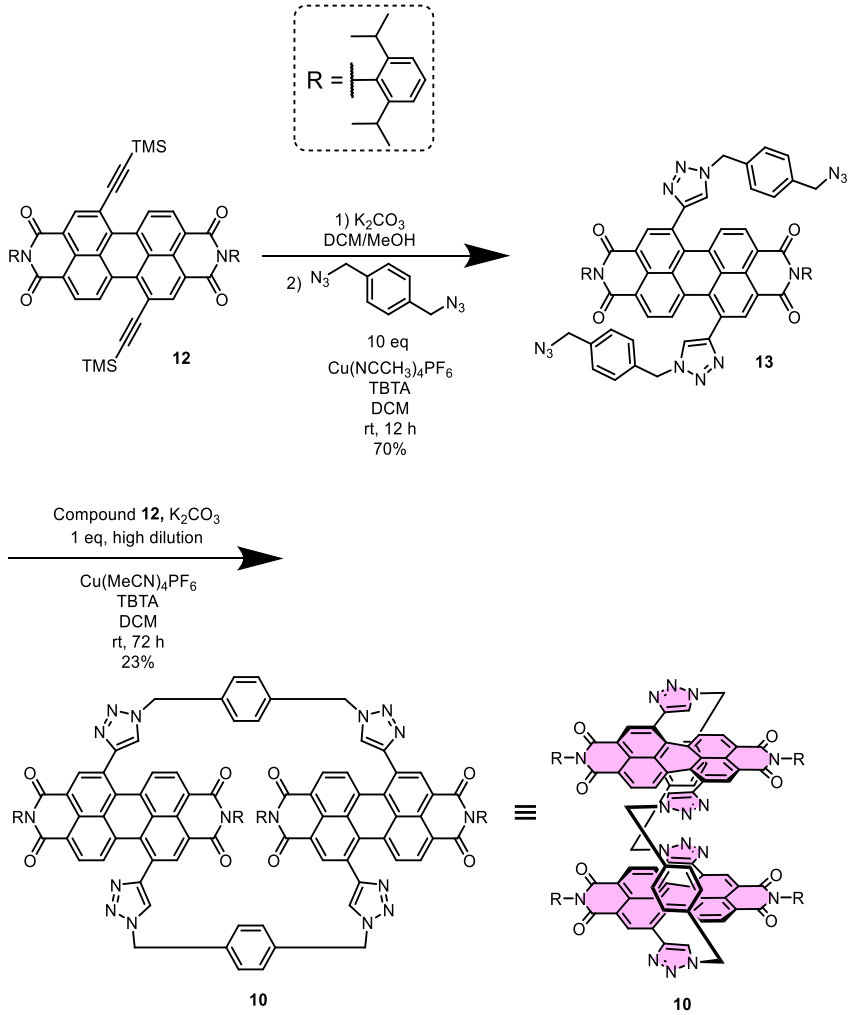

Multistep synthesis of bis-PDI macrocycle **10**.

Acyclic bis-triazole PDI 13

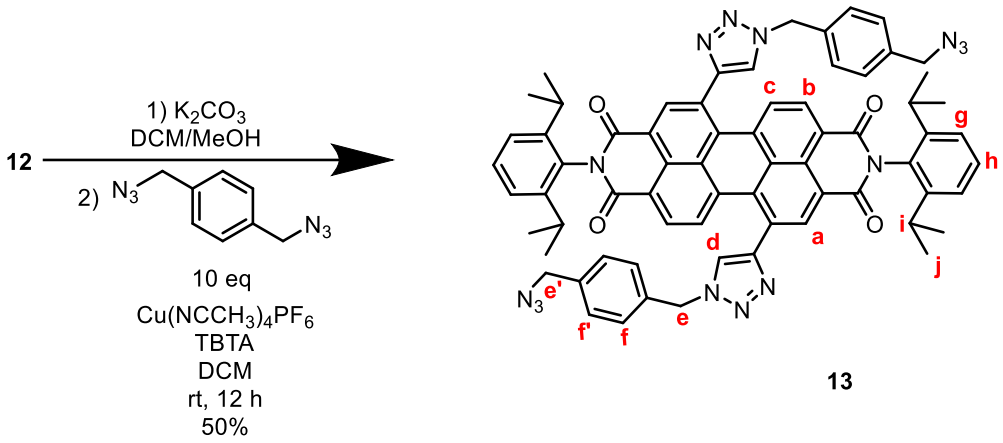

To a solution of TMS-protected bis-alkyne PDI **12** (50 mg, 79 µmol) in DCM (20 ml) was added K_2CO_3 (30 mg) in MeOH (10 ml). The mixture was stirred at rt for 3 min, and completion of the reaction was confirmed by TLC. The solution was then washed with water (2 x 30 mL) and brine (30 ml). The organic layer was then dried over anhydrous $MgSO_4$ and concentrated to dryness in vacuo to afford the deprotected PDI bis-alkyne which was used immediately without further purification. This PDI bis-alkyne was immediately re-dissolved in dry DCM (30 mL). To this was added 1,4- bis(azidomethyl)benzene (148 mg, 790 µmol, 10 equiv) and tris((1-benzyl-4- triazolyl)methyl)amine (TBTA) (8.4 mg, 16 µmol, 0.2 equiv). The solution was then de-gassed with argon. The copper (I) catalyst $Cu(CH_3CN)_4PF_6$ (5.9 mg, 16 µmol, 0.2 equiv) was then added and the solution was once again de-gassed with argon. The reaction was stirred at rt for 12 h. The solvent was then removed in vacuo. The resulting residue was purified by silica gel flash column chromatography (1:199 MeOH-DCM) affording the title compound as a purple solid (44 mg, 39 µmol, 50%).

^{1}H NMR (500 MHz, Chloroform-*d*, 1,7 isomer) δ 8.72 (s, $2H_a$), 8.26 (d, J = 8.1 Hz, $2H_b$), 7.93 (d, J = 8.0 Hz, $2H_c$), 7.81 (s, $2H_d$), 7.50 (t, J = 7.8 Hz, $2H_h$), 7.40 (s, $8H_f$), 7.37 – 7.33 (m, $4H_g$), 5.69 (s, $4H_e$), 4.38 (s, $4H_{e'}$), 2.72 (hept, J = 6.9 Hz, $4H_i$), 1.21 – 1.13 (m, $24H_j$).

^{13}C NMR (126 MHz, Chloroform-*d*) δ 165.08, 163.15, 163.07, 148.12, 138.75, 136.86, 135.31, 135.01, 134.56, 133.97, 132.73, 130.79, 130.22, 129.99, 129.50, 129.43, 129.29, 129.22, 129.08, 128.78, 128.67, 128.64, 128.60, 122.69, 122.49, 122.11, 121.93, 81.57, 54.39, 54.28, 28.35.

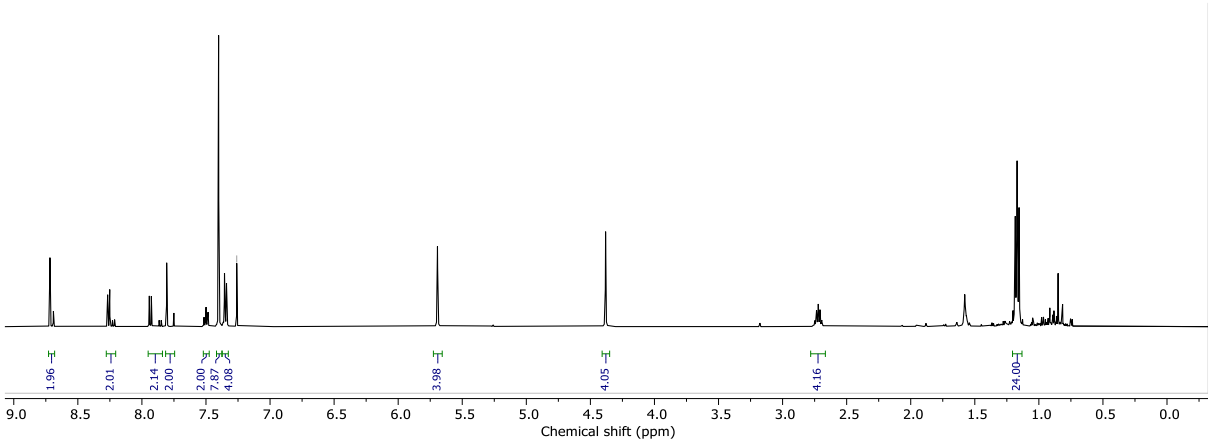

^{1}H NMR spectrum of compound **13** (chloroform-*d*, 298 K, 500 MHz).

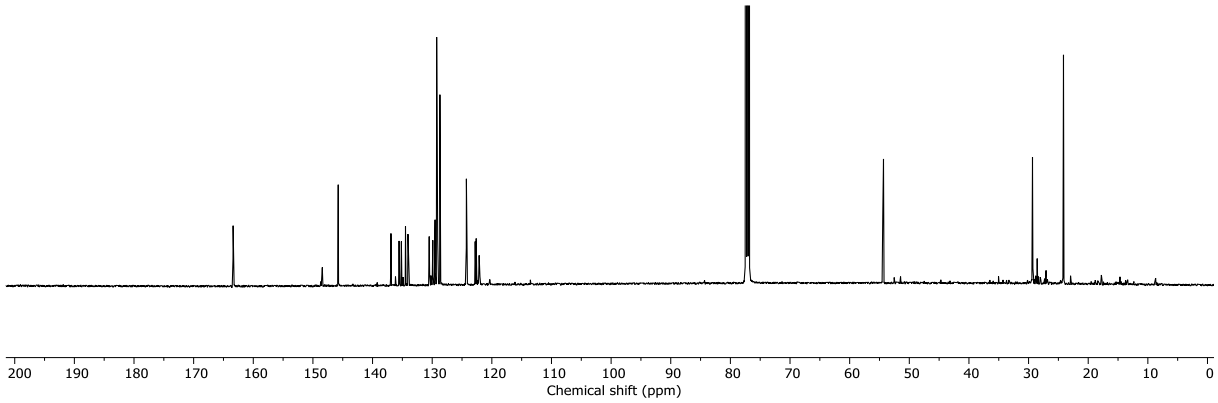

^{13}C NMR spectrum of compound **13** (chloroform-*d*, 298 K, 126 MHz).

Bis-PDI macrocycle 10

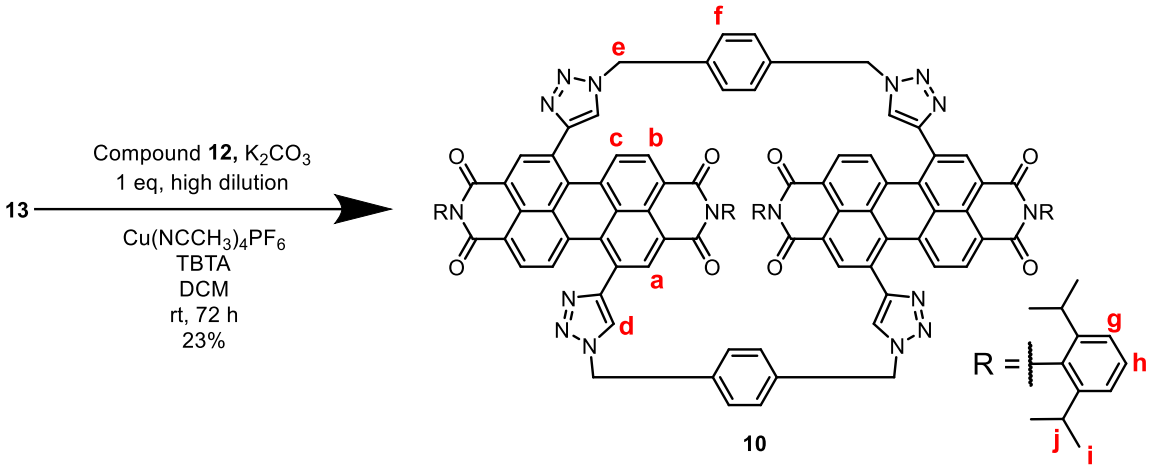

TMS-protected bis-alkyne PDI **12** (29 mg, 38 µmol) was dissolved in DCM (20 mL). To this was added K_2CO_3 (20 mg) in MeOH (10 mL). The reaction was monitored by TLC (1:99 MeOH:DCM). Upon completion the reaction mixture was thoroughly washed with water in a separating funnel (3 x 100 mL) and dried with $MgSO_4$ to yield crude deprotected bis-alkyne PDI in DCM, which was used immediately without further purification due to its tendency to aggregate and crash out of solution over time. This was added to a flask, along with acyclic bis-triazole PDI **13** (44 mg, 38 µmol, 1 equiv), tris((1-benzyl-4-triazolyl)methyl)amine (TBTA) (8 mg, 16 µmol, 0.4 eq) and a further 350 mL of DCM. The reaction mixture was thoroughly de-gassed with N_2. The copper catalyst $Cu(CH_3CN)_4PF_6$ (6 mg, 16 µmol, 0.4 equiv) was then added and the reaction mixture was thoroughly de-gassed again. The reaction was stirred at rt for 36 h and monitored by TLC (2:98 MeOH-DCM). The solvent was then removed *in vacuo*. Attempts were made to purify macrocycle **10** using preparative silica TLC. Unfortunately, macrocycle **10** could only be isolated in trace amounts (< 1mg) and was only detectable by mass spectrometry. This is likely because the large steric bulk of the imide groups severely hinders the formation of the macrocycle. Indeed, MALDI mass spectrometry analysis of the crude reaction mixture revealed the formation of a tris-PDI oligomer in preference to the macrocycle. Because of the failure to make macrocycle **10**, macrocycle **11** was designed with the same goals in mind but with somewhat reduced bulk at the *ortho* position on the imide groups, to aid formation of the macrocycle.

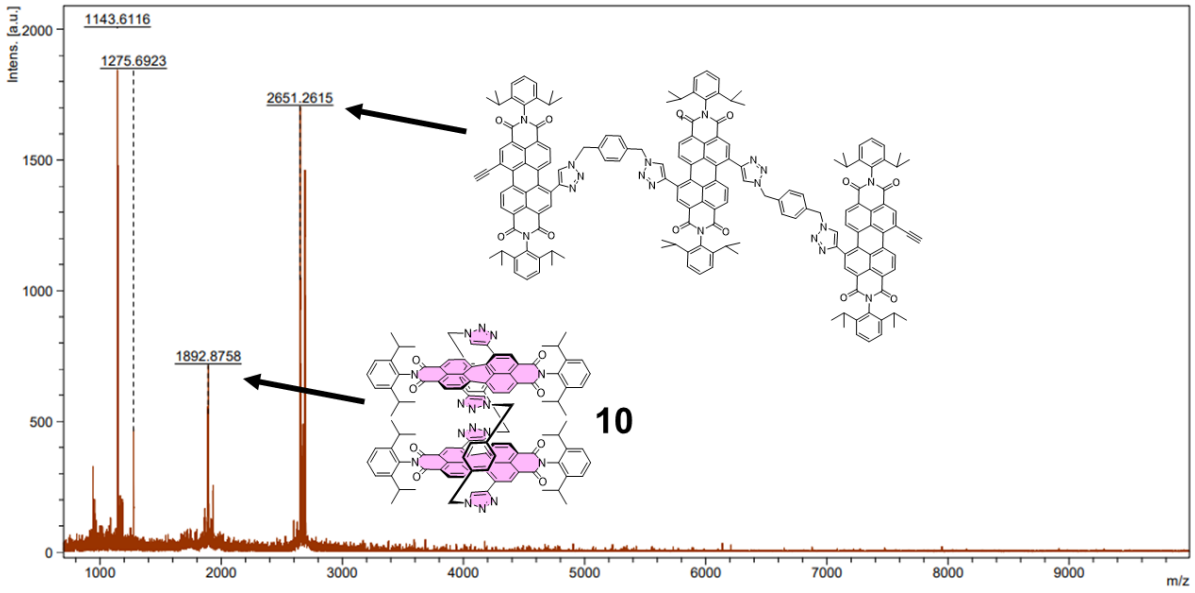

MALDI mass spectrum for the crude reaction mixture of the final macrocyclisation step in the synthesis of macrocycle **10**, after filtration to remove insoluble impurities (which are likely longer PDI oligomers).

4.7.3 Synthesis of macrocycle 11

The synthesis of bis-PDI macrocycle **11** was carried out as shown below. Compounds **14-16** were isolated as a mixture of 1,6- and 1,7- regioisomers. 1,4- bis(azidomethyl)benzene was prepared by Angus Yeung following the **safety precautions for the handling of organic azide compounds described in section 2.9.2**.

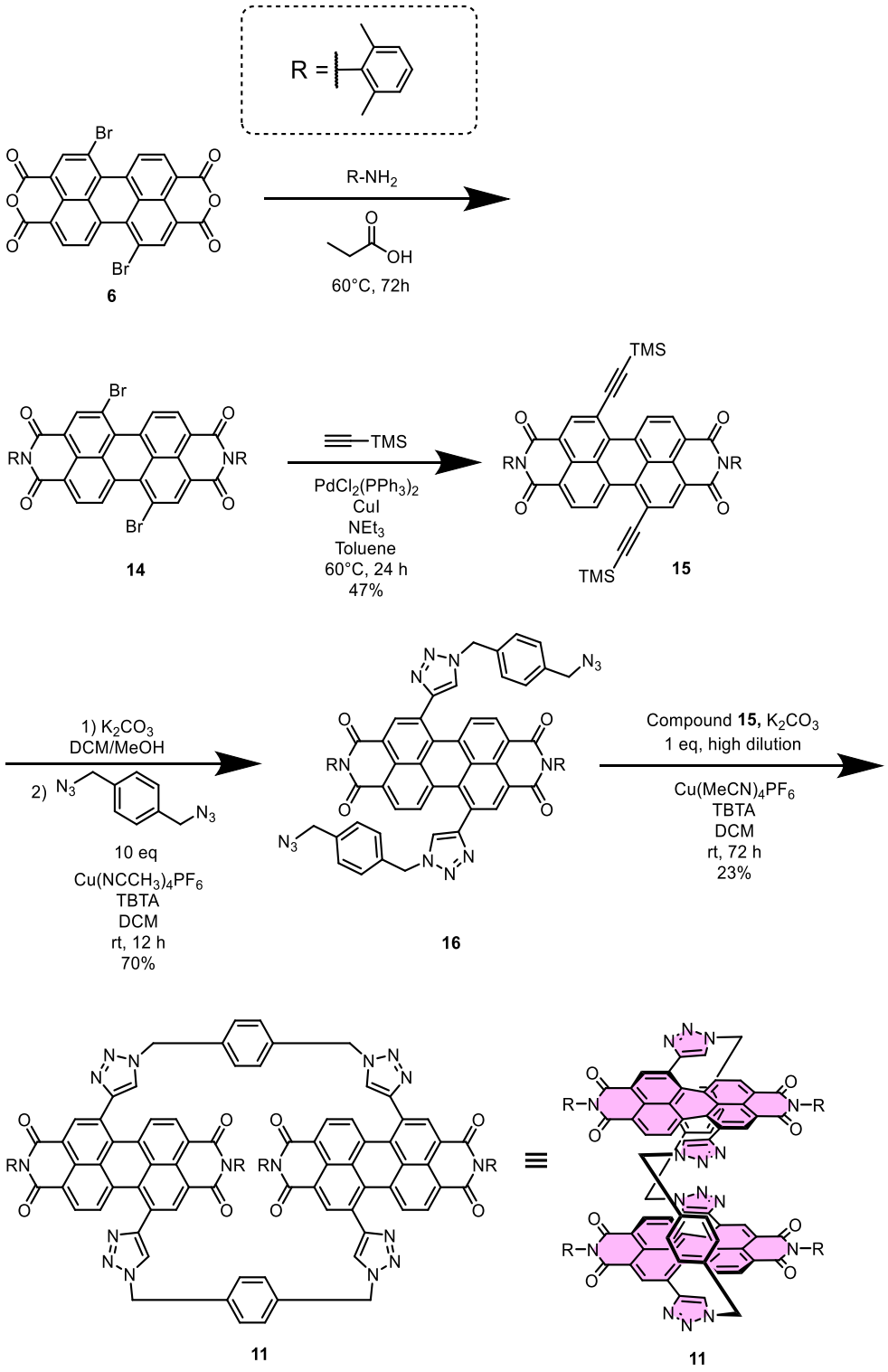

Multistep synthesis of bis-PDI macrocycle **11**.

Bis-bromo PDI 14

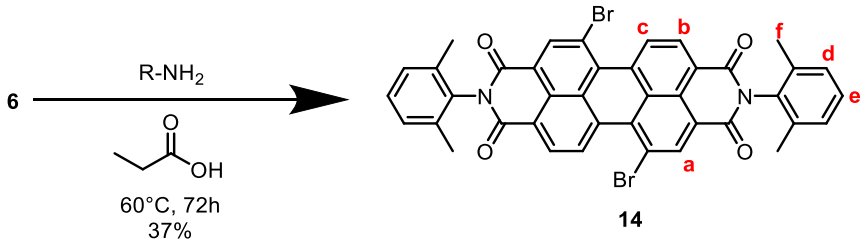

Compound **6** (a mixture of mono-, bis-, tris- and tetra-bromo perylenetetracarboxylic dianhydride, 5 g) was added to a flask. To this was added propionic acid (100 mL) and tert-butyl 4-aminobenzoate (6 mL, 50 mmol, 5.5 equiv). The mixture was purged with nitrogen and heated at 140°C for 72 h. The reaction mixture was then cooled to rt, which yielded a red precipitate. This was washed with water (200 mL) and methanol (50 mL). The resulting red residue was then purified by silica gel flash column chromatography (1:1 n-hexane:CH_2Cl_2), affording compound **14**[17] as a mixture of 1,6 and 1,7 bis-bromo isomers (2.54 g, 3.4 mmol, 33% yield if compound **6** was pure bis-bromo perylenetetracarboxylic dianhydride, taking into account the presence of DCM in the final product (50 mol % by NMR, which results in 10% of the isolated mass being DCM).

^{1}H NMR (500 MHz, Chloroform-*d*, 1,7-isomer) δ 9.58 (dd, *J* = 8.1, 3.2 Hz, $2H_a$), 9.02 (s, $2H_b$), 8.81 (dd, *J* = 8.1, 3.6 Hz, $2H_c$), 7.33-7.25 (m, $6H_{d-e}$), 2.18 (s, $12H_f$), consistent with literature report. [17]

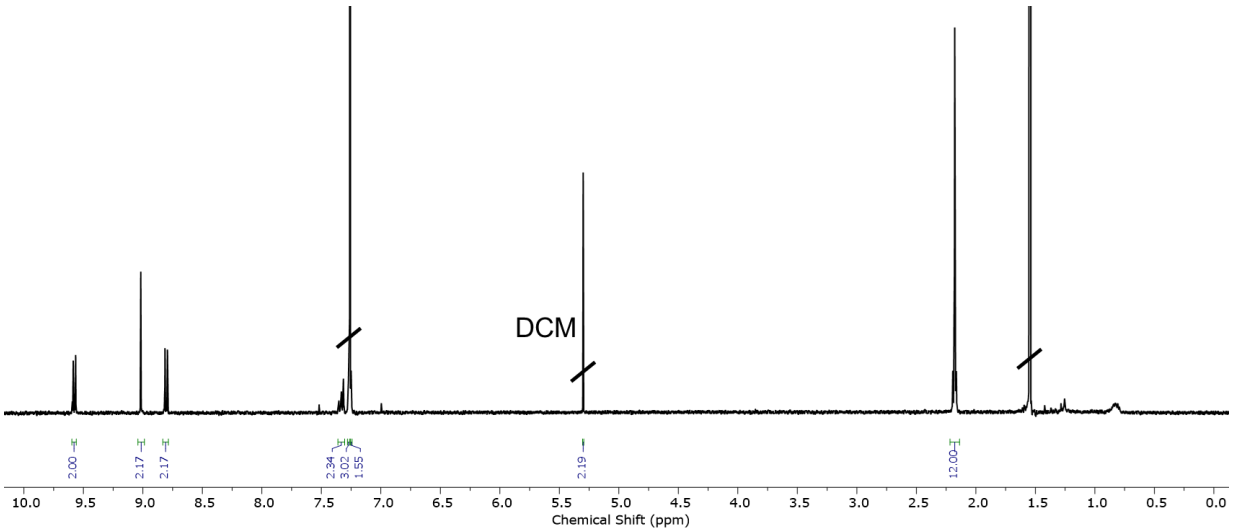

^{1}H NMR spectrum of compound **14** (chloroform-d, 298 K, 500 MHz)

TMS-protected bis-alkyne PDI 15

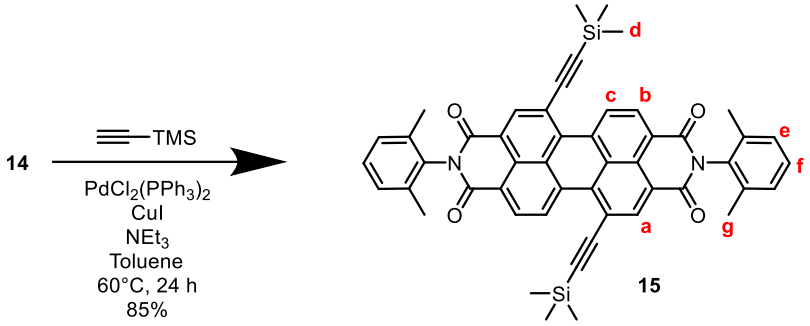

To a solution of bis-bromo PDI **7** (580 mg, 644 µmol) in 1:1 dry NEt_3-toluene (250mL) under a nitrogen atmosphere was added $Pd(PPh_3)_2Cl_2$ (27 mg, 39 µmol, 0.06 equiv), CuI (14 mg, 73 µmol, 0.11 equiv) and trimethylsilylacetylene (316 mg, 458 µL, 3.22 mmol, 5 equiv). The mixture was thoroughly de-gassed with nitrogen and stirred at 60 °C for 24 h. The solvent mixture was then removed in vacuo. The resulting residue was then re-dissolved in DCM (100 mL) and washed with 1 M HCl (50 mL) and water (3 x 50 mL); dried over anhydrous $MgSO_4$ and concentrated to dryness in vacuo. The resulting residue was purified by silica gel flash column chromatography (1:1 n-hexane:DCM) affording the title compound as a red solid (515 mg, 550 µmol, 85%).

^{1}H NMR (500 MHz, Chloroform-*d*, 1,7 isomer) δ 10.26 (d, *J* = 8.2 Hz, $2H_b$), 8.91 (d, *J* = 7.8 Hz, $2H_a$), 8.74 (d, *J* = 8.2 Hz, $2H_c$), 7.33– 7.24 (m, $6H_{e\text{-}f}$), 2.18 (s, $12H_g$), 0.39 (s, $18H_d$).

^{13}C NMR (126 MHz, Chloroform-*d*) δ 162.70, 162.38, 138.96, 138.62, 135.66, 135.00, 134.67, 133.59, 131.11, 129.25, 128.79, 128.74, 128.54, 128.10, 128.02, 127.80, 123.44, 122.32, 120.38, 106.56, 105.53, 18.10, 18.05.

HRMS (ESI) (m/z) calculated for $C_{50}H_{43}N_2O_4Si_2$ $[M+H]^+$ 791.2761, found 791.2773.

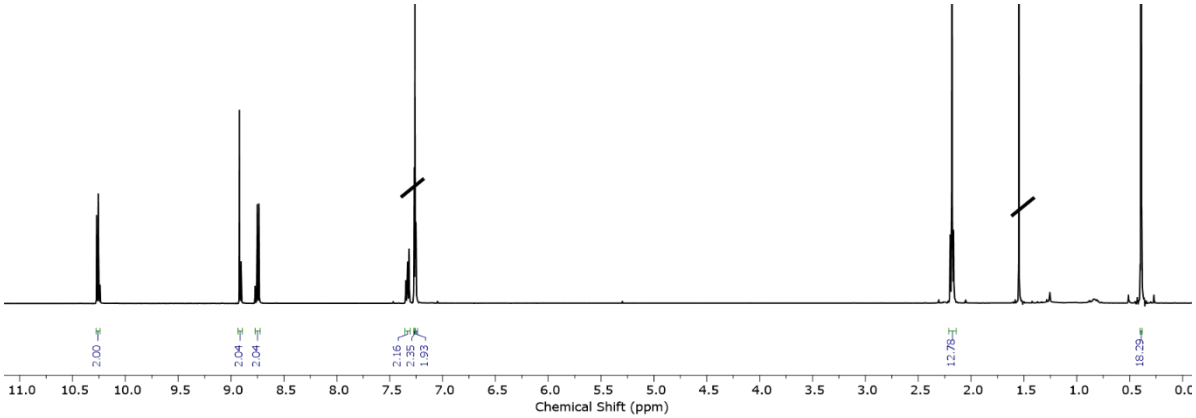

^{1}H NMR spectrum of compound **15** (chloroform-d, 298 K, 500 MHz).

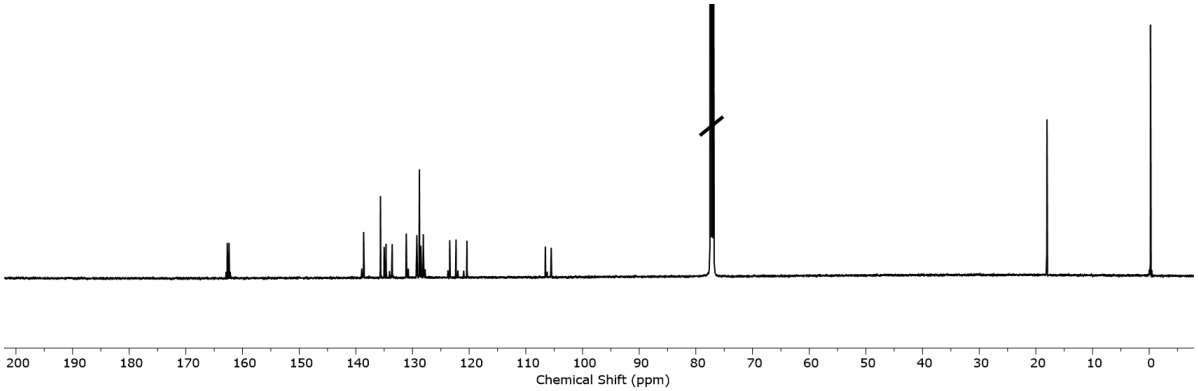

^{13}C NMR spectrum of compound **15** (chloroform-d, 298 K, 126 MHz)

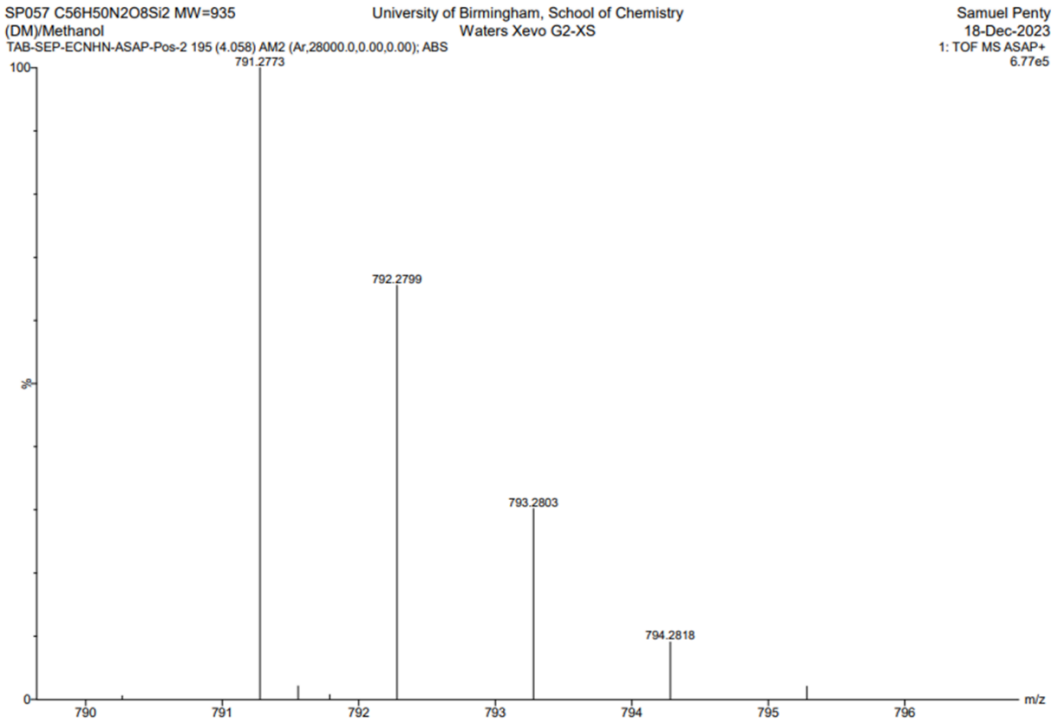

Observed ESI MS data for compound **15**.

Acyclic bis-triazole PDI 16

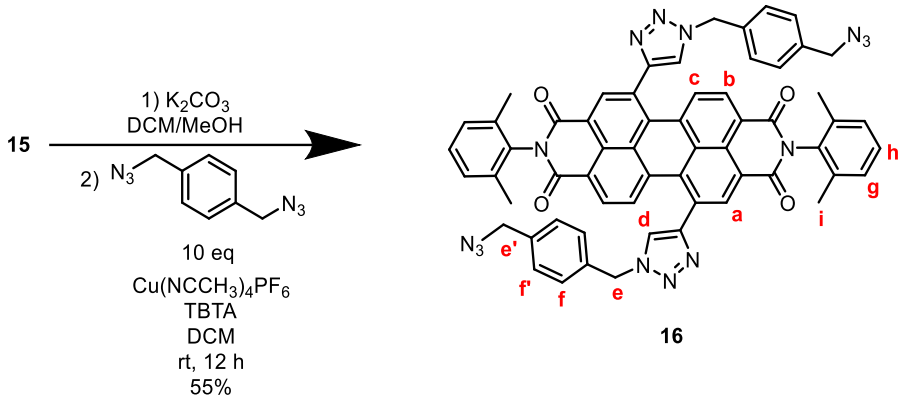

To a solution of TMS-protected bis-alkyne PDI **15** (155 mg, 194 µmol) in DCM (20 ml) was added K_2CO_3 (30 mg) in MeOH (10 ml). The mixture was stirred at rt for 3 min, and completion of the reaction was confirmed by TLC. The solution was then washed with water (2 x 30 mL) and brine (30 ml). The organic layer was then dried over anhydrous $MgSO_4$ and concentrated to dryness in vacuo to afford the deprotected PDI bis-alkyne which was used immediately without further purification. This PDI bis-alkyne was immediately re-dissolved in dry DCM (30 mL). To this was added 1,4- bis(azidomethyl)benzene (182 mg, 971 µmol, 5 equiv) and tris((1-benzyl-4- triazolyl)methyl)amine (TBTA) (20 mg, 39 µmol, 0.2 equiv). The solution was then de-gassed with argon. The copper (I) catalyst $Cu(CH_3CN)_4PF_6$ (15 mg, 39 µmol, 0.2 equiv) was then added and the solution was once again de-gassed with argon. The reaction was stirred at rt for 12 h. The solvent was then removed in vacuo. The resulting residue was purified by silica gel flash column chromatography (1:199 MeOH-DCM) affording the title compound as a purple solid (110 mg, 108 µmol, 55%).

^{1}H NMR (500 MHz, Chloroform-*d*, 1,7 isomer) δ 8.74 (s, $2H_a$), 8.24 (d, J = 8.0 Hz, $2H_b$), 7.93 (d, J = 8.0 Hz, $2H_c$), 7.72 (s, $2H_d$), 7.43 – 7.21 (m, $10H_{f,g,h}$), 5.67 (d, J = 2.2 Hz, $4H_e$), 4.37 (d, J = 2.4 Hz, $4H_{e'}$), 2.14 (s, $12H_i$).

^{13}C NMR (126 MHz, Chloroform-*d*) δ 162.49, 162.44, 148.20, 136.77, 135.47, 135.32, 135.01, 134.42, 133.95, 133.50, 130.19, 129.41, 129.30, 129.22, 129.11, 129.08, 128.91, 128.65, 128.52, 128.48, 122.68, 122.49, 122.00, 54.27, 54.17, 17.89

HRMS (MALDI-MS) (m/z) calculated for $C_{60}H_{41}N_{14}O_4$ [M-H] 1021.3435, found 1021.4322.

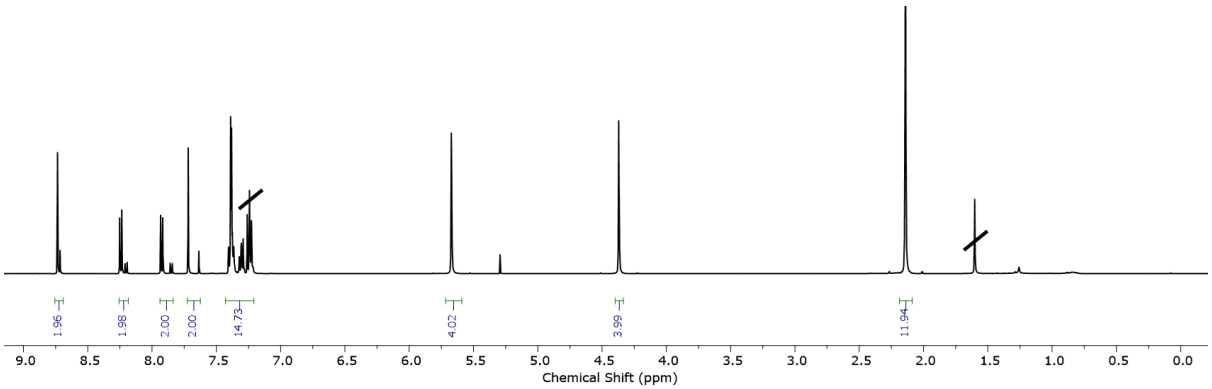

^{1}H NMR spectrum of compound **16** (chloroform-*d*, 298 K, 500 MHz).

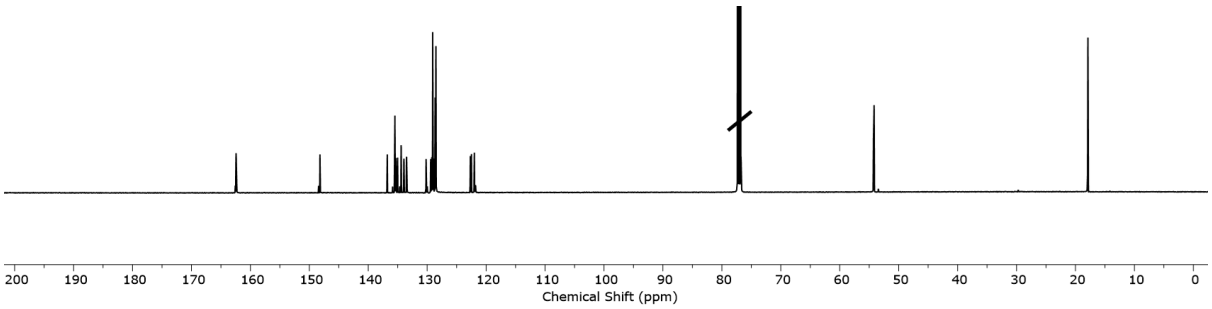

^{13}C NMR spectrum of compound **16** (chloroform-*d*, 298 K, 126 MHz).

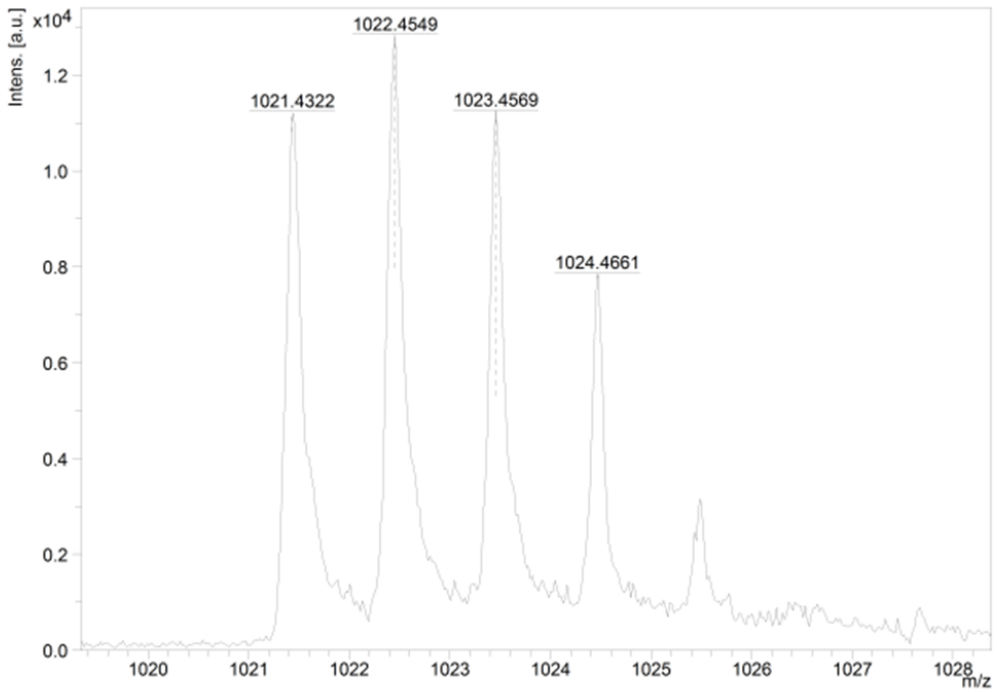

Observed (bottom) MALDI-MS data for compound **16**.

Bis-PDI macrocycle 11

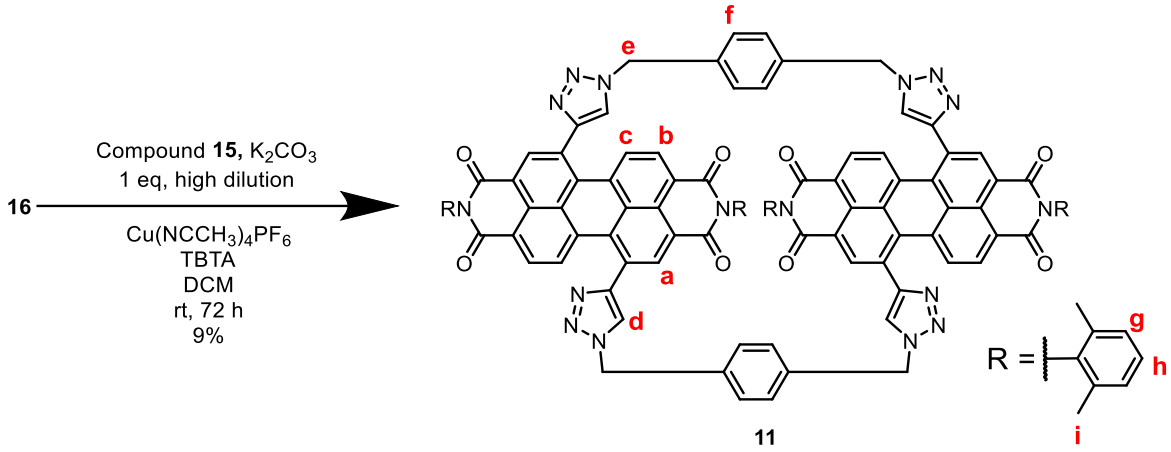

TMS-protected bis-alkyne PDI **15** (77 mg, 97 µmol) was dissolved in DCM (20 mL). To this was added K_2CO_3 (20 mg) in MeOH (10 mL). The reaction was monitored by TLC. Upon completion the reaction mixture was thoroughly washed with water in a separating funnel (3 x 100 mL) and dried with $MgSO_4$ to yield crude deprotected bis-alkyne PDI in DCM, which was used immediately without further purification due to its tendency to aggregate and crash out of solution over time. This was added to a flask, along with acyclic bis-triazole PDI **16** (99 mg, 97 µmol, 1 equiv), tris((1-benzyl-4-triazolyl)methyl)amine (TBTA) (21 mg, 39 µmol, 0.4 eq) and a further 350 mL of DCM. The reaction mixture was thoroughly de-gassed with N_2. The copper catalyst $Cu(CH_3CN)_4PF_6$ (14 mg, 39 µmol, 0.4 equiv) was then added and the reaction mixture was thoroughly de-gassed again. The reaction was stirred at rt for 36 h and monitored by TLC (2:98 MeOH-DCM). The solvent was then removed *in vacuo*. The resulting residue was dissolved in DCM and filtered through cotton wool and the filtrate was then purified by HPLC (COSMOSIL Buckyprep 250 x 10 mm, eluted with a gradient going from 1:1 (v/v) DCM:n-hexane eluent to 7:3:1 (v/v/v) DCM:n-hexane:isopropanol) affording the title compound as a purple solid (isolated 15 mg including both the homochiral and heterochiral diastereomers, 97 µmol, 9%).

^{1}H NMR (homochiral stereoisomer, 400 MHz, 343K, TCE-d_2) δ 8.76 (s, 4H_a), 8.33 (d, J = 8.1 Hz, 4H_b), 7.95 (d, J = 8.2 Hz, 4H_c), 7.41 – 7.21 (m, 24$H_{d,f,g,h}$), 5.73 (d, J = 15.2 Hz, 4H_e), 5.62 (d, J = 15.2 Hz, 4H_e), 2.17 (d, J = 6.6 Hz, 12H_i), 2.04 (s, 12H_i).

^{13}C NMR (101 MHz, TCE-d_2) δ 162.54, 162.17, 148.11, 136.07, 135.99, 135.57, 135.23, 134.72, 133.73, 133.69, 130.23, 129.76, 129.24, 129.07, 129.02, 128.74, 122.99, 122.93, 121.41, 120.60, 74.45, 74.17, 73.90, 54.30, 18.13, 17.94.

HRMS (MALDI-MS) (m/z) calculated for $C_{104}H_{68}N_{16}O_8$ [M-H] 1667.5327, found 1667.5328

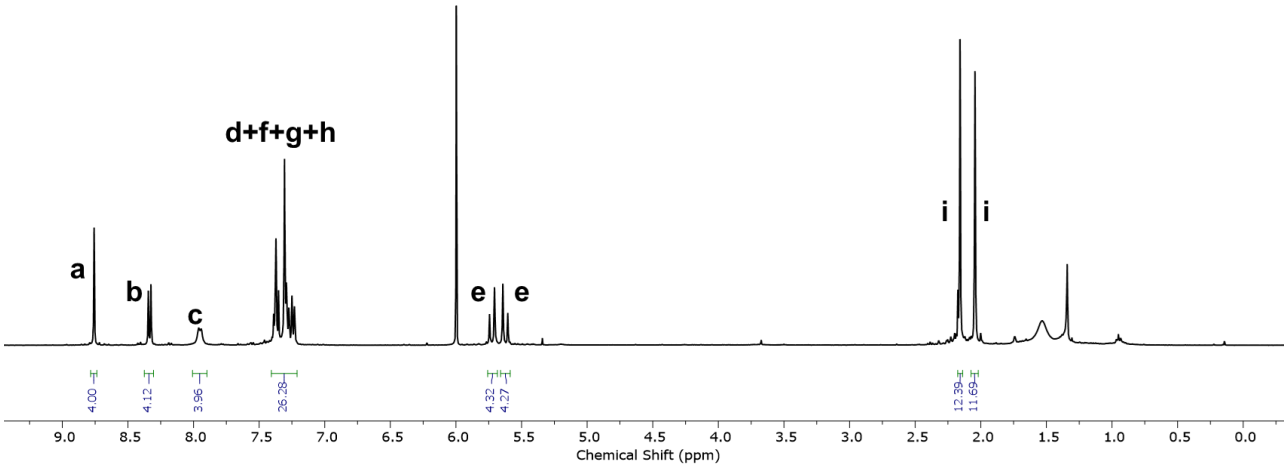

^{1}H NMR spectrum of macrocycle **11** (homochiral diastereomer, TCE-d_2, 343 K, 400 MHz).

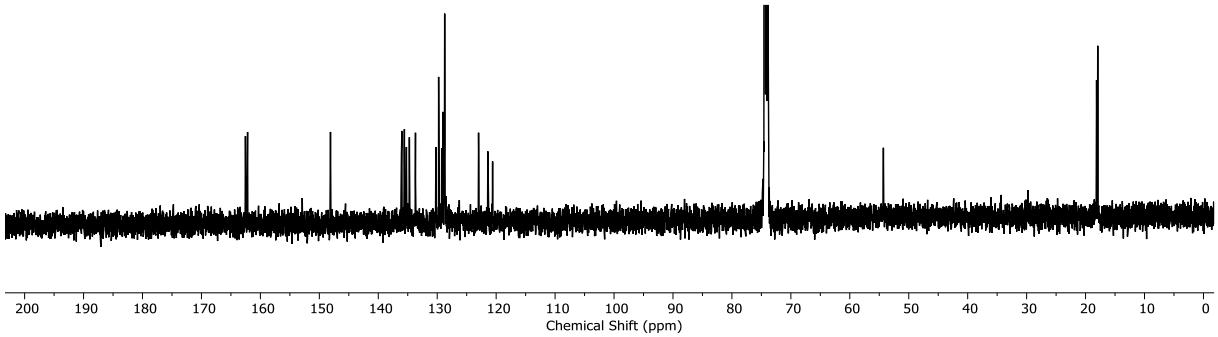

^{13}C NMR spectrum of macrocycle **11** (TCE-d_2, 343 K, 400 MHz)

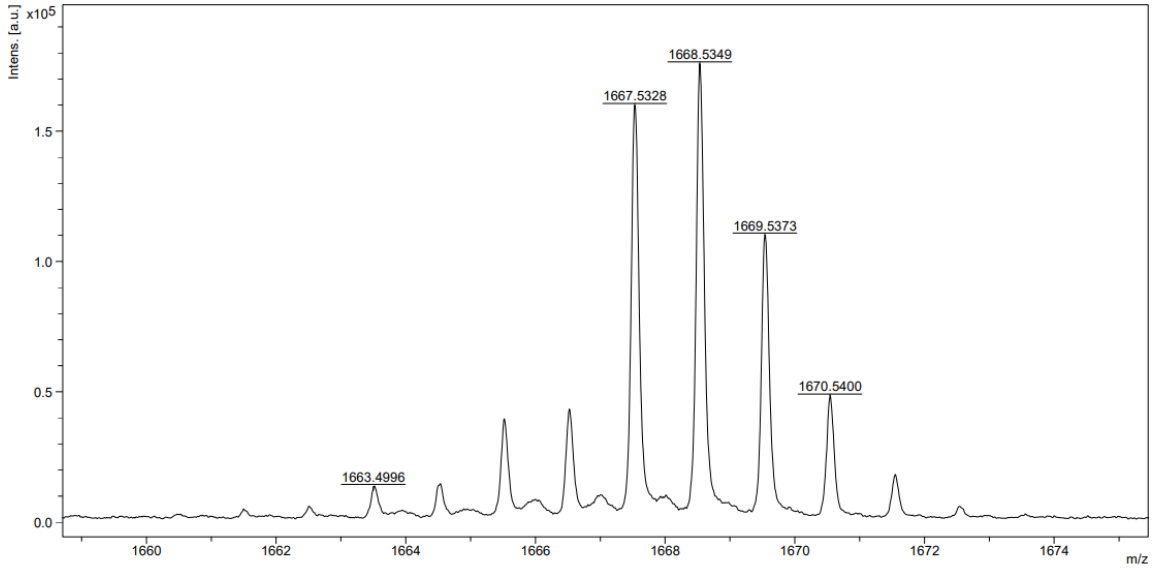

Observed MALDI-MS data for macrocycle **11**.

4.7.4 Chiroptical studies

Circular dichroism

Circular dichroism (CD) spectra were recorded on a Jasco J-1500 CD spectrophotometer with a wavelength accuracy ± 0.2 nm (250 to 500 nm), ± 0.5 nm (500 to 800 nm) and a CD root mean square noise < 0.007 mdeg (500 nm). A quartz cuvette with 1 mm path length was used. The spectra were recorded at a concentration of 10 μM. The enantiomers were assigned by corroboration of the samples with the crystal structure of enantiopure **5-*PP***, as well as by comparison of their CD spectra to the computationally predicted CD spectra (see Appendix A for further details).

Circularly polarised luminescence

CPL was measured with a home-built (modular) spectrometer.[18] The excitation source was a broad band (200 – 1000 nm) laser- driven light source EQ 99 (Elliot Scientific). The excitation wavelength was selected by the incorporation of an Acton SP-2155 monochromator (Princeton Instruments); the collimated light was focused into the sample holder (1 cm quartz cuvette). Emission was collected perpendicular to the excitation direction with a lens (f = 150 mm). The emission was fed through a photoelastic modulator (PEM) (Hinds Series II/FS42AA) and through a linear sheet polariser (Comar Optics). The light was then focused into a second scanning monochromator (Acton SP-2155) and subsequently on to a photomultiplier tube (PMT) (Hamamatsu H10723 series). The detection of the CPL signal was achieved using the field modulation lock-in technique. The electronic signal from the PMT was fed into a lock-in amplifier (Hinds Instruments Signaloc Model 2100). The reference signal for the lock-in detection was provided by the PEM control unit. The monchromators, PEM control unit and lock-in amplifier were interfaced to a desktop PC and controlled by a custom-written Labview graphic user interface. The lock-in amplifier provided two signals, an AC signal corresponding to (I_L- I_R) and a DC signal corresponding to (I_L + I_R). Background subtraction was achieved post data collection The emission dissymmetry factor was, therefore, readily obtained from the experimental data as 2 AC/DC.

Spectral calibration of the scanning monochromator was performed using a Hg-Ar calibration lamp (Ocean Optics HL-3P-CAL). A correction factor for the wavelength dependence of the detection system was constructed using a calibrated lamp (Ocean Optics HL-3_CAL). The

measured raw data was subsequently corrected using this correction factor. The validation of the CPL detection systems was achieved using light emitting diodes (LEDs) at various emission wavelengths. The LED was mounted in the sample holder and the light from the LED was fed through a broad band polarising filter and $\lambda/4$ plate (Comar Optics) to generate circularly polarised light. Prior to all measurements, the $\lambda/4$ plate and a LED were used to set the phase of the lock-in amplifier correctly. The emission spectra were recorded with 0.5 nm step size and the slits of the detection monochromator were set to a slit width corresponding to a spectral resolution of 0.25 nm. CPL spectra (as well as total emission spectra) were obtained through an averaging procedure of several scans.

4.7.5 Photophysics

UV-vis-NIR absorption and emission spectra in solution

All steady state electronic absorption and emission spectra were recorded at a concentration of 10 µM (unless otherwise stated) at 298 K. For UV-vis-NIR spectroscopy a Shimadzu UV-3600i Plus spectrophotometer was used, with a wavelength accuracy ± 0.2 nm in the UV-vis range and absorbance accuracy ± 0.002 Abs. For fluorescence spectroscopy a Jasco FP-8500 was used with emission and excitation wavelength accuracies ± 1.0 nm. The detector base sensitivity is 8500:1. Quartz cuvettes with 1 cm path length were used.

4.8 References

1. M. Ball, B. Fowler, P. Li, L. A. Joyce, F. Li, T. Liu, D. Paley, Y. Zhong, H. Li, S. Xiao, F. Ng, M. L. Steigerwald and C. Nuckolls, *Journal of the American Chemical Society*, 2015, **137**, 9982-9987.
2. S. E. Penty, G. R. F. Orton, D. J. Black, R. Pal, M. A. Zwijnenburg and T. A. Barendt, *Journal of the American Chemical Society*, 2024, DOI: 10.1021/jacs.3c13191.
3. N. J. Hestand and F. C. Spano, *The Journal of Chemical Physics*, 2015, **143**.
4. E. Sebastian, A. M. Philip, A. Benny and M. Hariharan, *Angewandte Chemie International Edition*, 2018, **57**, 15696-15701.
5. G. Bressan, S. E. Penty, D. Green, I. Heisler, G. Jones, T. A. Barendt and S. Meech, *Angewandte Chemie International Edition*, 2024, **63**, e202407242.
6. E. Lee, H. Ju, I.-H. Park, J. H. Jung, M. Ikeda, S. Kuwahara, Y. Habata and S. S. Lee, *Journal of the American Chemical Society*, 2018, **140**, 9669-9677.
7. T. Ogoshi, R. Shiga, T.-a. Yamagishi and Y. Nakamoto, *The Journal of Organic Chemistry*, 2011, **76**, 618-622.
8. I. Shioukhi, H. Batchu, G. Schwartz, L. Minion, Y. Deree, B. Bogoslavsky, L. J. W. Shimon, J. Wade, R. Hoffman, M. J. Fuchter, G. Markovich and O. Gidron, *Angewandte Chemie International Edition*, 2024, **63**, e202319318.
9. L. Miton, É. Antonetti, D. García-López, P. Nava, V. Robert, M. Albalat, N. Vanthuyne, A. Martinez and Y. Cotelle, *Chemistry – A European Journal*, 2024, **30**, e202303294.
10. M. Lago-Silva, M. M. Cid, E. Quiñoá and F. Freire, *Journal of the American Chemical Society*, 2024, **146**, 752-759.
11. C. D. Schmidt, N. Lang, N. Jux and A. Hirsch, *Chemistry – A European Journal*, 2011, **17**, 5289-5299.
12. T. E. Kaiser, H. Wang, V. Stepanenko and F. Würthner, *Angewandte Chemie International Edition*, 2007, **46**, 5541-5544.
13. M. Hecht and F. Würthner, *Accounts of Chemical Research*, 2021, **54**, 642-653.
14. S. E. Penty, G. R. F. Orton, D. J. Black, R. Pal, M. A. Zwijnenburg and T. A. Barendt, *Journal of the American Chemical Society*, 2024, **146**, 5470-5479.
15. T. R. Chan, R. Hilgraf, K. B. Sharpless and V. V. Fokin, *Organic Letters*, 2004, **6**, 2853-2855.
16. M. Bagui, T. Dutta, H. Zhong, S. Li, S. Chakraborty, A. Keightley and Z. Peng, *Tetrahedron*, 2012, **68**, 2806-2818.
17. M. Queste, C. Cadiou, B. Pagoaga, L. Giraudet and N. Hoffmann, *New Journal of Chemistry*, 2010, **34**, 2537-2545.
18. R. Carr, R. Puckrin, B. K. McMahon, R. Pal, D. Parker and L.-O. Pålsson, *Methods and Applications in Fluorescence*, 2014, **2**, 024007.

Chapter 5: Linker variation in Pink Box-type macrocycles

5. Linker variation in Pink Box-type macrocycles

5.1 Introduction

The Chapters 2, 3 and 4 in this thesis focused on the effects of varying the imide groups in "Pink Box" type bis-PDI macrocycles while keeping the linker group (para-xylene) constant. Changing the imide group was found to impact the configurational stability, chiroptical and self-assembly properties of these macrocycles. However, a key feature of these "Pink Box" macrocycles is that the linker groups can also be modulated as they are incorporated into the molecular architecture in the penultimate stage of the synthesis via "click" chemistry. Using linker groups with different lengths and rigidities is expected to affect the PDI-PDI intramolecular distance and relative rotation (**Figure 5.1**), which in turn may affect the nature of the PDI-PDI interaction and the population of chiral conformations. Furthermore, varying the imide groups may give access to a larger macrocyclic cavity for binding polycyclic aromatic hydrocarbon (PAH) guests.[1] Indeed, the intermolecular π–π recognition characterised in Chapter 3 indicates that bis-triazole PDIs have the correct shape complementarity for binding PDIs (i.e. self-recognition), but that the bis-PDI macrocycle cavity may be too small for binding a bis-triazole PDI guest. Systematic variation of the linker groups has been previously studied in imide-linked bis-PDI macrocycles,[2] but has yet to be studied in bay-connected bis-PDI macrocycles.

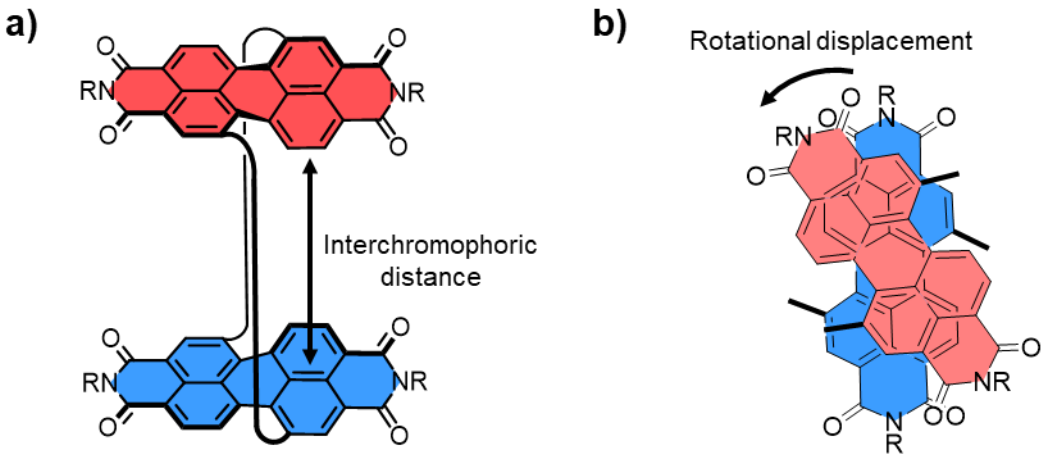

Figure 5.1: Cartoon depiction of **(a)** variation pf interchromophore distance, and **(b)** variation of PDI-PDI relative rotation, in a 1,7-bay-connected bis-PDI macrocycle.

This chapter focuses on the effects of varying the linker group while keeping the imide group constant. For this purpose, a series of macrocycles bearing the same branched alkyl "C_{11}" imide groups, but with different linkers connecting the PDIs, were synthesised. These are shown in **Figure 5.2**, alongside the previously discussed macrocycle **1a** which bears short and rigid para-xylene linker groups. This aromatic linker is progressively extended to afford the biphenyl analogue macrocycle **17** and the terphenyl analogue macrocycle **18**. Additionally, macrocycle **19** linked by more flexible *n*-hexyl chains, was also synthesised. These macrocycles are studied by ^{1}H NMR and UV-vis spectroscopy alongside chiral HPLC to characterise the nature of the intramolecular PDI-PDI interaction in each case, and how this might influence the population of the various chiral conformations presented in Chapter 4. Additionally, attempts are made to use these macrocycles as hosts for the binding of PAHs. The analysis in this chapter is complemented by computational studies carried out by Prof. Martijn Zwijnenburg to aid interpretation of the experimental work. These studies are referred to throughout this Chapter, and full details are given in Appendix A.

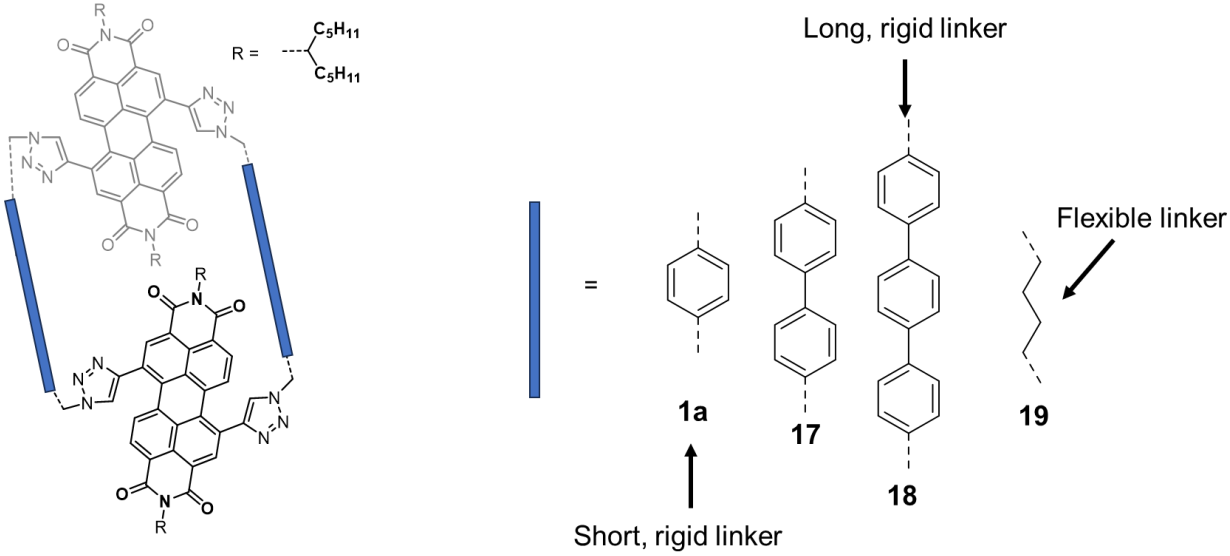

Figure 5.2: Structures of macrocycles **1a**, **17**, **18** and **19**, designed to study the effects of linker group length and rigidity on the properties of "Pink Box"-type macrocycles.

5.2 Synthesis of bis-PDI macrocycles 17-19

Macrocycles **17-19** were synthesised using the same strategy as for the original "Pink Box" macrocycle **1a** described in Chapter 2. To begin with, bis-alkyne PDI **2a** was reacted with an excess of the appropriate bis-azide linker to yield compounds **20-22** via copper(I)-catalysed azide–alkyne cycloaddition (CuAAC) "click" reactions (**Scheme 5.1**).

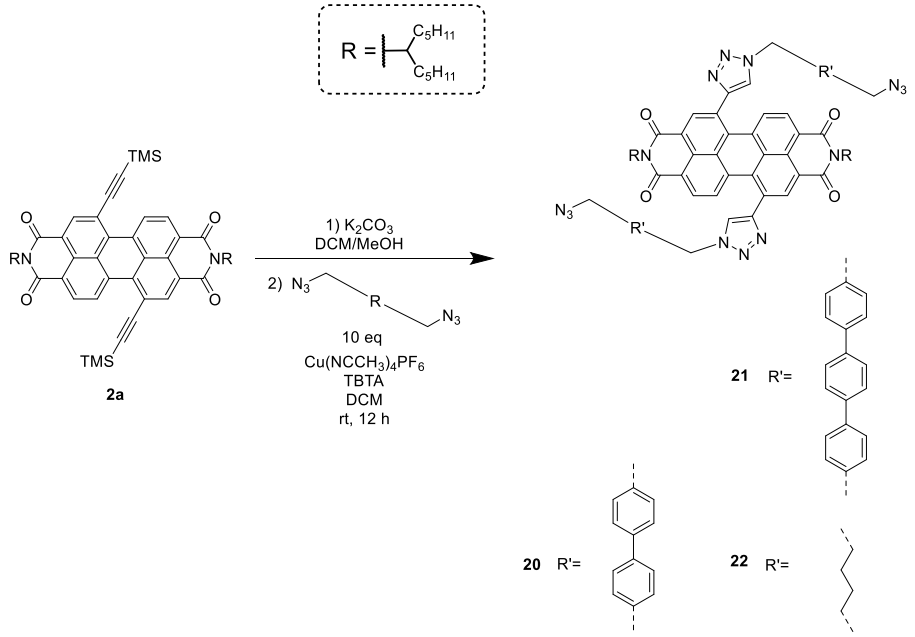

Scheme 5.1: Synthesis of the bis-triazole acyclic PDIs **20-22**.

While the biphenyl and hexyl bis-azide linkers have been previously reported[3, 4] and were kindly provided by another group member (Angus Yeung), the terphenyl linker **24** is a novel compound and was synthesised according to **Scheme 5.2**

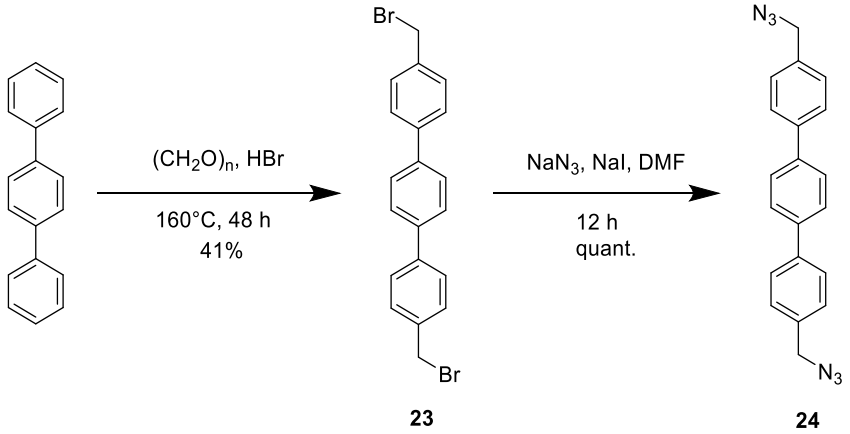

Scheme 5.2: Synthesis of terphenyl bis-azide linker **24**.

Bis-azide PDI compounds **20-22** were then reacted with a stoichiometric amount of bis-alkyne PDI **2a** under relatively high dilution conditions (0.3 mM) to favour macrocyclisation,[5] once again under CuAAC "click" chemistry conditions. This yielded macrocycles **17-19 (Scheme 5.3)**. Interestingly, for the aromatic linkers, the yield of macrocycle in this final macrocyclisation step decreases as the linker length increases, going from 39% for phenyl-linked **1a** to 17% for terphenyl-linked **19**. This may be explained by weaker PDI-PDI templation through co-facial π–π interactions[6] in macrocycles containing longer rigid linkers. For macrocycle **22**, with flexible hexyl linkers, the yield is similar to that of phenyl-linked **1a**. All novel compounds were fully characterised by ^{1}H NMR spectroscopy and high-resolution mass spectrometry. Further details are also provided in the experimental section 5.9.

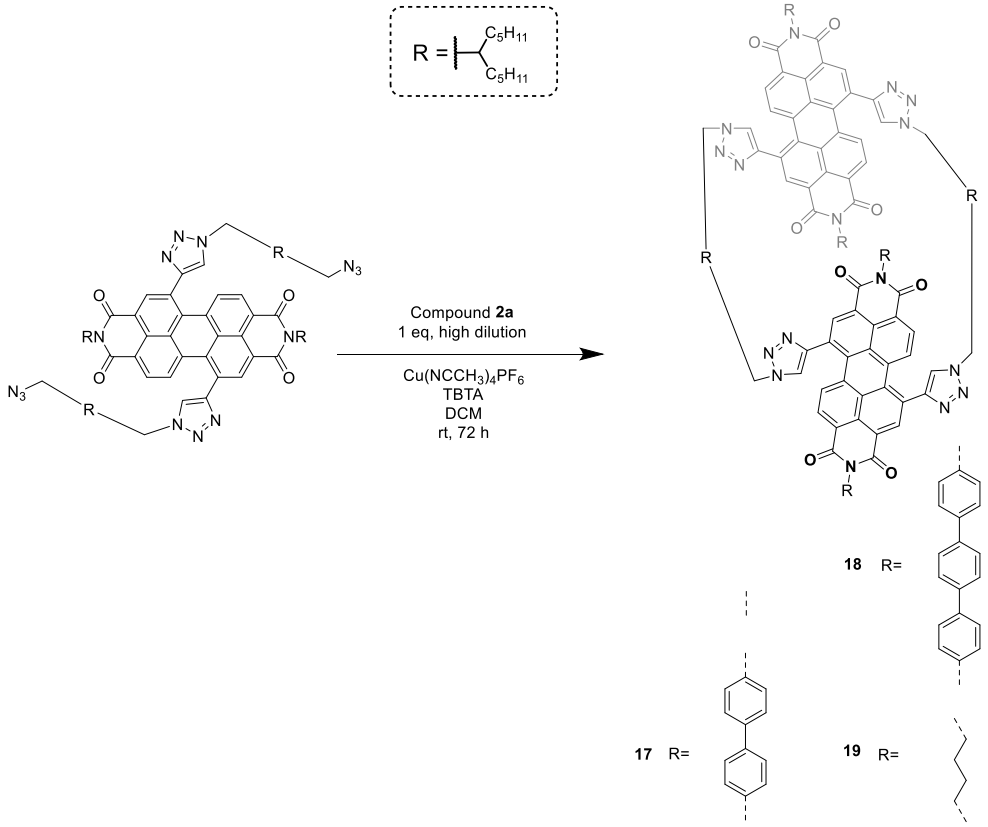

Scheme 5.3: Synthesis of the bis-PDI macrocycles **17-19**.

5.3 Photophysical studies

5.3.1 UV-vis absorption spectroscopy

As discussed extensively in Chapters 2 and 4, the strength of intramolecular PDI-PDI excitonic coupling in xylene-spaced macrocycle **1a** displays a dramatic solvent dependence, as a result of a conformational change between toluene and chlorinated solvents. The strength of PDI-PDI excitonic coupling can be measured from the intensity ratio of the 0-0 and 0-1 vibronic bands within the $S_0 \rightarrow S_1$ band in the UV-vis absorption spectrum of these macrocycles. Therefore, the first experiment with macrocycles **17-19** was to measure their UV-vis spectra in toluene and TCE and compare their behaviour to that of **1a** (**Figure 5.3**).

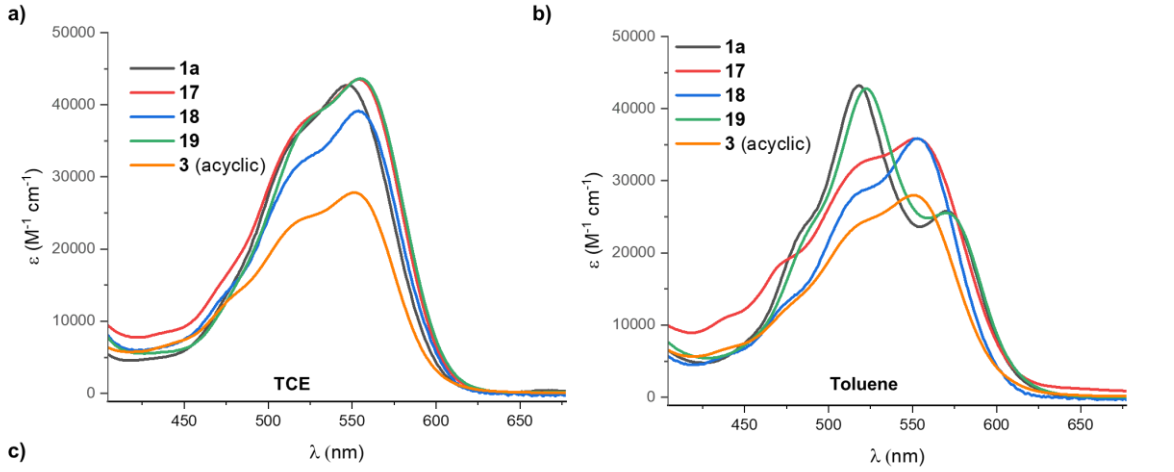

Compound	$\varepsilon_{0-0}/\varepsilon_{0-1}$	
	TCE	Toluene
1	1.19	0.58
17	1.16	1.08
18	1.17	1.22
19	1.16	0.58
3	1.16	1.20

Figure 5.3: a) UV-vis absorption spectra of macrocycles **1a** and **17-19** alongside acyclic PDI monomer **3** in TCE. **b)** UV-vis absorption spectra of macrocycles **1a** and **17-19** alongside acyclic PDI monomer **3** in toluene. **c**) Ratio of the 0-0 and 0-1 vibronic bands in the $S_0 \rightarrow S_1$ band in the UV-vis absorption spectrum of macrocycles **1a**, **17-19** and acyclic PDI monomer **3**.

In TCE, the UV-vis spectra of macrocycles **1a**, **17-19** are very similar to each other, and to that of acyclic PDI monomer **3** (**Figure 5.3a**), with $\varepsilon_{0-0}/\varepsilon_{0-1}$ ratios ranging from 1.16 to 1.19, showing that intramolecular PDI-PDI excitonic coupling is very weak in chlorinated solvents for all of these macrocycles.

However, in toluene clear differences in the excitonic coupling in these macrocycles can be observed (**Figure 5.3b**). As discussed in Chapter 2, **1a** exhibits strong H-type excitonic coupling since $\varepsilon_{0-0}/\varepsilon_{0-1} = 0.58$ and λ_{max} is blue-shifted from 547 nm in TCE to 516 nm in toluene. Gradually increasing the linker length leads to a decrease in excitonic coupling strength, with $\varepsilon_{0-0}/\varepsilon_{0-1}$ = 1.08 for biphenyl-spaced macrocycle **17** and $\varepsilon_{0-0}/\varepsilon_{0-1}$ = 1.22 for terphenyl-spaced macrocycle **18**. For hexyl-spaced macrocycle **19** the UV-vis spectrum in toluene is very similar to that of **1a** in toluene, but λ_{max} is slightly less blue-shifted (λ_{max} = 516 nm for **1a**, 522 nm for **10**). This indicates that **19** forms an intramolecular PDI-PDI H-type aggregate in toluene very similar to that of **1a**, but perhaps with a slightly different conformation as a result of the more flexible hexyl linkers.

One possible explanation for weaker intramolecular PDI-PDI excitonic coupling in macrocycles **17** and **18** is that the longer linkers position the PDIs further apart. However, as explained in Chapter 1 (section 1.6), the strength and nature of excitonic coupling not only depends on interchromophore distance but is also extremely sensitive to small changes in slip angle or rotational angle between the two PDI cores (see **Figure 1.8** in Chapter 1)[7, 8] Indeed, as established in Chapter 4 (section 4.3) for macrocycle **1a**, these macrocycles are conformationally-flexible, such that "triazoles" in vs "triazoles out" conformations are likely to affect the distance and relative orientation of the PDI cores in macrocycles **17** and **18**.

In addition, so far in this thesis PDI-PDI excitonic coupling has mainly been discussed in terms of Kasha's model where it is treated as a long-range Coulombic interaction between the electric transition dipole moments of the molecules.[9] Whilst this model successfully accounts for the optical properties of many PDI aggregates,[10] there are also examples of PDI aggregates with smaller interchromophore separations where "short-range" coupling, which arises from orbital overlap between adjacent chromophores, cannot be neglected.[7, 11] In fact, PDI aggregates have even been reported where the "long-range" and "short-range" coupling energies have similar magnitudes but opposite signs, leading to an overall "null aggregate" with monomeric optical properties.[11, 12]

With UV-vis spectroscopy identifying a correlation between excitonic coupling strength and linker length, attention then turned to experimental and theoretical studies that could inform on the macrocycle conformation(s) responsible for this trend.

5.4 NMR spectroscopy

5.4.1 ^{1}H NMR spectroscopy at room and high temperature

Proton NMR spectroscopic studies were carried out to gain insight into the conformations of macrocycles **17-19** in solution and draw comparisons with macrocycle **1a**.

As a reminder, the ^{1}H NMR spectrum of macrocycle **1a** is broad at room temperature (25°C) due to restricted molecular motion (**Figure 5.9**). Heating the sample in TCE-d_2 causes sharpening (**Figure 5.9**), which was analysed in depth in Chapter 2 but is used here to highlight two features indicating restricted molecular motion in **1a**. Firstly, the presence of a second set of peaks corresponding to the heterochiral ***MP*** stereoisomer shows that PDI "somersaulting" is slow on the NMR timescale. Secondly, the signal corresponding to proton H_e exhibits diastereotopic splitting into two roofed doublets, due to the proximity of this methylene group to the chiral bis-triazole PDI. Importantly, this diastereotopic splitting is only observed when the interconversion of PDI enantiomers is restricted since no splitting is observed in the ^{1}H NMR spectrum of the acyclic bis-triazole PDI **3** due to rapidly interconverting atropisomers. Therefore, diastereotopic splitting of H_e provides a useful handle for identifying restricted PDI "somersaulting" in bis-PDI macrocycles.

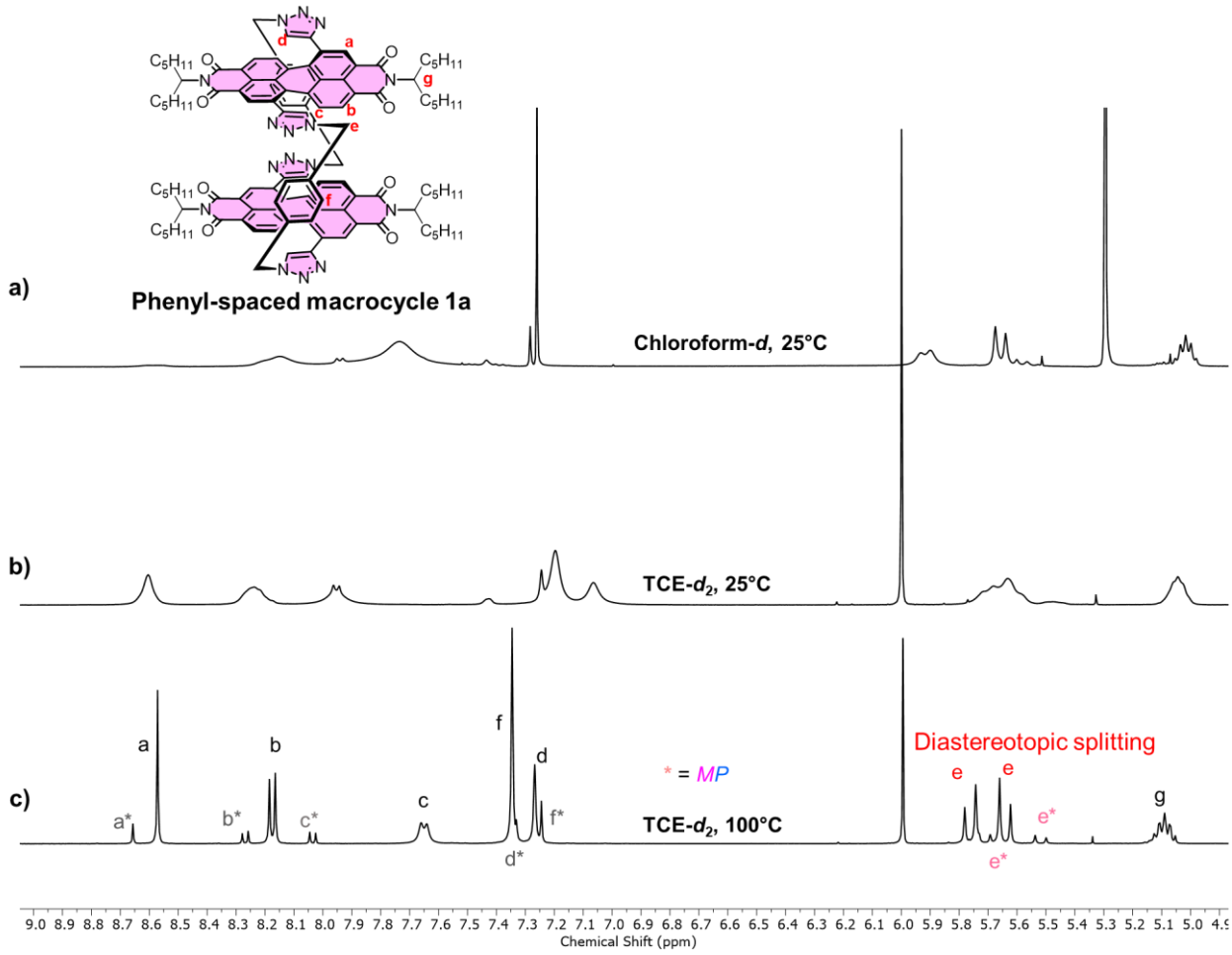

Figure 5.4: NMR spectra of macrocycle **1a** (400 MHz) in **a)** chloroform-*d*, 25°C, **b)** TCE-d_2, 25°C and **c)** TCE-d_2, 100°C.

In contrast to **1a**, biphenyl-spaced macrocycle **17** and terphenyl-spaced macrocycle **18** exhibit sharp ^{1}H NMR spectra in chloroform-*d* at room temperature (25°C), suggesting that molecular motion in these macrocycles is less restricted as a result of their longer linkers(**Figure 5.5**). Furthermore, macrocycles **17** and **18** do not exhibit diastereotopic splitting of the methylene proton signals H_e and no separate set of signals for the ***MP*** diastereomer were detected, also indicating that for these macrocycles, intramolecular somersaults are fast on the NMR timescale. Overall, the ^{1}H NMR spectra of macrocycles **17** and **18** are consistent with more conformational flexibility than that exhibited by macrocycle **1a** with shorter, rigid phenyl linkers.

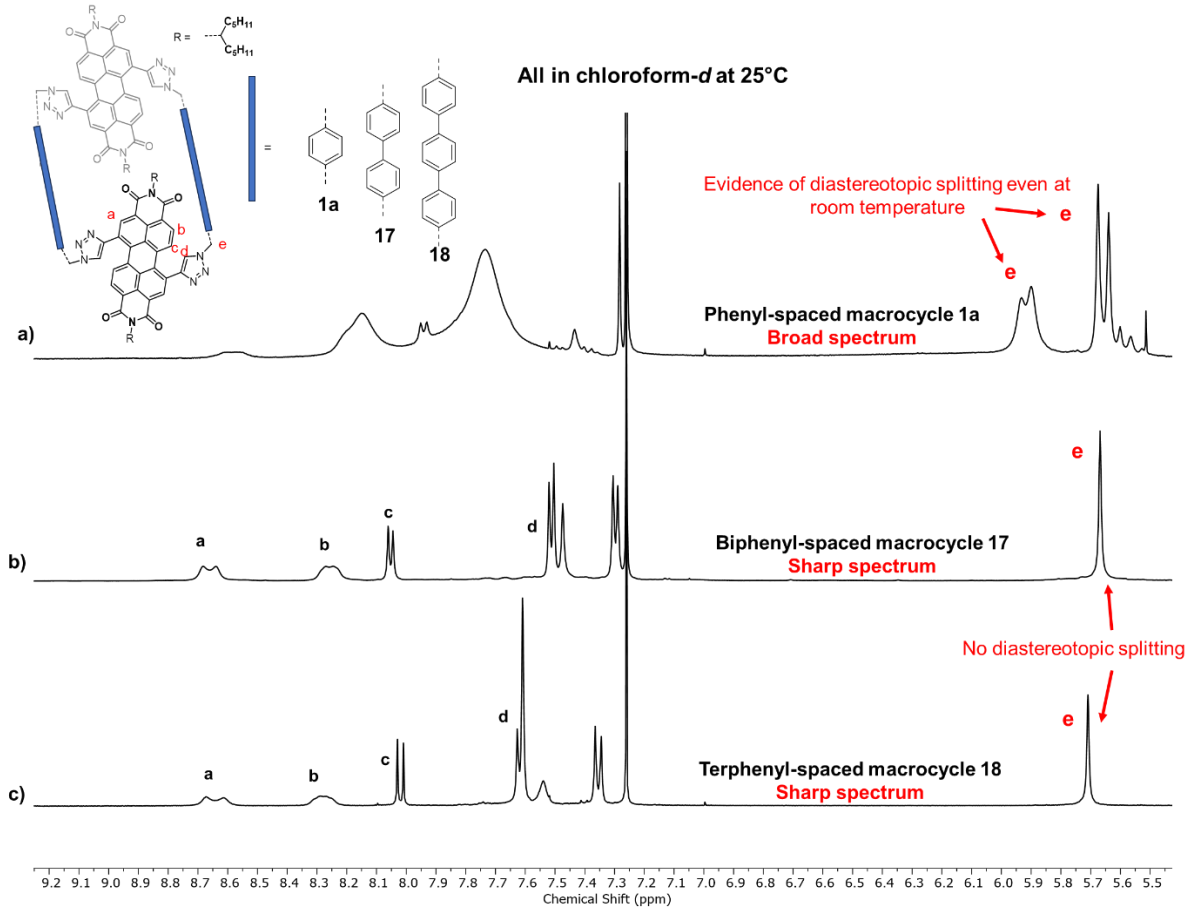

Figure 5.5: NMR spectra (chloroform-*d*, 400 MHz, 25°C) of macrocycles **a) 1a**, **b) 17** and **c) 18**.

Additionally, *n*-hexyl-linked macrocycle **19** was also studied by ^{1}H NMR spectroscopy in TCE-d_2 (**Figure 5.6**). Like macrocycle **1a**, the ^{1}H NMR spectrum was broad at room temperature, suggesting restricted molecular motion. Indeed, the length of the hexyl spacers is similar to that of the xylyl linkers in macrocycle **1a**, based on an equal count of six carbon atoms linking the triazole groups. As for **1a**, the ^{1}H NMR spectrum of macrocycle **19** in TCE-d_2 sharpens at higher temperatures (**Figure 5.6**), allowing the spectrum to be fully assigned. However, in contrast to **1a**, for macrocycle **19** there is no second set of signals corresponding to the heterochiral ***MP*** diastereomer, suggesting that, at least at high temperatures, "intramolecular somersaults" are fast on the NMR timescale. Additionally, there is no diastereotopic splitting of the analogous methylene H_e proton signal, suggesting the stereoisomers of **19** are not configurationally stable due to the more flexible hexyl linkers.

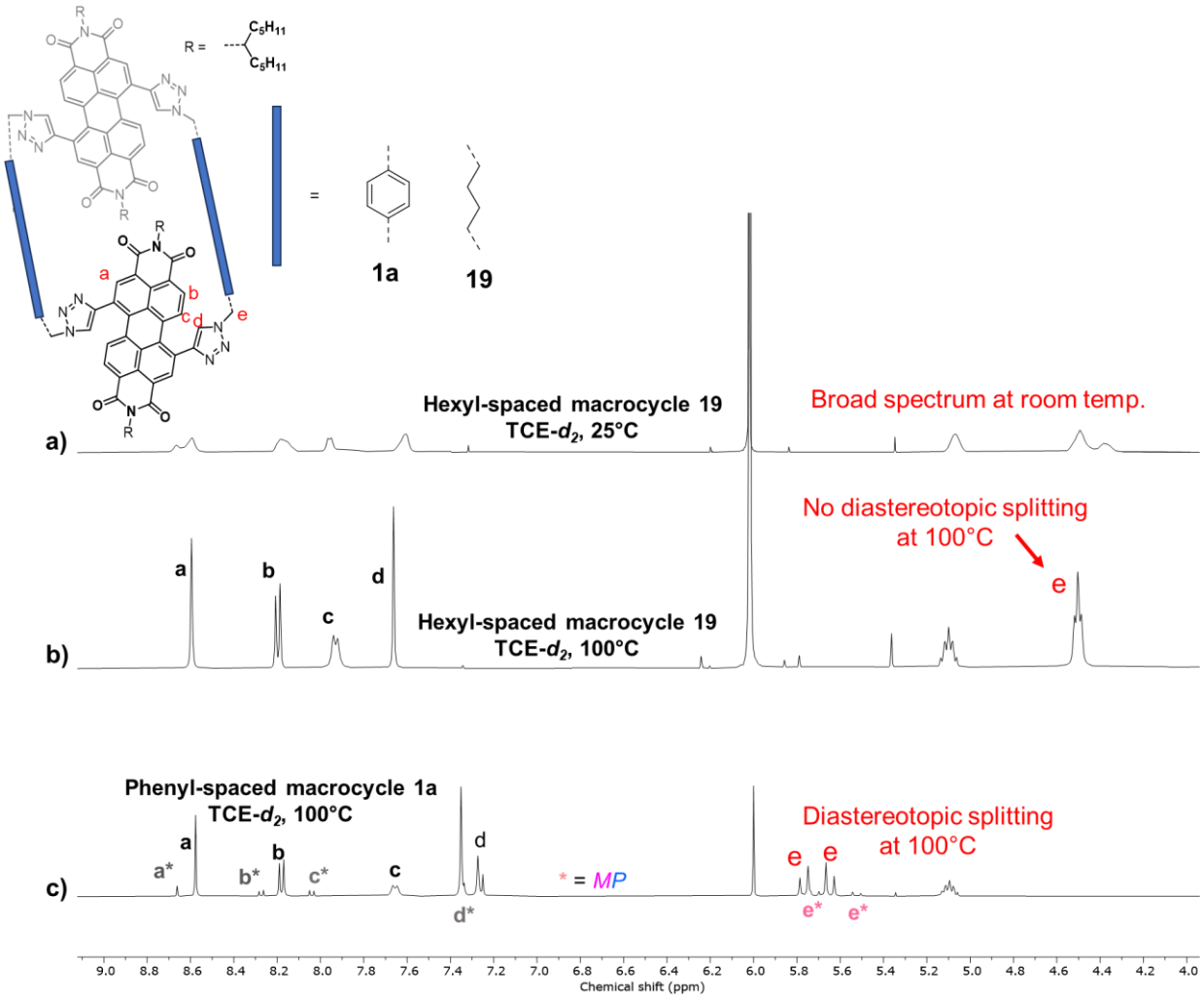

Figure 5.6: NMR spectra (TCE-d_2, 400 MHz) of macrocycles **a) 19**, 25°C **b) 19**, 100°C and **c) 1a**, 100°C.

As seen in **Figure 5.3b**, the UV-vis absorption spectra indicate that hexyl-linked macrocycle **19** forms an intramolecular PDI-PDI H-type aggregate in toluene very similar to that of phenyl-spaced **1a**. Therefore, the ^{1}H NMR spectrum of **19** was measured in toluene-d_8 and is shown alongside the ^{1}H NMR spectrum of **1a** in TCE-d_2 and toluene in **Figure 5.7**. As for **1a**, the proton signal H_c in macrocycle **19** shifts upfield in toluene, indicative of intramolecular π–π stacking, albeit by a lesser extent (0.4 vs 2.1 ppm) and so perhaps a weaker interaction than in **1a**. The H_c signal, as well as other proton signals such as H_a and H_d, are also considerably broader in toluene for **19** compared to **1a**. All of this is likely the result of greater conformational flexibility in **19**, and so potentially less restricted intramolecular PDI somersaulting.

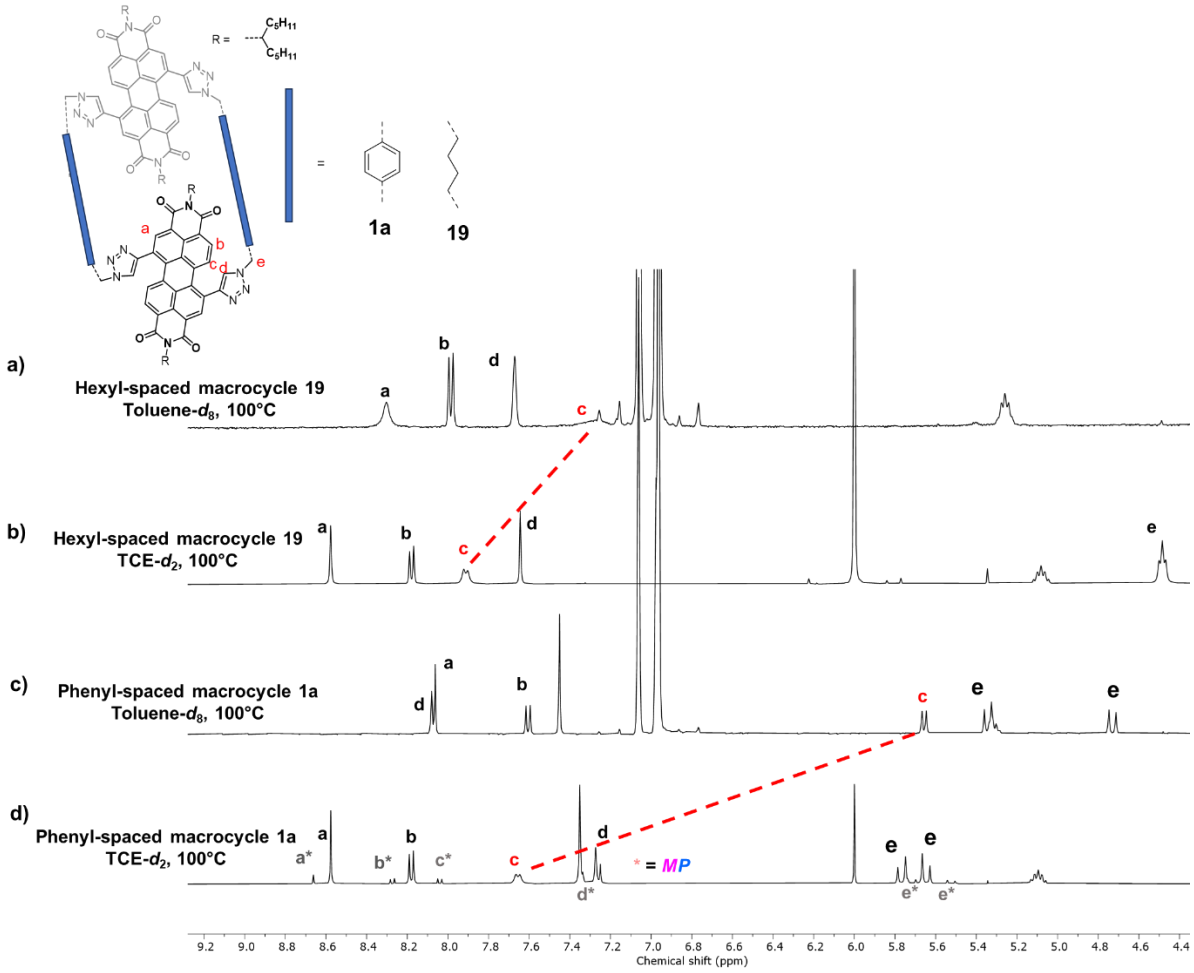

Figure 5.7: Stacked NMR spectra (400 MHz, 100°C) of macrocycles **19** (**(a)** and **(b)**) and **1a** (**(c)** and **(d)**) in TCE-d_2 and toluene-d_8.

5.4.2 Low temperature NMR studies

Out of the macrocycles discussed in this section, only macrocycle **1a**, with its short, rigid phenyl linkers, exhibits a separate set of signals in its ^{1}H NMR spectrum corresponding to the heterochiral ***MP*** diastereomer. This is likely because for the other macrocycles, with longer or more flexible linkers, the energy barrier for stereoisomer interconversion via PDI somersaulting (***MM*⇆*MP*⇆*PP***) is lowered, such that they cannot be observed as separate species on the NMR timescale. It was therefore hypothesised that it might be possible to observe the ***MP*** stereoisomer by measuring ^{1}H NMR spectra at low temperatures.

A low temperature ^{1}H NMR spectrum was first acquired for biphenyl-spaced macrocycle **17**. Unfortunately, this ^{1}H NMR was too broad at −30 °C for identifying, assigning and analysing a separate set of proton signals arising from the ***MP*** stereoisomer (**Figure 5.8**). A possible explanation for this result is that additional molecular motions such as PDI twisting, alongside PDI somersaulting, may be slowed down upon cooling.

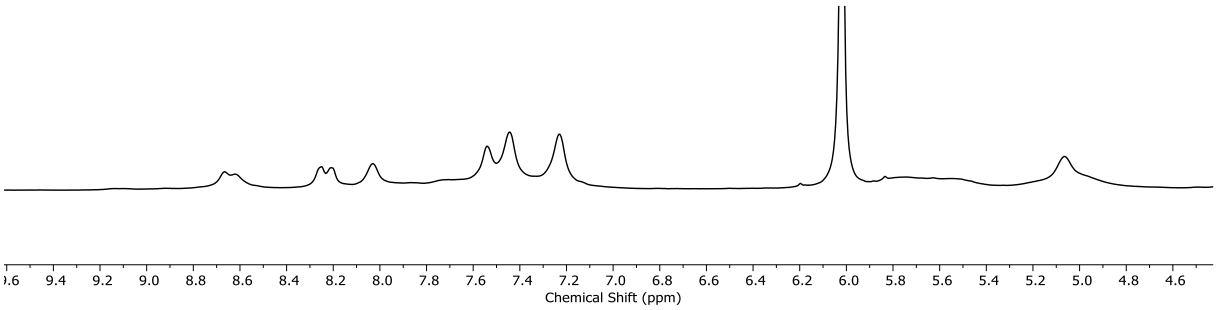

Figure 5.8: ^{1}H NMR spectrum of macrocycle **17** (TCE-d_2, 400 MHz, -30°C).

However, with hexyl-spaced macrocycle **19** some clearer changes to the ^{1}H NMR spectrum are observed upon gradual cooling from 100 °C to -30 °C (**Figure 5.9**). The spectrum is initially sharp at 100°C, but becomes significantly broader at 50°C and 25°C. In doing so however, some proton signals, most noticeably H_a, H_c, and H_e each appear to split into two signals. The second signal in each instance here could be the heterochiral ***MP*** diastereomer being observed, as the rate of "somersaulting" of the PDIs is being decreased with temperature. However, further cooling of the sample down to −30°C sees these signals split into more peaks. For example, proton signal H_a is a sharp singlet at 100°C but becomes two broad signals at 25°C before splitting into what appears to be four sharper signals at −30°C. Here, it is speculated that these additional signals may correspond to chiral conformers that are related by PDI

twisting (e.g., ***MM*⇆*P*P****) as well as somersaulting (e.g., ***MM*⇆*MP***), as discussed in Chapter 4. This would give four sets of (symmetrical) conformers, ***MM*/*PP***, ***M*M**/*P*P****, ***MP***, ***M*P****, that may be distinguishable by ^{1}H NMR spectroscopy due to their slow exchange on the NMR timescale at low temperature. However, further experimental and computational studies would be needed to prove this theory conclusively.

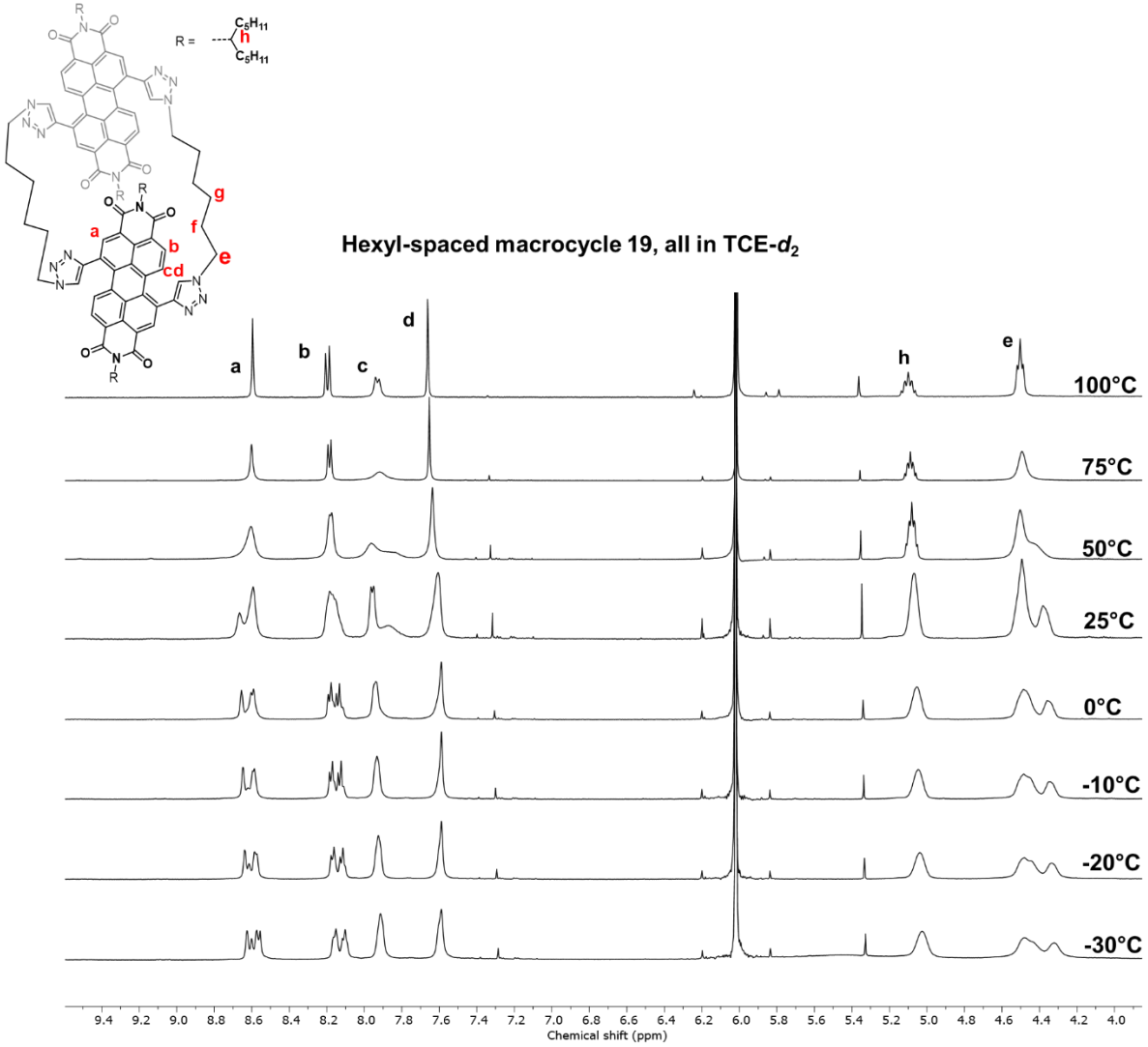

Figure 5.9: Stacked ^{1}H NMR spectra of macrocycle **19** (TCE-d_2, 400 MHz) at various temperatures ranging from -30°C to 100°C.

5.5 Chiral HPLC studies

As more than one species can be observed by ^{1}H NMR spectroscopy for *n*-hexyl-spaced macrocycle **19** at lower temperatures, the next step was to see whether these additional species, particularly the ***MP*** stereoisomer, could also be observed, and perhaps even isolated, by chiral HPLC. Unfortunately, chiral HPLC chromatograms of **19** revealed one (albeit broad) peak (**Figure 5.10b**). This can be explained by the slower timescale (minutes vs. seconds) and higher temperature (25 °C vs −30 °C) of the HPLC experiment in comparison to the ^{1}H NMR spectroscopy measurements. Therefore, while seemingly two or more species can be observed by ^{1}H NMR spectroscopy, they are still interconverting too quickly to be observed by HPLC. Similarly, the chiral HPLC chromatograms of biphenyl-spaced macrocycle **17** also only revealed one peak (**Figure 5.10c**). This contrasts with the chiral HPLC chromatogram of phenyl-spaced macrocycle **1a** in 70:30 DCM:hexane which reveals three peaks corresponding to the homochiral pair of enantiomers in addition to the heterochiral ***MP*** diastereomer.

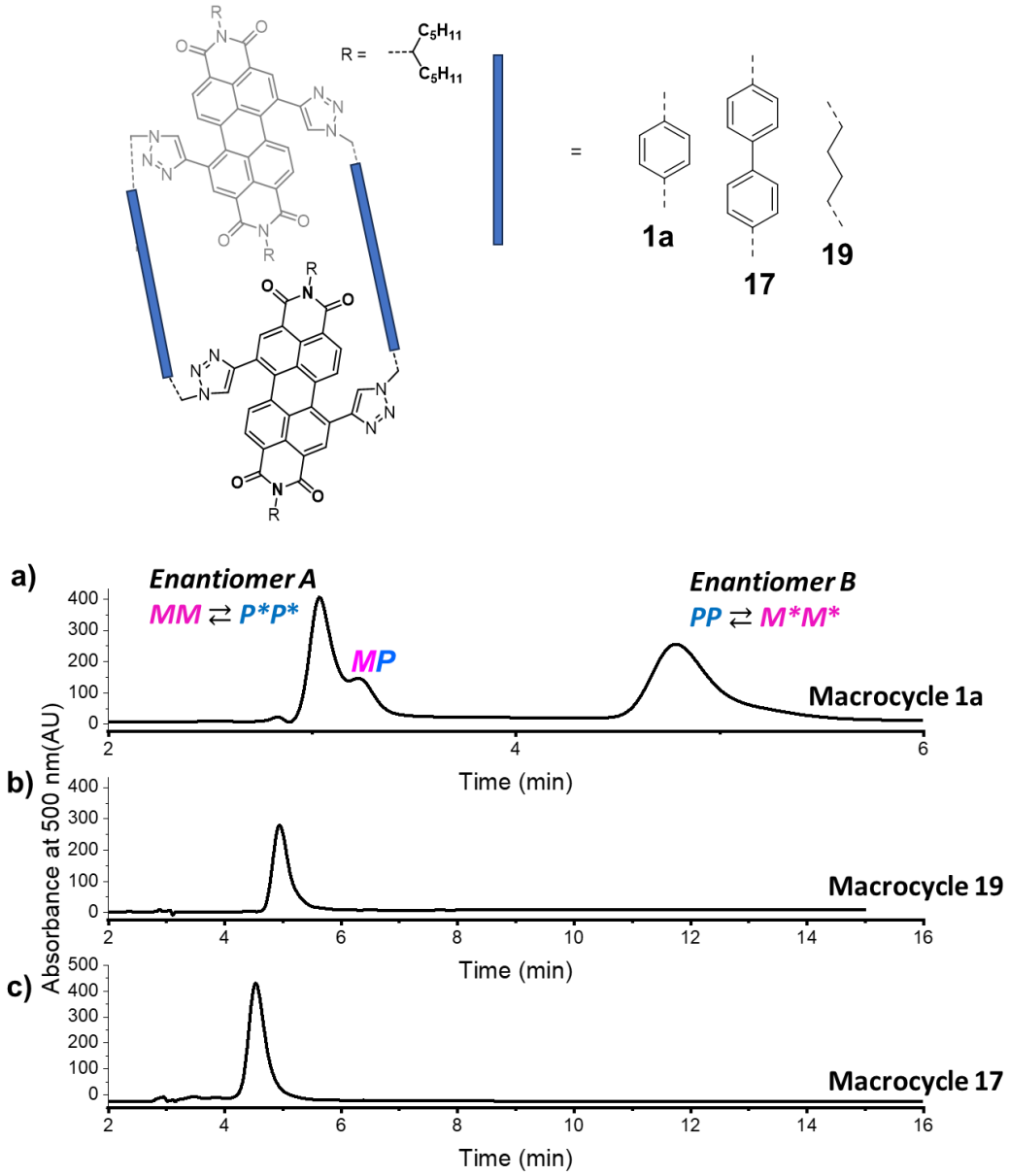

Figure 5.10: Chiral HPLC chromatograms (Phenomenex i-Amylose-1, 250 x 4.6 mm, 7:3 (v/v) DCM:n-hexane eluent) of macrocycles **a) 1a**, **b) 19** and **c) 17**.

Overall, the chiral HPLC results are consistent with NMR data suggesting that increasing the length of the linkers (as is the case for biphenyl-spaced macrocycle **17**) and increasing their flexibility (as is the case for *n*-hexyl-linked macrocycle **19**) lowers the barrier to interconversion between the ***MM***/***PP*** enantiomer pair and the heterochiral ***MP*** diastereomer relative to phenyl-spaced macrocycle **1a**. As established before, this interconversion between bay-connected bis-PDI stereoisomers occurs via an "intramolecular somersault" of the PDI imide heads through the centre of the macrocyclic cavity. For macrocycles **17**, **18**, and **19**,

interconversion between stereoisomers via somersaulting occurs on the order of seconds, as determined by chiral HPLC and ^{1}H NMR spectroscopy. According to a study by LaPlante and co-workers, this means that the energy barrier for interconversion is < 80 kJ mol^{-1},[13] which is lower than that for macrocycle **1a** (~ 93 kJ mol^{-1}).

5.6 Density functional theory studies

In the absence of a crystal structure for the biphenyl-spaced macrocycle **17**, a DFT conformer search was performed by Prof. Martijn Zwijnenburg. This macrocycle was chosen over the *n*-hexyl linked system **19** because the more rigid linkers may reduce degrees of freedom (and hence calculation times) and it allows comparisons with calculations of the phenyl-connected macrocycle **1**.

The lowest energy conformations for phenyl-spaced macrocycle **1** and biphenyl-spaced macrocycle **17** (both simplified, with methyl groups at the imide position) predicted by DFT are given in **Figure 5.11**. At first glance, the conformations of both macrocycles appear similar, with a PDI-PDI centroid-centroid distance of 3.7 Å and 3.6 Å and a rotational angle of 20° and 17° respectively. Therefore, the calculated ground state conformation of **17** does not appear to explain the experimental results of weaker intramolecular PDI excitonic coupling with increasing linker length. Kasha's excitonic coupling theory predicts that coupling becomes weaker as interchromophore distance increases or as rotational angle increases from 0° to 90°, but the DFT conformer of biphenyl-spaced macrocycle **17** does not show this occurring.

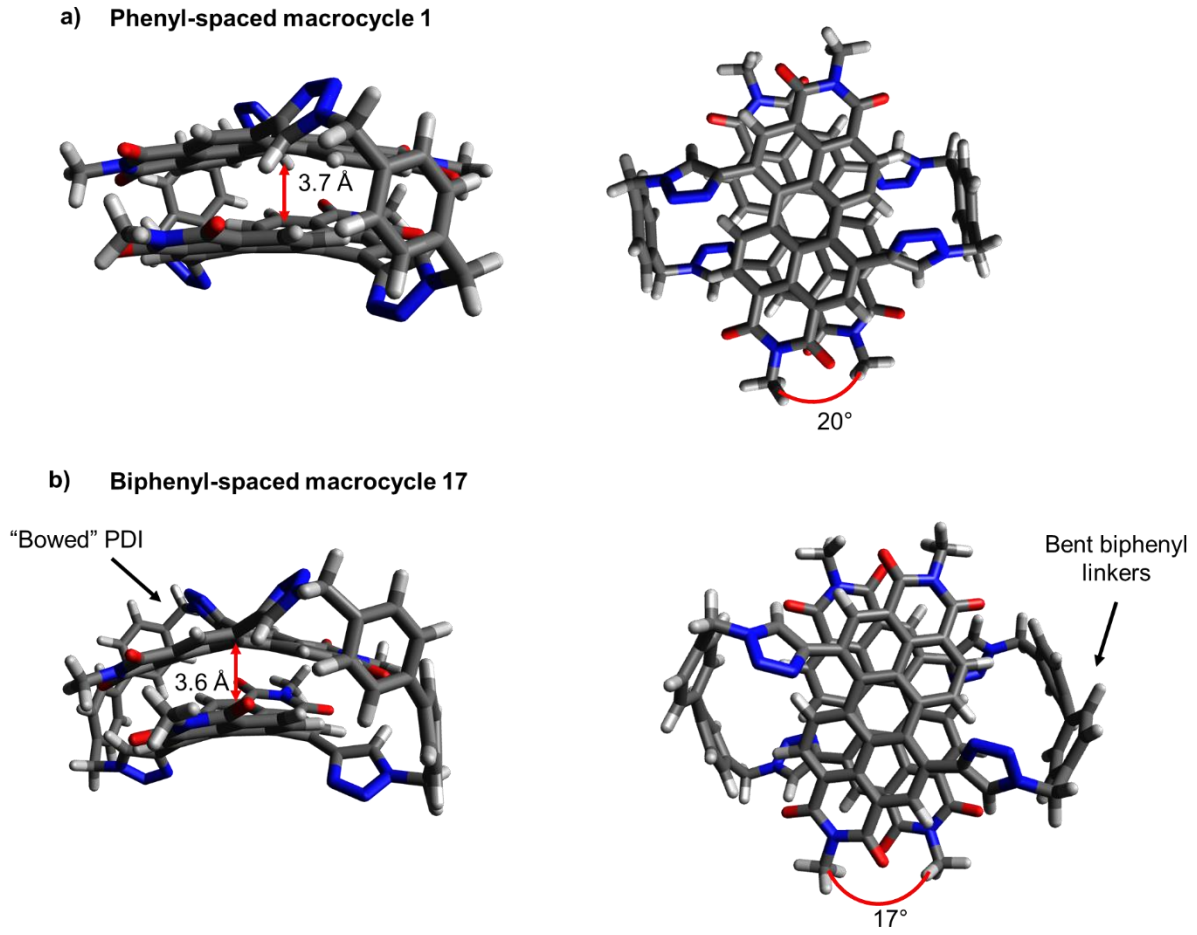

Figure 5.11: Lowest energy predicted DFT structures of macrocycles **1a** ("conformer **A**") and **17**. These calculations were carried out on simplified model macrocycles bearing methyl groups at the imide positions.

Upon closer inspection, the ground state conformation of **17** is considerably more strained than that for **1a** to facilitate an intramolecular PDI-PDI interaction. This is most notable in two parts of the macrocycle. Firstly, the biphenyl linkers in **17** are bent, and secondly the PDI units are bowed, both of which appear to be required to afford a small interchromophore distance (π–π stacking) between the two PDI units. This bending of the linkers or bowing of the PDIs is not observed in macrocycle **1a** with shorter phenyl linkers. Therefore, it is possible that, for biphenyl-spaced macrocycle **17**, a more stable conformer is gained from the PDI-PDI interaction than is lost by straining the macrocycle. However, since these calculations were performed in the gas phase, it is possible that macrocycle **17** may adopt a more "breathed out" conformation in solution, in which the energetic penalty of disrupting the intramolecular PDI-PDI interaction is paid back by solvation of the macrocycle cavity as well as an "unbowing" of the PDIs and an "unbending" of the biphenyl linkers.

5.7 Guest binding studies

As discussed in Chapter 1, several bis-PDI macrocycles have been reported that are able to bind polycyclic aromatic hydrocarbons (PAHs), with this molecular recognition being readily detectable by UV-vis spectroscopy.[1, 14-18] Unfortunately, macrocycle **1a** did not exhibit any binding of PAHs (**Table 5.1**) in either toluene or chlorinated solvents, which is likely due to the small cavity size of the macrocycle in either conformation (***MM/PP*** or **M*M*/P*P***). In toluene, the absence of binding may also be explained by the reasonably strong intramolecular PDI-PDI interaction (ΔG_{agg} = -11.1 ± 0.1 kJ mol^{-1}), which the PAH guest must outcompete for binding. In chlorinated solvents, it is proposed that the PDI units are better solvated,[19, 20] meaning that PAH guests must now outcompete PDI–solvent interactions, making this a potentially more competitive solvent for binding.

Therefore, it was thought that macrocycles with longer linkers, such as biphenyl-spaced **17** and terphenyl-spaced **18** may exhibit stronger binding, as the longer linkers had been shown to disrupt the PDI-PDI interaction (sections 5.3-5.4) and may create a larger cavity size for PAH encapsulation. It was thought that PAH binding might be most favourable in toluene, due to it being a poorer solvent for PDIs than chlorinated solvents. [19, 20] Moreover, in toluene, intramolecular PDI-PDI aggregation is weaker for biphenyl-spaced **17**, while for terphenyl-spaced **18** the UV-vis spectrum appears monomeric, suggesting that the intramolecular PDI-PDI interaction is absent altogether.

Therefore, UV-vis spectroscopic host–guest binding studies were performed with macrocycles **1a**, **17**, **18**, and **19** as hosts and with a wide range of PAH guests and in a number of different solvents (**Table 5.1**). This included both planar (e.g. anthracene, 1,5-dihydroxynaphthalene, pyrene, perylene) and non-planar (e.g. BINOL) PAH guests. In a binding experiment, the UV-vis spectrum of the macrocycle host (10 μM) was measured in the absence and presence of one up to several thousand equivalents of the PAH guest and the S_0-S_1 main PDI absorption band was monitored. Unfortunately, there was no significant change to the main PDI absorption band for any host–guest combination and in any solvent tested, which indicates that, under these conditions, none of the bis-PDI macrocycles exhibited PAH binding. The current possible explanations for this outcome include poor size and/or shape complementarity of the bis-PDI macrocycles, arising due to triazole bay substituents which

create a cavity with sterically encumbered and twisted aromatic surfaces that are unsuitable for π–π molecular recognition of the PAH guests tested.

Table 5.1: Summary of guest binding attempts with various solvent systems for macrocycles **1a**, **17**, **18** and **19**.

Bis-PDI macrocycle (Host)	PAH (Guest)	Solvents tested
1a	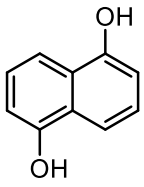 1,5-dihydroxynaphthalene	Toluene, DCM, various MeOH:DCM ratios (1% up to 50% MeOH), Hexane:DCM (1:1), toluene:DCM (1:1), TCE, various TCE:MeOH ratios (1% up to 50% MeOH).
	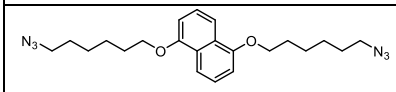	Toluene, DCM, various MeOH:DCM ratios (1% up to 50% MeOH), Hexane:DCM (1:1), toluene:DCM (1:1), TCE
	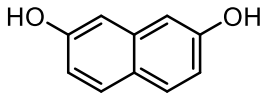 2,7-dihydroxynaphthalene	Toluene, DCM, various MeOH:DCM ratios (1% up to 50% MeOH), Hexane:DCM (1:1), toluene:DCM (1:1), TCE
	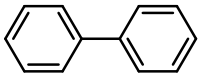 Biphenyl	Toluene, DCM, various MeOH:DCM ratios (1% up to 50% MeOH), Hexane:DCM (1:1), toluene:DCM (1:1), TCE
	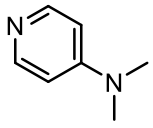 DMAP	Toluene, chloroform, DCM, various MeOH:DCM ratios (1% up to 50% MeOH), Hexane:DCM (1:1), toluene:DCM (1:1), TCE
	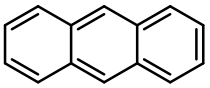 Anthracene	Toluene, chloroform, DCM, various MeOH:DCM ratios (1% up to 50% MeOH), toluene:DCM (1:1), TCE
	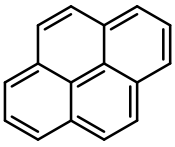 Pyrene	Toluene, chloroform, DCM, various MeOH:DCM ratios (1% up to 50% MeOH), toluene:DCM (1:1), TCE
	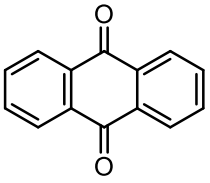 Anthraquinone	Toluene, chloroform, various MeOH:chloroform ratios (1% up to 50% MeOH), toluene:DCM (1:1), TCE

	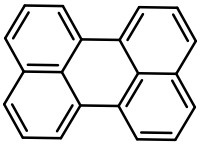 Perylene	Toluene, chloroform, various MeOH:chloroform ratios (1% up to 50% MeOH), toluene:DCM (1:1), TCE
	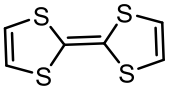 TTF	Toluene, DCM, various MeOH:DCM ratios (1% up to 50% MeOH), toluene:DCM (1:1), TCE
17	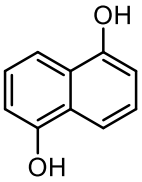 1,5-dihydroxynaphthalene	Toluene, DCM, various MeOH:DCM ratios (1% up to 50% MeOH), toluene:DCM (1:1), TCE
	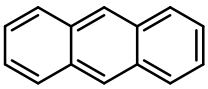 Anthracene	Toluene, DCM, various MeOH:DCM ratios (1% up to 50% MeOH), toluene:DCM (1:1), TCE
	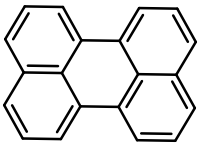 Perylene	Toluene, DCM, various MeOH:DCM ratios (1% up to 50% MeOH), toluene:DCM (1:1), TCE
	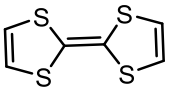 TTF	Toluene, DCM, various MeOH:DCM ratios (1% up to 50% MeOH), toluene:DCM (1:1), TCE
	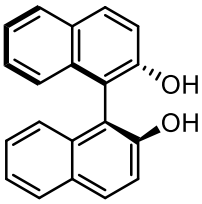 S-Binol	Toluene, DCM, various MeOH:DCM ratios (1% up to 50% MeOH), toluene:DCM (1:1), TCE
18	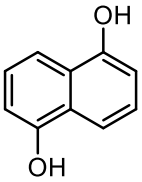 1,5-dihydroxynaphthalene	Toluene, DCM, various MeOH:DCM ratios (1% up to 50% MeOH), toluene:DCM (1:1), TCE
	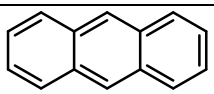 Anthracene	Toluene, DCM, various MeOH:DCM ratios (1% up to 50% MeOH), toluene:DCM (1:1), TCE

	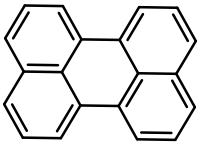 Perylene	Toluene, DCM, various MeOH:DCM ratios (1% up to 50% MeOH), toluene:DCM (1:1), TCE
	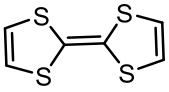 TTF	Toluene, DCM, various MeOH:DCM ratios (1% up to 50% MeOH), toluene:DCM (1:1), TCE, various TCE:MeOH ratios (1% up to 50% MeOH)
	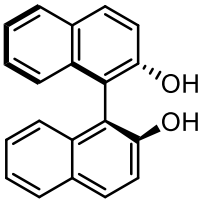 S-Binol	Toluene, DCM, various MeOH:DCM ratios (1% up to 50% MeOH), toluene:DCM (1:1), TCE, various TCE:MeOH ratios (1% up to 50% MeOH)
19	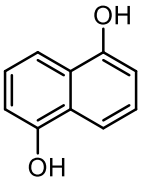 1,5-dihydroxynaphthalene	Toluene, DCM, various MeOH:DCM ratios (1% up to 50% MeOH), Hexane:DCM (1:1), toluene:DCM (1:1), TCE
	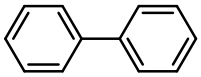 Biphenyl	Toluene, DCM, various MeOH:DCM ratios (1% up to 50% MeOH), toluene:DCM (1:1), TCE
	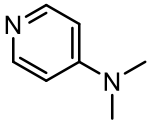 DMAP	Toluene, DCM, various MeOH:DCM ratios (1% up to 50% MeOH), toluene:DCM (1:1), TCE
	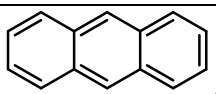 Anthracene	Toluene, DCM, various MeOH:DCM ratios (1% up to 50% MeOH), toluene:DCM (1:1), TCE
	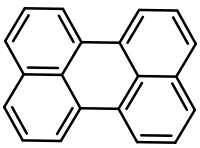 Perylene	Toluene, DCM, various MeOH:DCM ratios (1% up to 50% MeOH), toluene:DCM (1:1), TCE
	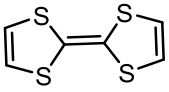 TTF	Toluene, DCM, various MeOH:DCM ratios (1% up to 50% MeOH), (toluene:DCM (1:1), TCE

5.8 Summary and future work

This chapter sought to explore the effects of varying the groups linking the two PDI chromophores in "Pink Box" type bis-PDI macrocycles. It was found that elongating the rigid aromatic linkers systematically from phenyl to biphenyl to terphenyl leads to a progressive reduction in PDI-PDI excitonic coupling strength in toluene, being switched off completely in the latter macrocycle. This may be explained by an increase in rotational displacement of the PDI cores or an increase in the intramolecular PDI-PDI distance. Further experimental (2D NMR, crystallography) and computational studies are needed to confirm the ground state conformation(s) of these macrocycles. Proton NMR spectroscopy suggests that this will present a significant challenge since variable temperature studies revealed that increasing the length and flexibility of the linkers leads to greater conformational flexibility, which also makes their chirality dynamic. For example, the ***MP*** diastereomer of *n*-hexyl-linked macrocycle **19** could not be observed by chiral HPLC at room temperature, unlike the more rigid phenyl-linked macrocycle **1a**. Only at low temperature was preliminary evidence for the ***MP*** diastereomer obtained by splitting of ^{1}H NMR signals of the PDI units.

It was hoped that inhibiting intramolecular PDI–PDI interactions might make the macrocycles receptors for PAH guests. Unfortunately, however, no binding was observed by UV-vis spectroscopy for any of the attempted PAH guests in a range of different solvents. This is most likely due to poor size and shape complementarity between the π-surfaces of the bis-PDI macrocycle's cavity and PAH guests. Therefore, future work may seek to use planar PDIs and π-extended PDI derivatives (e.g. coronene diimides)[21] to increase the strength of the aromatic interactions that drive PAH complexation. Chiral analogues of these hosts may act as chiroptical sensors, with chiral guest recognition reported by UV-vis absorption and/or CD spectroscopy.

5.9 Experimental

5.9.1 Materials and methods

All commercial solvents and reagents were used as purchased, unless otherwise stated. Anhydrous solvents were degassed with N_2 and dried using an Innovative Technology PureSolv MD 5 solvent purification system. $Cu(MeCN)_4 \cdot PF_6$ was stored in a desiccator. Tris((1-benzyl-4-triazolyl)methyl)amine (TBTA) was prepared following a literature procedure.[22] Water was distilled and microfiltered using an ELGA DV 35 Purelab water purification system. Chromatography was undertaken using silica gel (particle size: 40-63 μm) or preparative TLC plates (20 × 20 cm, 1 cm silica thickness).

1,4-bis(azidomethyl)benzene, 4,4'-bis(azidomethyl)-1,1'-biphenyl,[23] and 1,6-diazidohexane[24] were prepared by Angus Yeung following the **safety precautions for the handling of organic azide compounds described in section 2.9.2**.

^1H and ^{13}C NMR spectra were recorded using Bruker AVIII400 (400 MHz), Bruker AV NEO 400 (400 MHz) and Bruker AV NEO 500 (500 MHz, with cryoprobe). Mass spectra were recorded using a Bruker UltrafleXtreme MALDI-TOF mass spectrometer or a Waters Synapt G2-S mass spectrometer for high resolution MS-ESI. Details of equipment used for other analytical techniques are provided in their appropriate sub-sections in this experimental section.

5.9.2 Synthesis of macrocycle 17

Acyclic bistriazole PDI 20

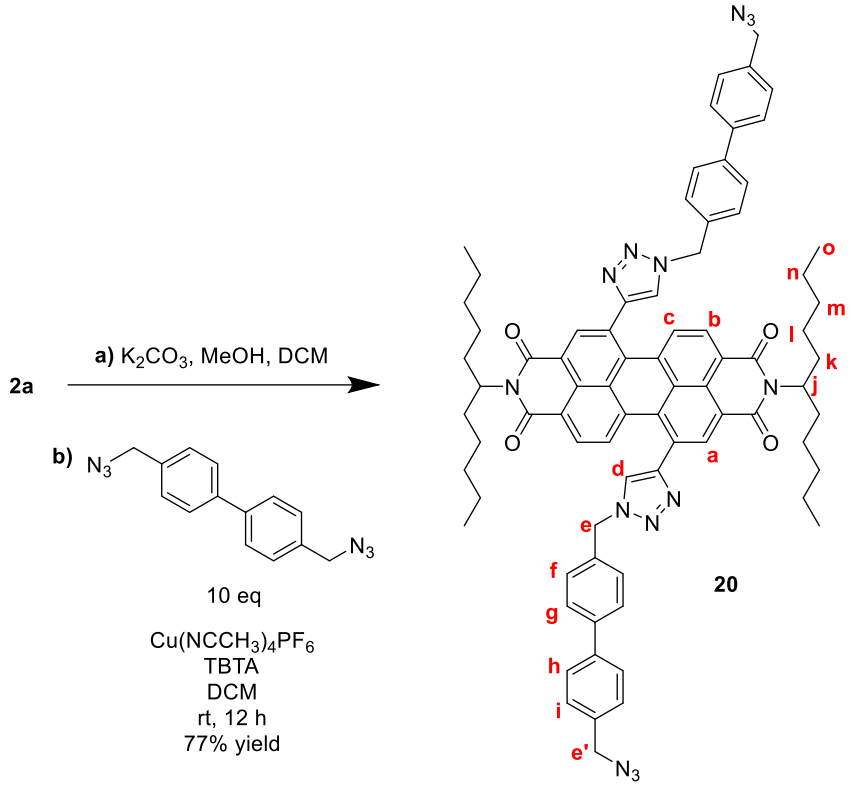

To a solution of TMS-protected bisalkyne PDI **2a**[5] (100 mg, 111 µmol) in DCM (20 ml) was added K_2CO_3 (300 mg) in MeOH (10 ml). The mixture was stirred at rt for 3 min, and completion of the reaction was confirmed by TLC. A further 20 mL of DCM was added to the mixture. The mixture was then washed with 1 M HCl (2 x 30 mL), water (2 x 30 mL) and brine (30 ml). The mixture was then dried over anhydrous $MgSO_4$ and concentrated to dryness *in vacuo* to afford the PDI bis-alkyne, which was used immediately without further purification. To a solution of this deprotected PDI bis-alkyne (83 mg, 111 µmol) in dry DCM (10 ml) was added 4,4'-bis(azidomethyl)-1,1'-biphenyl (294 mg, 1.11 mmol, 10 equiv) and TBTA (12 mg, 22 µmol, 0.2 equiv). The solution was then de-gassed with Argon. The copper catalyst $Cu(CH_3CN)_4PF_6$ (8 mg, 22 µmol, 0.2 equiv) was then added and the solution was once again de-gassed with Argon. The reaction was stirred at rt for 12 h. The solvent was then removed *in vacuo*. The resulting residue was purified by silica gel flash column chromatography (1:99 MeOH-CH_2Cl_2) affording the title compound as a purple solid (110 mg, 86 µmol, 77%).

^{1}H NMR (500 MHz, chloroform-*d*) δ 8.62 (d, *J* = 8.0 Hz, 2H_b), 8.23 (s, 2H_a), 7.91 (d, *J* = 8.0 Hz, 2H_c), 7.75 (s, 2H_d), 7.70 – 7.63 (m, 8$H_{f,g}$), 7.47 – 7.39 (m, 8$H_{h,i}$), 5.72 (s, 4H_e), 5.15 (p, 2H_j), 4.40 (s, 4$H_{e'}$), 2.30 – 2.12 (m, 4H_k), 1.86 – 1.72 (m, 4H_k), 1.27 – 1.21 (m, 24H_{l-n}), 0.85 – 0.79 (m, 12H_o).

^{13}C NMR (126 MHz, chloroform-*d*) δ 164.60, 163.47, 148.82, 148.59, 141.62, 140.22, 135.52, 135.07, 134.67, 133.58, 130.48, 129.69, 129.33, 129.15, 128.89, 128.65, 128.18, 127.77, 123.25, 122.57, 121.98, 121.80, 54.62, 32.41, 31.84, 26.66, 22.68, 14.18.

HRMS ESI (m/z) calculated for $C_{78}H_{79}N_{14}O_4$ $[M+H]^+$ 1275.6409, found 1275.6381.

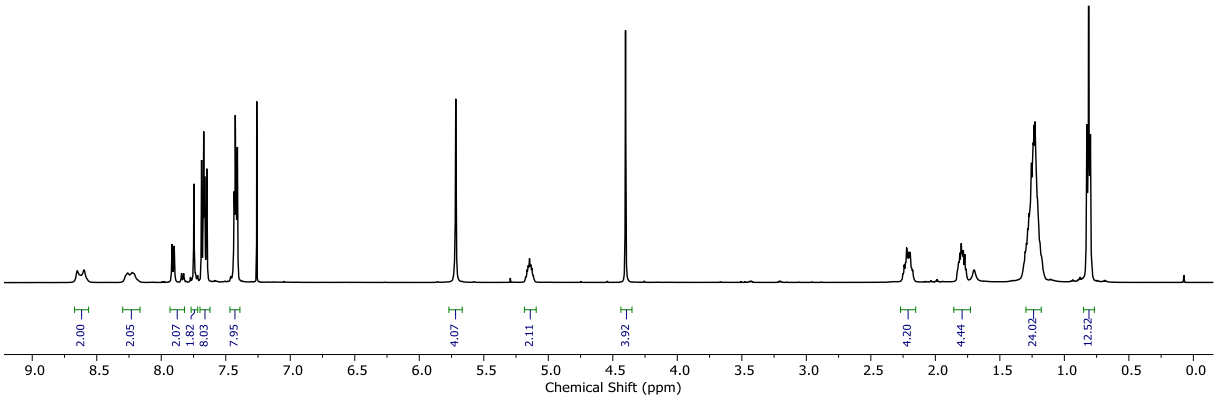

^{1}H NMR spectrum of **20** (Chloroform-*d*, 298 K, 500 MHz).

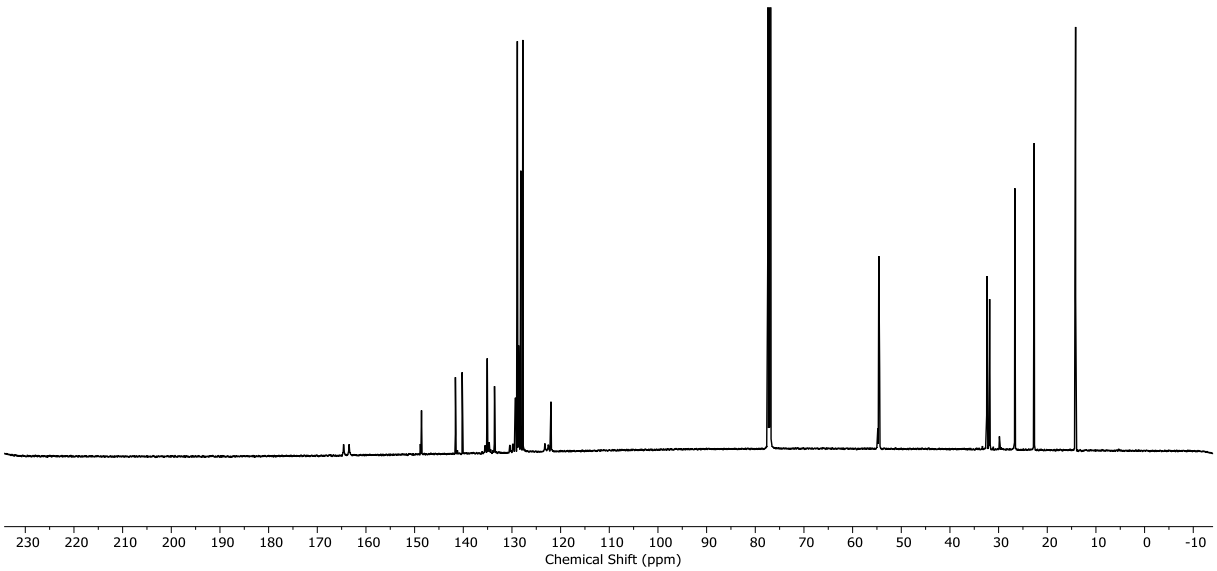

^{13}C NMR spectrum of **20** (Chloroform-*d*, 298 K, 101 MHz).

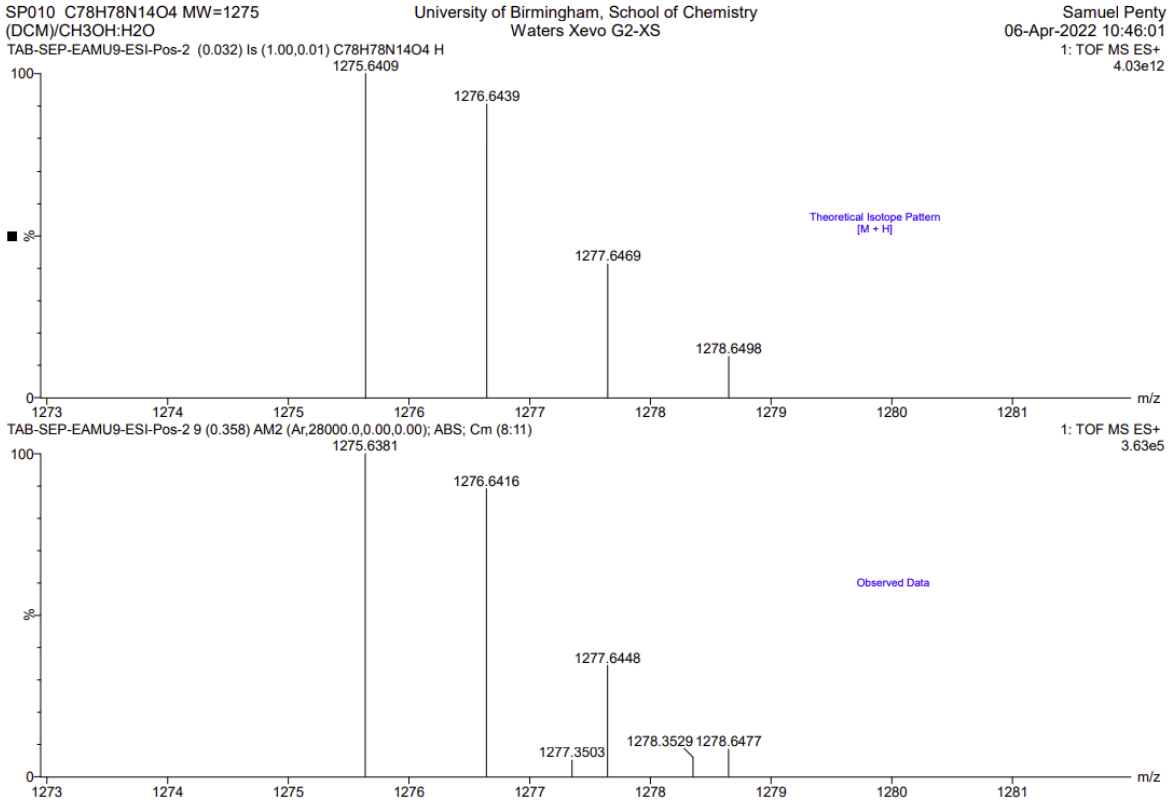

Calculated (top) and observed (bottom) ESI MS data for compound **20**.

Biphenyl-spaced bis-PDI macrocycle 17

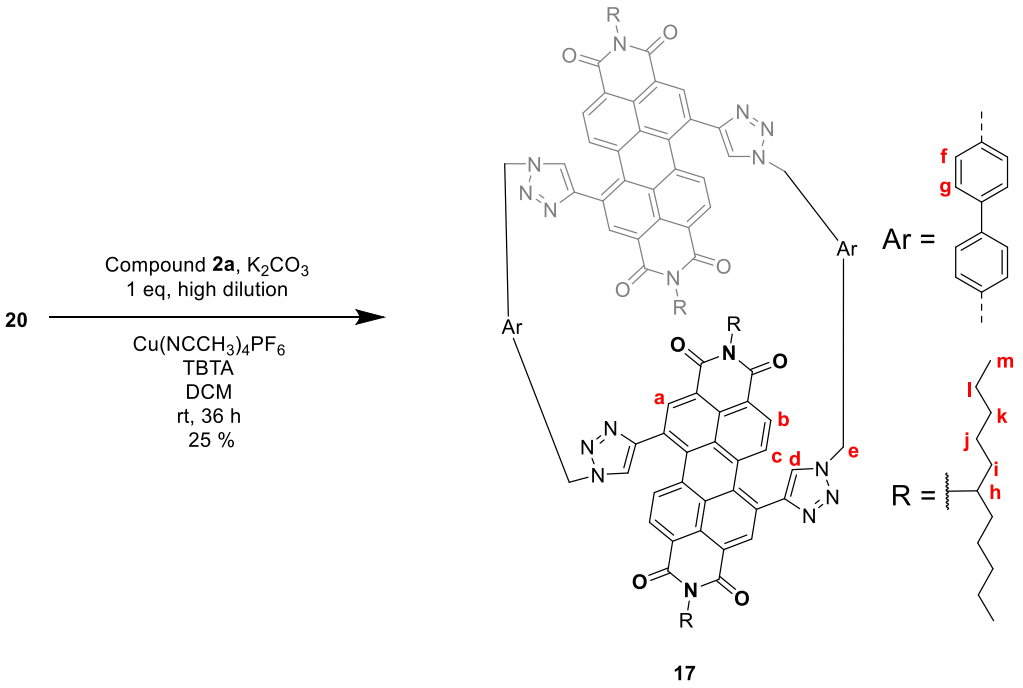

To a solution of TMS-protected bisalkyne PDI **2a**[5] (75 mg, 86 µmol) in DCM (20 ml) was added K_2CO_3 (300 mg) in MeOH (10 ml). The mixture was stirred at rt for 3 min, and completion of the reaction was confirmed by TLC. A further 20 mL of DCM was added to the mixture. The mixture was then washed with 1 M HCl (2 x 30 mL), water (2 x 30 mL) and brine (30 ml). The mixture was then dried over anhydrous $MgSO_4$ and concentrated to dryness *in vacuo* to afford the PDI bis-alkyne, which was used immediately without further purification. This was added to a solution of compound **20** (110 mg, 86 µmol) and TBTA (18 mg, 34 µmol, 0.4 equiv) in DCM (250 mL). The solution was then de-gassed with Argon. The copper catalyst $Cu(CH_3CN)_4PF_6$ (13 mg, 34 µmol, 0.4 equiv) was then added and the solution was once again de-gassed with Argon. The reaction was stirred at rt for 36 h. The solvent was then removed *in vacuo*. The resulting residue was purified by silica gel flash column chromatography (1:99 MeOH-CH_2Cl_2) followed by preparative silica TLC (0.5:99.5 MeOH-CH_2Cl_2), affording the title compound as a purple solid (44.8 mg, 23 µmol, 25%, noting the presence of some aliphatic impurities (estimated < 10 mol % by NMR)).

^{1}H NMR (500 MHz, chloroform-*d*) δ 8.66 (d, *J* = 8.1 Hz, 4H_b), 8.29 – 8.23 (s, 4H_a), 8.05 (d, *J* = 8.1 Hz, 4H_c), 7.51 (d, *J* = 8.0 Hz, 8H_f), 7.47 (s, 4H_d), 7.30 (d, *J* = 8.0 Hz, 8H_g), 5.67 (s,

8H_e), 5.11 (p, *J* = 9.8, 5.8 Hz, 4H_h), 2.16 (m, 8H_i), 1.77 (m, 8H_i), 1.16 (m, 48H_{j-l}), 0.86 (m, 24H_m).

^{13}C NMR (126 MHz, chloroform-*d*) δ 148.44, 140.79, 135.63, 134.97, 134.44, 133.74, 133.32, 129.64, 129.25, 129.09, 128.92, 128.77, 128.44, 127.95, 123.25, 122.52, 121.35, 54.44, 31.79, 29.85, 26.61, 22.65, 14.13.

HRMS ESI (m/z) calculated for $C_{127}H_{131}N_{16}O_8$ $[M+H]^+$ 2022.0492, found 2022.0446.

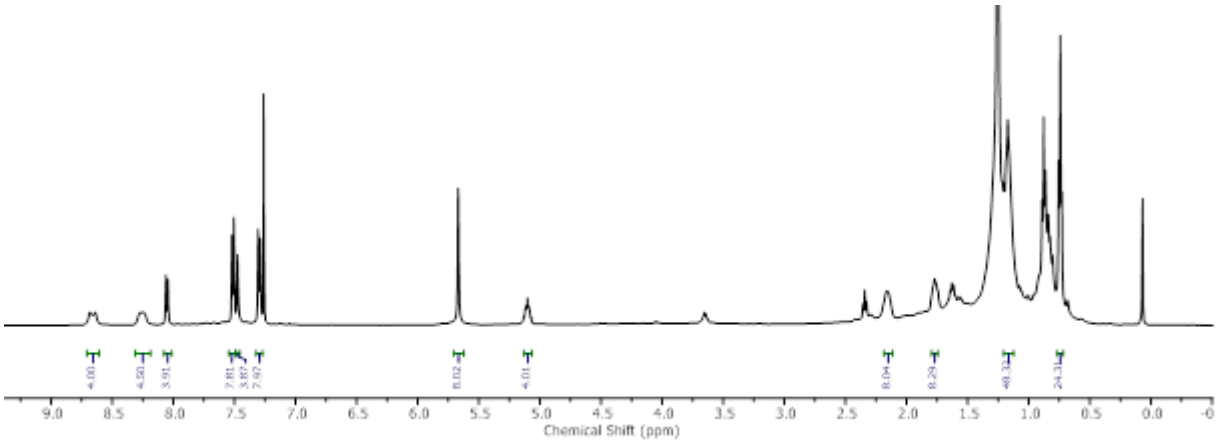

^{1}H NMR spectrum of macrocycle **17** (Chloroform-*d*, 298 K, 500 MHz).

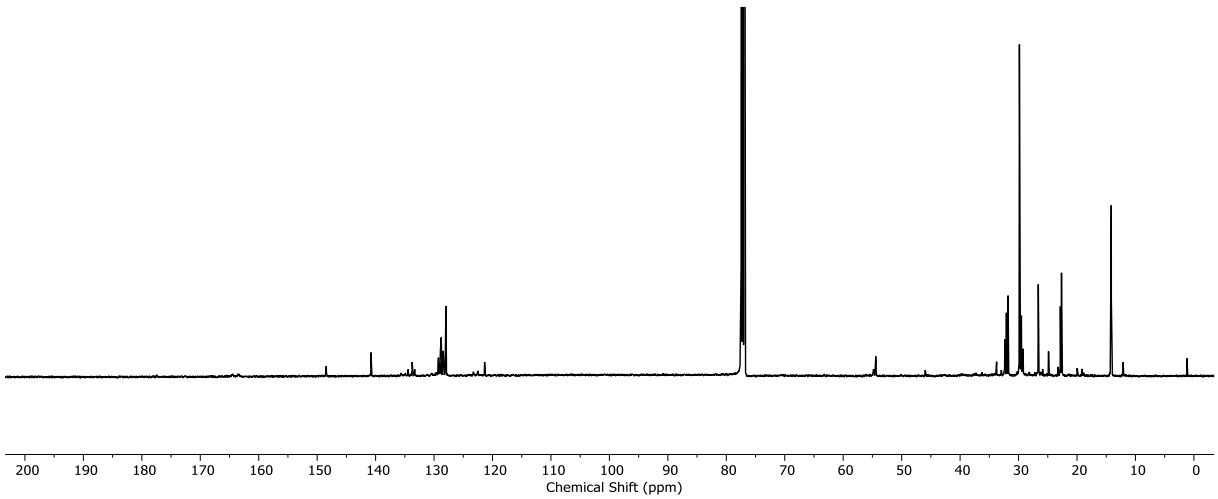

^{13}C NMR spectrum of macrocycle **17** (Chloroform-*d*, 298 K, 101 MHz).

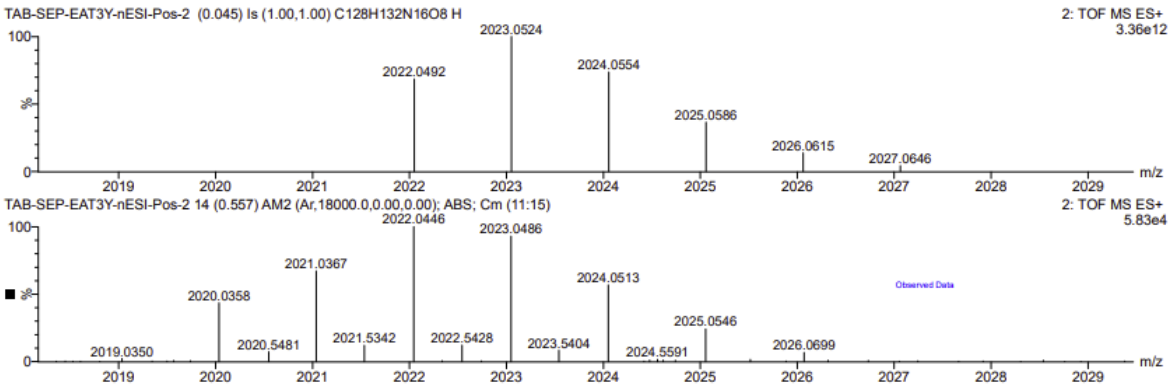

Calculated (top) and observed (bottom) ESI MS data for macrocycle **17**.

5.9.3 Synthesis of macrocycle 18

4,4‘-Bis(bromomethyl)-1,4-terphenyl 23 [25]

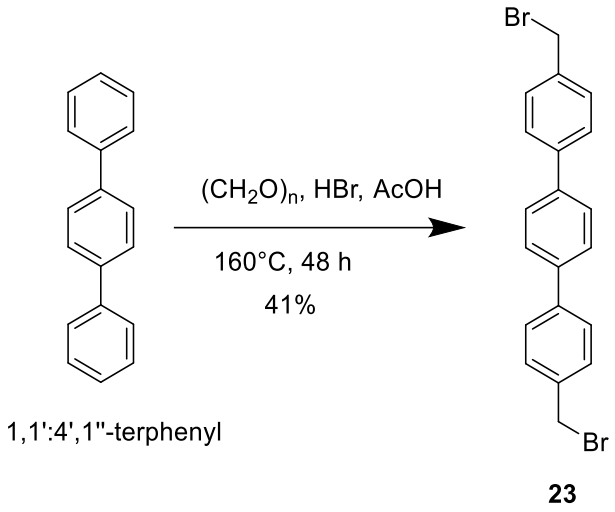

23

To a pressure vessel was added 1,1':4',1"-terphenyl (1.5 g, 6.5 mmol), paraformaldehyde (1.95 g, 6.5 mmol), and HBr (33% in acetic acid, 15 mL). The pressure vessel was sealed and heated at 160°C for 48h. The reaction vessel was then allowed to cool to rt, and was then carefully opened and the acetic acid was decanted. The remaining reaction mixture was sonicated for 30 min and then filtered. The residue was then washed with ethyl acetate (100 mL), and dried in an oven, affording the title compound as a white powder (1.12 g, 2.69 mmol, 41%).

^{1}H NMR (400 MHz, Chloroform-*d*) δ 7.67 (s, 4H), 7.64 – 7.59 (m, 4H), 7.51 – 7.47 (m, 4H), 4.57 (s, 4H), consistent with literature reports.[25]

HRMS ESI (m/z) calculated for $C_{20}H_{17}Br_2$ $[M+H]^+$ 493.9619, found 493.9627.

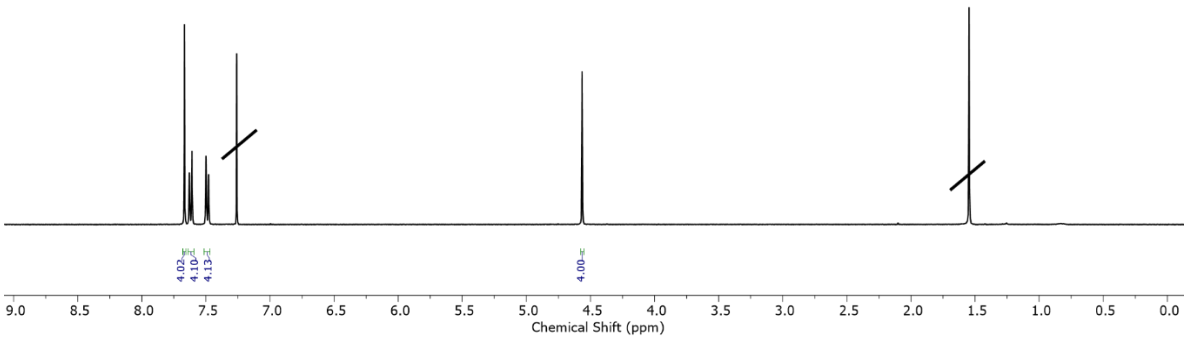

^{1}H NMR spectrum of compound **23** (Chloroform-*d*, 298 K, 500 MHz).

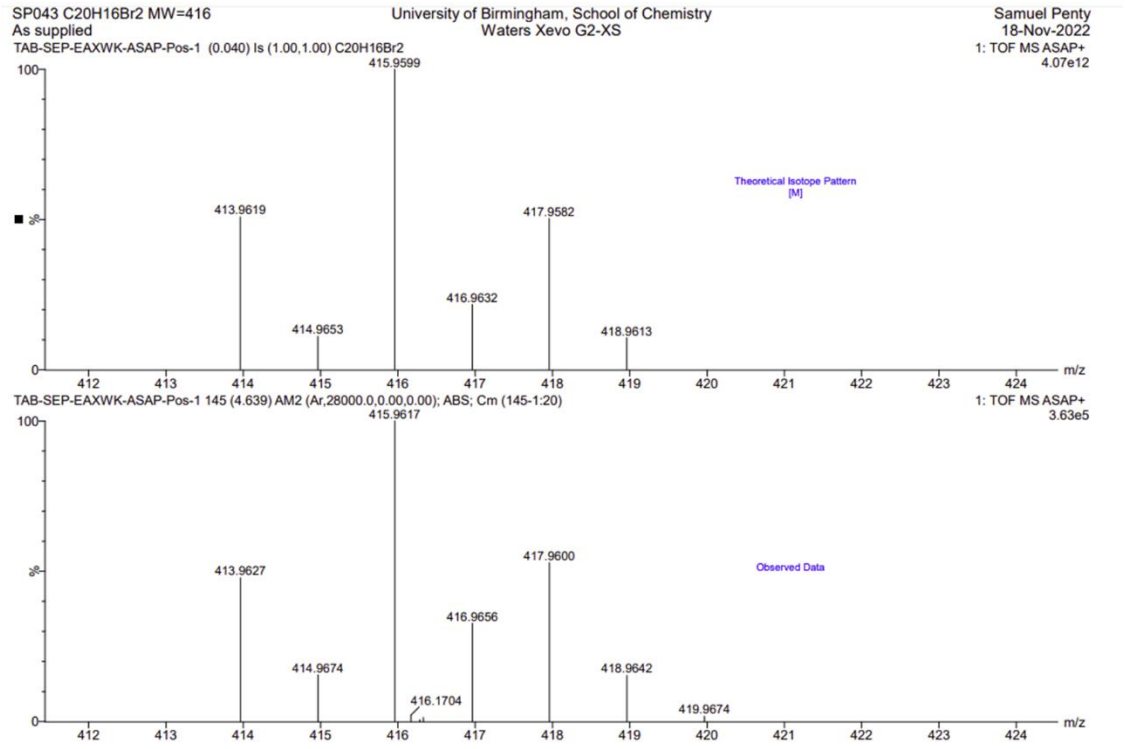

Calculated (top) and observed (bottom) ESI MS data for compound **23**.

4,4''-bis(azidomethyl)-1,1':4',1''-terphenyl 24

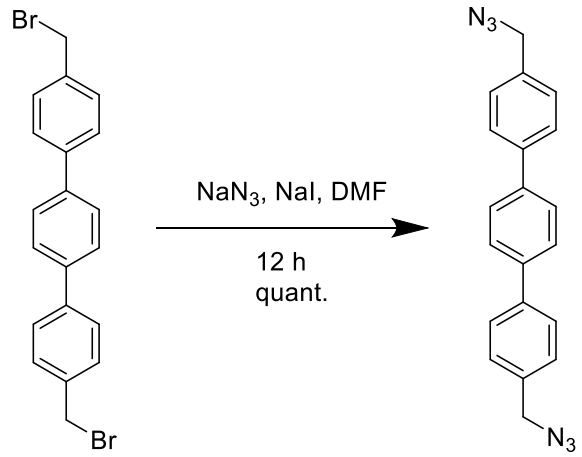

23 **24**

To a solution of compound **23** (1 g, 2.4 mmol) in DMF (5mL) was added NaN_3 (625 mg, 9.6 mmol, 4 equiv) and NaI (360 mg, 2.4 mmol, 1 equiv). The mixture was stirred at rt for 12 h. At this point a white precipitate was observed. The reaction mixture was then filtered, and the precipitate was washed with 10% LiCl in water solution (50 mL) and water (50 mL), affording the title compound as a white solid (817 mg, 2.4 mmol, quant.). It is worth noting that compound **24** has more than six carbon atoms per azide group and therefore is considered more stable to decomposition compared to the other organic bisazides discussed previously in this thesis.[26]

^{1}H NMR (400 MHz, Chloroform-*d*) δ 7.69 (s, 4H), 7.68 – 7.64 (m, 4H), 7.44 – 7.40 (m, 4H), 4.41 (s, 4H).

^{13}C NMR (101 MHz, Chloroform-*d*) δ 140.66, 139.67, 134.55, 128.75, 127.54, 127.47, 54.56.

HRMS ESI (m/z) calculated for $C_{20}H_{17}N_6$ $[M+H]^+$ 340.1436, found 493.1440.

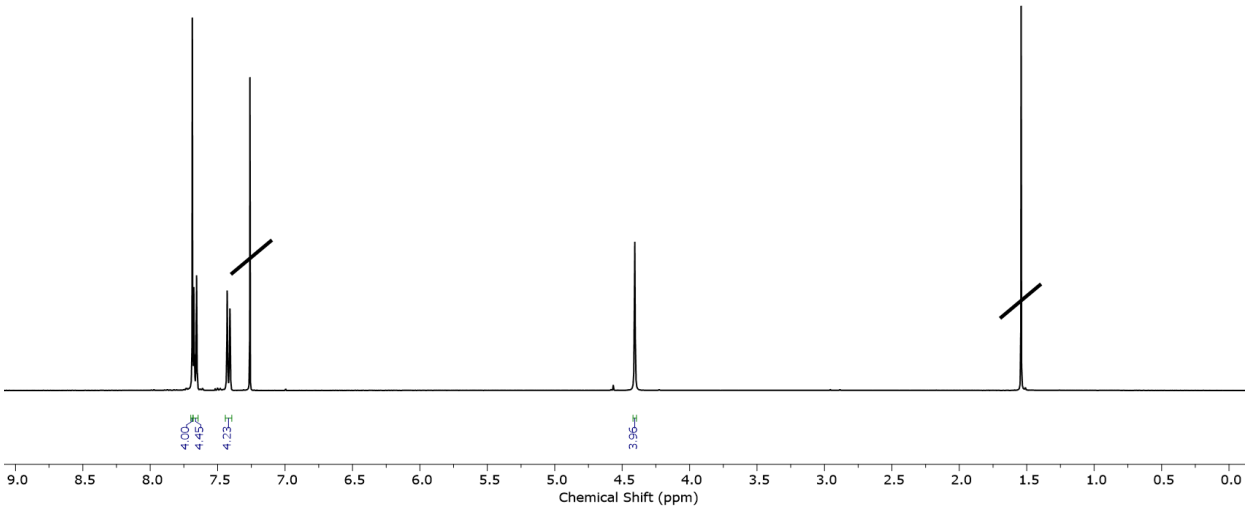

^{1}H NMR spectrum of compound **24** (Chloroform-*d*, 298 K, 500 MHz).

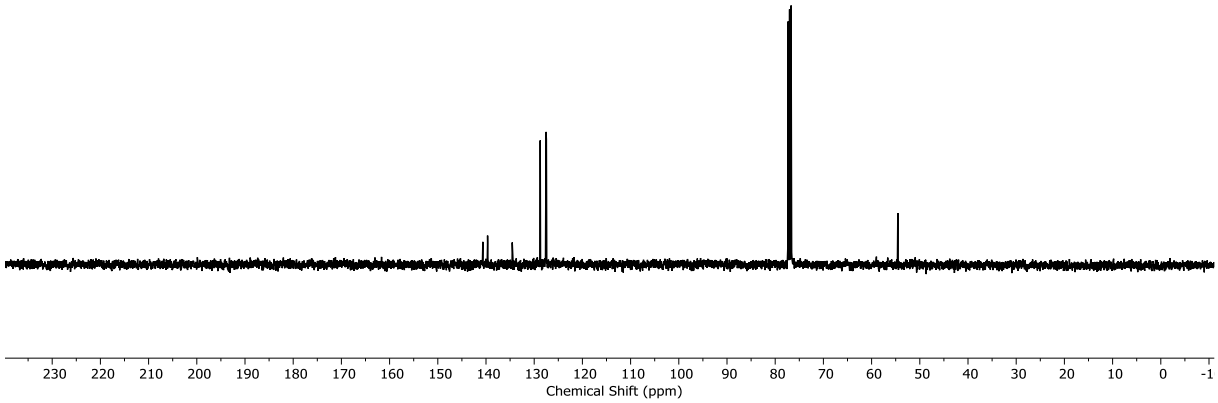

^{13}C NMR spectrum of compound **24** (Chloroform-*d*, 298 K, 101 MHz).

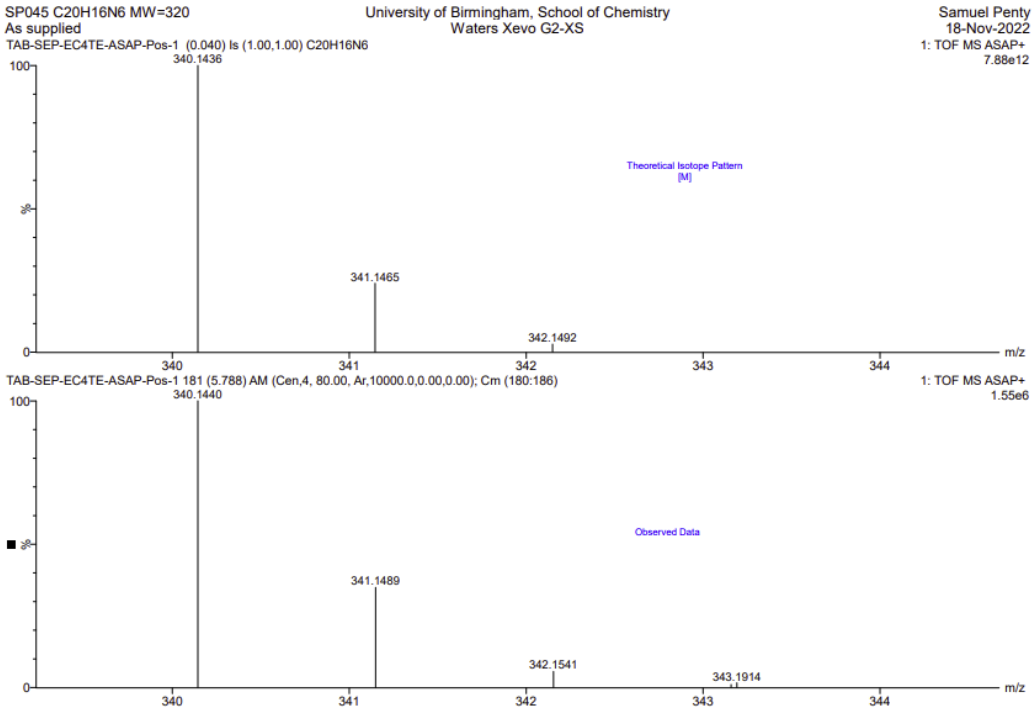

Calculated (top) and observed (bottom) ESI MS data for compound **24**.

Acyclic bistriazole PDI 21

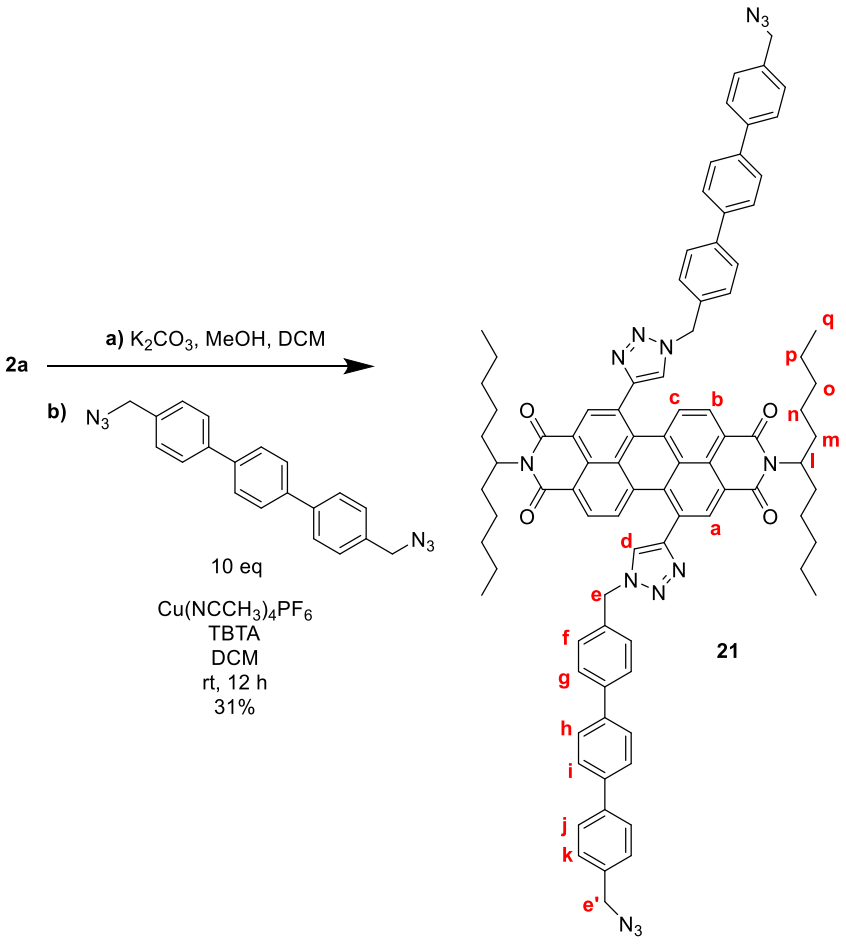

To a solution of TMS-protected bisalkyne PDI **2a**[5] (150 mg, 168 µmol) in DCM (20 ml) was added K_2CO_3 (300 mg) in MeOH (10 ml). The mixture was stirred at rt for 3 min, and completion of the reaction was confirmed by TLC. A further 20 mL of DCM was added to the mixture. The mixture was then washed with 1 M HCl (2 x 30 mL), water (2 x 30 mL) and brine (30 ml). The mixture was then dried over anhydrous $MgSO_4$ and concentrated to dryness *in vacuo* to afford the PDI bis-alkyne, which was used immediately without further purification. To a solution of this deprotected PDI bis-alkyne (125 mg, 168 µmol) in dry DCM (10 ml) was added compound **24** (569 mg, 1.68 mmol, 10 equiv) and TBTA (35 mg, 67 µmol, 0.4 equiv). The solution was then de-gassed with Argon. The copper catalyst $Cu(CH_3CN)_4PF_6$ (25 mg, 67 µmol, 0.4 equiv) was then added and the solution was once again de-gassed with Argon. The reaction was stirred at rt for 12 h. The solvent was then removed *in vacuo*. The resulting residue was purified by silica gel flash column chromatography (1:99 MeOH-CH_2Cl_2) affording the title compound as a purple solid (75 mg, 55 µmol, 31%).

^{1}H NMR (500 MHz, Chloroform-*d*) δ 8.63 (d(b), 2H_b), 8.24 (s(b) 2H_a), 7.92 (d, *J* = 8.1 Hz, 2H_c), 7.77 (s, 2H_d), 7.74 – 7.64 (m, 16H_{f-k}), 7.43 (m, 8H_{f-k}), 5.72 (s, 4H_e), 5.17 (p, 2H_l), 4.40 (s, 4$H_{e'}$), 2.22 (m, 4H_m), 1.87 – 1.76 (m, 4H_m), 1.33 – 1.20 (m, 24H_{n-p}), 0.85 – 0.76 (m, 12H_q).

^{13}C NMR (126 MHz, Chloroform-*d*) δ 164.48, 148.47, 141.51, 140.56, 139.88, 139.17, 134.63, 133.41, 129.23, 129.05, 128.92, 128.77, 128.56, 128.53, 128.45, 127.93, 127.63, 127.57, 127.45, 121.92, 54.69, 54.55, 54.33, 32.35, 32.31, 31.77, 31.74, 26.59, 26.57, 22.58, 14.10, 14.08.

HRMS MALDI (m/z) calculated for $C_{90}H_{86}N_{14}O_4$ [M]: 1426.6956, found 1426.8519.

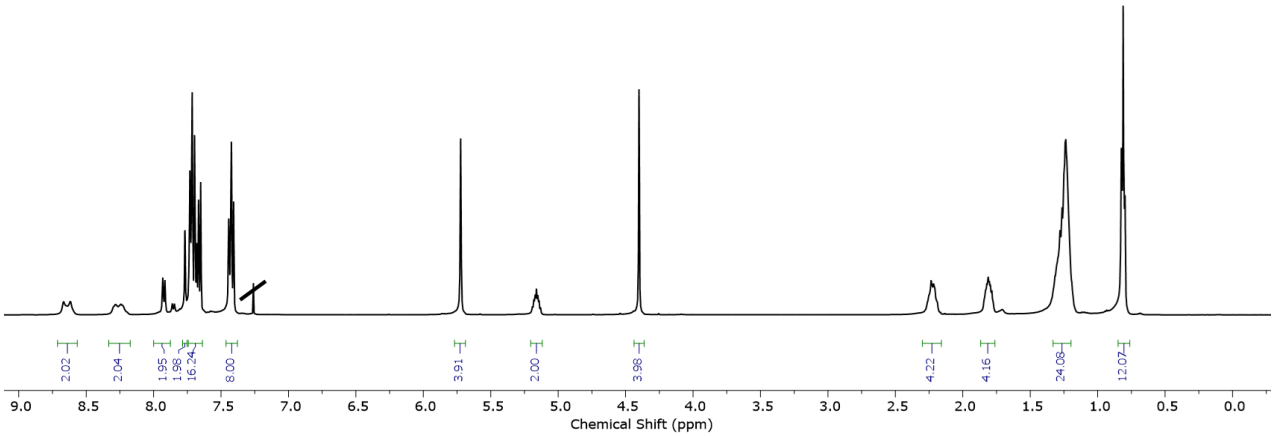

^{1}H NMR spectrum of compound **21** (Chloroform-*d*, 298 K, 500 MHz).

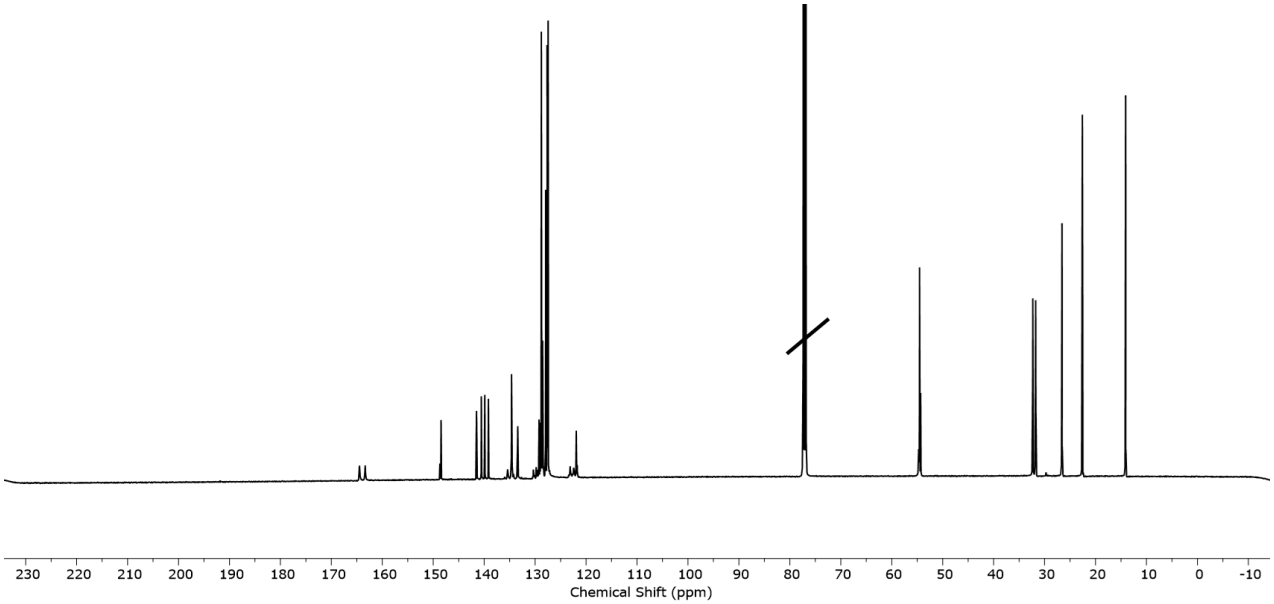

^{13}C NMR spectrum of compound **21** (Chloroform-*d*, 298 K, 101 MHz).

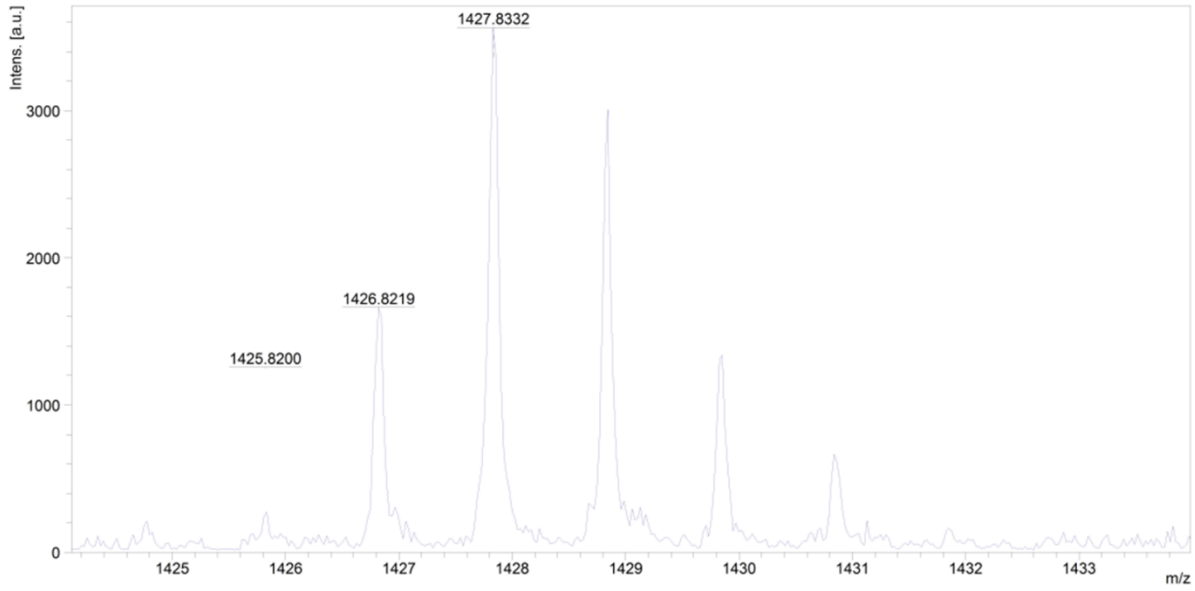

Observed MALDI MS data for compound **21**.

Terphenyl-spaced bis-PDI macrocycle 18

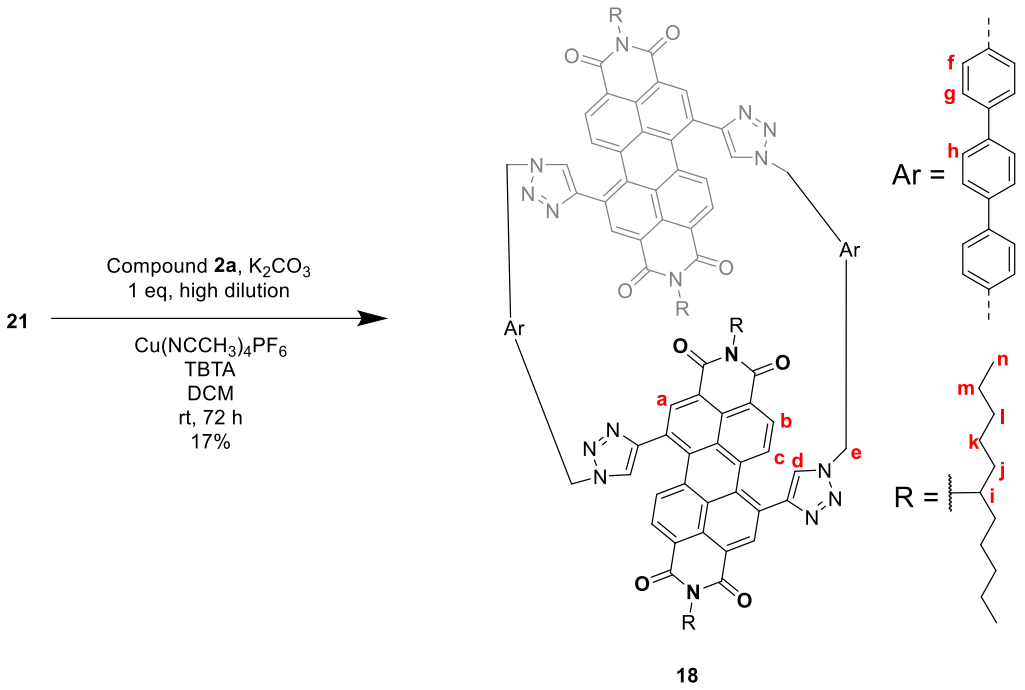

TMS-protected bis-alkyne PDI **2a** (50 mg, 56 µmol) was dissolved in DCM (20 mL). To this was added K_2CO_3 (20 mg) in MeOH (10 mL). The reaction was monitored by TLC (1:99 MeOH:DCM). Upon completion the reaction mixture was thoroughly washed with water in a separating funnel (3 x 100 mL) and dried with $MgSO_4$ to yield crude deprotected bis-alkyne PDI in DCM, which was used immediately without further purification due to its tendency to aggregate and crash out of solution over time. This was added to a flask, along with acyclic bis-triazole PDI **21** (75 mg, 56 µmol, 1 equiv), tris((1-benzyl-4-triazolyl)methyl)amine (TBTA) (12 mg, 21 µmol, 0.4 eq) and a further 350 mL of DCM. The reaction mixture was thoroughly de-gassed with N_2. The copper catalyst $Cu(CH_3CN)_4PF_6$ (8 mg, 21 µmol, 0.4 equiv) was then added and the reaction mixture was thoroughly de-gassed again. The reaction was stirred at rt for 72 h and monitored by TLC (2:98 MeOH-DCM). The solvent was then removed *in vacuo*. The resulting residue was dissolved in DCM and filtered through cotton wool and the filtrate was then purified by preparative silica TLC (2:98 MeOH-DCM), affording the title compound (as the pure 1,7-regioisomer) as a purple solid (20 mg, 9 µmol, 17%, noting the presence of some aliphatic impurities (estimated < 10 mol% by NMR).

^{1}H NMR (400 MHz, Chloroform-*d*) δ 8.57 (d, *J* = 8.2 Hz, 4H_b), 8.21 (s (b), 4H_a), 7.95 (d, *J* = 8.2 Hz, 4H_c), 7.58 – 7.43 (m, 20$H_{d,f-h}$), 7.32 – 7.24 (m, 8$H_{d,f-h}$), 5.64 (s, 8H_e), 5.05 (p, 4H_i), 2.10 (m, 8H_j), 1.76 – 1.68 (m, 8H_j), 1.11 (s, 48H_{k-m}), 0.68 (d, *J* = 6.8 Hz, 24H_n).

^{13}C NMR (126 MHz, Chloroform-*d*) δ 148.46, 141.22, 139.17, 128.85, 128.71, 128.41, 127.75, 127.47, 121.39, 54.46, 32.23, 31.94, 29.72, 29.68, 29.45, 29.38, 26.51, 22.71, 22.52, 14.14, 14.02.

HRMS MALDI (m/z) calculated for $C_{140}H_{140}N_{16}O_8$ [M] 2172.1045, found 2172.3493

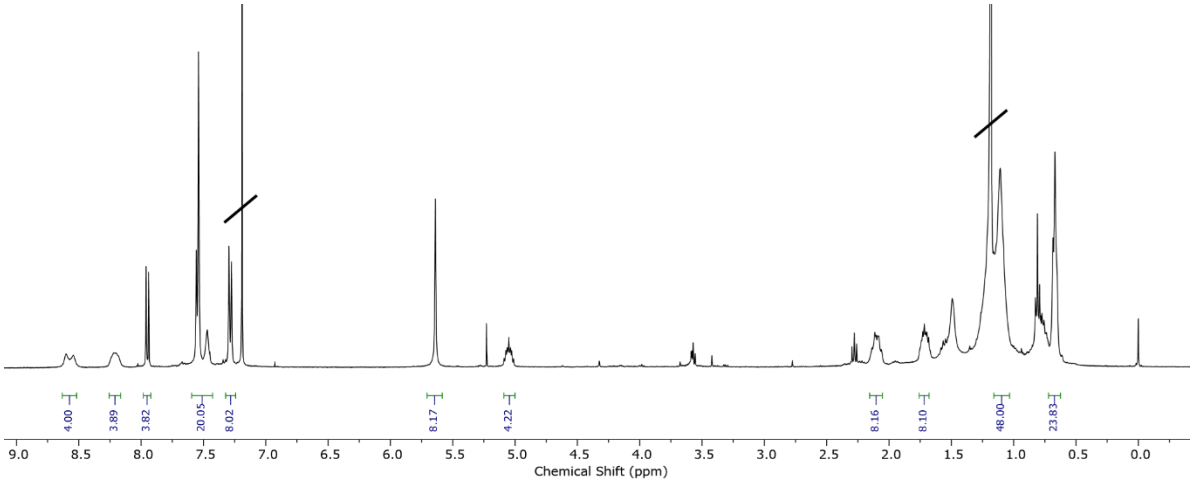

^{1}H NMR spectrum of macrocycle **18** (Chloroform-*d*, 298 K, 500 MHz).

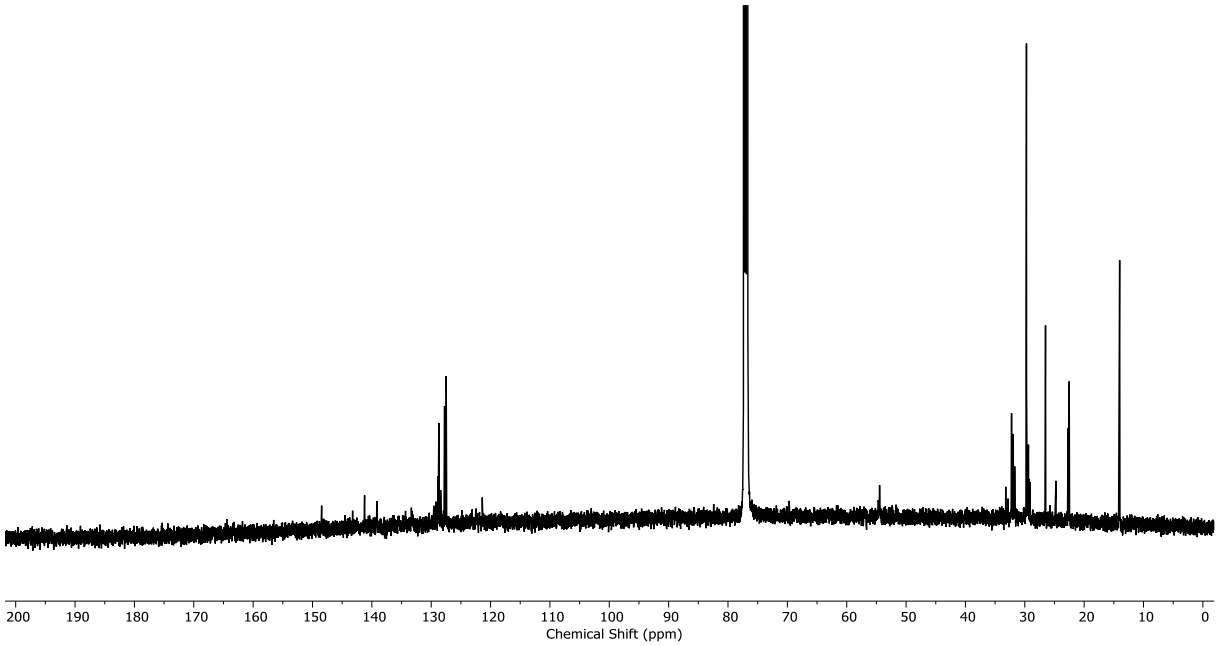

^{13}C NMR spectrum of macrocycle **18** (Chloroform-*d*, 298 K, 101 MHz).

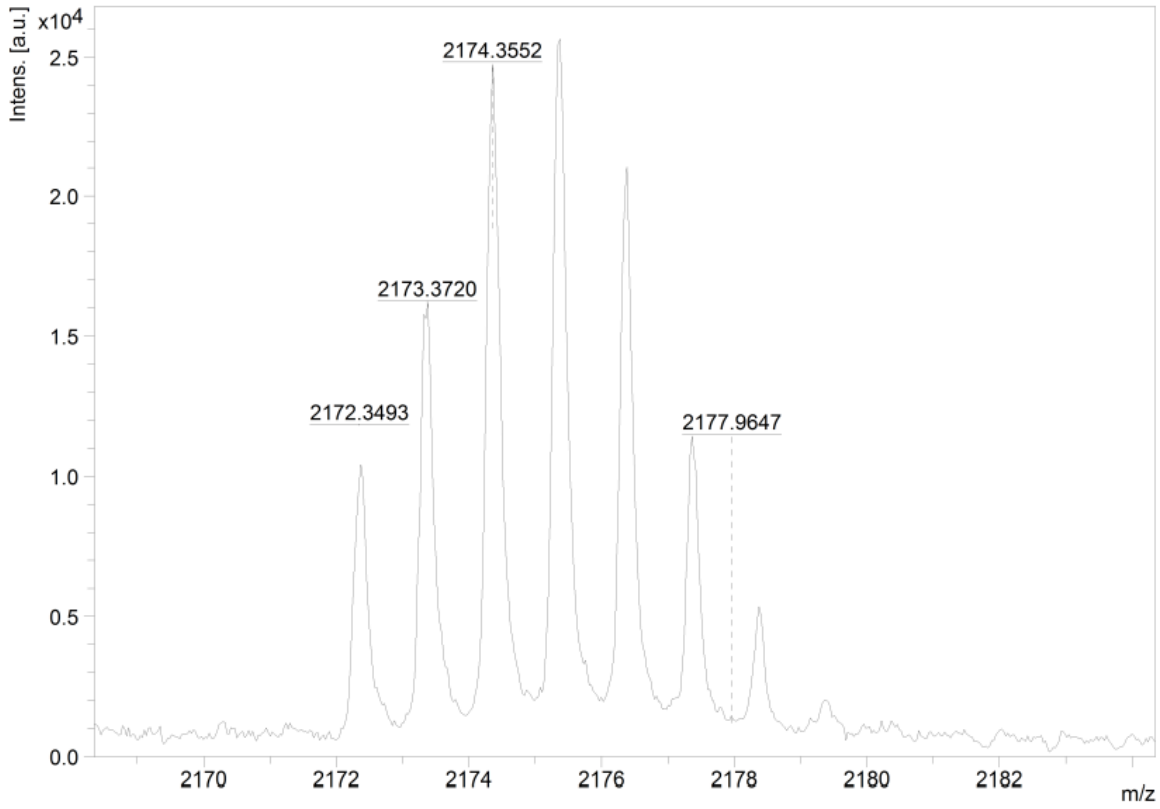

Observed MALDI MS data for macrocycle **18**.

5.9.4 Synthesis of macrocycle 19

Acyclic bistriazole PDI 22

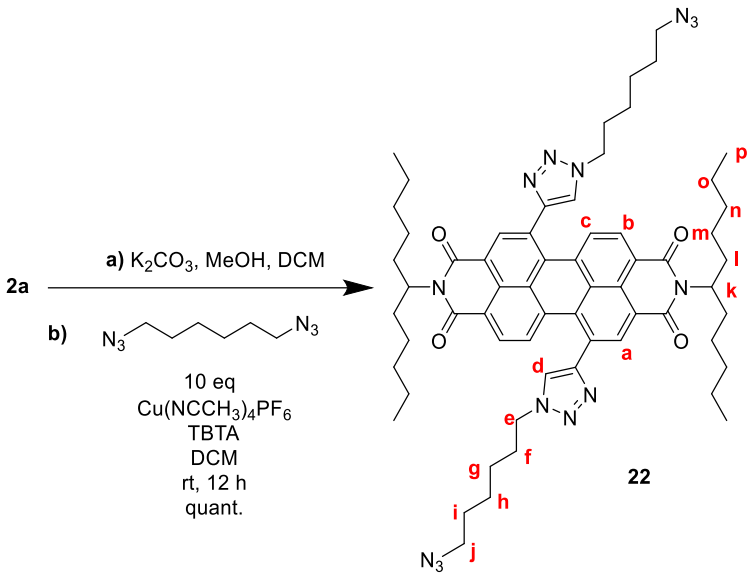

To a solution of TMS-protected bisalkyne PDI **2a**[5] (100 mg, 111 µmol) in DCM (20 ml) was added K_2CO_3 (300 mg) in MeOH (10 ml). The mixture was stirred at rt for 3 min, and completion of the reaction was confirmed by TLC. A further 20 mL of DCM was added to the mixture. The mixture was then washed with 1 M HCl (2 x 30 mL), water (2 x 30 mL) and brine (30 ml). The mixture was then dried over anhydrous $MgSO_4$ and concentrated to dryness *in vacuo* to afford the PDI bis-alkyne, which was used immediately without further purification. To a solution of this deprotected PDI bis-alkyne (83 mg, 111 µmol) in dry DCM (10 ml) was added 1,6-diazidohexane (300 mg, 1.14 mmol, 10 equiv) and TBTA (12 mg, 22 µmol, 0.2 equiv). The solution was then de-gassed with Argon. The copper catalyst $Cu(CH_3CN)_4PF_6$ (8 mg, 22 µmol, 0.2 equiv) was then added and the solution was once again de-gassed with Argon. The reaction was stirred at rt for 12 h. The solvent was then removed *in vacuo*. The resulting residue was purified by silica gel flash column chromatography (1:99 MeOH-CH_2Cl_2) affording the title compound as a purple solid (123 mg, 111 µmol, quant).

^{1}H NMR (500 MHz, chloroform-*d*, 1,7-regiosiomer) δ 8.68 (d, $2H_b$), 8.22 (s, $2H_a$), 7.89 (d, $2H_c$), 7.72 (s, $2H_d$), 5.20 – 5.10 (m, $2H_k$), 4.50 (t, *J* = 7.1 Hz, $4H_e$), 3.31 (t, *J* = 6.7 Hz, $4H_j$), 2.22 (m, $4H_f$), 2.03 (p, *J* = 7.1 Hz, 4H), 1.86 – 1.76 (m, 4H), 1.66 (dt, *J* = 12.1, 4.9 Hz, 4H), 1.48 (d, *J* = 34.8 Hz, 8H), 1.34 – 1.17 (m, 25H), 0.82 (t, *J* = 6.7 Hz, 12H).

^{13}C NMR (126 MHz, chloroform-*d*) δ 164.49, 163.36, 148.17, 147.94, 135.48, 134.75, 134.60, 134.19, 133.45, 130.23, 130.03, 129.92, 129.49, 129.10, 129.07, 129.03, 128.75, 128.43, 123.13, 122.41, 121.68, 121.49, 54.81, 54.70, 53.46, 51.27, 50.63, 32.33, 32.30, 31.77, 31.74, 30.29, 30.28, 28.69, 26.59, 26.56, 26.18, 26.10, 22.57, 14.08, 14.06.

HRMS ESI (m/z) calculated for $C_{62}H_{78}N_{14}O_4$ $[M+H]^+$ 1083.6409, found 1083.6373.

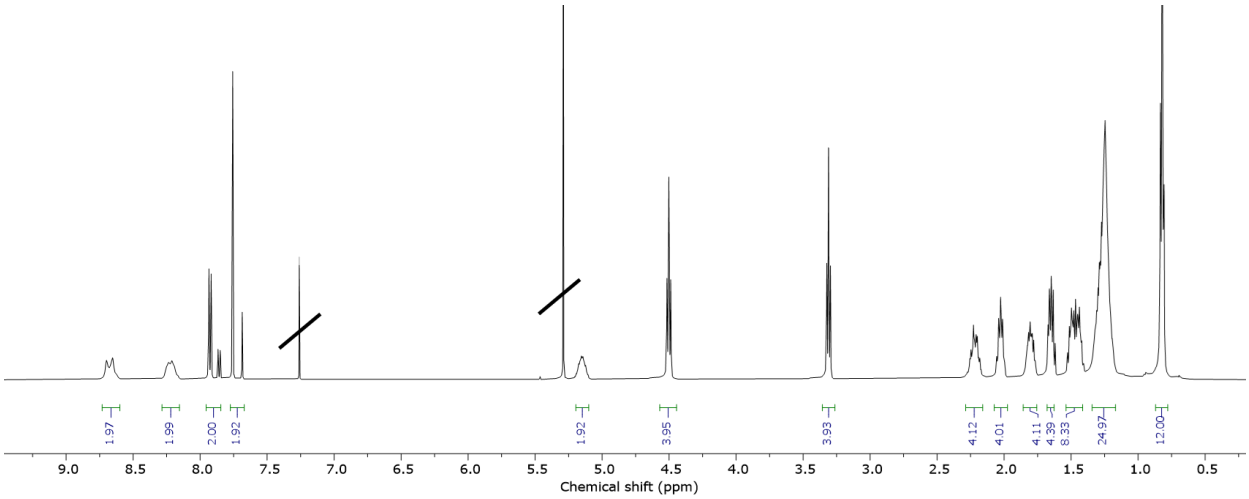

^{1}H NMR spectrum of compound **22** (Chloroform-*d*, 298 K, 500 MHz).

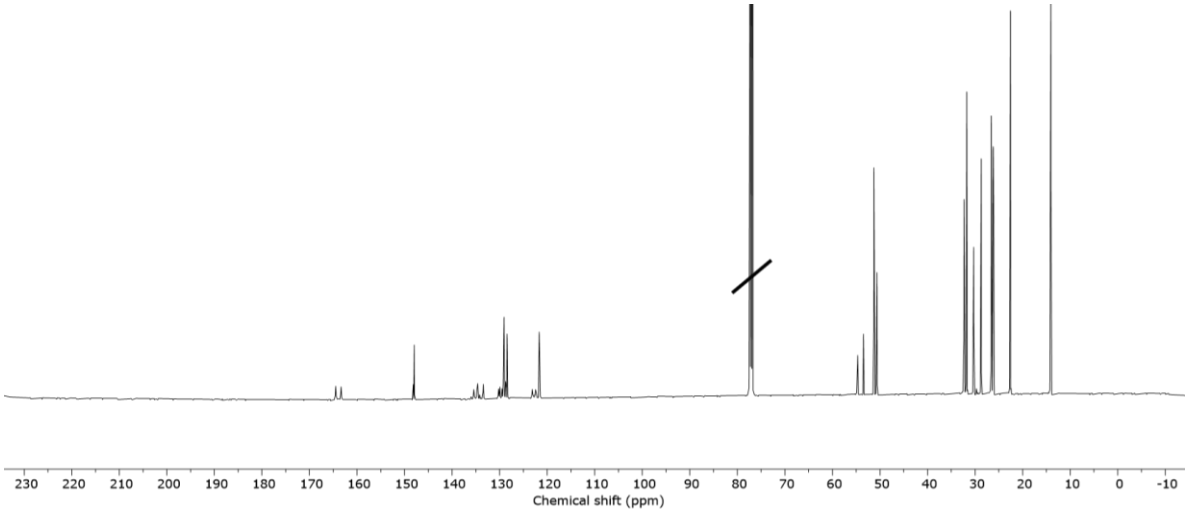

^{13}C NMR spectrum of compound **22** (Chloroform-*d*, 298 K, 101 MHz).

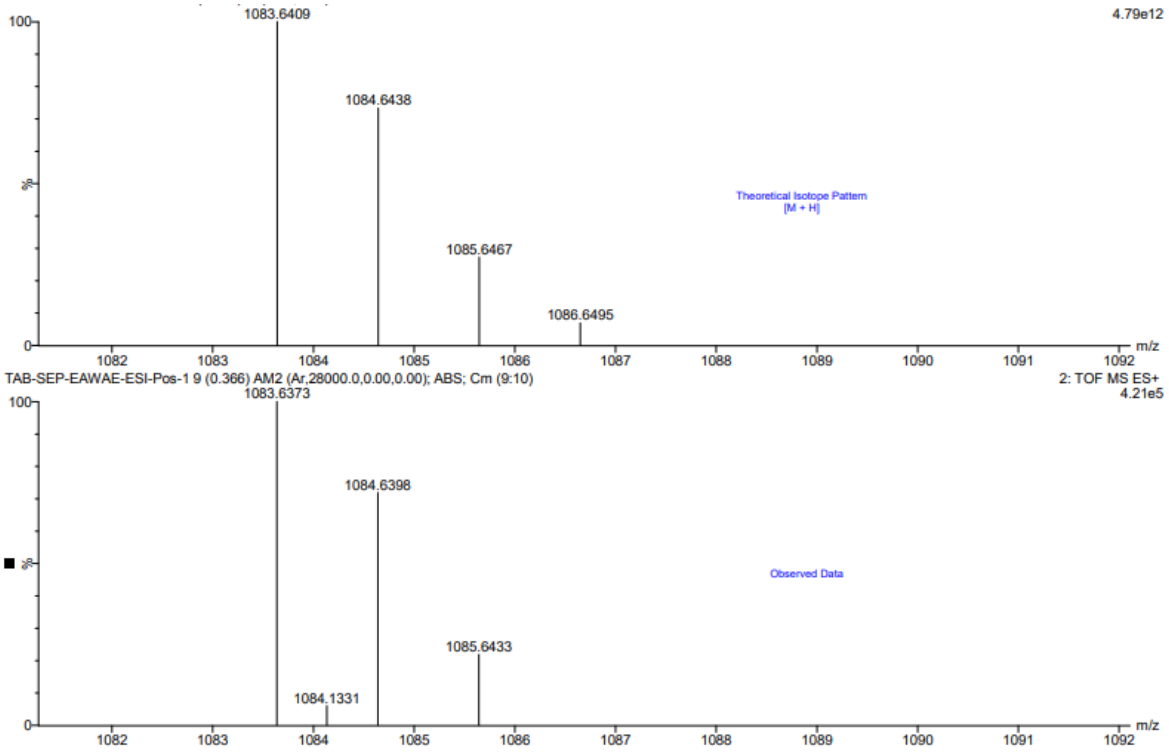

Calculated (top) and observed (bottom) ESI MS data for compound **22**.

Hexyl-spaced bis-PDI macrocycle 19

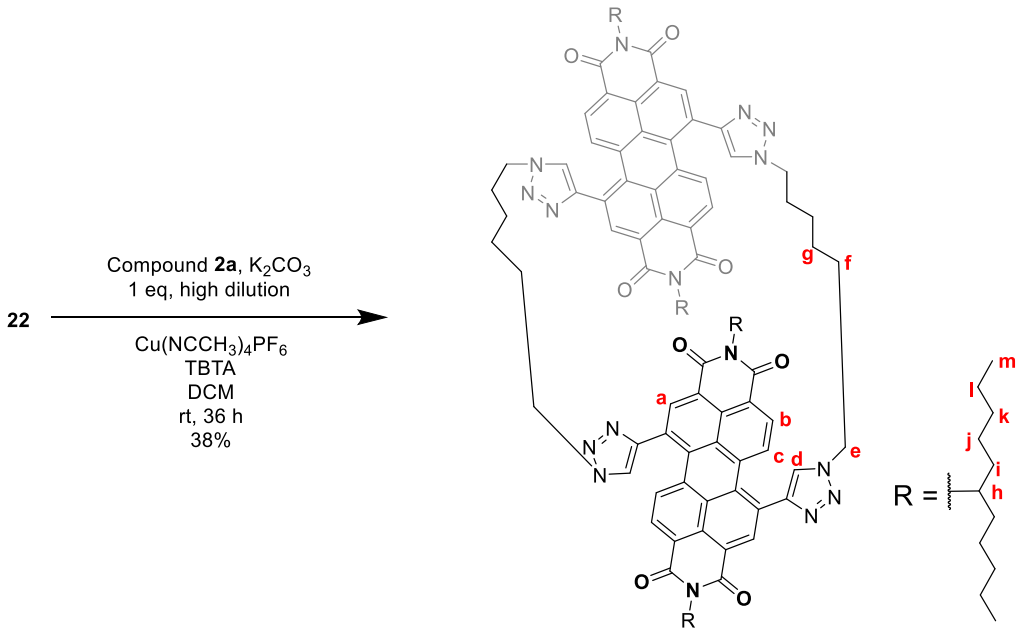

19

To a solution of TMS-protected bisalkyne PDI **2a**[5] (66 mg, 74 µmol) in DCM (20 ml) was added K_2CO_3 (300 mg) in MeOH (10 ml). The mixture was stirred at rt for 3 min, and completion of the reaction was confirmed by TLC. A further 20 mL of DCM was added to the mixture. The mixture was then washed with 1 M HCl (2 x 30 mL), water (2 x 30 mL) and brine (30 ml). The mixture was then dried over anhydrous $MgSO_4$ and concentrated to dryness *in vacuo* to afford the PDI bis-alkyne, which was used immediately without further purification. This was added to a solution of compound **22** (80 mg, 74 µmol, 1 equiv) and TBTA (16 mg, 30 µmol, 0.4 equiv) in DCM (250 mL). The solution was then de-gassed with Argon. The copper catalyst $Cu(CH_3CN)_4PF_6$ (11 mg, 30 µmol, 0.4 equiv) was then added and the solution was once again de-gassed with Argon. The reaction was stirred at rt for 36 h. The solvent was then removed *in vacuo*. The resulting residue was purified by silica gel flash column chromatography (1:99 MeOH-CH_2Cl_2) followed by preparative silica TLC (0.5:99.5 MeOH-CH_2Cl_2), affording the title compound as a purple solid (52 mg, 28 µmol, 38% noting the presence of some aliphatic impurities (estimated <10 mol % by NMR)).

^{1}H NMR (500 MHz, chloroform-*d*) δ 8.58 (s, 4H_a), 8.18 (d, *J* = 8.1 Hz, 4H_b), 7.91 (d, *J* = 8.2 Hz, 4H_c), 7.64 (s, 4H_d), 5.11 – 5.05 (m, 4H_h), 4.48 (t, *J* = 6.7 Hz, 8H_e), 3.26 – 3.21 (m, 8H_f),

2.12 (m, 8H$_i$), 1.99 (m, 8H$_i$), 1.88 (m, 8H), 1.69 (m, 8H), 1.53 – 1.48 (m, 24H), 1.09 (m, 16H), 0.87 (t, J = 6.7 Hz, 24H$_m$).

^{13}C NMR (126 MHz, chloroform-*d*) δ 163.89, 163.59, 134.73, 129.67, 128.44, 123.24, 99.98, 74.47, 74.19, 73.92, 55.13, 50.58, 32.64, 31.74, 29.76, 26.70, 22.48, 13.90.

HRMS ESI (m/z) calculated for $C_{112}H_{133}N_{16}O_8$ $[M+H]^+$ 1830.0492, found 1830.0424.

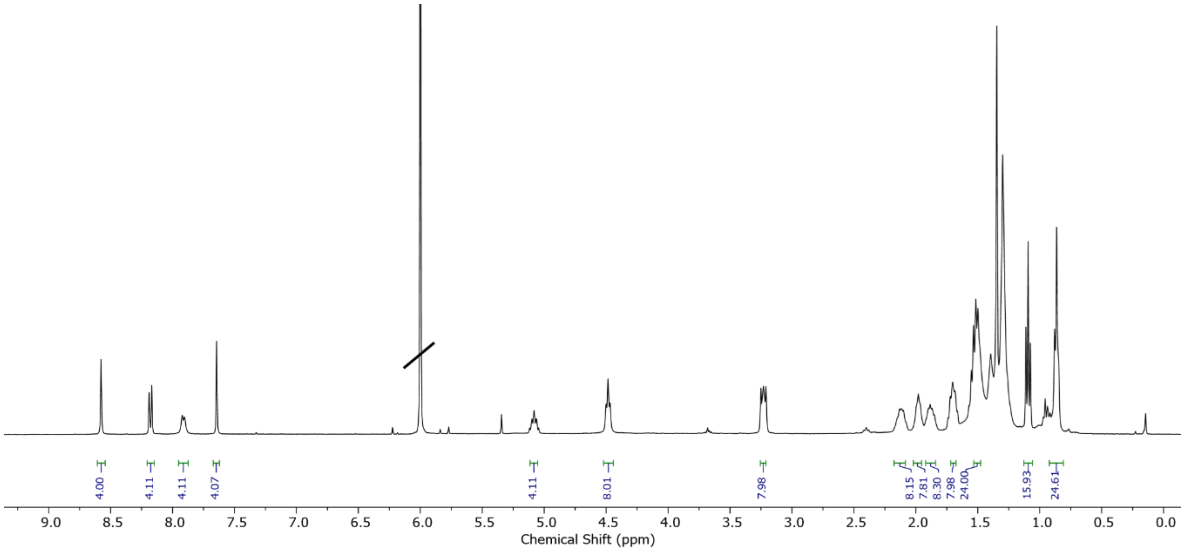

^{1}H NMR spectrum of macrocycle **19** (Chloroform-*d*, 298 K, 500 MHz).

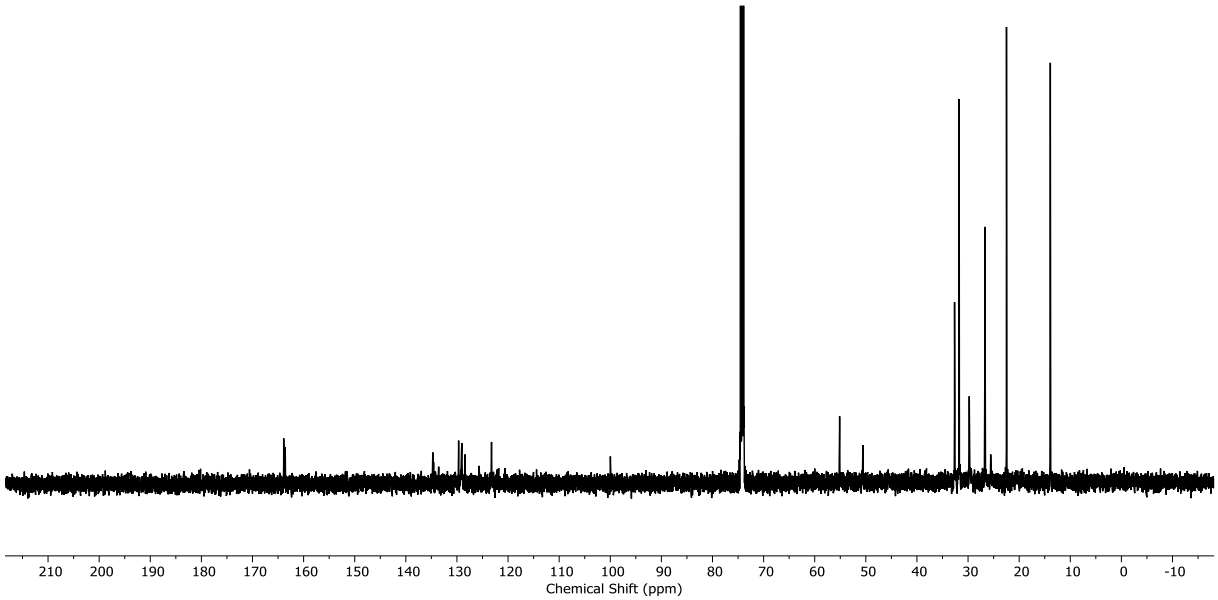

^{13}C NMR spectrum of macrocycle **19** (Chloroform-*d*, 298 K, 101 MHz).

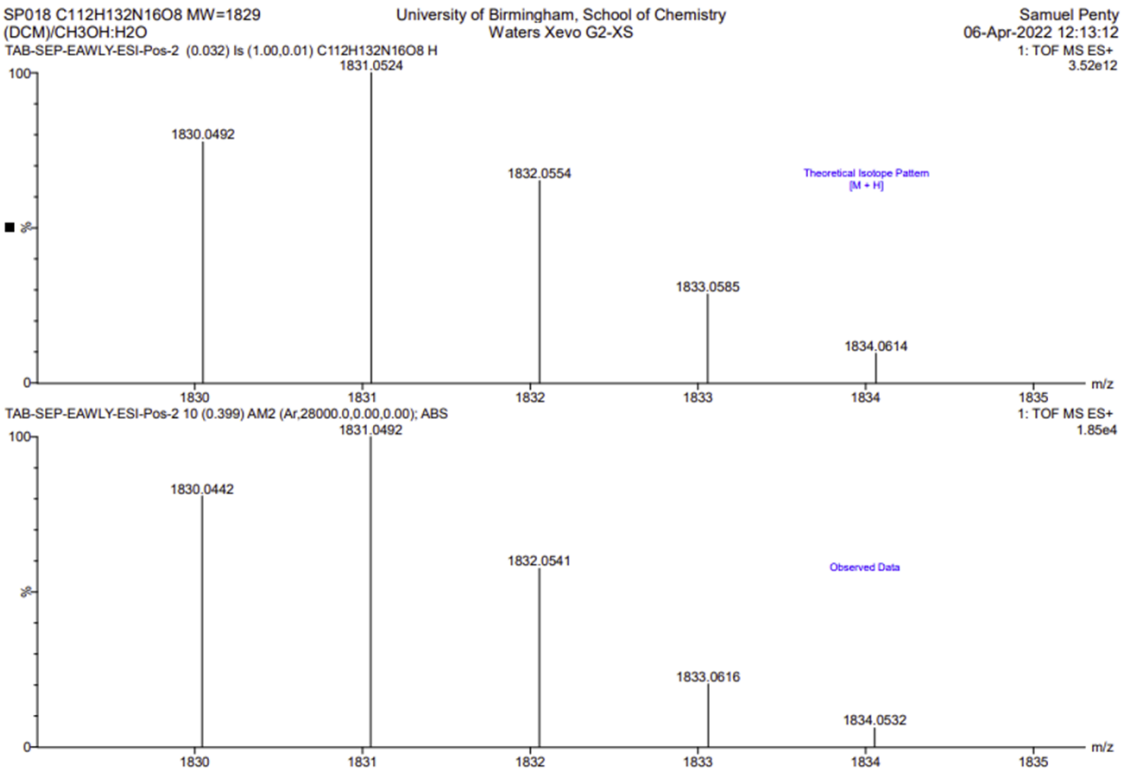

Calculated (top) and observed (bottom) ESI MS data for macrocycle **19**.

5.9.5 Photophysics

UV-vis-NIR absorption spectra in solution

All steady state electronic absorption and emission spectra were recorded at a concentration of 10 µM (unless otherwise stated) at 298 K. For UV-vis-NIR spectroscopy a Shimadzu UV-3600i Plus spectrophotometer was used, with a wavelength accuracy ± 0.2 nm in the UV-vis range and absorbance accuracy ± 0.002 Abs. For fluorescence spectroscopy a Jasco FP-8500 was used with emission and excitation wavelength accuracies ± 1.0 nm. The detector base sensitivity is 8500:1. Quartz cuvettes with 1 cm path length were used.

5.10 References

1. P. Spenst and F. Würthner, *Angewandte Chemie International Edition*, 2015, **54**, 10165-10168.
2. J. Rühe, D. Bialas, P. Spenst, A.-M. Krause and F. Würthner, *Organic Materials*, 2020, **02**, 149-158.
3. J. C. Rosa, D. Galanakis, C. R. Ganellin, P. M. Dunn and D. H. Jenkinson, *Journal of Medicinal Chemistry*, 1998, **41**, 2-5.
4. J. W. Lee, S. I. Jun and K. Kim, *Tetrahedron Letters*, 2001, **42**, 2709-2711.
5. C. D. Schmidt, N. Lang, N. Jux and A. Hirsch, *Chemistry – A European Journal*, 2011, **17**, 5289-5299.
6. S. E. Penty, G. R. F. Orton, D. J. Black, R. Pal, M. A. Zwijnenburg and T. A. Barendt, *Journal of the American Chemical Society*, 2024, **146**, 5470-5479.
7. N. J. Hestand and F. C. Spano, *The Journal of Chemical Physics*, 2015, **143**.
8. E. Sebastian, A. M. Philip, A. Benny and M. Hariharan, *Angewandte Chemie International Edition*, 2018, **57**, 15696-15701.
9. M. Kasha, H. R. Rawls and M. A. El-Bayoumi, *Pure and Applied Chemistry*, 1965, **11**, 371-392.
10. F. Wurthner, C. R. Saha-Moller, B. Fimmel, S. Ogi, P. Leowanawat and D. Schmidt, *Chem Rev*, 2016, **116**, 962-1052.
11. N. J. Hestand and F. C. Spano, *Chemical Reviews*, 2018, **118**, 7069-7163.
12. C. Kaufmann, D. Bialas, M. Stolte and F. Würthner, *Journal of the American Chemical Society*, 2018, **140**, 9986-9995.
13. S. R. LaPlante, P. J. Edwards, L. D. Fader, A. Jakalian and O. Hucke, *ChemMedChem*, 2011, **6**, 505-513.
14. M. Sapotta, P. Spenst, C. R. Saha-Möller and F. Würthner, *Organic Chemistry Frontiers*, 2019, **6**, 892-899.
15. M. Weh, A. A. Kroeger, O. Anhalt, A. Karton and F. Würthner, *Chemical Science*, 2024, **15**, 609-617.
16. M. Weh, A. A. Kroeger, K. Shoyama, M. Grüne, A. Karton and F. Würthner, *Angewandte Chemie International Edition*, 2023, **62**, e202301301.
17. M. Weh, J. Rühe, B. Herbert, A.-M. Krause and F. Würthner, *Angewandte Chemie International Edition*, 2021, **60**, 15323-15327.
18. M. Weh, K. Shoyama and F. Würthner, *Nature Communications*, 2023, **14**, 243.
19. Z. Chen, B. Fimmel and F. Würthner, *Organic & Biomolecular Chemistry*, 2012, **10**, 5845-5855.
20. S. E. Penty, M. A. Zwijnenburg, G. R. F. Orton, P. Stachelek, R. Pal, Y. Xie, S. L. Griffin and T. A. Barendt, *Journal of the American Chemical Society*, 2022, **144**, 12290-12298.
21. T. Ogawa and D. Kuzuhara, *ChemPlusChem*, 2021, **86**, 852-857.
22. T. R. Chan, R. Hilgraf, K. B. Sharpless and V. V. Fokin, *Organic Letters*, 2004, **6**, 2853-2855.
23. J. R. Thomas, X. Liu and P. J. Hergenrother, *Journal of the American Chemical Society*, 2005, **127**, 12434-12435.
24. D. D. Díaz, K. Rajagopal, E. Strable, J. Schneider and M. G. Finn, *Journal of the American Chemical Society*, 2006, **128**, 6056-6057.
25. K. N. Houk, S. Menzer, S. P. Newton, F. M. Raymo, J. F. Stoddart and D. J. Williams, *Journal of the American Chemical Society*, 1999, **121**, 1479-1487.

26. https://ehs.stanford.edu/reference/information-azide-compounds, (accessed 07/10, 2024).

Chapter 6: Conclusions

6. Conclusions

6.1 Conclusions

This thesis aimed to explore the non-covalent interactions between chiral core-twisted PDIs by developing a novel class of bis-PDI macrocyclic scaffold, nicknamed the "Pink Box" due to its colour in solution. The unique connectivity between the PDI units in this macrocycle, namely the use of non-conjugated linkers that connect the PDI units via their (1,7) bay positions, allows the tuning of intramolecular PDI–PDI π–π interactions, which impact a range of important properties for organic chiroptical materials. [1]

Chapter 2 outlined the development of the Pink Box macrocyclic scaffold, synthesising the 1st generation bis-PDI macrocycle (**1**),[2] and characterising its intramolecular PDI-PDI dimer by a range of experimental techniques. In toluene solvent and in the solid state it was found that the complementary π–π interactions between the chiral PDIs result in the co-facial intramolecular dimer being exclusively homochiral, with H-type excitonic coupling (**Figure 6.1**). These through-space π–π interactions (ΔG_{agg} = -11 kJ mol^{-1}) lead to a 400-fold enhancement in the stability of the macrocycle enantiomers (***MM*** and ***PP***), enabling their chiroptical properties to be measured. Excitingly, the enantiomers of **1** have the highest circularly polarized luminescence dissymmetry factor of any discrete PDI in solution (g_{lum} = 10^{-2} vs 10^{-3})[3] and are also amongst the most red-shifted (λ_{em} = 675 nm) of organic CPL emitters.[4-8] The conformation of this macrocycle is solvent-dependent, resulting in switchable chiroptical, electrochemical and photophysical properties, the latter being examined in further detail by Bressan, Meech *et al.*[9]

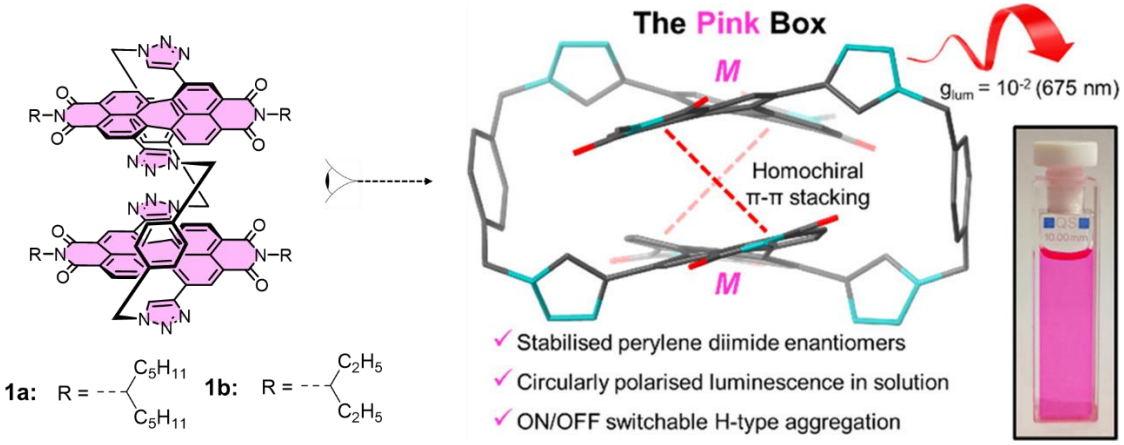

Figure 6.1: Summary of results for Chapter 2.

Chapter 3 introduced a strategy to make the Pink Box macrocycle chirally locked, developing a 2nd generation bis-PDI macrocycle (**5**)[10] that uses long, rigid imide groups (*tert*-butyl benzoate) to prevent the "intramolecular somersault" mechanism[11] for stereoisomer interconversion (**Figure 6.2**). The configurationally stable enantiomers of the macrocycle ($\Delta G^{\ddagger}$ > 155 kJ mol^{-1})[12, 13] were isolated and their chiroptical properties were shown to be persistent over time in solution, of potential value for solution-based manufacturing of chiral optoelectronic materials.[14] Configurational stability also led to the discovery that the synthesis of **5** is diastereoselective, forming exclusively as the pair of enantiomers ***MM*** and ***PP***, with none of the heterochiral ***MP*** macrocycle detected by HPLC. The *tert*-butyl benzoate imide groups make the outer π-surfaces of the macrocycle more accessible, allowing the π–π self-assembly of the macrocycle to be explored in both enantiopure and racemic mixtures. It was found that while the *intra*molecular PDI-PDI interaction is co-facial (H-type) and homochiral, further *inter*molecular self-assembly beyond the dimer limit is slipped-stacked (J-type) and heterochiral. From this new understanding, a general prediction can be made: when both π-surfaces of a twisted 1,7-disubstituted PDI are available for π–π self-assembly, homochiral H-type dimerization on the less sterically hindered face is expected to be followed by heterochiral J-type slipped-stacking on the remaining π-surface (**Figure 6.2**). Therefore, the work in Chapter 3 shows that the chirality of the disubstituted PDI building block provides a rational route to designing H- and J-type aggregates as well as materials that simultaneously contain both H- and J-type aggregates.

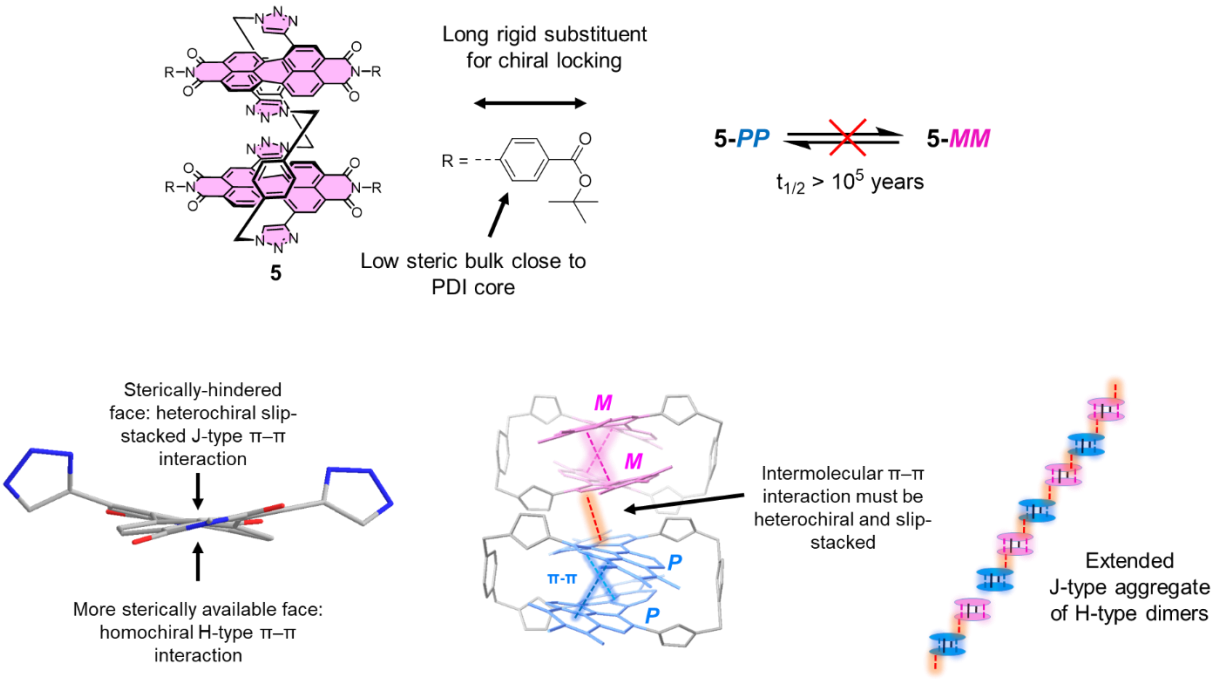

Figure 6.2: Summary of results for Chapter 3.

Chapter 4 sought to provide a fundamental understanding of the chiral conformations of "Pink Box" type macrocycles to further their potential as efficacious chiroptical materials. By considering isomerism of the twisted PDIs in the macrocycle design, it was realised that the three different stereoisomers (***MM***, ***PP***, and ***MP***) of a bis-PDI macrocycle may also adopt "triazoles in" and "triazoles out" conformations. These conformations interconvert via "twisting" of the PDI cores, which inverts the local axial chirality of the PDI cores, i.e. ***PP*** ⇄ ***M*M****, ***MM*** ⇄ ***P*P****, and ***MP*** ⇄ ***P*M**** (where the asterisk indicates a "triazoles in" conformation). However, this does not equate to true enantiomerisation, i.e. ***PP*** ⇄ ***MM***, which requires a "somersault" of the PDI imide heads through the centre of the macrocyclic cavity.[11] To provide evidence for this theory, a 3rd generation Pink Box macrocycle, **11** (**Figure 6.3**), was developed that is configurationally stable, such that racemisation does not occur, yet can still be switched between "triazoles out" and "triazoles in" conformations by changing the solvent. Inverting the local axial chirality of the PDI cores in **11** inverts the CD spectrum, a rare example of an achiral stimulus (solvent) being used to afford chiroptical switching.[15, 16] Additionally, a stable ***MP*** heterochiral diastereomer was isolated, where experimental and computational evidence is provided for an intramolecular "slip-stack" J-type dimer between the two PDIs, in contrast to the homochiral macrocycles which always form H-type intramolecular dimers (**Figure 6.3**).

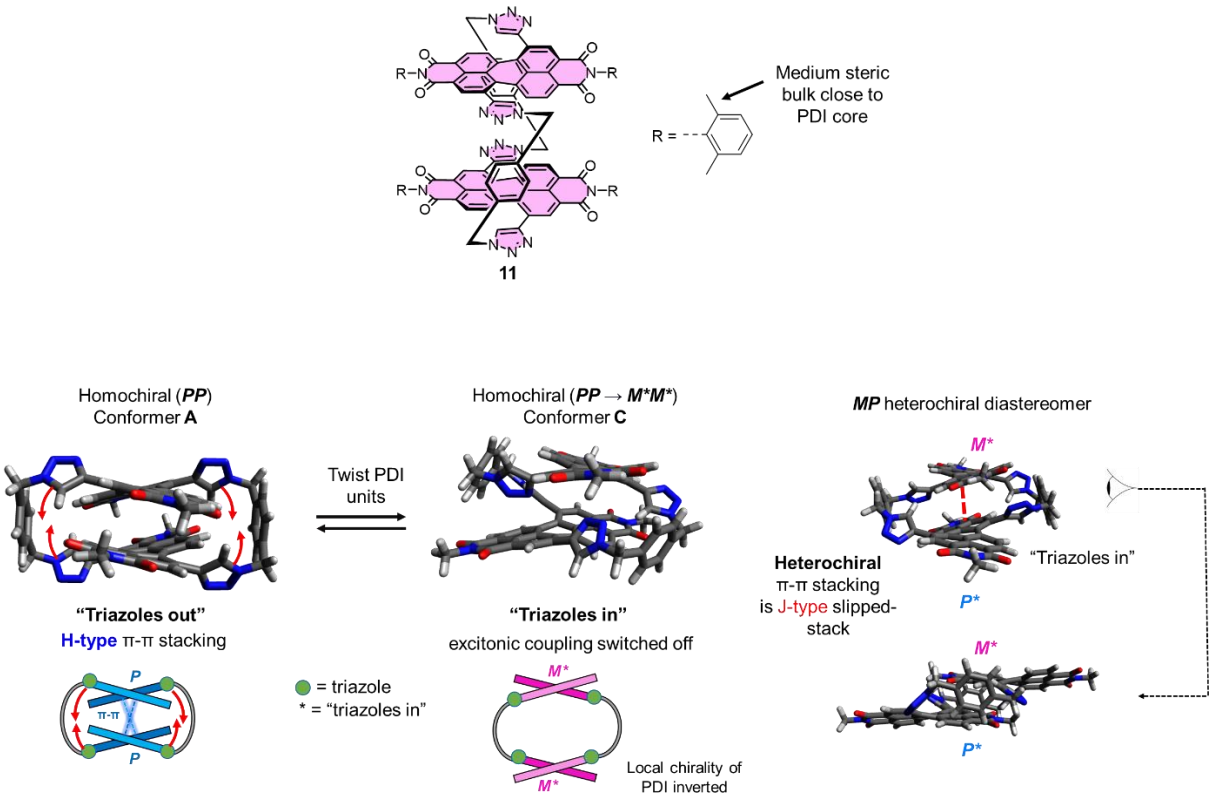

Figure 6.3: Summary of results for Chapter 4.

Finally, Chapter 5 explored the synthesis and characterisation of a series of Pink Box-type macrocycles with alternative linkers, to understand the impact of linker length and rigidity on the interaction between the PDI units in a bis-PDI macrocycle. Macrocycle **19**, which uses a flexible *n*-hexyl linker, has solvent switchable PDI-PDI excitonic coupling. It was found that elongating the rigid aromatic linkers systematically from phenyl (**1a**) to biphenyl (**17**) to terphenyl (**18**) leads to a reduction, and ultimately an absence, of excitonic coupling in toluene (**Figure 6.4**). It was hypothesised that this may be due to a larger macrocyclic cavity that increases the interchromophore separation, prompting supramolecular binding studies using a wide range of polycyclic aromatic hydrocarbon guests. Unfortunately, no binding was observed by UV-vis spectroscopy for any guests tested. This is ascribed to poor complementarity in terms of size and shape, thereby motivating the need for further structural information on the (chiral) conformation of larger Pink Box macrocycles with greater degrees of freedom.

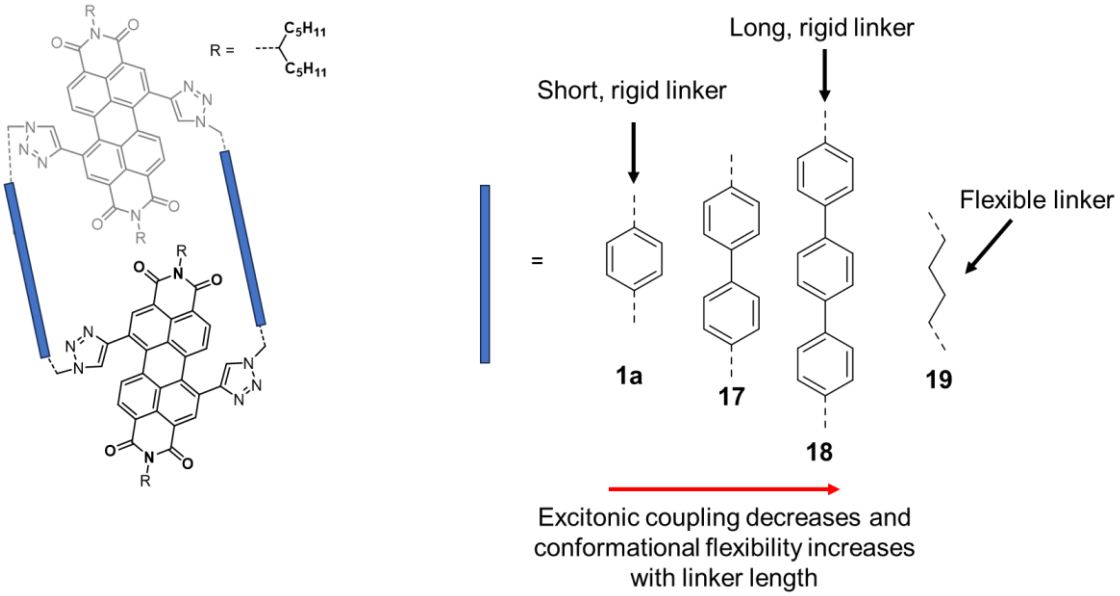

Figure 6.4: Summary of results for Chapter 5.

Overall, the work performed in this thesis makes significant contributions to the fundamental understanding of chiral π-π interactions between an important class of chiral organic dye molecules, PDIs. These interactions can be harnessed to optimise the chiroptical, photophysical and electrochemical properties of PDIs, and to direct their π-π self-assembly into chiral H- and J-type dimers and larger aggregates. Therefore, this body of work paves the way for exploring the electron-transport properties of these macrocyclic materials as the active layers in chiral photodetectors and light-emitting devices,[17-24] and for developing their potential as chiroptical probes or sensors to be used in biology and medicine.[25, 26]

6.2 References

1. F. Würthner, C. R. Saha-Möller, B. Fimmel, S. Ogi, P. Leowanawat and D. Schmidt, *Chemical Reviews*, 2016, **116**, 962-1052.
2. S. E. Penty, M. A. Zwijnenburg, G. R. F. Orton, P. Stachelek, R. Pal, Y. Xie, S. L. Griffin and T. A. Barendt, *Journal of the American Chemical Society*, 2022, **144**, 12290-12298.
3. R. Renner, B. Mahlmeister, O. Anhalt, M. Stolte and F. Würthner, *Chemistry – A European Journal*, 2021, **27**, 11997-12006.
4. M. Hasegawa, Y. Nojima and Y. Mazaki, *ChemPhotoChem*, 2021, **5**, 1042-1058.
5. E. M. Sánchez-Carnerero, A. R. Agarrabeitia, F. Moreno, B. L. Maroto, G. Muller, M. J. Ortiz and S. de la Moya, *Chemistry – A European Journal*, 2015, **21**, 13488-13500.
6. J. Zhao and P. Xing, *ChemPhotoChem*, 2022, **6**, e202100124.
7. J.-L. Ma, Q. Peng and C.-H. Zhao, *Chemistry – A European Journal*, 2019, **25**, 15441-15454.
8. J.-Q. Wang, X.-N. Han, Y. Han and C.-F. Chen, *Chemical Communications*, 2023, DOI: 10.1039/D3CC04187E.
9. G. Bressan, S. E. Penty, D. Green, I. Heisler, G. Jones, T. A. Barendt and S. Meech, *Accepted in ACIE on 3rd July 2024*.
10. S. E. Penty, G. R. F. Orton, D. J. Black, R. Pal, M. A. Zwijnenburg and T. A. Barendt, *Journal of the American Chemical Society*, 2024, **146**, 5470-5479.
11. M. Ball, B. Fowler, P. Li, L. A. Joyce, F. Li, T. Liu, D. Paley, Y. Zhong, H. Li, S. Xiao, F. Ng, M. L. Steigerwald and C. Nuckolls, *Journal of the American Chemical Society*, 2015, **137**, 9982-9987.
12. S. R. LaPlante, P. J. Edwards, L. D. Fader, A. Jakalian and O. Hucke, *ChemMedChem*, 2011, **6**, 505-513.
13. S. R. LaPlante, L. D. Fader, K. R. Fandrick, D. R. Fandrick, O. Hucke, R. Kemper, S. P. F. Miller and P. J. Edwards, *Journal of Medicinal Chemistry*, 2011, **54**, 7005-7022.
14. A. Knebel, A. Bavykina, S. J. Datta, L. Sundermann, L. Garzon-Tovar, Y. Lebedev, S. Durini, R. Ahmad, S. M. Kozlov, G. Shterk, M. Karunakaran, I. D. Carja, D. Simic, I. Weilert, M. Klüppel, U. Giese, L. Cavallo, M. Rueping, M. Eddaoudi, J. Caro and J. Gascon, *Nature Materials*, 2020, **19**, 1346-1353.
15. E. Lee, H. Ju, I.-H. Park, J. H. Jung, M. Ikeda, S. Kuwahara, Y. Habata and S. S. Lee, *Journal of the American Chemical Society*, 2018, **140**, 9669-9677.
16. T. Ogoshi, R. Shiga, T.-a. Yamagishi and Y. Nakamoto, *The Journal of Organic Chemistry*, 2011, **76**, 618-622.
17. J. R. Brandt, F. Salerno and M. J. Fuchter, *Nature Reviews Chemistry*, 2017, **1**, 0045.
18. D.-W. Zhang, M. Li and C.-F. Chen, *Chemical Society Reviews*, 2020, **49**, 1331-1343.
19. K. Baek, D.-M. Lee, Y.-J. Lee, H. Choi, J. Seo, I. Kang, C.-J. Yu and J.-H. Kim, *Light: Science & Applications*, 2019, **8**, 120.
20. Y. Deng, M. Wang, Y. Zhuang, S. Liu, W. Huang and Q. Zhao, *Light: Science & Applications*, 2021, **10**, 76.
21. Y. Yang, R. C. da Costa, M. J. Fuchter and A. J. Campbell, *Nature Photonics*, 2013, **7**, 634-638.
22. D. Zhu, W. Jiang, Z. Ma, J. Feng, X. Zhan, C. Lu, J. Liu, J. Liu, Y. Hu, D. Wang, Y. S. Zhao, J. Wang, Z. Wang and L. Jiang, *Nature Communications*, 2022, **13**, 3454.
23. Z. Ma, T. Winands, N. Liang, D. Meng, W. Jiang, N. L. Doltsinis and Z. Wang, *Science China Chemistry*, 2020, **63**, 208-214.

24. L. Zhang, I. Song, J. Ahn, M. Han, M. Linares, M. Surin, H.-J. Zhang, J. H. Oh and J. Lin, *Nature Communications*, 2021, **12**, 142.
25. P. Stachelek, L. MacKenzie, D. Parker and R. Pal, *Nature Communications*, 2022, **13**, 553.
26. B. Li, J. Zhang, L. Li and G. Chen, *Chemical Science*, 2021, **12**, 2504-2508.

Appendix A: Computational studies

I thank Prof. Martijn Zwijnenburg who carried out all Density Functional Theory (DFT) calculations which are referred to throughout this thesis and detailed in this appendix.

Computational methods

Conformer searches in toluene and dichloromethane for a simplified model of macrocycle **1**, in which the imide-based alkyl chains (R groups) are replaced with methyl groups, were performed using the combination of the CREST code,[1] the GFN2-xTB semiempirical tight-binding method[2] and the analytical linearized Poisson–Boltzmann (ALPB) implicit solvation model.[3] The lowest energy conformers found using CREST were subsequently reoptimized by means of density functional theory using either the B97-3c composite scheme[4] or the combination of the PBE density functional,[5] the D4 dispersion correction method[6] and the def2-TZVP basis-set.[7] Solvation effects in the DFT calculations were described using either the COSMO[8] (toluene, dichloromethane) or COSMO-RS[9] (toluene, dichloromethane) implicit solvation models. All DFT calculations, including the time-dependent DFT and NMR calculations, are performed using Turbomole 7.5.[10, 11] Vertical excitation and circular dichroism spectra of the DFT optimised conformers were calculated by single point calculations on the B97-3c optimised structures using the combination of the ωB97x density functional[12] and the def2-TZVPP basis-set.[7] ^{1}H NMR spectroscopy chemical shifts of DFT optimised conformers were predicted using the Gauge-Including Atomic Orbitals method[7] and PBE-D4/def2-TZVP for structures optimised with the same functional and basis-set combination.

Conformer searches

As discussed in Chapters 2 and 4, "Pink Box" macrocycles have solvent-switchable conformations, which leads to a change in photophysical, electrochemical and chiroptical properties. In order to shed light on these conformations and their structure-property relationships, Density Functional Theory (DFT) calculations were carried out.

Conformer searches were carried out in the gas phase and in toluene and dichloromethane solvents for a simplified model of macrocycle **1**, where the imide-based alkyl chains (R groups) are replaced with methyl groups. The initial conformer search in the gas phase gave the lowest energy conformers **A**-**H** shown below (**Figure A**.1). Conformations related by the simple rotation of the methyl group(s) at the imide position(s) were omitted. These structures can be found as .xyz files in the "DFT structures" folder in the supporting information of ref.[13].

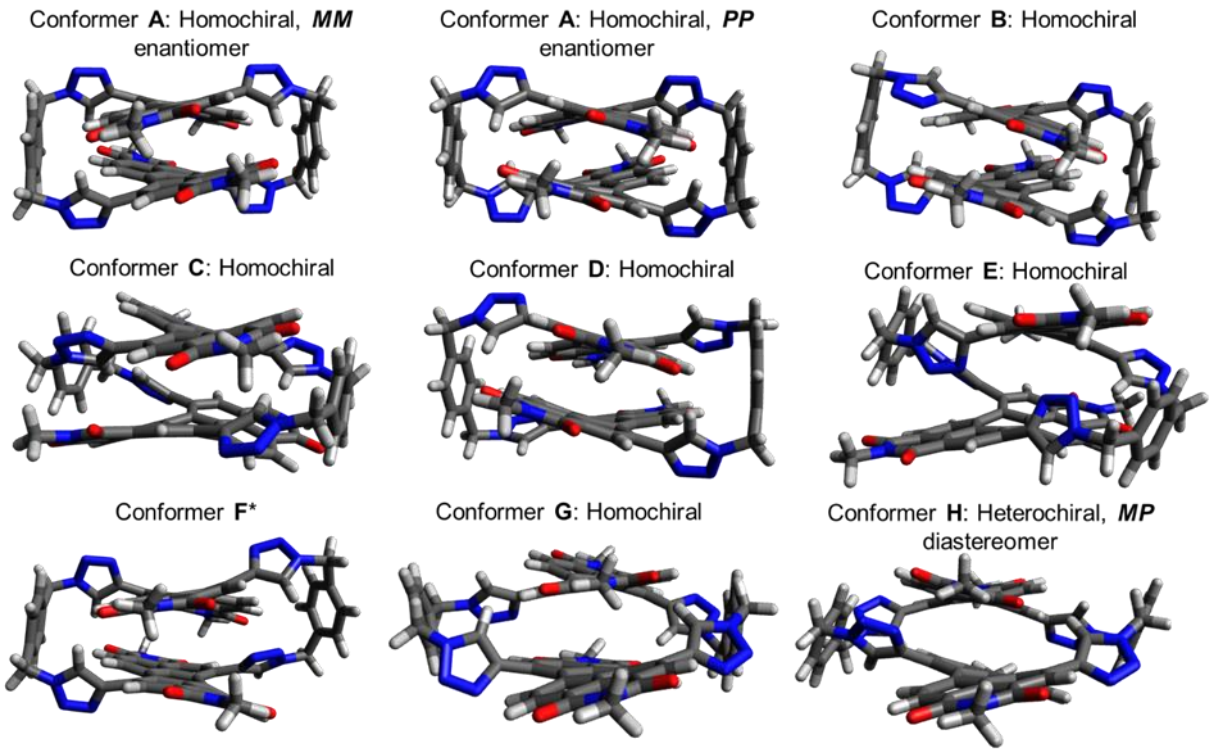

Figure A.1: Lowest energy conformers **A-H** (gas phase). The homochiral/heterochiral labels refer to the relationship between the two axially chiral PDI units. Conformer **F** cannot be labelled in this way since the perylene core of the bottom PDI is pseudo-planar. ***MM*** and ***PP*** assignments are included for conformer **A**, in agreement with the homochiral conformation of the macrocycle observed experimentally in toluene (**1a**) and the X-ray crystal structure (**1b**). The heterochiral ***MP*** assignment is given to the heterochiral conformer **H**.

The relative energies of conformers **A-H** obtained in the gas phase and in toluene and chlorinated solvents are shown below in **Table A2**. The lowest energy conformer, labelled **A** in **Figure A.1**, was found to be a *homo*chiral "triazoles out" structure (***MM***/***PP***) and is virtually identical to the X-ray crystal structure obtained for macrocycle **1b** (see section 1.3.1 below). The second lowest energy conformer (labelled **B**) is a simple variation of conformer **A** but with a rotated triazole. However, the third lowest energy conformation (labelled **C**) is substantially different, being a *homo*chiral "triazoles in" conformation (i.e. ***P*P****/***M*M****, where the asterisk indicates a "triazoles in" conformation in each PDI unit). The lowest energy heterochiral conformation was the eight-lowest energy conformation found (labelled conformer **H**), which is also "triazoles in" (i.e. ***M*P****).

Conformer **A** is predicted to be lowest energy conformer in the gas phase and in both DCM and toluene solvents. As discussed in Section 1.3 below, this agrees with experimental observations

in toluene. However, the energy landscape in chlorinated solvents predicted by density functional theory differs significantly from that observed experimentally, as NMR, UV-vis, fluoresence, CD, electrochemistry, and racemisation kinetics experiments all indicate the population of a different conformer(s) in chlorinated solvents. Indeed, as shown in section 1.4, it is conformer **C** that best explains the experimental results in chlorinated solvents.

Table A2: Relative energies in kJ/mol of conformers **A-H** in the gas phase and in different solvents described using different solvation models as calculated with B97-3c.

	gas phase	DCM	$CHCl_3$	Toluene	Toluene
	--	cosmo	cosmo-rs	cosmo	cosmo-rs
A	0	0	0	0	0
B	30	24	23	26	27
C	51	42	51	47	52
D	60	48	48	54	55
E	88	74	72	81	82
F	93	73	70	85	78
G	101	81	69	90	75
H	107	79	67	90	76

Table A.3: Relative energies in kJ/mol of conformers **A-H** in the gas phase and in different solvents described using different solvation models as calculated with PBE-D4/def2-TZVP.

	gas phase	DCM	$CHCl_3$	Toluene	Toluene
	--	cosmo	cosmo-rs	cosmo	cosmo-rs
A	0	0	0	0	0
B	28	21	21	25	25
C	47	38	47	43	49
D	56	43	44	49	51
E	78	64	63	70	71
F	85	69	66	78	73
G	88	68	55	76	61
H	97	67	56	70	66

Comparison of DFT conformer A to experiment

This section will show that conformer **A** is in excellent agreement with experimental results for macrocycle **1** in toluene and in the solid state.

Comparison to X-ray crystal structure

Conformer **A** is essentially identical to the conformation of macrocycle **1b** observed in the crystal structure (**Figure A.2**).

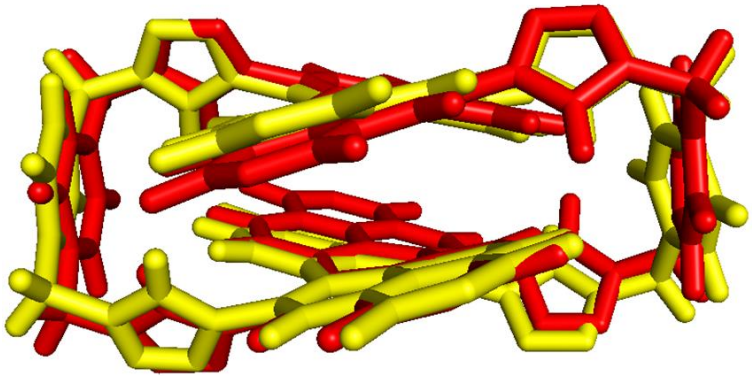

Figure A.2 An overlay of the DFT predicted conformer **A** (red) and the same fragment of the X-ray crystal structure (yellow) of macrocycle **1**. The methyl group (DFT structure) or alkyl chains (crystal structure) have been omitted to aid with comparison.

Predicted ^{1}H NMR spectroscopy chemical shifts

The calculated ^{1}H NMR spectrum of conformer **A** (H-type aggregate) shows a good agreement with the ^{1}H NMR spectrum measured in toluene-d_8 (**Table A.4**), and a poor agreement with the spectrum measured in TCE-d_2 (**Table A.5).** The PDI protons $H_{a\text{-}c}$ were chosen because they are informative of PDI–PDI π–π stacking interactions.

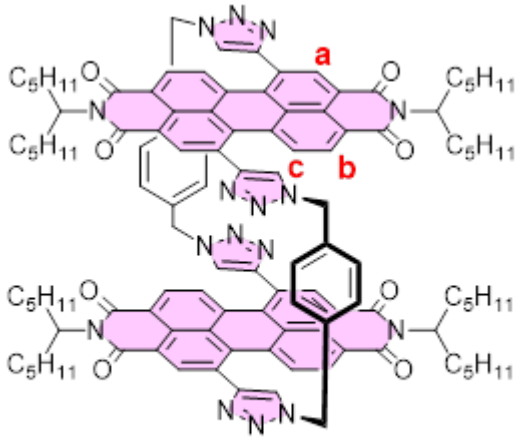

Macrocycle **1a**

Table A.4: Calculated (conformer **A** of macrocycle **1**) and measured (macrocycle **1a**, 373 K) ^{1}H NMR spectroscopy chemical shifts of PDI protons $H_{a\text{-}c}$ in toluene-d_8 (relative to TMS), showing good agreement.

Proton	Calculated δ in toluene (ppm)	Measured δ in toluene-d_8 (ppm)	|Δδ|
a	8.0	8.1	0.1
b	7.7	7.6	0.1
c	5.7	5.7	0

Table A.5: Calculated (conformer **A** of macrocycle **1**) and measured (macrocycle **1a**, 373 K) ^{1}H NMR spectroscopy chemical shifts of PDI protons $H_{a\text{-}c}$ in chlorinated solvent (relative to TMS), showing poor agreement.

Proton	Calculated δ in $CHCl_3$ (ppm)	Measured δ in TCE-d_2 (ppm)	|Δδ|
a	8.0	8.6	0.6
b	7.8	8.2	0.4
c	5.7	7.7	2.0

Predicted UV-vis absorption spectrum

The experimental (macrocycle **1a**, toluene) and calculated UV-vis absorption spectra (conformer A) are shown in **Figure A.3**. Due to excitonic coupling between the PDIs, there are two calculated transitions corresponding to the $S_0 \rightarrow S_1$ band. The lowest energy (most red-shifted) transition has a much lower oscillator strength than the second lowest energy transition, consistent with H-type excitonic coupling. This is consistent with the experimental spectrum of **1a** in toluene, which also displays clear signs of H-type excitonic coupling. However, the calculated transitions are blue-shifted relative to experiment (by ~ 40 nm), which is an artefact of the computational methods used. Overall, the predicted UV-vis spectrum of conformer **A** is consistent with the H-type excitonic coupling seen for macrocycle **1a** in toluene.

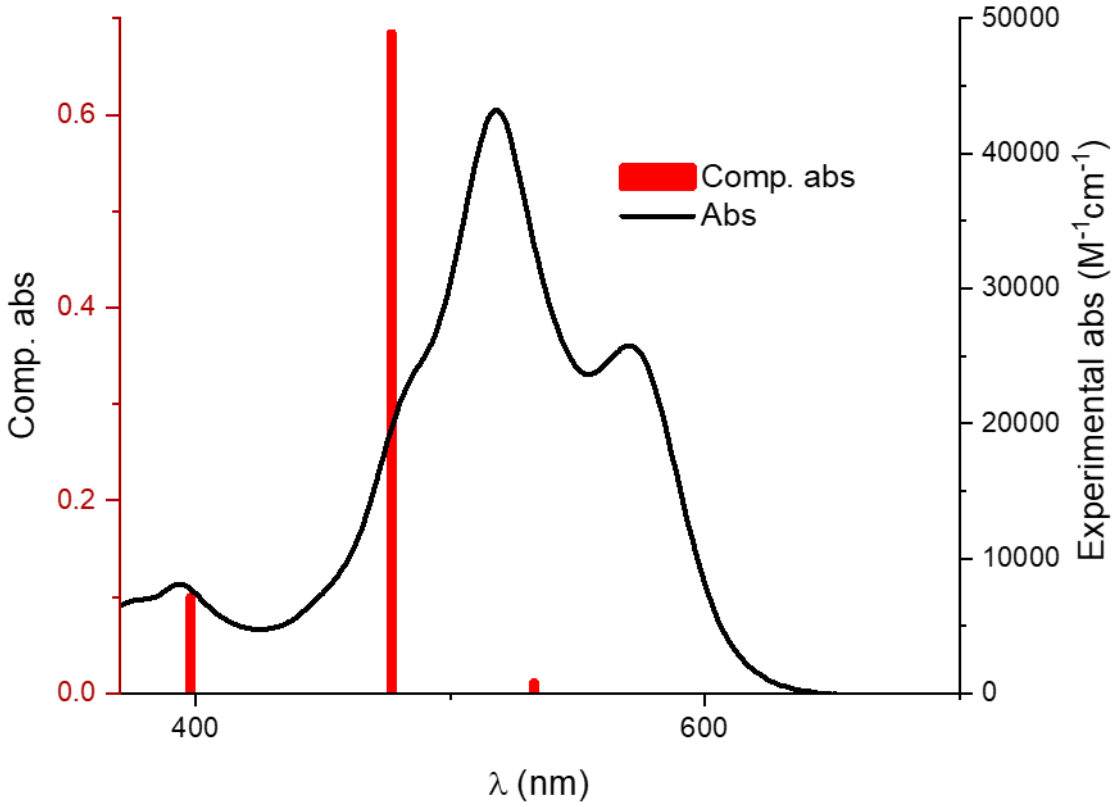

Figure A.3: Comparison of DFT-predicted (conformer A) and experimental UV-vis absorption spectra (macrocycle **1a**, toluene).

Table A.6: TD-ωB97x/def2-TZVPP predicted vertical excitation spectra conformer **A** in toluene (cosmo).

Exc.	excitation energy / eV	wavelength (nm)	oscillator strength
1	2.33	533	0.01202
2	2.60	477	0.68522
3	3.11	398	0.10038
4	3.16	392	0.00000

Predicted CD spectra

The experimental (***MM*** and ***PP*** enantiomers of macrocycle **1a**, toluene) and calculated CD spectra (conformer A, ***PP*** enantiomer) are shown in **Figure A.4** and **Table A**.7. As for the UV-vis spectra, the predicted CD transitions are blue-shifted relative to experiment as an artefact of the computational method used. However, if a 71 nm wavelength correction is applied to the CD spectra to account for this, it is apparent that the agreement between predicted spectra for conformer **A** and experimental spectra in toluene is very good (**Figure A.4**). Comparison of predicted and experimental CD spectra was also used to assign the isolated enantiomers of macrocycle **1**.

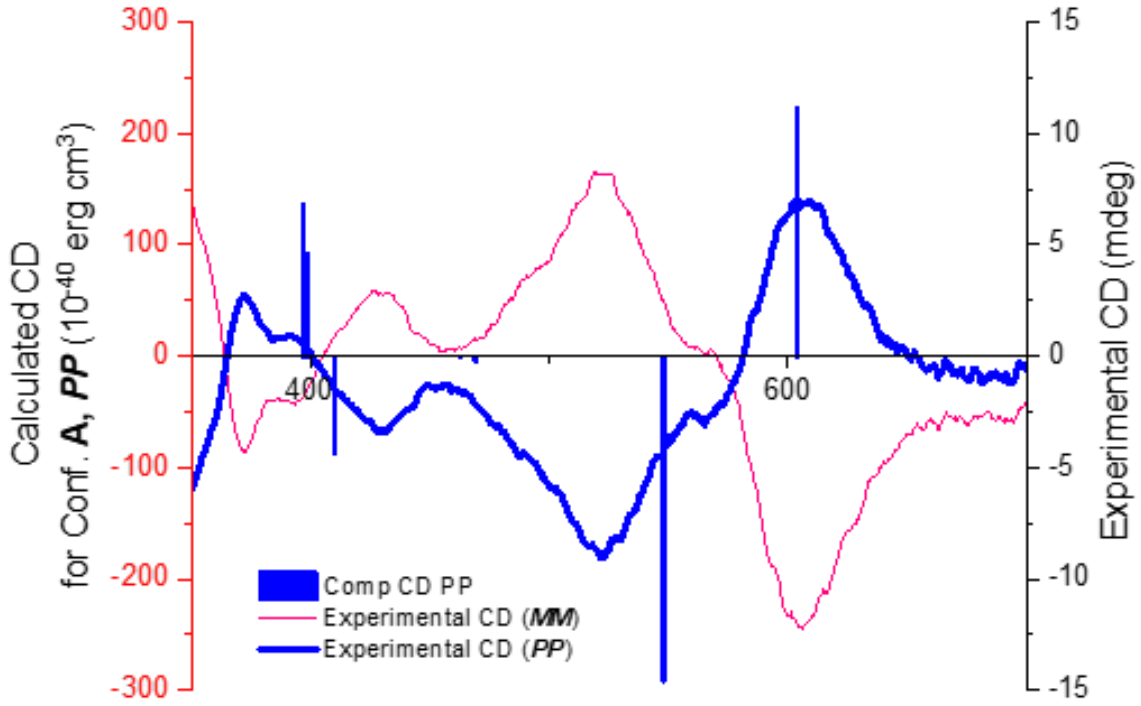

Figure A.4: Comparison of DFT-predicted (conformer **A**, corrected by applying a red-shift of 71 nm) and experimental CD spectra (macrocycle **1a**, toluene).

Table A.7: TD-ωB97x/def2-TZVPP predicted circular dichroism spectra for the ***MM*** and ***PP*** isomers of conformer **A** in toluene (cosmo).

	Excitation energy / eV (wavelength / nm)	Rotary strength / 10^{-40} erg cm^3	
		MM	*PP*
1	2.33 (533)	-223.26	223.35
2	2.60 (477)	292.31	-292.47
3	3.11 (398)	5.17	-5.08
4	3.16 (392)	-0.02	0.03
5	3.62 (342)	0.00	0.00
6	3.66 (339)	87.61	-87.62
7	3.78 (328)	-91.76	91.80
8	3.81 (326)	-136.50	136.45

Comparison of DFT conformer C to experiment

Compared to conformer **A**, in conformer **C** the PDIs are more rotated relative to each other (70° for conformer **C**, as opposed to the 20° rotation seen in conformer **A** and in the X-ray crystal structure, **Figure A.5**). There is no significant change in the PDI-PDI π–π distance in conformers **A** and **C** (3.7 Å), so it was proposed that it is the change in relative rotation between the PDIs that switches off excitonic coupling between the PDIs upon going from conformer **A** to conformer **C**. This section will explore this hypothesis and show that conformer **C** is in good agreement with experimental results for macrocycle **1** in chlorinated solvents.

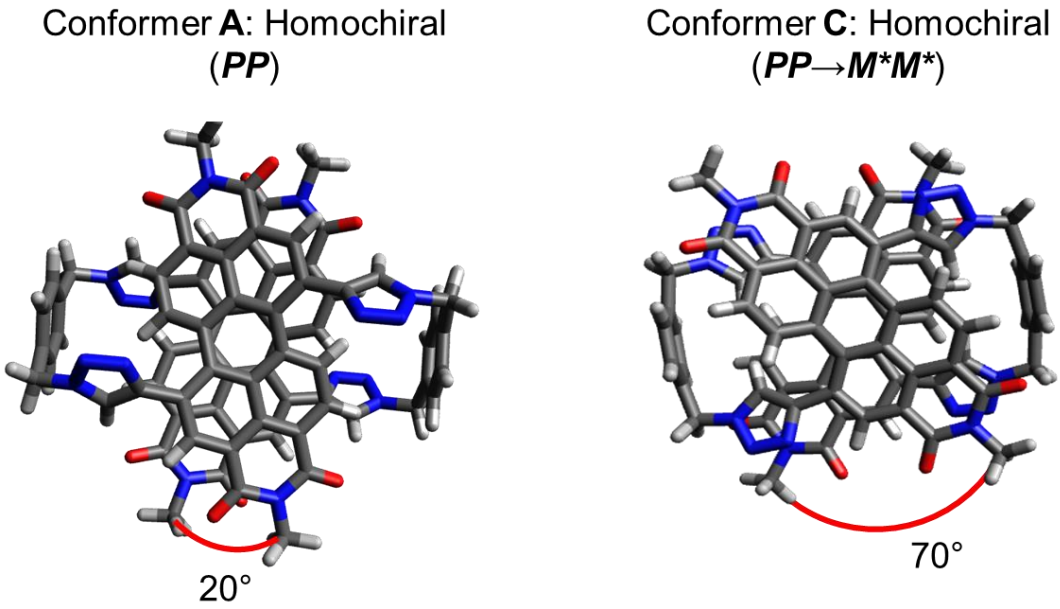

Figure A.5: A top-down view of conformer **C** shows the PDI units are rotated by 70° relative to one another. This contrasts with the 20° rotation in the H-type aggregated conformer **A** (π–π ON).

Predicted ^{1}H NMR spectroscopy chemical shifts

The calculated ^{1}H NMR spectrum of conformer **A** (H-type aggregate) shows a poor agreement with the spectrum measured in TCE-d_2 (**Table A.8**). Instead, the calculated ^{1}H NMR spectrum for conformer **C** shows a good agreement with the spectrum measured in TCE-d_2 (**Table A.9**).

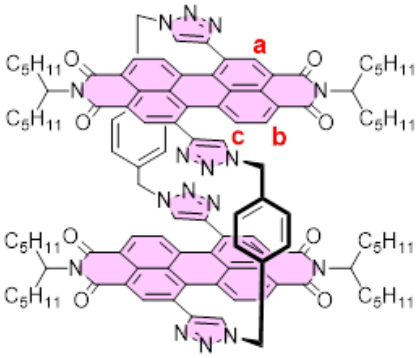

Macrocycle **1a**

Table A.8: Calculated (conformer **A** of macrocycle **1**) and measured (macrocycle **1a**, 373 K) ^{1}H NMR spectroscopy chemical shifts of PDI protons $H_{a\text{-}c}$ in chlorinated solvent (relative to TMS), showing poor agreement.

Proton	Calculated δ in $CHCl_3$ (ppm)	Measured δ in TCE-d_2 (ppm)	|Δδ|
a	8.0	8.6	0.6
b	7.8	8.2	0.4
c	5.7	7.7	2.0

Table A.9: Calculated (conformer **C** of macrocycle **1**) and measured (macrocycle **1a**, 373 K) ^{1}H NMR spectroscopy chemical shifts of PDI protons $H_{a\text{-}c}$ in chlorinated solvent (relative to TMS), showing good agreement.

Proton	Calculated δ in $CHCl_3$ (ppm)	Measured δ in TCE-d_2 (ppm)	|Δδ|
a	8.8	8.6	0.2
b	8.2	8.2	0
c	8.3	7.7	0.6

Predicted UV-vis absorption spectrum

The experimental (macrocycle **1a**, DCM) and calculated UV-vis absorption spectra (conformer **C**) are shown in **Figure A.6** and **Table A.10**. As for conformer **A**, the calculated transitions for conformer **C** are blue-shifted relative to the experimental spectra by ~ 40 nm, an artefact of the computational methods used. The lowest energy transition (excitation 1) in the spectrum of conformer **C** has a greater oscillator strength than the corresponding peak (excitation 1) in conformer **A** (**Figure A.6** and **Table A.10**). Additionally, the two lowest energy transitions are closer together in the predicted UV-vis spectrum of conformer **C** compared to conformer **A** ($\Delta\lambda$ =30 nm for **C** vs 56 nm for **A**), indicating weaker (H-type) excitonic coupling in conformer **C**. Overall, DFT predicts a more red-shifted $S_0 \rightarrow S_1$ band and weaker excitonic coupling for conformer **C** relative to conformer **A**, which is consistent with the macrocycle **1a** experiments on going from toluene to chlorinated solvents. Further support for this finding comes from recent photophysical experimental and theoretical calculations performed in collaboration with Bressan, Meech and co-workers.[14] This work shows that conformer **C** explains the monomer-like absorption spectrum for macrocycle **1** in chlorinated solvents due to a cancelling out of the long- and short-range electronic coupling between the PDI units,[15] otherwise known as a "null aggregate".[16, 17]

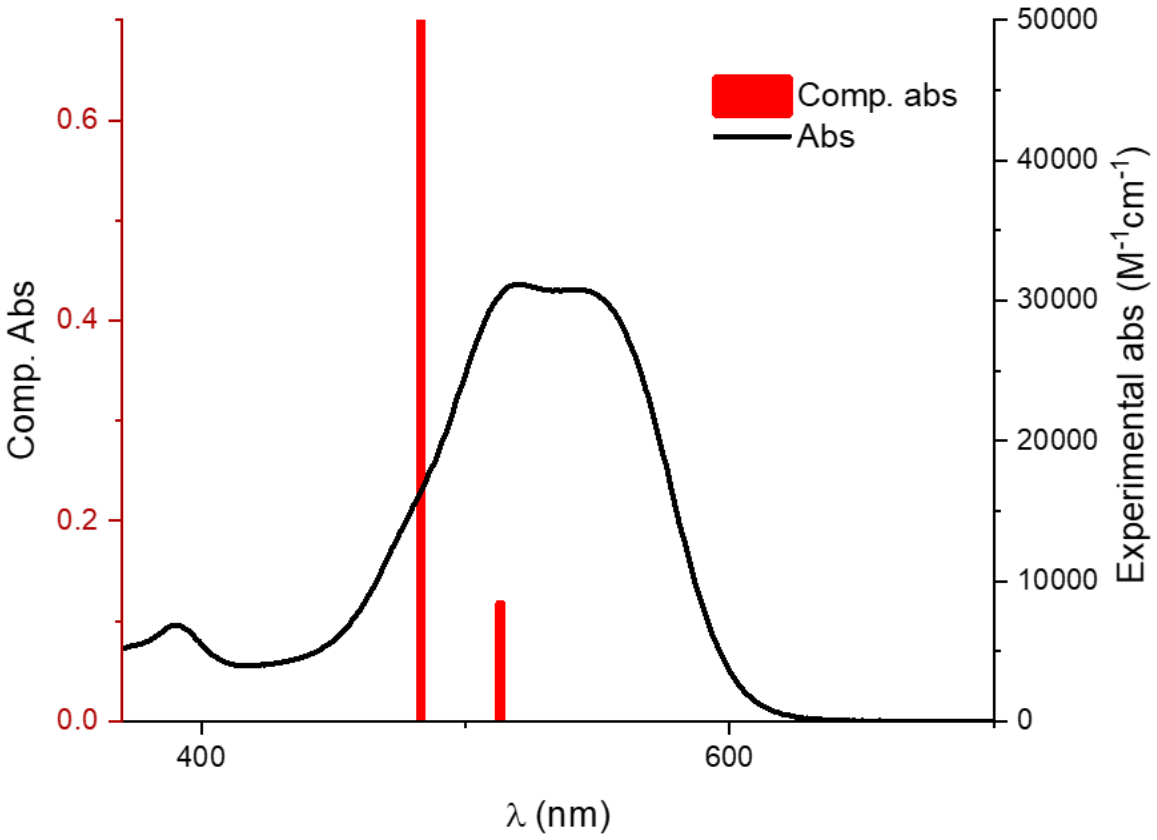

Figure A.6: Comparison of DFT-predicted (conformer C) and experimental UV-vis absorption spectra (macrocycle **1a**, DCM).

Table A.10: TD-ωB97x/def2-TZVPP predicted vertical excitation spectra conformer C (no H-type aggregation) in DCM (cosmo).

Exc.	**Excitation energy / eV**	**Wavelength (nm)**	**Oscillator strength**
1	2.42	513	0.11749
2	2.57	483	0.73674
3	3.37	368	0.02782
4	3.39	366	0.03303

Predicted CD spectra

As discussed in Chapter 2 (for macrocycle **1**) and Chapter 4 (for macrocycle **11-*homo***), the CD spectrum of the *same enantiomer* of the macrocycle (e.g., ***MM***) is solvent-switchable. It was hypothesised that this is due to the macrocycle adopting a different conformation (conformer **C**) in chlorinated solvents where: a) the H-type cofacial π–π stacking seen in toluene and in the crystal structure is disrupted and b) the core-twist of the PDI cores is inverted, such that they adopt the opposite axial chirality, but *homo*chirality is maintained (**Figure A.7**). This section details how the experimental findings that support this theory are underpinned by DFT calculations (using conformer **C**).

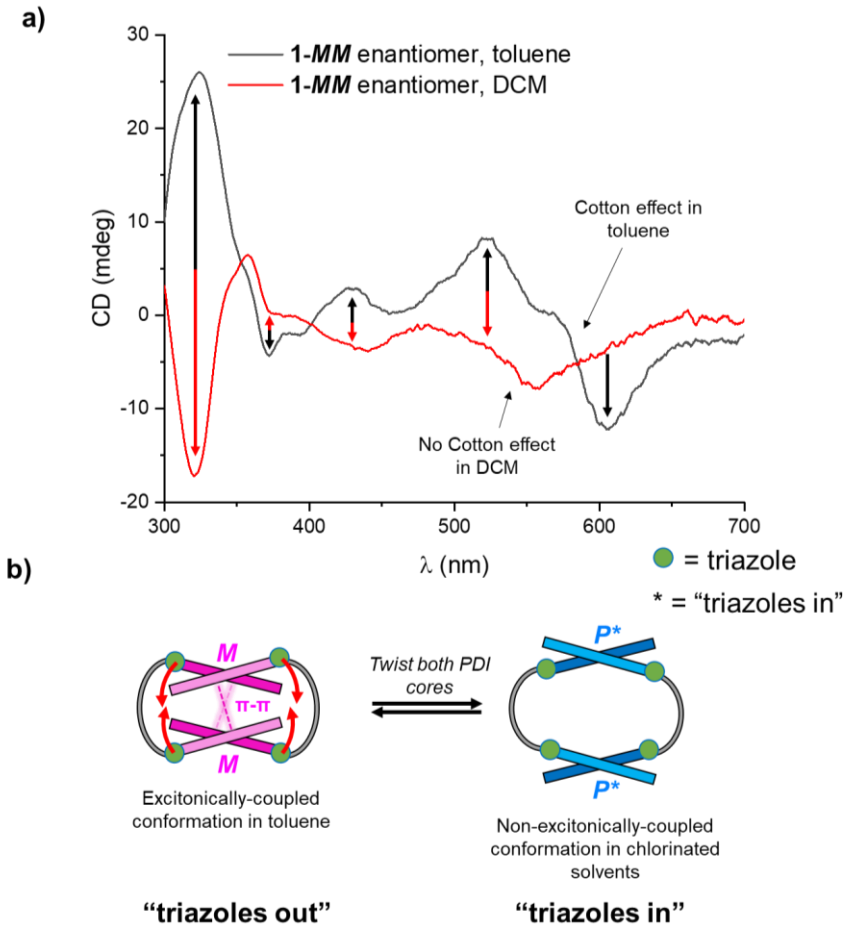

Figure A.7: a) CD spectra of the same enantiomer (assigned as **1-*MM*** in Chapter 2) in toluene (black trace) and DCM (red trace). **b)** Proposed solvent-induced conformational change that may explain the inversion of the CD spectra in **(a)**, where the PDI cores "twist", resulting in an inversion of the local axial chirality of the PDI cores. In the "triazoles in" conformation, excitonic coupling between the two PDIs is proposed to be "switched off", such that no cotton effect is seen in the $S_0 \rightarrow S_1$ transition.

Conformer **A** can convert into conformer **C** most easily by twisting the naphthalene units of the PDIs, such that the triazole groups, which point out of the macrocyclic cavity in conformer **A**, now point in towards the cavity in conformer **C** **(Figure A.8)**. This leads to a change in the axial chirality labels, i.e. the ***PP*** enantiomer of conformer **A** becomes the ***M*M**** enantiomer of conformer **C**, and the ***MM*** enantiomer of conformer **A** becomes the ***P*P**** enantiomer of conformer **C**.

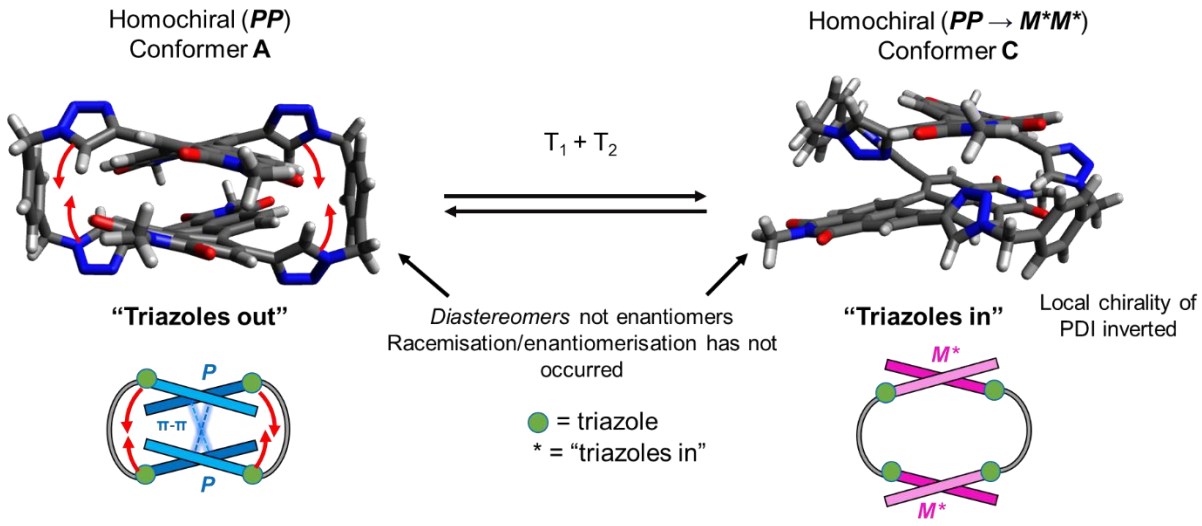

Figure A.8: Interconversion between DFT-predicted conformers **A** and **C** via a "twist" of the PDI cores.

Experimentally, the conformers ***M*M**** and ***P*P**** (DFT conformer **C**) exhibit negligible excitonic coupling and hence PDI monomer-like CD spectra. As such, these experimental CD spectra were compared with the experimental CD spectra of the atropisomers of a related chiral macrocycle prepared by Angus Yeung (**Mono-PDI macro**), that contains only a single twisted bis-triazole PDI chromophore **(Figure A.9)**.[18] There is excellent agreement between the experimental CD spectra of macrocycle **1a** in chlorinated solvents and the experimental spectra of **Mono-PDI macro**. This confirms the monomer-like character of the PDIs in ***M*M**** and ***P*P*** (conformer **C**) and inversion of their local axial chirality in chlorinated solvents relative to MM and PP in toluene (conformer **A**).

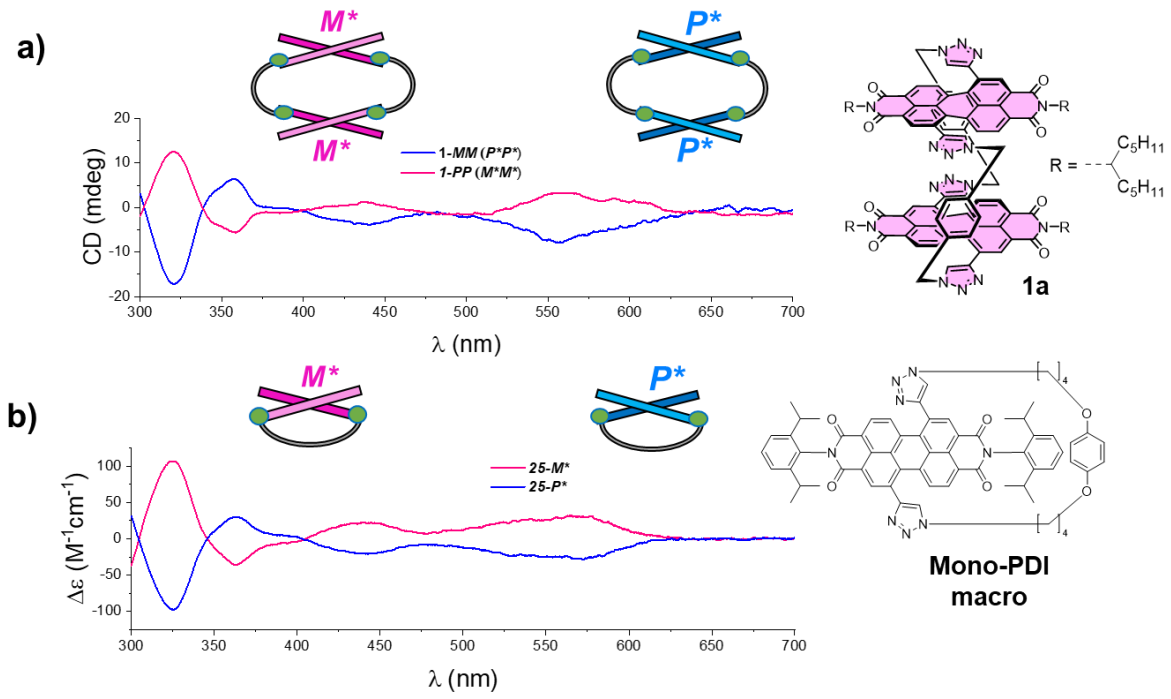

Figure A.9: Comparison of the experimental CD spectra of **a**) bis-PDI macrocycle **1a** (DCM) and **b)** mono-PDI macrocycle **mono-PDI macro** (chloroform). Note that **mono-PDI macro** was found to have a "triazoles in" conformation by single crystal x-ray diffraction,[18] and is thus labelled with chirality asterisks (***M**** and ***P******) for ease of comparison with the CD spectra of macrocycle **1a** (which exists in a "triazoles in conformation in DCM, i.e. conformer C).

References

1. P. Pracht, F. Bohle and S. Grimme, *Physical Chemistry Chemical Physics*, 2020, **22**, 7169-7192.
2. C. Bannwarth, S. Ehlert and S. Grimme, *Journal of Chemical Theory and Computation*, 2019, **15**, 1652-1671.
3. S. Ehlert, M. Stahn, S. Spicher and S. Grimme, *Journal of Chemical Theory and Computation*, 2021, **17**, 4250-4261.
4. J. G. Brandenburg, C. Bannwarth, A. Hansen and S. Grimme, *The Journal of Chemical Physics*, 2018, **148**, 064104.
5. J. P. Perdew, K. Burke and M. Ernzerhof, *Physical Review Letters*, 1996, **77**, 3865-3868.
6. E. Caldeweyher, C. Bannwarth and S. Grimme, *The Journal of Chemical Physics*, 2017, **147**, 034112.
7. F. Weigend and R. Ahlrichs, *Physical Chemistry Chemical Physics*, 2005, **7**, 3297-3305.
8. A. Klamt and G. Schüürmann, *Journal of the Chemical Society, Perkin Transactions 2*, 1993, DOI: 10.1039/P29930000799, 799-805.
9. S. Sinnecker, A. Rajendran, A. Klamt, M. Diedenhofen and F. Neese, *The Journal of Physical Chemistry A*, 2006, **110**, 2235-2245.
10. F. Furche, R. Ahlrichs, C. Hättig, W. Klopper, M. Sierka and F. Weigend, *WIREs Computational Molecular Science*, 2014, **4**, 91-100.
11. S. G. Balasubramani, G. P. Chen, S. Coriani, M. Diedenhofen, M. S. Frank, Y. J. Franzke, F. Furche, R. Grotjahn, M. E. Harding, C. Hättig, A. Hellweg, B. Helmich-Paris, C. Holzer, U. Huniar, M. Kaupp, A. M. Khah, S. K. Khani, T. Müller, F. Mack, B. D. Nguyen, S. M. Parker, E. Perlt, D. Rappoport, K. Reiter, S. Roy, M. Rückert, G. Schmitz, M. Sierka, E. Tapavicza, D. P. Tew, C. v. Wüllen, V. K. Voora, F. Weigend, A. Wodyński and J. M. Yu, *The Journal of Chemical Physics*, 2020, **152**, 184107.
12. J.-D. Chai and M. Head-Gordon, *The Journal of Chemical Physics*, 2008, **128**, 084106.
13. S. E. Penty, M. A. Zwijnenburg, G. R. F. Orton, P. Stachelek, R. Pal, Y. Xie, S. L. Griffin and T. A. Barendt, *Journal of the American Chemical Society*, 2022, **144**, 12290-12298.
14. G. Bressan, S. E. Penty, D. Green, I. Heisler, G. Jones, T. A. Barendt and S. Meech, *Angewandte Chemie International Edition*, **2024**, 63, e202407242.
15. N. J. Hestand and F. C. Spano, *Chemical Reviews*, 2018, **118**, 7069-7163.
16. N. J. Hestand and F. C. Spano, *The Journal of Chemical Physics*, 2015, **143**.
17. E. Sebastian, A. M. Philip, A. Benny and M. Hariharan, *Angewandte Chemie International Edition*, 2018, **57**, 15696-15701.
18. A. Yeung, M. A. Zwijnenburg, G. R. F. Orton, J. H. Robertson and T. A. Barendt, *Chemical Science*, 2024, **15**, 5516-5524.